Analysis of Height Stability of Object Points of Monolithic Construction

Slavomír LABANT[1)], Hana STAŇKOVÁ[2)], Pavel ŠUSTEK[4)], Lubomír LEICHER[5)], Tereza JADVIŠČOKOVÁ[6)], Martina HULANOVÁ[7)], Vladimír BRŮNA[8)], Štefan RÁKAY[3)]*

[1)] Technical University of Košice, Faculty of Mining, Ecology, Process control and Geotechnologies, Institute of Geodesy, Cartography and GIS, Letna 9, 04001, Košice, Slovak Republic; ORCID https://orcid.org/0000-0002-0666-4268
[2)] VŠB - Technical University of Ostrava, Faculty of Mining and Geology, Department of Geodesy and Mine Surveying, 17. listopadu 15, Ostrava - Poruba, 708 00, Czech Republic; ORCID https://orcid.org/0000-0003-0013-3666
[3)] Land and Forestry Department of the Kosice District Office, Hroncova 13, SK 04200 Kosice, Slovak Republic; ORCID https://orcid.org/0000-0002-0583-9783
[4)] VŠB - Technical University of Ostrava, Faculty of Mining and Geology, Department of Geodesy and Mine Surveying, 17. listopadu 15, Ostrava - Poruba, 708 00, Czech Republic; ORCID https://orcid.org/0009-0003-7930-9931
[5)] VŠB - Technical University of Ostrava, Faculty of Mining and Geology, Department of Geodesy and Mine Surveying, 17. listopadu 15, Ostrava - Poruba, 708 00, Czech Republic; ORCID https://orcid.org/0009-0008-7742-1176
[6)] VŠB - Technical University of Ostrava, Faculty of Mining and Geology, Department of Geodesy and Mine Surveying, 17. listopadu 15, Ostrava - Poruba, 708 00, Czech Republic; ORCID https://orcid.org/0009-0002-3739-996X
[7)] VŠB - Technical University of Ostrava, Faculty of Mining and Geology, Department of Geodesy and Mine Surveying, 17. listopadu 15, Ostrava - Poruba, 708 00, Czech Republic; ORCID https://orcid.org/0009-0008-7333-717X
[8)] VŠB - Technical University of Ostrava, Faculty of Mining and Geology, Department of Geodesy and Mine Surveying, 17. listopadu 15, Ostrava - Poruba, 708 00, Czech Republic; ORCID https://orcid.org/0000-0003-2789-860X
* Corresponding author: slavomir.labant@tuke.sk

http://doi.org/10.29227/IM-2024-01-87

Submission date: 10-05-2024 | Review date: 03-06-2024

Abstract

Geodetic measurements aim to monitor the behaviour of objects and prevent various degrees of non-functionality or destruction. By measuring vertical movements, the height stability of the monolithic building is monitored concerning the previous stages of measurement. The measurements were carried out using a digital levelling instrument, the Leica DNA03 and invar code bars GPCL2 with a length of 2 m. The object points were mainly stabilized in the supporting structure of the building, but stabilization in the ceiling was also necessary in problematic areas. Object points in the ceiling were measured using a special metal hanging holder for levelling rods. After the initial verification of the measured elevations, and whether they meet the accuracy criteria, processing followed by the application of the Gauss-Markov model based on the method of least squares corrections. The estimates of the unknown parameters from the stage measurements were used to calculate the height differences of the observed points, which characterize the behaviour of the monolithic object. Significant height changes were detected based on the accuracy of the estimated heights, determining whether they represented significant drops or just an accumulation of measurement errors. The height changes of the object points were graphically visualized in 1D as time series of decline and in 2D as isolines of vertical displacements based on the floor plan of the monolithic building.

Keywords: *monolithic construction, levelling, stability monitoring, height changes, isolines of movements*

1. Introduction

With the civilization's development, more complex constructions began to be built and more interventions by man into nature took place. Everything that is on the earth's surface, but also under it, is in constant motion. This is because different forces act on objects and their structures, which want to achieve mutual balance. Objects change their shape after some time and that negatively affects their functionality, and also their surroundings. Every change in the object's position and geometry (shape and dimensions) is a consequence of the action of various deformation forces. They are created by the action of various physical, chemical, biological, and other processes that affect the object and its surroundings. The effects of these forces cause internal as well as external changes, which geodesy and other measurement technologies can characterize and quantify with their procedures and methods [9]1. New and atypical building structures must be regularly geodetically monitored to prevent deformations in them. Horizontal, vertical, or even spatial changes occur on construction objects. The horizontal movement in the Cartesian system is given by the components ΔX a ΔY. A vertical displacement is either a rise or a fall and is denoted as ΔZ or Δh. When measuring the deformations of engineering structures (bridges, dams, tunnels, etc.), all three components are usually measured ΔX, ΔY, ΔZ and their 3D changes [7]7.

2. Determining movements of construction objects

As a result of the action of deformation forces, various horizontal and vertical displacements of the entire object or only parts of the object or various tilting of the object, shape changes of individual constructions, foundations and

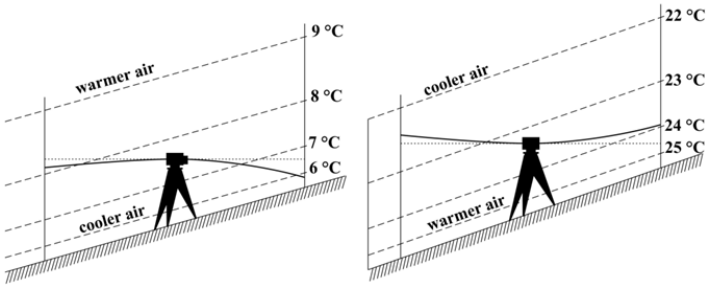

Fig. 1. Levelling refraction depending on the temperature of the air layers [2]
Rys. 1. Załamanie niwelacyjne w zależności od temperatury warstw powietrza [2]

Fig. 2. The building of the University Science Park Technicom
Rys. 2. Budynek Uniwersyteckiego Parku Naukowego Technicom

a) b) c) d) e) f)

Fig. 3. Reference points no. 193, 194, 195, 5001, and object points in the Technicom interior
Rys. 3. Nr punktów referencyjnych 193, 194, 195, 5001 oraz punkty obiektowe we wnętrzu Technicomu

subsoil of the object occur. When the soil is loaded with a construction object, it compresses and settles. For example, gravel and sand settle only a few millimetres, while on other very compressible soils, they may settle up to several decimetres. It is dangerous if the object sits unevenly, resulting in various cracks forming on the construction object that grows larger over time [7]. The purpose of measuring displacements and deformations of construction objects according to is [14]:

- to obtain materials for assessing the effects of construction on the foundation soil,
- to compare actual shift values with expected shift values in projects,
- and to monitor the condition, functionality, reliability, and safety of construction objects.

To monitor the stability of the construction object, a displacement measurement project will be developed. In the measurement project, the following shall be stated in particular [14]: the purpose and meaning of the measurement, data on the properties of the foundation soil, construction data, expected displacement values, required measurement accuracy, measurement methods, location of object and reference points, schedule for staged measurements, method of processing measurement results and their interpretation.

Measurement of vertical displacements and deformations is most often performed by geometric levelling, trigonometric method, photogrammetric methods, or physical methods [7]. Geometric levelling from the centre is the fastest, most used and most accurate method of measuring height differences [1]. High-precision levelling or precision levelling is most often used to measure vertical displacements. For demanding tasks, e.g. movements of the earth's crust, special-precision levelling is used [7]. For such tasks, a point field is also needed, which consists of:

- reference points – their location is chosen in places that are not affected by construction activity and deformation forces [14]. When stabilizing the reference points, the groundwater level and the depth of soil freezing (0.3 to 1.3 m) must also be considered [7]. When creating new reference points, the so-called heavy stabilization is firmly connected to the bedrock (concrete pillars and blocks) [9].
- object (observed) points – their position, density, number, and location of observed points are chosen to determine displacements and deformations of the observed building object. According to the project, they are stabilized on the monitored object with levelling marks, which are firmly inserted into the object in advance before the start of the measurement [14].

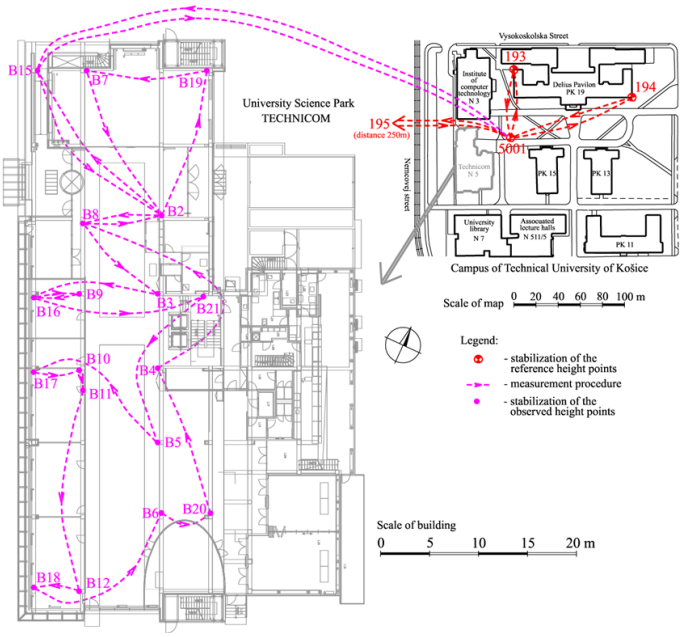

Fig. 4. Location sketch and measurement procedure of reference and observed height points

Rys. 4. Szkic lokalizacji i procedura pomiaru punktów odniesienia i obserwowanych wysokości

In Slovakia, the points of the geodetic foundations are also the points of the state levelling network (SLN). SLN points have determined exact normal heights according to Molodensky in the valid national implementation of the Baltic Vertical Datum – After Adjustment (BVD-AA) (1957) with EPSG code 8357 [15]. Altitudes in SLN refer to the mean level of the Baltic Sea in Kronstadt. Levelling marks are stabilized in permanent objects where it is assumed that the object is height stable (massive walls of public buildings, bridge piers, etc.). To stabilize object points, pin (on the object) or nail (into a solid foundation) marks are used. Pin levelling marks are firmly set into the object at a height of approx. 0.5 m above the ground with free space above the mark for the vertical position of the batten [10]. The problem arises if the pin mark is on a building that has been thermally insulated and left a small "window" around the pin mark.

The air layers above the earth's surface are not equally dense, and when a light beam passes through them, the beam is refracted, and refraction (curvature of the light beam) occurs (Fig. 1). According to [2], the transition of the beam between the layers is smooth and curved. The main source of heat is solar radiation, of which 42% is reflected, 15% is absorbed by the atmosphere and 43% falls on the earth's surface. Light beams pass through clean air and the air is heated from the surface of the soil. Due to the unevenness and roughness of the soil, masses of superheated air are created, which later rise in the form of bubbles in swirling movements. Cool air currents descend between them to warm up. This creates air circulation, where the layers are overheated at the bottom, air currents of different temperatures fall and rise in the middle, and the rising currents rotate at the top.

Only precise digital levelling is used for measurement in the SLN. According to [13] such measurements are subject to accuracy requirements:

a) the deviation ρ in elevation between two levelling points (double-run levelling) must not exceed the value of the extreme deviation which is:

- in 1st-order SLN $\rho \le \rho_{I.max} = 1.50\sqrt{R}$ [mm], (1)
- in 2nd-order SLN $\rho \le \rho_{II.max} = 2.25\sqrt{R}$ [mm], (2)

b) the standard deviation for 1 km double-run levelling:

$$m_0 = \frac{1}{2}\sqrt{\frac{1}{n_R}\cdot\sum_{i=1}^{n}\frac{\rho^2}{R}} \text{ [mm]}, \quad (3)$$

c) extreme deviation of the standard deviation for 1 km double-run levelling :

- for 1st-order SLN $m_0 \le m_{0\_I.max} = 0.40 + \sqrt{\frac{1}{n_R}}$ [mm], (4)
- for 2nd-order SLN $m_0 \le m_{0\_II.max} = 0.45 + \sqrt{\frac{1}{n_R}}$ [mm], (5)

d) the identity of the connection points must be verified according to the topography and by checking the elevation, the deviations between the original and the control elevation must not exceed the extreme deviation:

- for a section of the levelling network of the 1st-order: $2.00 + 1.5\sqrt{R}$ [mm], (6)
- for a section of the levelling network of the 2nd-order: $2.00 + 2.25\sqrt{R}$ [mm], (7)

where n_R is a number of sections, R is a haul length in km and ρ is deviation in elevation.

3. Materials and methods

Stability monitoring was carried out in stages at the building of the University Science Park (USP) Technicom (Fig. 2). This monolithic structure is located on the TUKE campus and has been geodetically monitored since 2016. During construction, the horizontality of individual floors was also determined using trigonometric levelling [8]. The USP Technicom building began to be built in 2013 in cooperation with the Technical University in Košice, the University of Prešov in Prešov and the University of Pavel Jozef Šafárik in Košice. USP Technicom according to [16]:

- creates an ecosystem for the acceleration of technological transfer, innovation, and business support,

a) b) c) d) e)

Fig. 5. Position of the invar bar code rod from the ceiling and on the point
Rys. 5. Położenie inwarowego pręta kodu kreskowego od sufitu i na punkcie

- provides space for the support of applied research and development,
- ensures the transfer of research and development results into economic and social practice and supports the creation and development of businesses,
- provides an incubation environment for the creation and development of innovative startup and spin-off companies.

Before commencing the initial stage of measurement, a reconnaissance of the existing point field surrounding the construction object and a proposal for the location of the observed points according to the designer's specifications was conducted. Within the vicinity of the constructed building, four reference height points were selected: 193, 194, 195, and 5001. Points 193 and 194 are secured by pin levelling marks in the foundations of the Delius Pavilion building (Fig. 3 a, b). A pin levelling mark anchors point 195 within the foundations of the Košice-Okolie District Office building (Fig. 3 c). Additionally, a steel geodetic nail embedded in the concrete block of the old foundations serves as point number 5001 (Fig. 3 d). These four reference points serve to check each other if any of them move and also serve to connect observed points by the levelling loop. The height connection to the Baltic Vertical Datum – After Adjustment was established using point no. 193 (Fig. 3 a) with its altitude denoted as H_{193} = 213.99480 m. The location and distribution of reference height points are illustrated in the situation sketch (Fig. 4 right). The observed points, after consultation with the designer, were secured within the supporting structure of the monolithic building. At the selected locations were anchored observed points B2 to B21 using steel measuring pins (Fig. 3 e, f). The position and distribution of points are outlined in the sketch (Fig. 4 left).

The determination of the heights of reference and observed points was carried out by the conditions established for high-precise levelling. For measurement used: the digital levelling instrument Leica DNA03 (Fig. 5 a), heavy wooden tripod Leica GST20-9 (Fig. 5 a), floor mat for the tripod (Fig. 5 b), two levelling invar bar code rod type GPCL2 (length 2 m) with a precise spirit level (Fig. 5 b), bipods for levelling rods (Fig. 5 b) and levelling pads. The Leica DNA03 is used for very accurate determination of heights and using an invar batten with parameters $\Delta L = \pm 0.02$ mm + $L \cdot 2 \cdot 10^{-5}$, and $\alpha_T <$ 1 ppm/°C achieves a standard deviation for 1 km double-run levelling $\sigma_{km} = \pm 0.3$ mm [12]. The resolution of the height reading on the invar bar code is 0.01 mm. The standard error in automatic measuring in laboratory conditions for the levelling measurement instrument of the Leica DNA03 with a 2-m invar bar code of the levelling rod was determined to be ±1.3 μm [4]. The Leica DNA03 instrument with battery weighs 2.4 kg, the heavy wooden tripod GST20-9 with extendable legs weighs 6.4 kg, and the 2 m long GPCL2 levelling bars weigh 4.2 kg. The levelling instrument needs visibility of at least 38 cm section of the levelling batten for 20 m without disturbing influences (shadow, vegetation). Before the measurement itself, the main axis condition of the levelling instrument was verified by the most accurate Näbauer procedure, which eliminates the effects of refraction and curvature of the Earth [11].

Levelling measurements were conducted in five stages: the 0th stage in March 2016, the 1st stage in June 2016, the 2nd stage in July 2017, the 3rd stage in June 2018, and the 4th stage in May 2019. These stage measurements were then divided into three levelling sections or moves. The first levelling section involved measurements through reference points 193, 194, 195, and 5001 (Fig. 4 right). The second levelling section extended from point 5001 through B15 to point B2, situated on the ground floor inside the building (Fig. 4 left). Within the building, on the ground floor, the third closed levelling loop was measured across 17 points, spanning from point B2 to B21. A digital levelling instrument (Fig. 5 a) was mounted on a tripod and placed on a special pad to prevent damage to the floor (Fig. 5 b). Most points were secured in the pillars of the monolithic structure using steel measuring pins, allowing for the levelling invar bar code rod to be placed without difficulty (Fig. 5 b, c). The rods were aligned vertically using a spirit-level vial and supported by a bipod. For points an-

Tab. 1. Assessment of the accuracy of measurement of levelling sections and loops

Tab. 1. Ocena dokładności pomiarów odcinków i pętli niwelacyjnych

Stage	Year/Month	1st levelling section			2nd levelling section			3rd levelling loop		
		ρ_1 [mm]	$\rho_{I,max}$ [mm]	test OK/NO	ρ_2 [mm]	$\rho_{I,max}$ [mm]	test OK/NO	m_0 [mm]	$m_{0\ I,max}$ [mm]	test OK/NO
0.	2016/03	0.17	1.11	OK	0.13	0.44	OK	0.15	0.64	OK
1.	2016/06	0.19	1.10	OK	0.06	0.43	OK	0.35	0.64	OK
2.	2017/07	-0.15	1.09	OK	-0.10	0.44	OK	0.02	0.64	OK
3.	2018/06	-0.18	1.11	OK	0.06	0.45	OK	0.21	0.64	OK
4.	2019/05	0.25	1.12	OK	0.03	0.44	OK	0.16	0.64	OK

chored in the ceiling, a special magnetic hanger was utilized to suspend the invar bar code rod from above (Fig. 5 a, d, e, point B11). As the network of observed points was planned in consultation with the designer before the construction of internal partitions, certain points in subsequent stages could not be observed due to changes in construction and were consequently omitted entirely.

4. Processing of measured data

Measured values of levelling measurements Δh to determine the heights of the observed points h, were processed using the Gauss-Markov model with the full rank of matrix A. It is about the application of MLS (method of least squares) as a conventional adjustment method. Point no. 193 was used as a reference point for the datum network fixation and its height was not changed by the processing. For the given network to be adjusted and in the result to determine the best possible estimates of the heights of the determined points, the condition of measurement redundancy (overdetermination of the network) must apply in the case of this adjustment: r = n – k.

The most used method for adjusting the height net is the Gauss-Markov model (GMM) with the full rank of the matrix A of the form:

$$\begin{aligned} &\mathbf{v} = \mathbf{A}\mathbf{d}\hat{\mathbf{h}} - \mathbf{d}\Delta\mathbf{h} = \mathbf{A}(\hat{\mathbf{h}} - \mathbf{h}^{\circ}) - (\Delta\mathbf{h} - \Delta\mathbf{h}^{\circ}), && \text{- funkcional part,} \\ &\boldsymbol{\Sigma}_{\Delta h} = s_0^2\mathbf{Q}_{\Delta h}, && \text{- stochastic part,} \end{aligned} \tag{8}$$

where v represents the correction (residuals) vector of the observed quantities Δh, dΔh = Δh – Δh° is the vector of reduced elevations, $\mathbf{d}\hat{\mathbf{h}} = \hat{\mathbf{h}} - \mathbf{h}^{\circ}$ is the vector of the estimates complements of determined heights and A is the configuration matrix (matrix of partial derivatives).

The adjusting procedure of measured levelling elevations between points and determination of estimates of unknown point's height consists of the following steps:

1. Arrangement of input data:

a) vector of measured elevations Δh among all points with a number n,

b) vector of approximate point heights h° with number k was determined using the reference height of point 193 and the measured elevations Δh,

c) cofactor matrix of measured elevations $Q_{\Delta h}$ characterizes the quality of elevation Δh, where used σ^2 is the apriori variance of the measurement method depending on the choice of weights.

2. Creation of model equations:

d) vector of the approximate elevations Δh° is determined from the difference in the approximate heights of the points h°,

e) vector of the reduced elevations dΔh is determined from the relationship Δh – Δh°.

3. Creation of configuration matrix:

f) design matrix A characterizes the tensile structure of the connection of points in the network and there are determined the partial derivatives of the functions of the approximate elevations Δh° according to approximate heights h°.

4. Calculation of estimates:

g) vector of estimates of determined heights $\hat{\mathbf{h}}$ is obtained by the sum of the vector complements of the height estimates $\mathbf{d}\hat{\mathbf{h}}$ and the vector of approximate heights h°.

h) vector of estimates of measured elevations $\Delta\hat{\mathbf{h}}$ is obtained by the sum of the vector of measured elevations Δh and vector of residuals v.

5. Expression of the accuracy of the parameters of the levelling network:

i) unit a posteriori variance s_0^2 is determined based on the minimization condition of MLS,

j) the covariance matrix of height estimates $\boldsymbol{\Sigma}_{\hat{\mathbf{h}}}$ contains the main diagonal empirical variances of the heights of individual points $\sigma_{\hat{h}_j}$,

k) the covariance matrix of elevation estimates $\boldsymbol{\Sigma}_{\Delta\hat{\mathbf{h}}}$ contains on the main diagonal the empirical variances of the elevation $\sigma_{\Delta\hat{h}_{j,j+1}}$ between the measured points.

The processing of the measured values was carried out by software, and after that, it was verified whether the measurements in individual stages were carried out at the same level of accuracy. This was done based on statistical testing with Fisher's test [9], where the test criterion T is determined by the proportion of unit posterior variances $s^2_{0(i)}$ from both stages, which was compared to the critical value F determined at the significance level α and the number of redundant measurements from both stages $f^{(i)}$, $f^{(i+1)}$:

$$T = \frac{s^2_{0^{(i+1)}}}{s^2_{0^{(i)}}} \approx F(\acute{a}, f^{(i)}, f^{(i+1)}) \tag{9}$$

In this case T < F it is possible to determine the significance of the height differences of the observed points between individual stages, which consisted according to [6] of:

1) estimates of determined heights of points obtained in stages $t^{(i)}$and $t^{(i+1)}$ were calculated the height differences of the observed points of the monolithic building $d\hat{h}_j^{(i,i+1)}$ according to the relationship:

$$d\hat{h}_j^{(i,i+1)} = \hat{h}_j^{(i+1)} - \hat{h}_j^{(i)} \tag{10}$$

2) variances of estimates of point heights obtained in stages $t^{(i)}$and $t^{(i+1)}$ were calculated variance values of height differences $\sigma^2_{d\hat{h}_j^{(i,i+1)}}$ according to the relationship:

$$\sigma^2_{d\hat{h}_j^{(i,i+1)}} = \sigma^2_{\hat{h}_j^{(i)}} + \sigma^2_{\hat{h}_j^{(i+1)}} \tag{11}$$

Tab. 2. Estimates of the parameters for all stages of monolithic building stability investigation

Tab. 2. Oszacowania parametrów dla wszystkich etapów badania stateczności budynku monolitycznego

0th measurement stage 2016/03				1st measurement stage 2016/06			2nd measurement stage 2017/07				3rd measurement stage 2018/06				4th measurement stage 2019/05			
Point	$\hat{\mathbf{h}}^{(0)}$	$\boldsymbol{\sigma}_{\hat{\mathbf{h}}}^{(0)}$	** Type	$\hat{\mathbf{h}}^{(1)}$	$\boldsymbol{\sigma}_{\hat{\mathbf{h}}}^{(1)}$	Δh (01)	$\hat{\mathbf{h}}^{(2)}$	$\boldsymbol{\sigma}_{\hat{\mathbf{h}}}^{(2)}$	Δh (12)	Δh (02)	$\hat{\mathbf{h}}^{(3)}$	$\boldsymbol{\sigma}_{\hat{\mathbf{h}}}^{(3)}$	Δh (23)	Δh (03)	$\hat{\mathbf{h}}^{(4)}$	$\boldsymbol{\sigma}_{\hat{\mathbf{h}}}^{(4)}$	Δh (34)	Δh (04)
	[m]	[mm]		[m]	[mm]		[m]	[mm]			[mm]				[m]	[mm]		
Reference points:																		
193	213.99480	0.00	LP	213.99480	0.00	0.00	213.99480	0.00	0.00	0.00	213.99480	0.03	0.00	0.00	213.99480	0.00	0.00	0.00
194	214.06152	0.02	LP	214.06150	0.05	-0.02	214.05872	0.10	-2.78*	-2.80	214.05876	0.08	0.04	-2.76	214.05872	0.09	-0.04	-2.80
195	214.29701	0.03	LP	214.29696	0.04	-0.05	214.29692	0.05	-0.04	-0.09	214.29686	0.06	-0.06	-0.15	214.29682	0.05	-0.04	-0.19
5001	213.28992	0.01	GN	213.28994	0.03	0.02	213.29004	0.06	0.10	0.12	213.29010	0.05	0.06	0.18	213.29012	0.03	0.02	0.20
Observed points:																		
B2	214.03935	0.05	SMP	214.03904	0.05	-0.31	214.03832	0.11	-0.72	-1.03	214.03750	0.08	-0.82	-1.85	214.03686	0.07	-0.64	-2.49
B3	214.02232	0.09	SMP	214.02218	0.13	-0.14	214.02146	0.12	-0.72	-0.86	214.02098	0.09	-0.48	-1.34	214.02022	0.08	-0.76	-2.10
B4	214.06471	0.10	SMP	214.06463	0.13	-0.08	214.06401	0.15	-0.62	-0.70	214.06350	0.12	-0.51	-1.21	214.06279	0.08	-0.71	-1.92
B5	214.06444	0.10	SMP	214.06427	0.18	-0.17	214.06355	0.17	-0.72	-0.89	214.06301	0.14	-0.54	-1.43	214.06240	0.09	-0.61	-2.04
B6	214.07217	0.10	SMP	214.07202	0.15	-0.15	214.07135	0.17	-0.67	-0.82	214.07057	0.14	-0.78	-1.60	214.06997	0.09	-0.60	-2.20
B7	214.13667	0.11	SMP	214.13651	0.11	-0.16	214.13584	0.12	-0.67	-0.83	214.13506	0.09	-0.78	-1.61	point is inaccessible			
B8	214.01755	0.07	SMP	214.01739	0.08	-0.16	214.01685	0.13	-0.54	-0.70	214.01600	0.10	-0.85	-1.55	214.01536	0.07	-0.64	-2.19
B9	214.00232	0.08	SMP	214.00247	0.14	0.15	214.00194	0.15	-0.53	-0.38	214.00115	0.12	-0.79	-1.17	214.00058	0.08	-0.57	-1.74
B10	214.01690	0.09	SMP	214.01636	0.18	-0.54	214.01545	0.17	-0.91	-1.45	214.01444	0.14	-1.01	-2.46	214.01342	0.09	-1.02	-3.48
B11	216.58603	0.10	SMP	216.58584	0.17	-0.39	216.58531	0.19	-0.84	-1.23	216.58446	0.17	-0.85	-2.08	216.58351	0.08	-0.95	-3.03
B12	213.99821	0.10	SMP	213.99814	0.18	-0.07	213.99680	0.19	-1.34	-1.41	213.99485	0.16	-1.95	-3.36	213.99339	0.09	-1.46	-4.82
B15	213.98742	0.05	SMP	213.98720	0.05	-0.22	213.98640	0.12	-0.80	-1.02	213.98578	0.09	-0.62	-1.64	213.98475	0.04	-1.03	-2.67
B16	214.01061	0.08	SMP	214.01067	0.14	0.06	214.00990	0.15	-0.77	-0.71	214.00912	0.12	-0.78	-1.49	214.00856	0.08	-0.56	-2.05
B17	214.05708	0.09	SMP	214.05694	0.18	-0.14	214.05641	0.17	-0.53	-0.67	214.05586	0.14	-0.55	-1.22	214.05553	0.09	-0.33	-1.55
B18	213.99836	0.10	SMP	213.99816	0.17	-0.20	213.99752	0.19	-0.64	-0.84	213.99684	0.16	-0.68	-1.52	213.99613	0.09	-0.71	-2.23
B19	214.03094	0.15	SMP	214.03106	0.11	0.12	214.03038	0.12	-0.68	-0.56	214.02962	0.09	-0.76	-1.32	point is inaccessible			
B20	214.01220	0.10	SMP	214.01205	0.15	-0.15	214.01145	0.15	-0.60	-0.75	214.01046	0.12	-0.99	-1.74	214.00967	0.09	-0.79	-2.53
B21	214.18229	0.10	SMP	214.18241	0.16	0.12	point was destroyed											

**Type: LP - levelling pin on building; GN - geodetic nail; SMP - steel measuring pin; -2.78* - facade repair

3) the critical value $dh_{j_{krit}}^{(i,i+1)}$ for the difference in height estimates $d\hat{h}_j^{(i,i+1)}$ of the observed point was calculated according to the relationship:

$$d\hat{h}_{j_{krit}}^{(i,i+1)} = t \cdot \sigma^2_{d\hat{h}_j^{(i,i+1)}}, \tag{12}$$

where t is confidence coefficient with value t = 2.5 according to the chosen significance level α = 0.01 with probability p = 98,8 %,

4) comparison of the height difference of the relevant observed point $d\hat{h}_j^{(i,i+1)}$ and its relevant critical value $dh_{j_{krit}}^{(i,i+1)}$ it is possible to conclude the significance of the height difference between stages $t^{(i)}$ and $t^{(i+1)}$ if this applies:

$$\left|d\hat{h}_j^{(i,i+1)}\right| < dh_{j_{krit}}^{(i,i+1)}, \tag{13}$$

it is possible to conclude that the point is stable, and the height difference is the effect of the accumulation of measurement errors, but in the case of:

$$\left|d\hat{h}_j^{(i,i+1)}\right| \geq dh_{j_{krit}}^{(i,i+1)}, \tag{14}$$

it is possible to conclude that the point is unstable, and the corresponding height difference is significant.

5. Results

After the completion of the levelling measurements in the individual stages of monitoring the height stability of the monolithic building, the data was pre-processed and verified whether the measurements met the required precision. The deviations and the standard deviation for 1 km double-run levelling of the individual stages (Tab. 1) met the required criteria according to equations 1–7 [13].

Estimation of the heights of the observed points $\hat{\mathbf{h}}$ and their standard deviations was performed using the Gauss-Markov model based on the MLS, where it was necessary to choose the measurement weight. If the weight of the levelling elevation is dependent on:

- the length of the section and the accuracy of the instrument used, then the measurement variance can be σ_{km} = ±0.3 mm for 1 km, and σ_0 is simple average of all σ_i value,
- the number of levelling instrument positions, then σ = ±0.018 mm for one instrument position, considering that with the average sight length approx. 30 m, possibly for one km approx. 1000m/(2·30m) ≈17 instrument positions, so σ_{km} = ±0.3 mm/km is divided by 17 instrument positions/km will be assigned ±0.018 mm on the one instrument positions [3], [5].

The measurement weights were used in the calculation depending on the length of the levelling sections and the accuracy of the instrument. If the weights of the measurements were used as the number of levelling instrument positions, the same measurement weights would be obtained, since in the interior only one instrument position was used between adjacent height points. That is, at the scales p = 1 the same corrections would thus be obtained v and $\sigma_{\Delta\hat{h}_{j,j+1}}$. The numerical values of height estimates and their standard deviations of all observed points, including their height differences $\mathbf{d\hat{h}}^{(i,i+1)} = \hat{\mathbf{h}}^{(i+1)} - \hat{\mathbf{h}}^{(i)}$ between the observed stages i and i+1, are arranged in Tab. 2. Over time, it happened that the points were unavailable or destroyed.

After the processing of the current stage of levelling measurements for tracking height changes, it was verified by the Fisher test from equation (9) whether the compared stages are at the same accuracy level. In the case of a positive result of the

Tab. 3. Verification of the stability of the observed points based on the previous stage

Tab. 3. Weryfikacja stabilności obserwowanych punktów na podstawie poprzedniego etapu

Point	Measur. stages 0-1 2016/03 – 2016/06				Measur. stages 1-2 2016/06 – 2017/07				Measur. stages 2-3 2017/07 – 2018/06				Measur. stages 3-4: 2018/06 – 2019/05			
	$d\hat{h}^{(01)}$	$\sigma^2_{d\hat{h}^{(01)}}$	$dh^{(01)}_{krit}$	sig	$d\hat{h}^{(12)}$	$\sigma^2_{d\hat{h}^{(12)}}$	$dh^{(12)}_{krit}$	sig	$d\hat{h}^{(23)}$	$\sigma^2_{d\hat{h}^{(23)}}$	$dh^{(23)}_{krit}$	sig	$d\hat{h}^{(34)}$	$\sigma^2_{d\hat{h}^{(34)}}$	$dh^{(34)}_{krit}$	sig
	[mm]	[mm]	[mm]		[mm]	[mm]	[mm]		[mm]	[mm]	[mm]		[mm]	[mm]	[mm]	
Reference points:																
194	-0.02	0.05	0.13		-2.78*	0.11	0.28	s	0.04	0.13	0.32		-0.04	0.12	0.30	
195	-0.05	0.05	0.13		-0.04	0.06	0.16		-0.06	0.08	0.20		-0.04	0.08	0.20	
5001	0.02	0.03	0.08		0.10	0.07	0.17		0.06	0.08	0.20		0.02	0.06	0.15	
Observed points:																
B2	-0.31	0.07	0.18	s	-0.72	0.12	0.30	s	-0.82	0.14	0.34	s	-0.64	0.11	0.27	s
B3	-0.14	0.16	0.40		-0.72	0.18	0.44	s	-0.48	0.15	0.38	s	-0.76	0.12	0.29	s
B4	-0.08	0.16	0.41		-0.62	0.20	0.50	s	-0.51	0.19	0.48	s	-0.71	0.15	0.36	s
B5	-0.17	0.21	0.51		-0.72	0.25	0.62	s	-0.54	0.22	0.55		-0.61	0.17	0.42	s
B6	-0.15	0.18	0.45		-0.67	0.23	0.57	s	-0.78	0.22	0.55	s	-0.60	0.16	0.41	s
B7	-0.16	0.16	0.39		-0.67	0.16	0.41	s	-0.78	0.15	0.38	s				
B8	-0.16	0.11	0.27		-0.54	0.15	0.38	s	-0.85	0.16	0.41	s	-0.64	0.12	0.31	s
B9	0.15	0.16	0.40		-0.53	0.21	0.51	s	-0.79	0.19	0.48	s	-0.57	0.14	0.36	s
B10	-0.54	0.20	0.50	s	-0.91	0.25	0.62	s	-1.01	0.22	0.55	s	-1.02	0.17	0.42	s
B11	-0.19	0.20	0.49		-0.53	0.25	0.64		-0.85	0.25	0.64	s	-0.95	0.19	0.47	s
B12	-0.07	0.21	0.51		-1.34	0.26	0.65	s	-1.95	0.25	0.62	s	-1.46	0.18	0.46	s
B15	-0.22	0.07	0.18	s	-0.80	0.13	0.33	s	-0.62	0.15	0.38	s	-1.03	0.10	0.25	s
B16	0.06	0.16	0.40		-0.77	0.21	0.51	s	-0.78	0.19	0.48	s	-0.56	0.14	0.36	s
B17	-0.14	0.20	0.50		-0.53	0.25	0.62		-0.55	0.22	0.55		-0.33	0.17	0.42	
B18	-0.20	0.20	0.49		-0.63	0.25	0.64		-0.68	0.25	0.62	s	-0.71	0.18	0.46	s
B19	0.12	0.19	0.47		-0.68	0.16	0.41	s	-0.76	0.15	0.38	s				
B20	-0.15	0.18	0.45		-0.60	0.21	0.53	s	-0.99	0.19	0.48	s	-0.79	0.15	0.37	s
B21	0.12	0.19	0.47													

Fisher test, differences in the height of the points to the previous and to the zero stage were created according to equation (10). These differences are due to the vertical movement of the observed points located on the construction object between stages $t^{(i)}$ and $t^{(i+1)}$. The results of the stability analysis of the observed points stabilized on the ground floor of the monolithic building according to equations (11–14) are monitored for the previous stage (Tab. 3) and the zero stage (Tab. 4). Statistically significant vertical movements of the observed points according to equation (13) are presented by the symbol in the "sig" column "s".

6. Discussion

Determination of the significance of height changes based on comparison with t times the variance of the height difference was carried out between neighbouring stages (Tab. 3) and to the zero stage (Tab. 4). The significance of the height changes at the observed points is a consequence of the real movement of the point and the symbol "s" has been indicated. But if it is a movement caused only as a result of the accumulation of measurement errors, then no symbol was given. When analysing the height changes of the adjacent stages, it is evident (Tab. 3) that the building usually decreases during the monitored period:

- between stages 0–1 there is a significant height change at 3 observed points (B2, B10 and B15), the average height change is = −0.12 mm, the maximum drop is at the point = −0.54 mm, the minimum drop is a point rise = −0.15 mm, while positive values are at 4 obse points while positive values are at 4 observed points (B9, B16, B19 a B21).
- between stages 1–2 there is no significant height change at 2 observed points (B11 and B17), the average height change is $\overline{\Delta\hat{h}^{(12)}} = -0.71$ mm, the maximum drop is at the point $\Delta\hat{h}^{(12)}_{B12} = -1.34$ mm, the minimum drop is at the point $\Delta\hat{h}^{(12)}_{B17} = -0.53$ mm, while the same decreases were also observed at the other 2 observed points (B9 and B11).
- between stages 2–3 there is no significant height change at 2 observed points (B5 a B17), the average height change is $\overline{\Delta\hat{h}^{(23)}} = -0.81$ mm, the maximum drop is at the point $\Delta\hat{h}^{(23)}_{B12} = -1.95$ mm, and the minimum drop is at the point $\Delta\hat{h}^{(23)}_{B3} = -0.48$ mm.
- between stages 3–4 there is no significant height change at 1 observed point (B17), the average height change is $\overline{\Delta\hat{h}^{(34)}} = -0.76$ mm, the maximum drop is at the point $\Delta\hat{h}^{(34)}_{B12} = -1.46$ mm, and the minimum drop is at the point $\Delta\hat{h}^{(34)}_{B17} = -0.33$ mm.

The single point B17 remained non-significant in all interstage analyses of height changes. When analysing the significance of height changes to the zero stage of the geodetic measurement, the drops between the individual stages were accumulated, so there is much less assumption that any point remained stable, or has significant height changes:

- between stages 0-2 there is no significant height change at 1 observed point (B9), the average height change is $\overline{\Delta\hat{h}^{(02)}} = -0.84$ mm, the maximum drop is at the point $\Delta\hat{h}^{(02)}_{B10} = -1.45$ mm, the minimum drop is at the point $\Delta\hat{h}^{(02)}_{B9} = -0.38$ mm.
- between stages 0-3 there is a significant height change at all observed points, the average height change is $\overline{\Delta\hat{h}^{(03)}} = -1.65$ mm, the maximum drop is at the point $\Delta\hat{h}^{(03)}_{B12} = -3.36$ mm, and the minimum drop is at the point $\Delta\hat{h}^{(03)}_{B9} = -1.17$ mm.
- between stages 0-4 there is also a significant height change at all observed points, the average height change is $\overline{\Delta\hat{h}^{(04)}} = -2.44$ mm, the maximum drop is at the point $\Delta\hat{h}^{(04)}_{B12} = -4.82$ mm, and the minimum drop is at the point $\Delta\hat{h}^{(04)}_{B17} = -1.55$ mm.

Based on the results of observing the significance between the mentioned stages, it was found that the B12 point with

Tab. 4. Verifications of the stability of the observed points based on the 0th stage

Tab. 4. Weryfikacja stabilności obserwowanych punktów na podstawie etapu 0

Point	Measur. stages 0-2 2016/03 – 2017/07				Measur. stages 0-3 2016/03 - 2018/06				Measur. stages 0-4 2016/03 – 2019/05			
	$d\hat{h}^{(02)}$	$\sigma^2_{d\hat{h}^{(02)}}$	$dh^{(02)}_{krit}$	sig	$d\hat{h}^{(03)}$	$\sigma^2_{d\hat{h}^{(03)}}$	$dh^{(03)}_{krit}$	sig	$d\hat{h}^{(04)}$	$\sigma^2_{d\hat{h}^{(04)}}$	$dh^{(04)}_{krit}$	sig
	[mm]	[mm]	[mm]		[mm]	[mm]	[mm]		[mm]	[mm]	[mm]	
Reference points:												
194	-2.80*	0.10	0.25	s	-2.76*	0.08	0.21	s	-2.80*	0.09	0.23	s
195	-0.09	0.06	0.15		-0.15	0.07	0.17		-0.19	0.06	0.15	s
5001	0.12	0.06	0.15		0.18	0.05	0.13	s	0.20	0.03	0.08	s
Observed points:												
B2	-1.03	0.12	0.30	s	-1.85	0.09	0.24	s	-2.49	0.09	0.22	s
B3	-0.86	0.15	0.38	s	-1.34	0.13	0.32	s	-2.10	0.12	0.29	s
B4	-0.70	0.18	0.45	s	-1.21	0.16	0.39	s	-1.92	0.13	0.32	s
B5	-0.89	0.20	0.49	s	-1.43	0.17	0.43	s	-2.04	0.13	0.34	s
B6	-0.82	0.20	0.49	s	-1.60	0.17	0.43	s	-2.20	0.13	0.33	s
B7	-0.83	0.16	0.41	s	-1.61	0.14	0.36	s				
B8	-0.70	0.15	0.37	s	-1.55	0.12	0.31	s	-2.19	0.10	0.25	s
B9	-0.38	0.17	0.43		-1.17	0.14	0.36	s	-1.74	0.11	0.28	s
B10	-1.45	0.19	0.48	s	-2.46	0.17	0.42	s	-3.48	0.13	0.32	s
B11	-0.72	0.21	0.54	s	-1.57	0.20	0.49	s	-2.52	0.13	0.32	s
B12	-1.41	0.21	0.54	s	-3.36	0.19	0.47	s	-4.82	0.14	0.34	s
B15	-1.02	0.13	0.33	s	-1.64	0.10	0.26	s	-2.67	0.06	0.16	s
B16	-0.71	0.17	0.43	s	-1.49	0.14	0.36	s	-2.05	0.11	0.28	s
B17	-0.67	0.19	0.48	s	-1.22	0.17	0.42	s	-1.55	0.13	0.32	s
B18	-0.84	0.21	0.54	s	-1.52	0.19	0.47	s	-2.23	0.14	0.34	s
B19	-0.56	0.19	0.48	s	-1.32	0.17	0.44	s				
B20	-0.75	0.18	0.45	s	-1.74	0.16	0.39	s	-2.53	0.13	0.33	s

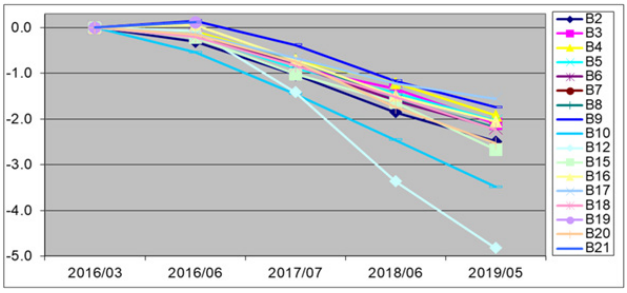

Fig. 6. Graphic presentation of the development of height changes of all observed points

Rys. 6. Graficzna prezentacja rozwoju zmian wysokości wszystkich obserwowanych punktów

the biggest decline was not the "winner" right from the start of the tracking, but only after it overtook the B10 point in the decline. The height changes of the observed points in the form of a decline time series (Fig. 6) of a monolithic building in 1D show that the entire building descends approximately evenly.

It is also clear from the visualization that the observed points have a uniform decrease in the interval of 1 mm, except for two points that have a more pronounced tendency to decrease over the entire observed period than was presented from the numerical values. Height changes were also plotted in the floor plan of the monolithic building in the form of isolines of subsidence, to determine their surface distribution. According to the designer, the network of observed points is not evenly distributed, and the graphic visualization of subsidence in the form of isolines can be significantly distorted. The biggest drops (Fig. 7) are to the right of the central part (around B10) and in the right part in the strip of dense isolines is a decrease from the junction B6-B18 there to the junction B12-B20.

Even the drops to the zero stage (Fig. 8), presented using isolines, are the same, that the biggest drops are to the right of the central part, which has a smaller slope than at the right edge of the monolithic structure.

Based on the above findings, it is necessary to continue monitoring the building with repeated geodetic measurements in the next period to monitor the further development of the vertical movements of the observed points of the monolithic structure, especially in the parts where the most significant decreases occur.

7. Conclusion

The measurement of displacements of building objects is constantly increasing because the available land with suitable foundation soils for construction within urban areas is decreasing and the construction of more complex buildings and architectural structures is progressing. These measurements make it possible to monitor the behaviour of the objects and to prevent various degrees of dysfunctionality or destruction, which can have catastrophic consequences. The aim of this article was to monitor the stability of a monolithic building by measuring its height using a Leica DNA03 digital levelling instrument. The measured elevations met the accuracy criteria imposed on such measurements, and based on them, height estimates of the observed points were determined at different stages with their corresponding accuracy. Subsequently, significant height differences between neighbouring stages and relative to the zero stage of levelling measurements were determined. The height changes of the observed points presented in the overview tables show that the most significant changes in height, compared to the zero stage, were observed at two points: B10 with a value of −3.48 mm and B12 with −4.82 mm., The average height changes from the last three

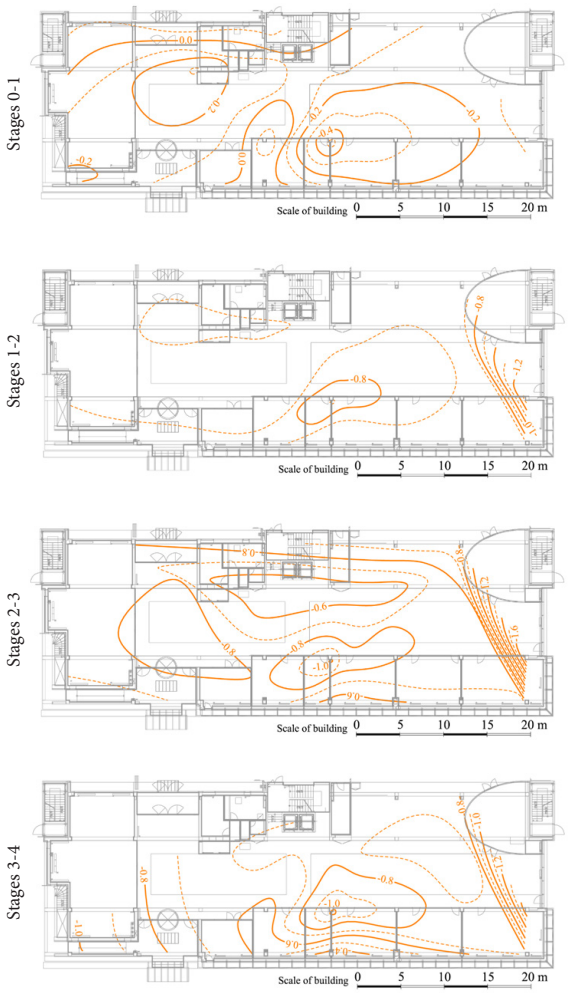

Fig. 7. Graphical visualization of height changes between neighbouring stages of geodetic measurement
Rys. 7. Graficzna wizualizacja zmian wysokości pomiędzy sąsiednimi etapami pomiaru geodezyjnego

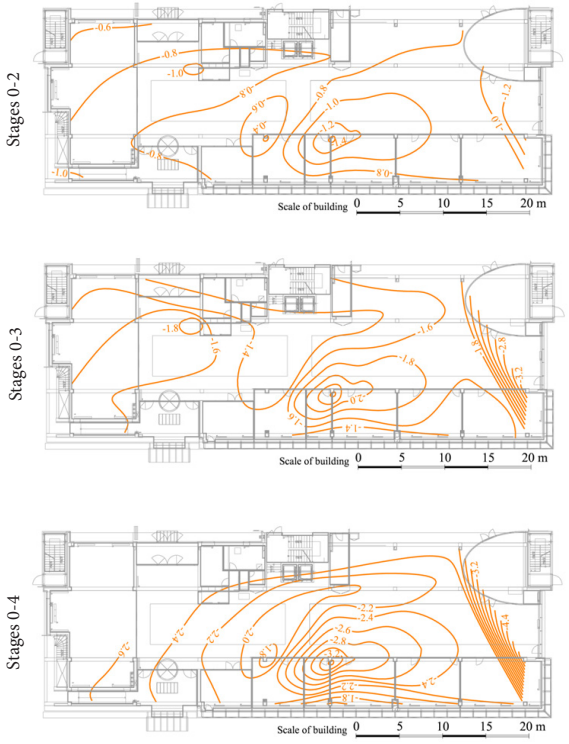

Fig. 8. Graphical visualization of height changes to the zero stage of geodetic measurement
Rys. 8. Graficzna wizualizacja zmian wysokości do zerowego stopnia pomiaru geodezyjnego

stages of monitoring were −0.76 mm. These height changes were plotted as a 1D grouped time series and as 2D isolines on the building floor plan to visualize the magnitude of these changes. However, due to the irregularity of the height point net according to the designer's intentions, and the fact that some observed points disappeared or were destroyed during construction, the graphical visualization may present significant results in a distorted manner.

Literatura – References

1. ABELOVIČ, J., MIČUDA, J., MITÁŠ, J. WEIGEL, J., Measurements in geodetic networks. Alfa, Bratislava, 1990, (in Slovak).
2. BOHM, J., SVOBODA, J. Geometric levelling. State publishing house of technical literature, Praha, 1960, (in Czech).
3. KLOBUŠIAK, M. Optimal software for processing measurements of horizontal and vertical displacements of water structures. Slovak surveyor and cartographer, 19(3), p. 8–14, 2014, ISSN 1335-4019.
4. KUCHMISTER, J., GOLUCH, P., CMIELEWSKI, K., RZEPKA, J., BUDZYN, G. A functional-precision analysis of the vertical comparator for the calibration of geodetic levelling systems. Measurement, 163(1), 107951, 2020, DOI: 10.1016/j.measurement.2020.107951.
5. LABANT, S., RÁKAY, S., GERGEĽOVA, M.B., LEICHER, L., SUSTEK, P. Vertical movements of tripods and their effect on the results of precise levelling measurements. Arabian Journal of Geosciences, 15(10), 980, 2022, DOI: 10.1007/s12517-022-09999-z.
6. MICHALČÁK, O., KOPÁČIK, A., LUKÁČ, Š., PÍŠ, D. Engineering geodesy: Selected engineering-geodetic methods. STU, Bratislava, 1995, (in Slovak).
7. MICHALČÁK, O., VOSIKA, O., VESELÝ, M, NOVÁK, Z. Engineering surveying I. Alfa, Bratislava, 1985, (in Slovak).
8. RÁKAY, Š., LABANT, S., BARTOŠ, K. Verification of floor planarity by trigonometrical measurement of heights on a 5-storey monolithic building. Geodesy and Cartography, 44(1), 14–21, 2018. https://doi.org/10.3846/gac.2018.269.
9. SABOVÁ, J., JAKUB, V. Geodetic deformation survey. Technical University of Košice, Košice, 2007, (in Slovak).
10. ŠUTTI, J. Surveying. Alfa, Bratislava, 1987, (in Slovak).
11. WITTE, B., SPARLA, P. Vermessungskunde und Grundlagen der Statistik für das Bauwesen. Wichmann, H., 2015.
12. Optics and optical instruments. ISO 17123-2:2001. Field procedures for testing geodetic and surveying instruments. Part 2: Levels., 1st ed., Geneva, 2001.
13. Guidelines for managing geodetic foundations. S 74.20.73.11.00. Geodesy, Cartography and Cadastre Authority of the Slovak Republic, Bratislava, 2006.
14. Measurement of deformation of building constructions. Slovak technical standard STS 73 0405. Slovak Office of Standards, Metrology and Testing, Bratislava, 2022, (in Slovak).
15. State levelling network. Geodesy, Cartography and Cadastre Authority of the Slovak Republic. [online]. [access: 2024-01-09]. https://www.geoportal.sk/sk/geodeticke-zaklady/body-gz-a-geodeticke-siete/statna-nivelacna-siet/.
16. University Science Park Technicom. Technical University of Košice. [online]. [access: 2023-12-04]. https://uvptechnicom.sk/uvp-technicom-faza-i/.

Analiza stabilności wysokości punktów obiektu o konstrukcji monolitycznej

Pomiary geodezyjne mają na celu monitorowanie zachowania obiektów i zapobieganie różnym stopniom ich niefunkcjonalności lub zniszczeniu. Mierząc przemieszczenia pionowe, monitoruje się stabilność wysokości budynku monolitycznego w odniesieniu do poprzednich etapów pomiaru. Pomiary przeprowadzono przy użyciu niwelatora cyfrowego Leica DNA03 oraz pasków kodowych invar GPCL2 o długości 2 m. Punkty obiektu stabilizowano głównie w konstrukcji nośnej budynku, lecz w miejscach problematycznych konieczna była także stabilizacja w stropie. Punkty obiektowe w suficie mierzono za pomocą specjalnego metalowego uchwytu do zawieszania łat poziomujących. Po wstępnej weryfikacji zmierzonych wysokości i tego, czy spełniają one kryteria dokładności, następuje obróbka, po której następuje zastosowanie modelu Gaussa-Markowa opartego na metodzie poprawek najmniejszych kwadratów. Oszacowania nieznanych parametrów z pomiarów etapowych posłużyły do obliczenia różnic wysokości obserwowanych punktów, które charakteryzują zachowanie obiektu monolitycznego. Znaczące zmiany wysokości wykryto na podstawie dokładności szacowanych wysokości, określając, czy reprezentują one znaczne spadki, czy po prostu kumulację błędów pomiarowych. Zmiany wysokości punktów obiektu zwizualizowano graficznie w 1D jako szeregi czasowe spadku oraz w 2D jako izolinie przemieszczeń pionowych na podstawie planu piętra monolitycznego budynku.

Słowa kluczowe: *konstrukcja monolityczna, poziomowanie, monitorowanie stateczności, zmiany wysokości, izolinie ruchów*

Mining Activites in the České Středohoří Mountains Protected Landscape Area

Jiří BERÁNEK[1)], Vít SLÁDEK[3)], Roman KAPICA[2)]*, Tereza JADVIŠČOKOVÁ[4)], Stanislav SMELIK[5)], Markéta SMELIKOVÁ[6)], Lukáš KUTIL[7)], Markéta LAŠTŮVKOVÁ[8)], Vladimír BRŮNA[9)]

[1)] VŠB - Technical University of Ostrava, Faculty of Mining and Geology, Institute of Combined Studies in Most, Dělnická 21, Most, Czech Republic; ORCID https://orcid.org/0000-0001-9167-1165
[2)] VŠB - Technical University of Ostrava, Faculty of Mining and Geology, Department of Geodesy and Mine Surveying, 17. listopadu 15, Ostrava - Poruba, 708 00, Czech Republic; ORCID https://orcid.org/0000-0003-1843-9823
[3)] VŠB - Technical University of Ostrava, Faculty of Mining and Geology, Department of of mining engineering and safety, 17. listopadu 15, Ostrava - Poruba, 708 00, Czech Republic; ORCID https://orcid.org/0009-0009-0696-9457
[4)] VŠB - Technical University of Ostrava, Faculty of Mining and Geology, Department of Geodesy and Mine Surveying, 17. listopadu 15, Ostrava - Poruba, 708 00, Czech Republic; ORCID https://orcid.org/0009-0002-3739-996X
[5)] VŠB - Technical University of Ostrava, Faculty of Mining and Geology, Department of Geodesy and Mine Surveying, 17. listopadu 15, Ostrava - Poruba, 708 00, Czech Republic; ORCID https://orcid.org/0000-0002-9731-2638
[6)] VŠB - Technical University of Ostrava, Faculty of Mining and Geology, Department of Geodesy and Mine Surveying, 17. listopadu 15, Ostrava - Poruba, 708 00, Czech Republic; ORCID https://orcid.org/0000-0002-6580-5235
[7)] VŠB - Technical University of Ostrava, Faculty of Mining and Geology, Department of Geodesy and Mine Surveying, 17. listopadu 15, Ostrava - Poruba, 708 00, Czech Republic; ORCID https://orcid.org/0009-0003-5564-5850
[8)] VŠB - Technical University Of Ostrava, Faculty of Mining and Geology, Institute of Combined Studies in Most, Dělnická 21, Most, Czech Republic; ORCID https://orcid.org/0000-0002-9887-7788
[9)] VŠB - Technical University Of Ostrava, Faculty of Mining and Geology, Institute of Combined Studies in Most, Dělnická 21, Most, Czech Republic; ORCID https://orcid.org/0000-0003-2789- 860X
* Corresponding author: roman.kapica@vsb.cz

http://doi.org/10.29227/IM-2024-01-88

Submission date: 21-05-2024 | Review date: 13-06-2024

Abstract

The České Středohoří Mountains Protected Landscape Area (hereinafter the ČSM PLA) is no doubt exclusive because of its volcanic relief, living nature and, of course, human activities – especially quarrying ones. There are two kinds of quarries here, according to their status, i.e. both abandoned (a huge majority) and still active ones, Concerning the brand of stone, we can find three substantial types – volcanic (crystalline) rocks, the Cretaceous sediments and even the Tertiary coal. Most of mining activities, especially related to building medieval towns and villages, were abandoned really long ago but some of modern quarries are still active as the source of superior construction and crushed stone which is utilized for building and maintaining roads and railways. Being in private hands, these quarries considerably harm the countryside and even endanger close environs, damaging buildings and public transportation ways. This situation leads to installing safety barriers, especially over railway lines and roads. On the other hand, the PLA suffer from transportation. Before the D8 highway was finished (and repaired after the 1914 landslide) almost the whole international transit had been concentrated along the river Labe. From the environmental point of view, it had been "in order", but the highway led through the least valuable part of PLA has initiated persisting animosities.

Keywords: *the České středohoří Mountains, Protected Landscape Area, volcanic relief, quarrying, human induced damages, D8 highway*

1. Introduction

The ČSM PLA was proclaimed in 1976, still being our second largest one (1068,9 km²). There are three typical parts which differ in their relief: The Louny Mountains are isolated hills or ridges which rise from their Cretaceous bedrocks, the Milešov Mountains (isolated hills rise from a huge mass of volcanic series) and the Verneřice Mountains in the form of volcanic "traps" (sills) with deep valleys formed by rivers and brooks. The border between the ČSM PLA and the neighboring Lužické Hory Mountains may be considered rather formal. The natural axis of the whole complex is formed by the Labe river flowing northwards to Saxony (Fig. 1).

There are several subjects of protection here: In fact, the PLA landscape is a unique combination of the nature-close and cultural countryside. The relief was formed by volcanic eruptions, later deeply eroded, and uplifted. Among particular hills people have been living and intensively managing all accessible places since medieval times, so forests are preserved in higher positions only. As the result we can say that this PLA is the least woody in the Czech Republic. On the other side, there are many rare plants and animals here, always typical for all three parts of the mountains.

According to Act no. 114/1992 Coll. (as amended) [19], the nature protection within Czech PLAs is very strict, similar to conditions in National Parks. However, these restrictions are still violated in the ČSM PLA (new constructions and communications, sports, intensive farming, active quarrying, etc.). Here we must especially emphasize the crushed stone production – there are several large quarries which have exceptions on the level of the PLA Administration. Following chapters are dedicated to this problem.

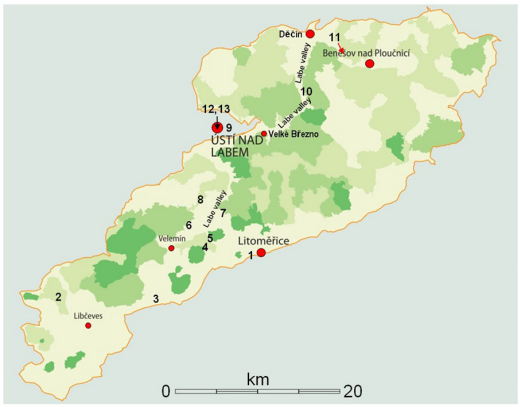

Fig. 1. The České středohoří mountains PLA

Rys. 1. Czeskie góry PLA

Fig. 2. The Písečný vrch near the village of Bečov

Rys 2. 2. Písečný vrch w pobliżu wsi Bečov

2. Geology of the area

This PLA forms a large part of the so-called Eger Graben [2], defined by [11] in 1971 and 1972, respectively. The valley is situated in the easternmost part of the Western European rift system, which may be compared to a huge birdclaw (triad) with the main axis heading from Oslo fiord down to the Rhone valley. Howevewer, in the České Středohoří Mts. the main graben volcanic activity was relatively short (43 to 16 Ma) and some authors deconstruct the rift´s real existence [6], [7]. They have serious reasons – the graben is assymetric, peripheral fault systems are doubtful and volcanic effusions do not follow the graben axis [14]. Moreover, the structure is very short, limited by two transversal fault zones. On the other hand, rocks – more or less – correspond with a typical rift volcanism. We can suppose a very cautious conclusion – this rift may represent a kind of aulacogene [13], i.e. a short living or even inactive lateral part of the triad, mentioned above. The graben itself consists of two main volcanic systems; the České Středohoří Mountains (laid bare volcanic funnels without erstwhile superstructures, but once much larger volcanic province, uplifted during the Late Tertiary and Quarternary) as well as the Doupovské Hory Mountains, a deeply eroded volcano with a mottled history [5]. Both residual provinces are divided by the Most coal Basin (the Sokolov Basin lies southwestwards from the Doupovské Hory Mts). Regarding the České středohoří mountains, conduits and faults pierce the Cretaceous and sometimes the Tertiary basement rocks; other volcanic products form so called multiple sills inside older beds. Because of erosion, many rocks are strongly altered; a very mottled rock composition is often complemented with tuffs and tuffites.

3. The area mining history

Some rocks in the area of question were extracted even in prehistoric times (for example quartzites inside the maar of Písečný Vrch – Sandy Hill – near the Village of Bečov) (Fig. 2). The main phase of utilizing local sources came with the medieval development of residential places. Nevertheless, there was no serious survey; old drawers simply used to set-up quarries and extract sources until they stroke altered rocks, tephra or their hardened forms.

This maar was a rich source of quality quartzite in prehistoric times. The hill is now covered with scrub (here the situation in 2009).

No problem – another quarry could be set up in any adjacent hill. That is why we can cee so many abandoned quarries and minor exposures there. Such a situation used to occur again and again until not a very late time. But modern miners cannot risk additional costs, so they spend money for necessary survey works (probing, boreholes). After 1989, active quarries were privatized and have still been exploited in the most intensive way. The result is pathetic – quarries have even violated the skyline. The end of ectracting basaltic rocks here is unsure. Companies shall try to utilize their property as long as their activities are profitable. They also "abuse" the so-called Mining Law (Act no 44/1988 Coll. (as amended); According to this law, miners are due to utilize deposits in the most complete way. Other sources – sediments, coal – were abandoned long ago for their little importance but they lef their traces in the countryside as well.

4. Volcanic and crystalline rocks

Several quarries – both abandoned and active – are described here. When necessary, photos or maps usefully complement the text.

Radobýl – described in the following chapter (underground limestone mining) it was also affected by a huge, abandoned shelf quarry (Fig. 3).

Fig. 3. The Radobýl is a lonely hill near Litoměřice and was exploited in two ways – in addition to a large wall quarry on the western slope, quality limestone was mined here by a system of underground chambers

Rys. 3. Radobýl to samotne wzgórze w pobliżu Litoměřic, które było eksploatowane na dwa sposoby – oprócz dużego kamieniołomu na zachodnim zboczu, wydobywano tu wysokiej jakości wapień za pomocą systemu podziemnych komór

Fig. 4. The Vršetín u Podsedic was abandoned in 2008. The quarry is situated inside the PLA and is an example of complete destruction of a landscape dominant

Rys. 4. Vršetín u Podsedic został opuszczony w 2008 roku. Kamieniołom położony jest na terenie PLA i jest przykładem całkowitego zniszczenia krajobrazu

Fig. 5. The Kubo quarry near Malé Žernosky is almost perfectly hidden from human eyes. Quarry stone as one of the products; here the filling of gabions

Rys. 5. Kamieniołom Kubo w pobliżu Malé Žernosky jest niemal idealnie ukryty przed ludzkimi oczami. Kamień łupkowy jako jeden z produktów; tutaj wypełnienie gabionów

Fig. 6. Panoramic image reveals a series of smaller wall quarry in the ortorula of the Czech Gate. The dark hill in the background of the picture is the Radobýl [21]

Rys. 6. Zdjęcie panoramiczne ukazuje szereg mniejszych kamieniołomów ściennych w ortoruli Bramy Czeskiej. Ciemne wzgórze w tle zdjęcia to Radobýl [21]

Vršetín – the hill is a typical example of an absolutely devastated landscape dominant. This hill mear the village of Podsedice lost its original profile, being only a torso now (Fig. 4).

Kubo – established in 1842, this open pit quarry is almost perfectly hidden in the terrain above the Labe river (left bank). Lying some 3 km from the City of Lovosice center, it is still the source of superior construction stone (walls, beddings, gabions, decorative elements (the stone is cut or cleaved and polished) and even of various crushed fractions for transportation purposes (Fig. 5). The stone is probably of the Carboniferous age, being a part of the so called Altenberg Caldera. [16]

Quarries in the Bohemian Gate (Porta Bohemica) – between the Villages of Velké Žernoseky and Libochovany, there are huge blocks of crystalline rocks [17] with several smaller quarries close to the railway line from Litoměřice to Ústí nad Labem (the Labe right bank), (Fig. 6). The stone was identified as a kind of red ortogneiss. The same material had to be removed from the left bank in the course of building the railway between Praha and Děčín (before 1850). Blocks were considered a result of vertical uplifts caused by the Tertiary lavas, other authors emphasize fault systems [3], [15]. Both railway lines are protected by safety nets now.

Dobkovičky – this is probably the most problematic active quarry within the PLA. It operates above the left Labe riverside, being a combination of the shelf and open pit quarry. In fact, this defile arose from older individual quarries, now

Fig. 7. The 2013 landslide at its largest extent. The thin silvery line represents the damaged and still non-functional railway line [20]
Rys. 7. Osuwisko w 2013 roku. Cienka srebrzysta linia przedstawia uszkodzoną i wciąż nieczynną linię kolejową [20]

Fig. 8. Deblík, the highest hill slightly to the right, is now only a technological base (left); mining takes place in neighbouring Trabice; Trabice and the broken horizon line (right)
Rys. 8. Dęblík, najwyższe wzniesienie (nieco po prawej stronie), to obecnie jedynie baza technologiczna (po lewej); wydobycie odbywa się w sąsiednich Trabicach; Trabica i przerwana linia horyzontu (po prawej)

Fig. 9. Natrolitic trachyte, mined by the quarry in Mariánská skála; fracturing of the rock as a result of stress relief during the outcrop of the massif (laccolith) during Saxon tectogenesis
Rys. 9. Trachit natrolitowy, wydobywany w kamieniołomie w Mariańskiej Skale; pękanie skały w wyniku odprężenia podczas wychodni masywu (lakkolitu) w okresie tektogenezy saksońskiej

being a very expressive landscape element. The enterprise suffers from very disfavourable geological conditions. There are layers of altered rocks (potential slide surfaces) but their exact extent is not well known. In 2013 (after heavy rains) a devastating landslide occurred below the bottom edge of the quarry. The slide destroyed a part of local railway between the cities of Teplice and Lovosice; it also covered the new D8 highway (Fig. 7).

After difficult sanitation works, the landslide was removed, and the adjacent slope stabilized. The highway contractors (as well as the Czech Ministry of Transport) have accused the quarry (and vice versa) – the plea still continues. According to public sources, contractors have been more successful, but the judgment has not been final yet. In any case, geologists claim the area to be highly unstable and the highway has to be carefully monitored: Now several words about the highway itself. Its construction was planned for more than 80 years with the only aim – to connect Prague and Dresden. Much later, (after 1989) the aim was to decrease the transit traffic load along the river Labe.

Libochovany – the series of basalt quarries is situated opposite to Dobkovičky on the right Labe riverside. The oldest quarry at the railway is full of debris; it was abandoned long ago as well as other minor developments. The first successful quarry was exploited inside the hill called Deblík (Fig. 8); because of altered rocks, working was shifted into the hill known as Trabice. This open pit quarry changes the hill into a torso as well.

Mariánská skála (Marienberg) in Ústí nad Labem – this open pit quarry was established inside a huge massif near the Ústí nad Labem center. In medieval times, the rock was a good source of construction material which enabled to build the whole borough by virtue of smaller quarries Originally the massif extended into the Labe river; rocks had to be partly blasted off because of building the railway line between Prague and Děčín (later Dresden). J. E. Hibsch, a famous Vienna mineralogist, called the stone Marienbergite (he often saw minor differences in mineral composition and called such rocks according to the place of their occurrence). Of course, from the present-day point of view it would be somewhat impractical – the rock is generally called phonolite and more exactly natrolitic trachyte (Fig. 9a) [8]. The quarry itself was opened inside the massif; because of strict spatial limits, it could only proceed downwards to the level of about 90 meters below the rock surface (present day situation). The stone seems crushed (Fig. 9b) but reasons are very different. The massif (called laccolith) was slowly uplifted and after opening the quarry, the internal stress got loose. The future of this quarry is not sure; spatial limits are still very strict.

Těchlovice – this not a very large shelf quarry is situated near the main volcanic center of the České Středohoří Mts. Well visible from the Labe left riverside, it forms another scar in its environs (Fig. 10).

Malá Veleň (Soutěsky) – this is a very obvious example of useless assets. The quarry was opened above the Ploučnice

Fig. 10. The quarry in Těchlovice, known for its position near the volcanic centre of the České Středohoří Mountains PLA and younger vertical intrusions
Rys. 10. Kamieniołom w Těchlovicach, znany ze swojego położenia w pobliżu centrum wulkanicznego PLA České Středohoří Mountains i młodszych pionowych intruzji

Fig. 11. Malá Veleň, Soutěsky: abandoned quarry in very poor condition (rock alteration)
Rys. 11. Malá Veleň, Soutěsky: opuszczony kamieniołom w bardzo złym stanie (przeróbka skały)

Fig. 12. The former coal mine (Kohlbruch) in Ústí nad Labem on a map from 1836 to 1852 [22]; view into part of the residual pit, blocked by a road embankment
Rys. 12 Dawna kopalnia węgla kamiennego (Kohlbruch) w Uściu nad Łabą na mapie z lat 1836–1852 [22]; widok na część pozostałości po wykopie, zablokowaną przez nasyp drogowy

river right bank (near the City of Děčín). Soon after opening, altered rocks occurred and became prevailing. After 1990, private owners tried to utilize one "healthy" basaltic vein in order to make decorative garden items. This activity has already been abandoned. The quarry thus accelerates erosive processes (Fig. 11).

5. Selected sources of sedimentary rocks the cretaceous and tertiary deposits

Along the Labe right riverside, there are minor quarries between the Lake of Píšťany and the Bohemian Gate) near the Village of Velké Žernoseky. These quarries used to extract marles and marlites for local purposes. These relatively soft rocks were apt for building houses, walls, terraces and other constructions. In the Village of Velké Žernoseky, these rocks were massively used within the local cemetery and its chapel in combination with other accessible stones. Sentry houses at famous vineyards (between Žernoseky and the Bohemian Gate) were built of marles as well. All small quarries were abandoned long ago, now being private dwelling and holiday estates. Sandstones were used as decorative components (arches, lintols or caps) because of their easy accessibility Abandoned quarries were also established in uplifted microblocks, for example in Ústí nad Labem and its environs [10]. Due to their unfavorable cementation, these rocks suffer from erosion. The reason is in fact very simple – surface water penetrates into subsurface zones, where cement is dissolved. It then impregnates the surface itself, forming a hard, reinforced crust. After this crust is damaged or eroded, loosened grains screen out and the process can continue deeper and deeper. There are also abandoned limestone deposits – for example Radobýl (Fig. 3 above) hill near the City of Litoměřice. The deposit was accessible via an adit below the volcanic complex. During the WWII, the underground labyrinth was utilized by Germans for producing aerial components, having its own "accessory" concentration camp and even its crematory. Now inaccessible, the mine serves as the deposit of radioactive wastes from hospitals and laboratories.

6. Tertiary coal

The Most coal basin used to be much larger, extending far away to the South-East. During vertical movements of particular crustal microblocks, peripheral basin parts were isolated and eroded into the form of small separate basins [4]. While some of them lie near the main sedimentation area (and not high above it), some others lie in very strange positions. These minor basins were either abandoned for their unfavorable geological conditions or completely exploited. Here are some of them:

Velké Březno – two small separate basins are reported southwards of the commune, particularly Byňov and Horní Zálezly. The booklet [18] informs about mining activities in these basins (beginning in 1765), writing about "black coal" or "anthracite" (allegedly of a pitch glance) which was very demanded especially in Litoměřice. The coal was transported via the Labe waterway, especially in autumn and early winter.

Fig. 13. A weathered coal seam (about 20 cm thick) in the excavation for the foundations of the building. It is clearly part of a separate basin, now almost 100 meters above the main basin. The Kohlbruch connection cannot be proven

Rys. 13. Zwietrzały pokład węgla (o grubości około 20 cm) w wykopie pod fundamenty budynku. Jest to wyraźnie część oddzielnego basenu, obecnie prawie 100 metrów nad głównym basenem. Nie można udowodnić związku Kohlbrucha

For shipmen it was a good opportunity to earn some money out of their main season. Coal seams were later abandoned – they became steep dipping and their quality worsened. Another interesting location is sometimes commemorated in the western part of Příbram village (eastwards from the Buková hora - Beech Mountain - transmitter). It is not sure whether it was a part of a larger separate basin; in any case, there are no visible remnants of mining here.

The question of "black coal" or even "anthracite" in this area is at least disputable. The nearest anthracite occurrence has been documented in Brandov (more than 50 km westwards) – nevertheless, this coal is not of the Tertiary but Carboniferous age. Thus, it is possible to consider some ways of thermal affecting the brown coal in separate basins because some volcanic rocks are younger than seams (for example natural coke in the main basin). Many authors – for example [12] claim that if an off-grade coal is despoiled of humidity (dessicated), the material becomes superior, comparable with hard coal regarding the purity and caloric value. [9]

Ústí nad Labem – the city of Ústí nad Labem forms a "bay" in the PLA boundaries (of course, such an industrial town cannot lie within them). However, there are several obvious records of exploiting the coal here.

The first one was visible in the course of building one of peripheral city parts, called Klíše. No coal can be found there now for intensive seam fires; however, porcelanites give good evidence of an erstwhile seam.

Another well-known place called "Kohlbruch" (coal pit) is well visible even in old maps (Fig 12a). Coal was exploited beyond the town walls from about 1750. Coal was transported by horse carts via reinforced ways. Although abandoned long ago, the pit is still well visible and modern blocks of houses and streets copy original pathways (Fig 12b). The third coal occurrence was incidentally found in the area of regional hospital. A weathered coal seam (about 20 cm thick) was visible and photographed inside the cut for a commercial building (Fig 13). There are more separate basins, but they lie beyond the PLA territory.

7. Bohemian garnets

The least invasive mining within the PLA is connected with tertiary maars, usually represented by small hills with a minimum of vegetation. Three of them – Linhorka, Granátka and Nová trubka (New Pipe) – are sources of pyropes which were transported from a deep subsurface during the Neogene volcanic activity. Pyropes are concentrated in quarternary deluvia (by the way, two Czech diamonds were found here as well). The mining area is relatively small, hidden in fields near the Village of Dlažkovice. This area is guarded, and it is not recommended to try to enter it. Even though the deposit is almost worked-out, subtle pieces of pyropes can be found in surrounding fields, especially after the rain.

8. Conclusion

The České středohoří mountains PLA represents an instance of a very disturbed landscape, historically inhabited, and utilized in a maximum possible way. The volcanic relief was affected by quarrying activities which moved from one hill to another because of a various quality of stone. Before the PLA was proclaimed, quarrying had not respected any rules of protecting the nature – some abandoned quarries evolved into debris and block fields which endanger near buildings and communications. Because of heavy traffic, rocks still loose and it is often necessary to protect railways and roads with catch nets and anchors. Moreover, several large quarries continue working and their activities affects the landscape (the D8 motorway landslide can be a very obvious example). In the past, quarrying and mining here was almost unlimited – while basaltic rocks found their use in medieval walls, sediments – especially sandstones – served as arches, lintels or caps. Brown coal was worked in the so-called separate basins and utilized for local purposes.

And what to say about the future of this beautiful but disturbed landscape? Before D8 was finished, the main traffic load had been concentrated along the river Labe. From this fact it implies that building the highway was a good (i.e. nature and people friendly) solution. Long time ago, the Labe represented an important waterway.

Literatura – References

1. BERÁNEK, J. KORANDOVÁ, B., ŽIŽKA, L., MUDRUŇKA, J. Zapomenuté pískovcové lokality v Ústí nad Labem a okolí. Most: Výzkumný ústav pro hnědé uhlí, Zpravodaj hnědé uhlí, 4, 2018. ISSN: 1213-1660
2. CAJZ, V. Současný stav poznatků o oherském riftu. Essentia, 33, 2003, 2004.
3. CAJZ, V. Nové vulkanologické poznatky z Litoměřicka. Praha: Zprávy o geologických výzkumech 37, 2004 (ZGV v roce 2003), pp. 16–19
4. CAJZ, V., ADAMOVIČ, J., MRLINA, J., Mach, K. Vulkanické centrum Českého středohoří, strukturní aspekty vývoje. Praha: Zprávy o geologických výzkumech 38, 2005 (ZGV v roce 2004), pp. 26–30
5. CAJZ, V., RAPPRICH, V., RADOŇ, M. Vulkanismus v okraji Doupovských hor – vulkanologická studie paleontologické lokality Dětaň. Praha: Zprávy o geologických výzkumech 39, 2006 (ZGV v roce 2005), pp. 13–16
6. CAJZ, V., VALEČKA, J. Tectonic settings of the Ohře/Eger Graben between the central part of the České Středohoří Mts. and the Most Basin, a regional study. Journal of Geosciences, 55, 2010. DOI: 10.3190/jgeosci.075
7. ELZNIC, A., PEŠEK, J., SKOPEC, J. Oherský rift v severozápadních Čechách – argumenty pro a proti. Uhlí – rudy – geologický průzkum, roč. 14, č. 10, 2007. ISSN: 1210-7697
8. HEJTMAN, Bohuslav. Petrografie. 3., oprav. vyd. Bratislava: ALFA, 1981.
9. HURNÍK, S., HAVLENA, V. Krušné hory Mts. and the piedmont brown coal basins as a part of a neotectonic megafold structure. Praha: Čas. Mineral. Geol., 29 (1), 1984.
10. JINDRICH, V. New Views in Tectonic Significance of Platform Sediments in the Bohemian Massif, Czechoslovakia. GSA Bulletin 82 (3), 1971.
11. KOPECKÝ, A. Zpráva o výzkumu neotektoniky Českého masivu v letech 1971 - 1981. Praha: Výzk. Práce Ústř. Úst. Geol., 20, 1982
12. MALKOVSKÝ, M. The Mesozoic and Tertiary basins of the Bohemian Massif and their evolution. Volume 137, Issues 1–4, 1 June 1987, Pages 31-42. Tectonophysics. DOI: 10.1016/0040-1951(87)90311-8
13. MILANOVSKY, E. E. Aulacogens and aulacogeosynclines: Regularities in setting and evolution. Volume 215, Issues 1–2, 10 December 1992, Pages 55-68. Tectonophysics. DOI: 10.1016/0040-1951(92)90074-G
14. MLČOCH, B. Character of the Contact between the Saxothuringian and Teplá-Barrandian Unit. Praha: Geolines 16, 2003.
15. MLČOCH, B. Problematika regionální příslušnosti krystalinika České brány k saxothuringiku. Praha: Zprávy o geologických výzkumech 36, 2003 (ZGV v roce 2002), pp. 31–32
16. MLČOCH, B., SKÁCELOVÁ, Z. Geometry of the Altenberg-Teplice Caldera revealed by the borehole and seismic data in its Czech part. Journal of Geosciences, 55, 2010, pp. 217-229, DOI: 10.3190/jgeosci.071
17. POUBOVÁ, M. Krystalinikum Opárenského údolí a České brány. Praha: Sbor. Geol. Věd, Geol., 2, pp. 79-99, 1963, Praha
18. ŠIDÁK, M. Březina 1167, Velké Březno 2017, 850 let od první písemné zmínky o obci. Velké Březno, 2017.
19. Úplné znění č. 460/2004 Sb. Úplné znění zákona č. 114/1992 Sb., o ochraně přírody a krajiny, jak vyplývá z pozdějších změn. [online]. [access: 2023-04-04]. https://www.psp.cz/sqw/sbirka.sqw?cz=460&r=2004
20. Hospodářské noviny. [online]. [access: 2023-04-04]. https://domaci.hn.cz/c1-65927400-soud-ani-napodruhe-nezacal-projednavat-sesuv-d8-setri-se-jestli-stat-nepodal-zalobu-na-kamenolom-pozde
21. Seznam.cz. Mapy.cz. [online]. [access: 2023-04-04]. https://mapy.cz/zakladni?source=base&id=1833555&gallery=1&x=15.6252330&y=49.8022514&z=8
22. oldmaps.geolab.cz. [online]. [access: 2023-04-04]. http://oldmaps.geolab.cz/map_viewer.pl?lang=cs&map_root=2vm&map_region=ce&map_list=W_4_I (access: 2023-04-04)

Działalność górnicza w Obszarze Chronionego Krajobrazu Gór České Středohoří

Obszar Chronionego Krajobrazu Gór České Středohoří (zwany dalej ČSM PLA) jest bez wątpienia wyjątkowy ze względu na rzeźbę wulkaniczną, przyrodę ożywioną i działalność człowieka – szczególnie górniczą. Istnieją tu dwa rodzaje kamieniołomów, ze względu na ich status, tj. opuszczone (w zdecydowanej większości), jak i czynne.

Jeśli chodzi o rodzaj kamienia, możemy wyróżnić trzy zasadnicze typy – skały wulkaniczne (krystaliczne), osady kredowe, a nawet trzeciorzędowy węgiel. Większość działalności górniczej, szczególnie związanej z budową średniowiecznych miast i wsi, została porzucona już dawno temu, lecz niektóre nowoczesne kamieniołomy nadal działają jako źródło najwyższej jakości materiałów budowlanych i kruszonego kamienia, który jest wykorzystywany do budowy i utrzymania dróg i linii kolejowych.

Będąc w rękach prywatnych, kamieniołomy te w znacznym stopniu szkodzą krajobrazowi, a nawet zagrażają bliskiemu otoczeniu, odziaływując niszcząco na budynki i środki transportu publicznego.

Sytuacja ta prowadzi do instalowania barier ochronnych, szczególnie nad liniami kolejowymi i drogami. Z drugiej strony, PLA odczuwa wpływ transportu. Przed ukończeniem autostrady D8 (i naprawą po osuwisku w 1914 r.) prawie cały tranzyt międzynarodowy koncentrował się wzdłuż rzeki Łaby. Z ekologicznego punktu widzenia było „w porządku", ale autostrada poprowadzona przez najmniej wartościową część PLA wywołała utrzymujące się animozje.

Słowa kluczowe: *Czeskie Góry, Obszar Chronionego Krajobrazu, rzeźba wulkaniczna, wydobywanie, szkody spowodowane działalnością człowieka, autostrada D8*

The Importance of Relative Slope Length Data in Flood Hazard Zoning: A Case Study of the Ngan Sau, Ngan Pho River Basin, Vietnam

Tuyet Minh DANG[1], Duyen Quang LE[2], Ba Dung NGUYEN[3]*

[1] Thuyloi University, 175 Tay Son street, Ha Noi, Vietnam; ORCID: https://orcid.org/0000-0001-8379-1087
[2] Hanoi University of Mining and Geology, Hanoi, Vietnam; ORCID: https://orcid.org/0000-0001-6953-4762
[3] Hanoi University of Natural Resources and Environment, Hanoi, Vietnam; ORCID: https://orcid.org/0000-0001-5378-0926
* Corresponding author: Duyen Quang LE, email: lequangduyen@humg.edu.vn

http://doi.org/10.29227/IM-2024-01-89

Submission date: 22-05-2024 | Review date: 01-06-2024

Abstract

Flood modeling provides useful information to assist manage flood hazards and lessen the effects of floods in locations that are vulnerable to flooding. The present research established flood hazard maps for the Ngan Sau, Ngan Pho river basin using GIS technology and the Analytical Hierarchy Process (AHP) method. The precision of flood simulation results is dependent on criteria that cause flooding. The goal of this study was to evaluate the role of relative slope length in flood hazard identification and delineation. The AHP method was used to determine the respective weights of six physical geography and meteorology factors including rainfall, slope, soil, land use, drainage density, and relative slope length. In the process of computing the model, these factors are classified into two groups: group 1 includes five criteria excluding the relative slope length criterion and group 2 has all six parameters. Based on flood warning levels at hydrological stations in the research area during past floods, the results of flood hazard zoning were verified. The obtained findings indicated that map developed from the group of criteria including the relative slope length are more accurate than those generated based on the remaining five factors. The results of the paper can be used as a reference when choosing criteria for creating flood hazard zoning models utilizing a combination the AHP and GIS technology.

Keywords: *Analytical Hierarchy Process, AHP, flood hazard, relative slope length, Ngan Sau, Ngan Pho river basin*

1. Introduction

The flood is one of the most devastating disasters affecting human's lives and the ecosystem, causing both life and material damage. The determination of the flood hazard is a necessary pre-requisite for flood risk evaluation [1]. Moreover, flood hazard map play an important role in assessing susceptibility of flood prone area, estimating the spatial extent of flood and flood depths [2]. To detect the flood potential areas, a variety of techniques, approaches, and models have recently been developed and implemented. With the development of satellite technology, geographic information system (GIS) and remote sensing images have gradually taken precedence to delineate flood potential regions [3]. In addition, flood hazard map can be generated by using various machine learning models, namely, random forest, support vector machine, gradient boosting model, decision tree, classification regression tree, and naïve Bayes [4]. Recently, several research have utilized Multi-Criteria Decision Analysis (MCDA) like the Analytical Hierarchy Process (AHP) to evaluate the possibility for flood hazard [5, 6]. The AHP algorithms can integrate with Delphi methods to assess the impact level of criteria on flood hazard [7]. In addition, this approach used in various fields such as groundwater [8], agriculture [9, 10], land slide [11], drought [12], etc. Their findings showed that AHP is the most widely used and effective method for creating accurate flood hazard maps in the GIS environment, and it is also appropriate for other hazard studies. Many scientists described AHP as an easy-to-use, affordable, and convenient approach for flood risk assessment. In particular, this approach can be applied for a large and complex river basin with data sparsity [13].

According to Dung et al. (2022), floods occur due to several reasons such as hydrological, orographic, geomorphologic, meteorological, cover, soil, infrastructure and socio-economic factors [14]. The relationships between flood hazard and these conditioning parameters have been studied by researchers. Many publications indicated the factors that have significant influence on flood potential including rainfall, slope, drainage density, soil, land cover, land use, etc. Although the slope length factor contributes significantly to flood formation, it has not been mentioned much. There were many research used this factor and most of them assessed that slope length plays an important role in sediment yield by rainfall impact of various land use types [15], soil loss for steep slopes [16], the size distributions of loess slides [17], runoff and erosion conversion [18], soil erosion [19], sediment concentrations [20], flood hazard [8, 21]. In most erosion studies, this factor is used in conjunction with the slope angle or slope gradient and is referred to as LS-factor. However, for flood hazard studies, slope length is used independently with other factors contributing to flood generation to develop the flood hazard model, such as rainfall, slope, drainage density, land use, soil, etc. Literatures found that slope length was strongly correlated with runoff [22]. According to Verrina et al. (2013), runoff is part of the precipitation that falls over the surface of land to bodies of water like lakes, rivers, ocean, etc. An increase in runoff volume is the cause of flooding problems in the downstream watershed [23]. Therefore, it is undeniable that, slope length has a significant contribution to flood hazard.

In this study, the slope length factor was applied to simulate the flood hazard index using AHP method in Ngan Sau,

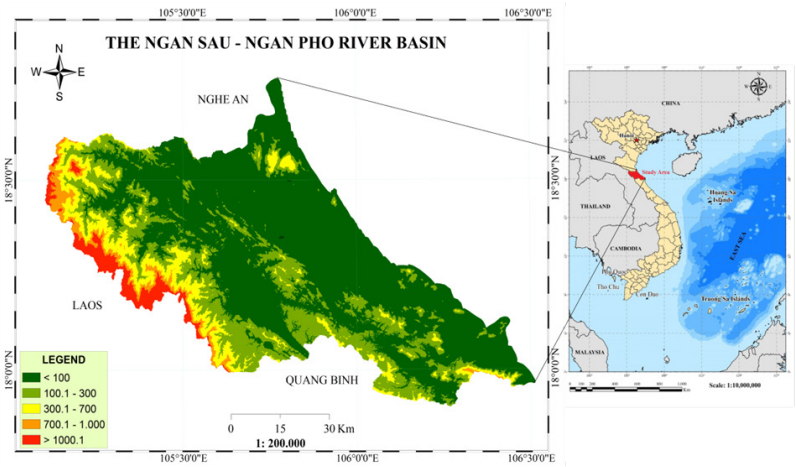

Fig. 1. The Ngan Sau – Ngan Pho river basin, Vietnam

Rys. 1. Dorzecze rzek Ngan Sau – Ngan Pho, Wietnam

Ngan Pho river basin. Flood hazard map generated from slope length and others was verified by the historical flood events. Accordingly, the important role of the slope length factor will be confirmed when establishing flood risk zoning maps using the AHP approach for the study area as well as other geographical regions.

2. Study area

The study area is in the North Central of Vietnam. It is located at longitudes of 105°07′00”E to 106°56′00”E and latitudes of 17°50′00”N to 18°37′58”N. The Ngan Sau, Ngan Pho river basin has an area of approximately 2061 km² and 1065 km² respectively consisting of Huong Son, Huong Khe, Vu Quang, Duc Tho districts [24, 25], as shown in Figure 1. The Ngan Pho River is the largest tributary of the La River, originating from the eastern slopes of the Truong Son Range, while the Ngan Sau river system is the second largest tributary of Ca river. The main stream of the Ngan Sau river is 100km, the river is narrow and steep with an average width of 30–50m. The river flows through the area with high annual rainfall reaching 2,200–2,400mm [6, 26].

The Ngan Pho River is 70 km long with the average river width of 30–35m, and the river bed is steep and short. The study area is located in the tropical monsoon area, which is hot and humid, with a lot of rain. The soil is mainly suitable for growing food crops and short-term industrial crops. Forests in the river basin are concentrated in two districts of Huong Son and Huong Khe, Ha Tinh province [6]. Ha Tinh province in north central Vietnam is frequently the hardest damaged by floods, in particular in the Ngan Sau, Ngan Pho river basin [24].

3. Data and Research methodology

3.1 Impact of slope length on flood hazard

Slope length is significant topographic criterion influencing flood occurrence. Slope length is the distance between the site of origin of overland flow and the point at which either the slope gradient reduces sufficiently for deposition to start or the runoff water enters a well-defined channel, which may be a drainage network or a manmade channel [27]. Thus, it can be understood as the slope length is equivalent to the measurement between the valley line and the watershed line. This parameter can control the variations along the slope water flow energy by altering the area that receives rain, which in turn, influences how water moves. Slope length is key influence on both the volume and velocity of surface runoff. Longer slopes deliver more runoff to the base of slopes [28]. According to He et al. (2022), slope length was significantly positive correlation with flow velocity and runoff [22]. This can be inferred as the further the slope length, the greater the volume of water, flow speed, and inertia force. This result is in accordance with the study of Begarello and Ferro (2010), Yongmei et al. (2011), and Liu & Singh (2004). Their findings have indicated that the volume of the flow rises with an increasing slope length. A flood occur when large runoff volumes flow rapidly into streams and rivers [29]. Therefore, the closer the distance to the watershed line, the less the flow kinetic energy, the smaller the flow velocity, leading to a reduction in flood hazard [21]. In addition, Kittipongvises et al. (2020) revealed that the higher the runoff, the greater the hazard of flooding [30]. Thus, there will exist a proportional relationship between slope length with runoff and flood hazard.

In addition to affecting the runoff, the slope length also impacts the flow accumulation. Theoretically, the longer the slope, the more runoff will accumulate, gathering speed and gaining its energy [31]. This judgment is the agreement with Balasubramanian's assessments, the slope length increase leads to a greater accumulation of runoff [32]. That means, if slopes are long, when rainfall reaches the soil, the speed and extent to which the flow accumulates on the soil surface strengthen. Furthermore, the proportional relationship between slope length and flow accumulation is also shown in the following formula [33]:

$$LS = \left(\frac{Flow\ Accumulation * Cell\ size}{22.12}\right)^{0.4} * \left(\frac{sin\theta}{0.0896}\right)^{1.3} \quad (1)$$

where LS is slope length and slope steepness factor, cell size is the pixel size of the DEM, θ is slope steepness in degree.

As such, on a slope, the quantity of water, runoff speed, and the capacity to accumulate water will all gradually rise when water moves from the ridge line to the water concentration areas. Additionally, the time of water concentration affects the water accumulation amount on the same slope.

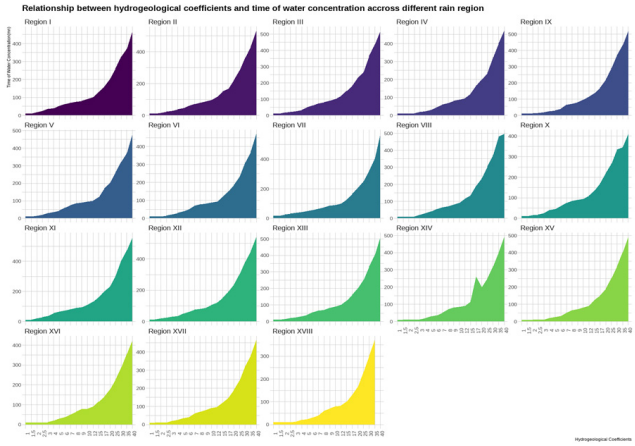

Fig 2. Relationship between hydrogeological coefficients and time of water concentration in the different rain regions of Vietnam [34]
Rys. 2. Zależność współczynników hydrogeologicznych od czasu koncentracji wody w różnych regionach deszczowych Wietnamu [34]

According to Directorate for Roads of Vietnam (2013), the water concentration time on a slope relies on the hydrogeological coefficient of the slope and the rain zone. The larger the geomorphology and hydrological coefficient of the slope, the longer the time of water concentration on the slope. This coefficient is proportional to the slope length and is calculated by the following equation [34]:

$$\Phi_{sd} = \frac{L_{sd}^{0.6}}{m_{sd} J_{sd}^{0.3} (\varphi H_P)^{0.4}} \quad (2)$$

where: Φ_{sd} is the geomorphology and hydrological coefficient of the slope; L is the average slope length of the watershed; J is the slope in percentage; φ is the flood flow coefficient depending the soil type, design daily rainfall and basin area; H_P is the design daily rainfall; msd is parameter of roughness characteristics on the slope relying on the surface condition of the basin slope.

Equation 2 indicates that, the longer the slope length increases, the greater the hydrogeological coefficient of the slope. In addition, the proportional relationship between this coefficient and the time of water concentration in different rain regions is shown on the chart (Figure 2) [34]. Where, the horizontal axis represents Φ_{sd} and the vetical axis shows the water concentration time. The above evidences show that there is a positive correlation between hydrogeological coefficient, time of water concentration and slope length. This demonstrates that the flood hazard increases with the increase of water concentration time and slope length. Therefore, it can be confirmed that slope length is an important parameter affecting flood hazard.

According to Nguyen et al. (2020), there are currently two different types on the concept of slope length including absolute and relative slope length. The former is often determined in length measurement units, making it "absolute" in terms of quantitative sense, while the latter is hierarchized depending on the proportion of the absolute slope length, so it denotes "relative" in terms of quantitative concepts. The concept of absolute slope length is widely used in erosion studies or hydrological and hydraulic calculations, but it is challenging in the hierarchy to establish the flood hazard zone map [21]. Therefore, the present study used the concept of the relative slope length to generate a hierarchical map of slope length, thereby combining with other maps to create a map of flood hazard zoning in the study area.

3.2 AHP method

There are different kinds of flood risk evaluations, which combine qualitative, semi-quantitative, and quantitative techniques [35]. However, the AHP technique is being utilized most frequently to resolve different flood hazard assessment [36]. The AHP is a decision-making methodology created by Thomas Saaty in the 1970s that can evaluate and analyze complex multiple problems [37]. In flood hazard evaluation, AHP can be integrated with various criteria to calculate the flood hazard index. In this paper, to delineate the flood-prone areas, based on the decision makers' consideration, the integration between the AHP algorithm and GIS technology has been applied to determine the weight of factors contributing to flood generation in the study area, including slope length factor. The AHP model involves creating a pair-wise matrix, calculating eigenvalue and weighting coefficients, and enables the calculation of a consistency ratio (CR) to assess the consistency of the priority ranking. The following equation has been used to compute the CR:

$$CR = CI / RI \quad (3)$$

When CR is the consistency index, RI is the random consistency index that depends on the number of criteria used in the AHP model, and CI is the consistency index calculated as follows:

$$CI = (\lambda_{max} - n)/(n-1) \quad (4)$$

when λ_{max} denotes the largest eigenvalue of the pair-wise comparison matrix; n is the number of parameters.

The AHP result is acceptable if the CR is less than or equal to 0.1. If this value is greater than 0.1, the result is inconsistent with continuing the evaluation and the approach needs to be revised [38].

3.3 Generating flood hazard zone map

Tab. 1. Type data, data sources, and output layers

Tab. 1. Typ i źródła danych, warstwy wyjściowe

Data type	Description	Source	Output layer
Topography map	Scale 1:50 000	Ha Tinh Department of Natural Resources and Environment	DEM, slope map, drainage density map, relative slope length map
Existing Land use map			Land cover map
Soil classification map			Soil map
Rainfall data	In the period from 1961 to 2020	National Centre for Hydro-Meteorological Forecasting	Annual rainfall map
Flood water level in reality of flood events	October 2010, 2013, 2016, 2020	Ha Tinh Department of Natural Resources and Environment	Used to validate the flood hazard zoning map

Tab. 2. Relative weight for thematic layers

Tab. 2. Współczynniki wagowania dla warstw tematycznych

Factors	RF	SI	DD	S	LU	RSI	Weights	
							Group 1	Group 2
Rainfall (RF)	1	3	5	7	5	5	50.3	45.8
Slope (SI)	1/3	1	3	5	5	3	27.3	25.3
Drainage Density (DD)	1/5	1/3	1	1	1	1	8.1	7.6
Soil (S)	1/7	1/5	1	1	1	1	6.8	6.6
Land Use (LU)	1/5	1/5	1	1	1	1	7.4	7.1
Relative Slope Length (RSI)	1/5	1/3	1	1	1	1		7.6
CI							0.03	0.02
CR							0.027	0.016

After determining the weights and ratings of each criterion, the following equation has been applied to calculate the flood hazard index. Accordingly, the flood hazard zone map can be developed with help of the raster calculator tool in ArcGIS. This map can show all areas that are at hazard of floods.

$$\mathrm{FHI} = \sum_{i=1}^{n}(W_i * X_i) \quad (5)$$

when X is the weight of factor i; W is the weight value of each parameter

3.4 Datasets

There are two kinds of data to feed into the AHP model including primary data and secondary data. The former was acquired by interviewing people living in the study area and asking for experts' judgment with questionnaires and recorded in the field notes. The latter in this study is defined as data gathered from some institutions.

These data are preliminary information about the study region such as topography map, land use map, population, climate situations, and rainfall. The datasets used in this study are described accordingly in Table 1. Based on this data, the flood hazard zoning map was created to detect flood-prone areas with various hazard levels.

4. Results and Discussion

4.1 Assessment of the importance of factors affecting to flood hazard

In this paper, two groups of influencing factors are used to map the flood hazard zone of the study area. Group 1 includes five criteria that are rainfall, slope, drainage density, soil, and land cover. Group 2, in addition to the five factors in group 1, also includes the relative slope length. The weight of criteria affecting flood hazard was based on their reaction to the occurrence of flood and expert's judgments. A factor with a high weight shows a great impact on flood potential, whereas a variable with a low weight indicates a minor influence. With values ranging from 1 to 9, Saaty's scale of relative importance was used to determine each parameter's weight. These values were allocated relied on previous research, together with experts' judgments. In this study, relative weights are assigned to each thematic layer, as indicated in Table 2.

AHP algorithm allows determining the normalized weight of each factor, as shown in Table 2. The study findings indicate that rainfall have a higher value than others, which means this rainfall is the most important parameter. Slope shows the prospect for high flood hazard, whereas high soil permeability implies low hazard flood. In this study, there are many factors that influence on flood potential listed in increasing order as follows: Soil, land use, drainage density, relative slope length, slope, and rainfall. To assess the appropriateness of the weights assigned to each criterion, the consistency ratio was determined based on the formula (1). The consistency index (CI) value obtained by the calculation is 0.03 (group 1) and 0.02 (group 2). Accordingly, the calculated consistency ratio is 0.027 and 0.016 respectively which are less than 0.1, this means that the weights assigned to the parameters are appropriate for further study.

4.2 Generating the flood hazard zone map

The flood hazard zone map in the study area is produced based on appropriate ratings for thematic layers, their classes on flood potentiality, and their weights. The flood hazard potential zones of the research region were determined by multiplying the influencing factor weight by the cell value of that criterion class and adding the resulting cell values together as following equation:

$$\text{For Group 1: FHI} = Rf_w*Rf_r + Sl_w*Sl_r + Dd_w*Dd_r + S_w*S_r + Lu_w*Lu_r \quad (6)$$

$$\text{For Group 2: FHI} = Rf_w*Rf_r + Sl_w*Sl_r + Dd_w*Dd_r + S_w*S_r + Lu_w*Lu_r + Rsl_w*Rsl_r \quad (7)$$

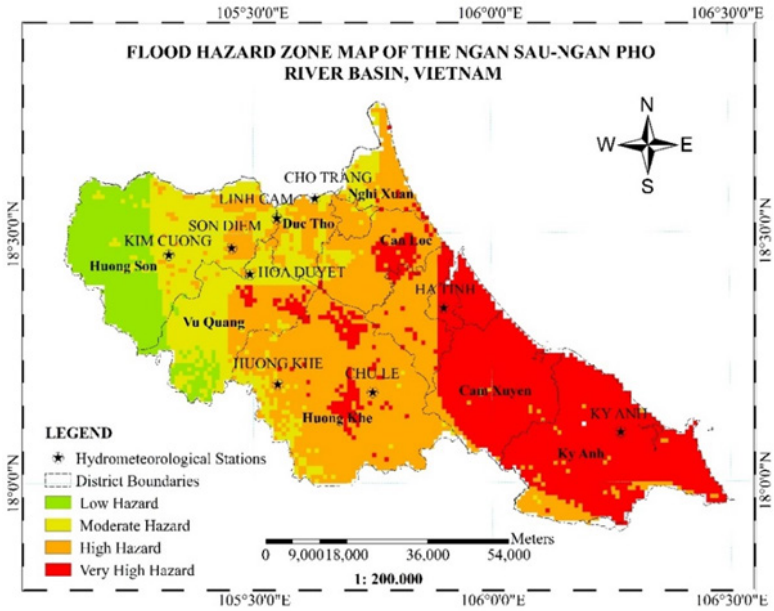

Fig 3. Flood hazard zone map of the study area (created for 5 factors affecting flood formation)

Rys. 3. Mapa stref zagrożenia powodziowego obszaru badań (stworzona dla 5 czynników wpływających na powstawanie powodzi)

where the symbol "w" shows the weight of 1 thematic layer, and the symbol "r" indicates the rating of subclasses in each layer.

The total values calculated by Equation (6) and (7) are classified into an assessment scale of low, moderate, high, and very high. The values of flood hazard zones range from 1.28 to 8.53 (for group 1) and from 1.3 to 8.4 (for group 2). Natural breaks classification of ArcGIS software is used to classify this flood potential zones as Figure 3 and Figure 4.

After opening the command window to perform the analysis of remote sensing image data from GEE, the integration of terrain data DEM, Sentinel 2 remote sensing image with a resolution of 10 × 10 meters, and real-life river cross-section data was performed (Figure 6). Nowadays, Sentinel images can alleviate the effects of clouds, allowing for analysis across more time layers. During the driest periods, the water level in the Ba River remains only in the main channels with the lowest water level. Therefore, the riverbanks and edges of the main channels are without water. Using Sentinel images helps determine the elevation of these areas.

4.3 Validation of flood hazard zone

Verification was performed between the flood hazard zone map and levels of a flood warning at hydrological stations of typical floods. In this study, three flood events were used to verify including floods in October 2010; October 2013; October 2016; and October 2020. In addition, water level data and flood alarm levels at Chu Le, Son Diem, and Hoa Duyet hydrological stations are also used to assess (Table 3). The total accuracy was calculated using the following equation [39]:

$$\text{The Accuracy (\%)} = (\text{number of correct sampled/total number of samples}) \times 100 \quad (8)$$

In this study, water level data from four flood events in three hydrological stations (that means the total number of samples is 12) were utilized as a point of reference for determining the accuracy of mapping the flood hazard zones. Accuracy is calculated for two cases as follows:

The total accuracy for group 1: (4/12)* 100 = 33%
The total accuracy for group 2: (9/12)* 100 = 75%

Thus, the identification of flood potential areas by six factors affecting flood formation (group 2) has much higher accuracy than the determination based on five factors (group 1). The findings indicated that there is a considerable level of agreement in using factors affecting flood potential of second group to establish the flood hazard zone map with the total accuracy of 75%. This assessment also shows a good connection between flood potential zones in the map and actual flood hazard information. This proves that adding the relative slope length factor to develop the AHP model helps to improve the precision of flood prone area delineation in the study area.

This study is useful in decision making, flood management, and as a guide for future flood monitoring in the study area. Based on the obtained results of this study, it can be concluded that integrated AHP method and GIS technology are very useful, time-efficient, and affordable tools for modeling flood hazard zones, in particular for the data spare areas such as flood prone regions. However, it is necessary to consider carefully before deciding which factors affecting flood generation to include in the calculation model. This selection depends not only on the physical geography characteristics of the study area, but also on the availability of data. This is not simple, especially for the ever-changing subject of flood. In addition, the number of criteria also needs to be considered, just choosing from 5 to 9 factors is enough. Moreover, in order to improve accuracy and increase the level of agreement between predicted results and actual happens, the data used to develop the model should be real-time data or data closest to prediction time.

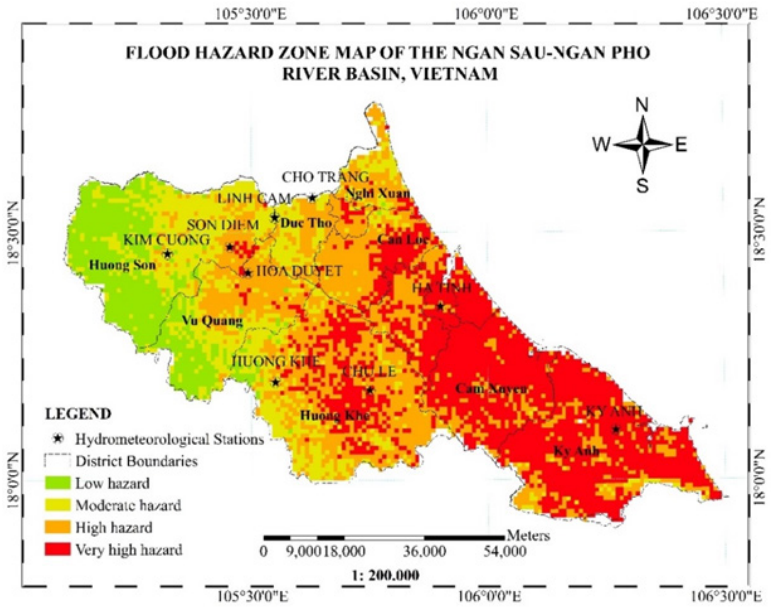

Fig. 4. Flood hazard zone map of the study area (created for 6 factors affecting flood formation)

Rys. 4. Mapa stref zagrożenia powodziowego obszaru badań (stworzona dla 6 czynników wpływających na powstawanie powodzi)

Tab. 3. Validation of flood hazard zone using data of flood evens (Data Source: Ha Tinh Committee for Flood and Storm Control)

Tab. 3. Walidacja strefy zagrożenia powodziowego na podstawie danych o zjawiskach powodziowych

River	Hydrologic-al stations	Flood even	Actual description			Expected description			
			Water level (m)	Flood danger level	Hazard level	Group 1	Agreement	Group 2	Agreement
Ngan Sau	Chu Le	16-18 October, 2010	16.56	Above warning level 3 (3.06 m)	Very high	High	Disagree	Very high	**Agree**
	Hoa Duyet		12.37	Above warning level 3 (1.87 m)	Very high	Very high	**Agree**	Very high	**Agree**
Ngan Pho	Sơn Diem		13.0	Above warning level 3 (0.78 m)	Very high	High	Disagree	Very high	**Agree**
Ngan Sau	Chu Le	15, 16 October, 2013	14.42	Above warning level 3 (0.92 m)	Very high	High	Disagree	Very high	**Agree**
	Hoa Duyet		11.26	Above warning level 3 (0.76 m)	Very high	Very high	**Agree**	Very high	**Agree**
Ngan Pho	Sơn Diem		14.62	Above warning level 3 (1.62 m)	Very high	High	Disagree	Very high	**Agree**
Ngan Sau	Chu Le	15, 16 October, 2016	15.64	Above warning level 3 (2.14 m)	Very high	High	Disagree	Very high	**Agree**
	Hoa Duyet		10.91	Above warning level 3 (0.41 m)	Very high	Very high	**Agree**	Very high	**Agree**
Ngan Pho	Sơn Diem		12.8	Under warning level 3 (0.2 m)	High	High	**Agree**	Very high	Disagree
Ngan Sau	Chu Le	19 October, 2020	14.5	Above warning level 3 (0.5 m)	Very high	High	Disagree	Very high	**Agree**
	Hoa Duyet		9.41	Above warning level 2 (0.41 m)	High	Very high	Disagree	Very high	Disagree
Ngan Pho	Sơn Diem		10.5	Above warning level 1 (0.5 m)	Moderate	High	Disagree	Very high	Disagree

5. Conclusions

In the present study, the AHP approach along with GIS technology was used to determine the flood prone zones of Ngan Sau, Ngan Pho river basin, based on influential variables in two groups. This procedure successfully achieves the satisfactory findings with regard to the identification of flood potential areas. The AHP analysis reveals that meteorological factor such as rainfall, physical criteria such as slope, drainage density, relative slope length have greater impact on flood formation. Two flood hazard zone maps of the study areas were generated using two data groups. The result maps were verified based on flood warning levels of four historical flood evens. The results of predicting flood hazard areas that take into account this factor are much more accurate and reliable than those made without that criterion. Therefore, it can be asserted that it is necessary to include the relative slope length to delineate the flood potential zones in Ngan Sau,

Ngan Pho river basin. In addition, since data preparation is not too complicated, this parameter can also be considered for use in other geographical areas to identify flood prone zones.

Acknowledgements

This study was completed based on the results of the research project: Research on evaluating changes of slope length to flood risk zoning (case study: Ngan Sau and Ngan Pho river basins, Ha Tinh province), Hanoi University of Natural Resources and Environment. Topic code: 13.01.23.E.01.

Thanks to two anonymous reviewers and editorial comments for their valuable comments in the earlier version, which helped us to improve the manuscript's quality

Conflicts of Interest

The authors declare no conflict of interest.

Ethical statement

The authors state that the research was conducted according to ethical standards.

Funding body

This research is no funding.

Literatura – References

1. Yodying, A., Seejata, K., Chatsudarat, S., Chidburee, P., Mahavik, N., Kongmuang, C., and Tantanee, S. (2019) Flood hazard assessment using fuzzy analytic hierarchy process: A case study of Bang Rakam model in Thailand. In: Proceedings of the 40th Asian Conference on Remote Sensing, Daejeon Convention Center (DCC), Daejeon, KR, pp. 14-18.
2. Sriariyawat, A., Kimmany, B., Miyamoto, M., Kakinuma, D., Pc, S., and Visessri, S. (2022). An Approach to Flood Hazard Mapping for the Chao Phraya River Basin Using Rainfall-Runoff-Inundation Model. Journal of Disaster Research. 17(6), p. 864-876.
3. Alarifi, S.S., Abdelkareem, M., Abdalla, F., and Alotaibi, M. (2022). Flash Flood Hazard Mapping Using Remote Sensing and GIS Techniques in Southwestern Saudi Arabia. Sustainability. 14(21), p. 14145.
4. Singha, C., Swain, K.C., Meliho, M., Abdo, H.G., Almohamad, H., and Al-Mutiry, M. (2022). Spatial Analysis of Flood Hazard Zoning Map Using Novel Hybrid Machine Learning Technique in Assam, India. Remote Sensing. 14(24), p. 6229.
5. Ba, D.N., Quynh, N.N., Thi, L.P., and Tuyet, M.D. (2021). Evaluation and validation of flood hazard zoning using Analytical Hierarchy Process and GIS: A case study of Lam River basin (Vietnam). Вестник Санкт-Петербургского университета. Науки о Земле. 66(4), p. 831-851.
6. Minh, D.T. (2021). Flood hazard zoning in Ngan Sau, Ngan Pho river basin, Ha Tinh province using GIS and analytical hierarchical process HNUE JOURNAL OF SCIENCE. 66(1), p. 198-212.
7. Dung, N.B. and Minh, D.T. (2021). Assessment of flood influence criteria in the lam river basin using a combined Delphi-AHP method. Sustainable development of mountain territories. 13(3), p. 387-396.
8. Dang, T.M. and Nguyen, L.T.D. (2021). Integration of Delphi technique and analytical hierarchy process method in assessment the groundwater potential influence criteria: a case study of the Ba River Basin. Inżynieria Mineralna. 38(2).
9. Kumar, A. and Pant, S. (2022). Analytical hierarchy process for sustainable agriculture: An overview. MethodsX. 10.
10. Dung, N.B., Minh, D.T., An, B.N., and Nga, N.Q. (2021). Assessment of vulnerability In agricultural land in flood prone Areas and application of mobile smart Phone in providing flood hazard Information in lam river Basin (Vietnam). Sustainable development of mountain territories. 2(48), p. 254-265.
11. Teshnizi, E.S., Golian, M., Sadeghi, S., and Rastegarnia, A. (2022). Application of analytical hierarchy process (AHP) in landslide susceptibility mapping for Qazvin province, N Iran. Computers in Earth and Environmental Sciences, p. 55-95.
12. Minh D.T, Dung N.B. (2023). GIS-based multi-criteria approach for drought hazard modeling in the Ba river basin, Vietnam. Environmental Earth Sciences, 30(83):30.
13. Dung, N.B., Long, N.Q., An, D.T., and Minh, D.T. (2022). Multi-geospatial flood hazard modelling for a large and complex river basin with data sparsity: a case study of the Lam River Basin, Vietnam. Earth Systems and Environment. 6(3), p. 715-731.

14. Dung, N.B., Long, N.Q., Goyal, R., An, D.T., and Minh, D.T. (2022). The role of factors affecting flood hazard zoning using analytical hierarchy process: A review. Earth Systems and Environment. 6(3), p. 697-713.

15. Fu, X., Zhang, L., and Wang, X. (2016). The effect of slope length on sediment yield by rainfall impact under different land use types. Water resources. 43(3), p. 478-485.

16. Liu, B., Nearing, M., Shi, P., and Jia, Z. (2000). Slope length effects on soil loss for steep slopes. Soil Science Society of America Journal. 64(5), p. 1759-1763.

17. Qiu, H., Cui, P., Regmi, A.D., Hu, S., Wang, X., and Zhang, Y. (2018). The effects of slope length and slope gradient on the size distributions of loess slides: Field observations and simulations. Geomorphology. 300, p. 69-76.

18. Fu, X., Zhang, L., and Wang, Y. (2019). Effect of slope length and rainfall intensity on runoff and erosion conversion from laboratory to field. Water Resources. 46(4), p. 530-541.

19. Huang, K., Liu, R.-L., Qin, L., Song, T., Liu, Z.-X., and Li, R. (2021). Effects of slope length on soil erosion of Karst slope under different rainfall conditions. Ying Yong Sheng tai xue bao= The Journal of Applied Ecology. 32(1), p. 271-280.

20. Kinnell, P. (2000). The effect of slope length on sediment concentrations associated with side-slope erosion. Soil Science Society of America Journal. 64(3), p. 1004-1008.

21. Nguyen, B.D., Minh, D.T., Ahmad, A., and Nguyen, Q.L. (2020). The role of relative slope length in flood hazard mapping using AHP and GIS (case study: Lam River Basin, Vietnam). Geography, Environment, Sustainability. 13(2), p. 115-123.

22. He, Z., Xiao, P., Yu, X., Hao, S., Jia, G., and Yang, C. (2022). A Field Study for the Effects of Grass Cover, Rainfall Intensity and Slope Length on Soil Erosion in the Loess Plateau, China. Water. 14(14), p. 2142.

23. Verrina, G.P., Anugerah, D.D., and Haki, H. (2013). Analisa runoff pada Sub DAS Lematang hulu. Jurnal Teknik Sipil Dan Lingkungan. 1(1).

24. Tran, H.T. and Nguyen, T.T. (2020). A GIS-based spatial multi-criteria approach for flash flood risk assessment in the Ngan Sau-Ngan Pho mountainous river basin, North Central of Vietnam. Environment and Natural Resources Journal. 18(2), p. 110-123.

25. Dang Tuyet Minh. (2021). Flood hazard zoning in Ngan Sau, Ngan Pho river basin, Ha Tinh province using GIS and analytical hierarchical process. Journal of Science. 1.

26. Thanh, N.T., Huy, N.A., Huong, P.T.T., and Trang, T.T.T. (2023). Flash Flood Hazard Mapping Using Landsat-8 Imagery, AHP, And GIS In The Ngan Sau And Ngan Pho River Basins, North-Central Vietnam. Geography Environment Sustainability. 16(2).

27. Smith, D.D. and Wischmeier, W.H. (1957). Factors affecting sheet and rill erosion. Eos, Transactions American Geophysical Union. 38(6), p. 889-896.

28. Martin, O.M., Anthony, G.B., and Robert, M.S. (2011). Maryland Standards and Specifications for Soil Erosion and Sediment Control. Baltimore.

29. Konrad, C.P. (2003). Effects of urban development on floods.

30. Kittipongvises, S., Phetrak, A., Rattanapun, P., Brundiers, K., Buizer, J.L., and Melnick, R. (2020). AHP-GIS analysis for flood hazard assessment of the communities nearby the world heritage site on Ayutthaya Island, Thailand. International Journal of Disaster Risk Reduction. 48.

31. Roose, E. (1996). Land husbandry: components and strategy. Vol. 70: FAO Rome.

32. Balasubramanian, A. (2017). Soil erosion–causes and effects. Centre for Advanced Studies in Earth Science, University of Mysore, Mysore. 12(12).

33. Negese, A., Fekadu, E., and Getnet, H. (2021). Potential soil loss estimation and erosion-prone area prioritization using RUSLE, GIS, and Remote Sensing in Chereti Watershed, Northeastern Ethiopia. Air, Soil and Water Research. 14, p. 1-17.

34. Directorate for Roads of Vietnam, T. (2013). Calculating of flood flow characteristics (in Vietnamese with English summary).

35. Van Westen, C., Alkema, D., Damen, M., Kerle, N., and Kingma, N. (2011). Multi-hazard risk assessment: distance education course guide book. United Nations University-ITC School on Disaster Geo-information Management (UNU-ITC DGIM).

36. De Brito, M.M. and Evers, M. (2016). Multi-criteria decision-making for flood risk management: a survey of the current state of the art. Natural Hazards and Earth System Sciences. 16(4), p. 1019-1033.

37. Saaty, R.W. (1987). The analytic hierarchy process—what it is and how it is used. Mathematical modelling. 9(3-5), p. 161-176.

38. Mitra, R., Saha, P., and Das, J. (2022). Assessment of the performance of GIS-based analytical hierarchical process (AHP) approach for flood modelling in Uttar Dinajpur district of West Bengal, India. Geomatics, Natural Hazards and Risk. 13(1), p. 2183-2226.

39. Jensen, J.R. (1996). Introductory digital image processing: a remote sensing perspective. Prentice-Hall Inc.

Znaczenie danych o względnej długości zboczy w strefach zagrożenia powodziowego: studium przypadku Ngan Sau, dorzecze rzeki Ngan Pho, Wietnam

Modelowanie powodzi dostarcza przydatnych informacji, które pomagają zarządzać zagrożeniem powodziowym i łagodzić skutki powodzi w lokalizacjach narażonych na powodzie. W ramach niniejszych badań opracowano mapy zagrożenia powodziowego dla dorzeczy rzek Ngan Sau i Ngan Pho przy użyciu technologii GIS i metody Analytical Hierarchy Process (AHP). Dokładność wyników symulacji powodzi zależy od kryteriów powodujących powódź. Celem pracy była ocena roli względnej długości zbocza w identyfikacji i wyznaczaniu zagrożenia powodziowego. Do określenia odpowiednich wag w AHP wykorzystano sześć czynników geograficznych i metrologicznych — opady deszczu, nachylenie, gleba, użytkowanie gruntów, gęstość drenażu i względna długość zbocza. W procesie obliczania modelu czynniki te dzielone są na dwie grupy: grupa 2 obejmuje wszystkie sześć parametrów, natomiast grupa 1 obejmuje pięć kryteriów z wyłączeniem kryterium względnej długości nachylenia. W oparciu o stany ostrzeżeń powodziowych na stacjach hydrologicznych na obszarze badań podczas powodzi, które miały miejsce w przeszłości, zweryfikowano skutki wyznaczania stref zagrożenia powodziowego. Uzyskane wyniki wykazały, że mapy opracowane z grupy kryteriów uwzględniających względną długość nachylenia są dokładniejsze niż mapy wygenerowane na podstawie pozostałych pięciu czynników. Wyniki artykułu mogą posłużyć jako punkt odniesienia przy wyborze kryteriów tworzenia modeli stref zagrożenia powodziowego z wykorzystaniem kombinacji technologii AHP i GIS.

Słowa kluczowe: *proces hierarchii analitycznej, AHP, zagrożenie powodziowe, względna długość nachylenia, Ngan Sau, dorzecze rzeki Ngan Pho*

River Cross-Section Addition from the Google Earth Engine in Downstream of the Ba River

*Ba Dung NGUYEN[1)], Tuyet Minh DANG[2)]**

[1)] Hanoi University of Natural Resources and Environment, No 41 A Phu Dien Road, Phu Dien precinct, North-Tu Liem District, Hanoi, Vietnam; ORCID: https://orcid.org/0000-0001-5378-0926
[2)] Thuyloi University, 175 Tay Son, Hanoi, Vietnam; ORCID: https://orcid.org/0000-0001-8379-1087
* Corresponding author: Tuyet Minh DANG, email: dtminh@tlu.edu.vn

http://doi.org/10.29227/IM-2024-01-90

Submission date: 16-05-2024 | Review date: 30-05-2024

Abstract

Riverbed depth is the main and essential data to conduct hydrodynamic modeling research. Typically, riverbed topography data is collected directly from cross-sections arranged along the river at relatively distant intervals. This paper presents the results of applying Google Earth Engine technology and high-resolution Sentinel 2 remote sensing images combined with digital elevation model data and field-measured cross-sections to supplement the cross-sections of the downstream Ba River. The reliability of the cross-sections obtained using this technology has been verified against actual measurements at several locations on the mainstream of the Ba River. The research results indicate that most of the interpolated cross-sections are consistent with the actual measured data.

Keywords: *Google Earth Engine, river cross-section, Ba river basin*

1. Introduction

Collecting riverbed topography data is not an easy and simple task as it requires extensive field measurement time and data processing post-survey. However, traditional measurement methods cannot address the scarcity of riverbed topography data. Recently, remote sensing technology has rapidly developed with big data and cloud computing technology. Google Earth Engine (GEE) is an advanced cloud-based geospatial processing platform that utilizes large-scale open-source big data, including petabyte-scale global geospatial images and data [1]. This tool has the potential for exploiting, processing, and analyzing satellite images and other spatial data for various research purposes [2]. Additionally, this technology can overcome the processing issues that traditional satellite image processing methods are facing [3]. Globally, GEE technology can be applied in many fields such as mapping and monitoring land cover [4], land cover classification [5], agriculture [6], disaster management [7], forestry [8], supplementing river cross-sections [9], and determining river width [10], fluvial geomorphology [11], river discharge retrieval [12]. However, in Vietnam, the application of GEE is still quite new, and currently, there are not many studies utilizing this technology. Most studies focus on disaster management fields such as floods [2], droughts [1], and land use changes [13]. Hoang et al. (2020) applied the GEE platform to create drought monitoring maps for the Dong Nai river basin in the Southeast region. The research results demonstrated that the GEE platform is an effective and rapid tool for drought monitoring [1]. Nhung and Thy (2019) also showed the effective application of the GEE tool to analyze the change in forest area and land surface temperature in the Ba-Da Rang river basin [13].

Additionally, Long et al. conducted the exploitation, processing, and analysis of satellite images on the GEE system to extract flood developments and statistically analyze the flood-affected areas over the years in the Dong Thap province [2]. Forest dynamics monitoring in Lam Dong province was also carried out using a remote sensing method on the GEE platform. The results showed that GEE is an effective tool and brings significant efficiency to forest monitoring. Besides GEE applications in disaster management and land use change monitoring, this technology can be applied to supplement river cross-sections. [14] used this method to densify river cross-sections in downstream of the Ca river. The results are used to evaluate saltwater intrusion developments and establish a saltwater intrusion risk map, taking into account the impact of climate change and sea level rise.

Both domestic and international research results have demonstrated the effectiveness of GEE, allowing users to combine various types of spatial data for different analysis and processing purposes. Therefore, this study combined optical satellite images from Sentinel-2, DEM topographic data, and field survey cross-section data to supplement the cross-sections in downstream of the Ba river area for researching and evaluating water resources. The research results will contribute to perfecting the scientific basis for applying new technology in the planning and management of water resources in the study area.

2. Study area

The Ba River is the largest river in the central coastal region with a basin area of 13,508 km². The geographical coordinates of the basin are approximately 12°55' to 14°38' North latitude and 108°00' to 109°55' East longitude [15]. It borders the Tra Khuc River basin to the north, the Cai Ninh Hoa River and the Serepok River basins to the south, the Kone and Ky Lo River basins to the east, and the Sesan and Serepok River basins to the west. The Ba River originates from the peak of Ngoc Ro Mountain at an elevation of 1,549 meters in the Truong Son range. The total length of the main river is 374 km [16].

The Ba River basin (Figure 1) can be divided into various topographical types: the middle and upper reaches are pri-

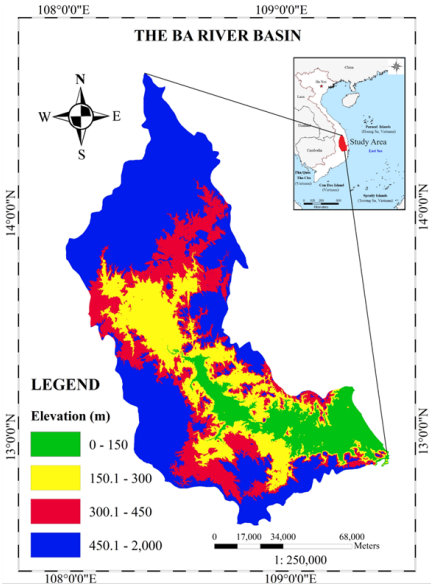

Fig. 1. Research process

Rys. 1. Obszar badawczy

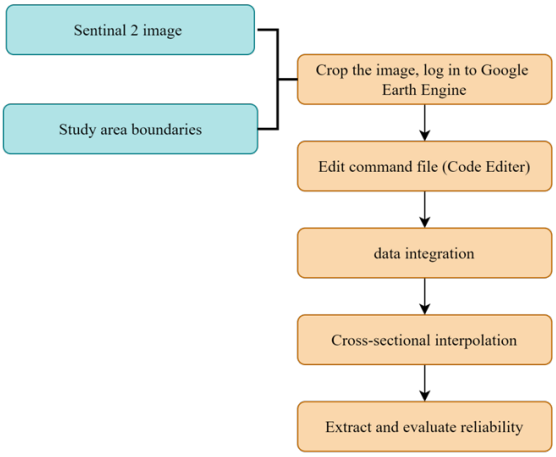

Fig. 2. Flow chart illustrating methodology of the study

Rys. 2. Schemat blokowy prezentujący metodykę analiz

marily mountainous and highlands; the lower reaches feature low hills, valleys, and coastal alluvial plains [17]. The flow in the Ba River basin not only varies greatly across different areas but also changes significantly over time, as evidenced by the fluctuations in seasonal flow and the monthly distribution of flow in various parts of the basin. In the Ba River, the minimum flow (or dry season flow) typically occurs in March or April for rivers and streams in the middle and upper regions, and in April or July for those in the downstream area [18].

3. Data and research methodology

3.1. Data

This study uses a Sentinel-2 remote sensing image with a resolution of 10x10 meters (with a cloud cover rate below 30%) and a Digital Elevation Model (DEM) created from topographic maps of the study area. Sentinel-2 images have a high revisit frequency (one scene per month), a clear processing procedure, and many automated steps. The Sentinel-2 data used in this study were obtained from GEE (ee.ImageCollection('COPERNICUS/S2_SR')) at processing level 2A, which includes atmospheric correction and geometric correction (converted to Bottom-of-Atmosphere Reflectance (RefBOA)). In addition to images and DEM, the study uses actual measured cross-section data to densify river cross-sections from the images. Currently, the actual measured cross-section data at the lower Ba River averages 1.2 to 1.5 km per cross-section.

3.2. Research methodology

Figure 2 shows the process of supplementing river cross-sections using GEE technology. GEE is a cloud computing platform that allows users to run geospatial analyses on Google's infrastructure. GEE operates through an online interface of a JavaScript application (API) called the Code Editor [19].

On this interface (Figure 3), the users can write and run scripts to share and reimplement the analysis process as well as cleaning and wrangling geospatial data. Code Editor helps users perform all features of Earth Engine. This interface is much more flexible than Explorer's and is even capable of conducting highly complex analysis procedures per user's request.

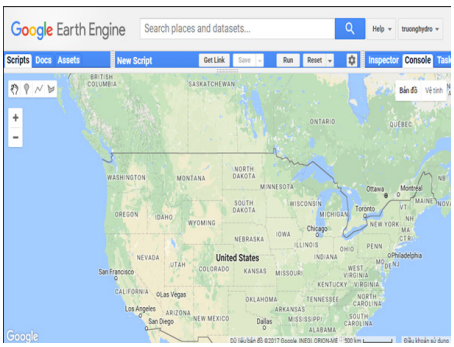

Fig. 3. Register domain to analyze remote sensing image data on Google Earth Engine

Rys. 3. Rejestracja do domeny analizy danych z obrazów teledetekcji w Google Earth Engine

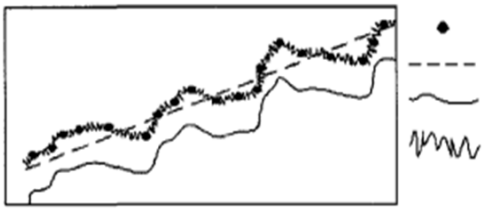

Fig. 4. Main components of Kriging Interpolation [20]

Rys. 4. Główne składniki interpolacji metodą krigingu [20]

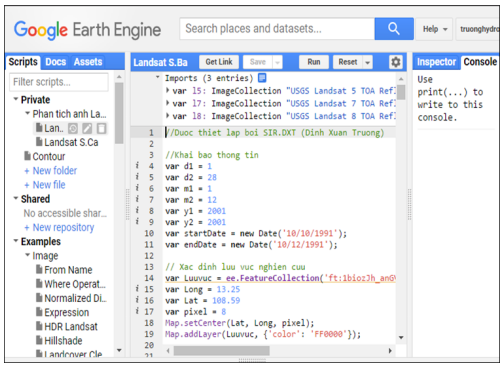

Fig. 5. Code editor in Google Earth Engine

Rys. 5. Edytor kodu w Google Earth Engine

In the Scripts library, there are many sample script files to showcase the capabilities and code that can be used in analyses. Users can review these samples to understand what Earth Engine can perform and then save them in their personal repository. The Docs tab contains a list of guide notes that help identify the types of objects and functions in GEE. Users will use the Inspector (similar to the Identify tool in ArcMap) to view information about map layers at specific locations on the map. The Console will display messages when running scripts and print information about data, products, and intermediate results. The Console will also log any detection messages (such as information or error messages when running scripts). The Tasks tab is used to manage the export of data and the final results of the analysis, which are saved in Google Drive via a Gmail account [19].

The study uses the Kriging interpolation method, which is based on the assumption that spatially varying variables can be represented by a sum of three main components. These are (a) the structural component, which has a constant mean or trend, (b) the random component, which is spatially correlated, and (c) random noise, which is independent of spatial correlation [20].

Figure 4 shows the main components of Kriging interpolation. In this interpolation method, assuming that X is a location in space, the value of a variable Z at that location can be expressed as follows [20]:

$$Z(x) = m(x) + e'(x) + e'' \quad (1)$$

In which: m(x) is a function describing the structured component of Z at X, e'(x) is the spatially correlated component, and e'' is the spatially independent Gaussian noise with a mean value of p = 0 and variance δ^2 [20].

4. Results and Discussion

After signing in to register the domain to analyze remote sensing image data from GEE, the next step is to enter the command file editing window (Code Editor). On the web page of the GEE platform, the JavaScript programming language is used to perform direct execution (Figure 5).

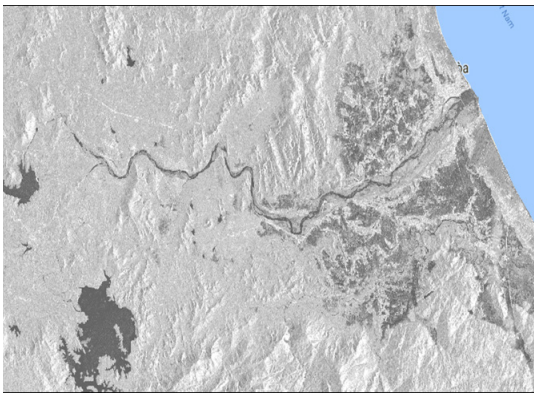

Fig. 6. Incorporation of DEM and Sentinel remote sensing image
Rys. 6. Włączenie DEM i obrazu teledetekcyjnego Sentiel

Fig. 7. Interpolation, supplement cross-section data for downstream of the Ba river area
Rys. 7. Interpolacja, uzupełnianie danych dla przekrojów w dole rzeki Ba

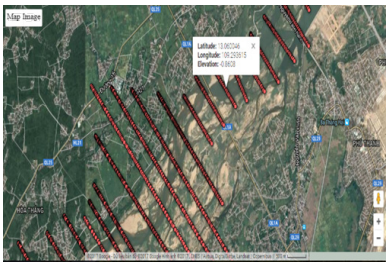

Fig. 8. Depth data of the cross-sections in downstream of the Ba river area
Rys. 8. Dane o głębokości w przekrojach w dole rzeki Ba

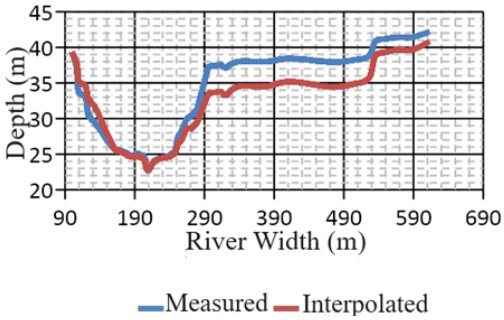

a) Actual measured cross-section and interpolation
a) Zmierzone i interpolowane przekroje

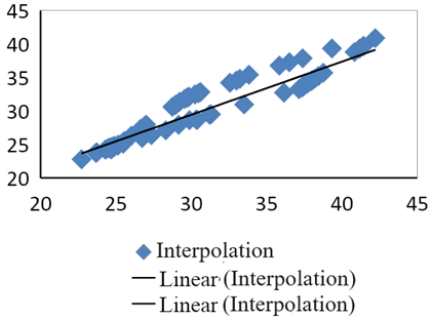

b) Evaluation of realiability of interpolation
b) Ocena wiarygodności interpolacji

Fig. 9. Cross section of the Ba river in Cung Son
Rys. 9. Przekroje dla rzeki Ba w Cung Son

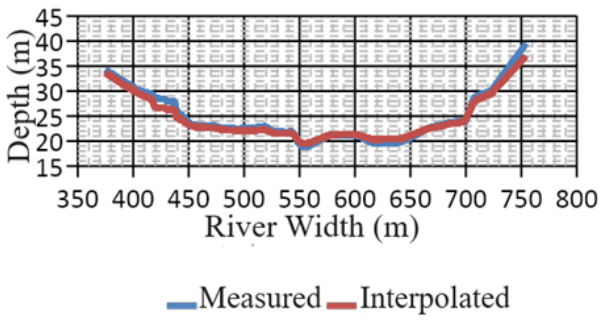

a) Actual measured cross-section and interpolation
a) Zmierzone i interpolowane przekroje

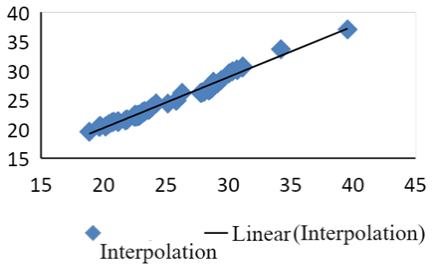

b) Evaluation of realiability of interpolation
b) Ocena wiarygodności interpolacji

Fig. 9. Cross section of the Ba river in Cung Son
Rys. 9. Przekroje dla rzeki Ba w Cung Son

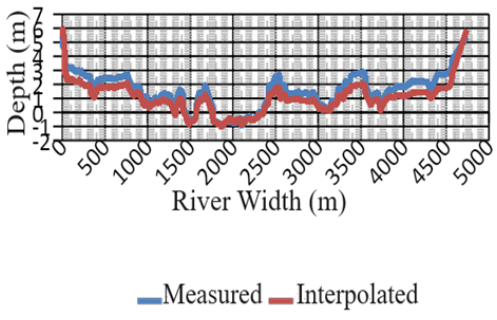

a) Actual measured cross-section and interpolation
a) Zmierzone i interpolowane przekroje

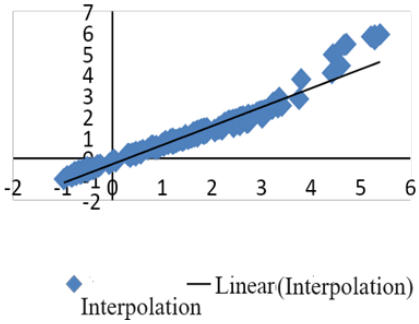

b) Evaluation of realiability of interpolation
b) Ocena wiarygodności interpolacji

Fig. 11. Cross section of the Ba river in Phu Lam
Rys. 11. Przekroje dla rzeki Ba w Phu Lam

After opening the command window to perform the analysis of remote sensing image data from GEE, the integration of terrain data DEM, Sentinel 2 remote sensing image with a resolution of 10 x 10 meters, and real-life river cross-section data was performed (Figure 6). Nowadays, Sentinel images can alleviate the effects of clouds, allowing for analysis across more time layers. During the driest periods, the water level in the Ba River remains only in the main channels with the lowest water level. Therefore, the riverbanks and edges of the main channels are without water. Using Sentinel images helps determine the elevation of these areas.

The terrain data below the water surface during the driest period is determined by interpolating from the data of actual measured cross-sections. Using GEE technology and the Kriging interpolation method, the cross-sections in the research area will be supplemented. Figures 7 and 8 illustrate the densified cross-sections and the depth data of the cross-sections in downstream of the Ba River area.

To evaluate the reliability of the interpolated cross-section results, the study extracts a number of experimental cross-sections to compare the interpolation results with the actually measured cross-sections at several locations along the mainstream of the Ba River, including Cung Son, Son Hoa, and Phu Lam. At these cross-section locations, the correlation relationship in depth between the measured and interpolated cross-sections is shown in Figures 9, 10, and 11. The results indicate a high correlation coefficient between the measured and interpolated cross-sections at the same location ($R \geq 0.9$), demonstrating the trustworthiness of the supplemented cross-sections for downstream of the Ba River.

5. Conclusions

The study has established a process for processing, calculating, and supplementing river cross-sections using Sentinel 2 satellite imagery, DEM terrain data, and actual measured river cross-section data on the GEE platform for the downstream of the Ba River. The results are compared with the data of the measured cross-sections at several locations such as Cung Son, Son Hoa, and Phu Lam, showing that the research method has high reliability, and the GEE platform is an efficient and effective tool for supplementing river cross-sections. Therefore, it can help reduce time, effort, and costs in measuring river cross-sections, contributing to improving the quality of research on flow regimes in rivers as well as issues related to erosion, channel morphodynamics, and river management.

Acknowledgements

Thanks to two anonymous reviewers and editorial comments for their valuable comments in the earlier version, which helped us to improve the manuscript's quality.

Conflicts of Interest

The authors declare no conflict of interest.

Ethical statement

The authors state that the research was conducted according to ethical standards.

Funding body

This research is no funding.

Literatura – References

1. Hoang N.V, Nhan H.T.K., Vuong N.D. (2020). Research and application of the Google earth engine platform to create a drought monitoring map in the Dong Nai river basin in the Southeast region. Journal of Resouces Science and Technology, 58.
2. Long V.H, Giang N.V., Hoa P.V. (2018). Applying Google Earth Engine cloud computing technology in flood research in Dong Thap, Downstream of the Mekong River. Journal of Resouces Science and Technology, 43.
3. Tiwari, V., et al. (2020). Flood inundation mapping-Kerala 2018; Harnessing the power of SAR, automatic threshold detection method and Google Earth Engine. PLoS One, 15(8): p. e0237324.
4. Tsai, Y.H., et al. (2018). Mapping vegetation and land use types in Fanjingshan National Nature Reserve using google earth engine. Remote Sensing, 10(6): p. 927.
5. Lee, J., J.A. (2018). Cardille, and M.T. Coe, BULC-U: Sharpening resolution and improving accuracy of land-use/land-cover classifications in Google Earth Engine. Remote Sensing, 10(9): p. 1455.
6. Xiong, J., et al. (2017). Nominal 30-m cropland extent map of continental Africa by integrating pixel-based and object-based algorithms using Sentinel-2 and Landsat-8 data on Google Earth Engine. Remote Sensing, 2017. 9(10): p. 1065.
7. Liu, C.-C., et al. (2018). Flood prevention and emergency response system powered by Google Earth Engine. Remote sensing, 10(8): p. 1283.
8. Jahromi, M.N., et al. (2021). Google Earth Engine and its application in forest sciences. Spatial Modeling in Forest Resources Management: Rural Livelihood and Sustainable Development, p. 629-649.
9. Pandya, U., Patel A., and Patel D. (2017). River Cross Section Delineation From The Google Earth For Development Of 1D HECRAS Model–A Case Of Sabarmati River, Gujarat, India. in International conference on hydraulics, water resources and coastal engineering, Ahmedabad, India (HYDRO). 2017.
10. Yang, X., et al. (2019). RivWidthCloud: An automated Google Earth Engine algorithm for river width extraction from remotely sensed imagery. IEEE Geoscience and Remote Sensing Letters, 17(2): p. 217-221.
11. Boothroyd, R.J., et al. (2021). Applications of Google Earth Engine in fluvial geomorphology for detecting river channel change. Wiley Interdisciplinary Reviews: Water, 8(1): p. e21496.
12. Riggs, R.M., et al. (2022). RODEO: An algorithm and Google Earth Engine application for river discharge retrieval from Landsat. Environmental Modelling & Software, 148: p. 105254.
13. Yen T.H, Thy P.T.M. (2019). Application remote sensing using google earth engine Platform to analysis the change of forest and Agricultural land in Ba/Da Rang river basin. GIS conference.
14. Truong D.X., Kieu T.D. (2018). Study on the development of saltwater intrusion risk maps taking into account the impacts of climate change in the downstream of the Ca River. Journal of Agriculture and Rural Development.
15. Nguyen, B.D., An B.N, and Minh D.T. (2021). Estimation of suspended sediment concentration in downstream of the Ba river basin using remote sensing images. Inżynieria Mineralna, 2.
16. Minh, D.T. and Dung N.B. (2024). GIS-based multi-criteria approach for drought hazard modeling in the Ba river basin, Vietnam. Environmental Earth Sciences, 83(1): p. 30.
17. Minh D.T. and Duong N.L.T. (2021). Integration of Delphi technique and analytical hierarchy process method in assessment the groundwater potential influence criteria: a case study of the Ba River Basin. Inżynieria Mineralna.
18. Minh, D.T., et al. (2022). Investigation of groundwater level fluctuations on the Ba river basin for water resources management and planning: a GIS-based approach. Sustainable Water Resources Management, 8(3): p. 86.
19. https://earthengine.google.com/.
20. Childs, C. (2004). Interpolating surfaces in ArcGIS spatial analyst. ArcUser, July-September, 3235(569): p. 32-35.

Pomiar przekrojów w dolnym odcinku rzeki Ba z uzupełnieniem Google Earth Engine

Głównymi i niezbędnymi danymi do prowadzenia badań modelowania hydrodynamicznego jest głębokość koryta rzeki. Zazwyczaj dane o topografii koryta zbierane są bezpośrednio z przekrojów rozmieszczonych wzdłuż rzeki w stosunkowo odległych odstępach. W artykule przedstawiono wyniki zastosowania technologii Google Earth Engine i wysokiej rozdzielczości obrazów teledetekcyjnych Sentinel 2 w połączeniu z danymi cyfrowego modelu wysokości i przekrojami pomierzonymi w terenie w celu uzupełnienia przekrojów poprzecznych dolnego biegu rzeki Ba. Wiarygodność przekrojów uzyskanych tą technologią została zweryfikowana w oparciu o rzeczywiste pomiary w kilku miejscach głównego nurtu rzeki Ba. Wyniki badań wskazują, że większość interpolowanych przekrojów jest zgodna z rzeczywistymi danymi pomiarowymi.

Słowa kluczowe: *Google Earth Engine, przekroje rzeki, dorzecze rzeki Ba*

Method of Predicting Surface Subsidence Caused by Underground Mining: A Review

Huy Dinh NGUYEN[1)], Trong Dinh TRAN[3)], Canh Van LE[2)], Stanisław PIETRZYK[4)]*

[1)] Faculty of Bridges and Roads, 55 Giai Phong Street, Hanoi University of Civil Engineering, Hanoi, Vietnam; ORCID https://orcid.org/0000-0002-2049-3338; * Corresponding author: huynd@huce.edu.vn
[2)] Faculty of Geomatics and Land Administration, 18 Vien street, Hanoi University of Mining and Geology, Hanoi, Vietnam; ORCID https://orcid.org/0000-0002-3838-9950
[3)] Faculty of Bridges and Roads, 55 Giai Phong Street, Hanoi University of Civil Engineering, Hanoi, Vietnam; ORCID https://orcid.org/0000-0002-8113-9949
[4)] AGH; ORCID https://orcid.org/0000-0002-2240-3332

http://doi.org/10.29227/IM-2024-01-91

Submission date: 16-05-2024 | Review date: 01-06-2024

Abstract

In recent years, there has been a global increase in energy demand, with the extraction of underground mineral energy sources such as coal playing a significant role in the energy supply. However, the extraction of these natural resources always faces many challenges and risks. This process has created large voids, causing an imbalance in the original stress state within the earth and resulting in surface terrain deformations. Therefore, ensuring efficient extraction must be accompanied by safety measures. Among these, predicting surface subsidence due to underground mining is a crucial task. This paper presents an overview of the current method of predicting mining subsidence and their application scope. The result synthesizes various methodologies applied to different regions worldwide. Finally, the findings of this research can provide guidelines for establishing essential requirements for the application of surface displacement forecasting technologies due to underground mining.

Keywords: *subsidence prediction, underground mining, artificial neural networks*

1. Introduction

Due to the increasing energy demand, open-pit mining is not only no longer sufficient to meet the needs, but also less effective, leading mining companies worldwide have been transitioning from open-pit mining to underground mining method. However, one of the main drawbacks of the underground mining method is that overlying rock mass tends to move down to regain its new equilibrium state of stress, leading to the upper surface of the ground subsiding correspondingly, forming hollows and trenches, open cracks in the earth, abrupt steps, and extensive subsidence troughs, creating dangers to underground engineering structures and natural and artificial structures on the ground surface. In actuality, underground mining has exerted many negative impacts on environment and structures underground as well as on the surface, causing serious human and wealth losses; therefore, the forecast of surface deformation is a concern for many countries, numerous scientific centers, and scientists worldwide, with particular focus on countries with developing mining industries such as Russia, Germany, China, Poland, the United States [1]. In addition, new theories along with modern technology are increasingly being applied to enhance the accuracy of forecasting.

Russian scientists have been at the forefront of researching surface subsidence forecasting in mining operations. Through years of observational data collected from coal mines within the Soviet territory, basic formulas for calculating and forecasting ground subsidence were developed [2]. The establishment of formulas and forecasting models based on field observations in various mining regions by the Mining Mechanics and Mine Surveying Institute (VNIMI) at Saint Petersburg Mining University was reported at the World Mining Science Conference in 2008 and is still being utilized in Russia and several other countries, including Vietnam [3]. Many Chinese scientists have focused on researching surface subsidence forecasting in mines. In 2000, in the Journal of Mining Mechanics, Cui X.M, Miao X.X., and Wang J.A. [4] proposed a method applying nonlinear geometric theory to improve the reliability of surface subsidence forecasting. In 2015, Lei Nie and colleagues published a new model applying inverse tangent functions to estimate mining-induced displacement and deformation [5]. Ki-Dong Kim and colleagues studied forecasting the degree of subsidence in Samcheok city due to the impact of coal mining [6]. In Poland, many research projects have laid the foundation and developed fundamental theories on displacement, mining deformation in general, and forecasting methods in particular. The most important and successful research is by Knothe Stanisław at the Academy of Mining and Metallurgy in Krakow. Knothe's method has paved the way for the development of many subsequent forecasting methods [7].

In recent years, alongside the continuous advancement of science and technology, many new theories and algorithms have been applied in mining subsidence forecasting. The support of algorithms and computer models has enabled overcoming the limitations of traditional methods. In 2003, Ambrozic T. and Turk G. [8] first published the results of applying artificial neural networks in forecasting subsidence due to coal mining at the Velenje mine, Slovenia, using a 2-layer feedforward neural network. In 2011, Kang Zhao and Si-ni Chen [9] announced the application of artificial neural networks in subsidence forecasting for metal mining in China.

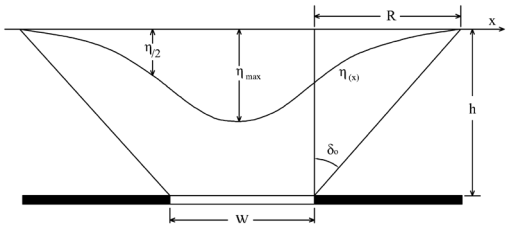

Fig. 1. Basic shifting cutting plane function [17]
Rys. 1. Podstawowa funkcja przesuwania płaszczyzny cięcia [17]

Hejmanowski and colleagues published a study applying artificial neural networks in forecasting surface mining displacement and deformation [10]. By 2017, author Kim Yangkyun and colleagues developed an artificial neural network (ANN) model to forecast subsidence in abandoned mines. The authors used survey results from 247 subsidence areas of 27 mines to validate the model [11]. To construct a map forecasting the impact of surface subsidence in the mine area, authors [12] utilized 7 input factors for ANN. In 2017, author [13] and colleagues used a feedforward neural network with a 9-7-6-1 structure to forecast the stability of transport and ventilation shafts of the Tabas mine, Iran. In Vietnam, Long and has applied the exponential function proposed by Knothe to forecast vertical displacement over time on the surfaces of Thong Nhat and Mông Dương mines [1], [14]. Research on forecasting vertical displacement of observation points on the surface over time was also addressed by author Khanh in a study applying the Kalman method in forecasting surface vertical displacement in mines [15]. Beside, Tam [16] and colleagues studied Prediction of underground mine's surface subsidence using a recursive multi-step forecasting model with an Artificial Neural Network shown that These results demonstrate that the proposed method and ANN model are suitable for the time-series monitoring data in mining areas.

2. Data and methodology

This study employed the systematic literature review approach to identify, evaluate, and interpret all pertinent research on the detection of surface displacements and deformations due to underground mining. The research on forecasting soil and rock displacement and surface deformation ultimately relies on data about geological characteristics, the physical properties of rock and soil layers, and mining technology. Researchers utilize suitable tools to estimate the values of displacement and deformation parameters as well as the displacement angles. Depending on the nature of the tool selection and problem-solving approach, forecasting methods can be categorized into different groups.

2.1. Group of methods based on empirical relationships

Common characteristics of this group of methods are based on empirical relationships determined based on actual measurement data in a specific area to predict surface deformations for that area. The more extensive and accurate the observational data, the higher the accuracy of the predictions. The broader the range of observational data, the more widely applicable the empirical relationship methods are for predicting surface deformations.

2.2. Group of cross-sectional function method

The group of methods involving the section function allows for the determination of vertical displacement at points on a cross-section perpendicular to the direction of the seam based on mathematical equations or descriptive tables of the displacement tank section. This research approach has been developed in many countries because it is relatively easy to use in forecasting and can be studied for application to new geological-mining conditions.

The coefficients in the equations or charts are determined experimentally from field survey data. The complexity of each method in the group depends on the number of factors considered in the geological-mining conditions, which are deemed important. The basic subsidence surface function has a form similar to equation (1) and has a shape as shown in Figure 1.

$$\eta = f(\eta, x, R) \tag{1}$$

This forecasting method can be subdivided into two groups: a group of formulas based on inflection points and a group of functions based on the center points of the mining area [17].

2.3. Group of Impact Function Methods

This method allows for the prediction of deformation at points on the ground surface. It is built on the theory that there is an influence zone surrounding the point to be predicted due to the extraction of an area within the sphere of influence affecting that point. A common assumption is that the influence zone has a circular shape. The hypotheses and scientific methods proposed by Keihorst have been applied and refined by later researchers, including Bals.

The advantage of the impact function method group is that it allows for the estimation of vertical displacement at any point on the ground surface within the influence zone of a mined area with an arbitrary shape. The application can be somewhat complex, and verifying accuracy is challenging. Moreover, drawing influence circles is only accurate in the case of flat-lying seam extraction, so this method is typically applied when extracting flat-lying and gently dipping seams.

2.4. Group of physical model methods

In many countries, small-scale material models representing different mining scenarios have been used for monitoring the vertical displacement process and have achieved varying degrees of success. By combining several materials such as sand, gelatin, a model of the mining panel similar to reality but on a smaller scale is built (Figure 2).

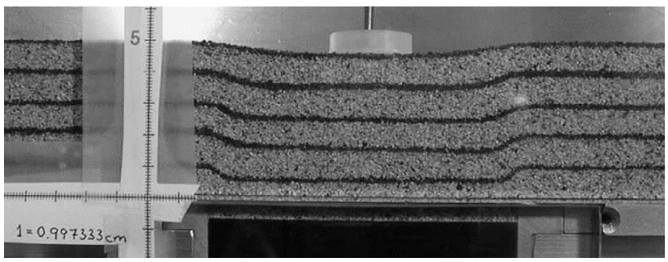

Fig. 2. Physical model made from dry sand [18]
Rys. 2. Model fizyczny wykonany z suchego piasku [18]

The advantage of this forecasting method is its ability to monitor the deformation and collapse mechanisms occurring in the rock and soil. It allows the observation of some characteristics that theoretical models may have difficulty representing. Importantly, this method can be applied to any geological and mining conditions, making it crucial for predicting the formation of displacement basins, especially suitable for studying new mining areas. It is also used as a supportive method alongside other approaches in forecasting surface displacement and deformation. The limitation of this group is the difficulty in constructing a model similar to the actual structure, so it mainly provides relatively qualitative results. Nowadays, thanks to the rapid development of information technology, this group of methods has been significantly improved, providing good efficiency and significantly increasing both qualitative and quantitative reliability.

2.5. Analytical Model Group

These models are based on examining ground displacement according to the laws of random environments, elastic environments, plastic environments, or viscoelastic environments, etc. Solutions from conventional models are typically sets of equations to predict vertical displacement, mainly in two-dimensional space. The finite element method and its variations are widely applied in modeling. Nonlinear analysis is also used to simulate the non-equilibrium state of soil and ground displacement.

A representative example of a random model is Litwiniszyn's research [18]. The author studied the movement of a random environment to explain the ground displacement process caused by mining. The results obtained are mathematical expressions recognized differently from expressions derived based on continuous environmental mechanics. It can be observed that because the random environment contains many factors with different degrees of freedom, solutions cannot be found in classical mechanics. Still, they can be found using other methods. Subsequent studies by the author using experimental models with dry sand confirmed that a random model can be used to study ground displacement processes.

2.6. Group of Impact Function Methods

Representative for the surface subsidence prediction method due to underground mining is the Knothe method, according to Knothe [7]. The relationship between the time parameter and the vertical displacement value can be described by a two-parameter exponential function. One parameter is influenced by geological and mining factors, obtained from observational data, while the other parameter represents the maximum vertical displacement. The formula proposed by Knothe allows predicting the quantity of vertical ground subsidence at a specific time.

However, subsequent studies have shown that the formula proposed by him does not fully describe the vertical displacement process due to mining activities, as the vertical displacement process of a point on the surface undergoes four stages, including the preparatory stage, the onset of displacement, the intense displacement stage, and the concluding stage. Therefore, an additional parameter is incorporated into Knothe's original formula to ensure that the graph accurately represents the entire vertical displacement process of the surface. Other methods have also been applied in forecasting surface deformation over time, such as the Kalman filtering method [15] and artificial neural networks [6], [11].

3. Application of artificial neural networks (ANN)

As mentioned above, forecasting surface displacements and deformations due to underground mining is a crucial task; therefor, new theories and algorithms are applied in forecasting mine displacement and deformation quantities, especially using artificial intelligence applications. Artificial Neural Networks are widely applied in various fields, including scientific forecasting. They have the ability to connect and integrate various parameters to identify and predict phenomena based on the cause-effect principle. Compared to forecasting methods based on formulas and coefficients determined from empirical data, the method of forecasting using artificial neural networks is considered a parameter-free approach and has the ability to forecast for areas with specific geological and topographical characteristics. This is a problem that needs to be addressed and applied in forecasting the displacement quantities due to the influence of mining processes. Forecasting the level of deformation due to mining using artificial neural networks is a modern approach. This method requires actual observational data from mining areas to train the network. However, this can be easily obtained and with much higher accuracy compared to collecting the necessary influencing factors as input for the aforementioned methods.

For many complex problems, to improve accuracy, the hidden layers should be increased, but this will complicate the network structure, increasing the time for training and adjusting the connection weights within the network [19]. According to Jeff Heaton [20], a neural network with two hidden layers can represent functions with any shape, so theoretically, there is no need to use networks with more than two hidden layers. Also, according to this author, problems requiring 2 hidden layers are rarely encountered, and in practice, there is no reason to use more than 1 hidden layer. More than one hid-

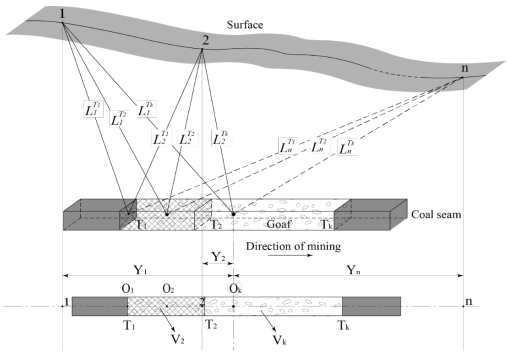

Fig. 3. Input factors of neural networks [1]
Rys. 3. Czynniki wejściowe sieci neuronowych [1]

den layer may be beneficial for some applications, but just one hidden layer is also sufficient [21]. Conversely, if there are too many neurons in the hidden layer, it can lead to issues such as "Overfitting" and long training times. Overfitting is when the output of the network is very accurate with the training set but performs poorly with new data (not in the training set). Recently, Nguyen Quoc Long [1] has researched and analyzed the factors influencing the deformation transfer process on the surface. We observe that the physical properties of soil and rocks will not change over time in the same exploitation area, so they are not chosen as input factors as shown in Figure 3.

4. Discussion

Base on a comprehensive review of the current methods for predicting mining subsidence and their application areas, the research findings can serve as a guide for setting up key requirements for the application of technologies to forecast surface displacement resulting from underground mining. Looking ahead, mineral extraction will continue to be a primary energy source, and forecasting subsurface displacement will remain a critical task in the geospatial industry. This review provides an overview of the current status of surface displacement forecasting, including current forecasting methods and their application scope. The findings reveal that the underground extraction process is highly complex, depending on numerous natural factors and mining technologies, leading to a variety of forecasting methods. Moreover, with the advent of new theories, algorithms, and artificial intelligence, surface displacement forecasting due to underground mining will become more accurate, ensuring safety in mining operations and reducing labor costs.

The discussion on the application of artificial neural networks (ANN) in forecasting surface displacements and deformations due to underground mining is particularly noteworthy. ANN, with its ability to connect and integrate various parameters to identify and predict phenomena based on the cause-effect principle, presents a promising approach to this complex problem. Unlike traditional forecasting methods that rely on formulas and coefficients determined from empirical data, ANN offers a parameter-free approach that can cater to areas with specific geological and topographical characteristics. However, the application of ANN in this context is not without its challenges. For instance, increasing the number of hidden layers to improve accuracy can complicate the network structure and increase the training time. Furthermore, having too many neurons in the hidden layer can lead to issues such as “Overfitting” and long training times. Overfitting is when the output of the network is very accurate with the training set but performs poorly with new data (not in the training set). Despite these challenges, the potential of ANN in forecasting surface displacement due to underground mining cannot be understated. With the continuous advancement of science and technology, it is expected that these challenges will be addressed, and the application of ANN in this field will become more widespread and effective. This will not only ensure safety in mining operations but also contribute to reducing labor costs, thereby making underground mining a more viable and sustainable solution to meet the escalating global energy demand.

The future of underground mining and the associated task of forecasting subsurface displacement looks promising, thanks to the advent of new theories, algorithms, and artificial intelligence. As the world continues to grapple with the escalating energy demand, these advancements will play a crucial role in ensuring the safety and efficiency of underground mining operations.

5. Conclusions

In the future, energy supply will still primarily rely on mineral extraction and forecasting subsurface displacement will remain a crucial task in the geospatial industry. This review provides an overview of the current status of surface displacement forecasting as well as current forecasting methods and their application scope. The obtained findings show that underground extraction process is highly complex, relying on numerous natural factors and mining technologies, leading to diversity in forecasting methods. Besides, with the new theories, algorithms and artificial intelligence, surface displacement forecasting due to underground mining will be more accurate, ensuring safety in mining operations and reducing labor costs.

Acknowledgements

This work was financially supported by Hanoi University of Civil Engineering, Hanoi, Vietnam grant number 01-2023/KHXD-TĐ.

Thanks to the anonymous reviewers and editorial comments for their invaluable comments in the earlier version, which helped us to improve the manuscript's quality.

Conflicts of Interest

The authors declare no conflict of interest.

Literatura – References

1. Long N.Q (2019), PhD thesis, Hanoi University of Miningand Geology (in Vietnamese).
2. Акимов А.Г.и др (1970), "Сдвижениже горных пород при подземной разработке угольных и сланцевых месторождений", "Недра", Москва.
3. Kha V.T, Long N.Q (2011), Research on selecting optimal methods for forecasting the displacement and surface deformation variables affected by the coal mining process in Thong Nhat coal mine., Journal of Mining and Earth Sciences, No. 34 (in Vietnamese).
4. Cui X.M, X.X, M., & J.A, W. (2000). Improved prediction of differential subsidence caused by underground mining. International Journal of Rock Mechanics and Mining Sciences, 37(4), 615-627.
5. Nie Lei, Hongfei, W., Yan, X., & Zechuang, L. (2014). A new prediction model for mining subsidence deformation: the arc tangent function model. Natural Hazards, 75(3), 2185-2198. doi:10.1007/s11069-014-1421-z.
6. Ki-Dong Kim, Lee, S., & Oh, H.-J. (2009). Prediction of ground subsidence in Samcheok City, Korea using artificial neural networks and GIS. Environmental Geology, 61-70.
7. Knothe S (2004), Prognozowanie wpływów eksploatacji górniczej. Wyd.Ślask., Poland.
8. Ambrožič Tomaž, & Goran, T. (2003). Prediction of subsidence due to underground mining by artificial neural networks. Computers & Geosciences, 29(5), 627-637.
9. Zhao Kang, & Si-ni, C. (2011). Study on Artificial Neural Network Method for Ground Subsidence Prediction of Metal Mine. Procedia Earth and Planetary Science, 2, 177-182. doi:10.1016/j.proeps.2011.09.029.
10. Hejmanowski Ryszard, & T., W. W. (2015). Suitability assessment of artificial neural network to approximate surface subsidence due to rock mass drainage. Journal of Sustainable Mining, 14(2), 101-107. doi:10.1016/j.jsm.2015.08.014.
11. Kim Yangkyun, Min, S., Hyun-Koo, M., & Seung-Ah, L. (2017). A study on the development of an artificial neural network model for the prediction of ground subsidence over abandoned mines in Korea. Geosystem Engineering, 20(3), 163-171. doi:10.1080/12269328.2016.1254573.
12. Lee Saro, Inhye, P., & Jong-Kuk, C. (2012). Spatial Prediction of Ground Subsidence Susceptibility Using an Artificial Neural Network. Environmental Management, 49(2), 347-358. doi:10.1007/s00267-011-9766-5.
13. Mahdevari Satar, Kourosh, S., Mostafa, S., & Dwayne, T. (2017). Stability prediction of gate roadways in longwall mining using artificial neural networks. Neural Computing and Applications, 28(11), 3537-3555. doi:10.1007/s00521-016-2263-2.
14. Long N.Q, V.C, M., & B.K, L. (2016). Divergency verification of predicted values and monitored deformation indicators in specific condition of Thong Nhat underground coal mine (Vietnam). Geoinformatica Polonica, 2016(2016)), 15-22.
15. Khanh, P. Q., & Long, N. Q. (2015). Research on the application of the Kalman filter method for predicting vertical surface displacement in mines. Mining Industry Journal, No. 5 (in Vietnamese).
16. Long Quoc Nguyen, Tam Thanh Thi Tam, Trong Gia Nguyen, Dinh Trong Tran (2023). Prediction of underground mine's surface subsidence using a recursive multi-step forecasting model with an Artificial Neural Network. Mining of Mineral Deposits, 17(4), pp 45-52.
17. Reddish D.J, Whittaker B.N (2012), Subsidence: occurrence, prediction and control, Elsevier, England..
18. Vardoulakis I., Graf B., Gudehus G. (1981), "Trap-door problem with dry sand: A statical approach based upon model test kinematics", International Journal for Numerical and Analytical Methods in Geomechanics, 5 (1), 57-78.
19. Zhao Kang, Chen Si-ni (2011), "Study on Artificial Neural Network Method for Ground Subsidence Prediction of Metal Mine", Procedia Earth and Planetary Science, 2, 177-182.
20. Heaton Jeff (2008), Introduction to neural networks with Java, Heaton Research, Inc.
21. Fausett Laurene (1994), Fundamentals of neural networks: architectures, algorithms, and applications, Prentice-Hall, Inc.

Metoda przewidywania osiadań powierzchni spowodowanych eksploatacją podziemną: przegląd

W ostatnich latach nastąpił globalny wzrost zapotrzebowania na energię, a wydobycie podziemnych mineralnych źródeł energii, takich jak węgiel, odgrywa znaczącą rolę w zaopatrzeniu w energię. Jednak wydobycie tych zasobów naturalnych zawsze wiąże się z wieloma wyzwaniami i ryzykiem. W procesie tym powstały duże puste przestrzenie, powodując brak równowagi pierwotnego stanu naprężeń w ziemi i powodując deformacje terenu na powierzchni. Dlatego zapewnieniu skutecznej ekstrakcji muszą towarzyszyć środki bezpieczeństwa. Wśród nich kluczowym zadaniem jest przewidywanie osiadań powierzchni na skutek eksploatacji podziemnej. W artykule przedstawiono przegląd dotychczasowych metod prognozowania osiadań górniczych oraz zakres ich zastosowania. W rezultacie dokonano syntezy różnych metodologii stosowanych w różnych regionach świata. Wreszcie, wyniki tych badań mogą dostarczyć wskazówek do ustalenia zasadniczych wymagań dotyczących stosowania technologii prognozowania przemieszczeń powierzchni w wyniku górnictwa podziemnego.

Słowa kluczowe: *predykcja osiadań, górnictwo podziemne, sztuczne sieci neuronowe*

Research on the Applicability of Polymer Injection Solution with Surfactant Compound for Lower Miocene, Bach Ho Field

Le Quang DUYEN[1)]*, Dinh Duc HUY[2)]

[1)] Hanoi University of Mining and Geology, 18 Vien street, Bac Tu Liem, Hanoi, Vietnam; ORCID https://orcid.org/0000-0001-6953-4762

[2)] Vietnam Petroleum Institute, 167 Trung Kinh Street, Cau Giay, Hanoi, Vietnam

* Corresponding author: lequangduyen@humg.edu.vn

http://doi.org/10.29227/IM-2024-01-92

Submission date: 01-05-2024 | Review date: 31-05-2024

Abstract

Similar to polymers, currently on the market there are many surfactants with reasonable prices and high activity. However, the simultaneous combination of surfactants and polymers in the same mixture has not been thoroughly studied. In this paper, the authors study the applicability of injecting a mixture of surfactants and polymers for Miocene objects in the lower Bach Ho field. The obtained results show that the technique of integrating the surfactant and polymer solution raise swept and sweep effectiveness, consequently increasing the oil recovery coefficient. Based on the simulation model, the recovery factor increased by 10% and the amount of oil increased by 36.6%. Additionally, findings indicated that the efficiency of increasing oil recovery coefficient from chemical injection via the combination of surfactants and polymers at well No. 1215 is much higher than that at well No. 1204. The research results can be used as a reference for studies with the same purpose conducted in areas with similar characteristics to Bach Ho field.

Keywords: *Enhanced Oil Recovery, injection of polymer solution, surfactants*

1. Introduction

Polymer injection is actually mixing a small amount of polymer into the injection water to increase the viscosity of water, reducing the mobility of the oil-pushing-phase in the reservoir. The polymer mixture, in addition to the ability to operate in high temperature and high pressure environment, also needs to be able to withstand water with great salinity and less adsorption on the rock surface. Currently, there are a number of polymers on the market that meet those extreme requirements and are easily available for purchase in industrial applications. Injection surfactant is essentially mixing a quantity of surfactant into water and injected into the reservoir, when contact with oil and water is made, the surfactant will reduce the interfacial tension between the two immiscible phases, so the trapped oil molecules can easily flow and escape from the holes or throat of pores to the extraction well.

According to recent estimations of Vietnam Government as well as Vietnam Petroleum Institute – VPI, productivity in crude oil and natural gas production of major fields in Vietnam will be less than 2 million tons per year by 2030. Additionlly, oil reserves of recently discovered reservoirs are moderate; most of these reservoirs are small and classified as marginal oil fields. Recently, many studies have been focussing on increasing the oil recovery factor of existing fields. In reality, oil production from Miocene layers accounts for 40% of the total yield of Bach Ho field, however, decline in oil production rate is considerably high with the decline rate of 12% per year. Thus, conducting research on the application of tertiary recovery solutions for the Miocene layer is imperative. Recently, several research works have been carried out to achieve this purpose [1, 2], in which the use of polymer chemicals and sufactants was found to be increase the propulsion coefficient and separate oil sweep, other studies have tried to combine these two kind of chemical elements for similar purpose [3]. In addition, [4] perform a review to study on polymeric surfactants for enhanced oil recovery. A summary of recent research in the literature that provides light on the characteristics, workings, and uses of polymeric surfactants in relation to enhanced hydrocarbon recovery is given in this review. Besides, [5] investigation on the effectiveness of surfactant/polymer flooding at Kumkol Oil Field to improve oil recovery through experimentation. The results indicate that while the polymer injection increases the sweeping front's efficiency, the polymer injection and polymer-surfactant-mixture slug can successfully replace the leftover oil. In order to improve oil recovery, [6] conducted a study on surfactant-polymer flooding and oil field surfactant. Using surfactant and surfactant-polymer slug, a series of flooding tests have been carried out in the present study to examine the increased oil recovery following water flooding. Similarly, [7] presented a new simulator for mixed surfactant/polymer flooding in the enhanced oil recovery processes. Findings showed that the interfacial, rheological, and adsorption rates of the polymer and surfactant are all influenced by each other. According to [8], one attempt to enhance oil recovery in oil reservoirs following the primary and secondary recovery phases is to use the enhanced oil recovery (EOR) approach. EOR screening based on reservoir rock and fluid 'N' parameters shows that alkali surfactant polymer (ASP) injection is the best approach. The laboratory test findings to improve the oil recovery in reservoir 'N' using ASP injection are presented in this study. According to [9], in order to reduce interfacial tension and promote oil recovery at the pore level during a soil decontamination or enhanced oil recovery procedure, a

Tab. 1. Physical properties of rock samples in Mioxen layer

Tab 1. Właściwości fizyczne próbek skał w warstwie Mioxen

Description	Unit	Value
Open porosity	%	16,92
Density of stone frame	g/cm^3	2,66
Air permeability	mD	162
Residual water saturation	%	50,7
Compressibilty	10^{-4} MPa	2,11

Tab. 2. Average values of main parameters of Lower Miocene oil

Tab. 2. Średnie wartości głównych parametrów ropy Dolnego Miocenu

Description	Unit	Northern Dome	Central Dome	South Dome
Saturation pressure	MPa	20.42	14.06	8.94
Gas content	m^3/t	141.4	95.14	42.7
Volume coefficient		1.399	1.3	1.149
Viscosity under seam condition	cP	1.074	1.76	4.879
Density in seam condition	kg/m^3	710.2	741.9	814.8
Separation oil density	kg/m^3	865.3	865.2	884.1

surfactant solution must first be injected. This is followed by the injection of a polymer solution to prevent the formation of preferential pathways and to conduct a uniform sweep of the reservoir. Thus, they conducted research on Polymer Surfactant Interactions in oil enhanced recovery processes. The results indicated that utilizing interacting polymer and surfactant systems can sometimes even be beneficial for oil recovery. In another study, the relationship between surfactant and polymer in aqueous solutions for chemically improved oil recovery was analyzed [10]. They confirmed that in EOR, polymer-surfactant partners are screened primarily by their interaction with the polymer. Additionally, research into polymeric surfactants for improved oil recovery, impact of surfactants in surfactant-polymer flooding on crude oil emulsion stability was presented in [11]. The findings showed that the two types of surfactants—petroleum sulfonate and anionic-nonionic composite surfactant—can both raise the surface potential of the oil droplets scattered in the O/W emulsion and reduce the interfacial tension between the oil phase and the aqueous phase, which can improve the stability of the W/O and O/W crude oil emulsions.

In addition to studying relationship between the polymer and surfactants, [12] found the best surfactant for EOR polymer injectivity. Good injectivities are guaranteed by this surfactant under a variety of circumstances. It offers value to polymer flooding projects as the surfactant that is more advantageous commercially. Moreover, [13] performed a study on surfactant-enhanced stimulation technology for polymer-injection wells. Lab test shows that the best results are obtained by using a flooding method that involves injecting an oxidant slug, a surfactant slug, and finally polymer flooding (the permeability to polymer fluid is improved by around 120%).

In Bach Ho field, there are some studies conducted in Lower Miocene reservoir. While [14] implemented seismic attribute analysis in Lower Miocene reservoir, [15] applied surfactant solution for lower oligocene formation, White Tiger field. Additionally, Giang et al. (2021) assesses the variables affecting the flooding process and suggests using a surfactant-polymer chemical flooding solution for the Lower Miocene formation of Bach Ho field South Block. Besides, an effective experimental use of the complex combination surfactant polymer VPI SP to improve oil recovery factor in the Bach Ho field during the Lower Miocene was presented in [16].

Nevertheless, suggested technique is still relatively novel to oil and gas industry, which brings about difficulties in chosing applicable methods to reach the optimun oil recovery factor, especially when using both polymer chemical and sufactants. This current paper presents studies on the suitability of surfactant-compound-infused polymer injection solution for lower Miocene Bach Ho field. The results of study can be used as as reference for research in areas with similar characteristics to Bach Ho field.

2. Properties of reservoir rock and lower Miocene fluid of Bach Ho mine

2.1 The petrographic-sedimentary characteristics of the rocks containing the Lower Miocene

In oder to examine the geotechnical characteristic of samples in Bach Ho field, 601.9m whole core was taken with 92.4% recovery of total lenght from 23 wells. All of these samples were located in the lower Miocene layer of Bach Ho field. Based on these core samples, the lithology and reservoir characteristic were studied. The laboratory analysis showed that the reservoir consistsing of sandstone, siltstone, sandy gravel with loose to medium dense.

Six sedimentary samples of Miocene layer taken from the lower wells namely BH-1203 were analyzed using X-ray method to determine 5 primary chemical components. The kaolinite content in clay minerals of lower Miocene layer ranges from 3.8% to 31.8%, average value of 17.33%; Chlorite content is from 3.8–12.4%, average of 7.53%. The ilite content is from 4.1–16.4%, the average is 10.58%; content of momtmorilonite 41–84.1%, the average of 60.93%; content of other minerals is 0.5–8%, average 3.82%. The laboratory analysis results that the primary element of clay samples located in the BH-1203 is momtmorilonite element (accounting for ~61%), followed by kaolinite (~17.1%), and the remaining minerals accounting for 21, 9%.

2.2 Physical characteristics of rocks containing the Lower Miocene

Lower Miocene reservoirs developed in the entire field, primarily in the north and central areas. The thickness of this reservoir varies between 11.6 and 576.6 m, with a northern average of 30.4 m. The lower Miocene has good quality (permeability = 0.1 - 2000 mD, porosity varying from 15.3÷22.9%) [17]. The author took samples of the lower Miocene layer in

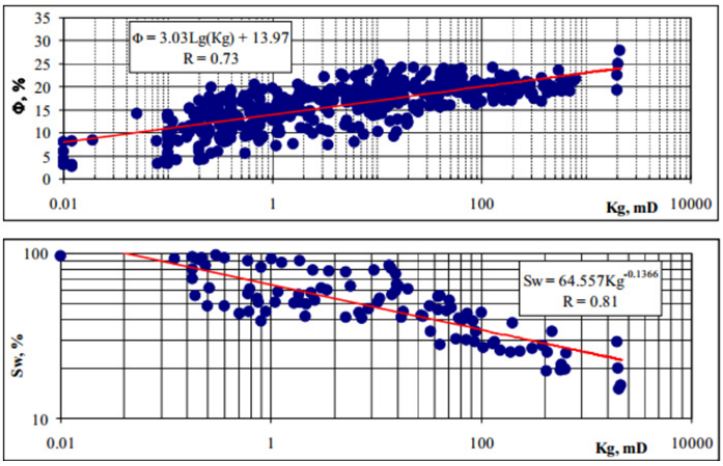

Fig. 1. The petrographic–physics relationships of rocks containing Lower Miocene, Northern dome of Bach Ho field
Rys. 1. Zależności petrograficzno-fizyczne skał zawierających Dolny Miocen, północną kopułę pola Bach Ho

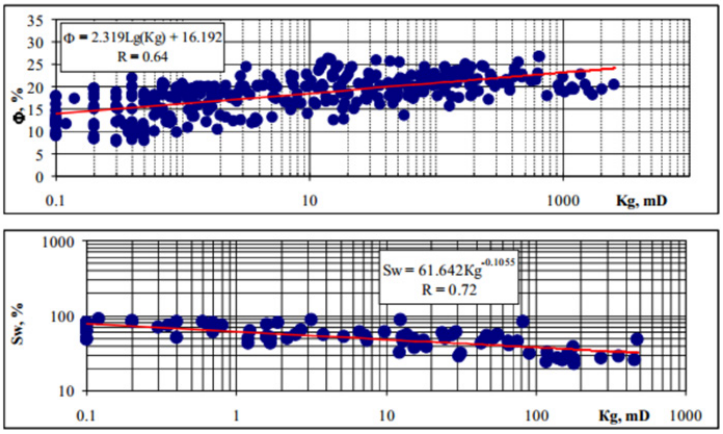

Fig. 2. The petrological relationships of the rocks containing the Lower Miocene, the central arch of the Bach Ho field
Rys. 2. Powiązania petrologiczne skał zawierających Dolny Miocen, centralny łuk pola Bach Ho

the Northern dome and the Central arch of the Bach Ho field to perform experiments to determine physical characteristics. Sampling complies with the procedures and regulations of the Ministry of Natural Resources and Environment. The physical properties of the sediment samples were analyzed based on experimental results of all samples taken from the lower Miocene stratum. The study analyzed sample characteristics including open porosity, density of stone frame, air permeability, residual water saturation, and compressibility. From the analysis results, the average value of the rock properties of the Miocene reservoir was determined (Table 1). In addition, the petrographic-physical relationship of the Lower Miocene reservoir rocks, the Northern dome and the Central arch of Bach Ho field were also determined through the above experiments. The petrographic-physical correlations of the Miocene are shown in Figure 1 and Figure 2.

2.3 Oil properties in reservoir condition

The accurately identification of the oil properties at the reservoir conditions have always been concerned with many experts in the field of oil industry. The correct recognition of these features results in the advancement of reservoir layers and enhances their performance. Reservoir-fluid characteristics are important in the designing and optimizing injection/production plans and surface facilities for effective reservoir management [18]. Therefore, in this study, 12 bottom hole oil samples were used to analyze the oil properties of Miocene reservoir seam including parameters: saturation pressure, gas content, volume coefficient, viscosity under seam condition, density in seam condition, and separation oil density. Analysis results show that the North crest has the highest saturation pressure (20.42 MPa) and the lowest viscosity (1.074 cP), meanwhile the South crest has the lowest saturation pressure (8.94 MPa) and highest viscosity (4.879 cP). The primary parameters of low Miocene reservoir seam oil for all three crests are shown in Table 2.

2.4 Characteristics of water beds in the Lower Miocene

Water in Miocene reservoir is characterized by weak acidic and weak alkali; medium and low mineralization, varying from 3,245–10,911 g/l in the North crest to 13,002–17,721 g/l in the Central crest, and reaching 27,524–30,408 g/l in the South crest (Table 3). From North to South of Bach Ho field, the mineralization of seam water gradually increases, and also the characteristic of water changes from sodium-bicarbonate to calcium chloride.

According to finding from previous publications [19], the water in Miocene layer is characterized by low content of sulphate and magnesium, varying between 25–413 mg/l and 1–88 mg/l, respectively. It is also found that the bicarbonate

Tab. 3. Water parameters of Miocene reservoir at Bach Ho field in reservoir condition

Tab 3. Parametry wody zbiornika mioceńskiego w polu Bach Ho w stanie zbiornikowym

Description	Central Dome		Northern Dome	
	Floor 23	Floor 24	Floor 23	Floor 24
Water gas ratio,m^3t.c/ton	3.153	3.245	3.376	3.446
Volume coefficient, unit part	1.0442	1.0454	1.0453	1.046
Viscosity, cP	0.255	0.255	0.265	0.265

Tab. 4 Laboratory results of matrix experiment for evaluation Polymer-Surfactant solution

Tab 4. Wyniki laboratoryjne doświadczenia matrycowego do oceny roztworu polimer-surfaktant

Test	Surfactant	Polymer	Lab procedure and results
Tolerance with sea water and formation water (salinity 25-35 g/liter)	√	√	Unprecipitate, stable properties and steady concentration
Stable at high tempeature (90-110°C)	√	√	Unprecipitate, stable properties and steady concentration
Reduce interfacial tension (IFT)	√		Interfacial tension of oil-water-chemical system less than 0.01 dynes/cm (IFT < 0.1 dynes/cm)
Stable viscosity		√	Viscosity > 10 cP
Improve recovery factor	√	√	Incremental of oil produced at outlet

content decreases from North to South direction, however, the calcium content gradually increased from several tens of mg/l up to thousands mg/l, and reaching 2,515 mg/l in the south (BH-7).

The bromine and iodine content are found relatively high, meanwhile the ammonia, phenol and naphthenic acid content is low value. One key noted that calcium and magnesium effect to the ability of chemical.

During the producing time, many different measures have been carried out such as seawater injection to maintain reservoir pressureand near-bottomhole treatment. This leads to the physical and chemical properties as well as the composition of ion-water is significantly altered. Besides, on the way reaching oil well, the injected water has interacted with the rock, seam-water and ion exchange taking place. As a result of this process, the calcium content of the water increases, and the content of magnesium, sulphate, bicarbonate and sodium decreases. It is implied that after the appearance of injected water at the extraction wells, the Miocene associated water changed properties, and becomes calcium chloride (XK) water.

3. Advanced mechanism for oil recovery when injecting surfactant and polymer combination

The adsorption of molecules of "Miocene" compound from the inside of the solution to the interface taking place with any concentration of "Surfactant" compound. As the concentration of Surfactant compound goes up, the concentration of surfactant at the interface also increases. When the concentration of Surfactant compound reaches a certain value, the aggregation of Surfactant compound is occurred inside of the solution, this process leads to dramatic change in the physical properties of the solution and the concentration of the solution is called the critical Micelle concentration (CMC). This group of elements is called as Micelle. This solution has a lower surface tension in comparison to that of oil phase, so it increases the mobility of oil trapped in the reservoir. Due to this effect, trapped oil could expel from pore throat and continue flowing into the well bore. Besides, the existence of Polymer chemical could control the mobility of Micelle solution and effectively impel the Micelle solution. As the Polymer solution is constantly injected, the viscosity of Polymer solution increase and able to prevent the dispersion of water penetrating the oil zone. This technique provides a high efficiency of oil recovery due to the simultaneous improvement of the sweeping and repel oil. The simulation results of Liaohe oil seam by Wu Wenxiang., etc (2014) [20] indicated the efficiency as injecting a combination of 0.3% of Surfactant and 1500 mg/l polymer with a molecular weight (MW) of 19 MDa could achieve a value of 30%.

4. Research on mixed injection in the laboratory to predict the results applied to the Ha Miocene, Bach Ho mine

4.1 Research on oil propulsion on reservoir physical model.

Firstly, dodecyl benzene sulfonate was neutralized by caustic soda to obtain sodium 2-dodecylbenzene sulfonate (SDBS). High concentration surfactant solution preparation was conducted. In order to prepare the main surfactant solution, a cup with magnetic stirrer bar was put on a magnetic stirrer. Water was poured into the cup and the stirrer was turned on. After that, AOS, sodium 2-dodecylbenzene sulfonate and isopropanol were added one by one and mixed about 2 hours until clear and homogeneous yellow solution appeared. Subsequently thiourea was added and stirred well until homogeneous and clear solution.

Aiming at evaluating the efficiency of improving oil recovery by using polymer injection solution with Surfactant solution, a simulation model for the Miocene object was built and simulated with a series of sensitivity assessments (Table 4). The primary basis of modelling work is based on performance of adjusted technology using for Bach Ho field along with the updates on the current state of exploitation to the end of 2018. Besides, the results from laboratory test of a combination of polymer and surfactant solution were also utilized as input parameters for the evaluation of oil sweep efficiency in the oil field.

Core flood are conducted on 02 set to evaluate the ability of solution chemical are shown in Figure 3 and Figure 4. Before core flooding test, all physical properties of the chemical are satisfied. The first core set is conducted with 02 stage chemical injection separately. The result showed that using compound solution polymer surfactant is more beneficial recovery than individual. The second core set was injected with complex solution SP after water flooded with no oil appeared at outlet.

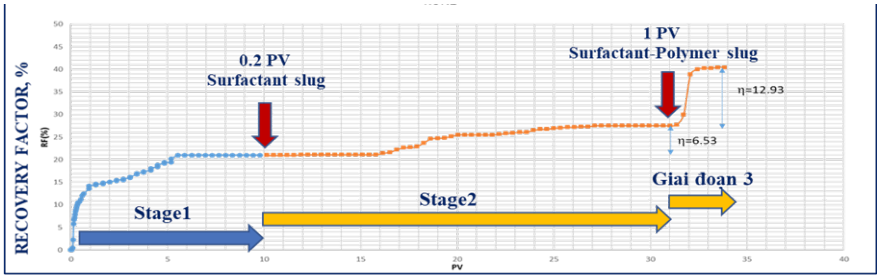

Fig. 3. Core flooding results of the first set core plug

Rys. 3. Wyniki pierwszego zalania rdzenia

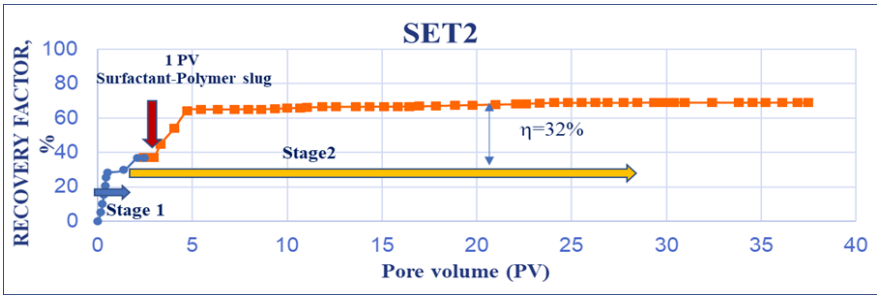

Fig. 4. Core flooding results of the second core plug set

Rys. 4. Wyniki drugiego zalania rdzenia

Set1: Process of 3-stage injection into core samples:

- Stage 1: Inject 10 PV of injection water through the core sample;
- Stage 2: Inject 0.2 PV Surfactant (concentration 20000ppm) through the sample.
- Stage 3: Inject 1 PV solution SP to increase oil recovery (20000ppm surfactant + 5000ppm polymer). Continue inject water to increase oil recovery.

Set2: Process of 2-stage injection into core samples

- Stage 1: Inject 3.5 PV of injection water through the core;
- Stage 2: Inject 1 PV solution SP to increase oil recovery (20000ppm surfactant + 5000ppm polymer). Continue inject water to increase oil recovery.

The results of increased oil recovery on fluid samples and core samples of lower Miocene when injecting show that the injection method of polymer + SURFACTANT mixture can be applied to the research object.

4.2. Research on oil propulsion on reservoir simulation model

Based on the analysis of geological characteristics, the properties of rock-fluid interactions, and the current state of exploitation. The South dome, specifically the BK-14/16 region, was selected as the primary input for the model due to its unique geological features and current exploitation status. This decision was made after a thorough examination of the geological characteristics of the area, including the composition and structure of the rocks, and the properties of the fluids they contain.

The simulation model constructed for this study is quite comprehensive, consisting of more than 400,000 active cells. This high number of active cells allows for a detailed and accurate representation of the geological structure of the South dome are shown in Figures 5. The model also includes a total of 27 flowing wells, providing a realistic depiction of the oil extraction process. Of these wells, 23 are production wells, which are primarily responsible for extracting oil, while the remaining four are injection wells, used for injecting substances to aid in oil recovery.

The simulation model provides an updated production history of the Miocene object until the end of March 2020. This update is crucial as it allows for the tracking of changes in production over time, providing valuable insights into the efficiency and effectiveness of the oil extraction process. Remarkably, the model shows a high degree of accuracy, with a total match of over 90% of wells. This high match percentage indicates that the model accurately represents the real-world conditions of the wells, further validating its reliability and effectiveness.

This data was used to design parameters for a test reagent system, which are set out in Table 5. These parameters were carefully designed based on the test program data to ensure the effectiveness of the reagent system. The reagent system plays a crucial role in the oil extraction process, and the careful design of its parameters is essential for optimizing oil recovery. Therefore, Table 5 is an important component of the study, providing detailed information on the designed parameters of the test reagent system.

Given the logistical imperatives and the infrastructural constraints specific to the pilot area, it becomes evident that judiciously administering a minute quantity of chemical agents during brief and targeted injection intervals into the injector wells is a prudent course of action. The empirical evidence corroborating this approach is succinctly summarized in Table 6, which meticulously outlines the observed enhancements in oil production for the two wells, namely 1203 and 1203B. To facilitate comprehensive pumping tests, we deliberately opted for a subset of wells strategically situated within

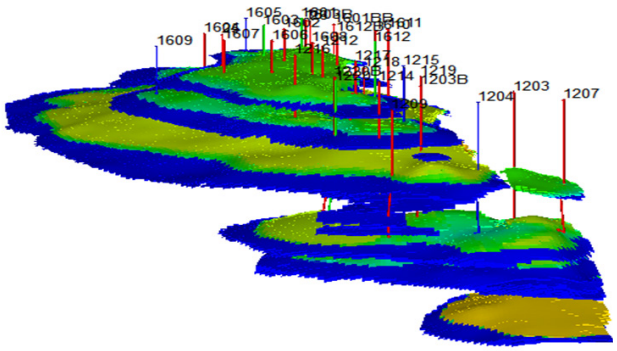

Fig. 5. Simulation model of Lower Miocen, Southern dome, field Bach Ho
Rys. 5. Model symulacyjny Dolny Miocen, kopuła południowa, pole Bach Ho

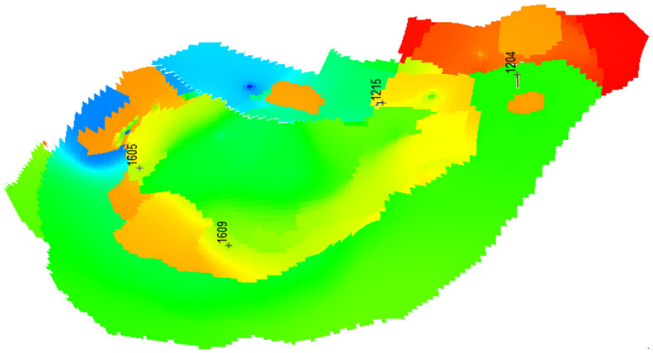

Fig. 6. Location of injection wells on the simulation model of Lower Miocen, Southern dome, Bach Ho field
Rys 6. Lokalizacja odwiertów zatłaczających na modelu symulacyjnym złoża Dolny Miocen, kopuła południowa w polu Bacha Ho

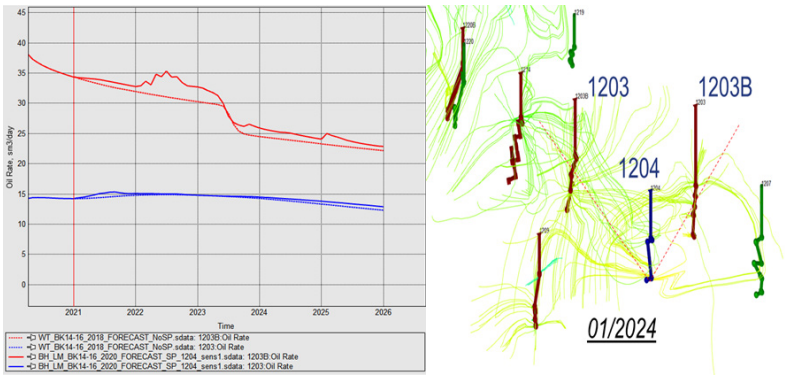

Fig. 7. Increased efficiency of oil recovery from the pump well 2014 to 2024
Rys. 7. Zwiększona efektywność wydobycia ropy z odwiertu pompowego w latach 2014–2024

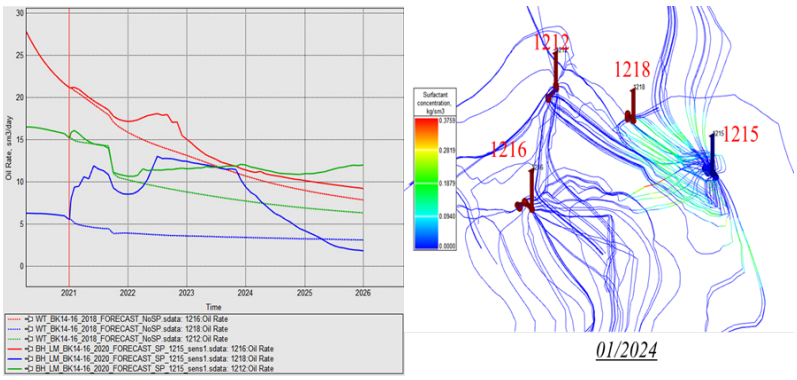

Fig. 7. Increased efficiency of oil recovery from the pump well 2014 to 2024
Rys. 7. Zwiększona efektywność wydobycia ropy z odwiertu pompowego w latach 2014–2024

Tab. 5. Parameters for the experimental chemical system

Tab. 5. Parametry doświadczalnego systemu chemicznego

Viscosity of complex solution SP		**Adsorption of chemical**		**IFT**	
concentration of polymer, kg/sm^3	Viscosity of solution, cP	Concentration of polymer, kg/sm^3	Adsorp chemical, kg/kg	Concentration, kg/sm^3	IFT, mN/m
0	1	0	0	0	26.3
2	5.3	0.0003	0	0.01	0.1
3	7.2	2.5	0.00012	0.1	0.05
4	12.5	9.5	0.00025	1	0.01

Tab. 6. Increase production oil of 2 well 1203 1203B

Tab 6. Zwiększenie wydobycia ropy z 2 odwiertów 1203 i 1203B

	Natural flowing (well: 1203 1203B)				Inject SP complex to 1215 well, Observe area (wells: 1212 1216 1218)			
	Applied SP	Water injection	Incremental in comparison with natural flow		Applied SP	Water injection	Incremental comparison with natural flow	
	th.tons	th.tons	th.tons	th.tons	th.tons	th.tons	th.tons	%
1st year	14.4	14.0	0.3	2.4	12.7	10.8	1.9	17.7
2nd year	28.7	27.6	1.1	4.1	24.5	18.9	5.6	29.5
3th year	41.6	40.0	1.5	3.8	35.2	25.9	9.3	35.8
4th year	**53.1**	**51.2**	**1.9**	**3.8**	**43.7**	**32.0**	**11.7**	**36.6**

the southern perimeter of the Bach Ho field. These selected wells were subsequently subjected to rigorous pumping simulations, the results of which are meticulously documented in Figure 6, providing valuable insights into the hydrodynamic behavior and reservoir response within this geologically significant context.

In the course of conducting rigorous simulation tests on a carefully selected subset of wells, the empirical evidence presented in Figures 7, 8, and 9 unequivocally substantiates the efficacy of implementing targeted strategies aimed at augmenting oil recovery over the ten-year period spanning from 2015 to 2024. These illustrative figures serve as compelling visual proof, demonstrating that the adoption of such measures represents a judicious and well-founded approach to enhancing the overall oil extraction performance within the geologically significant lower Miocene Bach Ho field. The implications of these findings are far-reaching, as they underscore the strategic importance of optimizing oil production in this specific geological context, thereby contributing to the sustainable management of hydrocarbon resources in the region.

5. Conclusion

The research presented in this paper has demonstrated the significant potential of a combined surfactant and polymer solution in enhancing oil recovery. The study focused on the Miocene objects in the lower Bach Ho field, an area that has not been extensively explored in previous studies. Our findings reveal that the integration of surfactants and polymers in a single solution can effectively increase both the sweep and swept efficiencies, leading to a substantial improvement in the oil recovery coefficient. The simulation model used in our study further substantiates this, showing a 10% increase in the recovery factor and a 36.6% increase in the amount of oil recovered. A noteworthy observation from our research is the differential impact of the chemical injection at different wells. Specifically, well No. 1215 exhibited a significantly higher efficiency in increasing the oil recovery coefficient compared to well No. 1204. This suggests that the effectiveness of the combined surfactant and polymer solution may vary depending on the specific characteristics of the well. this study provides compelling evidence for the practical applicability of a combined surfactant and polymer solution in enhancing oil recovery. These findings could serve as a valuable reference for future studies aiming to optimize oil recovery in areas with similar characteristics to the Bach Ho field. However, further research is needed to fully understand the factors influencing the effectiveness of this approach at different wells.

Literatura – References

1. Firozjaii, A. and H. Saghafi, Review on chemical enhanced oil recovery using polymer flooding: fundamentals, experimental and numerical simulation, Petroleum 6 (2): 115–122, ISSN 2405-6561. 2020, DOI.
2. Massarweh, O. and A.S. Abushaikha, The use of surfactants in enhanced oil recovery: A review of recent advances. Energy Reports, 2020. 6: p. 3150-3178.
3. Raffa, P., A.A. Broekhuis, and F. Picchioni, Polymeric surfactants for enhanced oil recovery: A review. Journal of petroleum science and engineering, 2016. 145: p. 723-733.
4. Afolabi, F., et al., Polymeric surfactants for enhanced oil recovery: A review of recent progress. Journal of Petroleum Science and Engineering, 2022. 208: p. 109358.
5. Zhao, L., et al., Experimental study on the evaluation of surfactant/polymer flooding for enhancing oil recovery in Kumkol Oil Field. Journal of Petroleum Exploration and Production Technology, 2023. 13(3): p. 853-864.
6. Samanta, A., et al., Surfactant and surfactant-polymer flooding for enhanced oil recovery. Advances in Petroleum Exploration and Development, 2011. 2(1): p. 13-18.
7. Druetta, P. and F. Picchioni, Surfactant-polymer interactions in a combined enhanced oil recovery flooding. Energies, 2020. 13(24): p. 6520.
8. Tobing, E.M. and H. Ani, Study of Enhanced Oil Recovery with Alkaline Surfactant Polymer Injection Method by Using Laboratory Test. Scientific Contributions Oil and Gas, 2014. 37(3): p. 175-184.
9. Hamouma, M., et al., Polymer surfactant interactions in oil enhanced recovery processes. Energy & Fuels, 2021. 35(11): p. 9312-9321.
10. Kothencz, R., et al., Analysis of the interaction between polymer and surfactant in aqueous solutions for chemical-enhanced oil recovery. Particulate Science and Technology, 2018. 36(7): p. 887-890.
11. Dong, Z., et al., Influence of surfactants used in surfactant-polymer flooding on the stability of Gudong crude oil emulsion. Petroleum Science, 2010. 7: p. 263-267.
12. Gerlach, B., et al. Best surfactant for EOR polymer injectivity. in SPE Kuwait Oil and Gas Show and Conference. 2019. SPE.
13. Wang, Y., et al. Surfactant-enhanced stimulation technology for polymer-injection wells. in International Petroleum Technology Conference. 2005. IPTC.
14. Nguyen, H.M., et al., Application of seismic attribute analysis in Lower Miocene reservoir characterization, northeast Bach Ho field, Vietnam. Journal of Mining and Earth Sciences Vol, 2021. 62(6): p. 14-22.
15. Pham, T.H., et al., Application of Surfactant Solution for Lower Oligocene Formation, White Tiger Field. SPE Production & Operations, 2021. 36(04): p. 816-824.
16. Dinh, D.H., et al., A successful pilot application of the complex mixture surfactant polymer VPI SP to enhance oil recovery factor for the Lower Miocene, Bach Ho field. Petrovietnam Journal, 2022. 10: p. 19-27.
17. Nguyen, X.T., Reservoir modeling on the basis of seismic attributes and wireline logs analyses in Miocene formation of White Tiger oilfield (Cuu Long basin). Summary of Ph.D thesis. Hanoi Univeristy of Mining and Geology, Hanoi, Vietnam., 2011.
18. Al-Obaidi, S.H., A. Patkin, and N. Guliaeva, Advance use for the NMR relaxometry to investigate reservoir rocks. 2020.
19. Hai, N.H., et al., Selection of drilling fluid system for wells with high co2 content in Song Hong basin. Petroleum magazine, 2022. 5: p. 10-18.
20. Wu Wenxiang Study on Physical Simulation of Polymer Flooding System in the Block of Liaohe Oilfield Applied Mechanics and Materials (Volume 700) P 607-611.

Badania nad przydatnością roztworu wtryskiwania polimeru ze związkiem powierzchniowo czynnym dla Dolnego Miocenu, pole Bach Ho

Podobnie jak w przypadku polimerów, na rynku dostępnych jest wiele środków powierzchniowo czynnych o rozsądnych cenach i wysokiej aktywności. Niemniej jednak, jednoczesne połączenie surfaktantów i polimerów w tej samej mieszaninie nie zostało dokładnie zbadane. W niniejszej pracy autorzy badają możliwość wstrzykiwania mieszaniny surfaktantów i polimerów w celu zwiększenia wydajności wydobycia ropy na obiektach miocenu w dolnym polu Bach Ho. Uzyskane wyniki wskazują, że technika integrowania roztworu surfaktantu i polimeru zwiększa efektywność przepłukiwania i oczyszczania, co w konsekwencji prowadzi do wzrostu współczynnika odzysku ropy. Na podstawie modelu symulacyjnego wskaźnik odzysku wzrósł o 10%, a ilość wydobywanej ropy zwiększyła się o 36,6%. Ponadto wyniki badań wskazują, że efektywność zwiększania współczynnika odzysku ropy poprzez wstrzykiwanie chemiczne za pomocą połączenia surfaktantów i polimerów w odwiertach nr 1215 jest znacznie wyższa niż w odwiertach nr 1204. Wyniki tych badań mogą stanowić punkt odniesienia dla prac o podobnym celu prowadzonych w obszarach o podobnych cechach geologicznych jak pole Bach Ho.

Słowa kluczowe: *zwiększony odzysk ropy, wtrysk roztworu polimeru, środki powierzchniowo czynne*

Application of Terrestrial Laser Scanning and Global Navigation Satellite System in the Mining Area

Van Chung PHAM[1)], Tomasz LIPECKI[2)], Ngoc Dung VO[3)], Stanisław PIETRZYK[4)]*

[1)] Faculty of Geomatics and Land Administration, Hanoi University of Mining and Geology, Hanoi, Vietnam; ORCID https://orcid.org/0000-0002-6446-7860; * Corresponding author: phamvanchung@humg.edu.vn
[2)] Faculty of Geo-Data Sciences, Geodesy and Environmental Engineering, AGH University of Kraków, Poland; ORCID https://orcid.org/0000-0002-3204-7343
[3)] Faculty of Geomatics and Land Administration, Hanoi University of Mining and Geology, Hanoi, Vietnam; ORCID https://orcid.org/0000-0003-4095-3992
[4)] AGH; ORCID https://orcid.org/0000-0002-2240-3332

http://doi.org/10.29227/IM-2024-01-93

Submission date: 14-05-2024 | Review date: 07-06-2024

Abstract

Terrestrial Laser Scanning and Global Navigation Satellite System technologies are increasingly prevalent in geodetic mapping work, playing a significant role in mine surveying tasks such as drawing maps for volume calculation, monitoring displacement, and deformation of mine surfaces and structures above mine tunnels. Currently, there are many studies on the application of these technologies in various aspects of mine surveying work. This paper will synthesize these studies to evaluate the effectiveness of applying GNSS and TLS technologies in mining surveying. The authors has reviewed 44 papers/projects in recent years and found that these technologies are developing rapidly, with the accuracy of coordinate and altitude measurement increasingly improving to approximately millimeters in both horizontal and vertical directions.

Keywords: *Terrestrial Laser Scanning, Global Navigation Satellite System, mine mapping, displacement, deformation, subsidence, open-pit mine, mining*

1. Introduction

Surveying to establish maps, update terrain, and serve blasting in open-pit mines is a daily task. In addition, surface deformation monitoring due to mining impacts is also carried out on a monthly, quarterly, or annual cycle. Currently, terrain surveying work serving the above purposes mainly uses TLS and GNSS equipment, the advantages of these technologies are high accuracy up to millimeters, reducing fieldwork time compared to measurement with electronic total stations. Currently, there are many advanced GNSS and TLS devices capable of measuring coordinates and elevation with high accuracy, such as Trimble R8 GNSS/RTK dual frequency.

GNSS stands as one of the most sophisticated technological instruments in today's world. The advent of contemporary satellite positioning systems has led to the widespread application of GNSS technologies such as COMPASS, GPS, GLONASS, and GALLIEO in fields like spatial information science, military operations, transportation, and resource exploration [1]. Several reviews have been conducted to date on the topic of surface deformation determination due to mining. In the research [2], authors offers a comparative analysis of diverse methodologies employed to assess subsidence related to mining. The results obtained indicate that over the past two decades, the primary techniques for detecting and measuring land subsidence incidents have included GIS and remote sensing, Light Detection and Ranging (LiDAR), and Differential Interferometric Synthetic Aperture Radar (DiNSAR). In a similar vein, authors discuss surface displacement measurement techniques used at underground mining sites, drawing on a comprehensive review of a substantial body of scientific literature and relating these to geodetic and remote sensing approaches [3]. [4] undertakes an analysis of a considerable number of research publications on the mapping and assessment of mining-induced subsidence using geographic information systems, while [5] provides an overview of techniques for monitoring, calculating, and simulating ground subsidence caused by coal mining. Also contributing to the review of displacement determination methods, [6] endorses the perspective that InSAR is an effective and sufficiently precise method for tracking ground displacements triggered by mining-induced earthquakes. Furthermore, from a subsidence management viewpoint, [7] proposes recommendations and methodologies to enhance the existing mine stability evaluation methodologies.

An innovative advancement in the collection of spatial information data is the terrestrial laser scanner (TLS). This cutting-edge technology enables the capture of data with a level of precision and accuracy that was previously unimaginable [8].. When compared to traditional measurement methods, TLS technology offers a significantly faster means of acquiring three-dimensional (3D) point information. According to [9], 3D data can be gathered rapidly, efficiently, with high precision, and in great detail using TLS. The term "point clouds" is used to describe the sets of data points that are acquired through this process [10]. Owing to its precision, reliability, and efficiency, TLS technology has become an invaluable tool for a diverse range of applications. These include evaluating various tunnel characteristics [11], mapping building surfaces [12], civil engineering projects [13], 3D surveying tasks [14], and activities within the architecture, engineering, and con-

Fig. 1. Modern GNSS and TLS equipments. Source: (left) https://ts-geosystems.com/product/trimble-r8-rtk-gps/ and (right) https://ajhsurveyors.com/wp-content/uploads/2020/11/2-3.jpg

Rys. 1. Nowoczesne urządzenia GNSS (lewa) and TLS (prawa)

struction industries [15]. Additionally, it is applied in fields such as geology [16], engineering geodesy [17] and deformation and displacement monitoring [18]. Furthermore, the key features of 3D laser scanning technology — its high precision, rapid speed, and close proximity to the prototype — make it extensively used across various mapping and other sectors. This technology provides a comprehensive and highly accurate reconstruction scan that can be accessed physically and quickly [19]. Beyond these applications, TLS is recognized as an exceptional technology with potential uses in numerous other fields, including the mining sector. Within this domain, it can be applied in many publications for mining management [20] and is capable of performing various operations in both underground [8] and open-pit mining environments [9].

It can be observed that studies on the application of GNSS and TLS in open-pit mining have been relatively extensive, covering a diverse range of topics. These studies encompass the use of these technologies in mapping, supporting drilling and blasting operations, monitoring surface displacement and deformation, and environmental fluctuation surveillance. This research aims to catalog the projects that have been implemented to date and, based on this review, propose new research directions for the future.

2. Material and methodology

The process of conducting a systematic review involves identifying relevant works and concepts, transforming these into search terms and syntax, conducting a systematic search across various databases, and collecting a comprehensive collection of relevant literature. The review begins with the identification of key works and specific concepts that are relevant to the topic at hand. These identified works and concepts are then transformed into search terms and syntax that can be used to retrieve related studies. In the context of this particular research, the search terms and syntax have been established as follows: (1) The search syntax includes terms such as “Global Navigation Satellite System” or “GNSS”; “Terrestrial Laser Scanning” or “TLS”; “Mine surveying”; “Mapping”; “Subsidence” or “Displacement”; and “Mine”, “Mining”, or “Open-pit mine”. These terms are carefully chosen to ensure that the search results are as relevant as possible to the research topic; (2) This search syntax is then used to conduct a systematic search across various databases. The databases that are searched include Google Scholar, Scopus, Web of Science, and ScienceDirect. These databases are chosen for their extensive collection of academic and scientific literature; (3) The primary language used for conducting these searches is English. This is because English is the most commonly used language in scientific literature, and using English as the primary search language ensures that the search results are as comprehensive as possible; (4) The result of this systematic search is a comprehensive collection of scientific literature that covers many aspects of mapping and subsidence investigation by GNSS and TLS techniques. This collection of literature provides a wealth of information and insights into the topic at hand; (5) The types of literature that are collected include book chapters, conference proceedings, and original papers that have been published by international journals following a rigorous peer review process. These types of literature are chosen for their academic rigor and their relevance to the research topic.

3. Application of GNSS technology in mining area

The RTK method has become extensively utilized for monitoring deformation in mining sites. The application of the GNSS method in subsidence monitoring dates back to the early years of the last decade. To meet the precise requirements of surface deformation monitoring. In [21], authors proposed an innovative GPS RTK surveying technique that incorporates rod measurement. This technique mitigates the influence of multipath error in the U direction, effectively prevents the impacts of vertical deviation and shaking error of the surveying g rod, and further enhances positioning precision. Similarly, in the study [22], the GPS RTK approach has been adopted to improve the accuracy and reliability of mine surface subsidence monitoring. An in-depth analysis of the mechanism responsible for the primary systematic errors was conducted, drawing on several theories and techniques. This method can significantly increase the accuracy of estimations by completely eliminating inevitable shaking errors, vertical deflection, and to some extent, reducing the multipath effect. In this research [23], based on GNSS technology, findings from two years of ground deformation monitoring in coal mining regions in Upper Silesia, Poland, are presented. Real-time (RT) and near real-time (NRT) GNSS techniques were employed to verify long-term subsidence events, and these were cross-referenced with daily postprocessing solutions. Additionally, [24] provided the processing procedure and findings from their analysis of earth surface displacement data observations during coal mining at the Kostenko mine of the Coal Department of ArcelorMittal Temirtau JSC in the Karaganda Coal Basin using GNSS methods. The obtained results indicate that the proposed method of observing the displacement of the earth’s surface is more economically ad-

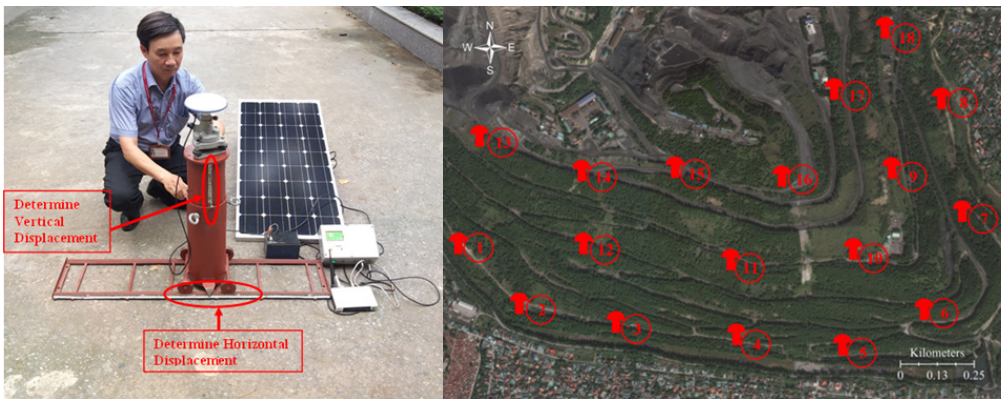

Fig. 2. GNSS/CORS-Based Technology for Real-Time Monitoring of Landslides on Waste Dump [27]
Rys. 2. Technologia oparta na GNSS/CORS do monitorowania w czasie rzeczywistym osuwisk na zwałowisku [27]

vantageous and requires significantly less time compared to traditional, expensive geodetic methods. According to [1], to establish real-time and quasi-real-time deformation monitoring methods, the GNSS Continuously Operating Reference Station (CORS) offers services for navigation based on pseudo range measurements and provides carrier phase information. Therefore, in light of mining technology for CORS, they suggested a large-area 3D deformation monitoring system for mining areas. The results showed that the proposed GNSS-RTK can improve both the temporal and spatial resolution of mine deformation monitoring. In another study, it has been demonstrated that it is possible to evaluate displacements both vertically and horizontally with great precision using geodetic networks. These networks consist of inclinometers and GPS networks to facilitate the detection of horizontal motions, while high-precision leveling systems are capable of estimating subsidence values. This study presented the results and observations on the use of a GPS geodetic network for continuous surface deformation monitoring in waste dumps of the Bages region of Catalonia (Spain) [24]. Furthermore, the utilization of GNSS satellite receivers and robotic total stations to monitor open pit mines is presented in [25]. This study demonstrated the combination of robotic total station equipment and GNSS receivers to provide a completely automated, accurate, efficient, and economical survey monitoring system for large open pit mines. The study [26] was shown that large-scale mobility in the mining area can be detected using continuous-time or GNSS location time series with high sample rates. Consequently, they presented a GPS method for monitoring seismic events and surface displacement that occurs during mining-induced tremors.

In the study GNSS/CORS-Based Technology for Real-Time Monitoring of Landslides on Waste Dump – A Case Study at the Deo Nai South Dump, Vietnam, the authors have self-produced a monitoring system using GNSS technology and tested it at the Deo Nai mine (Vietnam). The results demonstrated that this system operates well, with measurement accuracy comparable to major brands' monitoring equipment such as Leica and Topcon.

Moreover, the accuracy of the GNSS method is emphasized in various studies. For instance, [28] examined the duration necessary for GPS sessions in ground deformation measurements within mining areas. The findings revealed that a GPS session should last a minimum of twelve hours to achieve sub-centimeter precision in height coordinates at a 95% confidence level in a single observation session. Additionally, [29] conducted a study on monitoring local deformation using GNSS in an open-pit mine, addressing the challenge of achieving millimeter-level accuracy in displacement measurements with GPS. According to [29, high-accuracy geodetic surveys are essential for determining deformation indices in areas impacted by open-pit mining, facilitating the identification of potential hazards. Consequently, they discussed the fundamentals of precisely determining three-dimensional displacements using GPS technology. The results demonstrated that the 3-D coordinates of the observed points could be accurately determined to within mm accuracy.

In addition to determining deformation caused by mining, GNSS methods are extensively utilized for monitoring ground subsidence in mining areas. According to [30], the amplitude of ground subsidence in coal-mining regions can reach up to 10 cm per day, occurring continuously. This highlights the necessity for timely and accurate monitoring to ensure the safety of coal-mining areas. The study presents a real-time ground subsidence monitoring system that continuously operates on the Global Navigation Satellite System. Unlike traditional leveling surveying approaches, this method meets the precision requirements for ground subsidence monitoring and provides continuous subsidence information in real-time. Moreover, the application of GNSS methods extends beyond routine deformation monitoring to encompass large-scale subsidence observations. A high-precision GNSS monitoring system was constructed to precisely observe extensive mining subsidence areas. This system utilizes neighboring International GNSS Service (IGS) stations as reference points to enhance accuracy [31]. The proposed theory was successfully implemented to monitor mining subsidence in China's northern Anhui coal mine, demonstrating the system's efficacy in providing precise and reliable data. The significance of these advancements lies in their ability to provide real-time, continuous monitoring of ground subsidence, which is crucial for maintaining the integrity and safety of mining regions. Traditional leveling methods, while accurate, are often labor-intensive and time-consuming, limiting their effectiveness in providing immediate data necessary for proactive safety measures. In contrast, the GNSS-based systems leverage real-time data transmission, allowing for immediate analysis and response to subsidence events. This capability is particularly important

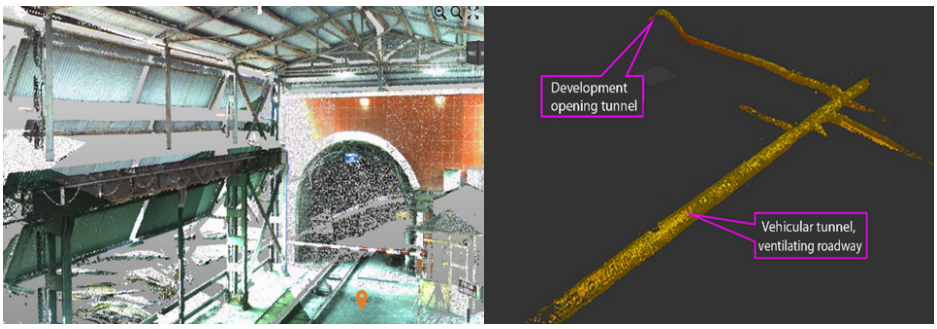

Fig. 3. Application of TLS in Khe Cham underground mine, (a) High definition mapping of inclined drift entrance; (b) Point cloud data of Khe Cham underground mine at the level of -170 m [40]

Ryc. 3. Zastosowanie TLS w podziemnej kopalni Khe Cham, (a) Mapowanie w wysokiej rozdzielczości pochyłego wejścia do sztolni; (b) Dane chmury punktów podziemnej kopalni Khe Cham na poziomie -170 m [40]

in coal-mining regions where subsidence can rapidly progress, posing risks to infrastructure and human safety. Furthermore, the integration of neighboring IGS stations as reference points, as detailed in [31],, enhances the precision of the GNSS monitoring system. These stations provide a stable and reliable framework for reference, enabling the system to detect even minute changes in ground levels with high accuracy. This approach not only improves the overall reliability of subsidence monitoring but also expands the system's applicability to larger geographic areas, thereby offering comprehensive surveillance over extensive mining regions. The study conducted in northern Anhui, China, exemplifies the practical application of this advanced monitoring technology. By implementing a high-precision GNSS system, researchers were able to obtain detailed subsidence data, which is critical for developing effective mitigation strategies and ensuring the long-term safety of the mining operations. The successful application of this technology in such a significant coal-mining area underscores its potential for widespread adoption in other regions facing similar subsidence challenges. The use of GNSS methods for monitoring ground subsidence in mining areas represents a significant leap forward in terms of precision, real-time data availability, and overall efficiency. These systems not only provide critical safety data but also facilitate a more proactive approach to managing the inherent risks associated with mining activities. By continuously monitoring subsidence and utilizing advanced reference frameworks, GNSS-based methods offer a robust solution for safeguarding mining regions and mitigating the impacts of ground deformation.

4. Application of TLS in mining site

The advent of modern technologies such as 3D laser scanning has opened new possibilities, especially for expansive and challenging environments like open pit mines [9], Systematic slope stability monitoring is essential to ensure safe and continuous mining operations. The application of 3D terrestrial laser scanning for tracking landslides and slope displacements in open pit mines has been extensively discussed in [9]. To overcome the limitations of traditional methods, , [32] proposes a TLS-based subsidence monitoring approach that operates without targets in mining regions. This method shifts the primary workload to the internal industry, reduces labor intensity, and simplifies the field measurement process. It is particularly suitable for monitoring surface subsidence in areas with difficult topography and harsh external conditions. Similarly, [33] describes a method for monitoring subsidence in mining areas using TLS without the need for targets. Compared to traditional techniques, this method transfers the main tasks to the internal industry, reduces labor demands, and optimizes the field measurement process. It is well-suited for environments with challenging topography and severe external conditions. Additionally, [34] discusses the use of optical transducers, 3D laser scanners, and digital image processing methods to physically describe the movement of strata related to mining. They presented physical modeling of mining-induced subsidence using various data processing techniques and innovative optical and laser-based monitoring instruments. In the study by [35], TLS was employed as the data acquisition tool to predict subsidence and horizontal displacement at Gubei Coal Mine in Huainan, China. The analysis results from a small observation area demonstrated that the mining subsidence monitoring approach described in this study could effectively capture surface deformation in a large mining-impacted area. Moreover, [36] developed an automated technique based on TLS point cloud data for extracting building deformation in mining locations. The absolute error between deformation values obtained by this method and those obtained manually was less than 8 mm, indicating a high degree of accuracy. This approach showed greater stability compared to manual extraction methods. Another study aimed to validate spatial variations (movements and deformations) in mining operations by applying this technique in situ at a chosen mining site in the Czech part of the Upper Silesian Coal Basin. At Lazy Mine, the primary goal of 3D laser scanning was to monitor the deformation of roadways as they approached the longwall face on the selected tailgate [37].

Additionally, [38] assessed the effectiveness of a stop-and-go laser scanning technique in a mine shaft to accurately determine the position, angle, and deviation of the bunton plates at Thembelani Mine. The findings revealed the significant advantages of laser scanning, particularly when continuous data analysis is required. Extensive laser scan datasets are available for off-site review and ongoing work by multiple departments and teams, supporting a wide range of applications including planning, design, engineering, safety, geology, and rock engineering. These advancements underscore the transformative impact of 3D laser scanning technology

in mining operations. The ability to conduct high-precision monitoring of slopes, subsidence, and structural deformations in real-time enhances safety and operational efficiency. By leveraging TLS, mining companies can reduce labor intensity, streamline field operations, and obtain highly accurate data critical for various applications. This technology is particularly beneficial in environments with complex topographies and harsh conditions where traditional methods fall short. The integration of 3D laser scanning with other modern monitoring tools and data processing techniques further expands its utility, enabling comprehensive and precise modeling of mining-induced ground movements. Overall, the adoption of these advanced monitoring approaches represents a significant step forward in ensuring the stability and safety of mining operations. Many projects use TLS for mines and tunnels, shaft, etc., which helps in detailed 3D simulation of these mines and displacement determination [8, 39]. In Vietnam, this technology has been tested at the Khe Cham coal mine [40]. In addition, TLS has also been tested in 3D modeling measurements at the Coc Sau coal mine. This shows that this technology is gradually being put into practical use in Vietnam [41].

According to [42], quickly determining the amount of raw material extracted from a surface quarry is a common challenge in the extraction of mineral resources, especially heterogeneous ones. To address this, a study was conducted comparing and evaluating laboratory and non-contact surveying methodologies to determine the bulk density of raw material under in situ conditions. Confirming the bulk density of extracted heterogeneous raw material is critical, and the study highlighted the effectiveness of TLS in achieving this. Additionally, the geometric characteristics of bucket-wheel excavators, essential for real-time mining management, can be accurately acquired using 3D laser scanning. This technology was used to establish mathematical models of the movement dynamics of these machines in three dimensions and determine their essential geometric properties [20]. Another significant application of terrestrial laser scanning (TLS) in open pit mines is volume estimation. This method is proving to be an invaluable tool for mining companies, enabling them to monitor and survey their operations more effectively, which in turn can enhance productivity and competitiveness in the market. This was demonstrated in [43], where field tests using two different types of TLS instruments for various mining applications, including volume estimations, were compared. The experiment revealed that volume could be calculated with significantly greater precision using TLS compared to traditional total stations. The results clearly indicate that TLS is a highly useful tool in the mining sector. Furthermore, the capability of TLS techniques to measure exploitative volumes in open-pit mines has been established in study [44].. This research proposed a coarse-to-fine method utilizing terrain-invariant zones to register temporal TLS surveys. According to experimental tests conducted in an open-pit mine in China, the proposed registration method outperformed state-of-the-art techniques, achieving superior performance in terms of convergence rate and registration accuracy.

The application of TLS for volume estimation in open pit mines allows for more accurate and efficient monitoring of extracted materials. The precision of TLS surpasses that of traditional methods, enabling mining companies to better manage resources and optimize their operations. This technology not only improves the accuracy of volume measurements but also facilitates the continuous monitoring of mining activities, providing real-time data that can be used for immediate decision-making. Moreover, the ability to measure bulk density of raw materials using non-contact surveying methods such as TLS offers significant advantages in terms of speed and safety. By avoiding the need for direct contact with the material, these methods reduce the risk of accidents and allow for quicker data collection. This is particularly important in the context of heterogeneous mineral resources, where the variability in material properties can make traditional sampling methods less reliable. The use of 3D laser scanning to capture the geometric properties of mining machinery further underscores the versatility and utility of TLS in the mining sector. By creating detailed models of equipment like bucket-wheel excavators, mining companies can better understand the dynamics of their machinery and optimize their use. This can lead to improvements in efficiency and reductions in maintenance costs, as well as enhanced safety for workers. The application of TLS in open pit mining for volume estimation, bulk density measurement, and equipment modeling represents a significant advancement in mining technology. The precision, efficiency, and safety benefits of TLS make it an indispensable tool for modern mining operations, enabling companies to remain competitive in a challenging market.

5. Conclusion

This in-depth study explores the application of TLS and GNSS techniques in mining areas, drawing from a wide range of publications that have emerged in recent years. The review embarked on a thorough analysis of 44 papers, all of which are related to mapping and displacement monitoring in mining areas using the TLS and GNSS methods. These papers, published in reputable scientific journals, provide a rich source of information on the subject. The results obtained from this comprehensive review demonstrate that both TLS and GNSS technologies can be effectively utilized to determine surface deformation in various mining environments, including underground mines, shafts, open-pit mines, and waste dumps. This capability to accurately measure and monitor displacement is crucial in maintaining the safety and efficiency of mining operations. As evidenced in this paper, the monitoring results achieved through these technologies are remarkably precise, with accuracy reaching the millimeter level. This high level of accuracy ensures the effective use of these technologies in the future, indicating that they can provide many long-term beneficial applications in mapping and monitoring movements in mining areas. This study, therefore, not only discusses the utilization of these techniques but also highlights their potential in transforming the way displacement is monitored in mining areas, thereby contributing to safer and more efficient mining operations areas.

Literatura – References

1. Jing-Xiang, G., H.J.P.E. Hong, and P. Science, Advanced GNSS technology of mining deformation monitoring. 2009. 1(1): p. 1081-1088.
2. Behera, A. and K.S. Rawat, A Comprehensive Review on Mining Subsidence and its Geo-environmental Impact. Journal of Mines, Metals & Fuels, 2023. 71(9).
3. Owczarz, K. A review of geodetic and remote sensing methods used for detecting surface displacements caused by mining. in IOP Conference Series: Earth and Environmental Science. 2020. IOP Publishing.
4. Suh, J., An overview of GIS-based assessment and mapping of mining-induced subsidence. Applied Sciences, 2020. 10(21): p. 7845.
5. Cai, Y., et al., A review of monitoring, calculation, and simulation methods for ground subsidence induced by coal mining. International Journal of Coal Science & Technology, 2023. 10(1): p. 32.
6. Hejmanowski, R., et al., An analysis applying InSAR of subsidence caused by nearby mining-induced earthquakes. Geosciences, 2019. 9(12): p. 490.
7. Yu, Y., et al., Subsidence mechanism and stability assessment methods for partial extraction mines for sustainable development of mining cities—A review. Sustainability, 2018. 10(1): p. 113.
8. Lipecki, T. and K.T.T. HUONG, The development of terrestrial laser scanning technology and its applications in mine shafts in Poland. Inżynieria Mineralna, 2020. 1(2).
9. Bazarnik, M. Slope stability monitoring in open pit mines using 3D terrestrial laser scanning. in E3S Web of Conferences. 2018. EDP Sciences.
10. Kekeç, B., et al., Applications of Terrestrial Laser Scanning (TLS) in Mining: A Review. Türkiye Lidar Dergisi, 2021. 3(1): p. 31-38.
11. Wang, W., et al., Applications of terrestrial laser scanning for tunnels: a review. Journal of Traffic and Transportation Engineering (English Edition), 2014. 1(5): p. 325-337.
12. Smits, J., Application of 3D terrestrial laser scanning to map building surfaces. Journal of Architectural Conservation, 2011. 17(1): p. 81-94.
13. Berenyi, A., T. Lovas, and A. Barsi, Terrestrial laser scanning–civil engineering applications. International Archives of Photogrammetry, Remote Sensing and Spatial Information Sciences, 2010. 38(Part 5): p. 80-85.
14. Fröhlich, C. and M. Mettenleiter, Terrestrial laser scanning–new perspectives in 3D surveying. International archives of photogrammetry, remote sensing and spatial information sciences, 2004. 36(Part 8): p. W2.
15. Wu, C., et al., Application of terrestrial laser scanning (TLS) in the architecture, engineering and construction (AEC) industry. Sensors, 2021. 22(1): p. 265.
16. Buckley, S.J., et al., Terrestrial laser scanning in geology: data acquisition, processing and accuracy considerations. Journal of the Geological Society, 2008. 165(3): p. 625-638.
17. Kuczyńska, G. and M. Stawska, Modern applications of terrestrial laser scanning. Горный информационно-аналитический бюллетень (научно-технический журнал), 2021(1): p. 160-169.
18. Mukupa, W., et al., A review of the use of terrestrial laser scanning application for change detection and deformation monitoring of structures. Survey review, 2017. 49(353): p. 99-116.
19. Fengyun, G. and X. Hongquan. Status and development trend of 3D laser scanning technology in the mining field. in 2013 the International Conference on Remote Sensing, Environment and Transportation Engineering (RSETE 2013). 2013. Atlantis Press.
20. Korandová, B. and M. Krupa, The application of terrestrial laser scanning for the management of mining in real time. International Multidisciplinary Scientific GeoConference: SGEM, 2018. 18(2.2): p. 1011-1018.
21. Liu, C., et al., Mine surface deformation monitoring using modified GPS RTK with surveying rod: Initial results. Survey Review, 2015. 47(341): p. 79-86.
22. Issabek, T., V. Dyomin, and D. Ivadilinova, Methods for monitoring the earth surface displacement at points of small geodetic network under the underground method of coal development. Natsional'nyi Hirnychyi Universytet. Naukovyi Visnyk, 2019(2): p. 13-20.
23. Tondaś, D., K. Kazmierski, and J. Kapłon, Real-time and near real-time displacement monitoring with GNSS observations in the mining activity areas. IEEE Journal of Selected Topics in Applied Earth Observations and Remote Sensing, 2023.
24. Costantino, D. and M.G. Angelini, Geodetic monitoring applied to a mine area. Applied Geomatics, 2011. 3: p. 61-74.
25. Brown, N., S. Kaloustian, and M. Roeckle. Monitoring of open pit mines using combined GNSS satellite receivers and robotic total stations. in Slope Stability 2007: Proceedings of the 2007 International Symposium on Rock Slope Stability in Open Pit Mining and Civil Engineering. 2007. Australian Centre for Geomechanics.

26. Szczerbowski, Z. and J. Jura, Mining induced seismic events and surface deformations monitored by GPS permanent stations. Acta Geodyn. Geomater, 2015. 12(3): p. 179.
27. Pham, C.K., D.T. Tran, and V.H. Nguyen, GNSS/CORS-Based Technology for Real-Time Monitoring of Landslides on Waste Dump–A Case Study at the Deo Nai South Dump, Vietnam. Inżynieria Mineralna, 2020. 1(2): p. 181-191.
28. Bazanowski, M., A. Szostak-Chrzanowski, and A. Chrzanowski, Determination of GPS session duration in ground deformation surveys in mining areas. Sustainability, 2019. 11(21): p. 6127.
29. Kim, D., et al., Local deformation monitoring using GPS in an open pit mine: initial study. GPS Solutions, 2003. 7: p. 176-185.
30. Tao, T., et al., Real-time monitoring rapid ground subsidence using GNSS and Vondrak filter. Acta Geophysica, 2019. 67: p. 133-140.
31. Bian, H.-f., et al., Monitoring large-area mining subsidence by GNSS based on IGS stations. Transactions of Nonferrous Metals Society of China, 2014. 24(2): p. 514-519.
32. Bing, S., et al., Reconstructing DEM using TLS point cloud data and NURBS surface. Transactions of Nonferrous Metals Society of China, 2015. 25(9): p. 3165-3172.
33. Gu, Y., et al., Study on subsidence monitoring technology using terrestrial 3D laser scanning without a target in a mining area: An example of Wangjiata coal mine, China. Bulletin of engineering geology and the environment, 2020. 79: p. 3575-3583.
34. Ghabraie, B., et al., Application of 3D laser scanner, optical transducers and digital image processing techniques in physical modelling of mining-related strata movement. International Journal of Rock Mechanics and Mining Sciences, 2015. 80: p. 219-230.
35. Li, J. and L. Wang, Mining subsidence monitoring model based on BPM-EKTF and TLS and its application in building mining damage assessment. Environmental Earth Sciences, 2021. 80(11): p. 396.
36. Wang, L., et al., Automatic deformation extraction method of buildings in mining areas based on TLS point clouds. IEEE Access, 2021. 10: p. 127817-127824.
37. Kukutsch, R., et al., Possibility of convergence measurement of gates in coal mining using terrestrial 3D laser scanner. Journal of sustainable mining, 2015. 14(1): p. 30-37.
38. Van der Merwe, J. and D.C. Andersen, Applications and benefits of 3D laser scanning for the mining industry. Journal of the Southern African institute of Mining and Metallurgy, 2013. 113(3): p. 00-00.
39. Jaśkowski, W., et al. Classical Measurement Methods and Laser Scanning Usage in Shaft Hoist Assembly Inventory. in E3S Web of Conferences. 2018. EDP Sciences.
40. Nghia, N.V., et al., Applied Terrestrial Laser Scanning for coal mine high definition mapping. World of Mining-Surface and Underground, 2019. 71(4): p. 237-242.
41. Long, N.Q., et al., Accuracy assessment of mine walls' surface models derived from terrestrial laser scanning. International Journal of Coal Science & Technology, 2018. 5: p. 328-338.
42. Blistan, P., et al., TLS and SfM approach for bulk density determination of excavated heterogeneous raw materials. Minerals, 2020. 10(2): p. 174.
43. Conforti, D. and T. Optech, Using Static and Mobile Laser Scanners to Measure and Manage Open Pit Mines. Canada: Optech Incorporated, 2017.
44. Xu, Z., et al., Registration of terrestrial laser scanning surveys using terrain-invariant regions for measuring exploitative volumes over open-pit mines. Remote Sensing, 2019. 11(6): p. 606.

Zastosowanie naziemnego skaningu laserowego i globalnego systemu nawigacji satelitarnej na obszarze górniczym

Technologie naziemnego skanowania laserowego (TLS) i globalnego systemu nawigacji satelitarnej (GNSS) są coraz bardziej powszechne w pracach związanych z kartowaniem geodezyjnym, odgrywając znaczącą rolę w zadaniach geodezyjnych w kopalniach, takich jak tworzenie map do obliczania objętości, monitorowanie przemieszczeń i deformacji powierzchni i konstrukcji nad wyrobiskami górniczymi. Obecnie prowadzonych jest wiele badań nad zastosowaniem tych technologii w różnych aspektach prac geodezyjnych w kopalniach. W artykule dokonana została synteza tych badań w celu oceny efektywności zastosowania technologii GNSS i TLS w górnictwie. Autorzy dokonali przeglądu 44 artykułów/projektów z ostatnich lat i stwierdzają, że technologie te bardzo szybko się rozwijają, a dokładność pomiaru współrzędnych i wysokości wzrasta do poziomu pojedynczych milimetrów zarówno w kierunku poziomym, jak i pionowym.

Słowa kluczowe: *Terrestrial Laser Scanning, Global Navigation Satellite System, mapowanie kopalń, przemieszczenie, deformacja, osiadanie, kopalnia odkrywkowa, górnictwo*

Application of Multi-Spectral Index from Sentinel-2 Data for Extracting Build-up Land of Hanoi Area in the Dry Season

*Le Thi THU HA[1,2], Nguyen HUU LONG[3], Nguyen VAN TRUNG[1,2], Pham THI LAN[1]**

[1] Hanoi university of Mining and Geology;
[2] Geomatics in Earth Sciences Research Group, Hanoi University of Mining and Geology, 18 Vien Str., Duc Thang Ward, Hanoi 100000, Vietnam
[3] Dong Thap University
emails: lethithuha@humg.edu.vn, nhlong@dthu.edu.vn, nguyenvantrung@humg.edu.vn; ORCID: 0000-0001-9459-787X; 0000-0002-3032-6808; 0000-0003-3982-1896
* Corresponding author: phamthilan@humg.edu.vn

http://doi.org/10.29227/IM-2024-01-94

Submission date: 17-05-2024 | Review date: 09-06-2024

Abstract

A remote sensing index is a simple and effective way to highlight a specific land cover. Therefore, in this study, we try to increase the accuracy of the urban land map developed for Hanoi city by focusing on determining the appropriate combination of spectral indices calculated from satellite image data. To conduct the study, four spectral indices were selected including namely normalized difference tillage index (NDTI), bare soil index (BSI), dry bare soil index (DBSI) and the normalized difference vegetation index (NDVI). All these spectral indices are calculated from Sentinel-2 data acquired in the dry season. The two combinations are created from the superposition of NDTI/BSI/NDVI and NDTI/DBSI/NDVI spectral index layers. The use of the "K-means" algorithm as an unsupervised classifier provides rapid and automatic urban land detection. The results show that the BSI index performs better than using the DBSI index. As a result, the BSI index brings improvements: bare soil types and accumulation processes are better differentiated, with overall accuracy increasing by 5.82% and Kappa coefficient increasing by 11.1%. The results show that the NDTI/BSI/NDVI multi-spectral index dataset is suitable for mapping urban areas with the potential to help better urban management during the dry season.

Keywords: *Sentinel-2 data, K-means algorithm, Bare Soil Index (BSI), Dry Bare Soil Index (DBSI), Normalized Difference Tillage Index (NDTI)*

1. Introduction

Remote sensing imagery constitutes a form of data suitable for monitoring and mapping of changes in built-up within within metropolitan regions, particularly as the effects of population expansion and urbanization escalate [1]. One of the main problems in mapping urban area is determining the change in land use from non-residential to residential [2-5]. Mapping the built-up in urban regions holds significance as the presence of such land type serves as an indicator of urban growth [6]. The techniques for extraction of built-up area from satellite imagery can be grouped into two types: (1) techniques based on conventional multi-spectral image classification such as supervised, unsupervised, object based or deep learning classification (2) techniques based on normalized difference indices such as normalized difference built-up index (NDBI), principal component analysis (PCA) based built-up area index (PCABI), enhanced built-up index (EBI), urban index (UI), etc [7].

Classification methods based on multispectral image classification techniques often fail to achieve reliable accuracy, typically below 80%, due to the spectral confusion of heterogeneous urban built-up land class compared to other land use classes [8]. Instead, many researchers have experimented with normalized difference indices using specific spectral bands for automatic extraction of built-up land from satellite images [9-17]. In practice, the use of spectral indices such as spectral bands perform better than using the original spectral bands [8] and spectral indices play an important role in extraction of built up [18].

With the availability of Landsat satellite archive i.e. the largest series of space-borne earth observation data as well as at good spatial resolution provides huge opportunities for urban mapping [15]. Many studies shown the suitability of Landsat data for urban mapping and monitoring [1-3,6,8,9,15]. However, studies including [5,7,19,20] have leveraged the advantages of Sentinel-2 satellite imagery data to propose various applications of built-up index in urban land classification. Furthermore, some studies such as the work of [19] concluded that Sentinel-2 provides higher accuracy for urban built-up areas compared to Landsat-8 satellite imagery data. Additionally, a study by [20] found that Sentinel-2 data performs better than Landsat-8 data in mapping urban built-up land cover by using a combination of different spectral indices. Valdiviezo-N et al., 2018 [21]suggests that all utilized built-up indices, such as the Normalized Difference Built-Up Index (NDBI), Index-Based Built-Up Index (IBI), New Built-Up Index (NBI), Band Ratio for Built-Up Area (BRBA), Normalized Built-Up Area Index (NBAI), Biophysical Composition Index (BCI), Modified Built-Up Index (MBI), Built-Up Area Extraction Index (BAEI), and Combinational Build-Up

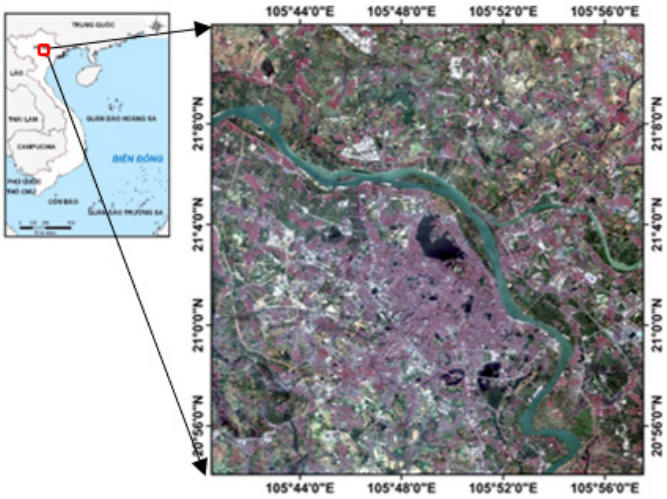

Fig. 1. Location of Study Area
Rys. 1. Lokalizacja obszaru badawczego

Tab. 1. Spectral bands and resolutions of Sentinel-2 MSI sensor
Tab.1 Pasma widmowe i rozdzielczości sensora Sentinel-2 MSI

Band Specification	Wavelength Range (nm)	Resolution (m)
Band 1 - Coastal	433–453	60
B2 - Blue	458–523	10
B3 - Green	543–578	10
B4 - Red	650–680	10
B5 - Red-edge 1	698–713	20
B6 - Red-edge 2	733–748	20
B7 - Red-edge 3	773–793	20
B8 - Near infrared (NIR)	785–900	10
B8A - Near infrared narrow (NIRn)	855–875	20
B9 - Water vapour	935–955	60
B10 - Shortwave infrared/Cirrus	1360–1390	60
B11 - Shortwave infrared 1 (SWIR1)	1565–1655	20
B12 - Shortwave infrared 2 (SWIR2)	2100–2280	20

Tab. 2. Different spectral indices were employed in this study on Sentinel-2 data
Tab. 2. Zastosowane różne wskaźniki widmowe dla danych z Sentinel-2

Index Name	Index Id	References	Formula on Sentinel -2 image
Normalized Difference Tillage Index	NDTI	Deventer, 1997 []	(B11-B12) / (B11+B12)
Bare Soil Index	BSI	Rikimaru and Miyatake, 1997 []	((B11+B4)-(B8+B2))/((B11+B4)+(B8+B2))
Dry Bare-Soil Index	DBSI	Rasul et al., 2018 []	((B11-B03)/(B11+B03)) –NDVI
Normalized Difference Vegetation Index	NDVI	Tucker, 1979 []	(B08-B04)/(B08+B04)

Index (CBI), are influenced by seasonal variations, particularly during dry months when the similarity between the spectra of bare soil and urban areas increases. As a result, these indices led to a less accurate mapping of urban areas during dry periods in the study area.

The outcomes discussed previously suggest an enhancement in mapping urbanized regions during dry seasons through the utilization of spectral indices layer stacking technique. Given that semi-arid zones are characterized by sparse vegetation and extensive bare soil, especially during dry periods, two bare soil indices were opted for. The initial one is the Bare Soil Index (BSI) introduced by Rikimaru and Miyatake, 1997 [13], aimed at improving the recognition of bare soil areas and fallow lands, thus distinguishing them from vegetative cover and other land cover types. Recently, the BSI index has seen widespread adoption in various studies, such as [13,23,24], the next index is the Dry Bare-Soil Index (DBSI), a recent creation by Rasul et al., 2018 [6], as an index for detecting bare areas in arid climates.

In recent years, a novel form of dataset emerged through the combination of different spectral indices. The research conducted by Ettehadi Osgouei et al., 2019 [24] employed the Normalized Difference Tillage Index (NDTI) – originally developed by Deventer, 1997 [25] and also utilized in studies by [12,23] – which has used SWIR bands of the Sentinel-2 images and succeeded in differentiating bare land and built-up area classes better than the other spectral indices used in the study. This approach effectively distinguished between bare land and built-up area categories, surpassing the performance of other spectral indices utilized in the investigation. Furthermore, the multi-index NDTI was subjected to classification using the machine-learning-based SVM algorithm [25], resulting in enhanced mapping accuracy of heterogeneous urban areas.

The research article explores the rapid and accurate map-

Fig. 1. Location of Study Area

Rys. 1. Lokalizacja obszaru badawczego

Spectral Indices	BSI	DBSI	NDTI	NDVI
BSI	1.000000	0.952421	0.173467	-0.305834
DBSI	0.952421	1.000000	0.124518	-0.332879
NDTI	0.173467	0.124518	1.000000	0.534376
NDVI	-0.305834	-0.332879	0.534376	1.000000

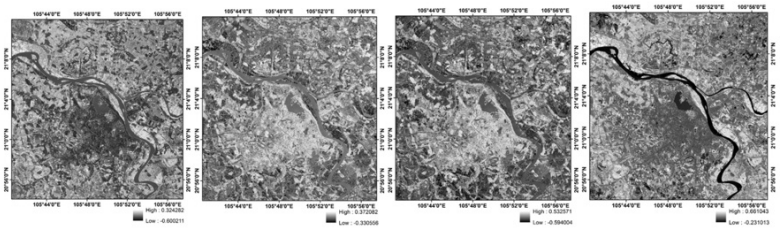

a) NDTI Index b) BSI Index c) DBSI Index d) NDVI Index

Fig. 2. Spectral indices result used in the study (a) NDTI (b) BSI (c) DBSI (d) NDVI

Rys. 2. Wyniki wskaźników widmowych wykorzystanych w badaniu (a) NDTI (b) BSI (c) DBSI (d) NDVI

Tab. 4. Statistical values of spectral indices were employed in this study on Sentinel-2 data

Tab. 4. Ocena statystyczna wykorzystanych wskaźników spektralnych w oparciu o dane Sentinel-2

Spectral indices	Min	Max	Mean	StdDev	Range value
BSI	-0.445267	0.552146	0.184725	0.052132	From -0.445267 to 0.552146
DBSI	-0.394781	0.573225	0.236719	0.073513	Từ -0.394781 đến 0.573225
NDTI	-0.326284	0.337416	0.071523	0.043426	Từ -0.326284 đến 0.337416
NDVI	-0.384516	0.901425	0.101642	0.072846	Từ -0.384516 đến 0.901425

ping of built-up land during the dry season through testing a new dataset that combines several spectral indices sourced from Sentinel-2 satellite imagery with the aim of identifying multi-spectral combinations for urban built-up land extraction. In this experiment, we leverage the advantages of the new Sentinel-2 satellite imagery data with a spatial resolution of 10 meters, which is widely used and freely available. We chose Hanoi city as the research area to carry out the process of distinguishing between bare land and urban built-up land during the dry season, surrounded by a large area and heterogeneous bare land.

2. Study area and data used

2.1 Study area

Research Area Hanoi is the capital city of Vietnam, covering an area of 3,359.82 square kilometers with a population of 8.4 million people. The terrain of the area includes the central plain region and hilly areas in the northern and western parts of the city. The climate of the Hanoi area is divided into two main seasons: the rainy season (from April to October) and the dry season (from November to March), but the weather is further categorized into four seasons due to transitional months. In 2023, Hanoi established the General Construction Planning for the Capital Hanoi until 2030 and vision until 2050 for a city with 9.1 million inhabitants by 2030 and over 10 million people by 2050. The location of the research area within the city is shown in Figure 1.

2.2 Data used

The Sentinel-2 sensor is a multispectral sensor that was launched in 2015. Sentinel-2 has 13 bands covering the VNIR region with 8 bands and the SWIR region with 2 bands having a spatial resolution of 10, 20, and 60 m. The swath width is 290 km. It consists of two multispectral satellites, Sentinel-2A and Sentinel-2B. The key mission objectives for Sentinel-2 are: (1) to provide systematic global acquisitions of high-resolution multi-spectral imagery with a high revisit frequency, (2) to provide enhanced continuity of multi-spectral imagery provided by the SPOT series of satellites, and (3) to provide observations for the next generation of operational products such as land-cover maps, land change detection maps, and geophysical variables. Consequently, Sentinel-2 will directly contribute to the Land Monitoring, Emergency Response, and Security services [26]. Data Used Sentinel-2 satellite imagery data was chosen for the research area because this satellite imagery data is freely available at https://scihub.copernicus.eu.

The Sentinel-2 satellite imagery data was acquired and processed at level 2A (product name: S2B_MSIL2A_20240212T032849_N0510_R018_T48QWJ_20240212T054533) and has been georeferenced. The dataset was collected on February 12, 2024, corresponding to the driest month of the year covering the research area, including Hanoi city. The selected satellite imagery data from this date provides good observation of both bare land and urban built-up areas, which can be distinguished because there is no mixed vegetation cover within the bare land due to the coincidence with the end of the harvest season in the region.

3. Methodology

3.1 Pre-processing

The data were provided as level L2A data captured under clear atmospheric conditions (cloud coverage = 0.01%) in the dry season. The process of overlayering spectral channels and cutting the research area is conducted using tools within version 8.0 of the SNAP software. The image processing tools for Sentinel-2 satellite imagery can be found at http://step.esa.int/main/download/.

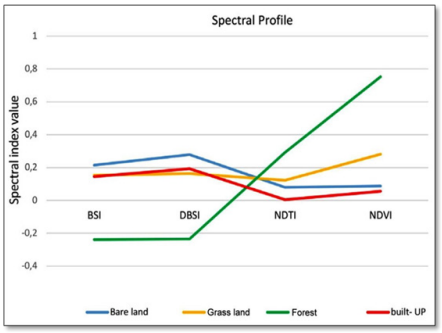

Fig. 3. Simplified spectral signatures represented by the mean of the major categories of Hanoi land cover for the multi-index image
Rys. 3. Uproszczone sygnatury widmowe reprezentowane przez średnią głównych kategorii pokrycia terenu Hanoi dla obrazu wieloindeksowego

Tab. 5 The built-up area extracted using both multi-index of Hanoi city in the Dry Season
Tab. 5. Powierzchnia zabudowana wyodrębniona przy użyciu obu wskaźników miasta Hanoi w porze suchej

Multi Index Used	Built-up area		Others		Total	
	Area (km²)	Area (%)	Area (km²)	Area (%)	Area (km²)	Area (%)
NDTI/BSI/NDVI	593,23	57,29	442,24	42,71	1035,47	100
NDTI/DBSI/NDVI	595,56	57,52	439,91	42,48	1035,47	100
NDTI	531,34	51,31	504,13	48,69	1035,47	100

3.2 Processing

3.2.1. Calculation of spectral indices

1. Normalized Difference Vegetation Index (NDVI)

Normalized Difference Vegetation Index (NDVI) is a remote sensing method that uses the reflectance of light in the visible and near-infrared (NIR) wavelengths to determine the amount and health of vegetation in an area. NDVI is widely used in agriculture, forestry, and ecology to monitor the growth and health of vegetation and to identify areas of stress or damage [27]. NDVI values can also be used to map and classify vegetation types, and to detect changes in vegetation cover over time. Simply put, the Normalized Difference Vegetation Index is an indicator of a plant's health entirely based on how the cell structures reflect the different light waves in visible and near-infrared bands.

NDVI is calculated by subtracting the reflectance of the NIR band from the reflectance of the red band and then dividing that value by the sum of the reflectance of the NIR and red bands. NDVI values range from -1 to 1, with -1 indicating no vegetation, 0 indicating bare soil or water, and values closer to 1 indicating greater amounts and healthier vegetation. The formula below for the evaluation of NDVI:

$$NDVI = (NIR-Red)/(NIR+Red) \quad (1)$$

The values range from -1 to +1. A higher or more positive value indicates greater plant vigor and general health.

2. Normalized Difference Tillage Index (NDTI)

The urban areas had higher blue reflectance than bare soil as a result of the type of building materials, mainly concrete, used for roof surfaces and walls. The NDTI index of van Deventer et al. 1997 [25], which is calculated as:

$$NDTI= (SWIR1-SWIR2) / (SWIR1+SWIR2) \quad (2)$$

3. Dry Bare-Soil Index (DBSI)

Inspection of the Sentinel-2 bands suggested that differentiation of these classes could be done based on spectral values in the SWIR1 and Green bands. In these bands, generally the digital number value (DN) of bare land is slightly higher than the DN of the built-up class [6].

$$DBSI = ((B11-B03)/(B11+B03)) – NDVI \quad (3)$$

The DBSI values can be between −2 to +2, and higher numbers represent more bare soil. An appropriate threshold for the bare soil class can be used for mapping bare soil and non-bare soil areas. Based on a test carried out with a sample of bare soil pixels, a DBSI value 0.26 and higher was delineated as bare soil for the study area, and areas with lower values were delineated as other classes.

4. Bare Soil Index (BSI)

Bare Soil Index (BSI) is a numerical indicator that combines blue, red, near infrared and short wave infrared spectral bands to capture soil variations. These spectral bands are used in a normalized manner. The shortwave infrared and the red spectral bands are used to quantify the soil mineral composition, while the blue and the near infrared spectral bands are used to enhance the presence of vegetation. BSI can be used in numerous remote sensing applications, like soil mapping, crop identification (in combination with NDVI) etc [13]. To calculate the BSI with the following formulas:

$$BSI = ((B11+B4) - (B8+B2))/((B11+B4) + (B8+B2)) \quad (4)$$

All the selected spectral indices are specifically described in (Table 2) and are calculated based on the spectral bands of Sentinel-2 MSI satellite imagery (Table 1).

3.2.2. Multi-Index development

The correlation coefficients between the selected spectral indices are shown in (Table 3). A high correlation is evident between both bare soil indices (BSI and DBSI) within the research area. Conversely, a low correlation is observed be-

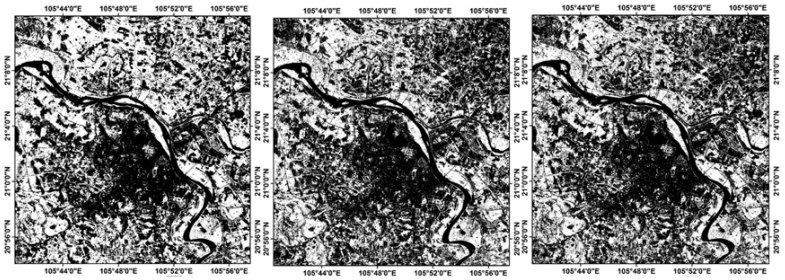

a) Binary of NDTI from K-means classifer (Black colour: Built-up area; White colour: Non Built-up area)

b) Binary of NDTI/BSI/NDVI from K- means classifer (Black colour: Built-up area; White colour: Non Built-up area)

c) Binary of NDTI/DBSI/NDVI from K- means classifer (Black colour: Built-up area; White colour: Non Built-up area)

Fig. 4. Binary image resulting from K- means classifer of (a) NDTI (b) Multi-Index (NDTI-BSI-NDVI) (c) Multi-Index (NDTI -DBSI-NDVI
Rys. 4. Obraz binarny wynikający z klasyfikatora K- oznacza (a) NDVI (b) Multiindeks (NDTI-BSI-NDVI) (c) Multiindeks (NDTI -DBSI-NDVI)

Tab. 6. Accuracy Assessment of binary Images resulting
Tab.6. Ocena dokładności uzyskanych obrazów binarnych

	NDTI Index		**Multi-Index NDTI/BSI/NDVI**		**Multi-Index NDTI/DBSI/NDVI**	
Accuracy types	User Accuaracy (UA) %	Producer Accuaracy (PA) %	User Accuaracy (UA) %	Producer Accuaracy (PA) %	User Accuaracy (UA) %	Producer Accuaracy (PA) %
Built-up	79.32	89.32	85.84	92.76	81.38	83.33
Non Built-up	91.22	83.84	95.26	91.22	89.28	88.46
Overall accuracy (%)	86.43		91.96		86.14	
Kappa Coefficient (%)	72.24		82.34		71.24	

tween the built-up area index (NDTI) and both BSI and DBSI. Meanwhile, the BSI index exhibits the lowest correlation with the NDVI index. The correlation between NDVI and NDTI indices is moderate.

Based on the degree of relationship discussed among the four spectral indices, two different combinations are proposed through a layer stacking process to enhance spectral differences between three main land cover classes (built-up area, bare soil, vegetation cover). The combinations are achieved by retaining both NDTI and NDVI indices, with the NDTI/BSI/NDVI trio being the first combination, and the NDTI/DBSI/NDVI trio being the second combination. These composite spectral indices are compared with the NDTI spectral index to determine the most accurate result for extracting built-up areas. Furthermore, to evaluate the impact of the bare soil index on the original NDTI/NDVI combination aimed at reducing misclassification between bare soil and built-up areas.

3.2.3 Extraction of urban built-up land by using the K-means method

Urban built-up land in the study area primarily comprises residential and industrial zones, roads, and other impervious surfaces. However, the non-urban built-up land includes forests, grasslands, and bare land. To achieve high-accuracy separation between these two main classes (built-up and non-built-up areas), binarization was utilized. However, the author Zuur et al., 2007 [28] reported that highlighting a specific land cover type by determining optimal thresholds is a major challenge.

3. Results and Discussion

3.1. Results of spectral indices

In this study, ENVI 5.1 software with the "Band Math" tool was used to calculate the spectral indices provided for further analysis. The calculated results of the spectral indices for the research area are presented in Figure 2.

The spectral profiles presented in Figure 3 show that the NDVI index highlights vegetation areas with large positive values, depicted by shades of gray and white observable in the 3D image (Figure 3). Additionally, the BSI and DBSI emphasize uncultivated and abandoned fields. Average values refer to built-up areas, while low values indicate vegetation cover. Vegetation and bare soil in areas with positive NDTI values and urban built-up land are represented by low positive NDTI values. Conversely, constructed structures yield negative values, depicted by darker pixels in Figure 3. Moreover, the statistical values of the four spectral indices can be found in Table 3, where low standard deviation values are observed for all the spectral indices used.

Based on the analysis of the spectral profiles presented in Figure 4, the process of mapping built-up land from other primary land cover types such as bare soil and vegetation can be easily achieved using the unsupervised classification algorithm K-means developed by [29]. The algorithm is applied for quick and accurate clustering of predefined classes [30]. The K-means algorithm has been successfully utilized to extract a specific land cover class in a region from a single spectral index result [9]. Additionally, the work of [31] has demonstrated the effectiveness of the algorithm for land cover classification based on multi-spectral datasets. The extraction of urban built-up land layers using the K-means algorithm is performed using ENVI 5.1 software.

3.2. Results of urban built-up land by using the K-means method

The results of the urban built-up land layer extraction using the NDTI index and the selected multi-spectral dataset

are presented in Figure 4. Statistical data generated from the classification results of spectral indices using the K-means algorithm are shown in Table 5.

Based on the surface area coverage values of each land cover type extracted from the multi-spectral dataset in Table 5, we observe that the area of built-up land classified from the NDTI/BSI/NDVI multi-spectral dataset is 593.23 km^2, accounting for approximately 57.29% of the total study area; this built-up land area is smaller than the corresponding area classified from the NDTI/DBSI/NDVI multi-spectral dataset, which is 2.32 km^2, and larger than the built-up land area when using only the NDTI index, which is 61.89 km^2.

3.3. Accuracy Assessment

The accuracy assessment was conducted using the stratified random sampling method [32], which recommends a minimum of 150 points for each class; 300 random points were distributed among the built-up and non-built-up classes. Additionally, high-resolution images from Google Earth taken on the same day were utilized as reference data. Subsequently, the error matrix [33] was computed as a result of assessing the classification accuracy, including overall accuracy and the Kappa coefficient, producer's accuracy (PA), and user's accuracy (UA). All accuracy metrics are presented in Table 5.

The error matrix presented in Table 5 indicates that the accuracy of the built-up land area is better when comparing the use of the NDTI/BSI/NDVI multi-spectral dataset with the NDTI/DBSI/NDVI multi-spectral dataset. The overall accuracy achieved is 91.96% and 86.14%, with corresponding Kappa coefficients of 82.34% and 71.24%, respectively. Therefore, the improvement in accuracy observed, with an increase of 11.1% in the Kappa coefficient and 5.82% in overall accuracy, is significant. Meanwhile, the NDTI/DBSI/NDVI multi-spectral dataset provides classification results for the built-up land class with similar accuracy in both overall accuracy and Kappa coefficient compared to the classification results using only the NDTI index in the study area. The error matrix shows that the user's accuracy of the built-up land class classified from the NDTI/BSI/NDVI multi-spectral dataset is 85.84%, an increase of 4.44% compared to the user's accuracy when classified from the NDTI/DBSI/NDVI multi-spectral dataset. Similarly, the producer's accuracy of the built-up land class classified from the NDTI/BSI/NDVI multi-spectral dataset is 92.76%, an increase of 9.43% compared to the producer's accuracy when classified from the NDTI/DBSI/NDVI multi-spectral dataset.

3.4 Discussion

Through visual observation of the classification results of built-up land illustrated in Figure 5, it is evident that using the NDTI index and developing multispectral indices has differentiated built-up land from other land types. Observations indicate that some vacant land pixels are misclassified as built-up, especially bright land and vice versa. The DBSI index generates a larger dynamic range compared to the BSI index. Therefore, the DBSI index delineates more built-up land surface than vacant land surface than the BSI index provides. This suggests that the BSI index influences the separation of vacant and built-up land by reducing misclassified pixels through minimizing spectral confusion of both classes. Thus, the BSI index has demonstrated effectiveness in mapping vacant land. As forest class has negative values for both classified vacant land outcomes illustrated in Figure 4, the addition of the NDVI index highlights vegetation with high positive values for the multispectral index, enabling automated classification to distinguish vegetation from vacant land during the classification process.

The analyses above have demonstrated that the BSI index in the multispectral index NDTI/BSI/NDVI yields the most accurate classification results for built-up land due to its enhanced ability to differentiate vacant land from built-up areas. Therefore, using multispectral imagery NDTI with the addition of BSI and NDVI indices proves to be more effective in extracting built-up land from vacant land when employing the K-means classification method.

These results support the method proposed by Ettehadi Osgouei et al., 2019 [24], which advocates a multispectral index-based approach centered on NDTI. Furthermore, the findings also contribute to the developments made by Li et al., 2017 [9] regarding classification methods based on stacking spectral indices as input datasets for K-means clustering. Therefore, the paper re-evaluated both multispectral indices in the classification of built-up and vacant land and compared their impacts since being used in conjunction with the NDTI index. Additionally, the results demonstrate the effective synergy among the three approaches of the aforementioned studies [9; 31] to enhance the discrimination between built-up land and other land types, developed from data tested in urban areas during the dry season.

4. Conclusion

Hanoi city (the capital of Vietnam) is characterized by a climate with distinct dry and rainy seasons, chosen as the research area. The main objective of this study is to find the best solution for combining multispectral indices to accurately extract the built-up land class from other land cover types, primarily vacant land, through experiments using a layer stacking method of various pre-selected spectral indices. Various remote sensing software tools were employed, including SNAP, ENVI, and ArcGIS, to process Sentinel-2 satellite image data.

Separating the built-up land has been the main problem in mapping urbanized areas. In general, both combinations of multispectral indices, NDTI/BSI/NDVI and NDTI/DBSI/NDVI, for Sentinel-2 satellite image data were tested for built-up land mapping through K-mean classification. The results obtained showed a fast classification process for built-up land. However, based on error matrices including overall accuracy and Kappa coefficient, the best results were observed when using multispectral indices comprising BSI in combination with NDTI and NDVI compared to the combination with DBSI.

Competing Interest

All authors declare no conflict of interest.

Funding

This research received no external funding.

Authors' Contributions

Conceptualization, L.T.T.H, N.H.L; data curation, formal analysis, P.T.L; investigation, L.T.T.H, N.H.L; methodology, N.V.T, N.H.L; project administration and supervision, P.T.L, N.H.L; visualization, L.T.T.H, N.H.L; writing original draft, L.T.T.H; writing, reviewing & editing, P.T.L, N.V.T. All authors commented on previous versions of the manuscript. All authors read and approved the final manuscript.

Consent for publication

Not applicable.

Literatura – References

1. Azad Rasul et al,.2018. Applying Built-Up and Bare-Soil Indices from Landsat 8 to Cities in Dry Climates. Land, 7, 81; doi:10.3390/land7030081
2. Bouzekri, S., Aziz Lasbet, A., Lachehab, A. 2015. A New Spectral Index for Extraction of BuiltUp Area Using Landsat-8 Data. Journal of the Indian Society of Remote Sensing, 43. https://doi.org/10.1007/s12524-015-0460-6
3. Bramhe, V., Ghosh, S., Garg, P. 2018. Extraction of builtup area by combining textural features and spectral indices from Landsat-8 multispectral image. ISPRS - International Archives of the Photogrammetry, Remote Sensing and Spatial Information Sciences, XLII-5, 727-733. https://doi.org/10.5194/isprsarchives-XLII-5-727-2018
4. Deng, C., Wu, C. 2012. BCI: A biophysical composition index for remote sensing of urban environments. Remote Sensing of Environment, 127, 247-259. https://doi.org/10.1016/j.rse.2012.09.009
5. Ettehadi Osgouei, P., Kaya, S., Sertel, E., Alganci, U. 2019. Separating Built-Up Areas from Bare Land in Mediterranean Cities Using Sentinel-2A Imagery. Remote Sensing, 11(3). https://doi.org/10.3390/rs11030345
6. Rasul, A., Balzter, H., Ibrahim, G.R.F., Hameed, H.M., Wheeler, J., Adamu, B.,... Najmaddin, P.M. 2018. Applying Built-Up and Bare-Soil Indices from Landsat 8 to Cities in Dry Climates. Land, 7(3), 81. https://doi.org/10.3390/land7030081
7. S.Vigneshwaran, S.Vasantha Kumar, 2018. Extraction of built-up area using high resolution sentinel-2A and google satellite imagery. The International Archives of the Photogrammetry, Remote Sensing and Spatial Information Sciences, Volume XLII-4/W9, International Conference on Geomatics and Geospatial Technology (GGT 2018), 3–5 September 2018, Kuala Lumpur, Malaysia
8. V. S. Bramhe1,* et al., 2018. Extraction of built-up area by combining textural features and spectral indices from landsat-8 multispectral image. The International Archives of the Photogrammetry, Remote Sensing and Spatial Information Sciences, Volume XLII-5, ISPRS TC V Mid-term Symposium "Geospatial Technology – Pixel to People", 20–23 November 2018, Dehradun, India
9. Li, H., Wang, C., Zhong, C., Su, A., Xiong, C., Wang, J., Liu, J. 2017. Mapping Urban Bare Land Automatically from Landsat Imagery with a Simple Index. Remote Sensing, 9(3), 249. https://doi.org/10.3390/rs9030249
10. Jieli, C., Manchun, L., Yongxue, L., Chenglei, S., Wei, H. 2010. Extract residential areas automatically by New Built-up Index. In Proceedings of the 18th International Conference on Geoinformatics, Beijing, China. https://doi.org/10.1109/GEOINFORMATICS.2010.5567823
11. Deng, C., Wu, C. 2012. BCI: A biophysical composition index for remote sensing of urban environments. Remote Sensing of Environment, 127, 247-259. https://doi.org/10.1016/j.rse.2012.09.009
12. Eskandari, I., Navid, H., Rangzan, K. 2016. Evaluating spectral indices for determining conservation and conventional tillage systems in a vetch-wheat rotation. International Soil and Water Conservation Research, 4(2), 93-98. https://doi.org/10.1016/j.iswcr.2016.04.002
13. Rikimaru, A., Miyatake, S. 1997. Development of Forest Canopy Density Mapping and Monitoring Model using Indices of Vegetation, Bare soil and Shadow. Paper presented at the Proceedings of the 18th Asian Conference on Remote Sensing (ACRS) 1997, Kuala Lumpur, Malaysia.
14. Sun, G., Chen, X., Jia, X., Yao, Y., Wang, Z. 2016. Combinational Build-Up Index (CBI) for Effective Impervious Surface Mapping in Urban Areas. IEEE Journal of selected topics in applied earth observations and remote sensing, 9(5), 2081-2092. https://doi.org/10.1109/JSTARS.2015.2478914
15. Waqar, M., Mirza, J., Mumtaz, R., Hussain, E. 2012. Development of New Indices for Extraction of Built-Up Area & Bare Soil from Landsat Data. Open Access Scientifc Reports, 1(1), 01-04
16. Xi, Y., Thinh, N.X., Li, C. 2019. Preliminary comparative assessment of various spectral indices for built-up land derived from Landsat-8 OLI and Sentinel-2A MSI imageries. European Journal of Remote Sensing, 52, 240-252. https://doi.org/10.1080/22797254.2019.1584737
17. Xu, H. 2008. A new index for delineating built-up land features in satellite imagery. International Journal of Remote Sensing, 29, 4269-4276. https://doi.org/10.1080/01431160802039957

18. Nur Hidayati, I., Suharyadi, R., Danoedoro, P. 2018. Developing an Extraction Method of Urban BuiltUp Area Based on Remote Sensing Imagery Transformation Index. Forum Geograf, 32. https://doi.org/10.23917/forgeo.v32i1.5907
19. Xi, Y., Thinh, N.X., Li, C. 2019. Preliminary comparative assessment of various spectral indices for built-up land derived from Landsat-8 OLI and Sentinel-2A MSI imageries. European Journal of Remote Sensing, 52, 240-252. https://doi.org/10.1080/22797254.2019.1584737
20. Pal, M., Antil, K. 2017. Comparison of Landsat 8 and Sentinel 2 data for Accurate Mapping of Built-Up Area and Bare Soil. Paper presented at the 38th Asian Conference on Remote Sensing, New Delhi, India.
21. Valdiviezo-N, J., Téllez-Quiñones, A., Salazar-Garibay, A., López-Caloca, A. 2018. Built-up index methods and their applications for urban extraction from Sentinel 2A satellite data: discussion. Journal of the Optical Society of America A, 35, 35-44. https://doi.org/10.1364/JOSAA.35.000035
22. Rikimaru, A., Miyatake, S. 1997. Development of Forest Canopy Density Mapping and Monitoring Model using Indices of Vegetation, Bare soil and Shadow. Paper presented at the Proceedings of the 18th Asian Conference on Remote Sensing (ACRS) 1997, Kuala Lumpur, Malaysia.
23. Daughtry, C.S.T., Serbin, G., Reeves, J.B., Doraiswamy, P.C., Hunt, E.R. 2010. Spectral Reflectance of Wheat Residue during Decomposition and Remotely Sensed Estimates of Residue Cover. Remote Sensing, 2(2), 416-431. https://doi.org/10.3390/rs2020416
24. Ettehadi Osgouei, P., Kaya, S., Sertel, E., Alganci, U. 2019. Separating Built-Up Areas from Bare Land in Mediterranean Cities Using Sentinel-2A Imagery. Remote Sensing, 11(3). https://doi.org/10.3390/rs11030345
25. Deventer, A., Ward, A.D., Gowda, P.H., Lyon, J.G. 1997. Using Thematic Mapper Data to Identify Contrasting Soil Plains and Tillage Practices, Photogrammetric Engineering and Remote Sensing, 63(1), 87-93.
26. F. Spoto et al., "Overview Of Sentinel-2," 2012 IEEE International Geoscience and Remote Sensing Symposium, Munich, Germany, 2012, pp. 1707-1710, doi: 10.1109/IGARSS.2012.6351195. keywords:
27. A. K. Bhandaria, A. Kumara, and G. K. Singhb,*. Feature Extraction using Normalized Difference Vegetation Index (NDVI): a Case Study of Jabalpur City. Procedia Technology 6, 612 – 621. doi: 10.1016/j.protcy.2012.10.074
28. Zuur, A.F., Ieno, E.N., Smith, G.M. 2007. Principal component analysis and redundancy analysis. In Analysing Ecological Data. Statistics for Biology and Health. Springer, New York, NY. pp. 193-224. https://doi.org/10.1007/978-0-387-45972-1
29. MacQueen, J. 1967. Some Methods for Classifcation and Analysis of Multivariate Observations. Paper presented at the In L.M. Le Cam & J. Neyman (eds.) Proceedings of the 5th Berkeley Symposium on Mathematical Statistics and Probability. University of California Press, Berkeley, CA, USA.
30. Gllavata, J., Ewerth, R., Freisleben, B. 2004. Text detection in images based on unsupervised classifcation of high-frequency wavelet coeffcients. In Proceedings of the 17th International Conference on Pattern Recognition, 2004. ICPR 2004. https://doi.org/10.1109/ICPR.2004.1334146
31. Gašparović, M., Zrinjski, M., Gudelj, M. 2019. Automatic cost-effective method for land cover classifcation (ALCC). Computers, Environment and Urban Systems, 76, 1-10. https://doi.org/10.1016/j.compenvurbsys.2019.03.001
32. Congalton, R. 1991. A Review of Assessing the Accuracy of Classifcations of Remotely Sensed Data (Vol. 37). https://doi.org/10.1016/0034-4257(91)90048-B
33. Foody, G.M. 2002. Status of land cover classifcation accuracy assessment. Remote Sensing of Environment, 80(1), 185-201. https://doi.org/10.1016/S0034-4257(01)00295-4

Zastosowanie wielospektralnego indeksu z danych Sentinel-2 do ekstrakcji terenów zabudowanych w rejonie Hanoi w sezonie suchym

Wskaźnik zdalnego wykrywania jest prostym i skutecznym sposobem na wyróżnienie określonego pokrycia terenu. Dlatego w tym badaniu staramy się zwiększyć dokładność mapy terenów miejskich opracowanej dla miasta Hanoi, skupiając się na określeniu odpowiedniego połączenia wskaźników spektralnych obliczanych z danych obrazów satelitarnych. Do przeprowadzenia badania wybrano cztery wskaźniki spektralne, a mianowicie znormalizowany wskaźnik różnicy uprawy (NDTI), wskaźnik gołej gleby (BSI), wskaźnik suchej gołej gleby (DBSI) i znormalizowany wskaźnik różnicy wegetacji (NDVI). Wszystkie te wskaźniki spektralne są obliczane z danych Sentinel-2 uzyskanych w sezonie suchym. Dwie kombinacje są tworzone z nakładania się warstw wskaźników spektralnych NDTI/BSI/NDVI i NDTI/DBSI/NDVI. Użycie algorytmu "K-means" jako klasyfikatora nienadzorowanego zapewnia szybkie i automatyczne wykrywanie terenów miejskich. Wyniki pokazują, że wskaźnik BSI działa lepiej niż użycie wskaźnika DBSI. W rezultacie wskaźnik BSI przynosi poprawki: typy gołej gleby i procesy akumulacji są lepiej zróżnicowane, a ogólna dokładność wzrasta o 5,82%, a współczynnik Kappa wzrasta o 11,1%. Wyniki pokazują, że zestaw danych wielospektralnych wskaźników NDTI/BSI/NDVI jest odpowiedni do mapowania obszarów miejskich z potencjałem pomocy w lepszym zarządzaniu miastem podczas sezonu suchego.

Słowa kluczowe: *dane Sentinel-2, algorytm K-means, Bare Soil Index (BSI), Dry Bare Soil Index (DBSI), Normalized Difference Tillage Index (NDTI)*

Application of Robust Estimation for Adjustment Analysis in Geodetic Networks with Outliers in the Control Points

Tuan Anh LUU [1)]*

[1)] Faculty of Geomatics and Land Administration, Hanoi University of Mining and Geology, Hanoi, Vietnam; ORCID https://orcid.org/0009-0001-7738-9718

* Corresponding author: luuanhtuan@humg.edu.vn

http://doi.org/10.29227/IM-2024-01-95

Submission date: 15-05-2024 | Review date: 03-06-2024

Abstract

In the field of data analysis, the method of least squares has been a go-to approach when dealing with measurements that contain random errors. However, this method shows its limitations when faced with real-world data, which, in addition to accidental error, often contains outlier. These outlier can significantly skew the results, leading to inaccurate conclusions if not properly addressed. In response to this challenge, Robust Estimation has emerged as an effective method for handling outlier. Unlike traditional methods, Robust Estimation is designed to be less sensitive to outliers in the data, providing a more reliable and accurate estimate by reducing the impact of outlier on the final result. One of the key features of Robust Estimation is its flexibility. The outcome of each robust estimation method is influenced by the choice of its weight function, allowing the method to be tailored to the specific characteristics of the data. This paper applies the principles of Robust Estimation to the analysis of geodetic networks, which often contain original data errors. By doing so, it aims to provide a more accurate and reliable analysis of these networks, contributing to their improved utilization and management.

Keywords: *Robust Estimation, outliers, Geodetic Network*

1. Introduction

Currently, Vietnam's Ministry of Natural Resources and Environment is building and implementing the project "Modernizing the national geodetic network system for planning, construction, socio-economic development and response to climate change in some large cities and coastal areas". The goal of important national work is to complete and modernize the sustainable and stable national coordinate and elevation system to ensure accurate and consistent determination of elevations of points and locations throughout the country and meet the increasing requirements of socio-economic development, national security and defense, and response to climate change. Tasks that need to be implemented include calculating and adjusting the national coordinate and elevation network and announcing the new National Elevation System. The network has various types of measurement values such as complete measurements of the modern national elevation network connecting "century benchmarks", GNSS CORS points, repeated measurements of the vertical displacement monitoring network in cities of Hai Phong, Hanoi, Da Nang, Ho Chi Minh, Can Tho and the Mekong Delta region using leveling method to analyze, evaluate and determine the causes of subsidence.

Robust estimation method is used in many applications such as GPS positioning [1, 2], GPS coordinate transformation [3], polynomial modelling [4], study of relationship between lake's water area and water level [5], data reconciliation [6], robotics [7], evaluation of the air quality area [8], etc. Various robust estimating techniques are employed to identify minor outliers that could exist in geodetic measurements. Comparative assessment of several resilient estimating techniques for deformation analysis was presented in [9]. Among these techniques are the Danish approach, the Least Absolute Sum, and robust M-estimators.

Thus, when modernizing the construction of the geodetic network, it is natural to make measurements connected to points with higher accuracy and then there is a case where the original points contain errors. Therefore, it is necessary to research data processing methods in this case. On the other hand, the measurement data of the control network cannot avoid outliers. For such a control network system, a data processing tool with coarse error detection and network reliability analysis is needed. In this article, the application of the Robust estimation method is chosen as a solution to solve the problem of data processing and network analysis.

The construction and development of Robust estimation theory is mentioned in many publications [10-12]. The essence of Robust estimation theory is that in cases wh`ere crude errors cannot be avoided, choose an appropriate estimation method so that the estimated values of the parameters are not affected. One of the robust estimation methods is robust estimation M proposed by Huber in 1964 and applied to geodetic data processing. Besides, some scientists have researched and successfully applied robust estimation methods such as Professor Zhow Jiangwen (1980) proposed the principle of estimating M in case the measured values are not of the same accuracy. The method of changing the weights during the adjustment process to achieve parameter stability is called the weight replacement method. Today, a number of scientists have been researching and applying robust estimates in different fields, including surveying. However, Vietnam's geodetic network has its own characteristics, so we research and modify a robust estimation method to process geodetic network data effectively in Vietnamese conditions.

According to [13], in the presence of measurement errors, robust estimation produces "less-biased" estimates than the least squares approach. The least median squares (LMS) approach is a reliable estimating technique. In other study, [14] conducted a study on application of robust estimation in geodetic networks. The obtained results indicated that least-squares adjustment of a geodetic network is the best alternative when neither gross nor systematic errors affect the observations nor the mathematical model. The most likely network solution is then provided by the least-squares adjustment. In order to address large mistakes in close-range photogrammetric data sets that call for a photo bundle correction solution, [15] evaluated the efficiency of robust estimate models. The findings of investigation show that, in comparison to the least squares approach, all robust approaches have the advantage of being able to identify and eliminate gross flaws, particularly when the observation contains large-scale errors. In addition, [16] used this method to detemine displacements in geodetic control network of dam. Then, the advantage of M-estimation over ordinary least squares adjustment in minimizing the impact of outliers on estimated network parameters is demonstrated in this study. Also related to identifing deformation, [17].

In Vietnam, there are not many studies mentioning this method. [18] applied a robust estimation method with a reasonable weight function to adjust and analyze the spatial ground network - GPS. The obtained results show that this method allows searching for raw measurement values, Therefore, “clean” measurement data can be generated and adjusted using the usual method. Also using this method, [19] detected coarse errors in the Son La hydropower construction grid based on robust estimates according to the posterior variance. The calculation results show that this method is effective. In addition to being able to determine the measurement value containing raw error, it can also determine the approximate value of the raw error in the measurement value, and moreover determine the exact value of the measurement value. get not just one but many gross errors in the measurement set. However, Vietnam's geodetic network has its own characteristics, so we research and modify a robust estimation method to process geodetic network data effectively in Vietnamese conditions.

2. Method of Robust estimation applied network adjustment containing the errors of control points

2.1 The Robust Estimation method

Assuming that the matrix of independent measurement called L_{nxl} and uknown vector is $\hat{X}_{txl}$; the observation equations can be rewritten that include residuals. The resulting set of equations is residual equation as [20]:

$$V_{nx1} = A_{nxt}\hat{X}_{tx1} + L_{nx1} = \begin{bmatrix} a_1 \\ a_2 \\ \dots \\ a_n \end{bmatrix}_{nxt} \begin{bmatrix} \hat{X}_1 \\ \hat{X}_2 \\ \dots \\ \hat{X}_t \end{bmatrix}_{tx1} + \begin{bmatrix} l_1 \\ l_2 \\ \dots \\ l_n \end{bmatrix} \quad (1)$$

where: A_{nxn} is the design matrix (coefficients matrix), a_i is the individual coefficients of ith, L_{nxl} is the vector of observation (freedom matrix).

From equation (1), the function of robust estimation has form as equation (2) [20]:

$$\rho(l_i, \hat{X}) = \rho(v_i) \quad (2)$$

Due to the measurements do not equal accuracy; so the weight P can be expressed in matrix form as equation (3):

$$P_{nxn} = \begin{pmatrix} p_1 & & & & \\ & p_2 & & & \\ & & \dots & & \\ & & & \dots & \\ & & & & p_n \end{pmatrix}_{nxn} \quad (3)$$

On the other hand, the ρ function must be minimized:

= min

$$\sum_{i=1}^{n} p_i \rho(v_i) = \sum_{i=1}^{n} p_i \rho(a_i \hat{X} + l_i) \quad (4)$$
$$= \min$$

Taking the derivative of expression (4) with respect to X, denoting $\varphi(v_i) = \frac{\partial \rho}{\partial v_i}$, setting the resulting equation equal to zero yields:

$$\sum_{i=1}^{n} p_i \varphi(v_i) a_i = 0 \quad (5)$$
$$= \min$$

Let $\bar{p}_i = p_i w_i$, $w_i = \frac{\varphi(v_i)}{v_i}$ we have:

$$\sum_{i=1}^{n} a_i^T \bar{p} v_i = 0 \quad (6)$$

or we can write equation (6) as equation (7):

$$A^T P V = 0 \quad (7)$$

Besides, replaceing the V matrix with given in Equation (7) yields the normal matrix of robust estimation M as equation (8):

$$A^T \bar{P} A\hat{X} + A^T \bar{P} L = 0 \quad (8)$$

where: $\bar{P}$ is the weight matrix, $\bar{p}_i$is the weight element, w_i is weight coefficients.

The $\hat{X}$ parameters of robust estimation M can be determined as:

$$\hat{X} = (A^T \bar{P} A)^{-1} x A^T \bar{P} L \quad (9)$$

The Function of weight Robust is described as the equation (10), where, c is constant value and select with c of 1.5.

$$\begin{aligned} &w_i = 1 && |\bar{v}_i| \le c \\ &w_i = \frac{c}{|\bar{v}_i|}; \bar{v}_i = \frac{v_i}{s_{v_i}}; \bar{p}_i = p_i w_i; && |\bar{v}_i| > c \\ &w_{ij} = w_{jj} = 1; && |\bar{v}_i| \le c; |\bar{v}_j| \le c; \\ &w_{ij} = \frac{c}{|\bar{v}_i|}; \bar{v}_i = \frac{v_i}{s_{v_i}}; w_{jj} = \frac{c}{|\bar{v}_j|}; \bar{v}_j = \frac{v_j}{s_{v_j}}; \bar{p}_j = p_j w_j; && |\bar{v}_i| > c; |\bar{v}_j| > c; \end{aligned} \quad (10)$$

2.1 Network adjustment containing the errors of control points

In this case, the control points are held fixed which is not perfect, meaning that they contain errors. Therefore, the unknown value is included coordinate of the control point.

For adjustment containing the errors of control points, we can choose B=0; β=E, the residual equation is [20]:

$$\begin{aligned} V &= A.X + a\hat{X} + L \\ V &= E.X + L \end{aligned} \quad (11)$$

Where: $\hat{X}$ is the unknown vector of the control point; X is the residual vector of approximate value $X^{(0)}$. If $X^{(0)}$ equal to L and to zero, the equation shows:

Tab. 1. Angle measurement

Tab. 1. Pomiar kąta

No	Angle			Value (0 ' ")		
		Occupy	Backsight	Backsight	Occupy	second
1	II	I	III	33	27	26
2	V	II	I	28	34	41
3	IV	II	V	50	51	39
4	III	II	IV	46	35	36
5	I	III	II	20	30	44
6	IV	III	I	40	44	55
7	II	IV	III	72	8	46
8	V	IV	II	71	13	18
9	II	V	IV	57	55	01
10	I	V	II	32	50	07
11	III	I	V	85	8	00

Tab. 2. Distance measurement

Tab. 2. Pomiar odległości

No	Distance		S(m)
	Occupy	Sight	
1	I	II	404.919
2	I	III	934.485
3	I	V	357.225
4	II	III	637.048
5	II	IV	586.833
6	II	V	655.743
7	III	IV	486.229
8	IV	V	537.194

Tab. 3. Baseline components ΔX, ΔY and their weight in rectangular coordinate system

Tab. 3. Składniki bazowe ΔX, ΔY i ich waga w prostokątnym układzie współrzędnych

No	Baselines		Observe		Weight		
	Occupy	Sight	ΔX	ΔY	Occupy	Sight	ΔX
1	I	II	-216.141	342.407	890914.68	-262093.59	323744.99
2	I	III	-851.811	384.289	682879.24	-195924.51	166977.63
3	I	V	-174.003	-311.984	667251.90	-229191.31	471605.13
4	II	III	-635.682	41.860	801837.10	-244621.72	197906.39
5	II	IV	-430.401	-398.913	1075012.79	-326412.03	341196.31
6	II	V	42.152	-654.398	2205098.64	-720459.46	1034072.38
7	III	IV	205.274	-440.776	216375.89	-113497.00	196044.45
8	IV	V	472.540	-255.501	1199357.84	-349210.59	403780.78

Tab. 4. The difference of residual angle between including outliers and without outliers

Tab. 4. Różnica kąta resztkowego pomiędzy uwzględnieniem wartości odstających i bez wartości odstających

No	Angle			v_i (") without outliers	Residual Difference $\Delta v_i = \lvert v_i - v_i' \rvert$ (second)	Including outliers
	Backsight	Occupy	Foresight	**1.07**	**0.84**	
1	II	I	III	-5.64	0.12	
2	V	II	I	-6.08	0.50	
3	IV	II	V	1.41	0.26	
4	III	II	IV	3.23	0.03	
5	I	III	II	-7.45	2.47	
6	IV	III	I	1.81	2.70	
7	II	IV	III	7.45	2.86	
8	V	IV	II	0.63	**15.63**	**+ 18"**
9	II	V	IV	3.33	1.50	
10	I	V	II	-0.77	0.84	
11	III	I	V	1.07	0.12	

Tab. 5. The difference of residual distance between including outliers and without outliers

Tab. 5. Różnica odległości resztkowej pomiędzy uwzględnieniem wartości odstających i bez wartości odstających

No	Distance		v_i (mm) without outliers	Residual Difference $\Delta v_i = \lvert v_i - v_i' \rvert$ (mm)	Including outliers (mm)
	Occupy	Sight			
1	I	II	-2.94	1.58	
2	I	III	-1.12	1.12	
3	I	V	-4.39	2.25	
4	II	III	-3.30	1.23	
5	II	IV	-5.17	5.17	
6	II	V	-1.94	2.01	
7	III	IV	-1.71	1.71	
8	IV	V	-0.58	**98.08**	**+100mm**

Tab. 6. The difference of residual baseline between including outliers and without outliers

Tab. 6. Różnica resztowej linii bazowej pomiędzy uwzględnieniem wartości odstających i bez wartości odstających

No	Baselines		v_i (mm) without outliers		Residual Difference $\Delta v_i = \lvert v_i - v_i \rvert$ (mm)		Including outliers
	Occupy	Sight					
1	II	I	-0.38	-2.62	97.62	0.38	Ax +100mm
2	III	I	-3.29	-5.61	1.17	0.14	
3	V	I	0.08	2.54	0.08	2.54	
4	II	III	3.33	3.77	1.21	0.24	
5	II	IV	2.10	4.12	3.21	4.15	
6	II	V	-2.46	-2.16	2.56	2.6	
7	IV	III	-3.77	1.65	4.42	3.91	
8	V	IV	-4.44	-5.72	5.66	6.31	

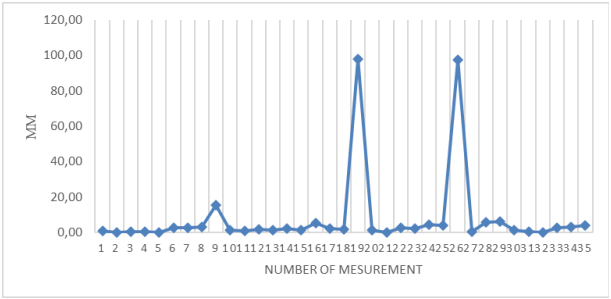

Fig. 1. Difference of residual between two cases: without and including outliers

Rys. 1. Różnica reszt pomiędzy dwoma przypadkami: bez wartości odstających i z uwzględnieniem wartości odstających

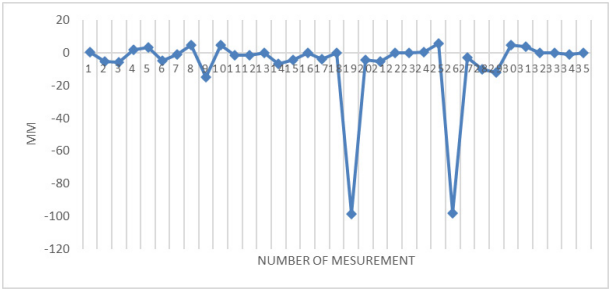

Fig. 2. Detecting outliers using robust estimates

Rys. 2. Wykrywanie wartości odstających przy użyciu solidnych szacunków

$$\begin{aligned} RX + Ra\hat{X} + b &= 0 \\ R_a^T X + R_X X + b_a &= 0 \end{aligned} \tag{12}$$

Where: $R_\alpha = A^T P\alpha;\ R_X = R_{\alpha\alpha} + P; R_{\alpha\alpha} = \alpha^T P\alpha;\ b_\alpha = \alpha^T PL$

From equation (12), it can be written as:

$$\begin{bmatrix} R & R_\alpha \\ R_\alpha^T & R_X \end{bmatrix}\begin{bmatrix} X \\ \hat{X} \end{bmatrix} + \begin{bmatrix} b \\ b_\alpha \end{bmatrix} = 0 \tag{13}$$

On the other hand, equation of residual equation (11) shows the block matrix:

$$\begin{bmatrix} V \\ \hat{V} \end{bmatrix} = \begin{bmatrix} A & \alpha & X \\ 0 & E & \hat{X} \end{bmatrix} + \begin{bmatrix} L \\ \hat{L} \end{bmatrix} \tag{14}$$

The problem of equation (14) can be solved with condiction as:

$$V^T PV + V^T Q_G^{-1} V = \min \tag{15}$$

Besides, the weight matrix has the form of a diagonal matrix as:

$$\bar{P} = \begin{bmatrix} P & \\ & Q_g^{-1} \end{bmatrix} \tag{16}$$

Therefore, the coefficient matrix of a system of linear equations can be written:

$$\begin{bmatrix} A^T & 0 \\ \alpha^T & E \end{bmatrix}\begin{bmatrix} P & \\ & Q_g^{-1} \end{bmatrix}\begin{bmatrix} A & \alpha \\ 0 & E \end{bmatrix} = \begin{bmatrix} A^T PA & A^T P\alpha \\ \alpha^T PA & \alpha^T P\alpha + Q_g^{-1} \end{bmatrix} \tag{17}$$

Finally, the standard deviation was calculated (mo) as:

$$m_0 = \sqrt{\frac{[PVV]}{n-t}} \tag{18}$$

Where:

$$[PVV] = V^T PV + V^T Q_G^{-1} V \tag{19}$$

2.4 Steps to calculate robust estimates in adjustment containing the errors of control points

Step 1: Setting up the residual equation

Assume that $w_1=w_2=w_3=...=w_n=1$

W = I, P = E , so $\bar{P}^{(0)} = \begin{bmatrix} P & 0 \\ 0 & Q_g^{-1} \end{bmatrix}$

Where: P is the weight matrix.

Step 2: Solving problem of equation (13), we can obtain the estimated value the first time X, $\hat{X}$ and equation (14) calculates the residual V flowing:

$$\hat{V}\begin{bmatrix} X \\ \hat{X} \end{bmatrix}^{(1)} = -\begin{bmatrix} A^T PA & A^T P\alpha \\ \alpha^T PA & \alpha^T P\alpha + Q_g^{-1} \end{bmatrix}^{-1}\begin{bmatrix} b \\ b_\alpha \end{bmatrix}$$

$$\begin{bmatrix} V \\ \hat{V} \end{bmatrix}^{(1)} = \begin{bmatrix} A & \alpha & X \\ 0 & E & \hat{X} \end{bmatrix} + \begin{bmatrix} L \\ \hat{L} \end{bmatrix}$$

Step 3: From this $V^{(1)}$, the weight matrix can be estimated based on equation (10), and then solving general equation (13) to obtain a matrix of $X^{(2)}$ and $X^{(2)}$. Calculating the residual matrix $V^{(2)}$ and $V^{(2)}$ by equation (20).

Step 4: Similar to step 3, from matrix of $\hat{X}^{(2)}$, $\bar{P}^{(2)}$ the equation of (13) can be calculated. This process was repeated and stopped until the different values twice in a row were less than 10^{-6} mm.

Step 5: Final result is determined from equation (21):

$$\begin{bmatrix} X \\ \hat{X} \end{bmatrix}^{(2)} = -\begin{bmatrix} A^T P^{(1)} A & A^T P^{(1)} \alpha \\ \alpha^T P^{(1)} A & \alpha^T P^{(1)} \alpha + Q_g^{-1} \end{bmatrix}^{-1}\begin{bmatrix} b \\ b_\alpha \end{bmatrix}\begin{bmatrix} V \\ \hat{V} \end{bmatrix}^{(2)} = \begin{bmatrix} A & \alpha & X^{(2)} \\ 0 & E & \hat{X}^{(2)} \end{bmatrix} + \begin{bmatrix} L \\ \hat{L} \end{bmatrix} \quad (20)$$

$$\begin{bmatrix} X \\ \hat{X} \end{bmatrix}^{(k)} = -\begin{bmatrix} A^T P^{(k-1)} A & A^T P^{(k-1)} \alpha \\ \alpha^T P^{(k-1)} A & \alpha^T P^{(k-1)} \alpha + Q_g^{-1} \end{bmatrix}^{-1}\begin{bmatrix} b \\ b_\alpha \end{bmatrix}\begin{bmatrix} V \\ \hat{V} \end{bmatrix}^{(k)} = \begin{bmatrix} A & \alpha & X^{(k)} \\ 0 & E & \hat{X}^{(k)} \end{bmatrix} + \begin{bmatrix} L \\ \hat{L} \end{bmatrix} \quad (21)$$

3. Data and experiment

The Lang Son geodetic network consists of two control points and three unknown points. In this network, there are 11 angles, 8 distances, and 8 baseline vectors. Besides, the weight of the control point is equal to PX = PY = 50.000. Note that, the network will adjust in the rectangular coordinate system. Network adjustment containing the errors of control points based on least squares. Assuming that the blunder in angle is (II-V-IV) + 18'' and distance is S(IV-V)+ 100 mm, while baseline is ΔX(I-II) +100 mm. To detect the blunders, we use adjustments combined containing the errors of control points and robust estimates. Creating the data without blunder to adjust using the principle of least squares or robust estimates to possess the outliers (errors) in order to calculate the most probable value.

Note that, the Total point has error of measurements are mS = ±(2mm + 1ppm.D) and $m_{\beta i}$=3'' for distance and angles, respectively.

From the result of the experiment shown in Tables 4, 5, 6, and Figure 1 and Figure 2; it can be shown that The outliers were detected accurately, and the magnitude of the estimated outlier is approximately equal to the raw error value included in the experimental model.

4. Conclusion

The Robust estimation method is investigated in this paper, with the selection of a reasonable weight function to detect measurements containing blunders, processing and analyzing the quality of the geodetic network containing the errors of control points for reliable results. Combining the Robust estimation algorithm with the model of network adjustment containing the errors of control points, brings dual efficiency as it detects outliers while also addressing the impact of the errors in control points on the estimation results. This method allows for the identification of outliers, thereby assisting data processors in generating 'clean' measurement data and adjusting network according to conventional methods.

Literatura – References

1. Baselga, S. and L. García-Asenjo, Global robust estimation and its application to GPS positioning. Computers & mathematics with applications, 2008. 56(3): p. 709-714.
2. Gaglione, S., et al. Robust estimation methods applied to GPS in harsh environments. in 2017 European Navigation Conference (ENC). 2017. IEEE.
3. Ge, Y., Y. Yuan, and N. Jia, More efficient methods among commonly used robust estimation methods for GPS coordinate transformation. Survey Review, 2013. 45(330): p. 229-234.
4. Borowski, L. and M. Banas. Application of robust estimation in polynomial modelling. in 2018 Baltic Geodetic Congress (BGC Geomatics). 2018. IEEE.
5. Lv, J., et al., Application of Robust Estimation Method in Study of Relationship Between Lake's Water Area and Water Level. Journal of the Indian Society of Remote Sensing, 2018. 46: p. 1595-1603.
6. Llanos, C.E., M.C. Sanchez, and R.A. Maronna, Robust estimators for data reconciliation. Industrial & Engineering Chemistry Research, 2015. 54(18): p. 5096-5105.
7. Bosse, M., G. Agamennoni, and I. Gilitschenski, Robust estimation and applications in robotics. Foundations and Trends® in Robotics, 2016. 4(4): p. 225-269.
8. Solci, C.C., et al., Empirical study of robust estimation methods for PAR models with application to the air quality area. Communications in Statistics-Theory and Methods, 2020. 49(1): p. 152-168.
9. Hassan, K.M.Z., Comparative evaluation among various robust estimation methods in deformation analysis. Spatial Information Research, 2016. 24: p. 485-492.
10. Huber, P.J., Robust estimation of a location parameter, in Breakthroughs in statistics: Methodology and distribution. 1992, Springer. p. 492-518.
11. Huber, P.J., Robust estimation of a location parameter. Annals of Mathematical Statistics, 1964. 35: p. 73-101.
12. Huber, P.J., Robust statistics - A review. Annals of Mathematical Statistics, 1972. 43: p. 1041-1067.
13. Yetkin, M., Application of robust estimation in geodesy using the harmony search algorithm. Journal of Spatial Science, 2018. 63(1): p. 63-73.
14. Valero, J.L.B. and S.B. Moreno, Robust estimation in geodetic networks. Física de la Tierra, 2005. 17: p. 7.
15. Zaky, K.M. and A.A. Ghonem, Application of Robust Estimation Methods for Detecting and Removing Gross Errors from Close-Range Photogrammetric Data. Am. Acad. Sci. Res. J. Eng. Technol. Sci, 2019. 55: p. 111-120.
16. Banaś, M. Application of robust estimation methods to displacements determination in geodetic control network of dam. in 2017 Baltic Geodetic Congress (BGC Geomatics). 2017. IEEE.
17. Nowel, K., Robust M-estimation in analysis of control network deformations: Classical and new method. Journal of surveying engineering, 2015. 141(4): p. 04015002.
18. Hoang Ngoc Ha, L.A.T., Applying the Robust Estimation method for variance adjustment and analysis of GPS ground space networks. Journal of Geodesy and Cartography (in Vietnamese), 2019(39): p. 42-46.
19. Pham, K.Q. and T.K.T. Nguyen, Application of the method of robust estimation by posterior variance in detecting the raw error of geodetic control network. Journal of Mining and Earth Sciences Vol, 2021. 62(2): p. 57-64.
20. Ha, H.N., Adjustment computations geodetic network and GPS. Scientific and technical publisher, Hanoi (in Vietnamese), 2006.
21. Anh Tuan Luu, N.G.L., Application of weighting robust estimation in geodetic networks. GMMT2016 - International symposium on Geo-Spatial and Mobile mapping technologies and summer school for Mobile mapping technology, 2016.
22. Luu Anh Tuan, The study of optimal design methods and adjustment of combined GPS and terrestrial measurement applications in Vietnamese conditions. PhD thesis, Hanoi (in Vietnamese). 2020.
23. Luu Anh Tuan, Application of Robust Estimation Method for Establishing 3D Combined Terrestrial and GNSS Network: case study in Lang Son quarry (Vietnam). Journal of the Polish Mineral Engineering Society, 2020.
24. Wang Xinhou, T.B., QiuWeining, Yao Yibin (Translated form Chineses by Phan Van Hien), Advanced surveying adjustment 2015.

Zastosowanie Robust Estimation do analizy korekty w sieciach geodezyjnych z wartościami odstającymi w oryginalnych punktach kontrolnych

W dziedzinie analizy danych, metoda najmniejszych kwadratów była podstawowym podejściem przy radzeniu sobie z pomiarami zawierającymi błędy losowe. Jednak ta metoda pokazuje swoje ograniczenia w obliczu rzeczywistych danych, które oprócz błędów losowych często zawierają błędy grube. Te błędy grube mogą znacznie zniekształcić wyniki, prowadząc do nieprecyzyjnych wniosków, jeśli nie zostaną odpowiednio uwzględnione. W odpowiedzi na to wyzwanie, Robust Estimation pojawiła się jako skuteczna metoda radzenia sobie z błędami grubymi. W przeciwieństwie do tradycyjnych metod, Robust Estimation jest zaprojektowana tak, aby była mniej wrażliwa na wartości odstające w danych, dostarczając bardziej niezawodne i precyzyjne oszacowanie poprzez zmniejszenie wpływu błędów grubych na końcowy wynik. Jedną z kluczowych cech Robust Estimation jest jej elastyczność. Wynik każdej metody Robust Estimation ma wpływ przez wybór jej funkcji wagowej, co pozwala dostosować metodę do specyficznych cech danych. Ten artykuł stosuje zasady Robust Estimation do analizy sieci geodezyjnych, które często zawierają błędy pierwotnych danych. Robiąc to, ma na celu dostarczenie bardziej precyzyjnej i niezawodnej analizy tych sieci, przyczyniając się do ich lepszego wykorzystania i zarządzania.

Słowa kluczowe: *Robust Estimation, wartości odstające, sieć geodezyjna*

Monitoring Coastal Erosion and Deposition in Sam Son City, Vietnam – a Contribution from Remote Sensing Data

Lan Thi PHAM[1)], Dung Kim LE[2)], Son Si TONG[3)], Ha Thi Thu LE[4)]*

[1)] Faculty of Geomatics and Land Administration, Hanoi University of Mining and Geology, Hanoi, Vietnam; ORCID: https://orcid.org/0000-0003-3982-1896
[2)] Hong Duc University, Thanh Hoa, Vietnam.
[3)] Department of Space and Applications, Vietnam France University, Hanoi, Vietnam
[4)] Faculty of Geomatics and Land Administration, Hanoi University of Mining and Geology, Hanoi, Vietnam
* Corresponding author: phamthilan@humg.edu.vn

http://doi.org/10.29227/IM-2024-01-96

Submission date: 11-05-2024 | Review date: 01-06-2024

Abstract

Studying the trends in shoreline erosion and accretion is essential for a wide range of investigations conducted by coastal scientists, and coastal managers. Shoreline erosion and accretion occur as a result of both natural and human influences. Some areas along shoreline in Sam Son are eroded and deposed by natural coastal processes and human actions, such as storm, wave, tourism activities. Purpose of this work is to study the erosion and deposition in Sam Son over 33 years (1989–2022). Coastlines were extracted using multi-temporal Landsat images, and the shoreline change rate was determined using Digital Shoreline Analysis Systems (DSAS). The results of this paper inlustrated that the shoreline change in Sam Son undergoes significant and varied fluctuations across different areas. At the Hoi estuary, erosion rates vary from -2.22 m/year to -40.32 m/year. The construction of FLC Sam Son is one of the factors contributing to sedimentation loss in the northern part of Sam Son City, which is situated adjacent to the East Sea and next to the Ma River. Furthermore, the accretion rate has strongly increased, reaching 9.7 m/year in the Do River estuary. The phenomenon of sediment deposition serves as the basic for constructing hotels to cater to tourism in Sam Son.

Keywords: *erosion, deposition, remote sensing, DSAS, Sam Son*

1. Introduction

The coastal region is a crucial component of the Earth's surface, as it undergoes changes over both long and short time span [1]. Both coastal management and engineering design necessitate knowledge of the current shoreline location, its past positions, and its projected future positions [2]. Therefore, there is a pressing need to improve our understanding of the long-term dynamics of coastal change to offer scientific support for decision-making in coastal restoration efforts.

Coastal change is affected by natural and anthropogenic activities [3]. The shoreline is the most basic indicator of changes in the coastal environment, implying erosion, deposition, and subsequent recovery [4]. Assessing coastal erosion and accretion in coastal areas is essential for proposing strategies to address future sea-level rise [5]. The rise in sea levels caused by global warming, combined with coastal erosion, is resulting in the loss of shoreline infrastructure [6].

Coastal erosion, defined as the loss of land adjacent to a body of water, is assessed by monitoring the rate of change or horizontal displacement of a shoreline over time [7]. The erosion caused by wave and current action and the disappearance of mangrove vegetation are both attributable to the long-term impacts of human activities [8], disrupt the balance of dynamic coastal actions in the coastal process, leading to the long-term loss of sediment in the coastal zone and resulting in the destructive process of coastline retreat and beach erosion [9]. Coastal erosion represents a serious issue leading to the damage or loss of residences, hotels, and other coastal infrastructure, as well as the undermining of roads. Additionally, it contributes to the degradation and loss of valuable land and disrupts activities such as fishing, navigation, and recreation [10]. In erosion and deposition studies, there is an ongoing discussion about the degree to which coastal erosion is shaped by natural factors in contrast to anthropogenic distribution, encompassing tourism services and urbanization [11].

In contrast to erosion, the deposition process often involves the accumulation of sediment. Deposition happens when a body of water becomes overloaded with suspended or dissolved substances [12]. The rate of sediment deposition is influenced by wave action, seafloor topography [13], winds [14], and fine or light sediment [12]. Beside, the construction of coastal projects also affects the accumulation. For example, the wave barrier embankment outside the estuary significantly reduces the influx of sediment from the sea, causing sediment deposition [13]. In addition, the coastline is also extended seaward by land reclamation to facilitate the development of tourism and urban areas.

The requirement to define the coastline's position and analyze its changes across space and time is especially critical due to the extensive prolonged human habitation in the coastal region [15]. To address the consequences of coastal erosion in the future, we need to gather appropriate data and choose effective methods to determine the coastline position and evaluate shoreline changes. The shoreline change analysis was conducted to determine the rate of shoreline alteration, utilizing a series of multiple shoreline positions over time [16]. The rate of Shoreline changes are evident through erosion and accretion rates.

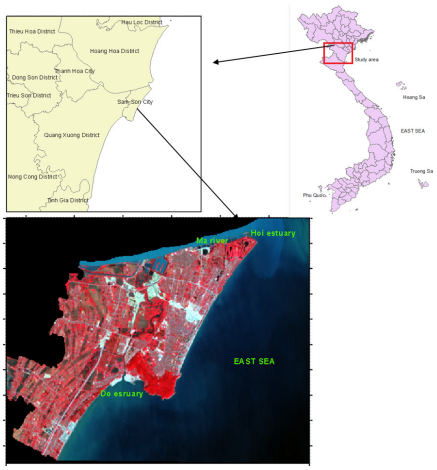

Fig. 1. Study area

Rys. 1. Obszar prowadzonych analiz

Tab. 1. List of satellite data (L8 – Landsat 8; L5 – Landsat 5 TM)

Tab. 1.Dane pozyskiwane z satellitów (L8 – Landsat 8; L5 – Landsat 5 TM)

Type os sensors	Date of acquisition	Bands	Tidal height (m)
L8	2022	2,3,4,5,5,7	3.21
L8	2013.12.27	2,3,4,5,5,7	3.01
L5	2001.09.29	1,2,3,4,5,7	2.81
L5	1989.11.23	1,2,3,4,5,7	2.8

Utilizing geospatial technology demonstrates potential as a valuable asset in delivering comprehensive coverage via multitemporal satellite imagery of coastal regions at diverse resolutions, facilitating the assessment of shoreline changes over time [16]. Various data sources have been utilized for shoreline detection, including historical land-based photographs, aerial photography, coastal maps and charts, GPS field surveys, and remote sensing data [17]. Beside, remote sensing methods for detecting shorelines encompass the extraction of the Green/Near-Infrared ratio [18], applying histogram thresholding to band 5 [19], and NDWI [20]. Recent researches, leveraging the planetary-scale analysis capabilities of Google Earth Engine (GEE), has successfully mapped shoreline change [21]. In addition to using images with average resolution to determine shoreline changes, high resolution satellite images were also used to detect coastal erosion monitoring [22]. Subsequently, aerial photographs and Landsat products were integrated these datasets to determine the magnitude of shoreline fluctuations [23]. In this study, the site-specific rate of erosion and accretion is evaluated using the historical shorelines extracted from the temporal Landsat 5 and Landsat 8 for the period 1989–2022.

Sam Son is the famous coastal city of Thanh Hoa province, is located about 16 km away from the Thanh Hoa city [24]. Despite being favored by tourists, Sam Son tourism also has to face many challenges such as inappropriate resource exploitation, climate change, and rising sea levels. Climate change and rising sea levels have significantly impacted the processes of coastal erosion and sediment deposition. According to research conducted by Cong Quan Nguyen and V.H. Pham (2016), The northern and southern coasts of the Hoi River estuary experience an accretion rate ranging from 5 to 10 meters per year, whereas erosion at the mouth of the Hoi River occurs at a slower rate of approximately 3-5 meters per year [25]. The reduction in width caused by coastal erosion in Sam Son has directly affected livelihoods, infrastructure, tourism attractions, cultural and historical landmarks, seasonality, and all tourism-related activities in the region [24].

This paper aims to evaluate the extent of coastal erosion and sediment deposition along the Sam Son beaches over a span of 33 years (1989–2022) through the analysis of remote sensing data. Coastal erosion and deposition are indicators of shoreline dynamics. The alterations of coastlines were identified through the analysis of NDWI of Landsat images. Furthermore, the Digital Shoreline Analysis System (DSAS) was utilized to calculate the rates of coastal deposition and erosion [26]. The erosion and deposition change were illustrated the results based on five statistical variables: Net Shoreline Movement (NSM), End Point Rate (EPR), and Linear Regression Rate (LRR).

2. Study area

The Coastal Sam Son City is located in Thanh Hoa province, which is famous for its picturesque beaches, drawing a large number of tourists from Vietnam and abroad. The landscape of Sam Son is distinctly divided into four zones: the tidal saltwater zone, the high sandbar zone, the coastal zone, and the mountainous zone. The territory of Sam Son consists of two parts: mainland and sea. This is an advantage for Sam Son to develop its maritime economy, aiming to become a strong coastal city in the near future. However, Sam Son faces challenges related to natural disasters such as flooding, climate change, rising sea levels, and shoreline change.

The coastline of Sam Son stretches approximately 26 kilometers from Quang Tho Ward, along the Ma River and the sea, to Quang Dai Commune. In recent years, the coastline of Sam Son City has experienced notable changes, influenced by both factors of natural origin and anthropogenic. Human activities such as building hydroelectric dams and sand mining contribute to coastal erosion and sedimentation. In addition,

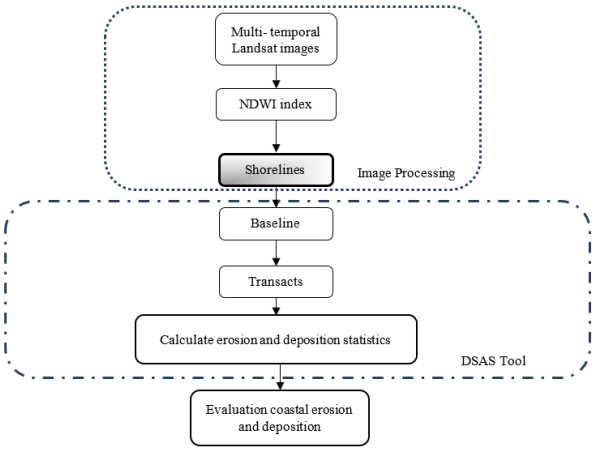

Fig. 2. Flowchart of the overall methodology for assessing coastal erosion and deposition
Rys. 2. Schemat blokowy ogólnej metodologii oceny erozji i osadzania się wybrzeża

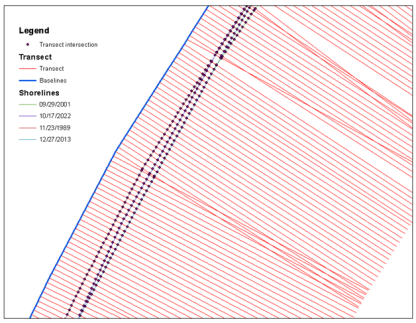

Fig. 3. Initiating transects from the baseline in parallel to the coastline vectors
Rys. 3 . Inicjacja transektów od linii bazowej równolegle do wektorów linii brzegowej

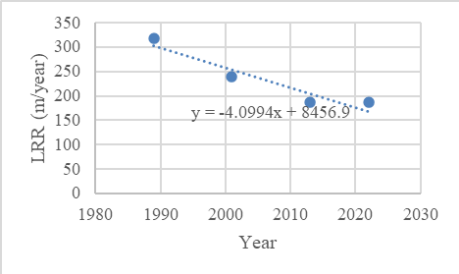

Fig. 4. Representation of a typical cross-plot showing LRR for shoreline change
Rys. 4. Reprezentacja typowego wykresu krzyżowego przedstawiającego LRR dla zmiany linii brzegowej

natural factors such as climate change and rising sea levels also lead to coastal erosion and sedimentation. The diminishing beach area and alterations to the shoreline can profoundly affect tourism activities of Sam Son City, considering the beaches are a primary draw for tourists. Moreover, coastal erosion poses a threat to coastal infrastructure, leading to economic losses.

In conclusion, the complexity of coastline change in Sam Sơn City demands a multifaceted approach for effective resolution. Continuously monitoring the shoreline and implementing suitable measures are essential to guarantee the long-term sustainability of both the coastal environment and the economic development in Sam Son.

3. Methodology and data

We obtained historical multi- temporal Landsat images by downloading it from the United States Geological Survey (USGS) earth explore website for the years 1989, 2001, 2013, and 2022. Landsat-8 OLI and Landsat 5 TM images are with the Word Geodetic System (WGS84) datum and projected using the Universal Transverse Mercator (UTM) System, specifically in zone 48N. The detailed parameters of those images are presented in Table 1.

The detailed methodology and objectives of the whole study is presented in Figure. 2. First, shorelines were extracted from Landsat in 1989, 2001, 2013 and 2022 using NDWI. The NDWI indexes were manually digitized the water – land boundary. The manual digitizing method is seen as the most straightforward technique for shoreline detection when dealing with study sites that are not extensive [27] like Sam Son city. The Digital Shoreline Analysis System (DSAS) tool was utilized to analyze the multi-date shorelines and compute statistics regarding shoreline change.

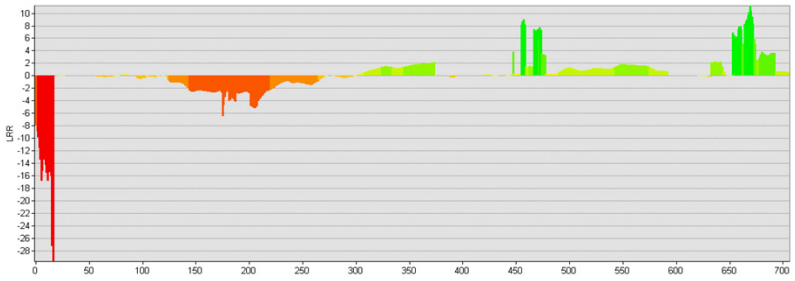

Fig. 5. Coastal accretion and erosion of Sam Son coast with LRR
Rys. 5. Akrecja przybrzeżna i erozja wybrzeża Sam Son z LRR

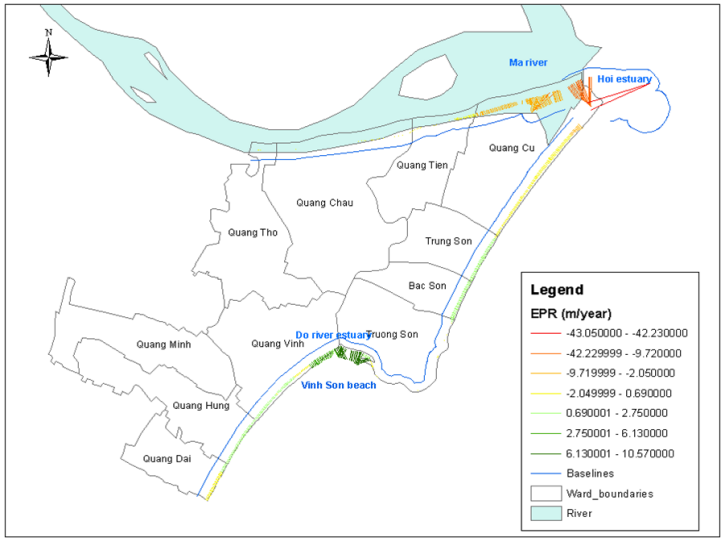

Fig. 6. Coastal accretion and erosion of Sam Son coast with EPR.
Rys. 6. Akrecja przybrzeżna i erozja wybrzeża Sam Son z EPR

3.1. Shoreline Determination

The process of coastline detection using satellite data involves the separation of land and water bodies [28]. There are several water indexes such as Normalized Difference Water Index (NDWI) [29], Automated Water Extraction Index (AWEI) [30], and Modification of normalised difference water index (MNDWI) [31]. In which, the normalized difference water index (NDWI) is a sensitive indicator to alters in body of water and it can be utilized for detecting aquatic entities. It is generated from the near-infrared and short-wave infrared bands of satellite images [32]. The normalized difference water index (NDWI) can be calculated from both the near-infrared and green bands of remote sensing data [29]. One of the most commonly used water indices for coastline extraction is the normalized difference water index (NDWI) [33]. In this paper, the NDWI values were calculated using the formula provided by Gao (1996) in Equation (1).

$$NDWI = (NIR-SWIR) / (NIR+SWIR) \quad (1)$$

Where: NIR is band 4 of Landsat 5 and band 5 of Landsat 8; SWIR is band 5 of Landsat 5 and band 6 of Landsat 8.

The NDWI is utilized for extracting coastlines by method of visual interpretation in shapefile format using QGIS. Therefore, There are four coastlines corresponding to the years 1989, 2001, 2013, and 2022.

3.2. Coastal erosion and deposition detection

Coastal erosion and accretion are determined by assessing the rate of shoreline change. The DSAS tool was utilized in this study to assess shoreline change. The alterations in the shoreline were evaluated by integrating the positions of the shoreline referenced to the established baseline. The changes in the coastline were established by analyzing the intersections of transects oriented perpendicular to the shoreline [20]. In addition

It is essential to establish the baseline next to the series of shoreline positions. Transects should be deployed perpendicular to this baseline at a spacing determined by the user to intersect the shorelines and establish measurement points. The orientation of the transect through the shorelines is significantly influenced by the position of the baseline. In this paper, 854 transverse transects, each 1700 meters long and positioned perpendicular to the offshore baseline, were created at 30-meter intervals along the shoreline (Figure. 3).

The DSAS modul was employed to assess the erosion and deposition rates of shoreline positions using the end point rate (EPR), rate of shoreline change(RSC) and linear regression (LRR) techniques. EPR was calculated as the ratio of the time elapsed between the oldest and most recent coastline positions. Beside, The calculation of the rate of shoreline change in the LRR method is based on the assumption of a linear trend between the earliest and latest shoreline dates (Figure. 4).

In addition, The coastal erosion and deposition changes were analysed respectively in period 1989–2001; 2001–2013,

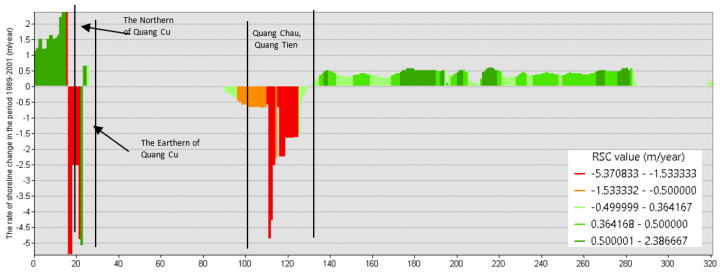

Fig. 7. The rate of erosion and deposition in the period 1989–2001 in Sam Son
Rys. 7. Tempo erozji i osadzania się w latach 1989–2001 w Sam Son

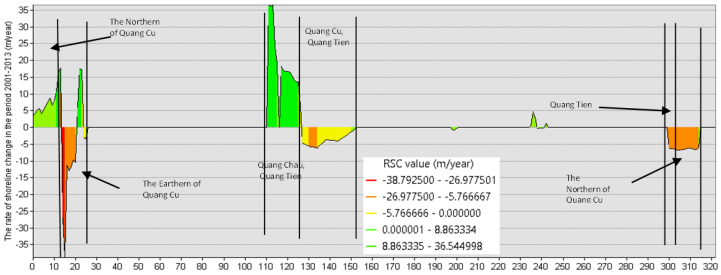

Fig. 8. The rate of erosion and deposition in the period 2001–2013 in Sam Son
Rys. 8. Tempo erozji i osadzania się w latach 2001–2013 w Sam Son

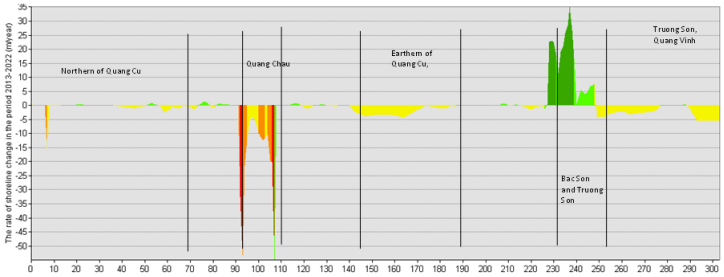

Fig. 9. The rate of erosion and deposition in the period 2013–2022 in Sam Son
Rys. 9. Tempo erozji i osadzania się w latach 2013–2022 w Sam Son

and 2013–2022 by rate of shoreline change(RSC) in following equation (2):

$$\text{RSC} = \text{NSM} / \text{time between oldest and most recent shoreline} \quad (2)$$

Where NSM (Net Shoreline Movement) is distance between oldest and most recent coastline

The RSC indicates nagative values of the coastal deposiston, while positive values of coastal erosion.

4. Results and discussion

4.1 Overall coastal erosion and deposition state

The identification of beach conditions, particularly coastal erosion, relies significantly on the geomorphological attributes of the coastline. The coastline is a dynamic system that undergoes rapid and continuous evolution, and its trends are monitored by mapping at different time intervals through field data collection or satellite imaging [34]. Coastal erosion and accretion are indicators of shoreline changes. The LRR method has been utilized to analyze the rate of shoreline change for Sam Son. According to the study, Sam Son exhibited both erosion and deposition along its coastline. The rate of 854 transects, erosion rates ranged from -0.12 m/year to -29.74 m/year, whereas the deposition rate along the coast ranged from 0.47 m/year to 11.22 m/year (Figure. 5)

Moreover, The end point rate (EPR) is calculated by dividing the distance of shoreline movement by the time elapsed between the oldest and the most recent shoreline. The EPR suggests that stable and negligible coastal deposition distances are concentrated in Bac Son, Trung Son, Quang Vinh, Quang Hung, and Quang Dai regions (Figure. 6). However, the EPR shows that significant coastal deposition distance are contributed in Quang Cu and Truong Son communes where the EPR reached from 0.69 m/year to 10.57 m/year. In addition, coastal in Quang Cu region is erosed strongly with EPR reached - 43.05 m/year.

The Figure. 7 shows the change of erosion and deposion from 1989 to 2001. The RSC vary between –5.37m/year and 2.39m/year. The coastal deposition was focused in the northern of Quang Cu ward from 0.5m/year to 2.39m/year and accretion is insignificant in Trung Son, Bac Son, Truong Son and Quang Vinh wards (below 0.5m/year). However, the shoreline was erosed from –5.37m/year to – 0.5m/year that was distributed in the Earthern of Quang Cu, Quang Chau and Quang Tien wards.

The change of erosion and deposition from 2001 to 2013 was shown in Figure. 8. Compared to the period from 1989

Tab. 2. Factors influencing coastal tourism in Sam Son (Source: Nguyen and Tran, 2020)

Tab. 2. Czynniki wpływające na turystykę przybrzeżną w Sam Son

Areas	Touristm activities	Limitations
Along the coast of Ho Xuan Huong	Hotels, Public swimming beaches, Shopping, Restaurant	Infrastructure has not fully invested, Sea level rise, Planning is not synchronized
Quang Cu commune		Natural disaster risks; erosion; Environmental pollution; Infrastructure is low; Services are not yet developed; Landslide

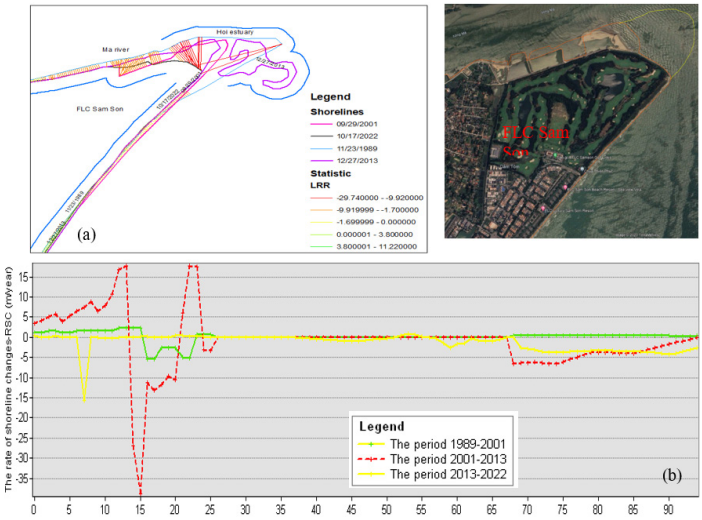

Fig. 10. The rate of shoreline change in Hoi estuary (LRR)

Rys. 10. Tempo zmian linii brzegowej w ujściu rzeki Hoi (LRR)

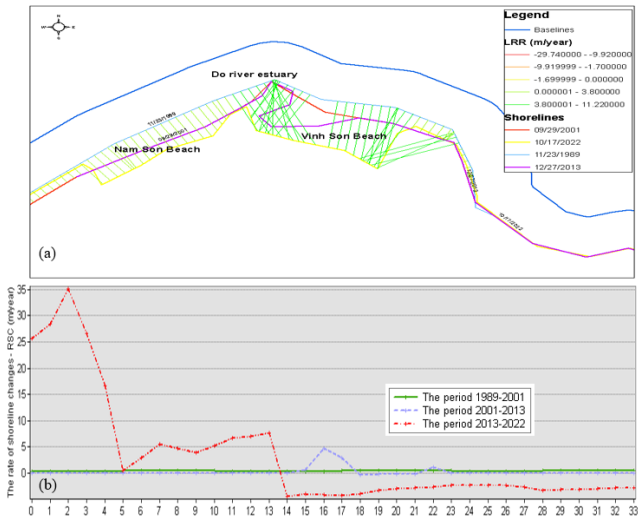

Fig. 11. The rate of shoreline change in Do river estuary

Rys.11. Tempo zmian linii brzegowej u ujścia rzeki Do

to 2001, the shoreline change in the period 2001–2013 was increased rate strongly which ranged from -38.79 m/year to 36.54/year.

In the Quang Cu ward where is located adjacent to the East Sea and next to Ma river in the Northern. In the Northern of Quang Cu ward, the shoreline was occurred both erosion and deposition which was the same phenomenon in the period of 1989–2001. However, the rate of erosion and deposion in the period of 2001–2013 were higher one of the period of 2001–2013. The value of erosion rate varied from -6.0 m/year to -6.67m/year, while the deposition rate value ranged from 4.22 m/year to 17.7 m/year. Beside, the rate of shoreline changes in the Earthern of Quang Cu ward were also different between the period 1989–2001 and the period 2001–2013. In there, shoreline was deposited about 0,6 m/year in the period 1989–2001 and 17.36 m/year in the period 2001–2013, whereas one was eroded significantly to -38.79 m/year in the period 2001–2013. In the Quang Chau and Quang Tien ward, the shoreline was deposed strongly from 6.5 m/year to 36.5 m/year. In addition, Quang Tien ward where was next to Quang Cu was erosed about -6.67m/year.

In the period 2013–2022, the shoreline change in Sam Son city was popular erosion (Figure. 9). The rate of erosion was largest in Quang Chau ward reaching – 55 m/year approximately. On the contrary general erosion trend, Bac Son and Truong Son were deposed strongly from 5 m/year to 35.1 m/year.

5. Discussion

Analysis of the results of the shoreline changes method, which we may regard as the reference method, reveals that the Sam Son coastline has experienced both erosion and deposition between 1989 and 2022. However, coastal erosion and deposition were different on each regions in period 1989–2001, 2001–2013, and 2013–2022 respectively. Overall, the rate of coastal erosion and deposition of Sam Son were most notably characterized by the rate of shoreline changes in Hoi estuary (Figure. 10) and Do river estuary (Figure. 11). In this section, we used LRR to analysis general the rate of erosion and deposition in during 1989–2022. Beside, we also applied RSC to evaluate particularly about the rate of erosion and deposition in each period 1989–2001, 2001–2013, and 2013–2022.

Figure. 10(a) shows LRR ranged from -1.7 to – 29.74. the LRR values proved that the shoreline was erosed in during period 1989–2022. However, as depicted in RSC in Figure. 10(b), the deposition process is specifically concentrated in the southern part of the Hoi estuary, with rates reaching 17.69 meters per year during the period 2001–2013. This accretion rate is the result of the transportation of sediment by the Ma River. The Hoi estuary is situated in the downstream area of the Ma River system, annually releasing millions (around 5.17 million) of tons of sediment into the sea. [35]. Contrastingly, the northern region of the Hoi estuary witnessed substantial erosion, characterized by erosion rates of -4.2m/year in period 1989–2001, -38.79 m/year, and -6.67 m/year in period 2013–2022. In this region, coastal erosion is attributed to a combination of natural elements and activities related to land exploitation. Natural elements comprise climatic events like storms, waves and increasing sea levels [36, 37]. Land exploitation activities contribute to coastal erosion, including urban development, sand mining, infrastructure construction. One of the notable land exploitation activities involves the establishment of tourism accommodation facilities, such as the Sam Son FLC complex and Van Chai resort. Consequently, sand mining in this tourist area has depleted the sediment deposition source, and this activity also generates a turbulent wave current that washes away the sediment, resulting in coastal erosion.

Furthermore, after consulting with stakeholders in the field, it has been recognized that the significant implications of analysis outcomes have impacted infrastructure of tourism [24], such as coastal erosion. The impacts of coastal erosion on marine tourism services in Sam Son are presented in Table 2:

The Do river mouth, situated to the west of the Truong Le mountain range, is the site where sedimentation and the formation of Vinh Son Beach and Nam Sam Son Beach occur. As a result of wave and tide action, sediment and sand get deposited, leading to an accumulation rate of up to 11.22 m/year (Figure. 11(a)) in during 1989–2022. In the region of Do river estuary, deposition processes was dominated with RSC value reaching 35.1 in period 2013–2022 (Figure. 11(b)). The sediment deposition at the mouth of the Do River provides the foundation feature for the development of resort areas aimed at catering to tourism. Currently, this area has undergone sand filling and the establishment of boundaries to facilitate the construction of resorts and hotels.

6. Conclusion

This study has utilized freely distributed multi-temporal Landsat satellite data and image processing techniques to demonstrate that Sam Son city has experienced extensive erosion and deposition between 1989 and 2022. In general, deposition is more significant in the most part of Do River estuary. However, erosion has been remarkable around the area of Hoi estuary. Erosion and deposition of shoreline in Sam Son are closely related to tourism activities. Therefore, addressing the issue of coastline changes in Sam Son City is essential to ensuring the sustainability of the local economy and the long-term attractiveness of the region as a preferred tourist destination.

Acknowledgements

We would like to express our thanks to the internal project coded T24-31, funded by the Hanoi University of Mining – Geology.

Conflicts of Interest

The authors declare no conflict of interest.

Literatura – References

1. Bouchahma, M. and W. Yan, Monitoring shoreline change on Djerba Island using GIS and multi-temporal satellite data. Arabian Journal of Geosciences, 2013. 7(9): p. 3705-3713.
2. Boak, E.H. and I.L. Turner, Shoreline Definition and Detection: A Review. Journal of Coastal Research, 2005. 214: p. 688-703.
3. Oyedotun, T.D.T., A. Ruiz-Luna, and A.G. Navarro-Hernández, Contemporary shoreline changes and consequences at a tropical coastal domain. Geology, Ecology, and Landscapes, 2018. 2(2): p. 104-114.
4. Davidson, M.A., et al., Annual prediction of shoreline erosion and subsequent recovery. Coastal Engineering, 2017. 130: p. 14-25.
5. Kaliraj Seenipandi, K.K. Ramachandran, and N. Chandrasekar, Modeling of coastal vulnerability to sea-level rise and shoreline erosion using modified CVI model. Remote Sensing of Ocean and Coastal Environments, 2021. Earth Observation: p. 315-340.
6. Zhang, K., B.C. Douglas, and S.P. Leatherman, Global Warming and Coastal Erosion. Climatic Change, 2004. 64(1/2): p. 41-58.
7. Haddow, G.D., J.A. Bullock, and D.P. Coppola, Natural and Technological Hazards and Risk Assessment, in Introduction to Emergency Management. 2020. p. 33-84.
8. Prasetya, G., Chapter 4: Protection from coastal erosion, in The role of coastal forests and trees in protecting against coastal erosion 2023, Agency for the Assessment and Application of Technology, Indonesia: FAO. p. 103-131.
9. Yincan, Y. and et al., Coastal Erosion, in Marine Geo-Hazards in China. 2017. p. 269-296.
10. Balasuriya, A., Coastal Area Management: Biodiversity and Ecological Sustainability in Sri Lankan Perspective, in Biodiversity and Climate Change Adaptation in Tropical Islands. 2018. p. 701-724.
11. Huu Duy NGUYEN., et al., Impacts of urbanization and tourism on the erosion and accretion. Urbanism. Arhitectură. Construcţii, 2020. 11: p. 123-156.
12. Willis, B., Conditions of sedimentary deposition. The journal of geology. 1893: p. 476-520.
13. Vinh, V.D., et al., Sediment transport and cause of the deposition in Nai Lagoon (Ninh Thuan province) (in vietnamese). Vietnam Journal of Marine Science and Technology, 2016. 16(3): p. 283-296.
14. Li, B., J.P. Liu, and Y. Jia, Comparison of the Causes of Erosion-Deposition between Yellow River, Yangtze River and Mekong River Subaqueous Deltas II: Comparative Analysis. Water, 2022. 15(1).
15. Burningham, H. and M. Fernandez-Nunez, Shoreline change analysis, in Sandy Beach Morphodynamics. 2020. p. 439-460.
16. Saravanan, S., K.S.S. Parthasarathy, and S.R. Vishnuprasath, Monitoring Spatial and Temporal Scales of Shoreline Changes in the Cuddalore Region, India, in Coastal Zone Management. 2019. p. 99-112.
17. Bouchahma, M. and W. Yan, Automatic Measurement of Shoreline Change on Djerba Island of Tunisia. Computer and Information Science, 2012. 5(5).
18. Lan, P.T., et al., Application of Remote Sensing and GIS technology for monitoring coastal changes in estuary area of the Red river system, Vietnam. Journal of the Korean Society of Surveying, Geodesy, Photogrammetry and Cartography, 2013. 31(6_2): p. 529-538.
19. A. A. Alesheikh, A. Ghorbanali, and N. Nouri, Coastline change detection using remote sensing. Int. J. Environ. Sci. Tech, 2007. 4(1): p. 61-66.
20. Kuleli, T., et al., Automatic detection of shoreline change on coastal Ramsar wetlands of Turkey. Ocean Engineering, 2011. 38(10): p. 1141-1149.
21. Yongjing. Mao, et al., Efficient measurement of large-scale decadal shoreline change with increased accuracy in tide-dominated coastal environments with Google Earth Engine. ISPRS Journal of Photogrammetry and Remote Sensing, 2021. 181: p. 385-399.
22. Vassilakis, E., A. Tsokos, and E. Kotsi, Shoreline Change Detection and Coastal Erosion Monitoring Using Digital Processing of a Time Series of High Spatial Resolution Remote Sensing Data. Bulletin of the Geological Society of Greece, 2017. 50(3).
23. Murray, J., et al., Monitoring Shoreline Changes along the Southwestern Coast of South Africa from 1937 to 2020 Using Varied Remote Sensing Data and Approaches. Remote Sensing, 2023. 15(2).
24. Nguyen Xuan Hai and T.D. Thanh. Sam Son marine tourism adaptation to climate change. in Sustainable tourism: Shaping a Better Future. 2020. Bangkok, Thailand: Kasetsart University.
25. Cong Quan Nguyen. and V.H. Pham., The topographic and dynamic landscape characteristics of the coastal river mouth area of the Ma River, Thanh Hoa province. Vietnam Journal of Earth Sciences, 2016(1): p. 59-65 (in Vietnamese).
26. Baig, M.R.I., et al., Analysis of shoreline changes in Vishakhapatnam coastal tract of Andhra Pradesh, India: an application of digital shoreline analysis system (DSAS). Annals of GIS, 2020. 26(4): p. 361-376.

27. Moore, L.J., P. Ruggiero, and J.H. List, Comparing Mean High Water and High Water Line Shorelines: Should Proxy-Datum Offsets be Incorporated into Shoreline Change Analysis? Journal of Coastal Research, 2006. 224: p. 894-905.

28. Kim Dung Le and T.L. Pham, Shoreline Changes and Their Impacts on Tourism: A Case Study of Sam Son City, Thanh Hoa Province, Vietnam. European Geographical Studies, 2022. 9(1): p. 12-20.

29. McFeeters, S.K., The use of the Normalized Difference Water Index (NDWI) in the delineation of open water features. International Journal of Remote Sensing, 2007. 17(7): p. 1425-1432.

30. Feyisa, G.L., et al., Automated Water Extraction Index: A new technique for surface water mapping using Landsat imagery. Remote Sensing of Environment, 2014. 140: p. 23-35.

31. Xu, H., Modification of normalised difference water index (NDWI) to enhance open water features in remotely sensed imagery. International Journal of Remote Sensing, 2007. 27(14): p. 3025-3033.

32. Gao, B.C., NDWI - A Normalized Difference Water Index for Remote Sensing of Vegetation Liquid Water From Space. Remote Sens. Environ, 1996. 58: p. 257-266.

33. Liu, Y., et al., Analysis of Coastline Extraction from Landsat-8 OLI Imagery. Water, 2017. 9(11).

34. Mendonça Diniz, M.T., et al., Variation of the Coastline Between the Years of 1984 and 2017 in the State of Sergipe, Northeast Region, Brazil. Journal of Coastal Research, 2020. 95(sp1).

35. Van Cu Nguyen. and H.T. Pham., Coastal erosion in Central Vietnam. 2003, Hanoi: Science and technics publishing house (in Vietnamese).

36. Manh Hung Le. and V.C. Ho, Analyze the landslide development and determine the causes of the morphological changes of the Sam Son coastline in Thanh Hoa province. Journal Science and Technology Water Resources, 2013. 16: p. 119-126 (in Vietnamese).

37. Viet Cuong Ho. and M.H. Le., Study the impact of the dynamic hydrological regime in the coastal zone, affecting the development of erosion on the Sam Son coastline in Thanh Hoa. Journal Science and Technology Water Resources, 2012. 10: p. 2 -9 (in Vietnamese).

Monitorowanie erozji i osadzania się na wybrzeżu w mieście Sam Son, Wietnam – wkład danych z teledetekcji

Badanie trendów erozji i akrecji linii brzegowej jest istotne dla szerokiego zakresu badań prowadzonych przez naukowców nadmorskich i menedżerów wybrzeża. Erozja i akrecja linii brzegowej występują zarówno w wyniku procesów naturalnych, jak i wpływu człowieka. Pewne obszary wzdłuż linii brzegowej w Sam Son ulegają erozji i akrecji w wyniku naturalnych procesów przybrzeżnych i działań ludzkich, takich jak burze, fale, działalność turystyczna... Celem tej pracy jest zbadanie erozji i akrecji w Sam Son na przestrzeni 33 lat (1989–2022). Linie brzegowe zostały wyodrębnione z wykorzystaniem wieloczasowych obrazów satelitarnych Landsat, a wskaźnik zmian linii brzegowej został określony przy użyciu systemów cyfrowej analizy linii brzegowej (DSAS). Wyniki tej pracy ilustrują, że zmiany linii brzegowej w Sam Son podlegają znacznym i zróżnicowanym fluktuacjom w różnych obszarach. W ujściu rzeki Hoi wskaźniki erozji wahają się od -2,22 m/rok do -40,32 m/rok. Budowa FLC Sam Son jest jednym z czynników przyczyniających się do utraty osadów w północnej części miasta Sam Son, która sąsiaduje z Morzem Wschodnim i rzeką Ma. Ponadto, wskaźnik akrecji znacząco wzrósł, osiągając 9,7 m/rok w ujściu rzeki Do. Zjawisko osadzania się osadów służy jako podstawa do budowy hoteli obsługujących turystykę w Sam Son.

Słowa kluczowe: *erozja, osadzanie się, teledetekcja, DSAS, Sam Son*

Automatic Detection and Analysis of Offsets in GNSS Position Time Series Using RMS Sliding-Window Method and Synthetic Model

Dinh Trong TRAN [1)]*

[1)] Faculty of Bridges and Roads, 55 Giai Phong Street, Hanoi University of Civil Engineering, Hanoi, Vietnam; ORCID https://orcid.org/0000-0002-3838-9950;

* Corresponding author: trongtd@huce.edu.vn

http://doi.org/10.29227/IM-2024-01-97

Submission date: 11-05-2024 | Review date: 01-06-2024

Abstract

This paper presents a method for automatically detecting and analyzing offsets in GNSS (Global Navigation Satellite System) position time series using the RMS (Root Mean Square) sliding-window approach. This technique identifies anomalies that indicate offsets within the time series. To adjust parameters such as linear trends, seasonal signals, and offsets accurately, synthetic model of GNSS position time series is utilized. The method is implemented in an automated program, pygps_ts, programmed by Python. The effectiveness of this approach is validated using both synthetic and real data from CORS (Continuously Operating Reference Station) stations in Vietnam. The results show that the program can accurately and efficiently detect and analyze offsets, identifying the epochs and magnitudes of these offsets in various scenarios. This study offers a practical tool for GNSS data processing, which is especially useful for tectonic studies and geodetic applications in Vietnam, where the continuous GNSS network is still developing. The study demonstrates the potential of this method for broader applications in monitoring and analyzing GNSS data in different regions. s accuracy and efficiency in offset detection and analysis.

Keywords: *GNSS position time series, displacement tectonic, offset, sliding-window, CORS*

1. Introduction

In recent decades, the Global Navigation Satellite System (GNSS) has emerged as an indispensable tool in the field of geodetic monitoring of Earth's crustal movements. Continuous GNSS stations, campaign GNSS stations, and continuously operating reference stations (CORS) observe signals from GNSS satellites [1], including USA's GPS, Russia's GLONASS, Europe's Galileo, Japan's QZSS, and China's BeiDou, enabling the generation of position time series for monitoring stations. With the advantage of continuous data and dense observation stations, these networks of GNSS stations facilitates the monitoring and analysis of both short-term and long-term variations in Earth's crust with millimeter-level accuracy [2]. These data are processed and analyzed to determine temporal displacements, including linear displacement, seasonal variations, and offsets due to earthquakes, land subsidence, or other geological phenomena. This information is crucial for earthquake forecasting and understanding the processes occurring within the Earth [3–5].

In processing and analyzing GNSS position time series using geodetic methods, determining a mathematical model to comprehensively describe the recorded phenomena is crucial. This approach helps in accurately and thoroughly identifying the movement parameters of the GNSS stations for various research purposes [6–9]. For GNSS stations monitoring crustal displacement in Vietnam, the recorded phenomena primarily include linear trends, periodic movements, and offsets (or jumps) in the position time series [7, 10–12]. These offsets can be caused by various factors, such as tectonic activities like earthquakes, or technical issues like station location changes, antenna changes, or other technical errors. These offsets significantly impact the accuracy of movement parameter estimates in the GNSS position time series if they are not detected and corrected [7, 13–16].

In the study on offset detection in GPS coordinate time series, Amiri-Simkooei et al. [6] developed a method using a functional model (including linear trends and periodic signals) and a stochastic model (including white noise and colored noise). By integrating both models, the offset detection method becomes more effective, improving the accuracy of GPS time series analysis and interpretation. Bruni et al. [17] applied the Sequential t-test Analysis of Regime Shifts method to identify the epoch and magnitude of offset in GNSS data sets, showing that the offsets identified are split into 48% true-positive, 28% false-positive, and 24% false-negative events with synthetic data. This method was successfully applied to a GPS time series spanning over 15 years in the Po Plain, Italy, and was validated as effective when compared with other observational techniques. Khazraei & Amiri-Simkooei [18] investigated improving the performance of the offset detection method in GNSS time series using a spline function, referred to as As-mode. The GNSS coordinate time series, including linear trends, seasonal signals, jumps, and white noise combined with colored noise, were simulated to compare performance. The results indicated a significant improvement in the overall performance of the algorithm, with the true positive detection rate increasing to 61.1%. Additionally, in 90% of cases, the velocities of the stations were estimated with an error of only 0.8 mm/year compared to the simulated values. A novel approach in GNSS position time series analysis involves the application of machine learning techniques for offset detection. Crocetti et al. [16] utilized ten machine learning algorithms to identify offsets in series attributed to seismic events in Japan. The results demonstrate

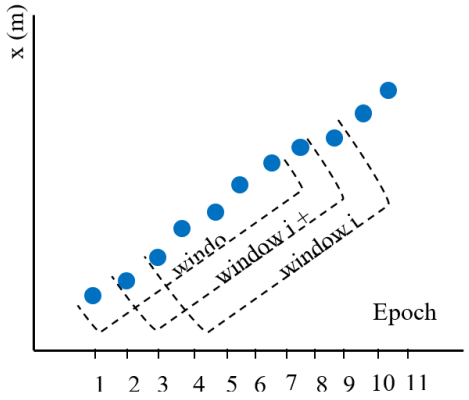

Fig. 1. Sliding-windows in GNSS position time series
Rys. 1. Przesuwne okna w szeregach czasowych pozycji GNSS

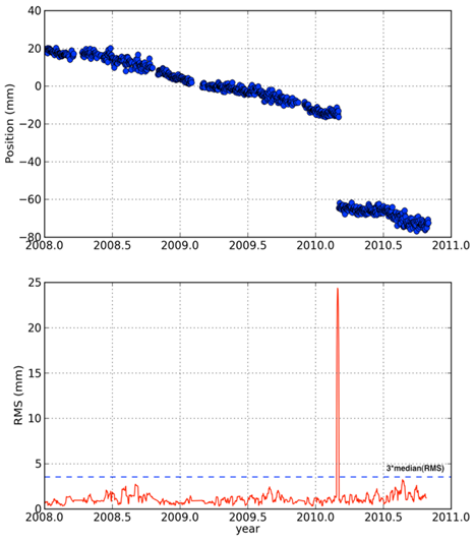

Fig. 2. The relationship between the offset and the RMS of the sliding-widow [22]
Rys. 2. Zależność przesunięcia od wartości skutecznej okna przesuwnego [22]

that the Random Forest method yielded the highest performance, though it only attained an F1 score of 0.77, a recall of 0.78, and a precision of 0.76.

In Vietnam, the application of GNSS in crustal displacement monitoring has been initiated and is in its early stages. GNSS data processing is largely conducted using softwares such as Gamit/GLOBK [19] or Bernese Bernese [20] with limited research on GNSS position time series analyzing. In a study on absolute displacements in the Tam Dao region, Vy Quoc Hai et al. [21] processed data of 6 mesurement cycles in 1996 and 2006 of GPS network using GPSurvey and Bernese software to determine the displacements of observation stations. Due to the availability of coordinate data at only 6 epochs, the motion of the observation stations was described using linear trend function.

In studies conducted by Tran et al. [7, 12], the authors processed data from the network of CORS stations across the territory of Vietnam to determine the velocity vector field. The daily GNSS position time series obtained were processed using a comprehensive motion model including linear trends, seasonal signals, and offsets. However, the epoch of the offsets was not automatically determined.

Thus, it is evident that in Vietnam, study on analyzing and processing the GNSS position time series to determine crustal displacement parameters is still limited, representing early-stage investigations. Studies in this field are crucial, particularly in light of the operationalization of the Vietnamese national satellite positioning network (VNGEONET) which is anticipated to catalyze continuous GNSS applications in Earth science research. Moreover, both globally and in Vietnam, continuous GNSS networks are expanding spatially, leading to an accumulation of increasingly voluminous data over time. Consequently, processing the position time series of these continuous GNSS networks will encounter challenges associated with large and complex datasets. Therefore, it is essential to study the application of algorithms and computational tools to facilitate swift, robust, and accurate analysis of GNSS position time series.

This paper focuses on developing a method for the automatic detection and analysis of offsets in GNSS position time series. The method utilizes an RMS (Root Mean Square) sliding-window approach to analyze consecutive coordinates within the time series. Subsequently, a synthetic model of the GNSS position time series is employed to accurately adjust the parameters of the model, including linear trends, seasonal signals, and offsets, which are common and significant phenomena at continuous GNSS stations in Vietnam. The

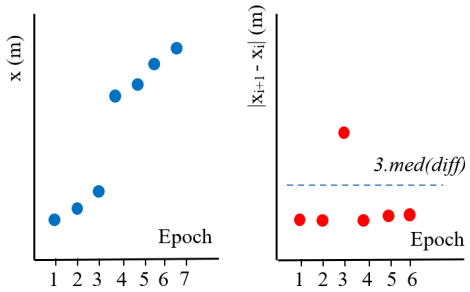

Fig. 3. Detecting the location of the offset in the sliding-window with anomalous RMS value
Rys. 3. Wykrywanie położenia przesunięcia w oknie przesuwnym z nieprawidłową wartością RMS

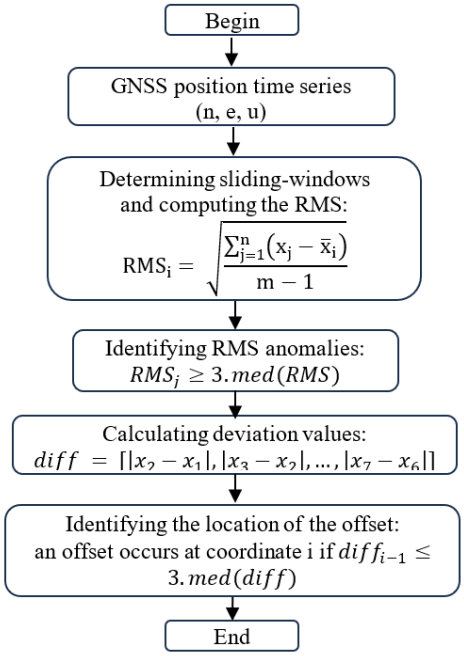

Fig. 4. Detecting the offsets in the GNSS position time series
Rys. 4. Wykrywanie przesunięć w szeregach czasowych pozycji GNSS

method is then implemented as an automated GNSS position time series analysis program using the Python programming language. The method and the developed program are tested using both simulated data and actual data from two CORS stations of the TAST network in Vietnam.

2. Methodology

2.1. RMS sliding-window method for offset detection

This method relies on the variation of the root mean square (RMS) of adjacent coordinates within a temporal window of GNSS position time series to detect offsets [22]. An anomaly is indicated when the RMS value of a corresponding window exceeds a threshold, indicating that this window contains an offset.

Sliding-window determination and RMS anomaly indentification:

Sliding-windows are determined by spanning consecutive coordinates within the time series. For instance, for a component coordinate $\{x_1,x_2,\ldots,x_n\}$, the first window spans from x_1 to x_{1+m}, the second window from x_2 to x_{2+m},…), and so forth, until the last coordinate (see Figure 1). Thus, with n coordinates, there are n-1 sliding-windows.

The RMS value for each window is computed using the formula (1):

$$RMS_i = \sqrt{\frac{\sum_{j=1}^{n}(x_j - \bar{x}_i)}{m-1}} \quad (1)$$

where x_j is the j-th coordinate of the i-th window, and $\bar{x}_i$ is the average coordinate of n coordinates in the i-th window.

The number of coordinates in the sliding window, denoted by m, is chosen to balance statistical significance and sensitivity to offsets. Here, m = 7 meets these criteria based on experimentation.

The threshold for indentifying RMS anomalies is set at 3 times the median value of RMS values, corresponding to a 99% confidence level [23], denoted as ε as per Formula (2):

$$\varepsilon = 3.med(RMS) \quad (2)$$

where med(RMS) represents the median of RMS values.

Figure 2 illustrates the relationship between the offset and the RMS of the sliding window. In Figure 2, the upper plot represents a time series of coordinates (green dots) from 2008 to 2011, exhibiting an offset at epoch 2010.175. The lower plot represents the RMS series of corresponding sliding-windows (red line), with anomaly RMS values corresponding to the

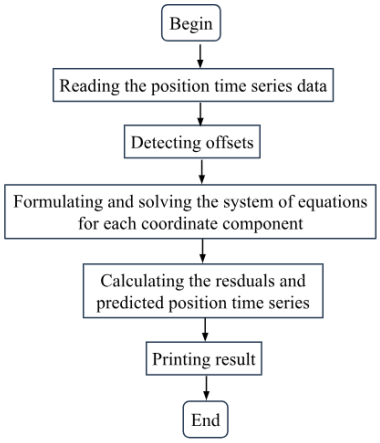

Fig. 5. Algorithm flowchart of pygps_ts program
Rys. 5. Schemat działania algorytmu programu pygps_ts

Tab. 1. Adjusted and design parameters of synthetic data
Tab. 1. Parametry korygowane i projektowe danych syntetycznych

Coordinate component		Initial position	Velocity	Seasonal motion				Offset at 2022.5
				Annual term		Semi-annual term		
		a (m)	b (m/năm)	c (m)	d (m)	e (m)	f (m)	g (m)
North	Designed	-0.0100	0.0200	-0.0010	0.0010	-0.0020	-0.0020	0.2000
	Adjusted	-0.0100	0.0201	-0.0010	0.0010	-0.0021	-0.0020	0.2000
	Deviation	0	-0.0001	0	0	0.0001	0	0
East	Designed	0.0100	0.0100	-0.0200	-0.0050	0.0050	-0.0050	0.2000
	Adjusted	0.0101	0.0100	-0.0200	-0.0049	0.0050	-0.0050	0.1999
	Deviation	-0.0001	0		-0.0001	0	0	0.0001
Up	Designed	-0.0010	0.0200	0.0100	0.0100	0.0100	0.0010	0.2000
	Adjusted	-0.0010	0.0200	0.0100	0.0101	0.0100	0.0010	0.1999
	Deviation	0	0	0	-0.0001	-0	0	0.0001

window containing the offset. It is evident that this anomaly value is substantial (24.1mm), significantly exceeding the threshold value (horizontal dashed green line).

Offset detection in sliding-windows:

After identifying the window containing an offset based on anomalous RMS values, offsets within this window are determined based on the deviation between consecutive coordinates. Specifically, the absolute differences between consecutive coordinates within the window are computed. For a window of 7 coordinates, this results in 6 deviation values calculated as per Formula (3).

$$diff = [|x_2 - x_1|, |x_3 - x_2|, \dots, |x_7 - x_6|] \quad (3)$$

Offset in the window occurs at the deviation with a value greater than 3 times the median of deviations within the window (3.med(diff)).

Figure 3 illustrates the determination of offsets within a window with anomalous RMS values. On the left side of Figure 2, there is a series of 7 consecutive coordinates (blue dots) with an offset at the 4th coordinate. On the right side, there is a series of 6 deviation values calculated from these 7 consecutive coordinates (red dots). It is evident that, corresponding to the offset at the 4th coordinate, the deviation value at the 3rd position is anomalous, significantly exceeding the 3.med(diff). Thus, within the window corresponding to anomalous RMS, an offset occurs at coordinate i if $diff_{i-1} \leq 3.med(diff)$.

The process of detecting offsets using the above method is accurate, fast, and automated as it can be programmed. The steps outlined above are summarized in the flowchart depicted in Figure 4.

This method of offset detection has been implemented as a module to automatically detect offsets in the GNSS coordinate time series analyzing program 'pygps_ts' using the Python programming language [24], which will be presented in Section 2.3.

2.2. Synthetic model of GNSS position time series and estimation of parameters of synthetic model

The GNSS position time series represents the spatial coordinates of a GNSS station over time within a three-dimensional coordinate system [25]. This time series is visually presented using mathematical equations to analyze the factors contributing to the displacements of observation stations. The predominant mathematical equation, or synthetic model, encompasses parameters that characterize these displacements, specifically: (1) the initial position of the series, (2) tectonic displacement, indicating the movement of the Earth's crust over time (velocity), (3) seasonal motion, which captures displacements based on seasonal patterns, and (4) steps. The GNSS position time series is mathematically modeled using equations for each coordinate component (North, East, Up), as delineated in Equation (4) [26]:

$$y(t_i) = a + bt_i + csin(2\pi t_i) + dcos(2\pi t_i) + esin(4\pi t_i) + fcos(4\pi t_i) + \sum_{j=1}^{n_g} g_j H(t_i - T_j) + v_i \quad (4)$$

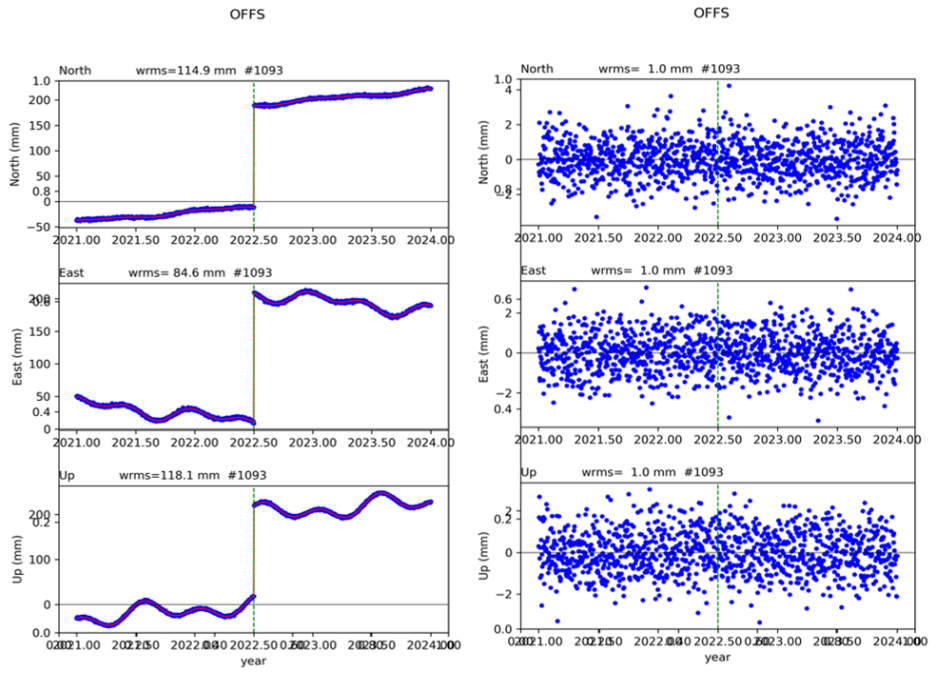

a) Measurement and predicted position time series
a) Pomierzone i przewidywane szeregi czasowe

b) Resdual position time series
b) Szeregi czasowe residuów pozycji

Fig. 6. Position time series of OFFS station
Rys. 6. Szereg czasowy pozycji stacji OFFS

where t_i represents the time of the coordinate y (referred to as measurement coordinate), t_i=1,2,3,…,n; a denotes the initial position; b indicates the displacement velocity; c, d, e, and f are parameters of seasonal motion (c and d are of annual term, e and f are of semi-annual term); g_j represents the magnitude of the offset at epoch T_j (n_g is the number of offsets in the series); $H(t_i\text{-}T_j)$ is the Heaviside function, $H(t_i\text{-}T_j)$=0=0 if $t_i \leq T_j$ and $H(t_i\text{-}T_j)$=1 if $t_i \leq T_j$; v_i represents the error term.

Assuming that the epochs T_j of the offsets are known, Equation (4) contains parameters representing the displacements of the GNSS observation stations as unknowns

$$x = [a\ b\ c\ d\ e\ f\ g_1\ g_2 \dots\ g_{n_g}]^T \tag{5}$$

it is expressed in matrix form as Equation (6)

$$y = Ax + v \tag{6}$$

in which: A is the design matrix, v is the residual vector, and y is the coordinate vector.

Equation (6) is adjusted by least squares. Neglecting the noise, the unknowns is determined by formula (7):

$$x = (A^T A)^{-1}(A^T y) \tag{7}$$

The predicted coordinates are calculated using formula (8):

$$\tilde{y} = Ax \tag{8}$$

The residuals, calculated using formula (9), represent the differences between the measurement coordinates and the predicted coordinates, thus indicating the best fit of the adjusted model.

$$v = y - \tilde{y} \tag{9}$$

Therefore, utilizing a synthetic model to depict the GNSS position time series enables us to estimate the parameters describing station displacement. A pivotal input parameter required for GNSS position time series featuring offsets is the epochs of these offsets. The method proposed for offset detection base on the RMS sliding-window approach as outlined in Section 2.1.

2.3. Development of an automated program for detection of offsets in GNSS coordinate time series

In order to analyze GNSS position time series automatically and accurately, we have developed a program in Python named pygps_ts. This program can automatically detect the epochs of offsets using the method we introduced above, and calculate the displacement parameters of the series. The program's algorithm flowchart is shown in Figure 5.

The steps for processing the position time series of pygps_ts include:

1. Reading the position time series data: The input data is a file containing the GNSS position time series in the format used by the GAMIT/GLOBK [27], which includes information on time and GNSS coordinate values over time.

2. Detecting offsets: Use the RMS sliding-window method to identify and determine the epochs of offsets in the position time series.

3. Formulating and solving the system of equations for each coordinate component of the position time series: Formulate the system of equations for each coordinate component using the determined epochs of offsets using Equation (4). Solve this system of equations using the least squares method to determine the unknowns, which are the displace-

Tab. 2. Adjusted displacement parameters of BD61 and BTIN

Tab. 2. Skorygowano parametry przemieszczenia stacji BD61 i BTIN

Displacement parameters		BD61			BTIN		
		North	East	Up	North	East	Up
Velocity (m/year)		-0.0104	0.0229	-0.0352	-0.0054	0.0424	0.0020
Seasonal motion (m)	Annual term	-0.0007	0.0012	-0.0004	-0.0009	-0.00004	0.0009
		0.0002	-0.0003	-0.0062	0.0008	0.0016	0.0006
	Semi-annual term	-0.0012	-0.0003	0.0010	0.0007	-0.0008	0.0007
		-0.0005	0.0015	-0.0020	-0.0001	0.0003	0.0006
Amplitude of offsets (m)	at 2020.0025	-0.0020	0.0115	0.0017	-	-	-
	at 2020.4540	-	-	-	-48.0265	-223.431	0.0023
	at 2020.8720	0.0031	0.0012	0.0267	-	-	-

ment parameters of the position time series (displacement velocity, seasonal motion, and offset amplitude).

4. Calculating the residual and predicted position time series: Calculate the predicted coordinate series using Equation (8) and the residuals using Equation (9).

5. Printing result: The output comprises the adjusted displacement parameters (displacement velocity, seasonal motion, and offset amplitude), along with the residual time series and predicted coordinates. The adjusted displacement parameters are saved in *.txt format, while the residual time series and predicted coordinates are saved in GAMIT/GLOBK format.

The program pygps_ts has been utilized as a complementary tool in various studies [7, 12, 22]. The entire source code of this program is now freely available via the link DOI 10.17605/OSF.IO/N7V4C.

3. Data, results, and discussion

To evaluate the accuracy and efficacy of the offset detection method and the developed program, two datasets were employed: synthetic data and real data. The synthetic data is a synthetic GNSS coordinate time series model deliberately designed with a predefined offset. Meanwhile, the real data comprises GNSS coordinate time series from two stations within the CORS network operated by Tường Anh Company, experiencing two offsets due to antenna changes during operation.

3.1. Synthetic data and results analysis

The synthetic GNSS coordinate time series model spans three coordinate components — North, East, and Up — over a three-year period from 2021.0 to 2024.0, for a station named OFFS (Offset). This synthetic model encompasses a linear trend, seasonal movements, and an offset at epoch 2022.5, with specific values detailed in Table 1. Subsequently, the data is perturbed with an error of $\sigma = \pm 1$mm following a normal distribution to generate the "measurement" coordinate time series. The designed GNSS coordinate time series for the OFFS station is plotted as blue dots along the time and coordinate axes in Figure 5.a.

The position time series of station OFFS is automatically analyzed by pygps_ts. The results demonstrate accurate identification of the epoch of the offset at 2022.5, with the parameters of the position time series determined nearly identical to their designed values (Table 1). The maximum deviation between the adjusted parameters and the designed ones is only ±0.0001 on the dataset perturbed by a random error of 1mm, as indicated in Table 1, which is negligible.

The processed coordinate time series of the OFFS station is depicted in Figure 6. In Figure 6.a, the red line represents the predicted coordinate series (fit line), closely aligning with the measurement coordinates. Figure 6.b illustrates the residuals of the measurement coordinate series, displaying a wrms of 1mm across all three coordinate components (North, East, and Up), matching the magnitude of the added error, indicating the accurate determination of the predicted coordinate series, closely resembling the designed values (Table 1). In both figures 6.a and 6.b, the vertical dashed blue line indicates the detected offset in the coordinate time series.

Thus, with the synthetic data, the pygps_ts program accurately identified the epoch of the offset at 2022.5, as designed in the synthetic GNSS coordinate time series. The motion parameters determined closely matched the designed values, with the maximum deviation being only ±0.0001, demonstrating the effectiveness of the method and the program. The wrms of the residual position time series precisely matches the 1 mm noise level, indicating that the predicted coordinate time series was accurately determined.

3.2. Real data and results analysis

The real data used in the study consists of GNSS coordinate time series from two typical CORS stations within the CORS network, operated by Tuong Anh Science and Technology Equipment Joint Stock Company (TAST) in Vietnam. The TAST network, consisting of nearly 200 stations, is renowned for its stability and accuracy, attributed to the utilization of Trimble's synchronous equipment technology. The selected stations, BD61 and BTIN, were continuously observed for approximately 1.5 years, spanning from 2020.0 to 2021.8. These stations were chosen due to their representation of typical motion patterns observed on the Earth's surface in Vietnam, encompassing linear trends, seasonal movements, and various offsets with differing amplitudes. Specifically, BD61 exhibits two small-amplitude offsets, while BTIN displays a single but large-amplitude offset (refer to Figure 7).

The position time series of BD61 and BTIN were automatically analyzed using the developed program pygps_ts, without any parameter intervention, providing results in less than a minute. The program accurately identified the epochs of the offsets, leading to precise adjustments of the displacement parameters, predicted coordinate time series, and residual coordinate time series of these stations.

Table 2 presents the adjusted displacement parameters of BD61 and BTIN. showcasing two offsets with relatively small am-

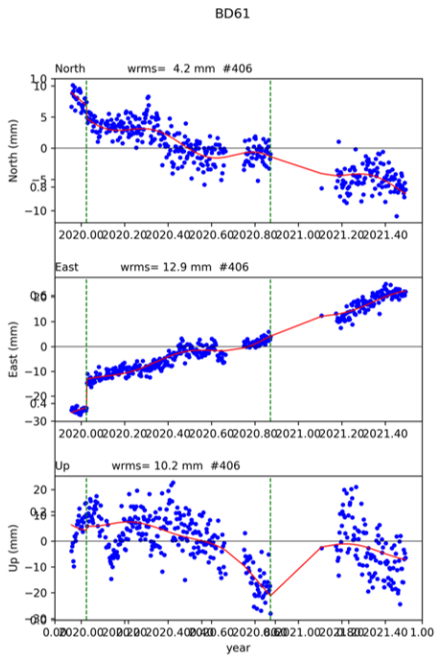

a) Predicted position time series of BD61 station
a) Przewidywany szereg czasowy pozycji stacji BD61

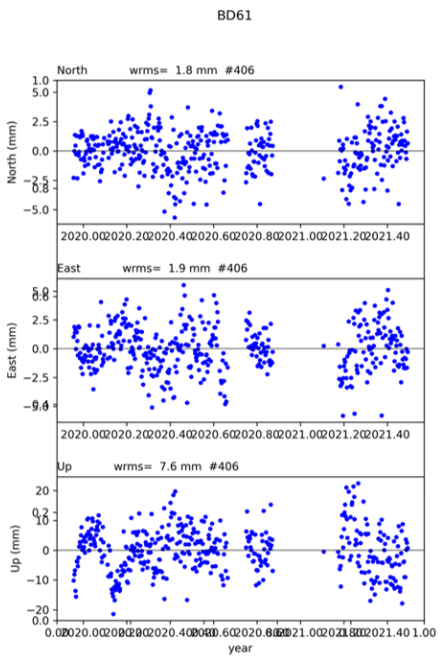

b) Residual position time series of BD61 station
b) Szereg czasowy residuum pozycji stacji BD61

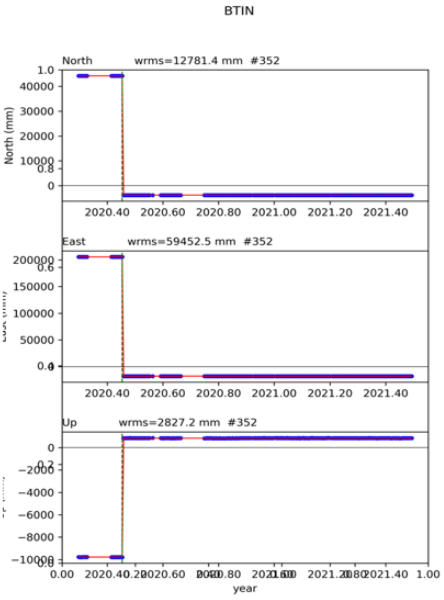

c) Predicted position time series of BTIN station
c) Przewidywany szereg czasowy pozycji stacji

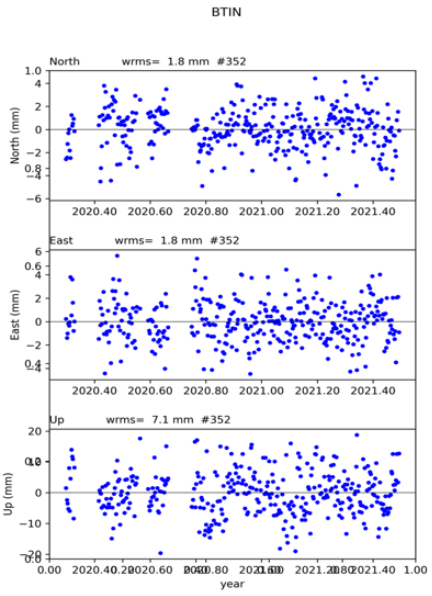

d) Residual position time series of BTIN station
d) Szereg czasowy residuum pozycji stacji

Fig. 7. Position time series of BD61 and BTIN stations
Rys. 7. Szeregi czasowe stacji BD61 and BTIN

plitudes detected in the position time series of BD61, occurring at epochs 2020.0025 and 2020.8720. At epoch 2020.0025, the offset in the East component is 0.0115 m, and at epoch 2020.8720, it is 0.0267 m in the Up component. The amplitudes in the other coordinate components are very small, on the order of millimeters, equivalent to the random noise of the time series.

Conversely, BTIN demonstrates a single offset at epoch 2020.4540, characterized by large amplitudes in the horizontal components, specifically -48.0265 m in the North and -223.431 m in the East, and minimal amplitude, 0.0023 m, in the vertical component (Up).

Figures 7.a and 7.c illustrate the position time series before (blue dots) and after adjustment (red line) for BD61 and BTIN, respectively, while Figures 7.b and 7.d depict the residual coordinate time series (blue dots). Vertical dashed blue lines indicate the identified epochs of offsets. The predicted position time series (red line) accurately calculated from result adjustment, as demonstrated by the residuals closely aligning with the horizontal "0" line. The wrms values are maximal at 1.9 mm for the horizontal components (North, East) and 7.6 mm for the vertical component (Up).

Thus, utilizing real data, the pygps_ts program processed swiftly and accurately. It effectively identified small-amplitude offsets at station BD61 and a large-amplitude offset at station BTIN, showcasing the method and program's flexibility across different scenarios. The wrms value of the adjusted coordinate time series indicates precise reflection of input data and effective handling of offsets.

4. Conclusions

This study presents a novel method for automatic detection and processing of offsets in GNSS position time series, utilizing the RMS sliding-window technique and synthetic models. The developed method was implemented through the pygps_ts program in Python and validated using synthetic and real data.

The program accurately identified the epoch and magnitude of offsets, while processing GNSS coordinate time series quickly and accurately. The results of processing synthetic data showed that the determined displacement parameters matched the designed values. The results of processing real data from two CORS stations in Vietnam, with small-amplitude offsets at station BD61 and large-amplitude offsets at station BTIN, were accurately identified, demonstrating the effectiveness and accuracy of the method and program applied.

The program effectively identified the epoch and magnitude of offsets while ensuring quick and accurate processing of GNSS coordinate time series. Evaluation with synthetic data revealed that the determined displacement parameters closely aligned with the designed values. Similarly, processing real data from two CORS stations in Vietnam successfully identified offsets of varying amplitudes, showcasing the method and program's efficacy and accuracy.

This study contributes a valuable method and tool for GNSS data processing, particularly beneficial in tectonic studies. Given the limited research and early deployment stage of continuous GNSS networks in Vietnam, the presented approach holds significant promise for advancing geodetic studies in the region.

Acknowledgements

We thank Tuong Anh Science and Technology Equipment Joint Stock Company for providing the CORS data, which was essential for this study. We also appreciate the helpful comments from the anonymous reviewers and editors on the earlier version of the manuscript.

Conflicts of Interest

The authors declare no conflict of interest.

Literatura – References

1. Amiri-Simkooei, A. R., Hosseini-Asl, M., Asgari, J., & Zangeneh-Nejad, F. (2019). Offset detection in GPS position time series using multivariate analysis. GPS Solutions, 23(1), 1–12. https://doi.org/10.1007/S10291-018-0805-Z/METRICS
2. Bruni, S., Zerbini, S., Raicich, F., Errico, M., & Santi, E. (2014a). Detecting discontinuities in GNSS coordinate time series with STARS: case study, the Bologna and Medicina GPS sites. Journal of Geodesy, 88(12), 1203–1214. https://doi.org/10.1007/S00190-014-0754-4
3. Bruni, S., Zerbini, S., Raicich, F., Errico, M., & Santi, E. (2014b). Detecting discontinuities in GNSS coordinate time series with STARS: case study, the Bologna and Medicina GPS sites. Journal of Geodesy, 88(12), 1203–1214. https://doi.org/10.1007/S00190-014-0754-4/METRICS
4. Cong Duong, C., Yun, H.-S., & Cho, J.-M. (2006). GPS measurements of horizontal deformation across the Lai Chau—Dien Bien (Dien Bien Phu) fault, in Northwest of Vietnam, 2002-2004. Earth, Planets and Space, 58(5), 523–528. https://doi.org/10.1186/BF03351949
5. Cox, A., & Hart, R. B. (2009). Plate tectonics: How it works. John Wiley & Sons.
6. Crocetti, L., Schartner, M., & Soja, B. (2021). Discontinuity Detection in GNSS Station Coordinate Time Series Using Machine Learning. Remote Sensing 2021, Vol. 13, Page 3906, 13(19), 3906. https://doi.org/10.3390/RS13193906
7. Dach, R., & Walser, P. (2015). Bernese GNSS Software Version 5.2.
8. Gazeaux, J., Williams, S., King, M., Bos, M., Dach, R., Deo, M., Moore, A. W., Ostini, L., Petrie, E., Roggero, M., Teferle, F. N., Olivares, G., & Webb, F. H. (2013). Detecting offsets in GPS time series: First results from the detection of offsets in GPS experiment. Journal of Geophysical Research: Solid Earth, 118(5), 2397–2407. https://doi.org/10.1002/JGRB.50152
9. Hazra, A. (2017). Using the confidence interval confidently. Journal of Thoracic Disease, 9(10), 4124–4129. https://doi.org/10.21037/jtd.2017.09.14
10. Herring, T., King, R., & McClusky, S. (2006). GLOBK reference manual—global Kalman filter VLBI and GPS analysis program release 10.3. Massachusetts Institute of Technology.
11. Khazraei, S. M., & Amiri-Simkooei, A. R. (2020). Improving offset detection algorithm of GNSS position time-series using spline function theory. Geophysical Journal International, 224(1), 257–270. https://doi.org/10.1093/GJI/GGAA453
12. Langley, R. B., Teunissen, P. J. G., & Montenbruck, O. (2017). Introduction to GNSS. Springer Handbooks, 3–23. https://doi.org/10.1007/978-3-319-42928-1_1
13. Métivier, L., Collilieux, X., Lercier, D., Altamimi, Z., & Beauducel, F. (2014). Global coseismic deformations, GNSS time series analysis, and earthquake scaling laws. Journal of Geophysical Research: Solid Earth, 119(12), 9095–9109. https://doi.org/10.1002/2014jb011280
14. Montillet, J.-P., & Bos, M. S. (2020). Geodetic Time Series Analysis in Earth Sciences (J.-P. Montillet & M. S. Bos, Eds.; 1st ed.). Springer International Publishing. https://doi.org/10.1007/978-3-030-21718-1
15. Montillet, J.-P., Williams, S. D. P., Koulali, A., & McClusky, S. C. (2015). Estimation of offsets in GPS time-series and application to the detection of earthquake deformation in the far-field. Geophysical Journal International, 200(2), 1207–1221. https://doi.org/10.1093/gji/ggu473
16. Nikolaidis, R. (2002). Observation of geodetic and seismic deformation with the Global Positioning System. University of California, San Diego.
17. Riel, B., Simons, M., Agram, P., & Zhan, Z. (2014). Detecting transient signals in geodetic time series using sparse estimation techniques. Journal of Geophysical Research: Solid Earth, 119(6), 5140–5160. https://doi.org/10.1002/2014JB011077
18. Thomas, H., & Simon, M. (2009, April 4). GAMIT/GLOBK MATLAB TOOLS. Http://Www-Gpsg.Mit.Edu/~tah/GGMatlab/.
19. Tian, Y. (2011). iGPS: IDL tool package for GPS position time series analysis. GPS Solutions, 15(3), 299–303. https://doi.org/10.1007/S10291-011-0219-7/METRICS
20. Tran, D. T. (2013). Analyse rapide et robuste des solutions GPS pour la tectonique [Université de Nice Sophia - Antipolis]. https://www.theses.fr/2013NICE4033
21. Tran, D. T., Nguyen, D. H., Vu, N. Q., & Nguyen, Q. L. (2023). Crustal displacement in Vietnam using CORS data during 2018-2021. Earth Sciences Research Journal, 27(1). https://doi.org/10.15446/esrj.v27n1.102630
22. Tran, D. T., Nguyen, Q. L., & Nguyen, D. H. (2021). General Geometric Model of GNSS Position Time Series for Crustal Deformation Studies – A Case Study of CORS Stations in Vietnam. Inzynieria Mineralna, 1(2). https://doi.org/10.29227/IM-2021-02-16
23. Tran, D. T., Nguyen, T. Y., Duong, C. C., Vy, Q. H., Zuchiewicz, W., Nguyen, Q. C., & Nguyen, V. N. (2013). Recent crustal movements of northern Vietnam from GPS data. Journal of Geodynamics, 69, 5–10. https://doi.org/10.1016/j.jog.2012.02.009

24. Van Rossum, G., & Drake, F. L. (2003). An introduction to Python. Network Theory Ltd. Bristol.

25. Vy Quốc Hải, Trần Đình Tô, & Ngô Văn Liêm. (2011). Determination of present crustal movements of Red River Fault Zone by the TamDao - BaVi GPS network (1994-2007). Vietnam Journal of Earth Sciences, 33(3), 474–479. https://doi.org/10.15625/0866-7187/33/3/438

26. Williams, S. D. P. (2008). CATS: GPS coordinate time series analysis software. GPS Solutions, 12(2), 147–153. https://doi.org/10.1007/s10291-007-0086-4

27. Wu, D., Yan, H., & Yuan, S. (2018). L1 regularization for detecting offsets and trend change points in GNSS time series. GPS Solutions, 22(3), 1–5. https://doi.org/10.1007/S10291-018-0756-4/METRICS

Automatyczne wykrywanie i analiza przesunięć w szeregach czasowych pozycji GNSS przy użyciu metody przesuwanego okna RMS i modelu syntetycznego

W artykule przedstawiono metodę automatycznego wykrywania i analizy przesunięć w szeregach czasowych pozycji GNSS (Globalnego Systemu Nawigacji Satelitarnej) z wykorzystaniem metody przesuwanego okna RMS (Root Mean Square). Technika ta identyfikuje anomalie wskazujące przesunięcia w szeregach czasowych. Aby dokładnie dostosować parametry, takie jak trendy liniowe, sygnały sezonowe i przesunięcia, wykorzystuje się syntetyczny model szeregów czasowych pozycji GNSS. Metoda jest zaimplementowana w zautomatyzowanym programie pygps_ts, napisanym w języku Python. Skuteczność tego podejścia potwierdza się na podstawie zarówno syntetycznych, jak i rzeczywistych danych ze stacji CORS (ciągle działającej stacji referencyjnej) w Wietnamie. Wyniki pokazują, że program może dokładnie i skutecznie wykrywać i analizować przesunięcia, identyfikując epoki i wielkość tych przesunięć w różnych scenariuszach. Niniejsze badanie oferuje praktyczne narzędzie do przetwarzania danych GNSS, które jest szczególnie przydatne w badaniach tektonicznych i zastosowaniach geodezyjnych w Wietnamie, gdzie ciągła sieć GNSS wciąż się rozwija. Badanie pokazuje potencjał tej metody do szerszego zastosowania w monitorowaniu i analizie danych GNSS w różnych regionach. dokładność i skuteczność w wykrywaniu i analizie przesunięć.

Słowa kluczowe: *szeregi czasowe pozycji GNSS, tektonika przemieszczeń, przesunięcie, okno przesuwne, CORS*

Solution to Improve the Horizontal and vertical Position Accuracy of Points Measured by GNSS/ CORS Technology in Creation of Large-Scale Topographic Maps in Vietnam

Tuan Anh LUU[1)], Thuy Thi Hoang[2)]*

[1)] Faculty of Geomatics and Land Administration, Hanoi University of Mining and Geology, Hanoi, Vietnam; ORCID https://orcid.org/0009-0001-7738-9718
[2)] Faculty of Geomatics and Land Administration, Hanoi University of Mining and Geology, Hanoi, Vietnam
* Corresponding author: luuanhtuan@humg.edu.vn

http://doi.org/10.29227/IM-2024-01-98

Submission date: 09-05-2024 | Review date: 29-05-2024

Abstract

In Vietnam, when creating large-scale topographic maps using Global Navigation Satellite Systems (GNSS) technology combined with Continuously Operating Reference Stations (CORS) and traditional electronic total station measurements, there will be shifts in both horizontal and vertical positions. To address this issue, we perform map adjustments by updating the map in an assumed coordinate system. In the assumed coordinate system, the shapes and elevation differences of the changed objects are accurately observed to meet the requirements corresponding to the map scale. The coordinates and elevations of clear points on the map or control points in the field obtained from different methods have differences that are larger than the permissible values according to the map scale. Applying a 2-dimensional coordinate transformation and the geoidal height calculated for each point with its weight, the coordinates and elevations of the points can be computed in a unified coordinate system.

Keywords: *GNSS accuracy, topographic map, Geodetic Network*

1. Introduction

Currently, Vietnam's Ministry of Natural Resources and A map is a scaled-down image that provides a generalized depiction of a large part of the Earth's surface on a plane applying various map projection methods. A topographic map is a type of general geographic map, of which the contents include information about natural elements such as terrain, hydrology, vegetation cover, and elements related to economy, culture, and society such as population, road systems, bridges, service facilities, public works, and administrative boundaries [1], [4].

In Vietnam, when creating large-scale topographic maps, an optimal solution that is being widely applied is the combination of GNSS/CORS technology and electronic total stations. The electronic total station is highly reliable, flexible, and efficient in residential areas and vegetated areas. In contrast, GNSS/CORS technology, such as Real-Time Kinematic (RTK) or Virtual Reference Station (VRS), enhances the accuracy and increases the distance from the base station. Additionally, RTK is advantageous in providing quick observations and economic efficiency in open areas, without relying on the construction of control networks. However, GNSS/CORS technology is based on the international WGS-84 coordinate system and ellipsoidal heights, while topographic maps are created on the national coordinate system of Vietnam (VN-2000) using the UTM reference system and leveling heights.

Despite its advantages, the VN-2000 system is not yet a 3D coordinate system and is not connected to the International Terrestrial Reference Frame (ITRF). This limits the exploitation of GNSS technology in determining spatial positions, data acquisition and sharing, and international cooperation to solve regional and global problems. Additionally, GNSS/CORS technology provides ellipsoidal heights with the reference ellipsoid, but the Vietnam national height system uses normal heights with the reference quasigeoid. To apply GNSS/CORS technology in height measurement, the difference between the quasigeoid and the ellipsoid at each point must be known. This requires a local quasigeoid model at the study area with sufficient accuracy for using GNSS/CORS technology as a replacement for traditional leveling methods [5].

In this study, a theoretical and experimental research is conducted to draw specific conclusions about the solution of combining surveying technologies in the creation of large-scale topographic maps in Vietnam. This is a new direction resquiring more extensive research and serious evaluation in practical production to best utilize the advantages of the various surveying methods in the creation of topographic maps in Vietnam.

2. Synchronization of topographic observation data

2.1 Coordinate Transformation between GNSS/CORS and ITRF

The transformation of the GNSS/CORS coordinates to the ITRF coordinate system ensures the consistency and accuracy of geographic data worldwide. The coordinate transformation between ITRF reference frames (ITRF, 2019) or between the VN-2000 coordinate system and ITRF is carried out using the general formula [6] as follows:

$$X_{(2)} = T + (1 + D)R^T X_{(1)} \quad (1)$$

where X(2) and X(1) are the coordinate vectors in the VN2000 and ITRF systems, respectively, T is the translation vector be-

tween the origions of the two systems, D is the scale factor, R is the rotation matrix about the axes in radians [7].

$$\boldsymbol{R^T} = \begin{vmatrix} 1 & -R_3 & R_2 \\ R_3 & 1 & R_1 \\ -R_2 & R_1 & 1 \end{vmatrix} \quad (2)$$

Since the value D.RT is a small quantity, the second-order term can be neglected, and therefore (1.1) can be written as:

$$\begin{bmatrix} X \\ Y \\ Z \end{bmatrix}_{(2)} = \begin{bmatrix} X \\ Y \\ Z \end{bmatrix}_{(1)} + \begin{bmatrix} T_1 \\ T_2 \\ T_3 \end{bmatrix}_{(1)} + D \begin{bmatrix} X \\ Y \\ Z \end{bmatrix}_{(1)} + \begin{bmatrix} 0 & -R_3 & R_2 \\ R_3 & 0 & -R_3 \\ R_2 & R_1 & 0 \end{bmatrix} \begin{bmatrix} X \\ Y \\ Z \end{bmatrix}_{(1)} \quad (3)$$

2.2 Conversion of the elevation of topographic points measured using GNSS/CORS technology to leveling height

There are different methods for height anomalies interpolation, in which polynomial, kriging, collocation, and spline interpolations are commonly applied. In this study, we apply the polynomial interpolation method for each measurement point by adding weighting factors, which are the inverse distances to the common points.

2.2.1 Interpolation of height anomalies using the polynomial model

In order to interpolate height anomalies, common points with known grid coordinates (x, y), ellipsoidal heights (H), and leveling heights (h^γ) are required, based on which the height anomalies can be calculated [3]:

$$\zeta = H - h^{\gamma} \quad (4)$$

Those points with both known ellipsoidal and leveling heights are termed as common points in this study. GNSS technology provides us with highly accurate ellipsoidal heights, but leveling heights are needed in practice. Therefore, the transformation from ellipsoidal heights to leveling heights is needed, which can be conducted using a global geoid model, such as OSU91A, EGM-96, or EGM2008. However, practical experiments indicated that global geoid models have low accuracy in Vietnam. Additionally, an accurate local geoid model has not been published so far in Vietnam.

To enhance the accuracy of height measurement using GNSS/CORS technology in the creation of topographic maps, we propose using high-precision level points in the surveying area to create a local geoid model by which to adjust the heights measured by GNSS technology. Based on the coordinates of points measured using GNSS technology (X, Y, Z) and leveling heights measured accurately in the national height system, we generate a geoid model at each surveyed point to transform the ellipsoidal heights to leveling heights as in [3]:

$$h^{\gamma} = H - \zeta \quad (5)$$

Depending on the number of existing common points in the surveying area, the local geoid model takes the form of a polynomial of zero-, first-, second-, or third-degree. The equation of the height anomaly is of the form:

$$\zeta i = F(xi, yi) \quad (6)$$

where ζi is the height anomaly of the point located at the coordinates xi , yi. The specific polynomial forms of the height anomaly are as follows:

With 3 common points, the first-degree polynomial function is used to calculate 3 coefficients ζ0, A, B. With 6 common points, the second-degree polynomial function is used, and with 10 common points, the third-degree polynomial function is used. When the number of common points exceeds the number of coefficients, the least squares method is employed to calculate the coefficients.

Taking ζ as the measurement with n common points, the system of measurement equations is formed as follows (for first-degree polynomial) [3]:

$$\begin{aligned} &\text{Zero-degre: } \zeta i = \zeta 0 \\ &\text{First-degre: } \zeta i = \zeta 0 + Axi + Byi \\ &\text{Second-degre: } \zeta i = \zeta 0 + Axi + Byi \\ &\qquad +Cxi\ 2 + Dyi\ 2 + Exiyi \\ &\text{Third-degre: } \zeta i = \zeta 0 + Axi + Byi + Cxi\ 2 + Dyi\ 2 \\ &\qquad + Exiyi + Fxi\ 3 + Gyi\ 3 + Hxi\ 2yi + Kxi\ yi\ 2 \end{aligned} \quad (7)$$

$$\begin{bmatrix} \zeta_1 \\ \zeta_2 \\ \cdots \\ \zeta_n \end{bmatrix} = \begin{bmatrix} x_1 & y_1 & 1 \\ x_2 & y_2 & 1 \\ \cdots & \cdots & \cdots \\ x_n & y_n & 1 \end{bmatrix} \times \begin{bmatrix} a \\ b \\ c \end{bmatrix} \quad (8)$$

Then, we can derive the system of correction equations:

$$\begin{bmatrix} v_1 \\ v_2 \\ \cdots \\ v_n \end{bmatrix} = \begin{bmatrix} x_1 & y_1 & 1 \\ x_2 & y_2 & 1 \\ \cdots & \cdots & \cdots \\ x_n & y_n & 1 \end{bmatrix} \times \begin{bmatrix} a \\ b \\ c \end{bmatrix} - \begin{bmatrix} \zeta_1 \\ \zeta_2 \\ \cdots \\ \zeta_n \end{bmatrix} \quad (9)$$

where vi is the correction for the anomalous height measurement ζi. With the number of common points exceeds the number of unknowns, the least squares method is applied ([vv]=Min) to form the system of normal equations [2]:

$$\begin{bmatrix} x_1 & y_1 & 1 \\ x_2 & y_2 & 1 \\ \cdots & \cdots & \cdots \\ x_n & y_n & 1 \end{bmatrix}^T \times \begin{bmatrix} x_1 & y_1 & 1 \\ x_2 & y_2 & 1 \\ \cdots & \cdots & \cdots \\ x_n & y_n & 1 \end{bmatrix} \times \begin{bmatrix} a \\ b \\ c \end{bmatrix} - \begin{bmatrix} x_1 & y_1 & 1 \\ x_2 & y_2 & 1 \\ \cdots & \cdots & \cdots \\ x_n & y_n & 1 \end{bmatrix}^T \times \begin{bmatrix} \zeta_1 \\ \zeta_2 \\ \cdots \\ \zeta_n \end{bmatrix} = 0 \quad (10)$$

In the matrix form:

$$A^T PA.X + A^T PL = 0$$

$$\text{where } A = \begin{bmatrix} x_1 & y_1 & 1 \\ x_2 & y_2 & 1 \\ \cdots & \cdots & \cdots \\ x_n & y_n & 1 \end{bmatrix}, X = \begin{bmatrix} a \\ b \\ c \end{bmatrix}, L = \begin{bmatrix} \zeta_1 \\ \zeta_2 \\ \cdots \\ \zeta_n \end{bmatrix}$$

We can then solve the parameter vector X and the uncertainty of the interpolation model:

$$X = \begin{bmatrix} a \\ b \\ c \end{bmatrix} = R^{-1} A^T PL = QA^T PL \quad (11)$$

$$m_0 = \sqrt{\frac{[pvv]}{n-t}} \quad (12)$$

Using the obtained model parameters to calculate the anomalous height for any GNSS measurement point P with coordinates (xP, yP) by Equation (11). In solving for the geoid model parameters, we consider the different influences of common points on the correction for each point. Specifically, for each measurement point, we calculate its own model parameters with weights assigned to common points as inversely proportional to the distances to the measurement point:

Pi = 1/Si or Pi = 1/Si2.

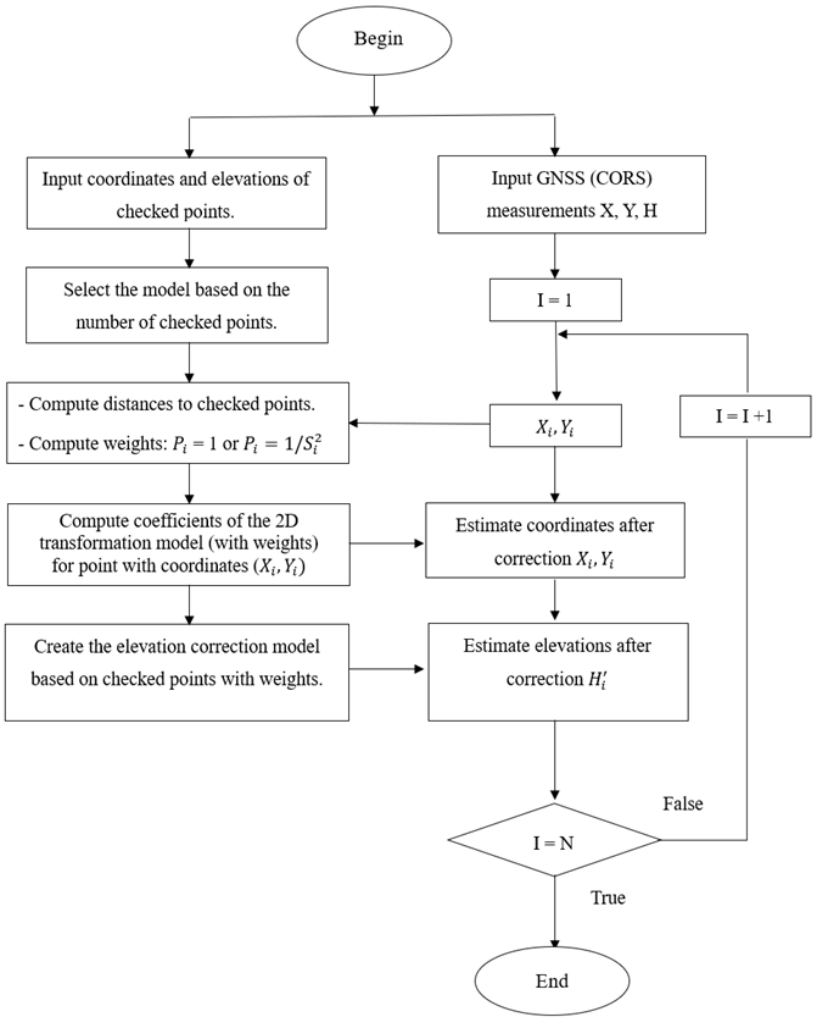

Fig. 1. Workflow of coordinate transformation and conversion of GNSS/CORS points
Rys. 1. Proces transformacji współrzędnych i konwersji punktów GNSS/CORS

2.2.2. Transformation between WGS-84 Geocentric and VN-2000 Grid Coordinates

With the coordinates of points (X, Y, Z) measured using GNSS technology in the global geocentric coordinate system WGS-84, we first transform them to the geocentric coordinates X1, Y1, Z1 in the VN-2000 coordinate system, and then to the geodetic coordinates B, L, H. Finally, the derived coordinates B, L are converted to grid coordinates using the UTM projection. At the same time, ellipsoidal heights are converted to leveling heights [3]:

(XYZ)WGS-84 ---> (XYZ)VN-2000 ----> (BLH)VN-2000 ---> (xyh)VN-2000

The transformation formulas are as follows:

a. Transformation of geocentric coordinates from WGS-84 to VN-2000

$$\begin{aligned} X1 &= \Delta X0 + k\,.\,(X - \omega 0\,.\,Y + \psi 0\,.\,Z) \\ Y1 &= \Delta Y0 + k\,.\,(\omega 0\,.\,X + Y - \varepsilon 0\,.\,Z) \\ Z1 &= \Delta Z0 + k\,.\,(-\psi 0\,.\,X + \varepsilon 0\,.\,Y + Z) \end{aligned} \quad (13)$$

where k is the scale factor, ω0, ψ0, ε0 are the Euler rotation angles about the X, Y, Z axes, and ΔX0, ΔY0, ΔZ0 are the coordinates of the center of the international WGS-84 system in the VN-2000 system.

b) Conversion from geodetic coordinates (B, L) to grid coordinates (x, y)

According to [3], we have:

$$\begin{aligned} (x - X) = {} & \frac{N}{2\rho''^2} \sin B \cos B\, 1''^2 + \\ & \frac{N}{24\rho''^4} \sin B \cos^3 B\,(5 - t^2 + 9\eta^2 + 4\eta^2)1''^4 + \\ & \frac{N}{720\rho''^6} \sin B \cos^5 B(61 - 58t^2 + t^4)1''^6 \end{aligned} \quad (14)$$

$$\begin{aligned} y = {} & \frac{N}{\rho''} \cos B\, 1'' + \frac{N}{6\rho''^3} \cos^3 B\,(1 - t^2 + \eta^2)1''^3 \\ & + \frac{N}{120\rho''^5} \cos^5 B\,(5 - 18t^2 \\ & + t^4 + 14\eta^2 - 58t^2\eta^2)1''^5 \end{aligned} \quad (15)$$

c) Conversion from grid coordinates (x, y) to geodetic coordinates (B, L)

According to [3], we have:

$$\begin{aligned} B_1 - B = {} & \frac{\rho'' t_1}{2M_1N_1} y^2 - \frac{\rho'' t_1}{2M_1N_1^3}(5 + 3t_1^2 + \eta_1^2 - 9t_1^2\eta_1^2)y^4 \\ & + \frac{\rho'' t_1}{720M_1N_1^5}(61 + 90t_1^2 + 45t_1^2)y^6 \end{aligned} \quad (16)$$

$$\begin{aligned} l = {} & \frac{\rho''}{N_1 \cos B_1} y - \frac{\rho''}{6N_1^3 \cos B_1}(1 + 2t_1^2 + \eta_1^2)y^3 + \\ & \frac{\rho''}{120N_1^5 \cos B_1}(5 + 28t_1^2 + 24t_1^4 + 6\eta_1^2 + 8t_1^2\eta_1^2)y^5 \end{aligned} \quad (17)$$

where X is the length of the meridian arc determined based on the known latitude B, N is the radius of curvature of the prime vertical. The coefficients l, M, N, t, h are calculated as follows:

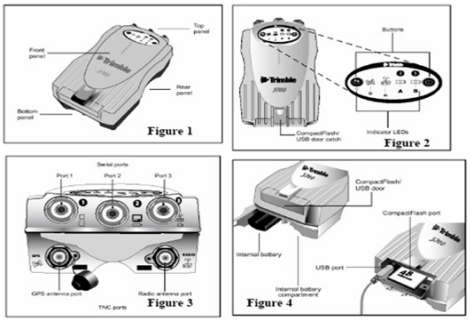

Fig. 2. Components of Trimble R7 GNSS receivers
Rys. 2. Komponenty odbiornika GNSS Trimble R7

Fig. 3. Trimble R7 GNSS antenna
Rys. 3. Antenna GNSS Trimble R7

l = L – L0, (L0 is the central meridian);
t = tgB; t1 = tgB1; h2 = e'2cos2B ;
$M = \frac{a(1-e^2)}{(1-e^2 \sin^2 B)^{3/2}}$;
$N = \frac{a}{(1-e^2 \sin^2 B)^{1/2}}$

e and e' are the first and second eccentricities, a is the semi major axis of the Ellipsoid.

d) Conversion from geodetic to geocentric coordinates

To convert from the geodetic coordinates B, L, H to the geocentric coordinates X, Y, Z of a point within the same coordinate system, we use the following equation [3]:

$$\begin{aligned} X &= (N + H)\cos B.\cos L \\ Y &= (N + H)\cos B.\sin L \\ Z &= [N(1 - e^2) + H)\sin B \end{aligned} \quad (18)$$

e) Conversion from geocentric to geodetic coordinates

According to [3], we have:

$$tgL = \frac{Y}{X}; \quad tgB = \frac{Z + Ne^2.\sin B}{R};$$
$$H = Z/\sin B - N(1-e2);$$
$$R = (X2 + Y2)1/2 \quad (19)$$

2.2.3 Transformation of coordinates measured by GNSS/CORS technology

The transformation of 2D coordinates from the first system (xoy)1 to the second system (xoy)2 is carried out using the Helmert transformation [2]:

$$\begin{pmatrix} x' \\ y' \end{pmatrix} = \begin{pmatrix} x_0 \\ y_0 \end{pmatrix} + m \begin{pmatrix} \cos\alpha & -\sin\alpha \\ \sin\alpha & \cos\alpha \end{pmatrix} \begin{pmatrix} x \\ y \end{pmatrix} \quad (20)$$

which can be rewritten as:

$$\begin{aligned} x' &= x_0 + (m.\cos\alpha)x - (m.\sin\alpha)y \\ y' &= y_0 + (m.\sin\alpha)x + (m.\cos\alpha)y \end{aligned} \quad (21)$$

with the notations $m.\cos\alpha = a;\ m.\sin\alpha = b;\ x_0 = c;\ y_0 = d.$

$$\begin{aligned} x' &= a.x - b.y + c \\ y' &= b.x + a.y + d \end{aligned} \quad (22)$$

we can from a system of correction equations as:

$$\begin{aligned} vx' &= x.a - y.b + 1.c + lx \quad \text{với} \quad lx = -x' \\ vy' &= y.a + x.b + 1.d + ly \quad \text{với} \quad ly = -y' \end{aligned} \quad (23)$$

Thus, we have a system of correction equations with 4 unknowns, which requires at least 2 common points to solve for the unknowns a, b, c, d.

2.3.4 Workflow of 2D coordinate transformation

The process of coordinate transformation and conversion of GNSS/CORS points to grid coordinates and leveling elevation is performed according to the workflow shown in Figure 1.

3. Experiment

3.1 Study area, data used, and instrument

The study area is located in Mu Cang Chai district, Yen Bai province, with an area of 400 km². Mù Cang Chải is a highland district located in the western part of Yen Bai Province. It is 185km away from the provincial center and 365km away from the capital city of Hanoi. The district covers an area of 120,095.83 hectares, most of which is mountainous terrain originating from the Hoang Lien Son mountain range. This includes many successive mountain ranges running in the northwest-southeast direction, with streams and valleys belonging to the Red River and Da River basins between them. The lowest absolute elevation is the Cao Pha field at 650m, and the highest is the Lung Cung peak in Nam Co commune at 2,963m above sea level. The terrain is heavily dissected, creating long slopes with an average gradient of 300m, though in some places it reaches over 450m. It borders Van Ban District of Lao Cai Province to the north, Muong La District of Son La Province to the south, Van Yen and Van Chan Districts to the east, and Than Uyen District of Lai Chau Province to the west.

The study area covers approximately 400km², encompassing the Mo De, Che Cu Nha, La Pan Tan, and De Xu Phinh communes (figure 4). There are 5 national geodetic control points 77423, 77432, 77434, 77437, and 77451, and 5 nation-

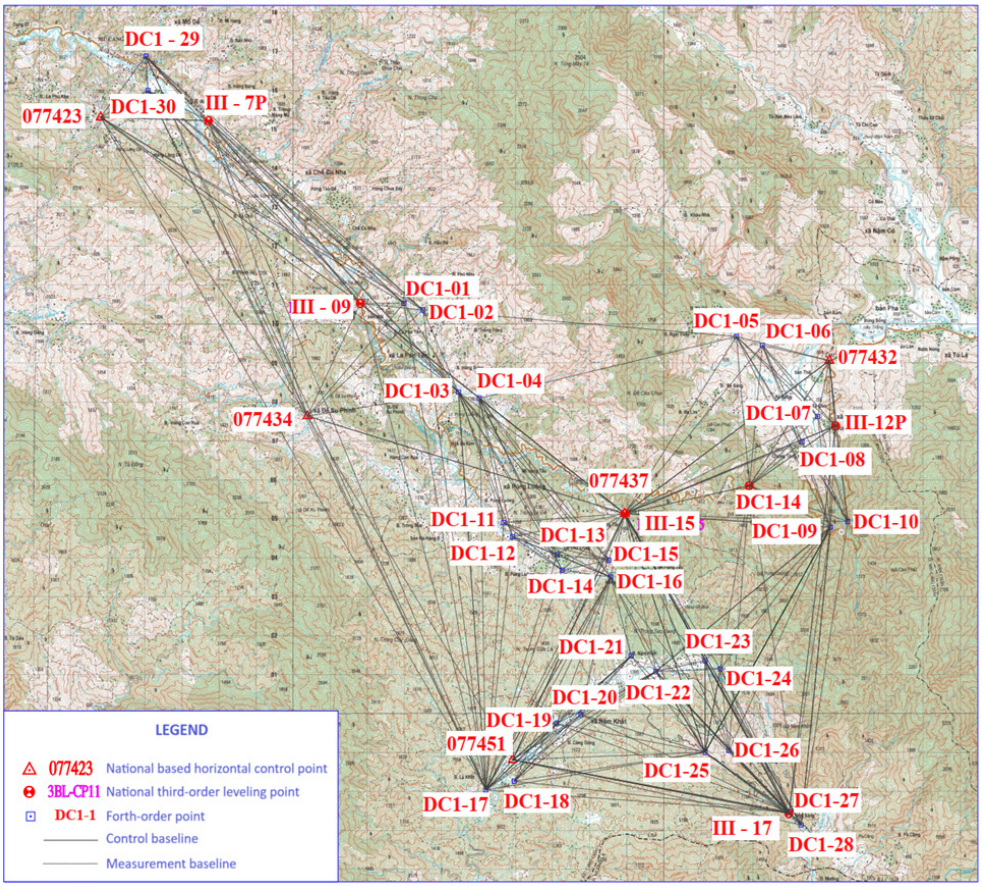

Fig. 4. Study area in Mu Cang Chai district, Yen Bai province
Rys. 4. Obszar objęty badaniami w okręg Mu Cang Chai, prowincja Yen Bai

al third-order level points III_09, III_7P, III_12, III_14, and III_17. The X, Y and H of these points are as in Table 1. The measurement network consists of those mentioned national geodetic control points and national third-order level points as well as 30 unknown first-order traverse points. The measurements are made using Trimble R7 GNSS receivers (figures 3 and 4), with horizontal and vertical fast static accuracies of 5mm + 0.5ppm and 5mm + 1ppm, respectively. The measurements were carried out with 6 receivers over 8 60-minute static measurement sessions.

3.2 Experimental procedure

The 30 GNSS points distributed across the entire study area are measured using Trimble R7 GNSS dual-frequency receivers based on the 5 national geodetic control points and 5 national third-order state leveling points. The observations are then processed by the Trimble Business Center software. The derived coordinates are subsequently adjusted using the 2D coordinate transformation, and the elevations of the measurement points are converted to leveling heights using the geoid undulation interpolation problem with the weight factor of P=1 and P = 1/Si2, where Si is the distance from the measurement point to the nearest control point. Finally, the results are analyzed and the experiment is concluded.

3.3 Results and discussion

The observations are processed using the Trimble Business Center (TBC) with the results shown in Table 2. The coordinates and elevations of the national third-order control points measured by GNSS and processed by the proposed workflow. The results are as shown in Table 3 and Table 4.

From Table 3, with coordinates and heights corrected according to the chosen weight factor P=1, we have: $[\Delta\Delta]$= 0.127303, n = 39, m = ±0.057 (m); with all corrections applied to the coordinates and levels of the control points are non-zero.

From Table 4, with coordinates and heights corrected according to the chosen weight factor $P=1/S^2$, we have: $[\Delta\Delta]$= 0.125443, n = 39, m = ±0.056 (m) with all corrections applied to the coordinates and levels of the control points are zero.

Tables 3 and 4 show the coordinates and elevations of the national third-order control points measured by GNSS and processed by the proposed workflow in this study. It is shown that the height deviations of the points III_09, III_7B, III_12, and III_14 are 0.023m, -0.012m, 0.013m, and -0.003m, respectively, when P=1 is applied, while those for the same points are 0.000m when $P=1/S^2$ is applied. Therefore, using weight $P=1/S^2$ has higher accuracy compared to using weight P=1.

From the corrections to convert GNSS-derived elevations to leveling heights, and the leveling heights shown in Table 4, we construct a site map and a height anomalies digital model as follows on Fig. 5.

Figure 5 shows a contour map of interpolated height anomalies determined based on the national leveling points, and Figure 6 shows their corresponding digital model. It can be concluded that the results based on the proposed workflow in this study applying $P=1/S^2$ is highly reliable.

Tab. 1. Coordinates and elevations of the national third-order level points and geodetic control points

Tab. 1. Współrzędne i wysokości krajowych punktów trzeciego rzędu i punktów kontroli geodezyjnej

No	Point name	Coordinates of the national third-order level points		
		X(m)	Y(m)	H(m)
1	77423	2415895.97	430623.605	1405.150
2	77432	2409679.742	450301.045	787.160
3	77434	2408234.513	436219.215	1400.972
4	77437	2405746.667	444786.447	1321.099
5	77451	2399421.409	441772.429	1361.617
6	III_09	2411130.052	437642.588	1127.604
7	III_7P	2415807.232	433534.639	971.193
8	III_12	2408008.217	450468.008	899.032
9	III_14	2406462.48	448147.867	1430.969
10	III_17	2398054.598	449225.164	1126.724

Tab. 2. GNSS processed coordinates

Tab. 2. Współrzędne przeliczone z pomiarów GNSS

No	Point name	WGS-84 coordinates		
		X(m)	Y(m)	Z(m)
1	77423	-1441162.2847	5746484.0925	2358410.7752
2	77432	-1460685.7912	5743315.5849	2352476.7272
3	77434	-1447312.2826	5747860.7325	2351315.7667
4	77437	-1455834.6258	5746570.7882	2349004.4970
5	77451	-1453518.3229	5749615.1725	2343131.8469
6	DC1-01	-1449556.8312	5746183.4792	2354019.5203
7	DC1-02	-1450065.5566	5746100.7344	2353854.8807
8	DC1-03	-1451155.0426	5746451.2906	2351834.1915
9	DC1-04	-1451722.2769	5746382.7343	2351690.8972
10	DC1-05	-1458256.3442	5743960.0941	2353139.8973
11	DC1-06	-1458935.1637	5743773.5249	2352894.2997
12	DC1-07	-1460515.8402	5743913.2417	2351145.3561
13	DC1-08	-1460186.5905	5744310.8179	2350568.6649
14	DC1-09	-1461207.5309	5745169.6658	2348641.9460
15	DC1-10	-1461615.2307	5744886.6552	2348732.7435
16	DC1-11	-1452921.8315	5747402.4856	2348380.3853
17	DC1-12	-1452661.0998	5747360.7446	2348730.8786
18	DC1-13	-1454143.7086	5747322.3845	2347985.2397
19	DC1-14	-1454318.0662	5747441.2862	2347617.8883
20	DC1-15	-1455520.0755	5747086.8324	2347881.1862
21	DC1-16	-1455611.5684	5747211.3012	2347471.4612
22	DC1-17	-1452896.1308	5750091.7296	2342416.8262
23	DC1-18	-1453617.7817	5749821.1209	2342633.0695
24	DC1-19	-1454583.1420	5749004.4930	2344009.4154
25	DC1-20	-1455195.3580	5748771.5598	2344227.1410
26	DC1-21	-1456369.5582	5747921.5992	2345646.8400
27	DC1-22	-1457054.9876	5747880.9472	2345270.8530
28	DC1-23	-1458330.1120	5747518.4952	2345559.8015
29	DC1-24	-1458748.2721	5747491.0286	2345362.9305
30	DC1-25	-1458552.9290	5748342.5893	2343366.9848
31	DC1-26	-1459173.9030	5748188.2307	2343424.6805
32	DC1-27	-1460835.6911	5748030.7095	2341827.6246
33	DC1-28	-1461161.2425	5748053.4930	2341518.9026
34	DC1-29	-1442102.0335	5745271.1303	2359726.5703
35	DC1-30	-1442234.0701	5745509.8574	2358883.8895
36	III_09	-1448356.6812	5746225.3194	2353908.9780
37	III_7P	-1443895.5225	5745411.8659	2358178.4849
38	III_12	-1461031.1133	5743974.7341	2350966.1604
39	III_14	-1459050.2383	5745582.2676	2349720.6425
40	III_17	-1460817.0764	5748051.2827	2341798.1099

The application of GNSS technology with the proposed algorithm to derive horizontal coordinates and leveling heights of points based on height anomalies of existing benchmarks in the study area for large-scale topographic mapping has both scientific and practical meanings in the context of Vietnam. This is because it meets technical requirements and economicly efficient for large-scale topographic mapping. The experiment over the study area of 400 km² with 5 to 10 benchmark points shows that the application of GNSS technology with the proposed workflow ensures required accuracy for large-scale topographic mapping in Vietnam. This method is particularly practical in Vietnam when mapping with GNSS technology in areas with difficult terrain such as border regions, coastal areas, and islands.

4. Conclusions

The algorithm proposed in this study, which focuses on the transformation of 2D coordinates and the determination of leveling heights based on the height anomalies of existing points within the designated study area, presents a compelling

Tab. 3. Corrections of GNSS to leveling heights using weight factor, P=1
Tab. 3. Korekty GNSS do wysokości niwelacyjnych z wykorzystaniem współczynnika wagowego, P=1

No	Point name	Coordinates P=1			Correction			Leveling height (m)	Level difference (m)
		X(m)	Y(m)	H(m)	dx(m)	dy(m)	dh(m)		
1	77423	2415895.970	430623.605	1405.155	-0.0002	0.0000	-3.830	1405.150	0.005
2	77432	2409679.742	450301.045	787.151	0.0001	0.0000	-3.373	787.160	-0.009
3	77434	2408234.513	436219.215	1400.960	0.0003	0.0000	-3.872	1400.972	-0.012
4	77437	2405746.667	444786.447	1321.090	0.0002	0.0000	-3.641	1321.099	-0.009
5	77451	2399421.409	441772.429	1361.620	-0.0001	0.0000	-3.764	1361.617	0.003
6	DC1-01	2411134.251	438816.271	1403.489	0.0006	0.0000	-3.812	1403.482	0.007
7	DC1-02	2410963.048	439328.991	1383.433	0.0006	0.0000	-3.802	1383.409	0.024
8	DC1-03	2408858.463	440291.355	1196.748	0.0005	0.0000	-3.787	1196.746	0.002
9	DC1-04	2408696.452	440857.368	1210.878	0.0005	0.0000	-3.772	1210.861	0.017
10	DC1-05	2410293.655	447790.181	1057.615	0.0004	0.0000	-3.505	1057.605	0.010
11	DC1-06	2410068.473	448493.152	953.719	0.0003	0.0000	-3.470	953.738	-0.019
12	DC1-07	2408245.295	449984.621	792.189	0.0000	0.0000	-3.388	792.196	-0.007
13	DC1-08	2407598.360	449565.609	860.805	-0.0001	0.0000	-3.410	860.768	0.037
14	DC1-09	2405405.192	450336.384	1153.487	-0.0004	0.0000	-3.361	1153.447	0.040
15	DC1-10	2405552.434	450801.616	1025.753	-0.0004	0.0000	-3.334	1025.696	0.057
16	DC1-11	2405143.900	441757.248	1174.905	0.0003	0.0000	-3.755	1174.901	0.004
17	DC1-12	2405508.911	441516.086	1207.803	0.0003	0.0000	-3.762	1207.807	-0.004
18	DC1-13	2404690.436	442959.544	1234.728	0.0002	0.0000	-3.714	1234.735	-0.007
19	DC1-14	2404290.284	443097.949	1245.489	0.0002	0.0000	-3.709	1245.489	0.000
20	DC1-15	2404548.398	444350.776	1297.871	0.0001	0.0000	-3.660	1297.830	0.041
21	DC1-16	2404114.718	444407.387	1279.092	0.0001	0.0000	-3.658	1279.044	0.048
22	DC1-17	2398645.450	441049.791	1385.024	-0.0001	0.0000	-3.790	1385.005	0.019
23	DC1-18	2398875.132	441816.383	1385.478	-0.0001	0.0000	-3.763	1385.476	0.002
24	DC1-19	2400354.647	442957.514	1378.558	-0.0001	0.0000	-3.718	1378.551	0.007
25	DC1-20	2400582.535	443608.796	1388.833	-0.0001	0.0000	-3.692	1388.795	0.038
26	DC1-21	2402094.565	444960.613	1416.317	-0.0001	0.0000	-3.635	1416.285	0.032
27	DC1-22	2401695.351	445633.474	1397.077	-0.0002	0.0000	-3.604	1397.013	0.064
28	DC1-23	2401973.284	446959.125	1468.860	-0.0003	0.0000	-3.540	1468.796	0.064
29	DC1-24	2401973.284	447370.374	1466.871	-0.0003	0.0000	-3.519	1466.785	0.086
30	DC1-25	2399620.923	446964.634	1451.031	-0.0005	0.0000	-3.536	1450.942	0.089
31	DC1-26	2399671.254	447604.477	1475.308	-0.0005	0.0000	-3.503	1475.186	0.122
32	DC1-27	2398087.617	449248.372	1123.538	-0.0009	0.0000	-3.406	1123.360	0.178
33	DC1-28	2397762.053	449557.178	1104.566	-0.0010	0.0000	-3.386	1104.364	0.202
34	DC1-29	2417464.371	431836.793	1015.054	0.0001	0.0000	-3.822	1015.075	-0.021
35	DC1-30	2416583.970	431902.953	946.175	0.0001	0.0000	-3.831	946.189	-0.014
36	III_09	2411130.052	437642.588	1127.627	0.0005	0.0000	-3.834	1127.604	0.023
37	III_7P	2415807.231	433534.639	971.181	0.0003	0.0000	-3.840	971.193	-0.012
38	III_12	2408008.217	450468.008	899.045	-0.0001	0.0000	-3.360	899.032	0.013
39	III_14	2406462.480	448147.867	1430.966	0.0000	0.0000	-3.484	1430.969	-0.003

Tab. 1. Coordinates and elevations of the national third-order level points and geodetic control points

Tab. 1. Współrzędne i wysokości krajowych punktów trzeciego rzędu i punktów kontroli geodezyjnej

No	Point name	Coordinates P=1/S²			Correction			Leveling height (m)	Level difference (m)
		x(m)	y(m)	h(m)	dx(m)	dy(m)	dh(m)		
1	77423	2415895.970	430623.605	1405.150	0.0000	0.0000	-3.835	1405.150	0.0000
2	77432	2409679.742	450301.045	787.160	0.0000	0.0000	-3.364	787.160	0.0000
3	77434	2408234.513	436219.215	1400.972	0.0000	0.0000	-3.860	1400.972	0.0000
4	77437	2405746.667	444786.447	1321.099	0.0000	0.0000	-3.632	1321.099	0.0000
5	77451	2399421.409	441772.429	1361.617	0.0000	0.0000	-3.767	1361.617	0.0000
6	DC1-01	2411134.251	438816.271	1403.469	0.0010	0.0000	-3.833	1403.482	-0.0130
7	DC1-02	2410963.047	439328.991	1383.414	0.0010	0.0000	-3.821	1383.409	0.0050
8	DC1-03	2408858.462	440291.355	1196.740	0.0007	0.0000	-3.795	1196.746	-0.0060
9	DC1-04	2408696.452	440857.368	1210.872	0.0006	0.0000	-3.779	1210.861	0.0110
10	DC1-05	2410293.655	447790.181	1057.621	0.0004	0.0000	-3.499	1057.605	0.0160
11	DC1-06	2410068.473	448493.152	953.727	0.0003	0.0000	-3.462	953.738	-0.0110
12	DC1-07	2408245.295	449984.621	792.183	0.0000	0.0000	-3.393	792.196	-0.0130
13	DC1-08	2407598.360	449565.609	860.801	0.0000	0.0000	-3.414	860.768	0.0330
14	DC1-09	2405405.192	450336.384	1153.480	-0.0003	0.0000	-3.369	1153.447	0.0330
15	DC1-10	2405552.433	450801.616	1025.744	-0.0003	0.0000	-3.344	1025.696	0.0480
16	DC1-11	2405143.901	441757.248	1174.908	0.0002	0.0000	-3.751	1174.901	0.0070
17	DC1-12	2405508.911	441516.086	1207.806	0.0002	0.0000	-3.759	1207.807	-0.0010
18	DC1-13	2404690.436	442959.544	1234.733	0.0001	0.0000	-3.709	1234.735	-0.0020
19	DC1-14	2404290.284	443097.949	1245.493	0.0001	0.0000	-3.704	1245.489	0.0040
20	DC1-15	2404548.398	444350.776	1297.878	0.0000	0.0000	-3.653	1297.830	0.0480
21	DC1-16	2404114.718	444407.387	1279.098	0.0000	0.0000	-3.652	1279.044	0.0540
22	DC1-17	2398645.450	441049.791	1385.019	0.0000	0.0000	-3.795	1385.005	0.0140
23	DC1-18	2398875.132	441816.383	1385.474	0.0000	0.0000	-3.767	1385.476	-0.0020
24	DC1-19	2400354.647	442957.514	1378.558	-0.0001	0.0000	-3.719	1378.551	0.0070
25	DC1-20	2400582.535	443608.796	1388.834	-0.0001	0.0000	-3.692	1388.795	0.0390
26	DC1-21	2402094.565	444960.613	1416.321	-0.0002	0.0000	-3.631	1416.285	0.0360
27	DC1-22	2401695.351	445633.474	1397.080	-0.0002	0.0000	-3.601	1397.013	0.0670
28	DC1-23	2401973.284	446959.125	1468.863	-0.0003	0.0000	-3.537	1468.796	0.0670
29	DC1-24	2401973.284	447370.374	1466.874	-0.0004	0.0000	-3.517	1466.785	0.0890
30	DC1-25	2399620.923	446964.634	1451.032	-0.0005	0.0000	-3.536	1450.942	0.0900
31	DC1-26	2399671.254	447604.477	1475.309	-0.0005	0.0000	-3.502	1475.186	0.1230
32	DC1-27	2398087.617	449248.371	1123.537	-0.0009	0.0000	-3.407	1123.360	0.1770
33	DC1-28	2397762.053	449557.178	1104.564	-0.0009	0.0000	-3.388	1104.364	0.2000
34	DC1-29	2417464.372	431836.793	1015.062	-0.0001	0.0000	-3.814	1015.075	-0.0130
35	DC1-30	2416583.970	431902.953	946.180	0.0000	0.0000	-3.826	946.189	-0.0090
36	III_09	2411130.052	437642.588	1127.604	0.0010	0.0000	-3.857	1127.604	0.0000
37	III_7P	2415807.232	433534.639	971.192	0.0000	0.0000	-3.828	971.192	0.0000
38	III_12	2408008.217	450468.008	899.032	0.0000	0.0000	-3.373	899.032	0.0000

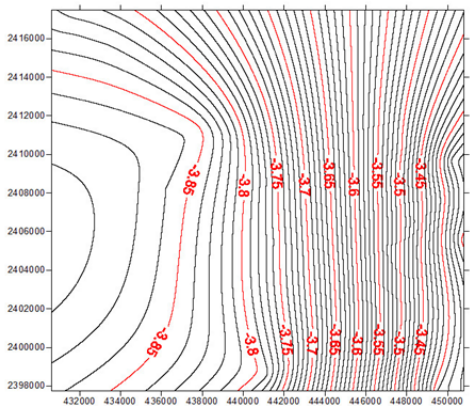

Fig. 5. Height anomalies map [m] determined based on the leveling heights in the Mu Cang Chai study area.

Rys. 5. Mapa anomalii wysokości [m] wyznaczona na podstawie wysokości niwelacyjnych na obszarze badań Mu Cang Chai

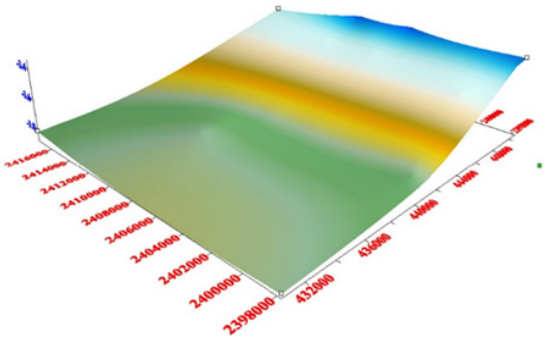

Fig. 6. Height anomalies digital model determined based on the level points in the Mu Cang Chai study area
Rys. 6. Cyfrowy model anomalii wysokości określony na podstawie punktów poziomu na obszarze badań Mu Cang Chai

case for the integration of GNSS technology. This integration, when combined with the measured leveling heights of points, has been shown to meet the stringent accuracy requirements necessary for the creation of large-scale topographical maps.

This innovative approach leverages the power of GNSS technology to capture precise measurements, thereby facilitating the accurate representation of geographical features on a large scale. The results obtained through this method not only meet but potentially exceed the standards set for topographical mapping, thereby offering significant potential for future applications.

In the context of Vietnam, this proposal is particularly relevant and feasible. The unique geographical conditions of Vietnam, characterized by diverse landscapes including border regions, coastal areas, and islands, pose unique challenges for mapping. The use of GNSS technology in these restricted areas offers a practical solution, enabling accurate mapping even in areas where traditional methods may fall short.

Literatura – References

1. Vietnam Ministry of Natural Resources and Environment (2015), "Circular No. 68/2015/TT-BTNMT of the Vietnam Ministry of Natural Resources and Environment: Technical regulations for terrestrial surveying for topographical maps and geographical information system databases at scales 1:500, 1:1000, 1:2000, 1:5000."
2. Hoang Ngoc Ha (2020), "Adjustment and computation of geodetic and GPS-GNSS networks," Science and Technical Publishing House.
3. Pham Hoang Lan (2014), "Physical geodesy textbook," Hanoi University of Mining and Geology.
4. Nguyen Trong San, Đao Quang Hieu, Đinh Cong Hoa (2015), "Surveying textbook", Construction Publisher.
5. Nguyen Van Sang (2013), "Computation of gravity anomalies and height anomalies in Vietnam from GOCE gravity satellite data," Journal of Mining and Geology. Issue 42.
6. Pham Thi Hoa et al. (2019), "Development of software for coordinate transformation between the VN-2000 coordinate system and International Earth Reference Frame (ITRF)," Journal of Mining and Geology. Issue 60.
7. TRF, 01/2019, from: http://itrf.ensg.ign.fr/ Jekeli, C., 2016, Geometric Reference Systems in Geodesy. Division of Geodesy and Geospatial Science, School of Earth Sciences. Ohio State University.

Rozwiązanie poprawiające dokładność pozycji poziomej i pionowej punktów mierzonych technologią GNSS/CORS przy tworzeniu wielkoskalowych map topograficznych Wietnamu

W Wietnamie, podczas tworzenia map topograficznych na dużą skalę przy użyciu technologii Global Navigation Satellite Systems (GNSS) w połączeniu z ciągle działającymi stacjami referencyjnymi (CORS) i tradycyjnymi pomiarami stacji całkowitej, wystąpią przesunięcia zarówno w pozycjach poziomych, jak i pionowych. Aby rozwiązać ten problem, dokonujemy korekt mapy, aktualizując mapę w założonym układzie współrzędnych. W założonym układzie współrzędnych kształty i różnice wysokości zmienionych obiektów są dokładnie obserwowane, aby spełniać wymagania odpowiadające skali mapy. Współrzędne i wysokości wyraźnych punktów na mapie lub punktów kontrolnych na polu uzyskanych z różnych metod mają różnice większe niż dopuszczalne wartości według skali mapy. Stosując dwuwymiarową transformację współrzędnych i wysokość nad geoidą, obliczaną dla każdego punktu z jego wagą, współrzędne i wysokości punktów mogą być obliczane w jednolitym układzie współrzędnych.

Słowa kluczowe: *dokładność GNSS, mapy topograficzne, osnowa geodezyjna*

Core Analysis Experience for Fractured Basement Rock at J/V "Vietsovpetro", Vietnam

Duyen Quang LE[1)]*, Dung The NGUYEN[2)]

[1)] Faculty of Petroleum and Energy, 108 Vien Street, Hanoi University of Mining and Geology, Hanoi, Vietnam; ORCID https://orcid.org/0000-0001-6953-4762

[2)] VIETSOVPETRO, 105 Le Loi street, Vung Tau city, Ba Ria-Vung Tau province, Vietnam; ORCID https://orcid.org/0009-0000-4018-3583

* Corresponding author: lequangduyen@humg.edu.vn

http://doi.org/10.29227/IM-2024-01-99

Submission date: 16-03-2024 | Review date: 22-06-2024

Abstract

This study presents a comprehensive methodology for core analysis of fractured basement rock at J/V "Vietsovpetro". The process begins with a detailed visual description of the core sample, followed by a fracture study to determine fracture density, azimuth, strike, and dip. Probe permeability and radioactivity are measured using traditional methods. The conventional core plug sampling approach is found to be unsuitable for highly heterogeneous fractured basement rock. A new core plug sampling approach is proposed, which involves increasing the core plug diameter and sampling frequency to better preserve vug-macrofractures. Post-cutting core plug analysis includes determining gas permeability, porosity, cut-off porosity, grain density, acoustic velocity, compressibility, capillary pressure curves, and wettability. The study also highlights the need for additional analysis of initial residual water saturation in the reservoir using preserved core, trace element analysis, and determination of radioisotope age. Certain parameters such as electrical properties and cation exchange capacity are deemed unnecessary for fractured basement rock. The findings of this study are crucial for improving the reliability of core analysis results and have significant implications for oil and gas exploration and production.

Keywords: *core analysis, fractured basement, Bach Ho*

1. Introduction

One of the key objectives of the most recent exploration plan is fractured basement [1]. According to [2], there are fractured basement reservoirs in over 25 basins in more than 30 nations. The most well-known is the White Tiger offshore oil field located in Vietnam's Cuu Long Basin. The reservoir has produced 180 MBBL cumulatively since it was found in 1986. Roughly 85% of Vietnam's hydrocarbon output comes from fractured basement rocks [1, 3]. In addition, when possible fractured basement play fairways are identified early on, oil companies may be encouraged to alter their drilling strategy and focus instead of avoiding basement targets by designing wells that optimally intersect the dominant fracture systems [4]. Therefore, determining the characteristics of fractured basement rocks is necessary. Some methods have been published by many scientists around the world, such as using high-resolution 3D seismic and logging datasets [2], geophysical well log data [5], several qualitative and quantitative well logging procedures [6], dual media approach [7], etc. In addition to using the available well logs, 2D seismic data, etc. the basement reservoirs can be detected and assessed using the core analysis results. These core analyses include description for the rocks and determination of porosity, permeability, fluid saturation and grain density [5]. In every stage of the petroleum business, core retrieval and analysis are crucial. Reducing uncertainty in reservoir appraisal is the primary objective of core analysis, which provides data typical of the reservoir under in-situ conditions. Coring and core analysis technology have been mentioned in many research. While [8] presented an overview of current and future trends and advancements in this technologies, [9] provided summary of hydrate coring management and analysis, [10] offered pressure-coring methods in boreholes and in situ pressure core analysis. For "intact" oil and gas reservoir features, core analysis offers the only precise and quantitative assessment available. It ought to offer the basis for evaluating formations in order to construct both static and dynamic reservoir models [11]. According to [12], core generated data have been merged with other field data to reduce reservoir uncertainties that can't be solved by other sources of information like well logging, well testing, or seismic. Therefore, in order to improve the reservoir evaluation procedures, they presented an overview of existing and emerging advancements and trends in core analysis and coring technologies. In addition, since core damage is a major problem during coring and handling, accurate data calibration for exploration is put at risk, therefore [13] have mainly focused on identifying and mitigating it. In this paper, they provided a useful manual for coring and downhole rock sampling as well as explaining and analyzing the various coring techniques. Recently, there area many studies have mentioned cores and core analysis. Developments in gas hydrate drilling investigations-related wireline pressure coring, core handling, and core analysis were presented in study [14]. The obtained results show that while gas hydrates have been the primary focus of these applications thus far, the technology can also be used to other unconventional hydrocarbon resources, particularly those associated with shale oil and gas. Besides, to assist and calibrate the estimation of rock properties, [15] discussed core analysis, applications, and coring types. The findings show that real reservoir rock samples can only be obtained via coring, and thus real reservoir rock can only be handled through core analysis. In other study, based on the analysis

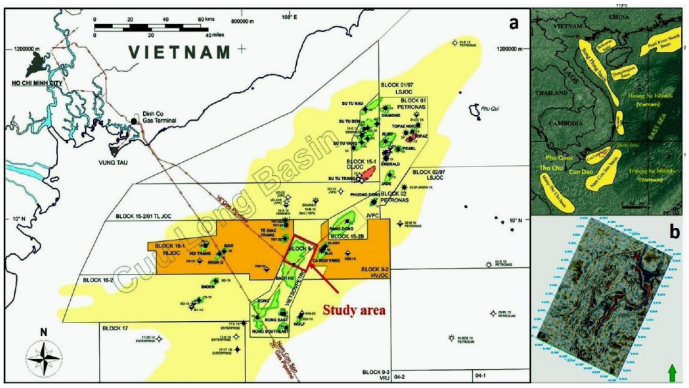

Fig, 1. Location map of study area [17]
Rys. 1. Mapa lokalizacyjna obszaru badań [17]

of core, properties of basement fracture reservoir were determied. By identifying the orientation of the fractures, the most suitable drill direction can be forecasted when looking for a reservoir [16]. In order to minimize data uncertainties and assure efficient quality control of test data, [11] described the necessity for a core analysis management architecture and a best practice guide for core analysis data collecting.

Up to now, a number of authors have conducted research at Bach Ho field. While [17] conducted eismic attribute analysis in Lower Miocene reservoir characterization, northeast Bach Ho field, [18] make an effort to analyze the basement reservoir's fracture distribution and to determine the variables affecting the reservoir's quality in this zone, [19] researched on the production performance of Bach Ho field's granite-fractured basement reservoir, [20] presented the procedure to generate chemical system at pilot scale and trial industrial application for miocene reservoirs in Bach Ho field. However, no studies have mentioned core analysis for fractured basement rock. Thus, the aim of this study is to perform provides a thorough approach for J/V "Vietsovpetro" core investigation of fractured basement rock. The results of this study have important influences for oil and gas exploration and production as well as for enhancing the dependability of core analysis results. The contents mentioned here are drawn from the experience of analyzing core for more than 35 years at Vietsovpetro combined with the requirements for core data that are necessary for the exploration, log interpretation, reserve assessment, building field development plan and enhancing oil recovery for Bach Ho fractured basement reservoir.

2. Study area

According to information from the Vietnam Energy Association, Bach Ho mine was discovered in 1975 and began operating on September 6, 1988. This is the largest oil field on the continental shelf of the Cuu Long basin, located in the Southeast, 145km from the coast of Vung Tau, exploited by Vietsovpetro. Vietsovpetro did not begin to develop the Bach Ho "buried-hill" until the middle of the 1980s. Figure 1 displays the location map of study area. At Bach Ho, igneous and metamorphic rocks that have not undergone significant alteration make up the majority of the matrix found in between hydrocarbon-filled fractures [18]. Basal andesite, poocfia diaba, and crystalline magmatic granitoid from the Jura and Cretaceous ages make up the basement.

The unusual nature of the oil pay zones in the fractured basement is attributed to their remarkably high levels of heterogeneity, anisotropy, and permeability. Because of the impact of the Cuu Long Basin's tectonic context, the research region is regarded as a narrow sub-thought and a tertiary structural unit of small scale [17]. Figure 2 shows basement distribution in the Bach Ho region, Cuu Long Basin, Vietnam.

3. Methodology and data

3.1. Core analysis before cutting core plugs (using original core set)

** Core description*

Visually describe the state of the core sample, color, preliminary petrographic characteristics, degree of fracturing, fracturing characteristics, oil trace... in order to preliminarily identify the rock type, porous-permeability characteristics and oil sign of the collected core set.

** Fracture study*

The fracture density, fracture azimuth, fracture strike and fracture dip are determined along entire oriented North-South core set using traditional method. Obtained results are presented in the form of histograms of fracture density, true azimuth, true strike and fracture dip, and that are used to correct FMS, FMI data, build an overall picture of fracture density and fracture development orientation for the whole reservoir. These results are useful for designing the new wells, building well trajectory, choosing perforation interval, selecting well completion techniques, etc. Therefore, it is necessary to take oriented core instead of traditional core to study fracture system for the fractured basement reservoir.

** Determination of probe permeability*

Probe permeability is measured along entire core set using traditional method. Obtained results were used to build the permeability profile by depth for quick assessment of productivity of the coring depth interval.

** Determination of radioactivity*

Total radioactivity and elemental spectrum radioactivity are measured along entire core set using traditional method. Obtained data will be used to correct the depth of log data (depth shift) and to calibrate gamma log data.

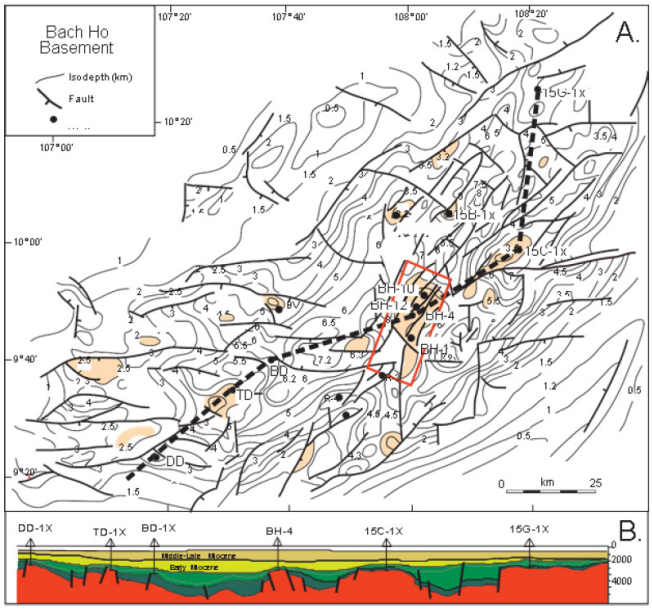

Fig. 2. Basement distribution in the Bach Ho region, Cuu Long Basin, Vietnam [18]
Rys. 2. Rozmieszczenie skał podłoża w regionie Bach Ho, Cuu Long Basin, Wietnam [18]

3.2. Core plug sampling approach for fractured basement rock

The conventional core plug sampling approach applied to homogeneous sedimentary rock is no longer suitable for highly heterogeneous fractured basement rock because the small diameter standard core plugs (Φ≤1.5") usually contain only microfractures and tight matrix (the rock part containing vug-macrofractures is often broken during cutting core plugs). This is the reason why the core analysis results will not accurately reflect the porous-permeability characteristics of the rock. In order to overcome this weakness, it is proposed to apply the new core plug sampling approach to best preserve the vug-macrofractures present in the rock by increasing the core plug diameter (Φ≥2") and increasing the core plug sampling frequency.

- Conventional core plug sampling approach (Figure 2): Standard diameter core plugs of Φ≤1.5" are cutted at regular intervals along the entire core set at a frequency of 3-4 plugs/1 m core.
- New core plug sampling approach (Figure 3): Full size cores are sampled from the top to the bottom of core set by cutting the entire core set into separated cylinders, or cutting large diameter core plugs (□>2") at a frequency of 10-15 plugs/1 m core.

3.3. Core analysis after cutting core plug (using core plug)

** Determination of gas permeability*

Full size cores or large diameter core plugs are proposed to use to determine vertical and horizontal permeability using traditional method, except some adjustments to the coreholder of measuring equipment. Thanks to the application of new core plug sampling approach, permeability for almost entire core set will be determined. The core permeability is used to correct the permeability interpreting results by log, FMS, FMI and welltest. Permeability data by FMS, FMI and welltest is used to design new well position, build well trajectory, choose perforating interval, build dynamic model.

** Determination of porosity*

Full size cores or large diameter core plugs are recommended to use to determine porosity using traditional method. Thanks to the application of new new core sampling approach, porosity for almost entire core set will be determined. The core porosity is used to correct the porosity interpreting results by log. Porosity by log interpretation is used to locate new well position, build well trajectory, choose perforation interval, assess OOIP, build geological model.

** Determination of cut-off porosity*

Cut-off porosity is an important value used in log interpretation to determine reservoir effective porosity. Effective porosity is used for assessing OOIP, building reservoir geological model.

For sedimentary rock: Porosity usually has a strictly linear relationship with gas permeability, therefore, porosity cut-off is determined based on relationship between gas permeability and porosity (Kg-Φ) corresponds to gas permeability cut-off (Kg*). Gas permeability cut-off is determined based on relationship between gas permeability and oil permeability when oil permeability is zero.

For fractured basement rock: Porosity has a very discrete relationship with gas permeability (core data shows correlation Kg-Φ has very low regression coefficient: <0.3), therefore, the determination of cut-off porosity by traditional method for sandstone is no longer applicable. Instead, porosity cut-off (Φ*) is recommended to be determined based on the correlation between dynamic porosity (Φdyn) and effective porosity (Φeff) when dynamic porosity equals to zero {Φdyn=Φeff*(1-Sro-Srw)}. The philosophy of this solution is that oil and water coexisted in the vug-fractures will be immobile when dynamic porosity is zero, i.e., then there is only residual water and residual oil in the pore space (Srw+Sro=1).

** Determination of grain density*

Grain density for fractured basement rock is determined by traditional method. Grain density is used to calculate the

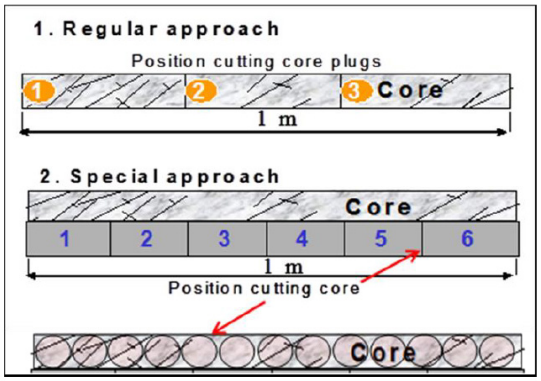

Fig. 3. Scheme of core plug sampling for fractured basement rock

Rys. 3. Schemat pobierania próbek korka rdzeniowego dla spękanej skały podłoża

porosity and correct the porosity interpreting results by log density.

** Determination of acoustic velocity*

Full size cores or large diameter core plugs are proposed to use for determining the rock acoustic velocity using traditional method. Acoustic velocity is used to calculate the porosity and correct the porosity interpreting results by log acoustic.

Noted that, the relationship between acoustic velocity and porosity for fractured basement rock is very weak, acoustic velocity for one core plug (one porosity value) can be quite difference when measuring direction changed (due to the effect of fracture development orientations in the core). Thus, caution should be taken when using porosity interpreting results by acoustic log for this type of rock.

** Determination of compressibility*

Full size cores or large diameter core plugs are proposed to use for determining compressibility using traditional method. Rock compressibility is used for OOIP assessment by material balance method, reservoir simulation, etc.

There are some contradictory opinions about skeletal effect for fractured basement reservoir. Specifically, effective overburden pressure increased due to reservoir pressure reduction during reservoir production will only impact on the skeletal frame of the reservoir and no impact on reservoir pore space (this can be occurred in the whole reservoir or only locally). Therefore, caution should be taken when using the compressibility for OOIP assessment and reservoir simulation.

** Determination of capillary pressure curves*

Full size cores or large diameter core plugs are proposed to use for determining capillary pressure curves using traditional method. Obtained capillary pressure curves showed the coexistence of microfractures and vug-macrofractures in the fractured basement rock. Those were well reflected by the presence of two parts of capillary pressure curve with different slope angles (that controlled by different forces – capillary and gravity: Capillary force impacts on fluids in microfractures and gravity impacts on fluids in vug-macrofractures). Based on this physical basis, the cut-off macrofractures aperture can be determined using capillary pressure value corresponding to the abrupt change point of slope angles on the capillary pressure curves. Calculated result shows that the cut-off macrofractures aperture for Bach Ho fractured basement rock is approximately 60 μm.

** Determination of wettability*

Full size cores or large diameter core plugs are proposed to use for determining the rock wettability using Amott method. The contact angle measuring method is not recommended because the fracture surfaces are often very rough due to the presence of secondary minerals, this leads to potential error for the measured contact angle.

The rock wettability has a decisive influence on the selection of fluid that employed for displacing oil in the secondary and tertiary production processes, decision of injecting gas or water depends on rock wettability (oilwet or waterwet).

** Determination of oil displacement efficiency*

It is necessary to determine the capillary oil displacement efficiency (imbibition displacement) and hydrodynamic oil displacement efficiency (forced displacement). Hydrodynamic oil displacement efficiency is determined by traditional method including water flood and gas injection. Full size core or large diameter core are suggested to use to increase the study pore volume and to increase the number of fractures in the core aiming to enhance the reliability of the experimental results. Oil displacement efficiency is used to calculate recoverable oil reserves and build FDP.

** Determination of relative permeability*

Full size core or large diameter core plug is suggested to use for experimental study to determine relative permeability. The relative permeability is used to build FDP and run reservoir simulation, etc. There are two methods for determining relative permeability: Steady-state flow and unsteady-state flow. The steady-state method is proposed to use to determine relative permeability for fractured basement rock based on:

- The rock specific porous structure (dual porosity and dual permeability).
- The physic of flows in fractured medium: Forced displacement in fractures only, not significant in matrix, only spontaneous mechanism is efficient for recovering matrix oil: expansion, capillarity, gravity drainage and dispersion.

- The nature of steady-state flow method: Several phases (oil, gas, and water) are injected simultaneously into the core sample at different volume ratio. At each volume scale: The effective permeability is determined directly using differential pressure between the two core ends and the saturation of each phase is determined directly for the entire core pore volume using the material balance method. For fractured basement rock: Simultaneous phases flow occurs mainly in macrofractures and at the same time occurs the mass transfer between fluid existed in the macrofractures and microfractures owed the phases flowing time in the core elongated. These factors make an important contribution to ensuring the high reliability of relative permeability determination results.
- The nature of unsteady-state flow method: Only one phase (gas or water) is injected into the sample to displace oil at a relatively high flow rate (high rate to eliminate the influence of capillary end effect). The effective permeability and its corresponding saturation of each phase are determined indirectly only at the core outlet end cross-section after the water/gas breakthrough by graphic or computed techniques. For fractured basement rock: Simultaneous phases flow quickly occurs only in macrofractures that driven by strong viscous force, no occurrence of mass transfer between fluid existed in macrofractures and microfractures, these cause large error to the determined results of effective permeability and saturation of each phase on the core output cross-section. Therefore, it is not to suggest to use this method to determine relative permeability for fractured basement rock.

** Determination of the secondary mineral compositions*

The secondary mineral compositions and their contents are determined by traditional methods. Obtained results are useful for designing well completion and choosing workover solutions.

** Determination of rock types*

Rock types are determined by petrographic analysis using thin section. Each basement rock type has specific mineral compositions and contents. The mineral composition and content significantly influence the logging results including GR, RHOB, NPHI. Thus, rock type is an important input data that used for interpreting log RHOB, NPHI to determine porosity (using BASROCK software).

4. Results and discussion

4.1 Parameters that do need to additionally analyze

** Determination of initial residual water saturation in the reservoir using preserved core*

For sedimentary rock (granular porous rock):

Residual water saturations are determined in laboratory by different techniques (restored state cells, centrifuging). The cut-off value of residual water saturation is determined by well-known laboratory correlation of gas permeability and residual water saturation (Kg-Srw) based on gas permeability cut-off value. This data is used in resistivity log interpretation to determine net pay and oil saturation for OOIP assessment.

For fractured basement rock: It is impossible to determine the residual water saturation cut-off value by method applied for sedimentary rock as mentioned due to the weak correlation between gas permeability with residual water saturation (regression coefficient is very low: < 0.3). For this reason, the residual water saturation (initial oil saturation) used to assess OOIP for the Bach Ho fractured basement reservoir was taken assumedly.

The potential error reserve of the Bach Ho fractured basement reservoir (calculated with the assumed residual water saturation value of 0.15 similar to the residual water saturation for oil reservoir in fractured carbonate rock according to world experience) and the fact that formation water has not been encountered in more than 35 years of production has posed the necessary to determine the actual residual water saturation for this reservoir in order to correct OOIP and improve production efficiency.

Residual water saturation of the Bach Ho fractured basement reservoir can be determined accurately in the laboratory using preserved core that taken with an oil-based mud (the sample should be taken at the moment before injecting water into the reservoir). However, due to the lack of previous experience working with fractured basement reservoir, Vietsovpetro did not carry out taking preserved core to determine the initial residual water saturation for the Bach Ho fractured basement reservoir.

** Trace element analysis*

Determination of trace elements, rare earth elements present in magma rock with extremely small concentrations in ppm to determine the origin and geodynamic context forming magma rock.

** Determination of radioisotope age*

Determine the absolute age of the rock (radioisotopic age U-Pb, Rb-Sr, Sm-Nd, K/Ar,..) and the source domain of the rock-generated magma lava (using isotope ratios - IR).

4.2 Parameters that do not need to analyze.

** Determination of electrical properties (formation factor and resistivity index)*

For sedimentary rock, formation factor and resistivity index are used to calculate water saturation by Archie's equation Swn=(a*Rw)/(□m*Rt) based on the abnormallyhigh resistivity at oil zones and abnormally low resistivity at water zones. Calculating water saturation for fractured basement rock according to Archie's equation is no longer appropriate because this rock has a very high resistivity, thus cannot distinguish oil-bearing zones from the tight matrix zones by log resistivity. Thus, it is no need to study core electrical properties for fractured basement rock.

** Determination of cation exchange capacity (CEC)*

CEC is perceived as the ability of some rock minerals (clay minerals) to exchange ions with the ions that existed in contacted water. This data is useful for correcting cementation factor (m) and saturation exponent (n) for sedimentary rock. However, as mentioned above, values of m and n were not

investigated for fractured basement rock, thus, no need to determine CEC for this type of rock.

5. Conclusions

This study introduces a novel core plug sampling method for fractured basement rock, aiming to enhance the reliability of core analysis results by better preserving vug-macrofractures in large diameter core plugs and full-size cores. The Amott method is advocated for determining wettability, while the steady-state method is recommended for ascertaining relative permeability for fractured basement rock. The type of rock is identified as a crucial input for log interpretation to determine porosity. When utilizing rock compressibility for fractured basement reservoirs, it is imperative to consider the skeletal effect. The study finds it unnecessary to determine the formation factor, resistivity index, or cation exchange capacity for fractured basement rock. Lastly, the study underscores the necessity of using preserved core taken with oil-based mud to determine the initial residual water saturation. This is a critical step for correcting Original Oil In Place (OOIP) for fractured basement reservoirs. These findings provide valuable insights and recommendations for future research and practices in the field of core analysis for fractured basement rock. This study contributes significantly to the body of knowledge and has potential implications for oil and gas exploration and production.

Acknowledgements

Thanks to the anonymous reviewers and editorial comments for their invaluable comments in the earlier version, which helped us to improve the manuscript's quality.

Conflicts of Interest

The authors declare no conflict of interest.

Literatura – References

1. Neff, P. The Habban Field and the fractured basement play in Yemen. in AAPG International Conference and Exhibition, Istanbul, Turkey. 2014.
2. Bawazer, W., A. Lashin, and M.M. Kinawy, Characterization of a fractured basement reservoir using high-resolution 3D seismic and logging datasets: A case study of the Sab'atayn Basin, Yemen. PloS One, 2018. 13(10): p. e0206079.
3. Gutmanis, J., et al., Hydrocarbon Production from Fractured Basements Formations. Geoscience Limited, 40 pp. 2010.
4. Rodriguez, K., N. Hodgson, and A. Intawong. Fractured basement initial identification methodology. in 80th EAGE Conference and Exhibition 2018. 2018. European Association of Geoscientists & Engineers.
5. El Sharawy, M., Fractured basement reservoir identification using geophysical well log data, Gulf of Suez, Egypt. Pelagia Research. Adv Appl Sci Res, 2015. 6(8): p. 17-35.
6. Abd El Rahman, A. and A. Lashin, Evaluation of the basement reservoir rocks in some selected wells in north Gulf of Suez and south Sinai. Annals of Geological Survey of Egypt, 2004. 27: p. 459-477.
7. Neff, P. Integrated 3D Modelling of an Unconventional Fractured Basement Reservoir. in EAGE/SPE Joint Workshop-Closing the Loop: Reservoir Simulation and Geophysical Measurements. 2011. European Association of Geoscientists & Engineers.
8. Al-Saddique, M., G. Hamada, and M.N. Al-Awad, State of the art: Review of coring and core analysis technology. Journal of King Saud University-Engineering Sciences, 2000. 12(1): p. 117-137.
9. Burger, J., et al., Overview on hydrate coring, handling and analysis. 2003, Westport Technology Center.
10. Schultheiss, P., M. Holland, and F. Rack, Borehole pressure coring techniques and core analysis at in situ pressure. Investigations in Geophysics, Society of Exploration Geophysicists, 2010.
11. McPhee, C., J. Reed, and I. Zubizarreta, Best practice in coring and core analysis, in Developments in petroleum science. 2015, Elsevier. p. 1-15.
12. Ubani, C., Y. Adeboye, and A. Oriji, ADVANCES IN CORING AND CORE ANALYSIS FOR RESERVOIR FORMATION EVALUATION. Petroleum & Coal, 2012. 54(1).
13. Ashena, R. and G. Thonhauser, Coring methods and systems. 2018: Springer.
14. Schultheiss, P., et al. Advances in wireline pressure coring, core handling, and core analysis related to gas hydrate drilling investigations. in Proceedings of the 9th International Conference on Gas Hydrates (ICGH 2017). 2017.
15. Badawy, A.M., et al., Coring and Core Analysis. Rock Properties and Reservoir Engineering: A Practical View, 2022: p. 9-15.
16. Riskha, H., et al., Characterization of Basement FRACTURE reservoir in FIELD 'X', South Sumatera Basin, based on the analysis of core and Fmi log. Journal of Geoscience, Engineering, Environment, and Technology, 2017. 2(2): p. 155-165.
17. Nguyen, H.M., et al., Application of seismic attribute analysis in Lower Miocene reservoir characterization, northeast Bach Ho field, Vietnam. Journal of Mining and Earth Sciences Vol, 2021. 62(6): p. 14-22.
18. Cuong, T.X. and J. Warren, Bach ho field, a fractured granitic basement reservoir, Cuu Long Basin, offshore SE Vietnam: A "buried-hill" play. Journal of Petroleum Geology, 2009. 32(2): p. 129-156.
19. Thuc., P.D., Enhanced oil recovery solutions and technologies for final phase of granite basement reservoir of Bach ho field Chapter 1: Granite fractured basement reservoir of Bach Ho field and production performance. Petrovietnam Journal, 2018. 2: p. 22-28.
20. Hoang, L., et al., Perfecting the technology to manufacture a chemical system to improve oil recovery coefficient on a pilot scale applying industrial testing to representative objects of Miocene sediments in Bach Ho field, Cuu Long basin = Technology improvement to create eor chemical system at pilot scale and trial industrial application for Miocene reservoirs in Bach Ho field, Cuu Long basin. 2022.(in Vietnames)

Doświadczenie w analizie rdzeniowej spękanej skały podłoża w J/V "Vietsovpetro" w Wietnamie

W pracy przedstawiono kompleksową metodologię analizy rdzeniowej spękanej skały podłoża w J/V "Vietsovpetro". Proces rozpoczyna się od szczegółowego wizualnego opisu próbki rdzenia, po którym następuje badanie pęknięć w celu określenia gęstości, azymutu, uderzenia i zanurzenia. Przepuszczalność sondy i radioaktywność mierzy się tradycyjnymi metodami. Stwierdzono, że konwencjonalna metoda pobierania próbek zatyczek rdzeniowych jest nieodpowiednia w przypadku bardzo niejednorodnych spękanych skał piwnicznych. Zaproponowano nowe podejście do pobierania próbek czopu rdzenia, które polega na zwiększeniu średnicy czopu rdzenia i częstotliwości próbkowania w celu lepszego zachowania makropęknięć typu vug. Analiza korka rdzeniowego po cięciu obejmuje określenie przepuszczalności gazu, porowatości, porowatości odcięcia, gęstości ziaren, prędkości akustycznej, ściśliwości, krzywych ciśnienia kapilarnego i zwilżalności. W pracy wskazano także na potrzebę przeprowadzenia dodatkowej analizy początkowego nasycenia resztkowego wodą zbiornika z wykorzystaniem konserwowanego rdzenia, analizy pierwiastków śladowych oraz określenia wieku radioizotopowego. Niektóre parametry, takie jak właściwości elektryczne i zdolność wymiany kationów, uważa się za niepotrzebne w przypadku spękanej skały piwnicznej. Wyniki tego badania mają kluczowe znaczenie dla poprawy wiarygodności wyników analiz podstawowych i mają znaczące implikacje dla poszukiwań i wydobycia ropy i gazu.

Słowa kluczowe: *analiza rdzenia, spękane podłoże, Bach Ho*

Koncepcja specjalnego urządzenia wspomagającego prace serwisowe w szybie naftowym podczas wymiany żerdziowej pompy wgłębnej

Fedorowicz Yaroslav TEODOROVYCH[1)], Tomasz WYDRO[2)], Michał BEMBENEK[3)], Oleh KHUHKRA[4)], Vasyl MYKHAILIUK[5)]

[1)] IFNTUNG; 76019, Ivano-Frankivsk, Ukraine, str. Karpatska 1; +38 0964151483, email: f e d o r o v y c h y t @ g m a i l . c o m https://orcid.org/0000-0002-7823-8938
[2)] AGH University of Krakow; Mickiewicza Av. 30, pav. B-2, pok. 7, 30-059 Cracow, Poland; +48 12 617 30 81, email: wydro@agh.edu.pl; ORCID https://orcid.org/0000-0003-4160-2238
[3)] AGH University of Krakow; Mickiewicza Av. 30, pav. B-2, pok. 7, 30-059 Cracow, Poland; +48 12 617 30 81, email: bembenek@agh.edu.pl; ORCID https://orcid.org/0000-0002-7665-8058
[4)] IFNTUNG; 76019, Ivano-Frankivsk, Ukraine, str. Karpatska 15; ORCID https://orcid.org/0000-0008-5879-4364
[5)] IFNTUNG; 76019, Ivano-Frankivsk, Ukraine, str. Karpatska 15; ORCID https://orcid.org/0000-0002-3329-2068

http://doi.org/10.29227/IM-2024-01-100

Submission date: 26-04-2024 | Review date: 18-06-2024

Abstrakt

W poniższym artykule przedstawiono i opisano urządzenie zaprojektowane w celu zapobiegania niekontrolowanemu napływowi i wypływowi gazu z warstwa odwiertu podczas operacji naprawczych (serwisowych) przy użyciu sprzętu wiertniczego do mechanicznego wydobycia ropy naftowej przy użyciu prętowej pompy wiertniczej.
W artykule opisano aktualność zastosowania urządzenia i zasadę jego użycia podczas wymiany pompy wgłębnej wtyczkowej. Opisano budowę, charakterystykę i zasadę działania urządzenia.

Słowa kluczowe: *szyb naftowy, prace serwisowe, specjalne urządzenia, wiertnictwo*

Wprowadzenie

Ze względu na korzyści ekonomiczne i stabilną produkcję, większość odwiertów naftowych w światowej praktyce jest wydobywana przy zastosowaniu prętowych wiertniczych pomp z prętem wsuwanym. Metoda ta wykazała, że jest wiarygodna, ekonomiczna, autonomiczna, łatwa w wykorzystaniu i obsłudze. Prostota konstrukcji urządzeń powierzchniowych i wgłębnych umożliwia produkcję szerokiej gamy rozmiarów i konfiguracji urządzeń dla różnych warunków wgłębnych i powierzchniowych. Konstrukcja urządzenia umożliwia adaptację procesu wydobycia do warunków eksploatacji przez regulację długości skoku tłoka, częstotliwość skoków oraz zmianę średnicy pompy. Podczas eksploatacji sprzęt wymaga systematycznej konserwacji i kontroli. Umożliwi to zapobiec usterkom i awariom sprzętu, a także przestojom w produkcji węglowodorów.

W celu przeprowadzenia obsługi technicznej i wymiany sprzętu wiertniczego, zostaje wyciągnięty z odwiertu . Proces ten jest niebezpieczny i niesie wiele zagrożeń. W celu bezpiecznego wykonania prac podczas wymiany sprzętu wiertniczego (pompy wgłębne), odwiert zostaje zamknięty (wypełniony ważoną płuczką). Jednak podczas podnoszenia pomp wgłębnych z odwiertu może dojść do niekontrolowanego wycieku gazu z warstwa, co prowadzi do awaryjnego wysadzenia odwiertu z powodu szybkiego spadku ciśnienia w warstwie produkcyjnej. Zjawisko to jest niebezpieczne dla środowiska, ma negatywny wpływ na dalszą eksploatację odwiertu, a jego likwidacja wymaga znacznych nakładów finansowych i czasu (Rys. 1).

W związku z tymi faktami zdecydowano się opracować urządzenie, które zapewni bezproblemowy proces wymiany pomp wgłębnych wtyczkowych do produkcji ropy naftowej bez zabijania odwiertu.

Analiza procesu wymiany układu z zastosowaniem tłokowej żerdziowej pompy wgłębnej w przypadku możliwości wystąpienia wysokiego zagrożenia wypływu gazu

Podczas eksploatacji odwiertu z zastosowaniem tłokowej żerdziowej pompy wgłębnej pewne wskaźniki ulegają zmianie, co wskazuje na potrzebę naprawy sprzętu do odwiertów naftowych. Brak zasilania, nagrzewanie się polerowanego pręta i dym wydobywający się z trójnika wskazują, że pompa przestała pompować produkty z odwiertu. Gaz, który jest uwalniany z wind olejowych przemieszcza się do głowicy obudowy wzdłuż rur wydobywczych, a płyn chłodzący urządzenia na głowicy odwiertu zostaje podgrzewany przez siły tarcia i nie spełnia funkcji chłodzenia. W takim przypadku konieczna jest naprawa pompy lub jej wymiany [1].

Naprawa odwiertów eksploatowanych za pomocą systemu tłokowej żerdziowej pompy wgłębnej polega na podnoszeniu oraz opuszczaniu rur wydobywczych, eliminowaniu pęknięć, odkręcaniu rur, sprawdzaniu i wymianie zaworów, wymianie pomp, zniszczonego tłoka, który utknął w cylindrze pompy [2]. Również potrzebę przeprowadzenia naprawy można zidentyfikować na podstawie wyników dynamogramu lub podczas pomiaru prędkości wynoszenia cieczy z dna odwiertu. Na podstawie powyższych czynników podejmowana jest decyzja o przeprowadzeniu prac remontowych na danym złożu.

Przed przystąpieniem do naprawy odwiertu, maszyna cofająca jest częściowo zdemontowana, jednostka podnosząca jest montowana, a odwiert jest wypełniony płynem w celu za-

Rys. 1. Erupcja płynów złożowych [6]
Fig. 1. Eruption of reservoir fluids [6]

blokowania odwiertu, która zależy od ciśnienia i wydajności odwiertu.

Podczas zamykania odwiertu przewód rurowy jest testowany pod kątem nieprzepuszczalności. Jeśli przewód rurowy jest zamknięty należy podnieś pompę wtykową na prętach i wymień ją. Jeśli przewód rurowy nie jest zamknięty, należy najpierw podnieść pompę na prętach, a następnie wykonać pełne podniesienie przewodu rurowego za pomocą wspornika blokady pompy. W przypadku wykrycia usterek w pompie należy ją wymienić na nową. Przewód rurowy jest napełniony wodą w celu sprawdzenia szczelności pompy i prawidłowego oznaczenia przeszkody oraz obrócenia jej z gniazda wspornika zamka. W tym przypadku woda z rur jest wysyłana w dół, zmywając brud i cząsteczki piasku z powierzchni prętów i wewnętrznej powierzchni rur, po czym pompa jest ponownie instalowana na miejscu, a rury są napełniane wodą. Następnie instalowane wyposażenie głowicy odwiertu i uruchamiony jest podnośnik pompy [2].

Główne zagrożenia wynikające z wymiany pomp podczas naprawy odwiertów

Odwierty są uważane za odwierty niebezpieczne, w których możliwe jest nagłe uwolnienie płynów warstwowych (woda warstwowa, ropa naftowa, gaz, kondensat gazu), co może prowadzić do pożarów, zniszczenia wind, wypadków obsługi i negatywnego wpływu na środowisko.

Najważniejszą częścią odwiertu jako konstrukcji inżynieryjnej jest głowica odwiertu, która jest połączona ze standardowym wyposażeniem zgodnie z zatwierdzonymi schematami, w zależności od złożoności projektu odwiertu. Podstawą prawidłowej pracy odwiertu jest wykwalifikowana i profesjonalna praca zespołu ludzkiego przy głowicy odwiertu [3].

W przypadku niekontrolowanego wypływu ciśnienia formacji ropy lub gazu z odwiertu w wyniku braku lub utraty szczelności urządzeń zapobiegających wybuchowi lub ich uszkodzenia, możliwe jest powstanie (otwartej) fontanny ropy naftowej i gazu (Rys. 1).

Otwarte fontanny swoim rozwojem wykraczają poza teren jednego obiektu (odwiertu) w strefie ochrony sanitarnej. W otwartych fontannach możliwy wpływ czynników szkodliwych (płyn w warstwie formacji) na środowisko. Wycieki występują w wyniku niekontrolowanego (awaryjnego) wypływu z odwiertu, pęknięcia rurociągów naftowych na znacznym obszarze, tworząc obszar skażenia.

Eksploatacja gazu i ropy naftowej jest uważana za najbardziej niebezpieczne miejsca w których może dojść do awarii w odwiertach, w których to przeprowadzane są bieżące naprawy i remonty. W związku z powyższym jeśli nie zostaną podjęte środki zapobiegawcze w celu ich wyeliminowania, eksploatacja gazu i ropy naftowej może doprowadzić do otwartej fantanny, której wystąpienie jest niebezpieczne dla środowiska poprzez niekontrolowane uwolnienie kondensatu gazu, ropy naftowej i wody złożowej do środowiska. Eliminacja otwartych fontann, nawet na obecnym poziomie rozwoju technologii, jest złożonym i kosztownym procesem [4,5].

Główną przyczyną procesu intensywnej penetracji znacznej ilości gazu lub płynu złożowego do odwiertu z jego późniejszym podniesieniem do głowicy odwiertu i pojawieniem się depresji w złożu, może być:

- stałe (podczas wiercenia, oczyszczania, operacji geofizycznych i przestojów);
- okresowy (przy podnoszeniu, przekraczaniu prędkości podnoszenia lub opuszczania, zjawisko „tłoka").

W przypadku braku depresji może wystąpić proces penetracji gazu lub płynu formującego, ale jego charakter i intensywność nie zależą od działań obsługi. Gaz lub ciecze występują w następujących warunkach:

- podczas płukania odwiertu i operacji awaryjnych, gdy ciśnienie hydrostatyczne jest mniejsze niż ciśnienie złożowe;
- w trakcie pracy określonej w poprzednim akapicie, po zatrzymaniu krążenia płuczki w odwiercie;
- podczas operacji podnoszenia urządzenia w odwiercie w wyniku drgań hydrodynamicznych;
- w wyniku długotrwałego braku obiegu wody w odwiercie w strefie nasyconej gazem;
- nagłe zaburzenia rur odwiertu, rur wiertniczych, rur do pompowania, a następnie zanik na dno odwiertu, które nie otrzymają wody do płukania z powodu zablokowania przestrzeni pierścieniowej.

Pojawienie się gazu lub nowej porcji ropy naftowej z dużą ilością gazu może również wystąpić przy wymianie pomp żerdziowych, może to prowadzić do niebezpiecznej sytuacji, która z kolei może nawet doprowadzić do erupcji ropy naftowej. Przejaw tego zjawiska odbywa się za pomocą przerywanej depresji na złożę. Wynika to ze zjawiska "tłoka", które

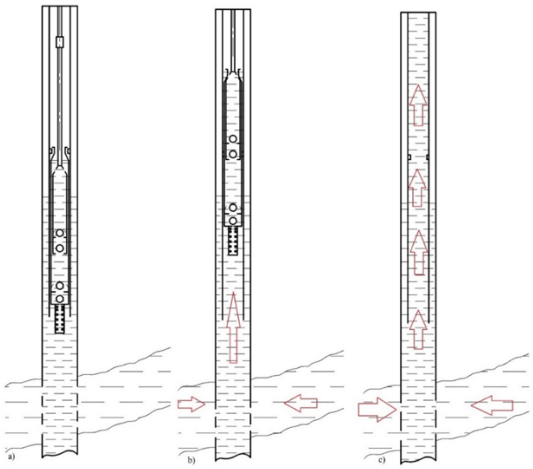

Rys. 2. Schemat procesu wymiany pompy wpuszczanej, a) wydobywania ropy naftowej, b) podniesienie pompy, c) podnoszenie pomp na powierzchnię
Fig. 2. Schematic of the sump pump replacement process, a) oil extraction, b) pump lift, c) pump lift to the surface

ma miejsce, gdy pompa jest podnoszona z kolumny rury (Rys. 2). Kiedy pompa zaczyna się podnosić w odwiercie, objętość pompy i rury wydobywcze, które zostały zanurzone w płuczce wiertniczej, są zastępowane przez płyn złożowy który dopływa ze złoża do odwiertu w ilości równej objętości sprzętu, która znajdowała się poniżej poziomu dynamicznego płynu w odwiercie i zaczyna podnosić się do góry, czyli w kierunku głowicy odwiertu. Proces ten jest bardzo nieprzewidywalny, ponieważ do odwiertu może trafić duża ilość gazu ze złoża, albo ropy naftowej, która jest nasycona gazem rozpuszczonym. Może się to zdarzyć, gdy gęstość płynu nie jest wystarczająca by stworzyć odpowiedni nacisk na złożę. Więc ciśnienie hydrostatyczne będzie mniejsze niż ciśnienie denne dynamiczne, co doprowadzi do nagłego i szybkiego wzrostu poziomu płynu złożowego w kolumnie rur wydobywczych ze względu na fakt, iż im więcej gazu w cieczy, tym mniejsza jego gęstość, tym mniejsze ciśnienie hydrostatyczne jest możliwe do wytworzenia [7]

Sposoby i środki zapewniające bezpieczną eksploatację procesu wymiany pomp prętowych z przyssawką

W celu zapewnienia bezpiecznej pracy przy naprawach odwiertów, na głowicy kolumny wydobywczej instalowany jest sprzęt zapobiegający wybuchom. Wyboru sprzętu zapobiegającego wybuchowi dokonuje się w zależności od rodzaju prac na odwiercie i ciśnienia w warstwie, charakterystyki sekcji oraz biorąc pod uwagę możliwość wykonania kolejnych operacji technologicznych. Aby zapobiec przelaniu się płynu i wyciekowi gazu na głowicy odwiertu podczas naprawy odwiertu, można zastosować następujące metody:

- zablokowanie odwiertu
- przy użyciu warstw odcinających, które są instalowane na dnie odwiertu
- zmniejszenie ciśnienia porowego poprzez ograniczenie wtrysku wody do sąsiednich odwiertów wtryskowych

Przygotowanie odwiertów do naprawy, jak wspomniano powyżej, obejmuje ich wyciszenie, czyli stworzenie warunków uniemożliwiających otwarte tryskanie i emisję ropy naftowej i gazu podczas demontażu wyposażenia głowicy odwiertu i podnoszenia sprzętu z odwiertu. Jest to metoda wyciszania odwiertów najczęściej stosowana przy naprawie odwiertów eksploatowanych za pomocą pompy wgłębną tłokową żerdziową [1].

Zakleszczenie odwiertu jest dozwolone, gdy płyn w odwiercie zostanie całkowicie lub częściowo wymieniony z przywróceniem obiegu lub bez niego. Jeśli częściowa wymiana płynu z odwiertu naftowego nie jest dozwolona, kolumna jest wypełniana płynem zakleszczającym podczas pompowania w celu absorpcji. Metoda zakleszczenia odwiertu jest wybierana w zależności od parametrów operacyjnych (współczynnik gazu, zawartość wody, odbiór, ciśnienie tłoczenia, ciśnienie porowe) i metody jego działania. Specjalny sprzęt do zakleszczenia obejmuje jednostki pompujące lub myjące oraz cysterny [1]. Zakleszczenie odwiertów wyposażonych w system pomp wgłębną tłokową żerdziową, jeśli to konieczne, odbywa się w dwóch lub więcej etapach. W przypadku niewielkiego wypływu płynu odwiert pozostawia się w spokoju na czas wyparcia płynu przez płyn zakleszczający i wykonuje kolejny cykl zakleszczenia. Jeśli nie ma powrotu ze zbiornika, to po wymianie objętości płynu od ujścia do wejścia pompy, odwiert jest zamknięty i czeka do momentu wymiany płynu w pompie. W przypadku zakleszczania odwiertów o wysokim współczynniku gazowym, dużym przedziale perforacji i absorpcji płynu zakleszczającego w wysoce przepuszczalnych interwałach (zwrot ze zbiornika 200–300 m^3/dobę przy ciśnieniu 10–12 MPa), objętość buforowa obszaru filtra jest przewidziana do pompowania płynu tłumionego lub płynu złożonego. Bufor płynu jest pompowany do przedziału perforacji, zatrzask głowicy odwiertu jest zamykany, a płyn jest wyciskany do formacji. Zawory są zamykane na 20–30 minut w celu wyrównania ciśnienia. Jeśli po otwarciu zaworów nie występują objawy gazowe, transfuzje, wchłanianie zakleszczonego płynu, rozpoczynają się prace naprawcze. Metoda ta jest dość efektywna, to znaczy zapewnia naprawę odwiertu bez wydobycia gazu i ropy naftowej, ale jest niedokładna, ponieważ trudno jest dobrać gęstość płynu, która zapobiegnie całkowitemu brakowi wydobycia gazu i ropy naftowej. Zajmuje to również dużo czasu i pieniędzy.

Podczas naprawy odwiertu wykorzystywany jest sprzęt zainstalowany u jego wylotu, który służy do eliminacji rozwoju gazu i ropy naftowej oraz tryskania z odwiertu. Takim sprzętem może być:

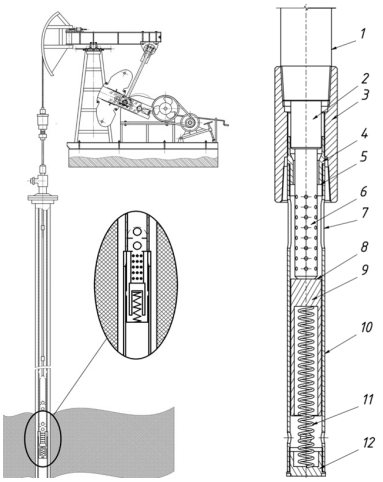

Rys. 3. Zawór zwrotny umieszczony w odwiercie oraz zasad pracy zaworu zwrotnego
Fig. 3. Check valve placed in the well and the working principles of the check valve

- prewenter;
- uszczelniacz;
- awaryjna płyta czołowa.

Po uzgodnieniu z serwisem, może być skierowany wniosek do firmy prowadzącej prace naprawcze o zabezpieczenie nieprzepuszczalności głowic odwiertów takimi urządzeniami które będą zapewniać warunki wypływu bezpiecznej fontanny i są wyprodukowane zgodnie z dokumentacją opracowaną techniczną i zatwierdzoną przez autoryzowany serwis [8].

Prewentery są zaprojektowane z myślą o nieprzepuszczalności w obecności lub braku rur w odwiercie.

Uszczelniacz jest przeznaczony do pokrywania przestrzeni rurowej kolumny rurowej, jeśli jest możliwość wycieku. To urządzenie jest podłączone do kolumny rurowej, która jest podnoszona z odwiertu w momencie rozpoczęcia manifestacji rozwoju gazu i ropy naftowej. W razie potrzeby kurek jest przesuwany do pozycji zamkniętej, co umożliwia uszczelnienie przestrzeni rurki i nie pozwala na przedostanie się płynu pod ciśnieniem do otwartej przestrzeni [5].

Awaryjna płyta czołowa z zaworem (kranem) jest przeznaczona do nakładania się na przestrzeń rurową obudowy produkcyjnej w sytuacjach awaryjnych w procesie wymiany pomp prętowych. Płyta czołowa jest przymocowana do kolumny produkcyjnej i połączona ze sprzętem głowicy odwiertu za pomocą sworzni i nakrętek. Jego konstrukcja zapewnia kontrolę nad przestrzenią rury.

Zaletami takiego sprzętu są prosta instalacja i obsługa. Wady obejmują fakt, że podczas instalacji przestrzeń rury jest otwarty i istnieje możliwość przerostu produkcji gazu i ropy naftowej do otwartej fantanny [6].

Dzisiaj istnieje również jeszcze kilka rodzajów sprzętu, który służy do zapobiegania otwartemu tryskaniu ropy i jest umieszczany bezpośrednio w odwiercie: korki, zawory sterujące, zawory głębokości powrotu.

Tak więc w omawianych powyżej urządzeniach nie ma gwarantowanej możliwości kontrolowanego zamknięcia odwiertu, a także odzyskania produkcji z odwiertu bez jego późniejszego zagospodarowania. W związku z tym istnieje potrzeba stworzenia urządzenia, które pozwoli na nałożenie się sznura rur, a następnie wznowienie pracy odwiertu bez użycia skomplikowanego sprzętu pomocniczego i rozwijania odwiertu.

Koncepcja specjalnego urządzenia wspomagającego prace serwisowe w szybie naftowym podczas wymiany żerdziowej pompy wgłębnej

Ponieważ istniejący sprzęt umożliwia częściową kontrolę procesu naprawy, a istniejące metody nie zapewniają bezpieczeństwa podczas naprawy odwiertu w związku z tym pojawiło się pytanie o stworzenie sprzętu, który stworzy bezpieczne warunki do przeprowadzania prac naprawczych w odwiercie, a mianowicie podczas wymiany systemu pompy wgłębnej tłokowej żerdziowej w warunkach wysokiego współczynnika zagrożenia wypływu gazu.

Mając na uwadze powyższe opracowano koncepcje zaworu zwrotnego pozwalającego na bezpieczne prace serwisowe.

Przedmiotowy zawór zwrotny (rys.3) jest przeznaczony do osłaniania przestrzeni rurowej pompy i sprężarki podczas wymiany pompy wgłębnej. Jednocześnie objętość płynu w odwiercie zostaje zachowana, w związku z tym niemożliwe staje się pobranie nowej porcji ropy naftowej lub gazu ze zbiornika. Ponieważ nie ma ropy naftowej nasyconej gazem lub gazu pochodzącego ze zbiornika, gęstość ropy naftowej na dnie nie zmniejsza się, a prawdopodobieństwo wypadków związanych z wydobyciem gazu i ropy naftowej jest wyeliminowane. Urządzenie pozwala również na naprawę i wymianę pomp bez zakleszczania odwiertu, co zmniejsza czas i pieniądze poświęcane na ten proces.

Zawór zwrotny składa się z cylindrycznego pływaka 9 z tworzywa sztucznego, wykonanego w formie "odwróconej góry", umieszczonego w środku cylindrycznego korpusu 10. Obudowa 10 jest połączona z adapterem 4, na którym wykonany jest koniec wsporczy 5, a adapter jest połączony z łącznikiem przejściowym 3, który jest połączony z rurą 1. W obudowie 10 zainstalowana jest sprężyna 11, która opiera się jednym końcem na pływaku 9, a drugim na pokrywie 12 i jest połączona z obudową za pomocą gwintu.

Podczas instalacji pompy 2 w odwiercie, filtr 6, który znajduje się pod pompami, przesuwa pływak w dół, jednocześnie ściskając sprężynę 11. W takim przypadku powierzchnie nośne powierzchni czołowej 5 i pływaka 8 są otwarte, a płyn ze

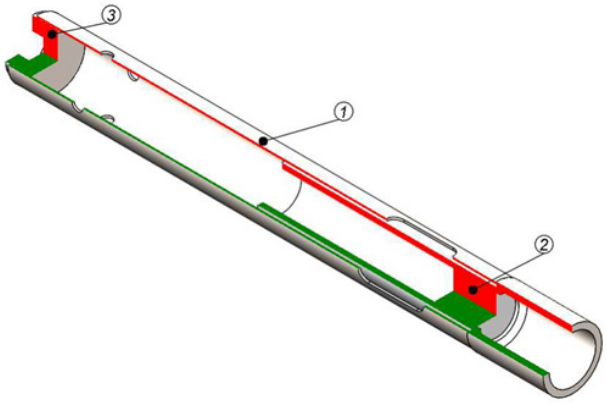

Rys. 4. Schemat wskazujący punkty do symulacji komputerowych: 1 – korpus, 2 – pływak, 3 – pokrywa obudowy
Fig. 4. Diagram indicating points for computer simulations: 1 – body, 2 – float, 3 – housing cover

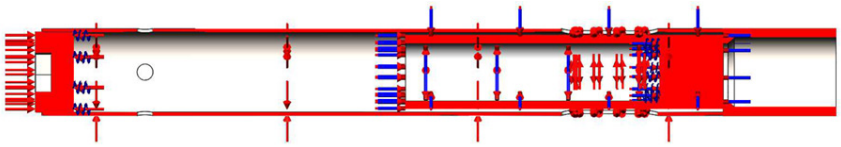

Rys. 5. Zastosowanie warunków brzegowych do badanego modelu
Fig. 5. Application of boundary conditions to the model under study

zbiornika przepływa przez otwory 7 korpusu urządzenia 10 do filtra pompy 6, a następnie do pompy 2. Podczas naprawy pompa z filtrem unosi się na powierzchnię, umożliwiając sprężynie przesunięcie pływaka w górę do styku końca nośnego pływaka 8 z końcem nośnym 5 adaptera 4. W takim przypadku przestrzeń rury kolumny rurowej jest zablokowana.

Szczególną cechą zaworu zwrotnego jest to, że obudowa jest zamontowana nie na kolumnie rurki 10, ale na złączu przejściowym 3. To umożliwia przymocowanie innych potrzebnych elementów do przewodu rurowego, takich jak trzon, kotwica gazowa (dobierana w zależności od warunków produkcji dla każdego odwiertu indywidualnie). Sprężyna 11, która znajduje się wewnątrz obudowy 10, pomaga pływakowi poruszać się w górę, pomimo obecności cząstek mechanicznych, które mogłyby zakłócać jego ruch i blokować przestrzeń rury kolumny rurowej.

Taka konstrukcja zaworów zwrotnych pozwala nie zmieniać układu elementów w odwiertach podczas ich użytkowania.

Zalety zaworów zwrotnych są więc następujące:

- możliwość wymiany pompy bez zatykania odwiertu (skraca czas naprawy i obniża jej koszty);
- zachodzenie na siebie dolnej części kolumny rur (zapobiega przedostawaniu się płynu ze zbiornika do odwiertu i tworzeniu sytuacji awaryjnej, która może prowadzić do otwartego tryskania).

Badanie funkcjonalności elementów konstrukcji zaworów zwrotnych z wykorzystaniem modelowania symulacyjnego [9]

Aby zbadać model 3D, należy najpierw rozważyć warunki pracy i materiały użyte do jego konstrukcji. Model może pracować w temperaturze do 120°C przy ciśnieniu 15 MPa. Wszystkie materiały zastosowane w modelu wykonane są ze stali 40 (chrom, nikiel), z wyjątkiem pływaka, który jest wykonany z poliamidu 610. Po przeanalizowaniu schematu sprężynowego zaworu głębokości (Rys. 3), stwierdzono, że w powyższych warunkach pracy wskazane jest zbadanie stanu naprężenia i odkształcenia następujących części: pływaka, obudowy i pokrywy obudowy.

Jednak w projekcie modelu występuje sprężyna, która jest zastępowana odpowiednią reakcją podczas symulacji. W tym celu należy użyć specjalnej funkcji programu "złącze-sprężyna" o wymaganej charakterystyce (normalna sztywność i napięcie wstępne).

Ponieważ model w warunkach roboczych będzie działał jako temperatura czynnika roboczego, ciśnienie i siła od działania sprężyny, te warunki brzegowe zostaną zastosowane jednocześnie (Rys. 5).

Tak więc, zgodnie z Rys. 6, maksymalna wartość naprężeń występujących w badanym modelu pod wpływem siły sprężyny, ciśnienia i temperatury wynosi 106 MPa. Ponieważ granica plastyczności części metalowych wykonanych ze stali 40 (chrom, nikiel) wynosi 245 MPa, współczynnik bezpieczeństwa jest równy 246/106=2,32. Przy tej wartości wytrzymałość konstrukcji jest zapewniona.

Maksymalny ruch jest obserwowany w pływaku i wynosi 0,3 mm. Ze względu na wielkość szczeliny pozostającej między korpusem a pływakiem, niemożliwe jest zablokowanie tego ostatniego.

Wartość ciśnienia kontaktowego między stykającymi się powierzchniami pływaka i obudowy (Rys. 7) wynosi 117 MPa, co jest wystarczające do zapewnienia nieprzepuszczalności.

Podsumowanie

Wymiana osadzonych pomp żerdziowych w systemach pomp wgłębnych tłokowych żerdziowych jest procesem niebezpiecznym ze względu na zjawisko "pompowanie tłokowe", które występuje w momencie podnoszenia pompy, niekontrolowany wypływ płynu ze zbiornika, a także niekontrolowane uwalnianie gazu z odwiertu. Może to prowadzić do wypadków (otwarta fontanna).

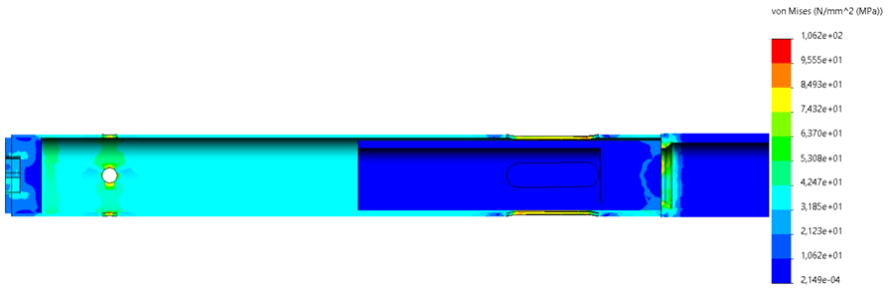

Rys. 6. Rozkład naprężeń równoważnych
Fig. 6. Equivalent stress distribution

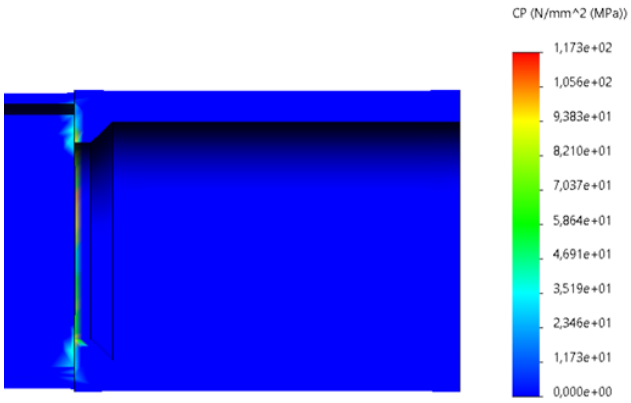

Rys. 7. Rozkład nacisku kontaktowego
Fig. 7. Distribution of contact pressure

Analiza istniejących metod narzędzi zapewniających bezproblemową wymianę pompy wgłębnych wykazała, że są one dość niedokładne i wymagają długiego czasu na dostosowanie parametrów, a także zawierają "czynnik ludzki". Na tej podstawie opracowano projekt zaworu odwiertu powrotnego w oparciu o dane z odwiertu "Dolina naftogazu". Opracowana konstrukcja urządzenia umożliwia zapewnienie bezpiecznego środowiska podczas wymiany pomp żerdiowych w systemie pomp wgłębnych tłokowych żerdziowych.

Za pomocą modelowania symulacyjnego zbadano elementy zaworu zwrotnego i potwierdzono ich działanie w określonych warunkach pracy, co zapewni skuteczność działania.

Literatura – References

1. Bargaev I. Y., Iostilevich G. B., Rez'bovle I flancevie Iwanofrankowsk 2013. S. 316
2. Czmochowski, J. 2008. Identyfikacja modeli modalnych maszyn urabiających w górnictwie węgla brunatnego. Oficyna Wydawnicza Politechniki Wrocławskiej
3. Jamroziak, K., Kosobudzki, M. and Ptak, J. 2013. Assessment of the comfort of passenger transport in special purpose vehicles. Eksploatacja i Niezawodnosc – Maintenance and Reliability. 15, 1 (2013), 25–30
4. Maślanka, M., Weber, F., Control, P., Mickiewicza, A. and Duebendorf, C. - Precise Stiffness Control with MR Dampers AGH University of Science and Technology , Faculty of Mechanical Engineering and Robotics, Empa , Swiss Federal Laboratories for Materials Science and Technology, Structural Engineering
5. Rusiński, E., Czmochowski, J., Iluk, A. and Kowalczyk, M. 2010. An analysis of the causes of a BWE counterweight boom support fracture. Engineering Failure Analysis. 1, 17 (2010), 179–191
6. Gamatudinova O.I. 1986, Spravochnaya kniga po dobyche nefti. — M.: Nedra, 1986. 332 s.;
7. I. Buhalenko. 1990 Nefteromislovanie: Sparvochnik – M. Nedra, 1990. s. 559.
8. Nikishenko S. L., Neftegazopromislovoe oborudovanie: Uchebnoe posobie – Volgograd: In-Folio, 2008. s. 416
9. Rusiński, E., Czmochowski, J. and Pietrusiak, D. 2012. Problems of steel construction modal models identification. Eksploatacja i niezadowność – Maintenance and reliability. 14, 1 (2012), 54–61
10. Rusiński, E., Kaczyński, P., Moczko, P. and Pietrusiak, D. 2012. Bucket Wheel Excavator Dynamics Optimization on The Stage of Preliminary Project. Górnictwo Odkrywkowe. 3-4, (2012), 25–28
11. Sapiński, B. 2011. Experimental study of a self-powered and sensing MR-damper-based vibration control system. Smart Materials and Structures. 20, 10 (Oct. 2011), 13pp
12. Weber, F., Feltrin, G., Maślanka, M., Fobo, W. and Distl, H. 2009. Design of viscous dampers targeting multiple cable modes. Engineering Structures. 31, 11 (2009), 2797–2800

Concept of a Special Device to Support Maintenance Work in an Oil Well during Replacement of a Rod Pit Pump

The following article introduces and describes a device designed to prevent uncontrolled inflow and outflow of gas from the wellbore layer during repair (service) operations with drilling equipment for mechanical oil recovery using a rod-style drilling pump.
The article describes the actuality of the application of the device and the principle of its use during the replacement of the plug plunge pump. The construction, characteristics and principle of operation of the device are described.

Keywords: *oil well, service work, special equipment, drilling*

Increasing the Efficiency of Froth Flotation to Maximize Production of Coking Coal Concentrates in the Aspect of Sustainable Management of Natural Resources

Daniel KOWOL[1)], Piotr MATUSIAK[2)], Sebastian JENDRYSIK[3)], Agata CZARDYBON[4)], Karina IGNASIAK[5)], Joanna BIGDA[6)]

[1)] KOMAG Institute of Mining Technology, 44-100 Gliwice, Poland; ORCID 0000-0001-5547-376X
[2)] KOMAG Institute of Mining Technology, 44-100 Gliwice, Poland; ORCID 0000-0002-9393-4309
[3)] KOMAG Institute of Mining Technology, 44-100 Gliwice, Poland; ORCID 0000-0002-6266-3411
[4)] Institute of Energy and Fuel Processing Technology, 41-803 Zabrze, Poland; ORCID 0000-0002-6115-0075
[5)] Institute of Energy and Fuel Processing Technology, 41-803 Zabrze, Poland; ORCID 0000-0001-9201-9937
[6)] Institute of Energy and Fuel Processing Technology, 41-803 Zabrze, Poland; ORCID 0000-0001-7083-5677

http://doi.org/10.29227/IM-2024-01-101

Submission date: 06-05-2024 | Review date: 11-06-2024

Abstract

Coking coal, due to its limited availability and the role and importance of steel as a raw material, essential in almost all industries, has been on the list of critical raw materials in the EU for many years. The article presents the results of laboratory tests of impact of the selected factors (feed parameters, process parameters, reagents) on the effectiveness of flotation, which is a commonly used method for beneficiation of fine coking coal grains. The large number of variables and significant differences in results clearly indicate the need for more detailed tests before each new application of flotation beneficiation technology. Selection of parameters that guarantee maximization of production from the point of view of rational and sustainable management of resources while minimizing the negative impact of the effects of this process on the environment should be the result of these tests.

Keywords: *mineral resources, coking coal, froth flotation, efficiency of the process*

1. Introduction

Coking coal, a critical raw material on the EU list [1], plays a key role in production of steel, one of the key materials used in construction and manufacture of machines, ships, cars and everyday items. Despite the technologies being developed to replace coke with green hydrogen, it is estimated that developing such a technology on a mass scale may still take several dozen years [2,3]. Difficulty in replacing the coking coal and its limited resources force the use of technological and design solutions that enable maximizing the production of high-quality concentrates while minimizing coal losses in waste.

In turn, steam coal, despite the ongoing decarbonization, resulting in a decline in its production and industrial use, will still continue to be a component of the energy mix in the coming years.

The production of hard coal with high quality parameters requires continuous improvement of the beneficiation technology and designs of the machines and devices used. The beneficiation process, depending on the grain size of the material (feed), is carried out in specialized machines and devices, including heavy media baths, dense medium cyclones, pulsating water jigs [4,5,6,7,8,9,10,11,12].

Very fine hard coal grains with a grain size below 0.5 mm are most often enriched by froth flotation [13,14,15,16,17].

Flotation can be used both for coking coal and steam coal, but in the case of the first one, much higher efficiency of the process is achieved.

Flotation is a physicochemical process based on the use of differences in the surface properties of useful mineral grains and waste rock, and above all, differences in hydrophobicity. In the case of hard coal, organic (coal) grains with hydrophobic surfaces are subject to flotation, while waste rock grains with hydrophilic surfaces, of high surface energy, do not float [18, 19,20,21].

The process of flotation of coal sludge generally is carried out in flotation machines, the so-called floaters.

A very important condition for an effective flotation separation process is the proper grain composition of the feed. The pioneer work on the relationship between particle size and flotation recovery was carried out by Gaudin et al. [22,23] Fig. 1 shows the dependence of flotation recovery on the grain size for a variety of raw mineral, including coal.

Although the coal flotation process is usually used for grains <0.5 mm, there are also reports in the literature of successful enrichment of grains coarser than <1 mm [24]. On the other hand, it was found in [25] that the maximum grain size that can be highly flotable is 0.589 mm.

A number of flotation kinetic models, which investigated the effect of particle size on the flotation process, can be found in the literature. Analysis of the available information showed that, despite significant differences in the grain size ranges, expected for maximum carbon recovery, the extreme grain sizes do not exceed 0.5 mm (maximum) and 0.074 mm (minimum) [22,26,27,28,29,30].

Increasing share of the finest grains <0.045 mm, with low floatability, in the flotation feed (grain class 0.5–0 mm) is an equally important problem that negatively affects the efficien-

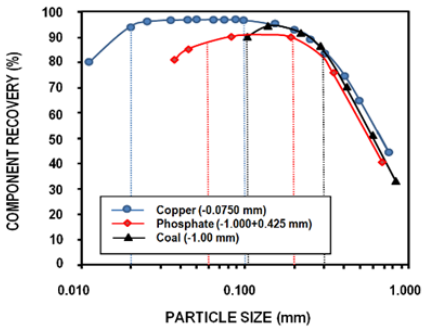

Fig. 1. Flotation recovery depending on the grain size for a variety of raw mineral [22,23]
Rys. 1. Odzysk flotacji w zależności od wielkości ziaren dla różnych surowców mineralnych [22,23]

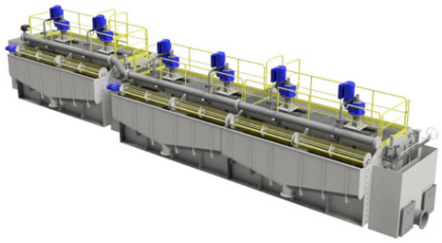

Fig. 2. IZ12K flotation machine [own elaboration]
Rys. 2. Maszyna flotacyjna IZ12K [opracowanie własne]

cy of the flotation process despite the possibility of flotation beneficiation of these grains. [31,32].

As a result of the most commonly used method of coal mining – longwall shearer technology – significant amount of very fine grains is formed, including grains <0.5 mm [33].

Such conditions justify research and development work aimed at increasing the efficiency of the flotation process in terms of both product quality parameters and process costs.

The article presents the test results on the efficiency of the flotation process for various ranges of grain size and different shares of each grain class in the feed.

2. Industrial flotation machines

The process of flotation of coal mud in a mass manner is carried out in flotation machines.

Flotation machines are most often classified according to the method of aerating the suspension [34,35]. Based on this criterion, three basic types of machines can be distinguished: mechanical flotation machines, in which the aeration and dispersion unit consisting of a rotor and a stator sucks in and agitates the flotation suspension and disperses the air sucked from the atmosphere, pneumo-mechanical flotation machines, in which the aeration and dispersion unit consisting of a rotor and a stator agitates the flotation suspension and disperses air supplied from the outside under pressure, pneumatic floating machines, in which there is no rotor, and special devices called aerators are used for air dispersion in the suspension. Compressed air is supplied from the outside or is sucked in from the atmosphere.

In addition, other types of flotation machines are known, not playing a significant role in industry, such as vacuum, cyclone, electro-flotation and combined machines.

Another division identifies five categories of flotation machines: mechanical agitation flotation machine, inflatable agitation flotation machine, flotation column, impeller flotation machine and rod flotation machine [36].

In the Polish processing plants, coal mud beneficiation by flotation almost exclusively uses pneumo-mechanical machines type IZ.

The KOMAG Institute of Mining Technology has developed a modernized version of the most popular pneumo-mechanical flotation machine – IZ12K (Fig. 2)

It is a trough-type machine and has a modular structure. It consists of three two-rotor units with two-sided intake of flotation foam.

Two-rotor units, each with a capacity of 13 m^3, are connected in a complete flotation machine in cascade, with the first level being one unit (two working compartments), and the next two units, set lower with a difference in the bottom levels of the working compartments of 400 mm, are connected with the previous one by an intermediate box. After the last working compartment, this flotation machine is equipped with a tailings container. Each section is equipped with two rotors, a mechanical driving system, a compressed air collector and stator located around the rotor as well as a bottom channel. The flotation machine is equipped with an automatic adjustment of the level of dregs in the trough. The coal beneficiation process takes place during the movement of dregs in the machine bed [37].

3. Laboratory tests

Two series of tests were performed, in which the grain size range in the feed and share of each grain class in the above-mentioned materials were different.

Testing the impact of coking coal feed size distribution on the efficiency of the flotation process was carried out at the KOMAG Institute of Mining Technology on a specialized laboratory stand using a chamber (cell) with a capacity of 1400 cm^3 (Fig. 3).

Fig. 3. Stand for testing the flotation process [32]
Rys. 3. Stanowisko laboratoryjne procesu flotacji [32]

Rys. 6. Rozkład naprężeń równoważnych
Fig. 6. Equivalent stress distribution

Grain class, mm	Feed 0.5–0 mm		Feed 0.3–0 mm	
	Output, %	Ash, %	Output, %	Ash, %
0.5–0.3	22.35	18.34		
0.3–0.045	39.21	23.83	50.49	23.83
<0.045	38.46	34.58	49.52	34.58
Suma	100.00	26.74	100.00	29.16

3.1. Testing methodology

The chamber (cell) of the flotation machine was filled with water from the water supply system (processing water). Then, a weighed portion of the feed was poured into the flotation chamber, a flotation reagent was added in a given dose, appropriate for a given portion of the feed, and the resulting mixture was conditioned for 30 seconds at the rotor speed of 600 rpm. Then the process air valve (output equal to 2 dm^3/min) supplied by the rotor was opened and the rotor speed was increased to 1040 rpm. The level of dregs in the flotation chamber was refill with water, so that it remained 1 cm below the overflow threshold. The flotation process was stopped after 180 s. The flotation products were filtered and dried at ambient temperature, and then weighed and the ash content was determined in accordance with PN-ISO 1171:2002.

To assess the flotation results, apart from the ash content in the products, recovery of combustible substance in the flotation concentrate (ε) was used, calculated according to the following relationship:

$$\varepsilon = \gamma \cdot \frac{100 - \lambda}{100 - \alpha} \quad (1)$$

where:
α – ash content in the feed %,
γ – concentrate output %,
λ – ash content in the concentrate %.

3.2. Test results

3.2.1. Test series No. 1

Two materials with a grain size of 0.5–0 mm and 0.3–0 mm were the object of tests. Tested materials were obtained, through dimensional classification, from the feed for a pulsating fine coal jig in the grain class of 30–0 mm from the selected coking coal mine.

The results of the granulometric analysis of the above-mentioned materials are given in the Table 1.

The tested material had a significant amount of the finest grains >0.045 mm, which amounted to 38.46% in the case of the 0.5–0 mm grain class and as much as 49.52% in the 0.3–0 mm grain class. Due to the high content of such grains, the feed with so narrowed grain size range should be considered as of very low floatability.

Two complex flotation agents, marked as R1 and R2, were used in the tests. The tests were carried out at densities of 60, 80 and 100 g/l. Agent doses of 0.4; 0.8 and 1.2 kg/Mg of dry material were used.

The test results, using the R1 agent, i.e. ash content in products and recovery of combustible substance are given in the Table 2.

The analysis of the results showed a clear effect of the flotation agent dose on the parameters of the products and the efficiency of the flotation process, especially in the case of feed of grain size 0.5–0mm. Impact of the dose of the flotation agent on the results concerned all the analysed quantities, i.e. products yield, their ash content and recovery of the combustible substance in the concentrate. With increasing the dose of the agent, the ash content in tailings increased from 77.45% (0.4 kg/Mg of dry material) to 80.97% (0.8 kg/Mg). The recovery of the combustible substance also increased from 64.01% (0.4 kg/Mg) to 68.51% (1.2 kg/Mg). At the same time, the ash content in the concentrate increased from 8.36% (0.4 kg/Mg) to 10.31% (0.8 kg/Mg).

The tests did not show the impact of material density on the efficiency of the flotation process (both feeds).

Despite lower ash content in the concentrate in testing the feed of grain size 0.3–0 mm, it should be stated that more favourable results and higher efficiency of the flotation process were obtained in tests with feed in the 0.5–0 mm class.

In most cases, for the 0.5–0 mm class, higher ash content in tailings was obtained. In tests, in which the ash content in tailings of 0.3–0 mm class was higher, lower ash content in the concentrate was obtained for the 0.5–0 mm class.

In all tests, the yield of combustible substance in the concentrate was higher in the tests with the feed of 0.5–0 mm.

A very important issue in terms of the effectiveness of the flotation process are the costs related mainly to the cost of

Tab. 2. Parameters of flotation with use of R1 agent [38]

Tab. 2. Zestawienie parametrów procesu flotacji z wykorzystaniem odczynnika R1 [38]

Feed 0.5–0 mm						
Concentration, g/l	Amount of agent, kg/Mg	Concentrate, %		Tailings, %		Recovery, %
		Yield, %	Ash, %	Yield, %	Ash, %	
60	0.4	77.23	9.15	23.77	77.45	64.01
	0.8	78.52	9.81	21.48	80.61	65.28
	1.2	80.36	10.12	19.64	77.56	68.51
80	0.4	75.39	8.36	24.61	75.97	61.71
	0.8	79.56	9.81	20.44	79.62	66.97
	1.2	79.38	10.01	20.62	79.78	66.69
100	0.4	77.86	9.16	22.14	76.77	65.02
	0.8	78.67	10.31	21.23	80.97	65.44
	1.2	79.95	10.01	20.05	80.52	67.39
Feed 0.3–0 mm						
Concentration, g/l	Amount of agent, kg/Mg	Concentrate. %		Tailings. %		Recovery, %
		Yield, %	Ash, %	Yield, %	Ash, %	
60	0.4	67.25	7.87	32.75	67.09	53.10
	0.8	65.87	8.18	34.13	62.68	52.52
	1.2	71.52	9.59	28.48	72.63	57.31
80	0.4	73.36	11.77	26.64	70.21	60.41
	0.8	70.10	8.49	29.90	68.70	56.30
	1.2	77.49	12.32	22.51	82.41	63.55
100	0.4	76.12	11.61	23.88	79.36	62.19
	0.8	70.90	9.60	29.10	72.03	62.79
	1.2	78.87	12.30	21.13	81.06	65.80

the agent. With comparable product parameters, the higher the reagent consumption, the lower the process effectiveness.

Therefore, special attention should be paid to the results of testing the use of lowest amounts of the agent (0.4 kg/Mg), especially in the case of the 0.5–0 mm grain size class. Regardless of the feed density, in each case the ash content in the concentrate was <10%, the ash content in tailings was higher than 75%, and the recovery of the combustible substance was not less than 64%.

Fig. 4 and 5 graphically show the comparison of parameters of flotation products for the tested grain classes, obtained at the extreme process parameters used during tests.

During the tests, a significant dispersion of results was observed regarding the ash content in the separation products and the recovery of combustible substance in the concentrate.

Use of the R2 reagent, despite the lower ash content in the concentrate, resulted in a significantly lower efficiency of the process due to the significantly lower ash content in tailings and lower recovery of combustible substance in the concentrate.

In most cases, there was a relationship between the dose of the flotation reagent and the parameters of products, especially of tailings, and the efficiency of the flotation process. With the increase in the dose of the agent, the yield of tailings decreased and, at the same time, the ash content in the above-mentioned product increased. In the case of the 0.3–0 mm grain class, a positive effect of the increase in flotation pulp density was also observed.

Fig. 6 and 7 show a graphical comparison of the parameters of flotation products for the tested grain classes, obtained at the extreme process parameters used in testing.

3.2.2. Test series No. 1

Three materials with a grain size of 0.5–0 mm, 0.25–0 mm and 0.125–0 mm, from the selected coking coal mine were tested. The granulometric-ash composition of the raw material is presented in Table 4.

The finest grains (<0.045 mm) had the largest share in the analyzed grain sizes – 65.84%.

Ash content increased inversely proportional to the grain size from 12.57% (0.5-0.25 mm) to 41.93% (<0.045 mm). Subsequent tested feeds with grain size of 0.5–0 mm, 0.25–0 mm and 0.125–0 mm had increasingly higher ash content.

Flotation agent R1 was used in the tests. The tests were carried out at densities of 60 and 100 g/l. Agent doses of 0.4, 0.8 and 1.2 kg/Mg of dry material were used.

Parameters of the flotation process such as yield and ash content in the products as well as the recovery of combustible substance are presented in Table 5.

Analysis of the results showed a clear effect of the dose of flotation agent and the density of flotation pulp on products parameters and the efficiency of the flotation process for all tested feeds.

With increase of the agent dose, the yield of the concentrate increased, but ash content in this product also increased. At the same time, the ash content in tailings increased. A similar dependence was observed during the recovery of a combustible substance. Increasing the density, for the same agent doses, resulted in an increase in the yield of the concentrate with a simultaneous increase in the ash content in tailings.

The tests clearly show the negative impact of narrowing the grain size class and reducing the upper range of grains on product parameters and process efficiency. As the size of grains in the feed decreased, the quality parameters of the separation products deteriorated. The ash content in concentrate of the tested classes of 0.5–0 mm, 0.25–0 mm and 0.125–0 mm increased and was in the range of 11.83–14.36%,; 12.44–16.43% and 15.01–18.48%, respectively, with a simultaneous increase in yields. The ash content in tailings decreased in the analyzed size classes, in the ranges 60.54–79.79%; 60.86–74.86% and 60.63–72.99% respectively.

Figures 8–10 show the impact of the extreme process parameters during tests on the products quality parameters.

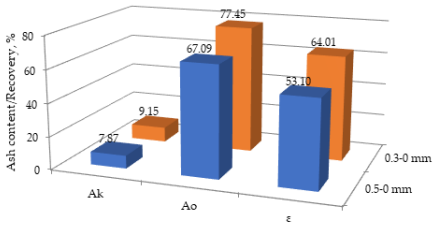

Fig. 4. Comparison of qualitative parameters of the flotation products – pulp density 60 g/l, agent dose 0.4 kg/Mg (Ak – ash content in the concentrate, Ao – ash content in tailings, ε – recovery of combustible substances in the concentrate) [38]

Rys. 4. Porównanie parametrów jakościowych produktów flotacji – zagęszczenie 60 g/l, dawka 0,4 kg/T (Ak – zawartość popiołu w koncentracie, Ao – zawartość popiołu w odpadach ε – uzysk substancji palnej w koncentracie) [38]

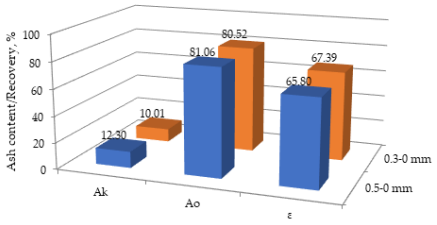

Fig. 5. Comparison of qualitative parameters of the flotation products (pulp density 100 g/l, agent dose 1.2 kg/Mg) [38]

Rys. 5. Porównanie parametrów jakościowych produktów flotacji (zagęszczenie pulpy 100 g/l, dawka odczynnika 1,2 kg/T) [38]

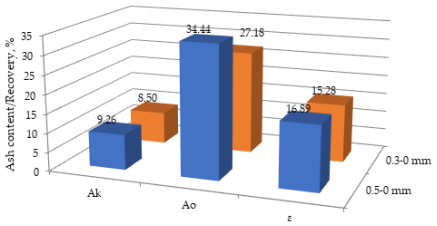

Fig. 6. Comparison of qualitative parameters of the flotation products (pulp density 60 g/l, agent dose 0.4 kg/Mg) [38]

Rys. 6. Porównanie parametrów jakościowych produktów flotacji (zagęszczenie 60 g/l, dawka 0,4 kg/T) [38]

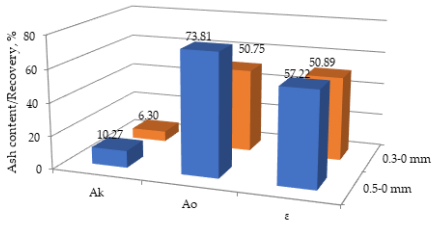

Fig. 7. Comparison of qualitative parameters of the flotation products (pulp density 100 g/l, agent dose 1.2 kg/Mg) [38]

Rys. 7. Porównanie parametrów jakościowych produktów flotacji (zagęszczenie pulpy 100 g/l, dawka odczynnika 1,2 kg/T) [38]

4. Conclusions

Reduced coal extraction associated with gradual decarbonization should not limit further development of technologies and design solutions for equipment used in the mining industry, including the coal processing. Due to the key role of coking coal in steel production, further R&D work allowing for a constant increase in the efficiency of both coal mining and processing is justified.

Froth flotation is one of the important methods for beneficiation of hard coal, including the stem coal.

Due to the increasing share of fine grains (<0.5 mm) in run-of-mine and material sent to flotation, selection of parameters, including the optimal grain range of the feed in terms of quality parameters of flotation products is an extremely important problem.

Testing the impact of the feed grain size distribution on the flotation efficiency showed that narrowing the grain size

Tab. 3. Parameters of flotation with use of R2 agent [38]

Tab. 3 Zestawienie parametrów procesu flotacji z wykorzystaniem odczynnika R2 [38]

Feed 0.5–0 mm						
Concentration, g/l	Amount of agent, kg/Mg	Concentrate, %		Tailings, %		Recovery, %
		Yield, %	Ash, %	Yield, %	Ash, %	
60	0.4	18.26	8.50	81.74	27.18	15.21
	0.8	43.92	9.94	56.08	35.29	36.98
	1.2	73.31	6.82	26.69	68.82	60.29
80	0.4	23.77	9.75	76.23	29.16	19.87
	0.8	56.06	6.50	43.94	47.19	45.34
	1.2	67.47	6.21	32.53	60.33	54.80
100	0.4	22.41	7.40	77.59	28.58	18.44
	0.8	64.39	7.51	35.61	55.14	52.59
	1.2	62.06	6.30	37.94	50.75	50.89
Feed 0.3–0 mm						
Concentration, g/l	Amount of agent, kg/Mg	Concentrate, %		Tailings, %		Recovery, %
		Yield, %	Ash, %	Yield, %	Ash, %	
60	0.4	21.58	9.26	78.42	34.44	16.89
	0.8	54.67	9.27	45.33	48.66	43.91
	1.2	65.58	8.30	34.42	64.57	51.73
80	0.4	27.02	8.19	72.98	35.80	21.09
	0.8	57.40	7.32	42.60	54.97	44.83
	1.2	65.76	9.33	34.24	63.97	52.19
100	0.4	28.93	7.75	71.07	33.95	23.09
	0.8	63.10	8.08	36.90	65.05	48.67
	1.2	71.67	10.27	28.39	73.81	57.22

Tab. 4. Granulometric-ash compositions of tested feeds for the flotation [38]

Tab. 4. Składy granulometryczno-popiołowe nadaw doświadczalnych do procesu flotacji [38]

Grain size mm	Feed 0.5–0 mm		Feed 0.25–0 mm		Feed 0.125–0 mm	
	Yield, %	Ash, %	Yield, %	Ash, %	Yield, %	Ash, %
0.5-0.25	11.32	12.57				
0.25-0.125	9.47	15.8	10.67	15.80		
0.125-0.045	13.37	18.24	15.08	18.24	16.88	18.24
<0.045	65.84	41.93	74.25	41.93	83.12	41.93
Suma	100.00	32.97	100.00	35.57	100.00	37.93

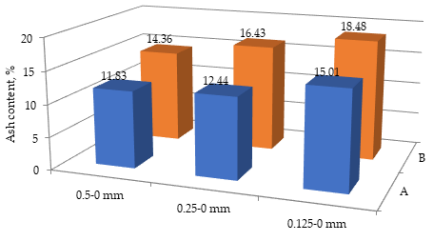

Fig. 8. Ash content in the concentrate depending on pulp density and agent dose (A – density 60 g/l, dose 0.4 kg/Mg; B – density 100 g/l, dose 1.2 kg/Mg) [38].

Rys. 8. Zależność zawartości popiołu w produkcie koncentratowym od zagęszczenia pulpy i dawki odczynnika (A – zagęszczenie 60 g/l. dawka 0,4 kg/T; B – zagęszczenie 100 g/l, dawka 1,2 kg/T) [38]

class and reducing the upper range of grain sizes in majority of tests resulted in deterioration of quantitative and qualitative parameters of the separation products and the decrease in the efficiency of flotation i.e. the recovery of combustible substance in the concentrate.

The test results clearly indicate that a high share of the smallest, very difficult to float grains <0.045 mm has a definitely negative impact on all product parameters. With the increase in the percentage of fine grains in the feed, the quality parameters of the products deteriorates. Therefore, it seems that the separation of the above-mentioned grains from the feed for flotation should significantly increase the process effectiveness.

The tests also confirmed the significant impact of the flotation agent type on the efficiency of recovery of combustible substance. The flotation agent, due to its high cost, is a significant component of cost effectiveness of the process, therefore it is extremely important to select the right type and dose of the agent in terms of the expected and acceptable parameters of the enrichment products.

Significant differences in the results require detailed tests before each new application of flotation enrichment technology. The tests, preceded by a grain size and ash analysis, should include the selection of the type of flotation agent, its dose, as well as other process parameters, including flotation pulp density.

Proper selection of the process parameters can significantly increase the efficiency of the flotation process, allowing both to reduce the production costs of coal concentrates and to maximize the production of high-quality assortments. The

Tab. 5. List of selected parameters of the flotation process [38]

Tab. 5. Zestawienie wybranych parametrów procesu flotacji [38]

Feed 0.5–0 mm						
Concentration, g/l	Amount of agent, kg/Mg	Concentrate, %		Tailings, %		Recovery, %
		Yield, %	Ash, %	Yield, %	Ash, %	
60	0.4	58.75	11.83	41.25	60.54	45.36
	0.8	70.41	14.33	29.59	75.77	55.46
100	0.4	66.67	13.07	33.33	68.80	52.14
	0.8	71.55	13.79	28.45	75.84	56.42
	1.2	73.67	14.36	26.33	79.79	58.85
Feed 0.25–0 mm						
Concentration, g/l	Amount of agent, kg/Mg	Concentrate, %		Tailings, %		Recovery, %
		Yield, %	Ash, %	Yield, %	Ash, %	
60	0.4	56.86	12.44	43.14	60.86	43.29
	0.8	66.99	14.35	33.01	76.33	50.98
100	0.4	63.25	14.19	36.75	67.04	48.93
	0.8	67.10	15.93	32.90	73.25	52.05
	1.2	69.83	16.43	30.17	74.86	55.10
Feed 0.125-0 mm						
Concentration, g/l	Amount of agent, kg/Mg	Concentrate, %		Tailings, %		Recovery, %
		Yield, %	Ash, %	Yield, %	Ash, %	
60	0.4	53.35	15.01	46.65	60.63	39.99
	0.8	61.21	16.43	38.79	67.93	46.57
100	0.4	59.50	16.13	40.50	64.08	45.72
	0.8	64.01	18.32	35.99	69.71	49.51
	1.2	66.04	18.48	33.96	72.99	51.04

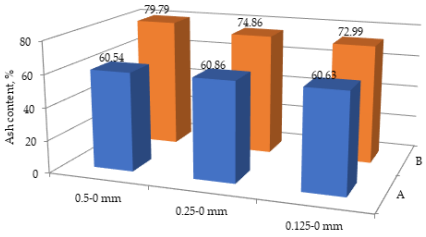

Fig. 9. Dependence of ash content in tailings on pulp density and the agent dose (A – density 60 g/l, dose 0.4 kg/Mg; B – density 100 g/l, dose 1.2 kg/Mg) [38].

Rys. 9. Zależność zawartości popiołu w produkcie odpadowym od zagęszczenia pulpy i dawki odczynnika (A – zagęszczenie 60 g/l. dawka 0,4 kg/T; B – zagęszczenie 100 g/l, dawka 1,2 kg/T) [38]

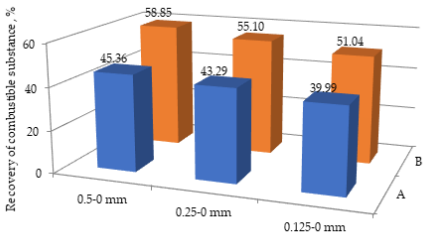

Fig. 10. Dependence of ash content in tailings on pulp density and the agent dose (A – density 60 g/l, dose 0.4 kg/Mg; B – density 100 g/l, dose 1.2 kg/Mg) [38]

Rys. 10. Zależność uzysku substancji palnej w produkcie koncentratowym od zagęszczenia pulpy i dawki odczynnika (A – zagęszczenie 60 g/l. dawka 0,4 kg/T; B – zagęszczenie 100 g/l, dawka 1,2 kg/T) [38]

end result will be a reduction in consumption of resources and, above all, in the case of combustion of steam coal concentrates, thus reduced emissions of pollutants.

The control system, which enables a wide selection of process parameters and its increased control is an important element that impacts the efficiency of the process and, as a result, the quality parameters of the products.

Higher efficiency of the process will also allow for the reduction of coal losses in tailings, which will have an additional positive impact on the natural environment by reducing the risk of spontaneous combustion of the material stored in post-mining landfills (heaps).

Literatura – References

1. https://www.euractiv.com/section/politics/news/coking-coal-remains-on-eu-critical-raw-materials-list-after-polish-pressure/ [access: 26.10.2023].
2. https://cleantechnica.com/2019/09/06/hydrogen-could-replace-coke-in-steelmaking-lower-carbon-emissions-dramatically/ [access: 26.10.2023].
3. https://www.linkedin.com/pulse/renewable-hydrogen-replace-coking-coal-simon-robeson [access: 26.10.2023].
4. Woodruff D. 2016. Dense Medium Baths and Drum Separators a Re-evaluation of Their Role in Modern Coal Preparation Plants. XVIII International Coal Preparation Congress pp 169–174. 2016. DOI 10.1007/978-3-319-40943-6_25.
5. Amini, S.H., Honaker, R., Noble, A. 2016 Performance evaluation of a dense-medium cyclone using alternative silica-based media. Powder Technology 297: 392-400.
6. Napier-Munn, T. 2018. The dense medium cyclone – past, present and future. Minerals Engineering. Volume 116: 107-113.
7. Matusiak, P., Kowol, D. 2020. Use of state-of-the-art jigs of KOMAG type for a beneficiation of coking coal. Min. Mach. nr1:46-55.
8. Kowol D., Matusiak, P. 2019. Improving the quality of hard coal products using the state-of-the-art KOMAG solutions in a pulsating jig nod. IOP Conference Series: Materials Science and Engineering, Volume 641, Number 1.
9. Liu, Y., Xie, J., Zhang, M., Kuang. Y. 2016. Study on the Model System of Jig with Flexible Air Chamber and Pulsating Current Characteristic. XVIII International Coal Preparation Congress: 797-802.
10. Kumar, S., Venugopal, R. 2020. Coal cleaning using jig and response surface approach for determination of quality of clean coal. International Journal of Coal Preparation and Utilization Volume 40, Issue 2.
11. Matusiak P., Kowol D., Suponik T., Franke D.M., Nuckowski P.M., Tora B., Pomykała R. 2021. Selective Crushing of Run-Of-Mine as an Important Part of the Hard Coal Beneficiation Process. Energies nr 14(11), 3167: 1-15, DOI: 10.3390/en14113167, ISSN 1996-1073.
12. Surowiak, A. Evaluation of the results of coal jigging process. In E3S Web Conf.; Mineral Engineering Conference MEC, 2017; Volume 18, p. 1030, doi:10.1051/e3sconf/201712301030.
13. Kaiser M. 1991 Investigations into the interactions of chemical agents during froth flotation of hardcoal. Proceedings of the International Conference on Coal Science, 16–20 September 1991, University of Newcastle-Upon-Tyne, United Kingdom: 953-956.
14. Dong, Z., Wang, R., Fan, M., Fu, X. Switching and optimizing control for coal flotation process based on a hybrid model. PLoS ONE 2017, 12, e0186553, doi:10.1371/journal.pone.0186553.
15. Bu, X.N, Xie, G.Y, Peng, Y.L. Chen, Y.R. 2016. Kinetic modeling and optimization of flotation process in a cyclonic microbubble flotation column using composite central design methodology. Int. J. Miner. Process. 157: 175-183.
16. Polat, M., Polat, H., Chander, S. 2013. Physical and chemical interactions in coal flotation. Int. J. Miner. Process. 72 (1-4): 199-213.
17. Sahu, L., Bhattacharya, S., Dey, S. 2019. Release analysis of coal fines: Evolution of the methodology and critical issues involved J. S. Afr. Inst. Min. Metall. 119, 6.
18. Wang, C., Wang, H., Fu, J., Liu, Y. 2015. Flotation separation of waste plastics for recycling—A review. Waste Management. Volume 41: 28-38.
19. Serranti S., Bonifazi G. 2019. Use of Recycled Plastics in Eco-efficient Concrete. A volume in Woodhead Publishing Series in Civil and Structural Engineering. Chapter 2. Techniques for separation of plastic wastes2019. ISBN 978-0-08-102676-2.
20. Treatise on Process Metallurgy Volume 3: Industrial Processes. 2014. doi.org/10.1016/C2010-0-67121-5.
21. Xing, Y., Gui, X., Liu, J., Cao, Y., Zhang, Y., Li, S. 2016. Flotation behavior of hard-to-separate and high-ash fine coal. Physicochem. Probl. Miner. Process. 52(2): 703−717.
22. Sokolovic J., Miskovic S. 2018. The effect of particle size on coal flotation kinetics: A review. Physicochem. Probl. Miner. Process., 54(4): 1172-1190.
23. Gaudin, A.M. Groh, J.O. Henderson, H.B. 1931. Effect of particle size in flotation. Am. Inst. Min. Metall. Eng. 1931.
24. Brozek, M., Mlynarczykowska, A. 2013. An analysis of effect of particle size on batch flotation of coal. Physicochem. Probl. Miner. Process. 49: 341–56.
25. Laskowski, J.S., G.H. Luttrell, G.H., Arnold, B.J. 2010. Coal flotation. XXV International Mineral Processing Congress (IMPC 2010), Brisbane, Australia.
26. Mohns, C.A. 1997. Effect of particle size on coal flotation kinetics. MSc. Thesis. Department of Mining Engineering, Queen's University, Kingston, Canada.

27. Abkhoshk, E., Kor, M., Rezai, B. 2010. A study on the effect of particle size on coal flotation kinetics using fuzzy logic. Expert Syst. Appl. 37 (7): 5201-5207.

28. Li, Y., Zhao, W., Gui, X., Zhang, X. 2013. Flotation kinetics and separation selectivity of coal size fractions. Physicochem. Probl. Miner. Process. 49: 387-395.

29. Ni, C., Xie, G., Jin, M., Peng, Y., Xia, W. 2016. The difference in flotation kinetics of various size fractions of bituminous coal between rougher and cleaner flotation processes. Powder Technol. 292: 210-216.

30. Liao, Y., Cao, Y., Liu, C., Zhao, Y., Zhu, G. 2017. Comparison of the effect of particle size on the flotation kinetics of a low-rank coal using air bubbles and oily bubbles. J. S. Afr. Inst. Min. Metall. 117 (6): 561-566.

31. Qu J., Tao X., Tang L., Xu N., He H. 2015. Flotation Characteristics and Particle Size Distribution of Micro-fine Low Rank Coal. Procedia Engineering 102: 159-166. DOI: 10.1016/j.proeng.2015.01.120

32. Kowol D., Łagódka M., Matusiak P., Gawliński A. 2014. Możliwości zastosowania procesu flotacji pianowej do wzbogacania "sedymentu" z wirówek sedymentacyjno-sitowych. KOMEKO, Innowacyjne i przyjazne dla środowiska techniki i technologie przeróbki surowców mineralnych. Bezpieczeństwo - Jakość - Efektywność, Instytut Techniki Górniczej KOMAG, Gliwice: 311-322; 0,62 ark. wyd., ISBN 978-83-60708-80-4

33. Kundel, H. 1983. Kohlengewinnung. Verlag Glückauf

34. Brzezina R., Sablik J. 1997. Investigations of two stage aeration of coal slurries In kolumn flotation. Proceedings of the XX Int. Min. Proc. Congress, Aachen. GDMB Clausthal – Zellerfeld.

35. Sablik J. 1998. Flotacja węgli kamiennych. Główny Instytut Górnictwa. Katowice.

36. https://www.miningpedia.cn/flotation/5-types-of-flotation-machines-working-principle.html [access: 26.10.2023]

37. http://www.innovator.com.pl/ [access: 26.10.2023]

38. Kowol D. i inni. 2021. Zwiększenie efektywności procesu wzbogacania miałów węgli koksowych w klasie 20(30)-0 mm w oparciu o zastosowanie nowoczesnych rozwiązań technologiczno-konstrukcyjnych ITG KOMAG (unpublished).

Zwiększenie efektywności procesu flotacji pianowej dla maksymalizacji produkcji koncentratów węgla koksowego w aspekcie zrównoważonej gospodarki surowcami naturalnymi

Węgiel koksowy z uwagi na jego ograniczoną dostępność oraz rolę i znaczenie stali jako surowca, który jest niezbędnym materiałem wykorzystywanym praktycznie we wszystkich gałęziach przemysłu, znajduje się od wielu lat na liście surowców krytycznych w UE. W artykule przedstawiono wyniki badań laboratoryjnych wpływu wybranych czynników (parametry nadawy, parametry procesowe, odczynnik) na skuteczność procesu flotacji, powszechnie stosowanej metody wzbogacania drobnych ziaren węgla koksowego. Duża liczba zmiennych i znaczące różnice w wynikach wyraźnie wskazują na konieczność prowadzenia szczegółowych badań przed każdym nowym zastosowaniem technologii wzbogacania flotacyjnego. Efektem tych badań powinien być dobór parametrów gwarantujących maksymalizację produkcji z punktu widzenia racjonalnej i zrównoważonej gospodarki zasobami przy zminimalizowaniu negatywnego oddziaływania efektów tego procesu na środowisko.

Słowa kluczowe: *zasoby mineralne, węgiel koksujący, flotacja pianowa, efektywność procesu*

Waste Management Analysis on the Example of a Leading University: VŠB-TUO (VŠB – Technical University of Ostrava)

*Oldřich ŠIGUT[1)], Leo KASPERČÍK[2)], Kamil KLACKO[3)], Martin ČECH[4)], Iva JANÁKOVÁ[5)], Martin TROJEK[6)], Jan JOSEFUS[7)], Tadeusz OLKUSKI[8)], Vladimír ČABLÍK[9)]**

[1)] VŠB-TUO; FMG; Department of Environmental Engineering; ORCID: 0009-0005-2154-5792
[2)] VŠB-TUO; FMG; Department of Environmental Engineering; ORCID: 0009-0001-2109-4531
[3)] VŠB-TUO; FMG; Department of Environmental Engineering
[4)] VŠB-TUO; FMG; Department of Environmental Engineering; ORCID: 0000-0003-1217-5062
[5)] VŠB-TUO; FMG; Department of Environmental Engineering; ORCID: 0000-0002-7892-9392
[6)] VŠB-TUO; FMG; Department of Environmental Engineering; ORCID: 0009-0004-6075-547X
[7)] VŠB-TUO; FMG; Department of Environmental Engineering; ORCID: 0009-0002-4863-1592
[8)] AGH University of Krakow; Faculty of Energy and Fuels; ORCID: 0000-0002-6256-9628
[9)] VŠB-TUO; FMG; Department of Environmental Engineering; ORCID: 0000-0001-8081-2348
* Corresponding author

http://doi.org/10.29227/IM-2024-01-102

Submission date: 10-05-2024 | Review date: 28-06-2024

Abstract

The paper concerns an analysis of waste management at VŠB – Technical University of Ostrava (VŠB-TUO). The paper focuses mainly on mixed municipal waste, and paper and cardboard waste, which make up the largest part of all waste generated at this university. The results of analyses of these three types of waste are presented. The analyses were carried out to determine the actual raw material composition of the contents of the collection bins and to determine how full they were on collection days. The studies were carried out within the framework of national waste legislation in line with European Union legislation. The results of these analyses served as the basis for the development of a waste management concept at the university.

Keywords: *waste management, municipal solid waste (MSW), mixed municipal waste (MMW), combustible waste, mixed municipal waste analysis, biodegradable waste (BDW)*

Introduction

Today's developed societies continue to struggle with a huge amount of waste generated, resulting in significant difficulties in waste disposal. The increase in waste generated seriously threatens human health and the environment. In order to promote efficient waste management, it is important to design and implement new tools that allow users to reduce the amount of waste generated and improve waste treatment. [1]

Today's universities can be compared to “small cities” with large areas and a wide range of human activities affecting the environment. State and international institutions require these universities to integrate sustainable strategies into all their activities in order to positively influence the social, economic, and environmental well-being of both their immediate surroundings and the wider environment. [2] The importance of universities in promoting sustainable development has been emphasised in various groundbreaking declarations including the Talloires Declaration (1990), the Halifax Declaration (1991), the Kyoto Protocol (1993), the Swansea Declaration (1993), the Copernicus Charta and others. [3]

VŠB – Technical University of Ostrava (VŠB-TUO) is a large university with an extensive campus and modern facilities. The total number of students is approximately 11,000. This number of students translates into the volumes of waste generated at the university. The purpose of this paper is to analyse the waste generated at VŠB-TUO and the current methods of waste disposal in a university environment. Particular attention is paid to mixed municipal waste and so-called combustible waste, which make up the largest part of waste generated at this university. The data obtained from the waste sampling process has been used to create a concept defining how the university will manage and treat waste. In practice, this means that, based on a study of the types and quantities of waste generated by the university, a proposal was developed for a strategy to manage waste in an efficient and environmentally-friendly way, and to minimise its impact on the environment and promote sustainability.

Current status

VŠB-TUO generates approximately 600 tonnes of waste annually [4,5,6,7,8], which is generated during the daily activities of students and university staff, or visitors to the area. According to Decree No. 8/2021 (Journal of Laws) on the catalogue of waste and the assessment of waste properties (Waste Catalogue), as amended [9], this waste is designated as "Other waste" (O), which is the largest amount in the university area, and "Hazardous waste" (H).

The largest part of the remaining waste is mixed municipal waste (hereinafter “MMW”) with the catalogue number 20 03 01, combustible waste which is listed under catalogue number 20 01 01 and bulky waste with catalogue number 20

Tab. 1. Observed SKO fractions depending on the classification level [15]

Tab. 1. Zaobserwowane frakcje SKO w zależności od poziomu klasyfikacji [15]

Poziom I	Poziom II	Poziom III
Paper	Packaging	Cardboard
		the remaining
	Not packaging	Magazines, leaflets, and similar papers
		Newspaper and office
	Other	
Plastics	Packaging	Foils
		Hard plastics
		PET colorless
		Colored PET
		PS
		the remaining
	Not packaging	
Bio	Kitchen	Fruits and vegetables
		Plant, fruit and vegetable remains
		Other foodstuffs
	From gardens and parks	
Wood	Only modified	
Glass	Packaging	
	Not packaging	
Metals	Packaging	Ferromagnetic
		Aluminum
		The remaining
	Not packaging	Ferromagnetic
		The remaining
Textiles	Clothes	
	Other textile materials	
Composite and beverage cartons	Beverage cartons (four-packs)	
	The remaining	
Electrical equipment		
Batteries and accumulators		
Other waste	Diapers and hygiene waste	
	Mineral waste	
	NO-other potentially hazardous waste	
	Composite products	
	Other	
Share less than 400 mm		
Share below 20 mm		Ash
		Other organic substances
Share less than 10 mm		Ash
		Other organic substances

Tab. 2. Collection dates and sample weights of 20 03 01 – Municipal solid waste (container)

Tab. 2. Daty odbioru i masa próbek 20 03 01 – Stałe odpady komunalne (pojemnik)

Date	19.05.2023	01.06.2023	13.07.2023	04.08.2023	13.09.2023	11.10.2023
Mass [kg]	18.7	39.1	24.5	17.1	61.6	45.2

Tab. 3. Collection dates and sample weights of 20 01 01 – Combustible waste (container)

Tab. 3. Daty odbioru i masa próbek 20 01 01 – Odpady palne (pojemnik)

Date	19.05.2023	01.06.2023	13.07.2023	04.08.2023	13.09.2023	11.10.2023
Mass [kg]	18.7	39.1	24.5	17.1	61.6	45.2

Tab. 4. Sampling period and total mass of 20 01 01 – Paper and cardboard (bag collection)

Tab. 4. Okres pobierania próbek i masa całkowita 20 01 01 – Papier i tektura (odbiór worków)

Date	24.05.2023	14.06.2023	12.07.2023	04.08.2023	19.09.2023	04.10.2023
Mass [kg]	17.3	27.4	18.4	17.9	38.3	46.5

Tab. 5. Sampling period and total mass of 20 03 01 – Municipal solid waste (bag collection)

Tab. 5. Okres pobierania próbek i masa całkowita 20 03 01 – Stałe odpady komunalne (zbieranie worków)

Sampling period	September – October 2023
Total mass [kg]	13.36

03 07. This waste is generated continuously throughout the year. Irregularly generated waste includes, for example, construction and demolition waste, and biodegradable waste from environmental maintenance. [10]

Waste management at VŠB-TUO is subject to the Waste Management Directive TUO_SME_05_005 version H [11], which sets out the obligations of waste producers at the university. Decision No. 194/22/OH, reference number SMO/804179/22/OŽP/MA, dated 30.11.2022, issued by the City of Ostrava (MMO). [12]

The decision approves the waiver of selective waste collection at VŠB-TUO. The decision could have been issued on the basis of § 30(5) of the Act No. 541/2020 on Waste [13] and is currently in force until 30 November 2026. [11,12] The omission applies to the following types of waste [11]: VŠB-TUO is obliged to classify mixtures of waste into the

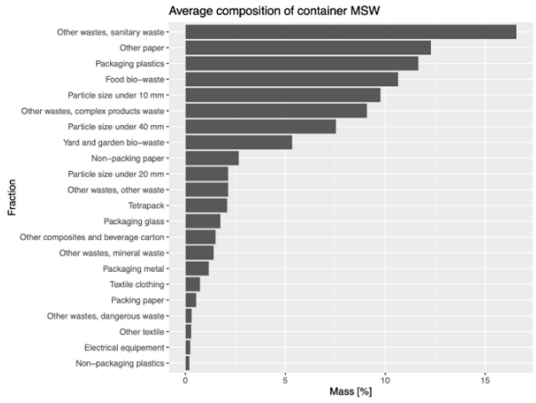

Fig. 1. Average raw material composition of mixed municipal waste in containers
Rys. 1. Średni skład surowcowy zmieszanych odpadów komunalnych w pojemnikach

predominant type of waste for record-keeping purposes and to classify the remaining mixture of unusable waste into the second category under the catalogue number 20 03 01 Mixed municipal waste". [11]

University waste management system

Within the university (e.g. in the Rector's building), waste is collected by staff and students in waste bins of different capacities (e.g. 50 dm³ or 25 dm³), which are placed in corridors, teaching rooms, offices, and lecture halls. The bins are labelled according to the type of waste that is collected in them (e.g. as "municipal" (MW) or "paper+plastic" (PP)).

From the waste bins located in the university buildings, the cleaning service staff collect selectively into three-ply paper sacks, which are then put into the bins according to the type of waste. These sacks are reused multiple times for their intended purpose. From the sacks labelled as paper and plastic, cleaning services staff segregate clean packaging paper and plastic waste, which is collected separately in a paper bin and a plastic bin. The remaining contents are stored in bins labelled as combustible waste, where smaller wood waste is also stored. It is this combustible waste and MMW that will receive the most attention in this paper. [14]

A total of 100 bins for waste types 20 01 01 and 20 03 01 [14] are available at VŠB-TUO in Ostrava-Poruba: 53 1100 dm³ bins for MMW, 2 240 dm³ bins for MMW, 7 120 dm³ bins for MMW, 37 1100 dm³ bins for combustible waste, 1 240 dm³bin for combustible waste. The remaining bins on the site are for clean waste, i.e. 8 240 dm³ bins for plastics and 8 240 dm³ bins for paper and cardboard. [15]

The contents of the MMW and combustible waste bins are collected from the university campus three times a week. The combustible waste (20 01 01), once collected from the site, is further processed (crushing, homogenisation) and used as certified fuel, which is burned in e.g. cement plants. MMW is no longer used and is landfilled. [15]

As part of the optimisation of waste management at VŠB--TUO, the project Supporting the Environmental Aspects of University Operations was implemented in 2022, which is in line with the university's strategic plan. As part of this project, an analysis of the production of all types of waste at the university over the past five years was carried out, with a particular focus on MMW and combustible waste, which account for the largest part of annual production. The results of the project identified deficiencies in waste segregation and deviations in waste records. The data from the continuous records are reported by an employee of the maintenance services to the Integrated System for the Performance of Reporting Obligations (ISPRP), set up by the Ministry of the Environment. The system is managed by the Czech Environmental Information Agency (CENIA) and its task is to provide administrative support, coordination, and development of this information system. Data is therefore managed in the ISPRP system, and the results from this data then allow the development of the production of individual types of waste and changes in waste production over different periods of time to be monitored. Forecasts of waste generation can then be made using mathematical models. [5]

In 2023, VŠB-TUO participated in the student grant competition for the Waste Management Optimisation project, which is based on the project Supporting the Environmental Aspects of University Operations and focuses on the analysis and optimisation of waste management at VŠB-TUO.

Methodology

Ministry of Environment (MŽP) methodology for determining the composition of MMW, MW

The methodology for determining the composition of MMW, MW is issued by the Ministry of the Environment (MŽP) in order to obtain and then statistically process information on individual components of MMW. [16] "The purpose of the methodology is to establish procedures that allow comparability and reproducibility of the results of field surveys aimed at determining the composition of MMW, but also of other types of MW (separately concentrated MW components)". [16]

The methodology divides the selected waste into three levels, from basic classification to detailed waste. The methodology identifies the first and second levels of sorting as mandatory. It then divides the waste into different fractions depending on the material. The waste is sorted on welded sieves with a mesh size of 40 × 40 mm, 20 × 20 mm, and 10 × 10 mm. Waste with a diameter greater than 40 mm is sorted by fraction and then shaken on individual sieves. The individual oversieve, intersieve and subsieve fractions are weighed and their weights recorded. [16]

The purpose of the waste sampling at the university was to determine the quality of sorting of individual components of

Fig. 2. Fraction of construction waste in a container for SKO
Rys. 2. Frakcja odpadów budowlanych w kontenerze dla SKO

municipal waste, and then to assess the possibility of proper waste management on the VŠB-TUO campus. The sampling process was carried out according to the methodology described above for determining the composition of MMW, MW. The sampling concerned 20 03 01 MMW, 20 01 01 Combustible waste and 20 01 39 Plastics.

Samples were taken in the area of the university's Rector's building, where waste is mainly generated in offices, meeting rooms, corridors, and toilets. This area is home to the largest container yard, where the majority of waste from university buildings is collected and taken away.

Staff and students separate their waste into bins labelled "municipal waste" and "paper and plastic". In the morning, the cleaning person segregates this waste into paper sacks, which are then taken to the outside containers. The sacks labelled "paper and plastic" are put into the combustible waste bin.

Sampling of the mixed municipal and combustible waste that was taken from the containers took place between May 2023 and October 2023 at monthly intervals. A total of six MMW containers with a total weight of 206.20 kg and six combustible waste containers with a total weight of 165.8 kg were sampled. In addition, MMW and paper and cardboard waste samples were taken from the sacks on an irregular basis, prior to being placed into the containers.

Sampling results

The figures for individual bin collections and their weights are shown in Tables 2 and 3. The number of retrievals from paper sacks for MMW waste, and paper, and plastics and their total weight are provided in Tables 4 and 5.

Figure 1 shows graphically the determined average raw material composition of the contents of the MMW bins. These average values were calculated from the six analyses carried out of the total weight of 206.20 kg of waste. Figure 2 clearly shows that the composition was dominated by the following: other waste (mainly sanitary waste), contaminated paper waste (mainly contaminated office paper), packaging plastic waste, biodegradable waste, and finer mesh fractions. The larger share of the remaining waste fraction was due to the presence of mineral waste (building materials, plaster, bricks), which, however, should be placed in large-capacity bins.

The largest part of the subsieve fraction consisted of smaller pieces of food, tea bags and paper up to 40 mm in diameter. The fraction up to 20 mm mainly contains soiled paper and smaller pieces of food, while the fraction up to 10 mm mainly consists of bio-waste such as coffee beans and dust. The samples also contained electrical equipment, including extension, and connecting cables, and wire residues.

Figure 3 shows graphically the determined average raw material composition of the contents of the combustible waste bins. These average values were calculated from the six analyses carried out of a total weight of 165.8 kg of waste. As can be seen from this sample, wastes were found that should not be placed in the 20 01 01 waste bins. These were specifically: glass, bio-waste, and electrical equipment (cables) and from the other waste group (minerals): waste, composite products such as shoes and bags, sanitary waste, ND). [16]

Figure 4 shows the average MMW raw material composition in the sacks before being put into the containers. The subsieve fraction was mainly of biological origin and included coffee beans and smaller pieces of food. The paper and cardboard fraction was mainly contaminated paper, including shredded office paper. The weight of this sample was 21.68 kg.

Figure 5 graphically shows the average raw material composition of the paper and cardboard waste collected from the sacks prior to being placed in the combustible waste bin. The total weight of the sample was 13.61 kg. Unlike the sample from the bin, it does not contain glass fractions. The sample consisted mainly of the paper and cardboard fraction, where shredded office paper predominated. The second largest component was plastic waste, consisting mainly of packaging material. Smaller pieces of bio-waste, coffee beans and pieces of paper from shredders were also present in all the subsieve fractions.

Figure 6 graphically shows the raw material composition of the waste collected from the plastic waste bin. The total weight of the sample was 13.81 kg. As can be seen, this sample included waste that should not be put into the plastic waste bins 20 01 39. These were in particular: composite products, soiled paper, biodegradable waste, metal waste, glass, wrapping paper and textile waste. The subsieve fractions mainly contained smaller pieces of bio-waste and coffee beans.

From the figures above, it can be seen that all MMW samples are dominated by the paper and cardboard fraction as well as plastic waste. In the paper and cardboard fraction, there was paper from shredders, ordinary office paper and wrapping paper. Although this type of paper is recyclable, by being concentrated in the bins designated for MMW, it is mixed with other fractions such as the bio-waste fraction, resulting in contamination and making it non-recyclable. There was also a significant proportion of the plastics fraction, which could be segregated appropriately into bins designated for plastic waste. There was a glass fraction in almost all samples. Glass should be disposed of separately in the glass waste bins located in the corridors of the University. For the MMW samples and combustible waste from the containers, waste elec-

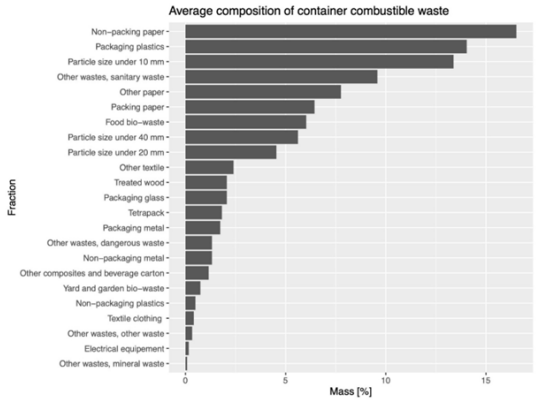

Fig. 3. Average raw material composition of combustible waste in containers
Rys. 3. Średni skład surowcowy odpadów palnych w pojemnikach

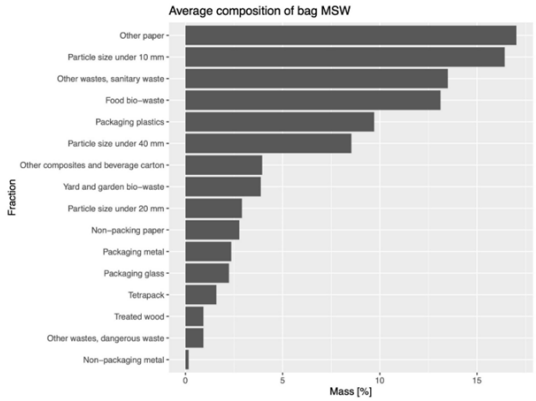

Fig. 4. Average raw material composition of mixed municipal waste in bags
Rys. 4. Średni skład surowcowy zmieszanych odpadów komunalnych w workach

trical equipment was found, including connection and power cables. These should also be separated for proper disposal or recycling. A one-off sampling of a plastic waste bin detected undesirable waste fractions, especially other waste, especially composite products, but also paper, metal, glass, textiles, and biodegradable waste.

The analyses also revealed that the containers are not filled effectively and are disposed of incompletely. Data from OZO Ostrava a.s. shows that the average weight of waste in a 1.1 m^3 bin is 54 kg for mixed municipal waste and 27 kg for combustible waste. The Czech Agency for Environmental Information (CENIA) reports [18] that the specific mass of mixed municipal waste is 160 kg per 1 m^3. In addition, it can be seen from Table 5 that during sampling carried out at VŠB TUO as part of the Waste Management Optimisation project at VŠB TUO, the average weight of waste in 1.1 m^3 bins on the day of collection was 34.4 kg for MMW and 30.2 kg for combustible waste.

From the above data, it can be concluded that the filling of bins is not optimal. The optimal solution would therefore be to obtain underground containers with a larger volume, equipped with a hydraulic press. This would lead to the export of filled containers and, at the same time, and to making the space on the VŠB-TUO campus more visually attractive.

Conclusions

The result of the analysis was that waste segregation at the university was not effective. Action has been taken to avoid these shortcomings. Inconsistent labelling of the collection bins is also a problem.

During sampling, it was found that the contents of the waste bins partly do not correspond to the composition of the waste that should be placed in the bins. Electrical equipment was found in the containers for MMW, which should be put in the bins intended for electrical waste, and mineral waste, which should be collected in large-capacity bins. A similar case was also found in the bins for combustible waste, where electrical waste was found. In addition, it was noted that there was a significant component of paper and cardboard in the MMW containers, including contaminated office paper. If this paper had been placed separately in the bins designated for paper and cardboard, it would not have needed to be mixed with other MMW components.

Proposals for measures to improve waste management at VŠB-TUO

- Increased education of operational services staff, university staff and students in the field of waste management.
- Switching to an underground bin system equipped with a hydraulic press as part of making the university grounds more visually attractive and in cooperation with the waste collection company. The advantage of underground containers is primarily to save space. Although they look like small rubbish bins at the top, their volume under the surface is usually

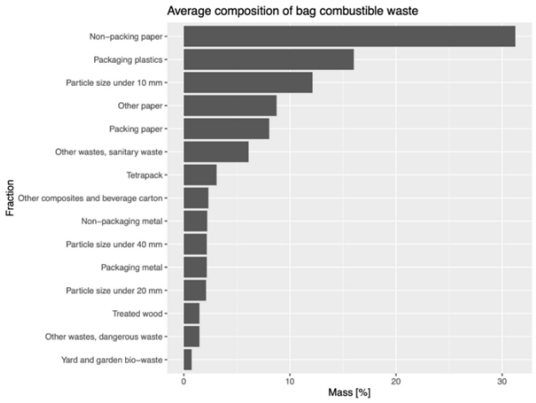

Fig. 5. Average raw material composition of combustible waste in bags
Rys. 5. Średni skład surowcowy odpadów palnych w workach

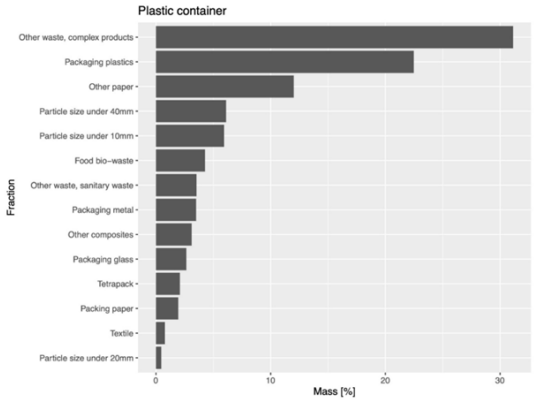

Fig. 6. Average raw material composition of plastic waste in a container
Rys. 6. Średni skład surowcowy odpadów tworzyw sztucznych w pojemniku

Tab. 6. Average mass of MSW and combustible waste in container (1m³) on the day of its export
Tab. 6. Średnia masa MSW i odpadów palnych w kontenerze (1m³) w dniu ich wywozu

Data origin	OZO Ostrava a.s.		Data obtained by sampling	
Types of waste	MSW	combustible waste	MSW	combustible waste
Average mass [kg]	54	27	34.4	30.2

three times that of a regular bin. Another advantage is undoubtedly making the surroundings more visually attractive, which consists primarily in the elimination of rubbish lying on the surface, but also in the minimisation of unpleasant odours, especially during the summer months. Due to their large volume, as well as the lower temperatures underground, they do not need to be emptied as often as classic above-ground containers.

- Ensuring selective collection of selected municipal waste (paper, plastics) preferably by 2025, but by 2030 at the latest. [14]. The transition to selective collection will therefore be smooth and there will be sufficient time for this.

Acknowledgement

This study was supported by student grant project SP2023/073 – Optimization of waste management VŠB-TUO.

Literatura – References

1. GALLARDO, A.; EDO-ALCÓN, N.; CARLOS, M. a RENAU, M. The determination of waste generation and composition as an essential tool to improve the waste management plan of a university. Online. Waste Management. 2016, roč. 53, s. 3-11. ISSN 0956053X. Dostupné z: https://doi.org/10.1016/j.wasman.2016.04.013. [cit. 2023-11-30].
2. ADENIRAN, A.E.; NUBI, A.T. a ADELOPO, A.O. Solid waste generation and characterization in the University of Lagos for a sustainable waste management. Online. Waste Management. 2017, roč. 67, s. 3-10. ISSN 0956053X. Dostupné z: https://doi.org/10.1016/j.wasman.2017.05.002. [cit. 2023-11-30].
3. GREYSON, James. An economic instrument or zero waste, economic growth and sustainability. Online. Journal of Cleaner Production. 2007, roč. 15, č. 13-14, s. 1382-1390. ISSN 09596526. Dostupné z: https://doi.org/10.1016/j.jclepro.2006.07.019. [cit. 2023-12-11].
4. Roční hlášení o produkci a nakládání s odpady za rok 2017, 2018. VŠB-TUO: 9556 – Provozní služby.
5. Roční hlášení o produkci a nakládání s odpady za rok 2018, 2019. VŠB-TUO: 9556 – Provozní služby.
6. Roční hlášení o produkci a nakládání s odpady za rok 2019, 2020. VŠB-TUO: 9556 – Provozní služby.
7. Roční hlášení o produkci a nakládání s odpady za rok 2020, 2021. VŠB-TUO: 9556 – Provozní služby.
8. Roční hlášení o produkci a nakládání s odpady za rok 2021, 2022. VŠB-TUO: 9556 – Provozní služby.
9. Vyhláška č. 8/2021 Sb., o Katalogu odpadů a posuzování vlastností odpadů (Katalog odpadů). In: Sbírka zákonů. 5.1.2021. ISSN 1211-1244.
10. HLAVATÁ, Miluše. Odpadové hospodářství. Ostrava: Vysoká škola báňská – Technická univerzita Ostrava, 2004. ISBN 978-80-248-0737-9.
11. Rozhodnutí č. 731/2004 č. j. ŽP/249.1/20119/2004. VŠB -TUO. 9556 – Provozní služby.
12. Odpadové hospodářství VŠB -TUO: TUO_SME_05_005 verze: G, 2022. VŠB -TUO: 9556 – Provozní služby.
13. Odpadové hospodářství VŠB-TUO: TUO_SME_05_005 verze: G, 2022. VŠB-TUO: 9556 – Provozní služby.
14. ČABLÍK, Vladimír; LAPČÍK, Vladimír; KASPERČÍK, Leo a KLACKO, Kamil. Podpora ekologických aspektů provozu univerzity: Odpadové hospodářství. Ostrava, 2022.
15. VŠB-vývozové dny, 2022. VŠB -TUO: 9556 – Provozní služby.
16. Metodika pro stanovení složení směsného komunálního odpadu z obcí a komunálního odpadu (Výsledek V4). [online]. In: Vysoké učení technické v Brně [cit. 2023-10-1]. Dostupné: https://www.mzp.cz/C1257458002F0DC7/cz/metodika_stanoveni_sko_ko/$FILE/OODP-V4_Metodika_slozeni_final-20211101.pdf
17. KLACKO, Kamil. Průměrná naplněnost sběrných nádob (1100 dm3) na SKO a spalitelný odpad [elektronická pošta]. Message to: oldrich.sigut@vsb.cz. 11. října 2023 07:15 [cit. 2023-10-11]. Osobní komunikace
18. Orientační přepočtová tabulka množství odpadů (aktualizace k 2.5.2007, aktualizace 13.5.2016). Online. Dostupné z: https://www.cenia.cz/wp-content/uploads/2019/02/Prepoctova_tabulka_07_2000_aktualizace_2016.pdf. [cit. 2023-12-18].

Analiza gospodarki odpadami na przykładzie wiodącej uczelni – VŠB-TUO

Artykuł dotyczy analizy gospodarki odpadami na Uniwersytecie Górniczo-Technicznym w Ostrawie (VŠB-TUO). W artykule zwrócono uwagę głównie na zmieszane odpady komunalne oraz odpady z papieru i tektury, które stanowią największą część wszystkich odpadów powstających w tej uczelni. Przedstawiono wyniki analiz tych trzech rodzajów odpadów. Analizy przeprowadzono w celu określenia rzeczywistego składu surowcowego zawartości pojemników zbierających oraz określenia stopnia ich zapełnienia w dniach odbioru. Badania przeprowadzono w ramach unijnego prawodawstwa dotyczącego odpadów. Wyniki tych analiz posłużyły jako podstawa do opracowania koncepcji gospodarki odpadami na uczelni.

Słowa kluczowe: *gospodarka odpadami, stałe odpady komunalne (TKO), zmieszane odpady komunalne (SKO), odpady palne, analiza zmieszanych odpadów komunalnych, odpady ulegające biodegradacji (BRO)*

Możliwości magazynowania gazu ziemnego i energii w utworach solnych na terenie Polski

Wacław ANDRUSIKIEWICZ[1)]

[1)] dr hab. inż., prof. AGH; Department of Mining Engineering & Occupational Safety, Faculty of Civil Engineering and Resource Management, AGH University of Krakow; email: andus@agh.edu.pl; ORCID: 0000-0002-4845-1404

http://doi.org/10.29227/IM-2024-01-103

Submission date: 13-05-2024 | Review date: 25-06-2024

Abstrakt

Bezpieczeństwo energetyczne państwa to m.in. zabezpieczenie potrzeb odbiorców w zakresie paliw i energii. Jednym z elementów polityki energetycznej jest infrastruktura magazynowa, która umożliwia przechowywanie zapasów gazu ziemnego oraz paliw. Jest realizowana poprzez magazyny powierzchniowe i podziemne. Szczególne ważna jest rola tych drugich z uwagi na oferowane pojemności, ale też możliwe do uzyskania parametry technologiczne procesu magazynowania.

Jednym z dogodnych miejsc do budowy magazynów podziemnych gazu i paliw są złoża soli kamiennej, w których wykonywane są kawerny magazynowe. Polska z racji korzystnego dostępu do solnych formacji geologicznych posiada w tym zakresie duże możliwości budowy podziemnej bazy magazynowej zarówno dla gazu ziemnego, jak i dla paliw płynnych.

Proces dekarbonizacji sektora energetycznego zmusza do poszukiwania nowych źródeł energii, które z czasem zastąpią w systemie energetycznym paliwa kopalne. Odpowiedzią na to wyzwanie stają się odnawialne źródła energii (woda, wiatr, słońce), których zaletą jest niewyczerpywalność, z drugiej zaś wadą ich niesterowalność z uwagi na uzależnienie od warunków klimatycznych/pogodowych.

W artykule omówiono możliwości budowy kawernowych podziemnych magazynów gazu oraz energii, zwracając uwagę na te drugie, jako przyszłościowe rozwiązania konieczne do wykorzystania w systemie energetycznym. Na tle bazy zasobowej soli kamiennej wskazano miejsca potencjalnej lokalizacji przyszłych magazynów kawernowych.

Słowa kluczowe: *złoża soli, kawerny solne, podziemne magazyny gazu, podziemne magazyny energii*

Wprowadzenie

Ustawowym celem polityki energetycznej państwa (PEP) jest zapewnienie bezpieczeństwa energetycznego rozumianego jako stan gospodarki, który umożliwia pokrycie bieżącego i perspektywicznego zapotrzebowania odbiorców na paliwa i energię w sposób technicznie i ekonomicznie uzasadniony, przy zachowaniu wymagań ochrony środowiska [16]. W 2021 r. został ogłoszony dokument Polityka energetyczna Polski do roku 2040 (PEP2040), w którym sprecyzowano 8 celów szczegółowych, obejmujących cały łańcuch dostaw energii – od pozyskania surowców, przez wytwarzanie i dostawy energii (przesył i rozdział), po sposób jej wykorzystania i sprzedaży [13]. Jednym z celów szczegółowych jest dywersyfikacja dostaw i rozbudowa infrastruktury sieciowej gazu ziemnego, ropy naftowej i paliw ciekłych.

W celu dalszego wzrostu bezpieczeństwa energetycznego państwa, założenia polityki energetycznej zakładają, że do sezonu zimowego 2030/2031 nastąpi rozbudowa podziemnych magazynów gazu. Planowane jest uzyskanie pojemności min. 4 mld m^3 (obecnie jest to ok. 3,3 mld m^3, tj. wzrost o blisko 1/3 aktualnej pojemności) oraz zwiększenie maksymalnej mocy odbioru gazu z instalacji magazynowych – z obecnych 53,5 mln m^3/dobę do min. 60 mln m^3/dobę (wzrost o ok. 1/6).

Gwałtowna zmiana sytuacji geopolitycznej w Europie, do której doszło na początku 2022 r., zmusiła wiele państw, w tym Polskę, do zweryfikowania stanu bezpieczeństwa energetycznego kraju. To z kolei wymusza aktualizację PEP2040, uwzględniając wcześniejsze założenia związane z dekarbonizacją energetyki. Miejsce węgla jako surowca energetycznego ma przejąć na pewien czas gaz ziemny, który docelowo będzie również eliminowany z rynku energii na rzecz odnawialnych źródeł energii (OZE) oraz energetyki jądrowej.

W tej perspektywie ważnym elementem mającym wpływ na bezpieczeństwo energetyczne państwa są zgromadzone rezerwy (zapasy) kluczowych nośników energii, w tym gazu ziemnego. Temu celowi służą podziemne magazyny gazu (PMG). Podejmowane są pierwsze próby przekształcania magazynów gazu na magazyny energii – w tym przypadku magazynowanym medium będzie wodór oraz powietrze.

Podziemne magazyny gazu

Magazynowanie gazu ziemnego może mieć charakter długoterminowy ze względów strategicznych na wypadek kryzysów (np. wojna, embargo, katastrofa), koniunkturalnych (związanych z ceną gazu na rynkach światowych) bądź sezonowy (wyrównanie popytu i podaży w zależności od pory roku). Może mieć też charakter krótkoterminowy (wyrównanie popytu szczytowego w okresie dobowym bądź kilkudniowym).

Klasyczne magazynowanie gazu ziemnego sprowadza się do budowy powierzchniowych zbiorników gazu [dotyczy tylko gazu w postaci skroplonej (LNG – Liquefied Natural Gas)], które narażone są na różnego rodzaju zagrożenia np. strategiczno-militarne. Zajmują przy tym tereny, które mogłyby być wykorzystane w inny sposób. Ponadto same w sobie stanowią potencjalne zagrożenie ekologiczne dla przyległego obszaru. Nie bez znaczenia są też koszty budowy i utrzymania takich magazynów, przy relatywnie niewielkiej kubaturze magazynowej.

Powyższe argumenty przemawiają za budową magazynów podziemnych różnych formacjach geologicznych, w tym złożach soli kamiennej.

Podziemny magazyn gazu to zbiornik o dużej pojemności magazynowej. Celem podziemnych magazynów gazu jest

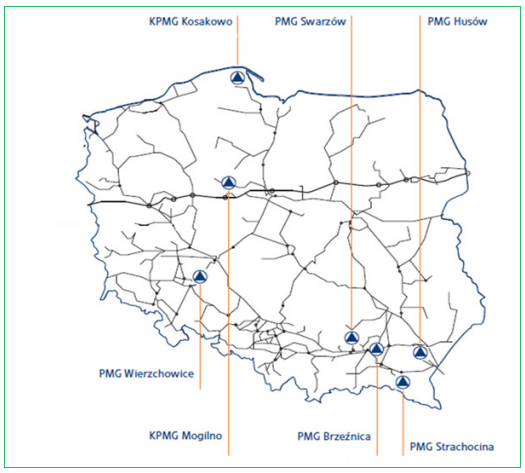

Rys. 1. Lokalizacja magazynów gazu w Polsce [5]
Fig. 1. Location of gas storage facilities in Poland [5]

Tab. 1. Podstawowe parametry magazynów gazu w Polsce [4]
Tab. 1. Basic parameters of gas storage facilities in Poland [4]

Magazyn	Pojemność czynna		Dobowa maksymalna moc		Dobowa maksymalna moc	
	mln m³	GWh	mln m³	GWh	mln m³	GWh
PMG Wierzchowice	1 300	14 729	9,60	107,5	14,40	158,4
PMG Husów	500	5 650	4,15	46,7	5,76	64,6
PMG Strachocina	460	5 212	3,84	43,7	3,36	37,9
PMG Brzeźnica	100	1 126	1,44	16,2	1,44	16,1
PMG Swarzów	90	1 013	1,00	11,2	0,93	10,4
PMG razem	***2 450***	***27 730***	***20,03***	***225,3***	***25,89***	***287,4***
KPMG Mogilno	581	6 471	9,60	106,9	18,00	200,5
KPMG Kosakowo	295	3 291	2,40	26,8	9,60	107,0
KPMG razem	***876***	***9 762***	***12,00***	***132,7***	***27,60***	***307,5***
ŁĄCZNIE	**3 326**	**37 492**	**32,03**	**358,0**	**53,49**	**594,9**

PMG – podziemny magazyn gazu w sczerpanym złożu gazu ziemnego
KPMG – kawernowy podziemny magazyn gazu w złożu soli kamiennej

sezonowe oraz strategiczne przechowywanie gazu ziemnego, co przyczynia się do zwiększenia niezawodności systemów gazowniczych i bezpieczeństwa energetycznego regionu oraz kraju.

Wyróżnia się trzy rodzaje zbiorników [19]:

- porowo-szczelinowe, do których zalicza się przestrzenie w sczerpanych lub częściowo wyeksploatowanych złożach węglowodorów oraz zawodnione struktury geologiczne;
- kawernowe, wykonane w pokładowych lub wysadowych utworach solnych;
- kubaturowe, poprzez wykorzystanie wyeksploatowanych kopalń np. węgla kamiennego, ale także w groty skalne.

Do tych zbiorników może być wtłaczany gaz pod odpowiednim ciśnieniem, który w normalnych warunkach zajmuje objętość miliardów metrów sześciennych.

W świetle ustawy [15] ten sposób magazynowania określany jest jako „…podziemne bezzbiornikowe magazynowanie substancji…" i dotyczy nie tylko gazu ziemnego, ale także np. ropy naftowej, wodoru, powietrza itp.

Pierwszy podziemny magazyn gazu powstał w 1915 r. w rejonie Ontario (Kanada). W krótkim czasie powstało ich kilkanaście na terenie USA. Polska w tym zakresie była pierwszym państwem europejskim, która już w 1954 r. stworzyła podziemny magazyn gazu w wyeksploatowanym złożu gazu ziemnego Roztoki koło Jasła. Utworzony wówczas magazyn miał pojemność ok. 35,5 mln m³ gazu i funkcjonował do 1980 r.

Na koniec 2023 r. na świecie działało 678 podziemnych magazynów gazu, z czego 446 w Ameryce Północnej, a 139 w Europie. Łączna pojemność wszystkich zbiorników wynosiła 429 mld m³, z czego 38% na terenie Ameryki Północnej, a 26% w Europie [2]. Na podstawie analizy dostępnych źródeł [2] [1] szacuje się, że w kawernach solnych zlokalizowano ok. 100 magazynów gazu (na kawernowy podziemny magazyn gazu może składać się od jednej do nawet kilkudziesięciu kawern) stanowiących ok. 8% globalnej pojemności PMG. Aktualnie w Polsce działa 7 magazynów – Rys. 1, a ich łączna pojemność wynosi ok. 3,3 mld m³ – Tab. 1.

Formacje solne i ich rozmieszczenie na terenie Polski

Na terenie Polski wyróżnia się trzy formacje solonośne: mioceńską, triasową oraz cechsztyńską [10]. Nie jest przesadą stwierdzenie, że sól kamienna zalega niemal na całym terytorium kraju, kwestią jest tylko głębokość, na jakiej występuje.

Mioceńskie sole kamienne występują w zapadlisku przedkarpackim i są reprezentowane przez 7 złóż, w tym złoża Wieliczka, Barycz, Łężkowice i Bochnia, gdzie eksploatacja została zakończona. Pozostałe 3 – Rybnik, Siedlec i Wojnicz, z racji dużej głębokości, skomplikowanej budowy geologicznej, zmiennej miąższości, zagrożenia wodnego i gazowego nie są brane pod uwagę jako potencjalnie możliwe do wykorzystania w kierunku magazynów gazu ziemnego [8].

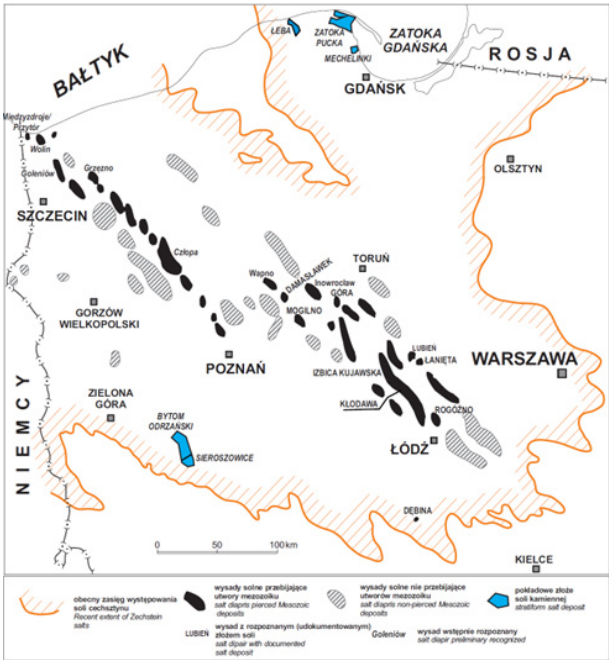

Rys. 2. Rozmieszczenie cechsztyńskich złóż soli w Polsce [7]
Fig. 2. Distribution of Zechstein salt deposits in Poland [7]

Złoża triasowe są zlokalizowane w dwóch rejonach Polski: pomiędzy Gorzowem Wielkopolskim i Zieloną Górą oraz pomiędzy Poznaniem i Łodzią. Zalegają na głębokości co najmniej 1100 m, a ich miąższość nie przekracza 25 m. Z tych dwóch powodów złoża te nie są uwzględniane w bilansie surowcowym Polski, jako że nie mają znaczenia gospo¬darczego, a z racji niewielkiej miąższości nie nadają się do budowania w nich kawern magazynowych gazu [10].

Cechsztyńska formacja solonośna stanowi około 93% udokumentowanych zasobów bilansowych soli kamiennej w Polsce. Osady solne tej formacji zajmują 2/3 powierzchni Polski i stanowią podstawowe źródło jej pozyskiwania. Złoża cechsztyńskie o znaczeniu gospodarczym można podzielić na trzy podstawowe rejony występowania: północny – obejmujący wyniesienie Łeby, środkowopolski pomiędzy Łodzią a Szczecinem, oraz południowo-zachodni obejmujący obszar Legnicko-Głogowskiego Okręgu Miedziowego – Rys. 2.

Sole cechsztyńskie występują w postaci dwóch form złożowych: pokładowej oraz jako wysady. Forma pokładowa jest charakterystyczna dla rejonu północnego oraz południowo-zachodniego, natomiast rejon środkowopolski stanowią wysady solne.

Największe złoża pokładowe rozpoznano w rejonie północnym [9]. Są to głównie sole najstarsze (Na1) budujące pokład o miąższości ponad 220 m, zalegający na głębokości od 490 do 1285 m. W obrębie tego pokładu rozpoznano w kategorii C1 i C2 trzy jego fragmenty: złoże Łeba o powierzchni około 50 km², złoże Zatoka Pucka o powierzchni około 100 km² oraz złoże Mechelinki o powierzchni około 9 km².

Złoże w rejonie północnym charakteryzuje się stosunkowo prostą budową i niewielkim stopniem zaangażowania tektonicznego. Zlokalizowane pomiędzy dwoma warstwami anhydrytu stanowiącego bardzo dobre horyzonty izolacyjne posiada dość jednolity stan mineralny.

W chwili obecnej zagospodarowywane jest jedynie złoże Mechelinki (rejon Kossakowa) w kierunku kawernowego podziemnego magazynu gazu. Perspektywicznie istnieje możliwość zagospodarowania złoża w kierunku KPMG w rejonie Władysławowa, Jastrzębiej Góry, Łebcza, Lisewa, Pucka i Białogardy. W rejonach tych miąższość złoża wynosi od 130 do 200 m, a głębokość zalegania mieści się w przedziale od 620 do 820 m.

Drugim rejonem występowania soli cechsztyńskich w formie pokładowej jest rejon południowo-zachodni (por. Rys. 2). Jest to monoklina przedsudecka, a sól kamienna występuje w nadkładzie rud miedzi na obszarze LGOM. W kategorii B rozpoznano fragment tej formacji należący do złoża Kaźmierzów na obszarze górniczym Sieroszowice I. Na obszarze tym występują najstarsze sole kamienne (Na1). Pokład o zmiennej miąższości, od kilkunastu do 200 m zawiera czystą sól kamienną o zawartości NaCl od 75,56 do 99,82%, średnio 98%. Pokład zalega na głębokości od 830 do 1270 m, nad pokładem rudy miedzi, od którego odizolowany jest warstwą anhydrytu dolnego (A1d), natomiast strop pokładu zamyka anhydryt górny (A1g). Pokład soli jest silnie zaburzony tektonicznie z pojawiającym się anhydrytem śródsolnym (A1s).

Na terenie LGOM w jego północno-zachodniej części występują jeszcze trzy złoża soli młodszych o miąższości 30–110 m występujących na głębokości około 1230 m (Na3) oraz 1340–1380 m (Na2), natomiast złoże soli (Na4) o miąższości do 44 m zalega 1100–1280 m poniżej poziomu terenu. Pokłady te – podobnie jak pokład soli najstarszych (Na1) – charakteryzują się skomplikowaną budową i tektoniką. Złoża te nie są obecnie zagospodarowane górniczo, choć najbardziej miąższe części pokładów soli mogą być brane pod uwagę jako potencjalne miejsce do KPMG, np. [14].

Trzeci rejon – środkowopolski – w istotny sposób odbiega w swojej formie i budowie od złóż tej samej formacji występujących w rejonach północnym i południowo-zachodnim. Jest to pas wysadów solnych rozciągających się od Łodzi po Szczecin (por. Rys. 2). Udokumentowano 9 wysadów, wśród których dwa zostały wykreślone z rejestru zasobów, a to za

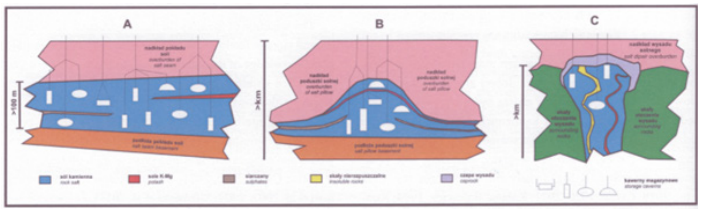

Rys. 3. Kawerny solne w trzech typach wystąpień solnych: A – pokład, B – poduszka solna, C – wysad [6]
Fig. 3. Salt caverns in three types of salt occurrences: A – seam, B – salt cushion, C – diapir [6]

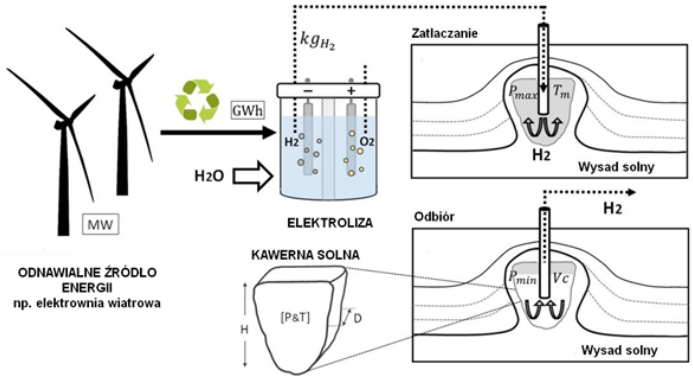

Rys. 4. Schemat wytwarzania, zatłaczania i odbioru wodoru [17]
Fig. 4. Scheme of hydrogen production, injection and collection [17]

przyczyną istniejących wcześniej, a obecnie zlikwidowanych kopalń w Wapnie i Inowrocławiu.

Aktualnie roboty górnicze prowadzone są na trzech wysadach: Mogilno, Góra i Kłodawa.

W dwóch pierwszych Inowrocławskie Kopalnie Soli „Solino" S.A. prowadzi eksploatację otworową „na mokro", a powstałe kawerny ukierunkowane są na podziemne magazyny paliw płynnych i gazu. W wysadzie kłodawskim od 1956 r. nieustannie wydobywa sól metodą „na sucho" Kopalnia Soli „Kłodawa" S.A., prowadząc roboty górnicze w 6 polach na głębokości od 475 do 820 m.

Możliwość budowy kawerny magazynowej w złożu soli zależy od wielu czynników. Ponieważ są to przestrzenie powstałe w procesie ługowania, istotnym czynnikiem jest podatność skał solnych na ługowanie. O ile sole kamienne i potasowo-magnezowe charakteryzują się wysoką lub bardzo wysoką podatnością na ten proces, tak występujące w złożach solnych skały węglanowe, siarczanowe itp. już ługowalne nie są. W związku z tym pierwszą przesłanką w wyborze lokalizacji kawerny będzie brak występowania soli potasowo-magnezowych (z uwagi na zbyt dużą podatność na ługowanie w stosunku do soli kamiennych) oraz skał nieługowalnych.

Równie istotną kwestią jest forma złoża. Złoża solne występują w formie pokładów, poduszek solnych i wysadów (diapirów) – Rys. 3.

Projektując kawernę w złożu pokładowym należy przy ustalaniu jej lokalizacji znaleźć takie miejsce, w których nie będą występowały sole potasowo-magnezowe oraz skały nieługowalne. Należy przy tym zwrócić uwagę na konieczność pozostawienia calizn solnych wokół kawerny, stanowiących filary międzykawernowe oraz stropową i spągową półkę bezpieczeństwa (por. Rys. 3A). Złoża pokładowe umożliwiają lokalizację wielu kawern w danym rejonie, jednak ich pojemność będzie uzależniona od miąższości pokładu, co przekłada się na wysokość kawerny. Złoża pokładowe wydają się być atrakcyjną lokalizacją dla kawern magazynowych z uwagi na stosunkowo prostą budowę geologiczną. Ograniczeniem może jest na ogół miąższość pokładu. W chwili obecnej eksploatowanych jest 10 kawern składających się na KPMG Kosakowo, wykonanych w złożu pokładowym.

Forma złożowa w postaci poduszki solnej wydaje się atrakcyjniejsza z uwagi na lokalnie zwiększoną miąższość pokładu (por. Rys. 3B), co może mieć bezpośredni wpływ na pojemność kawerny. Jest to jednak forma o bardziej skomplikowanej budowie wewnętrznej niż pokład – można spodziewać się wystąpień soli potasowo-magnezowych oraz utworów nieługowalnych. Kolejną trudność sprawia szczegółowe rozpoznanie geologiczne z uwagi na dużą głębokość zalegania oraz nieregularność złoża w rejonie poduszki. Z tych powodów obecnie nie przewiduje się wykonywania kawern w poduszkach solnych.

Atrakcyjną formą złożową dla posadowienia kawern magazynowych są wysady (diapiry) solne (por. Rys. 3C). Choć charakteryzują się skomplikowaną budową wewnętrzną, w tym wystąpieniami soli potasowo-magnezowych oraz utworów skalnych nieługowalnych, to wskutek rozpoznania robotami wiertniczymi można znaleźć lokalizacje, w których w całym profilu przyszłej kawerny występują miąższe i mniej więcej jednorodne utwory soli kamiennej. W takiej sytuacji możliwe jest wykonanie kawerny o znacznej wysokości, nawet ok. 1 km. Obecnie działający KPMG Mogilno eksploatuje 14 kawern wykonanych w wysadzie solnym.

Kawerna solna jako magazyn gazu ziemnego

Magazynowanie ciekłych węglowodorów w kawernach solnych uzyskanych w procesie ługowania zostało opatentowane w Niemczech w 1916 r., ale po raz pierwszy zastosowane dopiero w połowie XX w. (USA i Wielka Brytania). Techno-

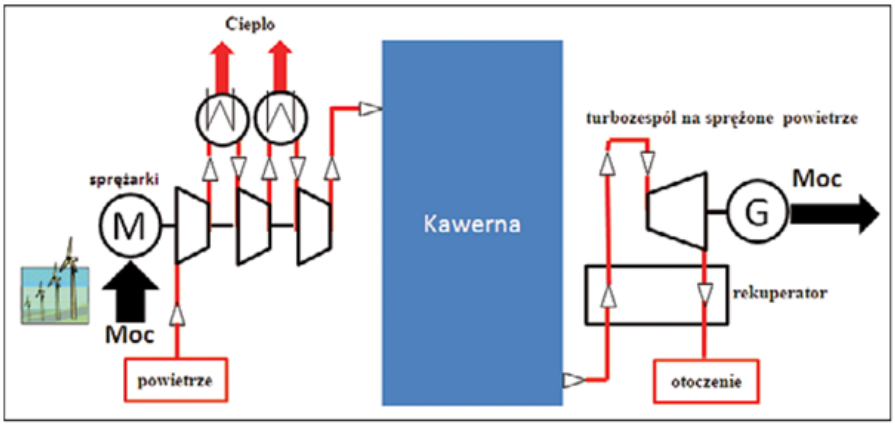

Rys. 5. Schemat sprężania powietrza i jego wykorzystania w turbinach [20]
Fig. 5. Diagram of air compression and its use in turbines [20]

logia ta zaczęła się gwałtownie rozwijać, a magazynowanym medium stał się również gaz ziemny. Szacuje się, że w chwili obecnej na świecie eksploatowanych jest ok. 1,5 tys. kawern ługowniczych w złożach soli. W Europie wykorzystywane są głównie na potrzeby magazynowania gazu ziemnego.

Niewątpliwie zalety tego sposobu magazynowania wynikają z szeregu czynników, które wskazują właśnie złoża soli kamiennej jako najkorzystniejsze środowisko, a wynikają z [11]:

- powszechności występowania złóż soli w wielu krajach;
- specyficznych warunki hydrogeologiczne panujące w złożach solnych – szczelność górotworu solnego;
- korzystnych właściwości geomechaniczne soli kamiennej, tj. zwięzłość, nieprzepuszczalność, plastyczność odkształceń;
- obojętności chemicznej soli względem większości magazynowanych substancji;
- dużej miąższości złóż solnych, umożliwiająca budowę magazynów podziemnych znacznej objętości.

Magazynowanie podziemne w znacznym stopniu eliminuje bądź ogranicza niebezpieczeństwa i uciążliwość dla środowiska, jaką stwarza magazynowanie powierzchniowe. Szczególnie istotne są trzy aspekty:

- bezpieczeństwo – podziemny magazyn jest mniej wrażliwy na pożar, atak terrorystyczny czy działania wojenne;
- ochrona terenu – w porównaniu ze zbiornikami na powierzchni mającymi pomieścić podobne ilości produktu co magazyny podziemne, muszą zająć duże powierzchnie. W odniesieniu do zbiorników podziemnych, efektem powierzchniowym są jedynie niewielkie instalacje obsługujące te zbiorniki, które staosunkowo łatwo można wkomponować w krajobraz lub w infrastrukturę – dotyczy to zwłaszcza magazynów gazu. W przypadku podziemnych magazynów produktów ciekłych sprawa jest bardziej złożona, gdyż na powierzchni muszą pozostać zbiorniki na solankę manewrową;
- finansowy – koszty inwestycyjne i później eksploatacyjne magazynów podziemnych, w porównaniu z kosztami budowy i eksploatacji tradycyjnych zbiorników podobnej pojemności na powierzchni są znacznie mniejsze.

Podstawowymi parametrami opisującymi KPMG są: pojemność czynna, moc zatłaczania gazu, moc odbioru gazu, wielkość bufora (poduszki gazowej) oraz możliwość wykonania wielu cykli w ciągu roku [19]. Jak wynika z dotychczasowych doświadczeń, magazyny kawernowe stwarzają najlepsze warunki w zakresie zatłaczania i odbioru gazu przy równoczesnym zapewnieniu wielocykliczności pracy (por. Tab. 1). Prócz wymienionych czynników technologicznych oczekuje się, że kawerna magazynowa będzie szczelna, zapewni odpowiednią temperaturę i ciśnienie magazynowania oraz zachowa długotrwałą stateczność geomechaniczną.

Kawerny przeznaczone na potrzeby magazynowania substancji użytecznych, w tym gazu ziemnego, muszą być szczelne. Niespełnienie tego warunku w przypadku magazynowania węglowodorów ciekłych może prowadzić do skażenia wód podziemnych, a w przypadku wydostania się gazu ziemnego może doprowadzić do eksplozji na powierzchni (wypadek taki miał miejsce w 2001 r. w Hutchinson, Kansas, USA, zginęły wówczas 2 osoby). Sól kamienna jako ośrodek o właściwościach plastyczno-lepkich oraz o przepuszczalności w normalnych warunkach rzędu 10–21 m² zapewnia szczelność podziemnego magazynu, jeśli tylko człowiek swą działalnością jej nie zniszczy. Zagrożeniem dla szczelności mogą być porowate przewarstwienia skał niesolnych w obrębie serii solnej, a także przewarstwienia szybko rozpuszczalnych soli magnezowo-potasowych, które mogą stworzyć drogi migracji magazynowanego produktu poza złoże soli. Dlatego kawerny magazynowe należy lokować w strefach złoża spełniających odpowiednie warunki geologiczne.

Magazynowanie gazu związane jest z wykorzystaniem jego ściśliwości. Kawerny solne po opróżnieniu z solanki wypełniane są gazem zmiennym ciśnieniem, ok. 10–20 MPa. W związku z tym pojemność robocza oznacza ilość gazu, jaka może być wtłoczona do kawerny. W związku z tym istotne są wartości minimalnego i maksymalnego ciśnienia gazu w kawernie. Utrzymywanie zbyt niskiego ciśnienia w kawernie będzie skutkowało przyspieszonym procesem konwergencji, a w konsekwencji zmniejszeniem objętości magazynowej. W skrajnym przypadku może doprowadzić do utraty przez kawernę stateczności geomechanicznej. Z kolei maksymalne ciśnienie gazu w kawernie nie może przekroczyć wytrzymałości skały solnej, co z kolei w przypadku zbyt wysokiego ciśnienia może doprowadzić do mikroszczelinowania górotworu, a tym samym do

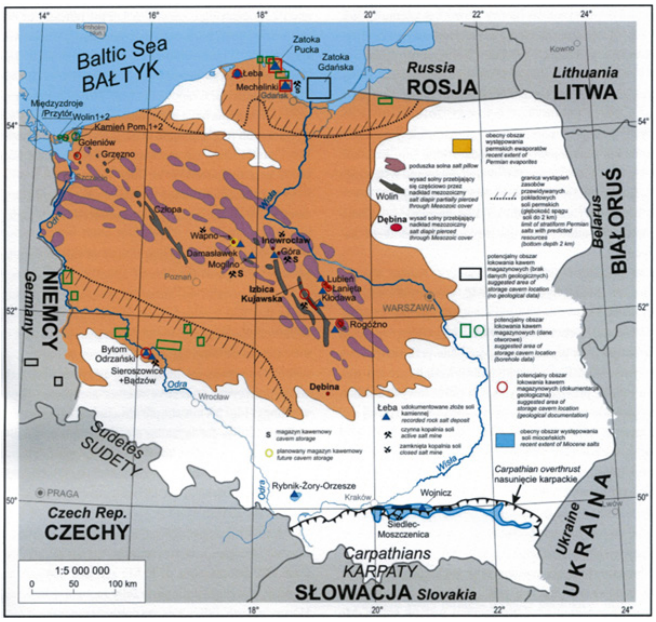

Rys. 6. Potencjalne miejsca lokowania kawern Magazynowych w utworach soli kamiennych w Polsce [6]
Fig. 6. Potential locations for locating storage caverns in rock salt formations in Poland [6]

utraty szczelności. Ponieważ rocznie odbywa się kilka, a czasem nawet kilkanaście cykli zatłaczania i odbioru gazu, należy liczyć się z postępującą konwergencją objętościową kawerny, wynikającą z własności reologicznych górotworu solnego. Szacuje się, że po 15 latach eksploatacji objętość kawern zmniejsza się średnio o ok. 13%, natomiast po 30 latach o ok. 24% [12].

Kawerna solna jako magazyn energii

Proces dekarbonizacji sektora energetycznego spowodował w ostatnich latach gwałtowny rozwój odnawialnych źródeł energii (OZE). Źródła oparte na energii słonecznej i energii wiatru są jednak niestabilne, silnie uzależnione od warunków pogodowych, ale także od pory dnia i pory roku. Na rynku pojawiają się nadwyżki energetyczne, w związku z czym operatorzy są zmuszeni do ograniczania produkcji energii elektrycznej w elektrowniach konwencjonalnych oraz jej pobór z OZE [3].

Częściowym remedium na te problemy jest magazynowanie energii elektrycznej, które może być realizowane m.in. w kawernach solnych. Nośnikiem energii elektrycznej w tym przypadku może być wodór, który jest traktowany jako paliwo przyszłości, zastępując w najbliższych latach paliwa kopalne. Obecnie trwają prace nad metodami jego szybkiej i wydajnej produkcji (z uwzględnieniem kwestii ekonomicznych), transportu oraz magazynowania.

Konwersja energii elektrycznej na wodór odbywa się w procesie elektrolizy wody, a więc w procesie wymagającym energii elektrycznej. Do tego procesu można wykorzystać nadwyżki energii z bieżącej produkcji przez OZE. Proces elektrolizy nie jest zbytnio skomplikowany, jest procesem bezpiecznym, a co najistotniejsze, jest procesem ekologicznym. Tak pozyskany wodór otrzymał przydomek „zielonego" wodoru, gdyż cykl produkcyjny jest zeroemisyjny. W kontekście energetyki odnawialnej tak pozyskany wodór wydaje się być bardzo atrakcyjny. Wodór można magazynować w kawernach solnych, które wg obecnej wiedzy są najlepszym rozwiązaniem w przypadku konieczności przechowania dużej ilości wodoru w dłuższym horyzoncie czasowym. Tak zmagazynowany wodór można wykorzystać do produkcji energii elektrycznej z wykorzystaniem np. turbin wodorowych napędzających generatory prądu czy też wodorowych ogniw paliwowych. Ten proces wytwarzania energii elektrycznej również jest zeroemisyjny. Schemat wytwarzania i magazynowania wodoru w kawernach solnych przedstawiono na Rys. 4.

W 2021 r. w Wielkiej Brytanii funkcjonowały 3 kawerny solne posadowione na głębokości 350–450 m o łącznej objętości 210 tys. m^3. 3 kolejne w USA na głębokości 800 m (strop kawerny) o objętości ponad 500 tys. m^3. Szacuje się, że kawerna solna o objętości 200 tys. m^3, posadowiona na głębokości 1000–1200 m p.p.t. i maksymalnym dennym ciśnieniu magazynowania 17 MPa pozwoli na zmagazynowanie około 2200–2400 Mg wodoru, tj. około 82,5 GWh [18].

Alternatywą dla wodoru jako nośnika energii może być sprężone powietrze. Nośnik ten jest uważany jako jeden z najdroższych, ponieważ proces sprężania jest niezwykle energochłonny. W związku z tym sprężanie powietrza może odbywać się w okresach, w których energia elektryczna jest tania (noc, weekendy) lub można wykorzystać energię pochodzącą z nadwyżek OZE. Do magazynowania energii w postaci sprężonego powietrza CAES (ang. Commpressed Air Energy Storage) można wykorzystać kawerny solne. Pierwsza tego typu instalacja powstała w 1980 r. w Niemczech zapewniając wytwarzanie 250 MW mocy elektrycznej [20].

Kawerny wykorzystywane obecnie do magazynowania gazu ziemnego mogą być w przyszłości wykorzystane jako magazyny energii w postaci wodoru lub sprężonego powietrza, pod warunkiem utrzymania dotychczasowych parametrów technologicznych takich jak: ciśnienie magazynowania nośnika energii, temperatura, dopuszczalne przepływy itp. Co najwyżej pewnym modyfikacjom będzie musiała ulec część naziemna, jak np. wymiana sprężarek gazowych na elektryczne, uzupełnienie instalacji o ekspander gazu sprzężony z generatorem, układy magazynowania ciepła i chłodu, układ połączeń.

Możliwość budowy nowych magazynów energii w polskich złożach soli kamiennej

Polska posiada bardzo duży potencjał magazynowania energii w utworach soli kamiennych, zarówno w złożach pokładowych, jak i wysadowych – Rys. 6. Potencjał ten ogranicza się do złóż cechsztyńskich, które występują na znacznych obszarach Polski. Złoża mioceńskie i triasowe z racji skomplikowanej budowy wewnętrznej i niewielkich miąższości nie są brane pod uwagę.

Miejsca potencjalnych lokalizacji kawern w formach pokładowych występują w północnej Polsce (5 obszarów, 3 udokumentowane złoża soli i 18 pojedynczych otworów wiertniczych), w części południowo-zachodniej kraju (11 obszarów, jedno udokumentowane złoże soli i 9 pojedynczych otworów wiertniczych). Potencjalne lokalizacje w formach wysadowych to północno-zachodnia Polska, region szczeciński (7 struktur wysadowych) oraz w Polsce centralnej (4 wysady).

Szczególnie atrakcyjne wydają się lokalizacje blisko wybrzeża Bałtyku, a to z racji możliwości poboru wody morskiej do ługowania kawern oraz zrzutu solanki do morza. W przypadku pozostałych lokalizacji głównym problemem może być odbiór solanki, ale też możliwości poboru wody do celów technologicznych na czas budowy kawerny.

Wskazane na Rys. 6 potencjalne lokalizacje w wielu przypadkach wymagają udokumentowania, gdyż są rozpoznane jedynie otworami wiertniczymi.

Z uwagi na skomplikowaną sytuację geopolityczną w Europie konieczne jak najszybsze podjęcie decyzji budowy kolejnych magazynów kawernowych, mając na uwadze, że proces budowy trwa ok. 5–10 lat.

Podsumowanie

Polska posiada doskonałą bazę zasobową złóż soli kamiennej, która z powodzeniem może być wykorzystana na potrzeby budowy podziemnych magazynów gazu i energii. Obecnie w strukturach solnych funkcjonuje jeden Podziemny Magazyn Ropy i Paliw (Góra k/Inowrocławia) oraz dwa Kawernowe Podziemne Magazyny Gazu (Mogilno k/Inowrocławia i Kosakowo k/Gdyni). W najbliższych latach przewiduje się budowę kolejnych kawernowych magazynów gazu. Niewątpliwie będzie to mieć korzystny wpływ na bezpieczeństwo energetyczne państwa, w szczególności w kontekście dekarbonizacji systemu energetycznego. Magazyny w złożach soli kamiennej, oprócz dużej pojemności operacyjnej, pozwalają na szybkie zatłaczanie i odbiór magazynowanego medium. Ma to istotne znaczenie w okresie, w którym węgiel brunatny i kamienny będzie zastępowany gazem ziemnym, co z kolei będzie wymagało stworzenie odpowiedniego zaplecza do magazynowania gazu.

Docelowo energetyka ma zostać oparta na odnawialnych źródłach energii, których wadą jest okresowość produkcji wynikająca głównie z warunków klimatycznych/pogodowych. W związku z tym będzie istniała konieczność budowy nowych magazynów energii, których zadaniem będzie buforowanie nadwyżek produkcyjnych energii i jej zwrot do systemu w okresach niedoboru. Oprócz nowych magazynów energii zajdzie konieczność przekształcenia na ten cel istniejących magazynów gazu, co jest technicznie możliwe.

Rozwój magazynów energii pozwoli na efektywny odbiór i konwersję energii elektrycznej pozyskiwanej za pośrednictwem odnawialnych źródeł energii. W wyniku przeprowadzonej konwersji medium magazynowym może zostać wodór lub sprężone powietrze. Odwrócenie procesu konwersji pozwoli za pomocą turbin gazowych i generatorów na wytworzenie energii elektrycznej.

Ponieważ odnawialne źródła energii postrzegane są jako przyszłość energetyczna Europy, eliminując z systemu energetycznego paliwa kopalne, niewątpliwie przyczyni się to do ochrony środowiska naturalnego. W tym kontekście Polska w perspektywie najbliższych lat może stworzyć pokaźną bazę magazynową energii w złożach soli kamiennej, która pozwoli na zachowanie bezpieczeństwa energetycznego państwa. Wskazanie potencjalnych lokalizacji przyszłych kawern magazynowych pokazuje, że część z nich może być zrealizowana bez istotnych szkód środowiskowych (dotyczy kawern zlokalizowanych w pasie nadmorskim). W przypadku pozostałych lokalizacji konieczna będzie budowa infrastruktury związanej z odbiorem i przeróbką uzyskanej solanki.

Literatura – References

1. Cornot-Gandolphe S. 2019 – Underground gas storage in the world – 2018 status. CEDIGAZ. https://cdn2.hubspot.net/hubfs/1982707/Overview-of-underground-gas-storage-in-the-world-2018-(1).pdf (01.06.2024)
2. Cornot-Gandolphe S. 2024 – Underground Gas Storage in the world – 2023 status. CEDIGAZ. www.europeangashub.com/underground-gas-storage-in-the-world-2023-status.html (01.06.2024)
3. https://globenergia.pl/czy-wylaczyli-ci-fotowoltaike-kolejne-wylaczenia-mocy-z-pv/ (01.06.2024)
4. https://ipi.gasstoragepoland.pl/pl/menu/transparency-template/?page=uslugi-i-infrastruktura/parametry-techniczne (01.06.2024)
5. https://pgnig.pl/podziemne-magazyny-gazu (01.06.2024)

6. Czapowski G., 2021: Lokalizacja kawern magazynowych w utworach solnych w Polsce – stare i nowe opcje. Przegląd Solny, (16), pp. 5-19.
7. Czapowski G., Bukowski K., (2012), Salt resources in Poland at the begining of the 21st century, Geology, Geophisics & Environment, vol. 38, No. 2.
8. Czapowski G., Bukowski K., Gientka M., (2008), Aktualny stan rozpoznania geologicznego złóż soli kamiennej w Polsce, Biuletyn Państwowego Instytutu Geologicznego, nr 429.
9. Czapowski G., Tomassi-Morawiec H., Chełmiński J., Tomaszczyk M., (2008b), Stopień rozpoznania i perspektywy zagospodarowania cechsztyńskich złóż soli w rejonie Zatoki Gdańskiej, Górnictwo Odkrywkowe, rocznik XLIX/2, nr 2-3.
10. Garlicki A., (1999): Złoża soli w Polsce i perspektywy ich wykorzystania, Prace Naukowe Uniwersytetu Śląskiego, nr 1809.
11. Kunstman A., Poborska-Młynarska K., Urbańczyk K., 2009: Geologiczne i górnicze aspekty budowy magazynowych kawern solnych, Przegląd Geologiczny, vol. 57, nr 9, 2009.
12. Lankof L., Tarkowski R. 2022. Potencjał magazynowy wodoru w permskich złożach soli kamiennej w Polsce. Przegląd Solny, (16), pp. 29-42.
13. Obwieszczenie Ministra Klimatu i Środowiska z dnia 2 marca 2021 r. w sprawie polityki energetycznej państwa do 2040 r. (Monitor Polski z 2021 r., poz. 264)
14. Ślizowski J., Urbańczyk K., Wiewiórka D., Kowalski M., Serbin K., (2011), Stateczność wyrobisk w pokładach ewaporatów LGOM w aspekcie budowy podziemnego laboratorium badawczego, seria „Studia, Rozprawy, Monografie", nr 168, Wydawnictwo Instytutu Gospodarki Surowcami Mineralnymi i Energią PAN, Kraków.
15. Ustawa z dnia 9 czerwca 2011 r. Prawo geologiczne i górnicze (t.j. Dz. U. z 2023 r. poz. 633 ze zm.)
16. Ustawa z dnia 10 kwietnia 1997 r. – Prawo energetyczne (Dz. U. z 2020 r. poz. 833 ze zm.) – wersja obowiązująca w chwili przyjęcia PEP2040
17. Valle-Falcones, L.M.; Grima-Olmedo, C.; Mazadiego-Martínez, L.F.; Hurtado-Bezos, A.; Eguilior-Díaz, S.; Rodríguez-Pons, R. Green Hydrogen Storage in an Underground Cavern: A Case Study in Salt Diapir of Spain. Appl. Sci. 2022, 12, 6081. https://doi.org/10.3390/app12126081.
18. Wilkosz P., Grzybowski Ł. 2021.Kawerny solne – najlepszy sposób wielkoskalowego podziemnego magazynowania wodoru. Przegląd gazowniczy, (9), pp. 46-47.
19. Wittman B., Wilkosz P., 2022: Bezpieczeństwo energetyczne – rola podziemnych magazynów gazu ziemnego. W: W służbie społeczeństwu. Polska w obronie praw człowieka na świecie i w kraju, red. J. Stala, M. Butrymowicz, Uniwersytet Papieski Jana Pawła II w Krakowie Wydawnictwo Naukowe, Kraków 2022, s. 159–182. DOI: https://doi.org/10.15633/9788374389891.10
20. Wojciechowski H. 2017. Technologie magazynowania energii. Cz. II. Instal, (3): pp. 16-27.

Possibilities of Storing Natural Gas and Energy in Salt Formations in Poland

The state's energy security includes, among others: securing customers' fuel and energy needs. One of the elements of energy policy is storage infrastructure, which enables the storage of natural gas and fuel stocks. It is carried out through surface and underground warehouses. The role of the latter is particularly important due to the capacities offered, but also the technological parameters of the storage process that can be obtained.

One of the convenient places to build underground gas and fuel storage facilities are rock salt deposits, where storage caverns are constructed. Due to favorable access to salt geological formations, Poland has great opportunities to build an underground storage base for both natural gas and liquid fuels.

The process of decarbonization of the energy sector forces us to look for new energy sources that will, over time, replace fossil fuels in the energy system. The answer to this challenge are renewable energy sources (water, wind, sun), the advantage of which is inexhaustibility, but on the other hand, the disadvantage is that they are uncontrollable due to their dependence on climate/weather conditions.

The article discusses the possibilities of building cavern underground gas and energy storage facilities, paying attention to the latter as future solutions necessary for use in the energy system. Against the background of the rock salt resource base, potential locations of future cavern storage facilities were indicated.

Keywords: *salt deposits, salt caverns, underground gas storage facilities, underground energy storage facilities*

Comprehensive Methodology for Geometrization of Mineral Deposits

Andrii PEREMETCHYK[1], Serhii CHUKHAREV[2], Serhii PYSMENNYI[3], Serhii FEDORENKO[4], Tatyana PODOYNITSYNA[5], Wiktoria SOBCZYK[6]

[1] Kryvyi Rih National University, Kryvyi Rih, Ukraine; ORCID https://orcid.org/0000-0001-6274-146X; email: peremetchyk@knu.edu.ua
[2] National University of Water and Environmental Engineering, Rivne, Ukraine; ORCID https://orcid.org/0000-0002-4623-1598; email: s.m.chukharev@nuwm.edu.ua
[3] Kryvyi Rih National University, Kryvyi Rih, Ukraine; ORCID https://orcid.org/0000-0001-5384-6972; email: psvknu@gmail.com
[4] Kryvyi Rih National University, Kryvyi Rih, Ukraine; ORCID https://orcid.org/0000-0001-5753-9603; email: fedorenkosa@knu.edu.ua
[5] Kryvyi Rih National University, Kryvyi Rih, Ukraine; ORCID https://orcid.org/0009-0000-9905-8912; email: podoinitsyna@knu.edu.ua
[6] AGH University of Science and Technology, Faculty of Energy and Fuels, Krakow, Poland; ORCID https://orcid.org/0000-0003-2082-9644; email: sobczyk@agh.edu.pl

http://doi.org/10.29227/IM-2024-01-104

Submission date: 03-05-2024 | Review date: 15-06-2024

Abstract

The article proposes a comprehensive methodology for geometrization of a mineral deposit. Based on existing concepts of geometrization, a set of methods for building a geometric model of a mineral deposit is developed. In the course of geometrization of mineral deposits, the authors of the research widely use geo-information systems. Geological exploration and survey data are used as the basis for geometrization. The most widely used estimation methods are considered when developing the methodology for estimating mineral reserves. The modified method of parallel vertical sections proves to be the most effective way to estimate the reserves of deposits of complex geometric shapes. The authors develop the methodology for determining optimal location of sections in relation to the mineral deposit under estimation. Both geostatistical estimation methods implemented in geo-information systems and a multidimensional heuristic estimation method developed by the authors of the research are used for geometrization purposes. This set of mining geometric methods enables actual and predictive geometrization of a mineral deposit and estimation of its reserves. The geometrization methodology developed by the authors makes it possible to rationally plan mining operations and increase mining enterprise efficiency.

Keywords: *comprehensive methodology for geometrization, geo-information system, geostatistical estimation methods, multidimensional heuristic estimation method, parallel vertical sections*

1. Introduction

Modern industrial production requires extraction of a large amount of mineral resources [1]. The current tendency of growing needs for raw materials in production leads to the need to increase the volume of mining. Quantitative and qualitative characteristics of minerals must meet modern requirements determined by complexity of production processes. Improving efficiency of mining operations involves solving a number of problems related to mining processes in different conditions of mineral deposit development. This requires a clear understanding of the mining enterprise and the rock massif. Geometrization of mineral deposits makes it possible to assess geological and technological characteristics of mineral deposits developed by mining enterprises [2-6].

Sustainable mining is an essential condition for providing the national economy with the necessary resources [7]. Development of mining depends on investments based on estimations of mineral reserves. Various methods of estimating mineral reserves are grounded on a comprehensive mining and geometric estimation of a mineral deposit [8]. Selecting the optimal, i.e. the most appropriate in different mining and geological conditions, method for estimating mineral reserves is the most important task of geometrization of a mineral deposit [9]. Comprehensive estimation and modelling of mining production can contribute to the efficient design and planning of performance of a mining enterprise or a system of mining enterprises [10].

A digital model of a deposit built on the basis of survey measurements and geological exploration data enables a comprehensive mining and geometric estimation of a mineral deposit [11–14]. Such a model can provide a qualitative ground for performing mining geometric calculations, creating mining and graphic documentation [15], building topographic surfaces and calculating volumes of minerals. The mining and geometric model of a mineral deposit based on its comprehensive geometrization is shown in Fig. 1.

Improvement of the technology for mining minerals is based on application of information on the geometric structure of a mineral deposit [16–17]. Efficient design of a mining enterprise is possible due to geometrically substantiated parameters of mining operations. Efficient extraction of minerals is a priority of mining production [18–21]. For example, in [22, 23], authors show that the results of scientific studies based on the geometrization data help solve not only the problems of the ore formation theory but also the practical tasks concerning improvement of methods for predicting the prospective areas within the deposit.

Mineral processing is an integral part of mining production. The technology for enrichment of minerals depends on their physical and chemical properties, water content, impacts of the nature of mineral occurrence in the rock mass on properties of the raw materials supplied to mining and processing enterprises. Geometrization-based information

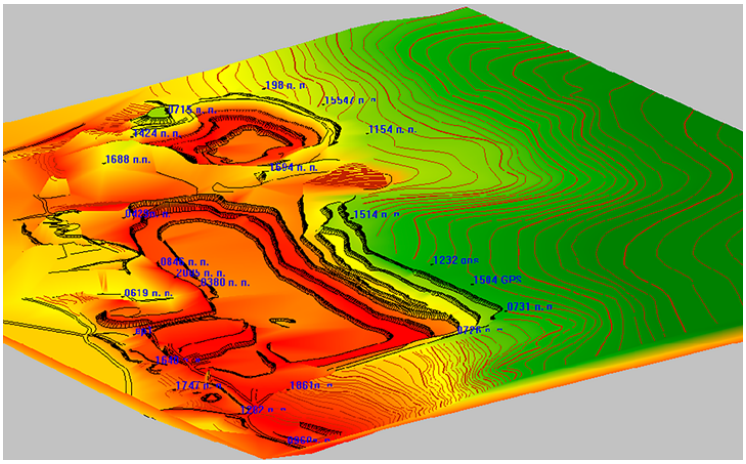

Fig. 1. Mining and geometric model of the deposit in the open pit of Slavyanskyi chalk-lime plant
Rys. 1. Model górniczy i geometryczny złoża odkrywkowego Zakładu Wapna Kredowego Slavyanskyi

provides the foundation for mineral deposit estimation and subsequent development of the mineral enrichment technology [24].

Various scopes of mining require monitoring mineral resources based on an integrated estimation of the mineral deposit. Exploitation of mineral deposits inevitably results in rock massif disturbances [25]. This leads to unstable geomechanical conditions of rocks and mine workings. Mining and geometric methods of estimation provide control of the rock massif condition, without which stable performance of the mining enterprise is impossible [26–28].

Concentration of stresses around mine workings may lead to losses of their integrity [29, 30]. Geometric methods for estimating geophysical processes are an integral part of mine safety [31]. The impact of mining operations on the surrounding rocks and the surface of the mining enterprise should be carefully estimated. Based on such estimations, activities are carried out to ensure stability of rocks [32–36].

The impact of mining on nature is an important issue. Different types of impacts have different consequences. Mineral mining and processing should be conducted in a way that minimizes their impact on nature and a mining enterprise. Estimating and modelling the environmental impact of a mining enterprise is the most important task that arises during the mining process. The amount of pollutants in the air is the most important indicator of the condition of the environment. This issue is particularly relevant in open pit mining, especially when it comes to minerals containing toxic useful components. Assessment of such pollution and reduction of its impact on the environment should be performed with a high degree of responsibility [37].

At mineral deposits with high geological variability, there is a problem of estimating the spatial occurrence of minerals. This reduces efficiency of mineral resources estimation based on the results of geological exploration. Geostatistical and heuristic methods of estimating geological characteristics of the deposit enable reducing the impact of variability on the mineral reserves estimation and determining geological characteristics of the deposit with higher accuracy [38–43].

Methods of heuristic self-organization are the most interesting methods of mining and geometric estimation of mineral deposits. They are characterized by various efficiency and based on different mathematical methods. They are the most flexible and adaptable as well. In combination with geostatistical methods for estimating mineral deposits, heuristic methods are very efficient for estimating deposits with high geological variability. Development and application of these methods is very promising for estimating and modelling mineral deposits [44–46].

Thus, the presented research aims to create a geometrization methodology allowing a comprehensive mining and geometric estimation of the mineral deposit, and ensuring efficient performance of the mining enterprise.

2. Methods

The majority of researches on geometrization of mineral deposits are based on P.K. Sobolevsky's concept on geometrization of shapes, properties, conditions of rock occurrence and subsoil processes [47].

This concept of geometrization underlies graphical and analytical methods of building a mining and geometric model of the deposit, estimating deposits of various geometric shapes as well as mineral reserves, that are developed and proposed by the authors. In addition, the authors of the present research have created a comprehensive methodology for mineral deposit geometrization.

A major disadvantage of the idea of geometrization based on the concept of the geochemical field and the topographic surface is that in the current system only one deposit characteristic is depicted. Simultaneous imaging of multiple characteristics is difficult and does not create a comprehensive model of the deposit if these characteristics are built as isolines. This disadvantage is addressed by applying mathematical operations with topographic functions according to certain rules that take into account genetic characteristics of the set of deposit characteristics. This formal set of characteristics provides a description of variability of the geological structure of the deposit parts or the entire deposit.

Under the general approach, variability arises when transiting, first, from considering individual characteristics to considering their totality; second, from studying the nature of spatial variability of individual characteristics to considering their combined impact on the overall variability factor, taking into account relationships between the characteristics.

Rys. 6. Potencjalne miejsca lokowania kawern Magazynowych w utworach soli kamiennych w Polsce [6]
Fig. 6. Potential locations for locating storage caverns in rock salt formations in Poland [6]

Any characteristic of the deposit P can be determined in a system of spatial-temporal coordinates P=f(x, y, z, t). In this case, location of a characteristic in the x coordinate system is commonly referred to as geochemical, geological, spatial, random. If in the coordinate system a multidimensional vector of various characteristics of the deposit P=f(P1, P2, ..., Pn) is determined, location of such a system of characteristics is called a vector field. However, such a name cannot be recognized as convenient. A system of spatially located deposit characteristics is called a spatial-factor field.

Each characteristic of this field can be formally described individually and exist as a spatial-factor field of an individual characteristic. The complete set of various characteristics of the deposit is specified by a system of spatial-factor fields of individual characteristics, which is described by a function of the type:

$$\begin{aligned} P_1 &= F\left[f_1(x,p);\phi_1(x,p)\right];\\ P_2 &= F\left[f_2(x,p);\phi_2(x,p)\right];\\ &\cdots\cdots\cdots\cdots\cdots\cdots\\ P_n &= F\left[f_n(x,p);\phi_n(x,p)\right], \end{aligned} \tag{1}$$

where f(x, p) is the regular component of the spatial-factor field; $\Phi_1 1(x, p)$ is the random component of the spatial-factor field or variance of the model.

The analysis of properties of individual fields and their systems is based on mining and geometric analysis of the deposit and topographic functions.

The variability model is expressed as a topographic function of the following type:

$$V = f(x, y, z). \tag{2}$$

This topographic function is scalar. If it is differentiated, it is transformed into a vector-topographic surface described by the expression:

$$q_v = \frac{\Delta P}{\Delta l} \tag{3}$$

where ΔP is the section of the isolines; Δl is the distance between adjacent profiles in the direction of the gradient.

To differentiate the variability at geological exploration network points located on the plan, values of the main gradients are calculated and the isogradients, which are derivatives of the given surface, are built on them. Isogradient surfaces are built on the basis of difference of the obtained characteristics in a given interval and allow finding any values within this interval and performing predictive modelling of deposit characteristics, as well as solving problems related to predicting and modelling spatial location of mineral reserves.

If necessary, coefficients of variability of the characteristics are calculated and accuracy of building the plans is assessed. If the accuracy of the model meets the requirements, the plans of the isolines are sufficiently informative.

The relationship between the network parameters and the error of determining the useful layer thickness is further established by comparing the amount of reserves obtained from the geological exploration data and that calculated from the exploitation data.

This error is determined as the mean square deviation of the surfaces of isothicknesses, built according to experimental parameters of the geological exploration networks, from the true surface, built according to the exploitation data, by the formula:

$$m = \pm\sqrt{\frac{\Sigma\Delta^2}{n}} \tag{4}$$

where $\Sigma\Delta^2$ is the total of squares of value deviations from the true surface; n is the number of points where deviations are determined.

Predictive modelling of mineral reserves is based on building vector-gradient fields of the useful layer thicknesses of mineral reserves. This process enables establishing regularities of spatial distribution of mineral resources, as well as managing reserves during exploration and exploitation of mineral deposits [48, 49].

These starting points for field differentiation and field gradient determination, known in the general rigorous mathematical field theory, enable new approaches to creating a geometric understanding of the deposit structure variability and solving problems of geological exploration and mining.

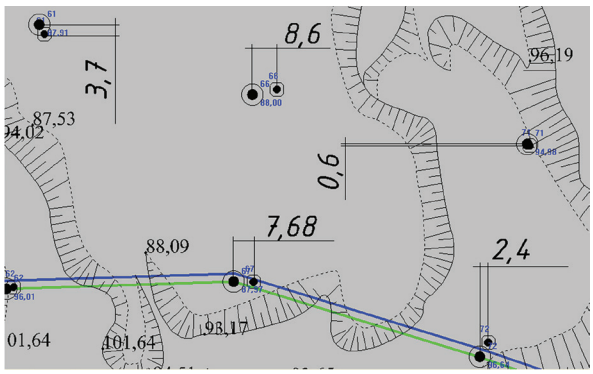

Fig. 2. Deviation of the position of boreholes plotted on the plan based on data of surveys and processed images

Rys. 2. Odchylenie położenia otworów wiertniczych, naniesione na planie na podstawie danych pomiarowych i przetworzonych zdjęć

The geostatistical analysis of the deposit provides an opportunity to assess the relationship between parameters of the exploration network and variability, to clarify distribution of the qualitative characteristics of the deposit, and improve accuracy of deposit reserves estimation. The geostatistical method of kriging is implemented in detail in geo-information systems used for geometrization of mineral deposits [50–52].

Within the framework of the comprehensive methodology for mineral deposit geometrization, the authors of the present research develop a method of mining and geometric modelling based on multidimensional heuristic self-organization of the function of deposit characteristics location [53]. The function looks like:

$$f_i = [c_i^p (a_{11}^p x_1^p + b_{11}^p x_1^p)^p \times (a_{12}^p x_2^p + b_{12}^p x_2^p)^p \cdot \ldots \cdot (a_{1n}^p x_2^p + b_{1n}^p x_2^p)^p \times (a_{21}^p x_1^p + b_{21}^p x_1^p)^p \cdot \cdot (a_{22}^p x_2^p + b_{22}^p x_2^p)^p \times \ldots (a_{mn}^p x_n^p + b_{mn}^p x_n^p)^p], \quad (5)$$

$$F_i(x_1, x_2, \ldots, x_n) = d_i^p [f_1(x_1, x_2, \ldots, x_n) + f_2(x_1, x_2, \ldots, x_n) + \ldots + f_n(x_1, x_2, \ldots, x_n)]^p + e^p, \quad (6)$$

$$P(x_1, x_2, \ldots, x_n) = g^p [F_1(x_1, x_2, \ldots, x_n) + F_2(x_1, x_2, \ldots, x_n) + \ldots + F_n(x_1, x_2, \ldots, x_n)]^p + h^p, \quad (7)$$

where x are the function arguments determined from reliable geological exploration data; a, b, c, e, g, h are the numerical coefficients obtained during modelling; p is the power calculated by (7).

In (5) – (7), the process of repetitive calculation cycles results in complicating the mathematical model of the deposit. The search for the functional relationship between the deposit characteristics takes place in worked-out areas of the deposit. While calculating, the factors are determined that impact distribution of the modelled characteristic most of all. Thus, the optimal type of functional relationship between geological characteristics is determined. The calculation cycles are performed according to the criterion of the modelling accuracy increase. The set of algorithms included in the described modelling method make this mathematical model very flexible, which allows it to be used in complex mining and geological conditions at deposits with high variability of geological characteristics. This makes it possible to describe very complex mathematical relationships between geological characteristics, distinguish the regular component of a multidimensional geochemical field, and estimate the error of modelling.

Large errors occur when processing maps and plans that can be used as a basis for modelling. These are made when building plans, or result from incorrect recognition of information on maps and plans due to their poor physical condition, or are related to inaccurate connection to the coordinate grids of the original image, etc.

To study these errors, two models are built for each open pit. One of them uses vectorized information from scanned plans, and the other is built on survey data. Then, the two models are compared for identity. Deviation of the values makes about 7% (Fig. 2).

Thus, accuracy of the volume calculations based on the data obtained by processing the scanned plans is much lower than that of the calculations based on the survey and geological exploration data. Survey and geological exploration data is a priority for geometrizaton of mineral deposits.

The comprehensive methodology for geometrization of mineral deposits created by the authors widely employs such geo-information systems as Micromine, K-mine, Surfer, and Autocad. These systems have detailed methods for estimation and geometrization of mineral deposits including geostatistical ones which are of particular interest given the complex geometry of mineral deposits. This methodology has been used for geometrization of Ukrainian mineral deposits of various shapes and complexity.

Mining enterprises most commonly use the following methods to calculate solid mineral reserves: vertical and horizontal sections, arithmetic mean, geological blocks, production blocks, polygons, triangles, isolines, isohypse, average dip, equal dip areas, etc.

The parallel section method is the most common for estimating reserves of ore deposits, as these deposits are characterized by highly variable morphology and very uneven distribution of the useful component. The section method divides the mineral body into a number of blocks located between parallel lines of the exploration network.

Depending on the geological exploration network, the method of vertical or horizontal sections can be used. For example, if the deposit is explored with vertical or inclined borehole profiles, the vertical section method provides the most complete direct use of all geological data obtained during exploration drilling.

To apply the horizontal section method in this case, it is necessary to average the geological data obtained from these boreholes and project them as individual points on the hor-

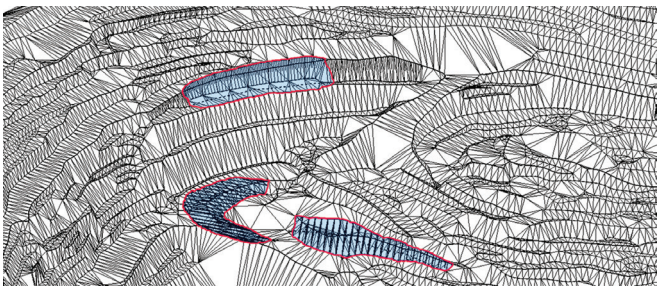

Fig. 3. A fragment of the triangulation surface of the digital model of the Pivdennyi GZK open pit. Experimental mine blocks are highlighted in color
Rys. 3. Fragment powierzchni triangulacyjnej cyfrowego modelu odkrywki Pivdennyi GZK. Eksperymentalne bloki kopalniane są wyróżnione kolorem

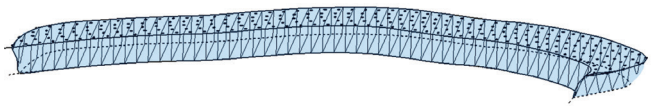

Fig. 4. Mine block with sections for calculating volumes
Rys. 4. Blok kopalniany z sekcjami do obliczania objętości

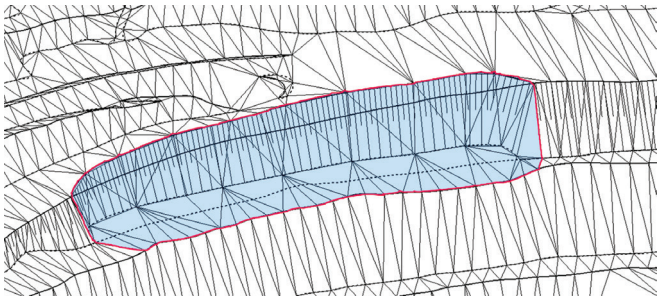

Fig. 5. Fragment of the triangulation surface of the pit after mine block extraction
Rys. 5. Fragment powierzchni triangulacyjnej wyrobiska po wydobyciu bloku kopalnianego

izontal section plane, which complicates the calculation of mineral reserves and inevitably reduces its reliability. On the contrary, if there are a number of mine working levels with underground horizontal boreholes, it is more expedient to use horizontal sections for calculating mineral reserves.

A huge advantage of the parallel section method is that it enables clear demonstration of geological features of the deposit, namely, the morphology of mineral bodies, the distribution of certain ore types and grades, the nature of mineralization changes along the dip, strike and thickness of the deposit. This method makes it possible to calculate reserves in the case of extremely complex deposit contours and availability of ore or non-ore layers.

In the general case of using the method of parallel sections, the volume of the block is calculated by the formula:

$$V = l_1\left(\frac{S_1 + S_2}{2}\right) + l_2\left(\frac{S_2 + S_3}{2}\right) + \ldots + l_n\left(\frac{S_n + S_{n+1}}{2}\right) \quad (8)$$

where S is the area of the section; l is the distance between the sections at the right angle to the dip; n is the number of sections.

When using the section method, the area of the ore body is determined for each section. Section areas are mostly determined by automated methods based on known plan-height coordinates of the digital section model. Depending on the shape and relative sizes of the areas in adjacent sections, volumes of blocks are calculated using the formulas of the pyramid, truncated pyramid, cone, wedge, etc. The average content of useful components in the sections is determined as the weighted average of the ore intervals of individual workings. If the geological sampling network of a mineral deposit is uneven, it is advisable to determine the content of the mineral component as a weighted average of the block areas using geostatistical estimation methods such as kriging.

The above data should be used for determining block parameters. Blocks are usually singled out between two exploration profiles, but in the case of a dense network of exploration workings, sometimes it is possible to include several sections in a block.

If the dip of mineral bodies is long, blocks formed by two sections are excessively large and it is advisable to divide them into several independent blocks, especially when there are significant vertical changes in the nature of the mineral distribution.

Most mineral deposits are limited by complex surfaces. It is impossible to accurately reproduce and identify them based on exploration data. Therefore, the principle of transforming complex bodies into simpler ones, within which reserves are estimated, underlies all geological exploration-based methods of reserve estimation.

The vertical section method is used to calculate volumes of complex block figures consisting of objects of different types that can be located in several different layers or pit benches and have a complex section profile.

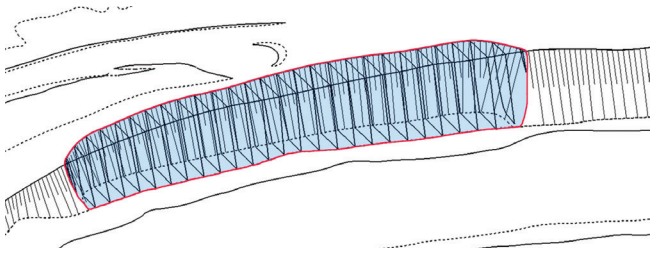

Fig. 6. Fragment of the triangulation surface of a mine block divided by parallel section planes
Rys. 6. Fragment powierzchni triangulacyjnej bloku kopalnianego, podzielonego równoległymi płaszczyznami przekroju

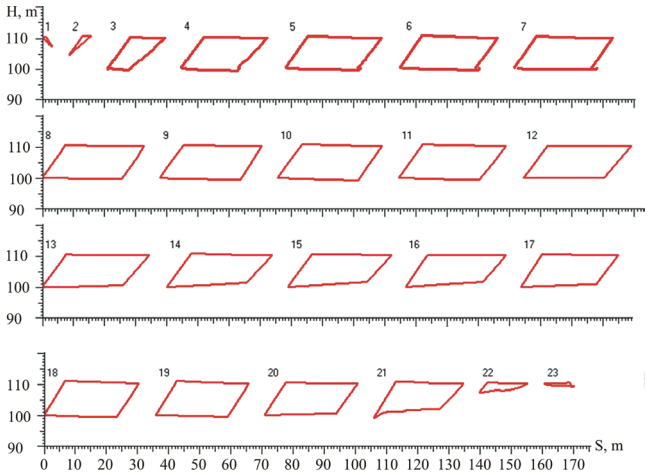

Fig. 7. Formation of sections to determine the volume
Rys. 7. Tworzenie przekrojów w celu określenia objętości

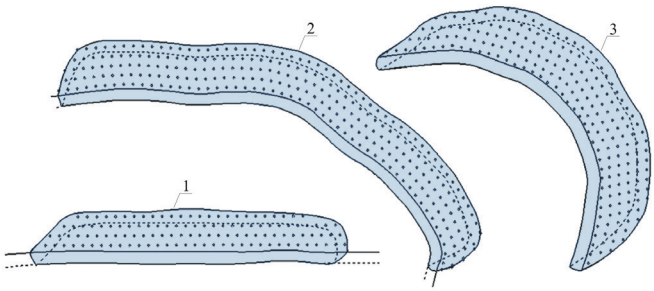

Fig. 8. Form of experimental mine blocks: 1 – straight elongated block; 2 – intermediate variation; 3 – block of a sharply rounded geometric shape
Rys. 8. Forma eksperymentalnych bloków kopalnianych: 1 – blok prosty wydłużony; 2 – zmienność pośrednia; 3 – bryła o ostro zaokrąglonym kształcie geometrycznym

3. Results and their discussion

The methodology for geometrization of mineral deposits developed in the present research has been applied to geometrization and modelling of Ukrainian mineral deposits, e.g. the deposit at Pivdennyi Ore Mining and Processing Plant (GZK).

The specifics of calculating volumes by the method of sections in geo-information systems used in the present research consists in building triangulation surfaces at the initial stage (Fig. 3).

The volume between two triangulation surfaces can be determined within a specified area of the mineral deposit limited by a closed contour exemplified in Fig. 4.

This method employs information on the condition of the pit surface at the beginning and the end of a certain time interval to calculate volumes with possible determination of volumes within a closed contour or multiple contours. For this, there should be indicated pit contours at the beginning and the end of the reporting period in different layers of the model. This information may be presented in the form of contours of workings, bench edges, surfaces, etc., which, in turn, are represented in the form of splines, polylines, surfaces, point elevation marks, etc. Based on these data, the contour of the mineral reserves in the XY plane is determined within which the reserves are estimated. A triangulation surface is built based on the set of objects describing information on the pit boundaries at the beginning and the end of the reporting period. The volume is found based on the difference in surfaces at the beginning and the end of the reporting period. Volumetric difference fragments with a positive mark are considered balance rock mass, and those with a negative mark are considered off-balance rock mass (Fig. 5)

Triangulation surfaces are built based on data from all objects included in each layer category. Triangulation surfaces are built for the new and old boundaries of a pit bench.

Next, the triangulation surfaces are intersected with vertical planes and the contours of intersection figures are deter-

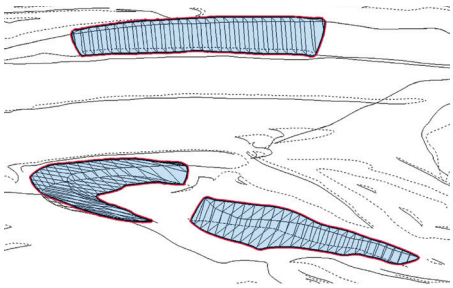

Fig. 9. Mine blocks of various shapes with sections for calculating volumes at the Pivdennyi GZK pit
Rys. 9. Bloki kopalniane o różnych kształtach z przekrojami do obliczania objętości w kopalni Pivdennyi GZK

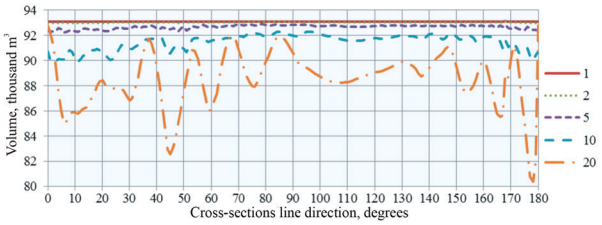

Fig. 10. Dependency of the calculated volume of a mine block of complex geometric shape on the direction of the line of vertical sections at different distances between the sections: 1, 2, 5, 10, 20 – dependencies at distances of 1 m, 2 m, 5 m, 10 m and 20 m, respectively
Rys. 10. Zależność obliczona objętości bloku kopalnianego o skomplikowanym kształcie geometrycznym od kierunku linii przekrojów pionowych, przy różnych odległościach między przekrojami: 1, 2, 5, 10, 20 – zależności w odległościach odpowiednio: 1 m, 2 m, 5 m, 10 m i 20 m

mined. Subsequently, the solution to the problem is reduced to solving the standard problem of calculating volumes by the method of parallel sections (Fig. 6).

This method is based on the parallel vertical section method and involves availability of a digital pit surface at the beginning and the end of the deposit mining. A contour, or a set of contours, that allows singling out the determined amounts of rock mass into categories is also taken into account. Such categories include, for example, accessed commercial mineral reserves, mineral reserves prepared for extraction, technological reserves, mineral reserves on individual mining horizons, balance and off-balance reserves within geological contours, reserves with a certain content of useful component.

At the same time, a reporting documentation package is generated for the calculated figure and all the necessary calculations are performed. The report contains a calculation table with calculations of the area for each section, as well as a graphical representation of each vertical section at a given scale (Fig. 7).

The method of estimating mineral volumes is studied on experimental modelled mine blocks of three main geometric shapes: a straight elongated block, a block of a sharply rounded geometric shape and the intermediate variation. For statistical data, the method of horizontal and vertical sections and that of arithmetic mean are used to calculate the volume of the obtained figures. The geometric shapes of the blocks are shown in Fig. 8.

The methods of horizontal and vertical sections employ sections located radially, parallelly and arbitrarily relative to each other. Each of the methods proves to produce more accurate results with certain shapes of the figures. That is, the method of parallel vertical sections provides a more reliable calculation of volume when applied to estimating a straight elongated block. The radial arrangement of vertical parallels provides higher accuracy in estimating rounded blocks. This is logical, since these methods are developed to determine amounts of rock mass in blocks of the geometric shape corresponding to these methods. To universalize the arrangement of vertical sections, the following procedure is employed: the point of the centre of the surface formed by the closure of the contour within which the volume is determined on the plan is used for arrangement of sections. Through this surface, in the north direction, a block strike line is drawn, perpendicular to which vertical sections are built. The line is then rotated at an angle of one degree, and the procedure is repeated. The obtained volumes are summarized in a table of calculated volumes of the block. As a result of these operations, angular ranges are determined within which the calculated values of volumes remain unchanged. These ranges are combined to provide minimum angular rotation values for calculating volumes and vary at different enterprises due to employment of different mining systems. The values of the rotation angles at which volumes of blocks differ sharply, become reference values for estimation of the block mineral reserves.

The calculation of volumes is carried out for mine blocks of different shapes at the Pivdennyi GZK pit, to clarify the impacts of different shapes of the calculated figures on calculation accuracy. Three shapes of mine blocks are chosen on different horizons: a straight elongated block, a sharply rounded block and the intermediate variation (Fig. 9).

At the same time, it is noted that reduction of distances between the sections leads to reduction of the difference between the obtained maximum and minimum values of the volumes calculated for all the section rotation options. Therefore, at the second stage of the experiment, an attempt is made to minimize the distance between sections. For this purpose, the volume in the given blocks is calculated several times with a gradual fixed reduction of the distance between the sections. The following distances are chosen for the volume calculation: 20 m; 10 m; 5 m; 2 m and 1 m (Fig. 10).

When analyzing the obtained results, it is concluded that with a certain reduction of the distance between sections, nu-

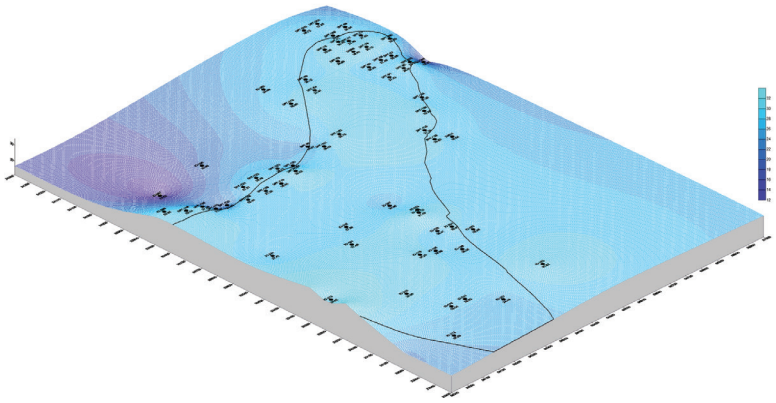

Fig. 11. Mining and geometric model of magnetic iron reserves distribution at the Pivdennyi GZK pit. The gradient shows the change in the percentage of the useful component content

Rys. 11. Model górniczy i geometryczny rozkładu zasobów żelaza magnetycznego w kopalni Piwdennyj GZK. Gradient pokazuje zmianę procentowej zawartości składników użytecznych

merical values of the calculated volumes of a block are equal at different orientation of the sections relative to the center of the surface formed by the closed limiting contour. In addition, the calculated values of volumes are equal to those obtained by other methods. It follows that this method can be used as a universal one for any geometric shape of the block with even greater accuracy. Volumes are calculated more accurately due to a greater number of sections that describe the contour of the figure, the volume of which is being calculated, in more detail. Optimal distances between sections are obtained empirically, their use confirms efficiency of the method of parallel vertical sections programmatically implemented in geo-information systems. A feature of the method is the ability to automatically arrange sections at optimal distances due to employment of geo-information systems. This eliminates the need to use other methods of calculating volumes of individual blocks of different geometric shapes.

Comprehensive estimation and geometrization of the deposit at the Pivdennyi GZK pit is performed employing geostatistical methods of estimation implemented in geo-information systems, as well as heuristic methods of estimation developed by the authors of the research. Comprehensive geometrization results in a mining and geometric model of mineral reserves distribution at the Pivdennyi GZK pit (Fig.11).

The resulting mining and geometric model of the deposit makes it possible to effectively plan both short- and long-term mining activities of the mining enterprise. The model describes the actual and predicted distribution of minerals by area and depth of the mineral deposit. The model enables geometrization of mineral deposits of complex geometric shapes with different detailing. The results of geometrization of individual parts of the deposit form the basis for creation of a complex mining and geometric model of a deposit.

4. Conclusions

Thus, the comprehensive methodology for geometrization of mineral deposits developed by the authors provides an opportunity of efficient geometrization of mineral deposits. The set of methods included in the methodology enables estimation and calculation of mineral deposit reserves with an error not exceeding 6–8%, depending on the amount of variability of the deposit characteristics. This results in rational and efficient mining operations.

It is advisable to perform geometrizaton of mineral deposits of various geometric shapes using the modified method of vertical parallel sections by selecting the optimal direction of sections and the optimal distance between them. It is expedient to determine the optimal arrangement of sections applying geo-information systems, which programmatically implement various ways of estimating mineral reserves.

Comprehensive geometrization of a mineral deposit requires extensive use of geostatistical and heuristic methods of estimation, which enable actual and predictive geometrization of a mineral deposit in conditions of high variability of the spatial occurrence of minerals.

Further development of the methodology for geometrization of mineral deposits consists in developing methods based on detailed geometrization of mineral deposits, as well as developing and creating geostatistical and heuristic methods of estimation enabling comprehensive geometrization of mineral deposits of various geometric complexity.

Acknowledgments

The work was supported by the Ministry of Education and Science of Ukraine within the framework of the state scientific themes “Investigation and scientific and practical substantiation of technological means for raw material control in mining ores on deep levels” (State registration 0122U000843).

Literatura – References

1. Stupnik, M., Kalinichenko, V. (2013). Magnetite quartzite mining is the future of Kryvyi Rig iron ore basin. Annual Scientific-Technical Colletion - Mining of Mineral Deposits 2013, 49–52.
2. Stupnik, N.I., Kalinichenko, V.A., Fedko, M.B. & Mirchenko, Ye.G. (2013). Prospects of application of TNT-free explosives in ore deposites developed by udergrounds mining. Naukovyi Visnyk Natsionalnoho Hirnychoho Universytetu, 1, 44–48.
3. Kalinichenko, O., Fedko, M., Kushnerov, I. & Hryshchenko, M. (2019). Muck drawing by inclined two-dimensional flow. E3S Web of Conferences, 123, 01015.
4. Stupnik, M.I., Kalinichenko, O.V. & Kalinichenko, V.O. (2012). Technical and economic study of self-propelled machinery application expediency in mines of krivorozhsky bassin. Naukovyi Visnyk Natsionalnoho Hirnychoho Universytetu, 5, 39–42.
5. Stupnik, M, Fedko, M, Hryshchenko, M, Kalinichenko, O & Kalinichenko, V. (2023). Study of Compensation Room Impacts on the Massif Stability and Mined Ore Mass Quality. Inżynieria Mineralna – Journal of the Polish Mineral Engineering Society, 1(51). 129–135. http://doi.org/10.29227/IM-2023-01-16.
6. Stupnik, N., Kalinichenko, V. (2012). Parameters of shear zone and methods of their conditions control at underground mining of steep-dipping iron ore deposits in Kryvyi Rig basin. Geomechanical Processes During Underground Mining – Proceedings of the School of Underground Mining, 15–17.
7. Malanchuk, Z.R., Moshynskyi, V.S., Korniienko, V.Y., Malanchuk, Y.Z., & Lozynskyi, V.H. (2019). Substantiating parameters of zeolite-smectite puff-stone washout and migration within an extraction chamber. Naukovyi Visnyk Natsionalnoho Hirnychoho Universytetu, (6), 11–18. https://doi.org/10.29202/nvngu/2019-6/2.
8. Bazaluk, O., Ashcheulova, O., Mamaikin, O., Khorolskyi, A., Lozynskyi, V., & Saik, P. (2022). Innovative activities in the sphere of mining process management. Frontiers in Environmental Science, (10), 878977. https://doi.org/10.3389/fenvs.2022.878977.
9. Malanchuk, Y., Moshynskyi, V., Khrystyuk, A., Malanchuk, Z., Korniienko, V., & Abdiev, A. (2022). Analysis of the regularities of basalt open-pit fissility for energy efficiency of ore preparation. Mining of Mineral Deposits, 16(1), 68–76. https://doi.org/10.33271/mining16.01.068.
10. Hryhoriev, Y., Lutsenko, S. & Joukov, S. (2023). Dominant Determinants of Adaptation of the Mining Complex in the Conditions of a Dynamic Environment. Inżynieria Mineralna – Journal of the Polish Mineral Engineering Society, 1(51). 15–21. http://doi.org/10.29227/IM-2023-01-02.
11. Bekbotayeva, A., & Dyussetay, S. (2023). Features of the geological structure of the Kogodai VMS deposit in the Kurchum block. Engineering Journal of Satbayev University, 145(5), 39–44. https://doi.org/10.51301/ejsu.2023.i5.06.
12. Uteshov, Y., Galiyev, D., Galiyev, S., Rysbekov, K., & Nauryzbayeva, D. (2021). Potential for increasing the efficiency of design processes for mining the solid mineral deposits based on digitalization and advanced analytics. Mining of Mineral Deposits, 15(2), 102–110. https://doi.org/10.33271/mining15.02.102.
13. Mendygaliyev, A., Arshamov, Y., & Yazikov, E. (2022). Orthogonal-contour geometrization of hydrogenetic ore mineralizations. Engineering Journal of Satbayev University, 144(3), 30–33. https://doi.org/10.51301/ejsu.2022.i3.05.
14. Kassymkanova, K.K., Istekova, S., Rysbekov, K., Amralinova, B., Kyrgizbayeva, G., Soltabayeva, S., & Dossetova, G. (2023). Improving a geophysical method to determine the boundaries of ore-bearing rocks considering certain tectonic disturbances. Mining of Mineral Deposits, 17(1), 17–27. https://doi.org/10.33271/mining17.01.017.
15. Rakishev, B.M. (2022). About the metallogeny of Kazakhstan and its significance for the forecast of mineral deposits. Engineering Journal of Satbayev University, 144(4), 25–33. https://doi.org/10.51301/ejsu.2022.i4.04.
16. Togizov, K., Issayeva, L., Muratkhanov, D., Kurmangazhina, M., Swęd, M., & Duczmal-Czernikiewicz, A. (2023). Rare earth elements in the Shok-Karagay Ore Fields (syrymbet ore district, northern Kazakhstan) and visualisation of the deposits using the geography information system. Minerals, 13(11), 1458. https://doi.org/10.3390/min13111458.
17. Issayeva, L., Togizov, K., Duczmal-Czernikiewicz, A., Kurmangazhina, M., & Muratkhanov, D. (2022). Ore-controlling factors as the basis for singling out the prospective areas within the Syrymbet rare-metal deposit, Northern Kazakhstan. Mining of Mineral Deposits, 16(2), 14–21. https://doi.org/10.33271/mining16.02.014.
18. Peremetchyk, A., Pysmennyi, S., Chukharev, S., Shvaher, N, Fedorenko, S., & Moraru, N. (2023). Geometrization of Kryvbas iron ore deposits. IOP Conference Series: Earth and Environmental Science, 1254(1), 012067. http://doi.org/10.1088/1755-1315/1254/1/012067.
19. Yechkalo, Y., Tkachuk, V., Hruntova, T., Brovko, D. & Tron, V. (2019). Augmented reality in training engineering students: Teaching methods. CEUR Workshop Proceedings, 2393, 952–959. http://ceur-ws.org/Vol-2393.
20. Bazaluk, O., Petlovanyi, M., Lozynskyi, V., Zubko, S., Sai, K., & Saik, P. (2021). Sustainable Underground Iron Ore Mining in Ukraine with Backfilling Worked-Out Area. Sustainability, 13(2), 834. https://doi.org/10.3390/su13020834.
21. Lozynskyi, V., Medianyk, V., Saik, P., Rysbekov, K., & Demydov, M. (2020). Multivariance solutions for designing new levels of coal mines. Rudarsko Geolosko Naftni Zbornik, 35(2), 23–32. https://doi.org/10.17794/rgn.2020.2.3.

22. Pysmennyi, S., Chukharev, S., Peremetchyk, A., Shvaher, N, Fedorenko, S., & Vu Trung Tien. (2023). Enhancement of the technology of caved ore drawing from the ore deposit footwall "triangle". IOP Conference Series: Earth and Environmental Science, 1254(1), 012065. http://doi.org/10.1088/1755-1315/1254/1/012065.

23. Petlovanyi, M., Lozynskyi, V., Zubko, S., Saik, P., & Sai, K. (2019). The infuence of geology and ore deposit occurrence conditions on dilution indicators of extracted reserves. Rudarsko Geolosko Naftni Zbornik, 34(1), 83-91. https://doi.org/10.17794/rgn.2019.1.8.

24. Stupnik, M., I., Peregudov, V., V., Morkun, V., S., Oliinyk, T., A. & Korolenko, M., K. (2021). Development of concentration technology for medium-impregnated hematite quartzite of Rryvyi Rih Iron ore basin. Science and Innovation, 16(6), 56–71. SOURCE-WORK-ID: PR1YE.

25. Bazaluk, O., Rysbekov, K., Nurpeisova, M., Lozynskyi, V., Kyrgizbayeva, G., & Turumbetov, T. (2022). Integrated monitoring for the rock mass state during large-scale subsoil development. Frontiers in Environmental Science, (10), 852591. https://doi.org/10.3389/fenvs.2022.852591.

26. Stupnik, N.I., Kalinichenko, V.A., Fedko, M.B. & Mirchenko, Ye.G. (2013). Influence of rock massif stress-strain state on uranium ore breaking technology. Naukovyi Visnyk Natsionalnoho Hirnychoho Universytetu, 2, 11–16.

27. Stupnik, M.I., Kalinichenko, V.O., Fedko, M.B. & Kalinichenko, O.V. (2018). Investigation into crown stability at underground leaching of uranium ores. Naukovyi Visnyk Natsionalnoho Hirnychoho Universytetu, 6, 20–25.

28. Stupnik, M.I., Kalinichenko, O.V. & Kalinichenko, V.O. (2012). Economic evaluation of risks of possible geomechanical violations of original ground in the fields of mines of Kryvyi rih basin. Naukovyi Visnyk Natsionalnoho Hirnychoho Universytetu, 6, 126–130.

29. Smoliński, A., Malashkevych, D., Petlovanyi, M., Rysbekov, K., Lozynskyi, V., & Sai, K. (2022). Research into Impact of Leaving Waste Rocks in the Mined-Out Space on the Geomechanical State of the Rock Mass Surrounding the Longwall Face. Energies, 15(24), 9522. https://doi.org/10.3390/en15249522.

30. Babets, D., Sdvyzhkova, O., Hapieiev, S., Shashenko, O., & Prykhodchenko, V. (2023). Multifactorial analysis of a gateroad stability at goaf interface during longwall coal mining – A case study. Mining of Mineral Deposits, 17(2), 9–19. https://doi.org/10.33271/mining17.02.009.

31. Bazaluk, O., Kuchyn, O., Saik, P., Soltabayeva, S., Brui, H., Lozynskyi, V., & Cherniaiev, O. (2023). Impact of ground surface subsidence caused by underground coal mining on natural gas pipeline. Scientific Reports, (13), 19327. https://doi.org/10.1038/s41598-023-46814-5.

32. Mussin, A., Imashev, A., Matayev, A., Abeuov, Ye., Shaike, N., & Kuttybayev, A. (2023). Reduction of ore dilution when mining low-thickness ore bodies by means of artificial maintenance of the mined-out area. Mining of Mineral Deposits, 17(1), 35–42. https://doi.org/10.33271/mining17.01.035.

33. Bazaluk, O., Petlovanyi, M., Zubko, S., Lozynskyi, V., & Sai, K. (2021). Instability Assessment of Hanging Wall Rocks during Underground Mining of Iron Ores. Minerals, 11(8), 858. https://doi.org10.3390/min11080858.

34. Pysmennyi, S., Chukharev, S., Peremetchyk, A., Fedorenko, S., & Matsui, A. (2023). Study of Stress Concentration on the Contour of Underground Mine Workings. Inżynieria Mineralna – Journal of the Polish Mineral Engineering Society, 1(51), 69–78. http://doi.org/10.29227/IM-2023-01-08.

35. Shashenko, O, Sobczyk, J, Shapoval, V, Konoval, V & Barsukova, S. (2023). Express-Method for Determination of Rock Heaving Parameters. Inżynieria Mineralna – Journal of the Polish Mineral Engineering Society, 1(51). 113–118. http://doi.org/10.29227/IM-2023-01-14.

36. Petlovanyi, M., Saik, P. & Lozynskyi, V. (2023). Substantiating and Assessing the Stability of the Underground System Parameters for the Sawn Limestone Mining: Case Study of the Nova Odesa Deposit, Ukraine. Inżynieria Mineralna – Journal of the Polish Mineral Engineering Society, 1(51). 79–89. http://doi.org/10.29227/IM-2023-01-10.

37. Stupnik, M., Kalinichenko, V., Fedko, M., Kalinichenko, O., Pukhalskyi, V. & Kryvokhin, B. (2019). Investigation of the dust formation process when hoisting the uranium ores with a bucket. Mining of Mineral Deposits, 13(3), 96–103. https://doi.org/10.33271/mining13.03.096.

38. Baltiyeva, A., Orynbassarova, E., Zharaspaev, M., & Akhmetov, R. (2023). Studying sinkholes of the earth's surface involving radar satellite interferometry in terms of Zhezkazgan field, Kazakhstan. Mining of Mineral Deposits, 17(4), 61–74. https://doi.org/10.33271/mining17.04.061.

39. Matheron, G. (1963). Principles of Geostatistics. Economic Geology, 58(8), 1246–1266. http://dx.doi.org/10.2113/gsecongeo.58.8.

40. Matheron, G. (1967). Kriging or polynomial interpolation procedures. CIMM Trans, 70, 240–244.

41. Kim, H.S., Chung, C.K. & Kim, J.J. (2018). Three-dimensional geostatistical integration of borehole and geophysical datasets in developing geological unit boundaries for geotechnical investigations. Quarterly Journal of Engineering Geology and Hydrogeology, 51(1), 79–95. https://doi.org/10.1144/qjegh2016-012.

42. Kim, H.S., Sun, C., G. & Cho, H.I. (2017). Geospatial Big Data-Based Geostatistical Zonation of Seismic Site Effects in Seoul Metropolitan Area. ISPRS International Journal of Geo-Information, 6(6), 174–191. https://doi.org/10.3390/ijgi6060174.

43. Yunsel, T. (2012). A practical application of geostatistical methods to quality and mineral reserve modelling of cement raw materials. Journal of the Southern African Institute of Mining and Metallurgy, 112, 239–249. https://bit.ly/37hhrJi.

44. Ivahnenko, A.G. (1982). Induktivnyj metod samoorganizacii modelej slozhnyh sistem. Kiev: Naukova dumka.

45. 4Muravina, O.M. & Ponomarenko, I.A. (2016). Programmnaya realizatsiya metoda gruppovogo ucheta argumentov pri unktsional'nom modelirovanii geologo-geofizicheskikh dannykh. Vestnik Voronezhskogo gosudarstvennogo universiteta. Ser. Geologiya, 2, 107–110. http://www.vestnik.vsu.ru/pdf/heologia/2016/02/2016-02-15.pdf.

46. Shurygin, D.N., Vlasenko, S.V. & Shastik, D.S. (2014). Modelirovanie optimalnoj teoreticheskoj variogrammy moshhnosti plasta na osnove metoda gruppovogo ucheta argumentov. Izvestiya vysshix uchebnyx zavedenij. Severo-Kavkazskij region. Seriya: Texnicheskie nauki, 4(179), 76–78.

47. Bukrinsky V.A. (1985). Geometriya nedr. Moscow: Nedra.

48. Pysmennyi, S., Peremetchyk, A., Chukharev, S., Fedorenko, S., Anastasov, D., & Tomiczek, K. (2022). The mining and geometrical methodology for estimating of mineral deposits. IOP Conference Series: Earth and Environmental Science, 1049(1), 012029. https://doi.org/10.1088/1755-1315/1049/1/012029.

49. Peremetchyk, A., Pysmennyi, S., Shvaher, N., Fedorenko, S., & Podoynitsyna, T. (2023). Modeling and Prediction of Iron Ore Quality Indicators. Inżynieria Mineralna – Journal of the Polish Mineral Engineering Society, 1(51). 127–136. http://doi.org/10.29227/IM-2023-01-15.

50. David, M. (1980). Geostatisticheskiye metody pri otsenke zapasov rud. Advanced Geostatistics in the Mining Industry. Leningrad: Nedra.

51. Huang, S. & Huaming, A. (2016). Application of geostatistics in the estimation of Sujishan graphite deposits, Mongolia Stavebn´ı obzor – Civil Engineering Journal, 27, 487–499. https://doi.org/10.14311/CEJ.2018.04.0039.

52. Hekmatnejad, A., Emery, X. & Alipour-Shahsavari, M. (2019). Comparing linear and non-linear kriging for grade prediction and ore/waste classification in mineral deposits. International Journal of Mining, Reclamation and Environment, 33(4), 247–264. https://doi.org/10.1080/17480930.2017.1386430.

53. Peremetchyk, A., Kulikovska, O., Shvaher, N., Chukharev, S., Fedorenko, S., Moraru, R., & Panayotov, V. (2022). Predictive geometrization of grade indices of an iron-ore deposit. Mining of Mineral Deposits, 16(3), 67-77. https://doi.org/10.33271/mining16.03.067.

Kompleksowa metodologia geometryzacji złóż minerałów

W artykule zaproponowano kompleksową metodologię geometryzacji złóż kopaliny. Na podstawie istniejących koncepcji geometryzacji opracowano zestaw metod budowy modelu geometrycznego złoża kopaliny. W procesie geometryzacji złóż kopalin autorzy badań szeroko wykorzystują systemy geoinformacyjne. Podstawą geometryzacji są dane z badań geologicznych. Przy opracowywaniu metodologii szacowania zasobów kopalin uwzględniane są najczęściej stosowane metody. Zmodyfikowana metoda równoległych przekrojów pionowych okazuje się najskuteczniejszą metodą szacowania zasobów złóż o skomplikowanych kształtach geometrycznych. Autorzy opracowują metodykę wyznaczania optymalnej lokalizacji przekrojów szacowanego złoża kopaliny. Do celów geometryzacji wykorzystywane są zarówno metody estymacji geostatystycznej stosowane w systemach geoinformacyjnych, jak i opracowana przez autorów wielowymiarowa metoda estymacji heurystycznej. Ten zestaw górniczych metod geometrycznych umożliwia rzeczywistą i predykcyjną geometrię złoża kopaliny oraz oszacowanie jej zasobów. Opracowana przez autorów metodologia geometryzacji pozwala racjonalnie planować działalność górniczą i zwiększać efektywność przedsiębiorstwa górniczego.

Słowa kluczowe: *kompleksowa metodologia geometrii, system geoinformacyjny, geostatystyczne metody estymacji, wielowymiarowa heurystyczna metoda estymacji, równoległe przekroje pionowe*

Modeling the Impact of Hydraulic Fracturing of Amber-Bearing Rocks by a Flooded Jet in the Erosion Chamber on Mining Productivity

Valerii KORNIYENKO[1)], Yevhenii MALANCHUK[2)], Vitalii ZAIETS[3)], Mykola KOZIAR[4)], Olexandr VASYLCHUK[5)], Wiktoria SOBCZYK[6)]

[1)] Doctor of Engineering, Professor, Department of Mineral Deposits Development and Mining Engineering, National University of Water and Environmental Engineering, Soborna str, 11, Rivne, Ukraine
[2)] Doctor of Engineering, Professor, Department of Automation, Electrical Engineering and Computer-Integrated Technologies, National University of Water and Environmental Engineering, Soborna str, 11, Rivne, Ukraine
[3)] PhD, Associate Professor, Department of Mineral Deposits Development and Mining Engineering, National University of Water and Environmental Engineering, Soborna str, 11, Rivne, Ukraine; email: v.v.zayets@nuwm.edu.ua
[4)] Doctor of Pedagogical Sciences, Professor, Department of Theoretical Mechanics, Engineering Graphics and Machine Sciences, National University of Water and Environmental Engineering, Soborna str, 11, Rivne, Ukraine
[5)] PhD, Associate Professor, Department of Mineral Deposits Development and Mining Engineering, National University of Water and Environmental Engineering, Soborna str, 11, Rivne, Ukraine
[6)] Prof. DSc, PhD, Eng. Faculty of Energy and Fuels, Dept. of Sustainable Energy Development, AGH University of Science & Technology, Krakow, Poland

http://doi.org/10.29227/IM-2024-01-105

Submission date: 13-05-2024 | Review date: 24-06-2024

Abstract

The article discusses the concept of socio-economic and strategic development of the Rivne region (Ukraine), especially the exploration, testing and industrial exploitation of strategic mineral resources. The concept envisages the use of energy-efficient technologies for raw material extraction, especially for amber deposits. It points out that conventional methods of amber extraction are harmful to the environment, and suggests the use of complex methods, such as mechanical and hydraulic technologies.

The article examines the challenge of implementing geotechnological methods at mining enterprises and assesses its complexity in mining science and practice. Scientific research in this area has been conducted, but comprehensive studies of the sampling and extraction methods of amber are still significant and relevant for the national interest.

Moreover, the article reports the results of research on the formation of a jet in a hydraulic monitor and the application of a telescopic hydraulic monitor to extend the range of rock fragmentation, including an analysis of jet parameters and the dynamics of hydraulic rock breaking, such as amber-bearing rocks. The conclusions relate to the linear expansion of the jet, the reduction of axial velocity with the increase of hydrostatic pressure and the efficiency of the telescopic hydromonitor to extend the fragmentation range.

Keywords: *amber, hydromonitor, submerged jet, destruction, parameters*

Introduction

The article outlines the concept of socio-economic and strategic development of the Rivne region of Ukraine, focusing on the exploration, testing and industrial exploitation of strategic mineral resources, located in the subsoil of this region. The concept proposes the creation and implementation of innovative energy-saving technologies for raw material extraction at various stages of sampling, testing and development of deposits, enhancing their energy efficiency through automation of technological processes, reducing costs, and ensuring environmental sustainability of operating conditions. Among other minerals, the development of amber deposits has been identified as a priority. However, the conventional and widespread open method is harmful to the environment. Analytical review and experience indicate that such technologies should rely on the use of integrated extraction methods that combine both mechanical and hydraulic technologies.

Evaluation of the problem status has revealed that the successful implementation of geotechnological methods at mining enterprises is one of the most promising tasks in this area, but also very challenging in mining science and practice.

To date, scientists have conducted research and achieved scientific results on this problem in the leading schools of mining and related sciences, but comprehensive studies of sampling and extraction methods, technology parameters for a significant improvement in the extraction completeness cannot be applied to amber deposits.

Therefore, the development of theoretical and applied foundations of mechanical-hydraulic technology for testing, trial operation and development of amber deposits is an urgent scientific and practical problem of important national importance.

1. Disintegration of Host Rocks by Hydromonitor Jets

The jet formation in the hydraulic monitor depends on the water flow encountering different supports on its way to the nozzle, which cause turbulization and cavitation of the flow, reducing the quality and parameters of the hydraulic monitor jet. The jet is finally formed in the nozzle, which transforms the static pressure of water into the kinetic energy of the jet, and as the nozzle cross-section decreases with a constant water flow rate, its speed increases. Meanwhile, the head loss in the nozzle increases, which is proportional to the square of

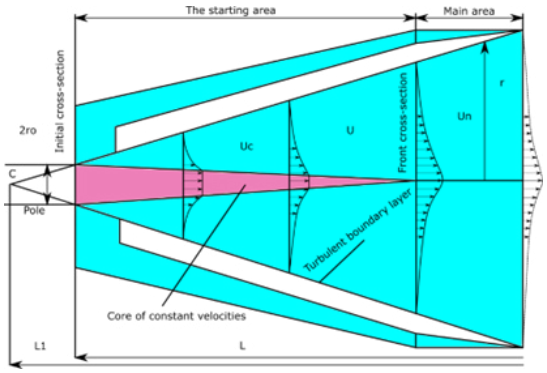

Fig. 1. Diagram of the flooded jet: r0 – nozzle radius; o – pole of jets; uo – initial jet outflow velocity; um – the speed of the jet along its axis; u – velocity of the jet at an arbitrary point along the cross-section; r – current jet radius; l – current jet length; l1 – jet length given pole

Rys. 1. Schemat zalanego strumienia: r0 – promień dyszy; o – słup dysz; uo – początkowa prędkość wypływu strumienia; um – prędkość strumienia wzdłuż jego osi; u – prędkość strumienia w dowolnym punkcie przekroju; r – aktualny promień strumienia; l – aktualna długość strumienia; l1 – długość strumienia na danym biegunie

the flow rate. In the final section of the nozzle, static pressure without head loss is converted into velocity head.

The speed of the jet departure, the water flow rate and the diameter of the hydraulic monitor nozzle are determined by the formulas:

$$u_o = \phi\sqrt{2gH} \tag{1}$$

$$Q = \mu S_H \sqrt{2gH} \tag{2}$$

$$d_H = 0,52\sqrt{\frac{Q}{\sqrt{H}}} \tag{3}$$

S_H – cross-sectional area of the nozzle outlet;
H – pressure;
Q – consumption;
φ – speed ratio (φ = 0,92–0,9b);
μ = αφ;
α – jet compression ratio (α≈1).

According to Prandtl's boundary layer theory, the jet dispersion is caused by the turbulent exchange between it and the surrounding fluid, and the viscosity is the reason for the formation of vortices at the interface between the jet and the liquid. These vortices impede the jet motion and increase its mass by drawing in fluid from the outside. Figure 1 illustrates the jet structure common to all types and its main elements.

The jet structure is defined by geometric (length of the initial and main jet sections, expansion angle) and hydraulic (initial flow speed from the nozzle, axial speed and flow speed across the jet cross-section) parameters [1-5].

The structure and initial parameters of the jet match the conditions for the water flow formation in the channels. Turbulence of the water flow in the supply channel, irregularity of the longitudinal speed profile of the jet, turbulence of the water flow at the nozzle entrance, and cavitation at high heads are factors that reduce the jet compactness and, consequently, its effective length. Besides them, the jet parameters are affected by the viscosity and density of the medium where the jet propagates. Hydraulic and geometric parameters determine the most important jet indicators in contact with the rock - impact force and specific dynamic pressure [6-11].

The decay of a free submerged jet is caused by its expansion due to turbulent exchange with the environment under the effect of inertial forces and surface tension [12-16]. In a non-free flooded jet, the same viscous friction forces and medium resistance have a greater role because of its higher density compared to the jet substance density (Figure 2).

The medium density can increase due to its pressure increase, for example, hydrostatic, because of the production deepening. As a result, the hydrodynamic parameters of the flooded jet worsen. This happens during hydraulic sandblasting of oil well bottomhole zones. The results of measuring the dynamic pressure of the jet at different depths are shown in figure 3. The graph shows that hydrostatic pressure up to a depth of 200-300 meters significantly deteriorates the jet parameters. Studies have also revealed that the effect of the medium density increase with the hydrostatic pressure increase is related to the presence of air bubbles in the liquid flowing out through the nozzle.

The hydromonitor jet, when traveling in the air at a certain distance from the nozzle at the end of the initial section, almost falls apart and can be described by a statistical analysis of the individual elements of the moving water-air mixture. The general form of the fluid mechanics equations for turbulent motion of discrete media has no solution.

Some researchers [23-28, 32] have found empirical relationships of jet parameters on the distance to the nozzle for specific conditions.

Hydromonitor jets can virtually break rocks of any hardness. However, jet fracture is mainly used in the development of weakly cohesive and loose rocks (sands, loams, clayey sandstones, siltstones, etc.) and less frequently semi-rocky rocks (coal, mudstones, marls, shales, limestone sandstones, and so on) [33-39].

According to the results of many experimental studies, it has been determined that the destruction mechanism is due to the simultaneous action of various forces and depends on the characteristics of rocks and the conditions of the jet flow [40-43]. With the destruction of weakly cohesive and loose rocks as a result of the pulsating action of the jet, the bond between the individual particles of the erosion rock is broken. As a result of filtration of part of the water into the pores of loose rocks, they are moistened and wetted, which leads to a change in the adhesion force of the particles. In addition, in an unflooded face, the mass of water of the jet, which accumulates in the funnel, bursts it and, as a result, stresses arise

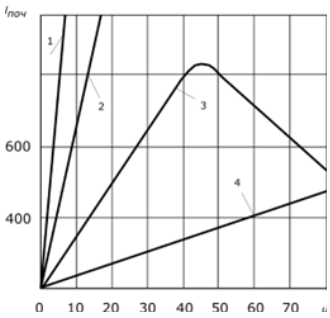

Fig. 2. Change in the length of the initial section of the jet depending on the outflow velocity: 1 – water; 2 – glycerin; 3 – oil: 4 – mercury; l_{init} – length of the initial section of the jet (mm); и – jet speed (m/s)

Rys. 2. Zmiana długości początkowego odcinka strumienia w zależności od prędkości wypływu: 1 – woda; 2 – gliceryna; 3 – olej: 4 – rtęć; $l_{pocz.}$ – długość początkowego odcinka strumienia (mm); u –prędkość strumienia (m/s)

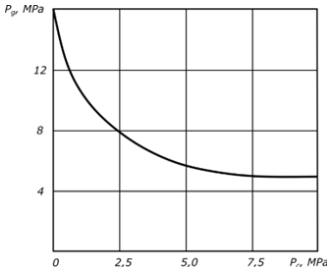

Fig. 3. Dependence of the dynamic head of the jet (P_g) on the hydrostatic pressure (P_c) of the aqueous medium at the pressure at the outlet of the nozzle of 20 MPa

Rys. 3. Zależność wysokości dynamicznej strumienia (P_g) od ciśnienia hydrostatycznego (P_c) ośrodka wodnego przy ciśnieniu na wylocie dyszy, wynoszącym 20 MPa

in the massif, contributing to the emergence of cracks and the detachment of individual pieces of rock.

The shear resistance of cohesive soils is expressed by Coulomb's formula

$$\tau = c + \sigma_e tg\ \varphi \quad (4)$$

σ_e – effective normal voltage;
τ – shear stress;
φ – angle of internal friction;
c – specific adhesion.

For cemented sands and similar rocks

$$\tau = c + (\sigma - p_\Gamma) tg\ \varphi \quad (5)$$

σ – full normal voltage;
p_Γ – neutral voltage equal to the hydrostatic pressure of water in the pores. For loose sands, you can take the specific adhesion to be zero.

To break weakly cohesive and loose rocks, the jet pressure at the contact must exceed the shear resistance [45-48].

The structure of the massif can be destroyed by creating a hydraulic gradient for very loose water-saturated soils and quicksand, which have a specific ratio of fractions and a degree of water saturation.

Investigation of hydrodynamic characteristics of the jet in mechanical-hydraulic extraction of amber. The study involved measuring the dynamic pressure of the flooded jet along its axis and across its cross-section at various distances from the nozzle depending on the nozzle diameters, water pressure, and the effect of the hydrostatic pressure of the amber deposit on the jet parameters.

To conduct field studies on the exposed layer of the Klesiv amber deposit in the Rivne region, a bench installation was built (Figure 4). A layer with a thickness of 3 meters from top to bottom consists of different-, medium- and fine-grained host rock, the strength of which is characterized by an adhesion coefficient of 0.03, 0.035 and 0.045 MPa. The telescopic barrel is placed at a distance from the face and closed with a jet cut-off to avoid erosion when measuring the fixed water pressure on the nozzle. Before the experiment, the pit was filled with water to a depth of more than 1 meter. In the course of the experiment, the time of operation of the jet and the pressure of water on the nozzle were fixed. After the experiment, the hydraulic mixture was pumped out of the chamber by a hydraulic elevator, and the formed cavity was measured [50, 53-54, 56, 58].

The bench installation enabled the experiment conditions to be as close as possible to the full-scale ones, to vary the pressure of the pressure water in front of the nozzle in a wide range and to measure the dynamic pressure of the jet along the axis and in its different sections.

It is well known that destructive processes are quite hard to model with physical similarity. It will be shown later that even a more stable process of mineral transportation is quite hard to model.

The dynamic pressure was measured by a receiving nozzle, which moved in three mutually perpendicular planes with the help of a system of adjusting bolts. The experiment started with mounting, centering and securing the nozzle and breaker plate. Then, a container measuring 2.5×1.5×1.5 m was filled with water, air was released from the impulse

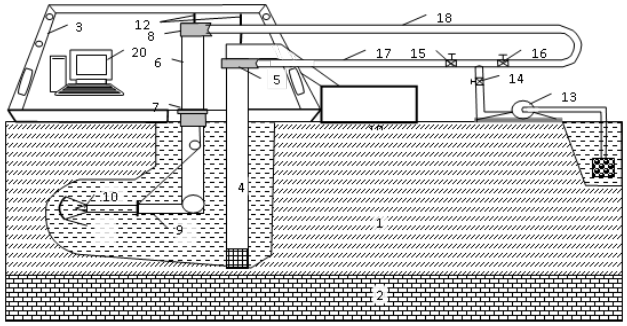

Fig. 4. Stand for field studies of hydraulic destruction of minerals in a flooded environment: 1 –mineral, 2 – underlying rocks; 3 – assembly crane; 4 – hydroelevator, 5 – hydraulic elevator header; 6 – hydromonitor device, 7 – rotator, 8 – headband, 9 – technological barrel, 10 – nozzle, 11 – jet cut-off, 12 – cable block system, 13 – pump, 14-16 – latches, 17, 18 – flexible high-pressure hoses, 19 – container for hydraulic mixture, 20 – control panel

Rys. 4. Stanowisko do badań terenowych hydraulicznego niszczenia minerałów w środowisku zalewowym: 1 – minerał, 2 – skały leżące pod spodem; 3 – dźwig montażowy; 4 – winda hydrauliczna, 5 – głowica windy hydraulicznej; 6 – urządzenie hydromonitorowe, 7 – rotator, 8 – opaska nagłowna, 9 – beczka technologiczna, 10 – dysza, 11 – odcięcie strumienia, 12 – układ bloków kablowych, 13 – pompa, 14-16 – zatrzaski, 17, 18 – elastyczne węże wysokociśnieniowe, 19 – zbiornik na mieszankę hydrauliczną, 20 – panel sterowania

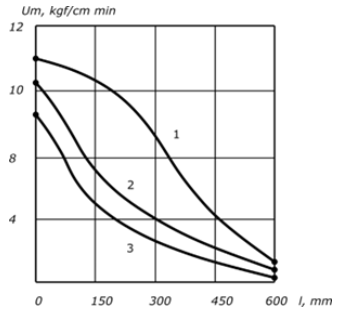

Fig. 5. Distribution of axial velocity (U_m) along the length of the flooded jet (l) for conoidal-cylindrical nozzles with diameters (mm) of 23 (curve 1), 15 (curve 2), 11 (curve 3), respectively at water pressures P_0 = 1.6 MPa

Rys. 5. Rozkład prędkości osiowej (U_m) na długości zalewanego strumienia (l) dla dysz stożkowo-cylindrycznych o średnicach (mm) odpowiednio 23 (krzywa 1), 15 (krzywa 2), 11 (krzywa 3), przy ciśnieniu wody P_0 = 1,6 MPa

tubes, the set pressure on the nozzle was set and measurements were taken.

As a result of the experiments, the distribution of the dynamic pressure of the jet along its axis for nozzles of different diameters was obtained (Figure 5). After processing the experimental data and presenting them in the form of a dimensionless dependence, it was established that this dependence of the tested nozzles and pressures at a hydrostatic pressure of 1 m of water column is described by an equation similar to [61-69]

$$\frac{u_{m}}{u_{o}} = \frac{0,96}{0,29 + \frac{a_o l}{r_н}} \quad (6)$$

u_o – initial jet outflow velocity;
l – jet length;
$u_т$ – axis jet velocity;
$r_н$ – nozzle radius;
a_o – jet structure coefficient at low hydrostatic pressure (a0 = 0,068).

On the stand, the distribution of the flow velocity along the cross-sections of the jet from different nozzles in the pressure range of 0.4–1.6 MPa at a distance from 1 to 20 nozzle diameters was determined. Figure 6 shows velocity diagrams in different cross–sections of a jet with a 23 mm nozzle. In the boundary layer, the flow velocity is low and its value fluctuates greatly due to the turbulent exchange of the jet and the environment. Therefore, in order to identify the pattern of expansion of the jet of the hydromonitor, there was a The dependence of the flow velocity on the distance on the axis of the jet $r_{0,5m}$, at which the velocity of the jet is half of the axial velocity in the same section, is constructed in a dimensionless form u=0,5 $u_т$ (Figure 6 a, 6 b)

$$\frac{u}{u_m} = \exp\left[-(\frac{r_o}{r_{0,5u_m}})^2 \ln 2\right] \quad (7)$$

Experimental data also show a linear expansion of the jet with an opening angle of α = 20°

$$r_{0,5u_m} / r_н = tg\frac{\alpha}{2} l / d_н \quad (8)$$

Study of the influence of the nozzle immersion depth on the parameters of the flooded jet. A special bench installation consisted of a chamber, which is a sealed pipe segment with a diameter of 400 mm and a length of 1500 mm, where the barrel of the hydraulic monitor is inserted. A measuring impulse tube of the pressure sensor is inserted from the other end of the chamber along the axis of the nozzle, which is secured and centered with a locking device.

The experiment starts with the installation and fixation of the nozzle and the receiving impulse tube at distances of 4, 10 and 20 nozzle diameters. When water is delivered to the chamber through the nozzle, the required value of hydrostatic pressure corresponding to the nozzle immersion is set in the

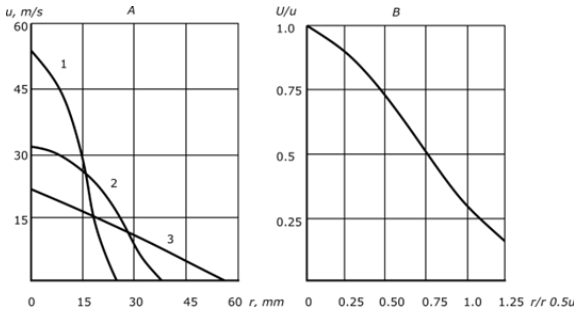

Fig. 6. Distribution of the flow velocity (u) of the flooded jet along the radius (r) of the cross–sections at distances from the nozzles (a) – 1 – 4 $d_н$; 2 – 10 dн; 3 – 20 d_0 (po = 1.6 MPa, dn = 23 mm); (b) – the same dependence in dimensionless form in the range of water pressure changes r_o = 0.4–1.6 MPa and nozzle diameters d_n = 11–23 mm

Rys. 6. Rozkład prędkości przepływu (u) zalanego strumienia wzdłuż promienia (r) przekrojów w odległościach od dysz (a) – 1 – 4 $d_н$; 2 – 10 $d_н$; 3 – 20 d_0 (po = 1,6 MPa, dn = 23 mm); (b) – ta sama zależność w postaci bezwymiarowej w zakresie zmian ciśnienia wody r_o = 0,4–1,6 MPa i średnic króćców d_n = 11–23 mm

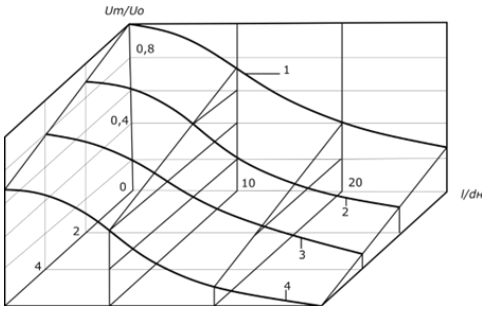

Fig. 7. Universal dimensionless dependence of the axial velocity of the flooded jet (U_m/U_0) of the hydromonitor nozzle on its length (l/dн) in sections 0, 1, 2, 3: 1 – at hydrostatic pressure p_r=1 meter of water column; 2 – p_r=20 meters of water column; 3 – p_r=40 meters of water column; 4 – p_r=60 meters of water column

Rys. 7. Uniwersalna bezwymiarowa zależność prędkości osiowej zalanego strumienia (U_m/U_0) dyszy hydromonitora od jej długości (l/dн) w przekrojach 0, 1, 2, 3: 1 – przy ciśnieniu hydrostatycznym p_r=1 metr słupa wody; 2 – p_r=20 metrów słupa wody; 3 – p_r=40 metrów słupa wody; 4 – p_r=60 metrów słupa wody

chamber using a relief valve and a pressure gauge. Then, the value of the axial dynamic pressure of the jet is measured.

The effect of hydrostatic pressure on the axial velocity increases with a decrease in the pressure at the nozzle outlet and practically does not depend on the nozzle diameters. The graph in Figure 7 shows that in the same jet cross–sections at a constant initial pressure with increasing hydrostatic pressure, the axial velocity decreases according to a linear law.

$$\frac{u_m}{u_0} = 1 - kp_0 \tag{9}$$

k – angular coefficient depending on initial pressure at nozzle inlet. For the conditions of the experiment k = 0,12–0,0054.

In the semi–empirical theory of the submerged jet [70, 73], the initial and boundary conditions of its flow are taken into account by the coefficient of the flow structure (a), empirically. Under our conditions, a dependence was obtained for differentinitial water pressures

$$a = \frac{1}{c - bp_0} \tag{10}$$

c – a constant equal to 16;
b – research coefficient.

Values of coefficient b are determined according to experimental data. For pressures (p0) 0.4; 0.8; 1.2; 1.6; 2.0 MPa; the b values are respectively 1.950; 1.471; 1.002; 0.560; 0.100.

The productivity of hydraulic fracturing per cycle was determined by dividing the volume of the product by the time of its formation. The specific water flow rate per 1 m^3 of destroyed mineral was calculated as the ratio of water flow through the nozzle to the mineral volume destroyed during this cycle. Specific energy intensity was defined as the ratio of jet power to hydraulic fracture productivity per cycle.

Figure 8 shows the dynamics of the host rock destruction. The graph shows three stages in the destruction process. At the first stage, a narrow channel 1.1–1.7 m long is formed intensively, the extraction volume reaches 27%; in the second – the channel is expanded and deepened, the extraction volume increases to an average of 57%; At the third stage, the destruction productivity drops sharply, on average, the extraction volume is 16% and the channel length hardly increases, reaching about 2 m after 2–2.5 minutes.

As the face moves away from the nozzle, the fracture rate decreases (Figure 9, a), and the specific water flow rate increases (Figure 9, b). The distance from the face, at which the destruction of the mineral occurs, increases with an increase in the diameter of the nozzle. For example, with a water pressure of 1.5 MPa and nozzles of 11, 15, 23 mm, this distance is 1.2, respectively; 1,8; 2.05 m (Figure 10). As the water pressure increases, the fracture rate increases, and the specific water flow rate decreases and remains practically constant at a pressure of 1–1.5 MPa. The same happens when the diameter of the nozzle increases.

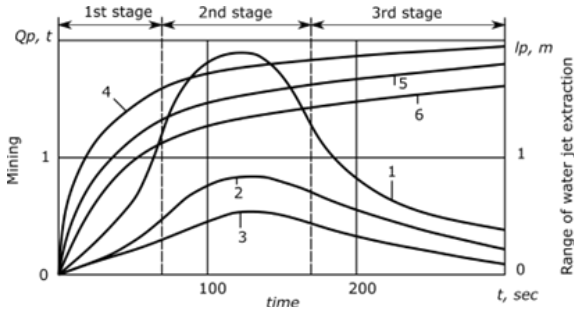

Fig. 8. Dynamics of hydraulic destruction of weakly cemented sand by a flooded jet from a single nozzle in time: 1, 2, 3 – Q_p=f(t); 4, 5, 6 – l p = f(t), respectively at p_0 = 1.5; 1.0; 0.5 MPa

Rys. 8. Dynamika niszczenia hydraulicznego piasku słabo zacementowanego przez zalany strumień z pojedynczej dyszy w czasie: 1, 2, 3 – Q_p=f(t); 4, 5, 6 – l p = f(t), odpowiednio przy p_0 = 1,5; 1,0; 0,5 MPa

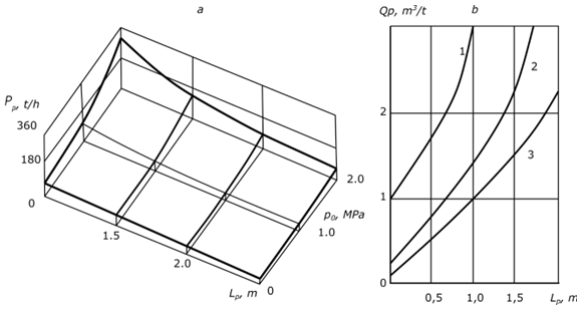

Fig. 9. Dependence of productivity (P_p) and specific flow rate (Q_p) and hydraulic fracture range or distance to face (L_p) on the value of pressure of pressure water (p_0): a – Pp =f(L_p); б – Q_p=f(L_p); 1, 2, 3 – for nozzle diameters of 11, 15 and 23 mm

Rys. 9. Zależność wydajności (P_p) i jednostkowego natężenia przepływu (Q_p) oraz zasięgu szczeliny hydraulicznej lub odległości od ściany (L_p) od wartości ciśnienia wody pod ciśnieniem (p_0): a – Pp =f(L_p); б – Q_p=f(L_p); 1, 2, 3 – dla dysz o średnicach 11, 15 i 23 mm

The productivity of destruction of a mineral flooded by a jet depending on (p_0 = 0,5–2 MPa, $d_н$=11–23 mm, L_p до 2 m) is described by empirical dependence (Figure 10).

One way to improve fracture performance is to use a special hydromonitor head, in which the jet of the side front nozzle rotates around the face perimeter. The head rotation is due to the jet reactive force. The jet of the central nozzle makes a cut in the host rock layer, and the rotating jet of the side nozzle, with one exposure plane, reflects the rock and widens the cut. As a result, a cavity will be formed, the size of which depends on the angle of the side nozzle inclination to the axis of the telescopic barrel and on the pressure of the pressurized water.

The fracture features and performance of the head are similar to those of a single nozzle. At the same time, the productivity is 2.5 times higher, and the minimum values of energy intensity and specific water consumption are 1.2–1.5 times lower. Increasing the side nozzle diameter, e.g. from 15 to 23 mm, gives a 50% increase in productivity at fracture. The optimal angle of the side nozzle is 50°.

The relationship between the main parameters of the flooded jet and the fracture is determined by the specific pressure needed for the destruction of a weakly cemented mineral with an adhesion coefficient of 0.030–0.045 MPa and an internal friction coefficient of 0.30–0.45. Table 1 shows the average values of the actual fracture range and specific pressure of the jet.

After analyzing the experimental data, generalized dependencies of fracture productivity (Pp) on jet power (N) were obtained

$$P_p = 2,0N^{0,933}, \text{ t/h} \quad (11)$$

Taking into account the well–known expression for the power of the jet, the formula will take the form

$$P_p = 165 d_н^{\,3} p_0^{2,4} \cdot 10^{-4}, \text{ t/h} \quad (12)$$

One way to improve fracture performance is to use a hydraulic monitor with a telescopic barrel. By delivering the fracture mechanism to the face with a telescopic shaft, the fracture range can be increased by the shaft length (up to 10 m) and the jet kinetic energy can be used effectively due to the nozzle constantly approaching the developing face.

The host rock destruction in the flooded face was tested by delivering the head to the massif with a telescopic shaft. During the tests, when the head was delivered to the face, the water pressure was 1.5 MPa, and when it was delivered back, it was 0.5 MPa. The destruction was done by sector approaches by undercutting the layer along the sole, made of the loosest rock. The undercutting roadway diameter stabilized and averaged 1.6–1.8 m in all tests.

One of the important aspects for the technology of mineral extraction is the calculation of the angle between two undercutting workings, which prevents the creation of an undestroyed pillar. With a cutting roadway width of 1.8 m and a chamber radius of 8–9 m, the optimal angle between approaches is 15°.

2. Conclusion

The modeling studies determined the distribution of the hydromonitor flow speed across the jet cross-sections in the pressure range of 0.4–1.6 MPa at a distance of up to 20 nozzle diameters. A linear expansion of the jet with an opening an-

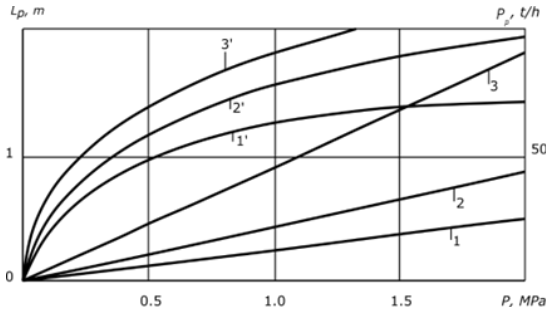

Fig. 10. Dependence of the average productivity (P_p) and fracture range (L_p) on water pressure (p_o): 1, 2, 3 – $P_p=f(p_o)$ d_H = 11, 15, 23 mm; 1', 2' ,3' – $l_p=f(p_o)$ at d_H = 11, 15, 23 mm

Rys. 10. Zależność średniej produktywności (P_p) i zasięgu pękania (L_p) od ciśnienia wody (p_o): 1, 2, 3 – $P_p=f(p_o)$ d_H = 11, 15, 23 mm; 1', 2',3' – $l_p=f(p_o)$ przy d_H = 11, 15, 23 mm

Tab. 1. Dependence of the fracture range of the host rock on the diameter of the nozzle

Tabela 1. Zależność zasięgu pękania skały macierzystej od średnicy króćca

Diameter nozzles, mm	Actual fracture range of the host rock, m	Distance from the nozzle, where the specific pressure jet is equal to 0.050 MPa
23	2,10	2,16
15	1,74	1,17
11	1,15	0,73

Tab. 2. Dependence of the Fracture Efficiency of the Host Rock on the Type destructive mechanism

Tab. 2. Zależność skuteczności pękania skały macierzystej od rodzaju mechanizmu niszczącego

Type of destruction mechanism	**Range destruction (limit), m**	**Average capacity, t/h**	**Pitoma vitrata waters, m³/t**	**Energy intensity, kWh/t**
Single nozzle diameter 11 мм 15 мм 23 мм	 1,15/(1,76) 1,74/(2,10) 2,10/(2,05)	 19,76/76,40 31,30/126,20 82,00/149,00	 0,76/0,197 1,10/0,28 0,72/0,50	 0,31/0,08 0,45/0,11 0,29/0,20
Hydromonitor head diameter 15 мм 23 мм	 2,0/(2,5) 2,6/(2,7)	 147,00/258 184,00/330	 0,603/0,340 0,680/0,375	 0,25/0,14 0,27/0,15
Hydromonitor head with telescopic barrel length 4.5 m, nozzle diameter 23 mm, feed rate 2.55 m/min	7,2/(7,3)	335/474	1,193/0,888	0,44/0,32

gle of 20° was established. In the same jet sections, the axial velocity decreases linearly with a coefficient of 0.12–0.0054, depending on the initial pressure at the nozzle outlet, as the hydrostatic pressure increases.

A flow structure coefficient of 0.068 was also found for different initial water pressures. The hydraulic destruction dynamics of rocks containing amber was studied, where three stages of the fracture process with different channel sizes and extraction volume intensities were identified respectively at 27%, 57% and 16%. The telescopic hydraulic monitor allows increasing the destruction range up to 10 m with stabilization of the undercutting roadway diameter of 1.6…1.8m.

Literatura – References

1. Dychkovskyi, R., Vladyko, O., Maltsev, D., & Cabana, E. C. (2018). Some aspects of the compatibility of mineral mining technologies. Rudarsko–Geološko–Naftni Zbornik, 33(4), 73–82. https://doi.org/10.17794/rgn.2018.4.7.
2. Perkovsky, E. E. (2017). Rovno Amber Caddisflies (Insecta, Trichoptera) from Different Localities, with Information about three New Sites. Vestnik Zoologii, 51(1), 15–22. https://doi.org/10.1515/vzoo–2017–0003.
3. Lustyuk M. G. Description of the technological scheme of the development of amber deposits / Bulletin of the NUVHP: Collection. of science works – Rivne, 2006. – No. 2 (34), part 1. – pp. 214–220.
4. Lustyuk M. G. Physico–technical basis of hydraulic extraction of lumpy minerals from placer deposits / Monograph – Rivne: Europ. Univ. PP DM – 2005. – 240 p.
5. Yussupov, Kh., Aben, Ye., Omirgali, A., & Rakhmanberdiyev, A. (2021). Analyzing a denitration process in the context of underground well uranium leaching. Mining of Mineral Deposits, 15(1), 127–133. https://doi.org/10.33271/mining15.01.127.
6. Begalinov, A., Khomiakov, V., Serdaliyev, Y., Iskakov, Y., & Zhanbolatov, A. (2020). Formulation of methods reducing landslide phenomena and the collapse of career slopes during open–pit mining. E3S Web of Conferences, 168, 00006. https://doi.org/10.1051/e3sconf/202016800006.
7. Shustov, O., Pavlychenko, A., Bondarenko, A., Bielov, O., Borysovska, O., & Abdiev, A. (2021). Substantiation into Parameters of Carbon Fuel Production Technology from Brown Coal. Materials Science Forum, (1045), 90–101. https://doi.org/10.4028/www.scientific.net/MSF.1045.90.
8. Zhanakova, R., Pankratenko, A., Almenov, T., & Bektur, B. (2020). Rational selection of the form of support for the formation of genetic composition of rocks in the conditions of the Beskempir field. News of the National Academy of Sciences of the Republic of Kazakhstan, (439), 106–113.
9. Begalinov, A., Almenov, T., Zhanakova, R., & Bektur, B. (2020). Analysis of the stress deformed state of rocks around the haulage roadway of the Beskempir field (Kazakhstan). Mining of Mineral Deposits, 14(3), 28–36. https://doi.org/10.33271/mining14.03.028.
10. Petlovanyi, M., Lozynskyi, V., Zubko, S., Saik, P., & Sai, K. (2019). The influence of geology and ore deposit occurrence conditions on dilution indicators of extracted reserves. Rudarsko Geolosko Naftni Zbornik, 34(1), 83–91. https://doi.org/10.17794/rgn.2019.1.8.
11. Telkov, S. A., Motovilov, I. Y., Barmenshinova, M. B., Medyanik, N. L., & Daruesh, G. S. (2019). Substantiation of Gravity Concentration to the Shalkiya Deposit Lead–Zinc Ore. Journal of Mining Science, 55(3), 430–436. https://doi.org/10.1134/s1062739119035769.
12. Korniienko, V., Malanchuk, Y., Zaiets, V., Semeniuk, V., Kucheruk, M. (2023). Research of the Dehydration Process of Amber–Containing Mining Mass. Inzynieria Mineralna, 1, 35–43. http://doi.org/10.29227/IM–2023–01–01.
13. Yulusov, S., Surkova, T. Y., Amanzholova, L. U., & Barmenshinova, M. B. (2018). On sorption of the rare–earth elements. Journal of Chemical Technology and Metallurgy, 53(1), 79–82.
14. Malanchuk, Z. V. Moshynskyi, Y. Malanchuk, V. Korniyenko, O. Vasylchuk, V. Zaiets, M. Kucheruk (2023). Impact by the operating and structural parameters of a screen on the technological parameters of vibratory basalt sieving. Mining of Mineral Deposits, 17(2), 35–43. https://doi.org/10.33271/mining17.02.035.
15. Begalinov, A., Shautenov, M., Almenov, T., Bektur, B., & Zhanakova, R. (2019). Prospects for the effective use of reagents based on sulfur compounds in the technology of extracting gold from resistant types of gold ore. Journal of Advanced Research in Dynamical and Control Systems, 11(8), 1791–1796.
16. Aben, E. K., Rustemov, S. T., Bakhmagambetova, G. B., & Akhmetkhanov, D. (2019). Enhancement of metal recovery by activation of leaching solution. Mining Informational and Analytical Bulletin, (12), 169–179. https://doi.org/10.25018/0236–1493–2019–12–0–169–179.
17. Remezova, O., Komsky M., Komliev O., Chukharev S., Vasylenko S. (2023). Study of Valuable Impurities of Ore–Forming Titanium Minerals in the Ukraine. Inzynieria Mineralna, 1, 189–194. http://doi.org/10.29227/IM–2023–01–24.
18. Bitimbaev, M. Z., Krupnik, L. A., Aben, E. K., & Aben, K. K. (2017). Adjustment of backfill composition for mineral mining under open pit bottom. Gornyi Zhurnal, (2), 57–61. https://doi.org/10.17580/gzh.2017.02.10.
19. Motovilov, I. Y., Telkov, S. A., Barmenshinova, M. B., & Nurmanova, A. N. (2019). Examination of the preliminary gravity dressing influence on the Shalkiya deposit complex ore. Non–Ferrous Metals, 47(2), 3–8. https://doi.org/10.17580/nfm.2019.02.01.
20. Arslanov, M. Z., Mustafin, S. A., Zeinullin, A. A., Kulpeshov, B. S., & Mustafin, T. S. (2020). Model for determining classification of filling materials hardening. News of National Academy of Sciences of the Republic of Kazakhstan, 5(443), 6–12. https://doi.org/10.32014/2020.2518–170x.98.
21. Mustakhimov, A., & Zeynullin, A. (2020). Scaled–up laboratory research into dry magnetic separation of the Zhezdinsky concentrating mill tailings in Kazakhstan. Mining of Mineral Deposits, 14(3), 71–77. https://doi.org/10.33271/mining14.03.071.

22. Pysmennyi, S., Fedko, M., Chukharev, S., Sakhno I., Moraru, R. and Panayotov, V. (2023). Enhancement of the rock mass quality in underground iron ore mining through application of resource–saving technologies. IOP Conf. Ser.: Earth Environ. Sci. 1156 012029. http://doi.org/10.1088/1755–1315/1156/1/012029

23. Malanchuk, Z.R., Korniyenko, V. Ya, Zaiets, V. V., Vasylchuk, O. Yu., Kucheruk, M. O. and Semeniuk, V. V. (2023). Study of hydroerosion process parameters of zeolite–smectite tuffs and underlying rock. IOP Conf. Ser.: Earth Environ. Sci. 1254 012051. https://doi.org/10.1088/1755–1315/1254/1/012051.

24. Malanchuk, Z.R., Khrystyuk, A.O., Stets, S.Ye. Semeniuk, V.V., Malanchuk, L.O. (2022). Substantiation of research results on energy efficiency of basalt crushing. Naukovyi Visnyk Natsionalnoho Hirnychoho Universytetu, (6), 41–46.https://doi.org/10.33271/nvngu/2022–6/041

25. Korniyenko, V.Ya, Vasylchuk, O.Yu, Zaiets, V.V., Semeniuk, V.V., Khrystyuk, A.O. and Malanchuk, Ye.Z. (2022). Research of amber extraction technology by vibroclassifier. IOP Conf. Ser.: Earth Environ. Sci. 1049 012027. https://doi.org/10.1088/1755–1315/1049/1/012027.

26. Malanchuk, Y., Moshynskyi, V., Khrystyuk, A., Malanchuk, Z., Korniienko, V., & Abdiev, A. (2022). Analysis of the regularities of basalt open–pit fissility for energy efficiency of ore preparation. Mining of Mineral Deposits, 16(1), 68–76. https://doi.org/10.33271/mining16.01.068.

27. Moshynskyi, V.S., Korniienko, V.Ya, Malanchuk, Ye.Z, Khrystyuk, A.O., Lozynskyi, V.H., Cabana, E.C. (2021). Simulation of amber extraction processes from sandy and clay rocks with stope filling. Naukovyi Visnyk Natsionalnoho Hirnychoho Universytetu, 6, 35–41. https://doi.org/10.33271/nvngu/2021–6/035.

28. Malanchuk, M., Zaiets, V., Tyhonchuk, L., Moshchych, S., Gayabazar G. and Dang T.(2021). Research of the properties of quarry tuff–stone for complex processing. E3S Web of Conferences. Volume 280 (2021) 01003 DOI:https://doi.org/10.1051/e3sconf/202128001003.

29. V. Korniyenko, V., Malanchuk Y., Khrystyuk, A., Kostrychenko V., Shampikova, A., Nogaeva K. and Kozhonov A. (2021). Modeling the distribution of rock mass and native copper output by size classes during crushing. E3S Web of Conferences. Volume 280 (2021) 01004 DOI:https://doi.org/10.1051/e3sconf/202128001004.

30. Dang, T., Malanchuk Z. and Zaiets T. (2021). Investigation of resistance and air leakage of auxiliary ventilation ducting in underground mine in Quangninh. E3S Web of Conferences. Volume 280 (2021) 08002 DOI:https://doi.org/10.1051/e3sconf/202128008002.

31. Nogaeva, K., Alpiyev, Y., Kozhonov, A., Korniyenko V. and Malanchuk Y. (2021). Technological basis of processing of serpentinite copper–gold ores in the Kyrgyz Republic. E3S Web of Conferences. Volume 280 (2021) 08005 DOI:https://doi.org/10.1051/e3sconf/202128008005.

32. Moshynskyi, V., Zhomyruk, R., Vasylchuk, O., Semeniuk, V., Okseniuk, R., Rysbekov K. and Yelemessov, K. (2021). Investigation of technogenic deposits of phosphogypsum dumps. E3S Web of Conferences. Volume 280 (2021) 08008 DOI:https://doi.org/10.1051/e3sconf/202128008008.

33. Malanchuk, Ye., Moshynskyi, V., Denisyuk, P., Malanchuk, Z., Khrystyuk, A., Korniienko, V., & Martyniuk, P. (2021). Regularities in the distribution of granulometric composition of tuff while crushing. Mining of Mineral Deposits, 15(1), 66–74. https://doi.org/10.33271/mining15.01.066.

34. Malanchuk, Ye., Korniienko, V., Malanchuk, L., Zaiets, V. (2020) Research into the moisture influence on physical–chemical tuff–stone characteristics in basalt quarries of the Rivne–Volyn region. E3S Web of Conferences. Volume 211 (2020) 01036 DOI:https://doi.org/10.1051/e3sconf/202020101036.

35. Small mining encyclopedia: in 3 volumes / edited by V. S. Biletskyi. — D.: Donbas, 2004. — T. 1: A — K. — 640 p. — ISBN 966–7804–14–3.

36. Svitlyi, Yu. G., Biletskyi V. S. (2009). Hydraulic transport (monograph). — Donetsk: Eastern Publishing House, Donetsk branch of the NTSh, "Editorial of the mining encyclopedia". 436 p. ISBN 978–966–317–038–1.

37. Korniyenko, V. , Nadutyi, V., Malanchuk, Y., Yeluzakh, M. (2020). Substantiating velocity of amber buoying to the surface of sludge–like rock mass. Mining of Mineral Deposits, 14(4), 90–96. DOI:https://doi.org/10.33271/mining14.04.090.

38. Malanchuk Z., Moshynskyi V.,Martyniuk P., Stets S., Galiyev D. (2020) Modelling hydraulic mixture movement along the extraction chamber bottom in case of hydraulic washout of the tuff–stone. E3S Web of Conferences. Volume 211 (2020) 01011 DOI:https://doi.org/10.1051/e3sconf/202020101011.

39. Malanchuk, Z., Moshynskyi, V., Malanchuk, Y.., Kor.niienko, V, Koziar, M. (2020). Results of Research into the Content of Rare Earth Materials in Man–Made Phosphogypsum Deposits. Key Engineering Materials, (844), 77–87. https://doi.org/10.4028/www.scientist.net/KEM.844.77.

40. Moshynskyi, V., Malanchuk, Z., Tsymbaliuk, V., Malanchuk, L., Zhomyruk, R., & Vasylchuk, O.(2020). Research into the process of storage and recycling technogenic phosphogypsum placers. Mining of Mineral Deposits, 14(2), 95–102. https://doi.org/10.33271/mining14.02.095.

41. Malanchuk Z., Korniyenko V., Malanchuk Ye., Khrystyuk A., Kozyar M. Identification of the process of hydromechanical extraction of amber. E3S Web of Conferences. Volume 166 (2020) 02008 DOI: https://doi.org/10.1051/e3sconf/202016602008.

42. Malanchuk, Z., Moshynskyi, V., Korniienko, V., Malanchuk, Y., Lozynskyi, V. Substantiating parameters of zeolite–smectite puff–stone washout and migration within an extraction chamber. Naukovyi Visnyk Natsionalnoho Hirnychoho Universytetu (2019). DOI: 10.29202/nvngu/2019–6/2.

43. Malanchuk, Z., Korniienko, V., Malanchuk, Y., Moshynskyi, V. Analyzing vibration effect on amber buoying up velocity.E3S Web of Conferences 123, 01018 (2019). Ukrainian School of Mining Engineering – 2019. DOI: 10.1051/e3sconf/201912301018.

44. Sai, K., Malanchuk, Z., Petlovanyi, M., Saik, P., Lozynskyi, V. Research of thermodynamic conditions for gas hydrates formation from methane in the coal mines. Solid State Phenomena (2019). DOI: 10.4028/www.scientific.net/SSP.291.155.

45. Malanchuk, Y., Korniienko, V., Moshynskyi, V., Soroka V., Khrystyuk, A., Malanchuk, Z. Regularities of hydromechanical amber extraction from sandy deposits. Mining of mineral deposits. – 2019. DOI: 10.33271/mining13.01.049.

46. Nadutyi, V., Korniyenko, V., Malanchuk, Z., Cholyshkina, O. Analytical presentation of the separation of dense suspensions for the extraction of amber. E3S Web of Conferences 109, 00059 (2019). Essays of Mining Science and Practice. DOI: 10.1051/e3sconf/20191090005.

47. Malanchuk, Z.V., Korniienko, V., Malanchuk, Ye., Soroka, V., Vasylchuk, O. (2018). Modeling the formation of high metal concentration zones in man–made deposits. Mining of Mineral Deposits, 12(2), 76–84. https://doi.org/10.15407/mining12.02.076.

48. Z. Malanchuk, Z., Moshynskyi, V., Malanchuk, Y., Korniienko, V. (2018). Physico–Mechanical and Chemical Characteristics of Amber. Non–Traditional Technologies in the Mining Industry. Trans Tech Publications Inc. Solid State Phenomena (Volume 277), pp. 80–89 doi: https://doi.org/10.4028/www.scientific.net/SSP.277.

49. Lozynskyi V., Saik P., Petlovanyi M., Malanchuk Z., Malanchuk Y. (2018). Substantiation into Mass and Heat Balance for Underground Coal Gasification in Faulting Zones. Inzynieria Mineralna. Journal of the Polish Mineral Engineering Society. DOI: 10.29227/IM–2018–02–36

50. Malanchuk Y., Moshynskyi V., Korniienko V., Malanchuk Z. (2018). Modeling the process of hydromechanical amber extraction. E3S Web Conf. Volume 60, Ukrainian School of Mining Engineering. https://doi.org/10.1051/e3sconf/20186000005.

51. Dychkovskyi, R.O., Lozynskyi, V.H., Saik, P.B., Petlovanyi, M.V., Malanchuk, Ye.Z., Malanchuk Z.R. (2018). Modeling of the disjunctive geological fault influence on the exploitation wells stability during underground coal gasification. Journal Archives of Civil and Mechanical Engineering. – 18(4), pp. 1183–1197. https://doi.org/10.1016/j.acme.2018.01.012.

52. Khomenko, O.Ye., Sudakov, A.K., Malanchuk, Z.R., Malanchuk, Ye.Z. (2017). Principles of rock pressure energy usage during underground mining of deposits. Scientific Bulletin of National Mining University/ Scientific and technical journal. Dnipro. Ukraine, PP KF «Gerda». №2(158). pp. 34–43.ISSN 2071–2227 UDC 622.831.24.0010.

53. Malanchuk, Z. (2017). Examining features of the process of heavy metals distribution in technogenic placers at hydraulic mining / Z. Malanchuk, Ye. Malanchuk, V. Korniyenko, I. Ignatyuk // Eastern – European Journal of Enterprise Technologies. № 1(10). – p. 45–51. – Режим доступу: http://nbuv.gov.ua/UJRN/Vejpte_2017_1(10)__7.

54. Malanchuk, Z., Korniienko, V., Malanchuk, Y. (2018). Results Of Research Into Amber Mining By Hydromechanical Method. Mining Of Mineral Deposits. T: 11. Vol. 1. p. 93–99. DOI: 10.15407/mining11.01.093.

55. Naduty, V., Malanchuk, Z., Malanchuk, E., Korniienko, V. (2016). Research results proving the dependence of the copper concentrate amount recovered from basalt raw material on the electric separator field intensity.Eastern – European Journal of Enterprise Technologies / PC «Technology Center», Kharkiv, Ukraine, Volume 5/5(83), p. 19–24. ISSN 1729–3774, UDC 622.277 DOI: 10.15587/1729–4061.2016.79524.

56. Malanchuk, Z., Malanchuk, Y., Khrystiuk, A. (2016). Mathematical Modeling Of Hydraulic Mining From Placer Deposits Of Minerals. Mining Of Mineral Deposits. T: 10. Vol. 2. p. 18–24. DOI: 10.15407/mining10.02.013.

57. Malanchuk, Y., Malanchuk, Z., Korniienko, V., Gromachenko, S. (2016). The Results Of Magnetic Separation Use In Ore Processing Of Metalliferous Raw Basalt Of Volyn Region. Mining Of Mineral Deposits. T: 10. Vol. 3. p. 77–83. DOI: 10.15407/mining10.03.077.

58. Malanchuk, Z., Korniienko, V., Malanchuk, E., Khrystiuk, A. (2016). Results of experimental studies of amber extraction by hydromechanical method in Ukraine. Eastern – European Journal of Enterprise Technologies / PC «Technology Center», Kharkiv, Ukraine, Vol.3/10(81), p. 24–28.(SCOPUS) ISSN 1729–3774, UDC 622.232.5:622.2 DOI: 10.15587/1729–4061.2016.72404.

59. Naduty, V., Malanchuk, Z., Malanchuk, E., Korniyenko, V. (2015). Modeling of vibro screening at fine classification of metallic basalt Text / Theoretical and Practical Solutions of Mineral Resources Mining, p. 441–443. doi: 10.1201/b19901–77.

60. Saik, P.B., Dychkovskyi, R.O., Lozynskyi, V.H., Malanchuk, Z.R., Malanchuk, Ye.Z. (2015). Revisiting the underground gasification of coal reserves from contiguous seams. New Developments in Mining Engineering: Theoretical and Practical Solutions of Mineral Resources Mining. №6. pp. 60–66. ISSN 2071–2227.

61. Fizyk, I., Prokhor, O., Kucheruk, M., Hrytsiuk, V. (2023). Ensuring environmental sustainability of forest ecosystems on disturbed lands with unauthorized amber mining. Key trends of integrated innovation–driven scientific and technological development of mining regions : multi–authored monograph. – Petroșani, Romania : UNIVERSITAS Publishing, p. 315–325. http://doi.org/10.31713/m1214.

62. Korniyenko, V.Ya. (2023). Research of deposits, their characteristics and features of amber occurence in amber bearing deposits of Ukraine and the world. Key trends of integrated innovation–driven scientific and technological development of mining regions : multi–authored monograph. Petroșani, Romani: UNIVERSITAS Publishing, p. 18–57. http://doi.org/10.31713/m1203.

63. Moshynskyi, V.S., Korniyenko V.Ya., Khrystyuk A.O., Solvar L.M. (2020). Research of energy effective parameters of the process of hydro mechanical extraction of amber from sandy deposits. Topical scientific researches into resource–saving technologies of mineral mining and processing. Multi–authored monograph. Sofia: Publishing House "St.Ivan Rilski", p. 24–38, 446 p. http://ep3.nuwm.edu.ua/17471.

64. Kryvoruchko, S.O. (2001). Products of the Rivne Region in Kyiv. S.O. Kryvoruchko: Khreshcha–tik newspaper.

65. Indutny, V.A. (1999). Stone colors of Ukraine: amber. V.A. Indutny. Geography and the basics of economics in school. No. 8. p. 26–31.

66. Kornienko, V. Ya. (2007). Analysis of modern technologies and the selection of equipment for the extraction of amber from sand deposits with the least technogenic and ecological impact on the environment / V. Ya. Kornienko // Bulletin of the NUVHP, Collection of Scientific Works, No. 2 (38). Rivne. p. 352–358.

67. Malanchuk, Z. R. (2009). Hydromining of minerals: scientific. study guide higher education closed. Z. R. Malanchuk, S. R. Boblyakh, E. Z. Malanchuk. National University of Water Management and Natural Resources Management. Rivne: NUVHP, 280 p.

68. The method of extraction of amber from the deposit. Patent of Ukraine (2000). No. 32201A dated 12/15. Bul. No. 7–II.

69. Arens, V.Zh. (1962). Investigation of parameters of hydromechanization during underground mining of ore deposits: author's review. thesis for obtaining sciences. candidate degree technical of Sciences / V.Zh. Ahrens. M. 137 p.

70. Kalabin, A.I. (1981). Extraction of useful minerals by underground leaching and other geotechnological methods / A.I. Kalabin. M.: Atomizdat, 1981. 302 p.

71. Kreiter V.M. (1960). Search and exploration of mineral deposits / V.M. Crater. – M.: Gosteoltekhizdat, t. I., 328 p.; 1961. Vol. II, 386 p.

72. Melnikov N.V. (1981). Mining engineers / N.V. Melnikov. M.: Nauka, 270 p.

73. Vlasyuk A.P. (1995). Numerical solution of one problem of dissolution and removal of formation salts from the base of hydraulic structures / A.P. Vlasyuk // Reports of the National Academy of Sciences of Ukraine. #8. p. 37–39.

74. Vabyshevich P.N. (1989). Adaptive nets of constant type in problems of mathematical physics / P.N. Vabyshevich // Journal. calculated mathematics and mathematics physicists. No. 6. pp. 902–914.

75. Burov A.P. (1952). Intructions for applying the classification of reserves of solid minerals. Al–Mazov rock deposits. A.P. Burov, G.I. Volarovich. M.: Gosgeolizdat, 40 p.

76. Vlasyuk A.P. (2005). Mathematical and computer modeling of the assessment of reserves of bulk minerals and the process of their extraction / A.P. Vlasyuk, M.G. Lustyuk. Abstracts of International Conference "Problems of decision making under uncertainties" (PDMU). Berdyansk, p. 107–109.

77. Burchakov A.S. (1985). Mine design / A.S. Burchakov, A.S. Malkin, M.I. Ustinov. M.: Nedra, 399 p.

78. Vabyshevich P.N. (1989). Adaptive nets of constant type in problems of mathematical physics / P.N. Vabyshevich. Journal. calculated mathematics and mathematics physicists. No. 6. p. 902–914.

Modelowanie wpływu hydraulicznego pękania skał bursztynośnych przez zalewany strumień w komorze erozji na wydajność górnictwa

W artykule omówiono koncepcję rozwoju społeczno-gospodarczego i strategicznego obwodu rówieńskiego (Ukraina), w szczególności poszukiwania, badania i przemysłowej eksploatacji strategicznych zasobów mineralnych. Koncepcja zakłada zastosowanie energooszczędnych technologii wydobycia surowca, zwłaszcza ze złóż bursztynu. Autorzy zwracają uwagę, że konwencjonalne metody wydobywania bursztynu są szkodliwe dla środowiska i sugerują stosowanie metod skomplikowanych, takich jak technologie mechaniczne i hydrauliczne.

W artykule podjęto problematykę wyzwań związanych z wdrażaniem metod geotechnologicznych w przedsiębiorstwach górniczych oraz dokonano oceny ich złożoności w nauce i praktyce górniczej. Prowadzono badania naukowe w tym zakresie. Kompleksowe badania metod pobierania próbek i wydobywania bursztynu są nadal istotne z punktu widzenia interesu narodowego.

Ponadto w artykule przedstawiono wyniki badań nad powstawaniem strumienia w monitorze hydraulicznym oraz zastosowania teleskopowego monitora hydraulicznego do poszerzania zasięgu fragmentacji skał, w tym analizę parametrów strumienia i dynamiki hydraulicznego kruszenia skał, m.in. skał bursztynonośnych. Wnioski dotyczą rozszerzalności liniowej strumienia, zmniejszania się prędkości osiowej wraz ze wzrostem ciśnienia hydrostatycznego oraz skuteczności hydromonitora teleskopowego w zwiększaniu zasięgu fragmentacji.

Słowa kluczowe: *bursztyn, hydromonitor, zanurzony strumień, zniszczenie, parametry*

Pneumatyczne źródło sejsmiczne do monitorowania prędkości fal sejsmicznych w warunkach podziemnej eksploatacji węgla

Przemysław SIERODZKI[1)], Leszek REMIORZ[2)], Zbigniew ISAKOW[3)], Rafał CZARNY[4)], Mateusz ĆWIĘKAŁA[5)]

[1)] mgr inż.; CTTEMAG Sp. z o.o. w Katowicach, Politechnika Śląska w Gliwicach
[2)] dr hab. inż. prof. w PolSl; Politechnika Śląska w Gliwicach
[3)] dr hab. inż.; CTTEMAG Sp. z o.o. w Katowicach
[4)] dr inż.; Uniwersytet Stanowy Pensylwanii, State College
[5)] mgr inż.; PGG S.A. Oddział KWK ROW Ruch Rydułtowy

http://doi.org/10.29227/IM-2024-01-106

Submission date: 17-05-2024 | Review date: 20-06-2024

Abstrakt

W artykule przedstawiono koncepcję pneumatycznego wzbudnika fal sejsmicznych oraz pierwsze rezultaty testu prototypu. W założeniach, konstrukcja źródła ma być dostosowana do warunków podziemnej eksplantacji węgla tj. z zachowaniem wymogów iskrobezpieczeństwa. Wzbudzanie ma odbywać się w krótkich odstępach czasu, rzędu kilku minut, co umożliwi wysokorozdzielcze w czasie monitorowanie prędkości różnych typów fal sejsmicznych. Quasi ciągły pomiar pozwoli na dokładniejsze śledzenie zmian pola naprężeń w rejonie wydobycia zmniejszając tym samym ryzyko wystąpienia tąpnięcia. Projektowane źródło będzie współpracowało z systemem sejsmoakustycznym ARES-5/E.

Słowa kluczowe: *źródło sejsmiczne, wzbudnik sejsmiczny, hazard sejsmiczny w kopalni, tąpnięcie górotworu, wstrząsy górnicze, system sejsmiczny*

1. Wprowadzenie

Dla bezpieczeństwa pracy w górnictwie kluczowym zagadnieniem jest utrzymanie stabilności wyrobisk. Proces wydobycia zaburza równowagę górotworu i powoduje występowanie niebezpiecznych koncentracji naprężeń mogących wywoływać tragiczne w skutkach tąpnięcia [1].

Bezpośredni, punktowy pomiar składowych naprężeń, jakkolwiek możliwy przy użyciu różnych czujników, to ze względu na trudny dostęp, objętość i zmienność kontrolowanego obszaru w otoczeniu ściany wydobywczej oraz koszty z tym związane nie jest stosowany praktycznie.

Zdecydowanie lepszym i tańszym sposobem do rozpoznania górotworu i oceny zmienności naprężeń jest wykorzystanie prędkości rozchodzących się w nim fal sejsmicznych wzbudzanych naturalnymi wstrząsami, które zazwyczaj występują w pobliżu miejsc koncentracji naprężeń lub odpalanymi ładunkami wybuchowymi.

W celu uniezależnienia rozpoznania pola naprężenia w górotworze od wstrząsów, ich rozkładu i ewentualnych błędów lokalizacji autorzy zaproponowali, skonstruowali oraz wstępnie przebadali quasi ciągły, impulsowy, tani i łatwy w użyciu wzbudnik fali sejsmicznej WZB Typ 2. Iskrobezpieczny, pneumatycznie sterowany wzbudnik WZB Typ 2 wykorzystywany będzie do wyznaczania prędkości rozchodzenia się fali sejsmicznej od miejsca jej wywołania do miejsca rejestracji przez czujniki geofonowe rozmieszczone w obrębie ściany wydobywczej. Pozwoli to uniknąć stosowania procedur związanych z użyciem małych ładunków wybuchowych w kopalniach metanowych.

2. Stan aktualny rozwoju systemów sejsmicznych do oceny zagrożenia tąpaniami z wykorzystaniem metod aktywnych stosowanych na bieżąco

W ostatnich latach w rozwoju systemów sejsmicznych do oceny zagrożenia tąpaniami w podziemnych zakładach górniczych obserwuje się dążenie do wdrażania aktywnych metod sejsmicznych szczególnie w rejonach ścian wydobywczych, gdzie to zagrożonych jest znaczące. Prace w tym kierunku zainicjowane zostały skonstruowaniem, wdrożeniem i przebadaniem w latach 2000–2003 w KWK Bielszowice w ramach projektu PCZ–003–20 realizowanego w Rudzkiej Spółce Węglowej wspólnie z Centrum EMAG, Centrum Mechanizacji i Automatyzacji Górnictwa KOMAG i Głównym Instytutem Górnictwa GIG systemu pt. „System monitorowania i wizualizacji oraz sterowania procesem pracy kompleksu ścianowego w restrukturyzowanych kopalniach węgla kamiennego". Opracowano wówczas pierwszy w Polsce system do kontroli i klasteryzacji zjawisk dynamicznych w stropie [2] i system GEOTOMO do określania względnych zmian naprężeń przed frontem ściany wydobywczej z wykorzystaniem organu urabiającego kombajnu [3]. Nowe możliwości funkcjonalne tych systemów umożliwiły dokonywanie na bieżąco oceny zagrożenia tąpaniami. Kolejnym krokiem rozwoju było opracowanie, w latach 2014–2016 systemu pt." Innowacyjne metody i system do oceny zagrożenia tąpaniami na podstawie probabilistycznej analizy procesu pękania i geotomografii online" o akronimie INGEO [4]. Prototyp niekomercyjny systemu INGEO, przeznaczony był do oceny zagrożenia tąpaniami w kopalni, w szczególności w rejonie ściany wydobywczej. System stanowił kontynuację rozwoju znanych i stosowanych w górnictwie systemów: sejsmicznego ARAMIS M/E i sejsmoakustycznego ARES-5/E. Cechowały go nowe, innowacyjne technologie (cyfrowa transmisja sejsmoakustyczna, światłowodowy dołowy koncentrator pomiarowy). Systemy wyposażone były również w narzędzia do sejsmicznej tomografii pasywnej [5]. Uzyskana nowa jakość

Rys. 1. Zdjęcia prototypu niekomercyjnego wzbudnika WZB Typ 1 w systemie INGEO
Fig. 1. Photos of non-commercial seismic source prototype WZB Type 1 as a part of INGEO system

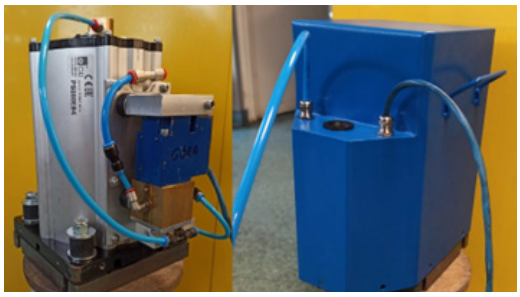

Rys. 2. Zdjęcia prototypu zoptymalizowanego wzbudnika WZB Typ 2 z płytą udarową i obudową
Fig. 2. Photos of the optimized seismic source prototype WZB Type 2 with an baseplate and steel case

Tab. 1. Porównanie parametrów wzbudnika WZB Typ 1 oraz WZB Typ 2
Tab. 1. Comparison of parameters of WZB Type 1 and WZB Type 2 inductor

Parametry	WZB Typ 1 (INGEO)	WZB Typ 2 (prototyp)
Energia uderzenia	~300 J	~150 J
Zasilanie (powietrze)	8-10 bar	3-6 bar
Gabaryty (bez uchwytów)	Ø 430 x 340 mm	350x200x280 mm
Waga (bez płyty udarowej)	~50 kg	~25 kg
Magazyn energii	Sprężyny	Powietrze
Konstrukcja kafara	CTT EMAG	PS-80 (OLI)

rejestrowanych danych stanowiła odpowiedź na rozwijające się trendy na świecie w wykorzystaniu systemów sejsmoakustycznych (mikrosejsmicznych) do monitorowania rejonu wyrzutów gazów [6] oraz przebiegu hydroszczelinowania. W projekcie INGEO podjęto również próbę rozszerzenia funkcjonalności systemu pomiarowego o nowe rodzaje czujników (deformacji, naprężeń, położenia kombajnu) oraz aktywnego wzbudnika sejsmicznego WZB Typ 1. Zasadniczą niedogodnością zaprojektowanego wzbudnika były waga oraz duże rozmiary, co zniechęcało potencjalnych użytkowników od jego stosowania i wdrożeń.

Dla utrzymania koncepcji systemu i dalszego doskonalenia podjęto zasadnicze działania upraszczając jego konstrukcję i zmniejszając jego rozmiar i wagę, kierując się doświadczeniami opisanymi w pracy [7]. Dążono również do zminimalizowania liczby stosowanych wzbudników w systemie i zmniejszenia liczby koniecznych przebudów.

3. Pneumatyczny wzbudnik fali sejsmicznej WZB Typ 2

Na rysunku 1 przedstawiono wzbudnik WZB Typ 1 zaprojektowany podczas realizacji projektu INGEO. Zasilaniem urządzenia jest sprężone powietrze kontrolowane przez iskrobezpieczny elektrozawór SEMI-2/P. Energia magazynowana jest w trzech sprężynach napinanych przez pneumatyczne siłowniki.

W celu zoptymalizowania konstrukcji wzbudnika zmieniono zasadniczo jego zasadę działania. Wyeliminowano sprężyny gromadzące energię potencjalną i napinające je siłowniki pneumatyczne, zastępując je masą i układem pneumatycznym pełniącym rolę sprężyny pneumatycznej nadającej masie udarowej wzbudnika w krótkim czasie dużą energię kinetyczną. Pozwoliło to zredukować wagę urządzenia ułatwiając jego stosowanie. Dużą zaletą jest również zastosowanie gotowego komponentu o sprawdzonej konstrukcji produkowanego seryjnie przez firmę OLI młota pneumatycznego typu PS-80 [8]. Korpus wzbudnika wykonano z odlewu aluminiowego, jednak ze względu na konieczność zapewnienia iskrobezpieczeństwa urządzenia dodano stalową osłonę. Na rysunku 3.2 przedstawiono zdjęcia konstrukcji prototypu wzbudnika WZB Typ 2. Konstrukcja składa się z młota pneumatycznego, iskrobezpiecznego sterowania oraz obudowy.

W tabeli 1 przedstawiono porównanie parametrów wzbudnika WZB Typ 1 z projektu INGEO, oraz nowego prototypu WZB Typ 2.

4. Karta pomiarowa REX_LAN Systemu ARES-5/E

Rejestrowanie i gromadzenie danych podczas pomiaru wzbudnikiem WZB Typ 2 umożliwia zmodyfikowana wersja popularnego systemu sejsmoakustycznego ARES-5/E. Modyfikacja polega na zamontowaniu karty REX_LAN do jednostki rejestrującej systemu ARES-5/E. Zmodyfikowana karta jest w pełni kompatybilna z dotychczas używaną kartą REX. Różnica polega na dodaniu 8 kanałowego przetwornika A/C oraz udostepnieniu wysokorozdzielczego cyfrowego

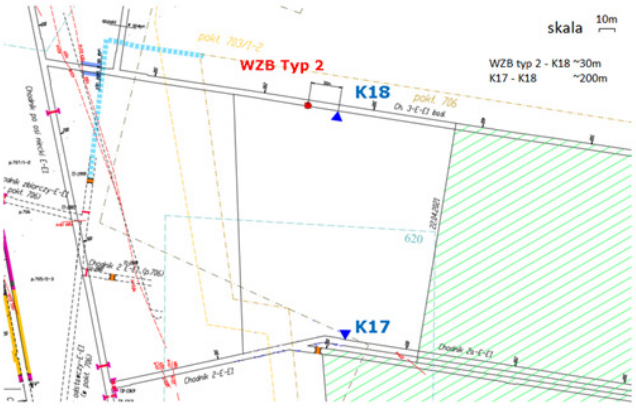

Rys. 3. Schemat pomiarowy testu wzbudnika WZB Typ 2 (czerwona kropka). K18 i K17 (niebieskie trójkąty) – czujniki geofonowe
Fig. 3. Underground settings of seismic source WZB Typ 2 (red dot) test. Geophones K18 and K17 are marked by blue triangles

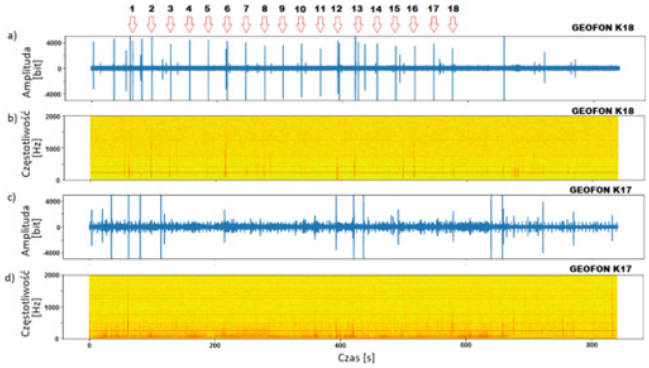

Rys. 4. Ponad 800 s ciągłej rejestracji systemem ARES 5/E wraz z nową kartą REX_LAN. Czerwoną strzałką zaznaczono18 wzbudzeń źródłem WZB Typ 2 odebranych geofonami K18 i K17. (a) rejestracja K18 w domenie czasu, (b) rejestracja K18 w domenie częstotliwości, (c) rejestracja K17 w domenie czasu, (d) rejestracja K17 w domenie częstotliwości
Fig. 4. Over 800 s continuous recording of the ARES 5/E with REX_LAN card. The red arrows the seismic source events are marked. (a) K18 in time domain, (b) K18 in frequen-cy domain, (c) K17 in time domain, (d) K17 in frequency domain

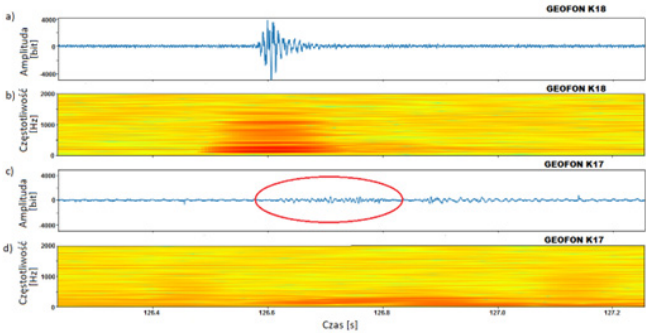

Rys. 5. Pojedyncze uderzenie wzbudnika WZB Typ 2 zarejestrowane przez geofony K17 oraz K18 .rejestracja K18 w domenie czasu (a) i częstotliwości (b), rejestracja K17 w domenie czasu (c) i częstotliwości (d)
Fig. 5. Single strike of the seismic source WZB Type 2 recorded by geophone K17 and K18. K18 in time domain (a) and frequency domain (b). K17 in time domain (c) and fre-quency domain (d)

strumienia danych sejsmicznych wysyłanych portem LAN. Rozwiązanie to konsoliduje sposób cyfrowej transmisji danych z systemów ARAMIS M/E, ARES-5/E oraz INGEO. Nowy sposób transmisji dostarcza cyfrowy zapis strumienia danych sejsmicznych oraz zasadniczo upraszcza współpracę systemu ARES z systemem ARAMIS. Modyfikacja umożliwia wykorzystanie programowego detektora impulsów sejsmoakustycznych oraz wykorzystanie rejestrowanych danych systemu do stosowania w nowo opracowanych metodach analiz systemu INGEO.

5. Testowanie prototypu wzbudnika WZB Typ 2

Testowanie wzbudnika przeprowadzono w KWK ROW Ruch „Rydułtowy" w dniu 24 kwietnia 2021 roku, w rejonie ściany III-E-E1, w pokładzie 713/1-2. W czasie pomiaru nie prowadzono robót wydobywczych. Wzbudnik został zamontowany w środku pokładu węgla na 4 kotwach o długości 2,5 m każda. Schemat pomiarowy przedstawiono na rysunku 3.

Fale sejsmiczne generowane wzbudnikiem WZB Typ 2 odbierano geofonami K18 oraz K17 (Rys. 3). Geofony o częstotliwości rezonansowej 28 Hz podłączono do iskrobezpiecz-

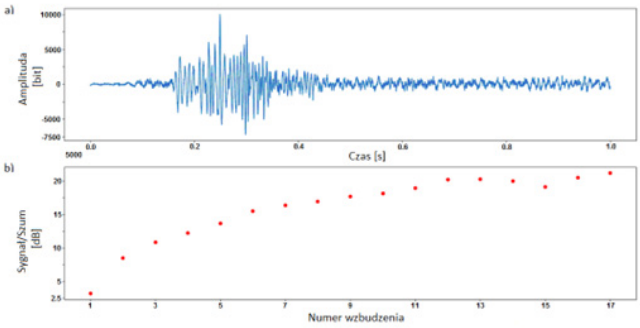

Rys. 6. Wynik sumowania 16 uderzeń prototypu wzbudnika WBZ Typ 2 jako sumarycznej rejestracji geofonu K17 (a) . Stosunek sygnału użytecznego do szumu w zależności od ilości uderzeń (b)

Fig. 6. The result of 16 shots stacking on the waveforms recorded at K17 (a) and correspond-ing S/N ratio (b)

nego systemu sejsmoakustycznego ARES-5/E. Rozmieszczono je odpowiednio 30 m od wzbudzenia (geofon K18) oraz około 200 m od wzbudzenia fali po przeciwległej stronie ściany, w chodniku nadścianowym 2-E-E1 (geofon K17). System ARES-5/E pracował w trybie ciągłej rejestracji z nową kartą REX_LAN. Częstotliwość próbkowania wynosiła 4000 Hz. Podczas testu zarejestrowano impulsy wywoływane uderzeniami wzbudnika podczas jego testowania. Na rysunku 4 przedstawiono rejestracje geofonów K18 oraz K17 w dziedzinie czasu i częstotliwości podczas 18 uderzeń wzbudnika dokonywanych w odstępach co 30 sekund. Na rejestracje nakładają się naturalne wstrząsy występujące na ścianie. Rejon badań był obszarem kopalni o dużej aktywności sejsmicznej.

Rysunek 5 przedstawia rejestrację pojedynczego uderzenia w dziedzinie czasu i częstotliwości. Trzeba zaznaczyć, że są to pomiary podczas postoju ściany i tło sejsmiczne jest bardzo niskie. Można zaobserwować, że sygnał odebrany 30 m od źródła sejsmicznego (geofon K18) charakteryzuje się częstotliwościami widma do około 1400 Hz. Ten sam sygnał odebrany po drugiej stronie ściany po przebyciu około 200 m (geofon K17) ma zredukowane widmo do około 500 Hz.

WZB Typ 2 w założeniach ma dostarczać wysokorozdzielczego zapisu sejsmicznego fal propagujących przez całą ścianę (na wzór aktywnej tomografii sejsmicznej) w krótkich odstępach czasu. Pojedyncze wzbudzenie, jak pokazuje rysunek 5c i 5d nie przedstawia wysokiego współczynnika sygnału użytecznego do szumu (S/N). Jednym ze sposobów poprawy S/N jest sumowanie sekwencji uderzeń. Na rysunku 6. przedstawiono wynik sumowania 17 uderzeń. Do sumowania wykorzystano korelację pomiędzy sejsmogramami z geofonu K18 następujących kolejno po sobie wzbudzeń (Rys. 4 czerwone strzałki). Po zsumowaniu około 10 uderzeń uzyskano znaczący wzrost S/N rzędu 20 dB. Otrzymana paczka fal sejsmicznych zaznacza się wyraźnie już od około 0,1 s do 0,5 s, sugerując obecność zarówno fal objętościowych jak i fal dyspersyjnych oraz przypuszczanie fal wielokrotnie rozproszonych.

5. Wnioski

Przeprowadzone testy prototypu zoptymalizowanego wzbudnika pneumatycznego WZB Typ 2 wykazały możliwość jego zastosowania do skutecznego wzbudzania fali sejsmicznej w warunkach podziemnej eksploatacji węgla. Głównym celem konstrukcji tego urządzenia jest umożliwienie łatwego i prawie ciągłego monitorowania prędkości rozchodzenia się fal sejsmicznych i pośrednio oceny występowania miejsc groźnych koncentracji naprężeń. Wykonane badania dowiodły, że system sejsmoakustyczny ARES-5/E z analogową transmisją sygnałów był w stanie zarejestrować fale sejsmiczne różnego typu po przeciwległej stronie ściany. W docelowym rozwiązaniu systemu wiele elementów wymaga udoskonalenia. Konieczna jest rejestracja zapisu bezpośrednio przy wzbudniku do wykorzystania jej jako znacznik czasowy sumowania, jak również oszacowania energii uderzenia czy poprawy rozdzielczości sumowanych sejsmogramów. Wzbudnik w wersji komercyjnej będzie mógł być wyzwalany z powierzchni, co pozwoli na pomiar podczas produkcji. Cyfrowa transmisja danych oraz nadajniki z przetwornikami A/C montowane przy geofonach (system INGEO) zwiększą dynamikę rejestracji. Z kolei uproszczona konstrukcja wzbudnika i zmniejszona jego masa do około 25 kg uczyni go bardziej przyjaznym w stosowaniu i przyczyni się do szerszego wdrażania najbardziej skutecznych aktywnych metod oceny zagrożenia tąpaniami w górnictwie.

Literatura – References

1. Mendecki A.J. 1996: Seismic monitoring in mine, Chapman $ Hall, London
2. Leśniak A., Isakow Z. 2009: Space–time clustering of seismic events and hazard as-sessment in the Zabrze - Bielszowice coal mine, Poland, International Journal of Rock Mechanics and Mining Sciences, Elsevier , 46/5, pp. 918-928.
3. Isakow Z. 2009: Geotomography with the help of a cutter–loader working organ as a source of imaging waves, International Journal of Rock Mechanics and Mining Sci-ences, Elsevier, 46/7, pp. 1235-1242.
4. Isakow Z. 2016: kierownik projektu i współredaktor wydania. Współautorzy rozdziałów: Augustyniak A., Cianciara A., Cianciara B., Isakow Z., Juzwa J., Kuciara I., Makola R., Piwowarski W., Pysik A., Siciński K., Sierodzki P., Słoka Z., Innowacyjne metody i system do oceny zagrożenia tąpaniami na podstawie probabilistycznej analizy procesu pękania i geotomografii online, Monografia - wynik realizacji projektu INGEO, Instytut Technik Innowacyjnych ITI EMAG, ISBN 978-83-63674-27-4, str. 1-156.
5. Dębski W. 2010: Seismic Tomography by Monte Carlo Sampling, Pure. Appl. Ge-ophys. vol.167, pp. 131-152.
6. Kozłowski B., Polak Z., Prokop P. 2014: Wyrzuty gazów i skał, Wydawnictwo Śląsk, str. 652.
7. almon Brian P., Goldswain G., Lynch Richard A., Rebuli Daryl, Olivier Jan C., and Kleynhans Waldo. 2019: Estimating changes in seismic wave velocity from a pneu-matic source in an operational mine, Geophysics,.
8. Instrukcja obsługi „Młot pneumatyczny typu PS-80" firmy OLI.

Pneumatic Seismic Source for Monitoring Velocity Changes of Seismic Waves in Underground Coal Mining Conditions

In the article, the concept and the first test of the seismic source WBZ Type 2 were presented. The idea is to construct the seismic source tailored for underground measurement requirements, including intrinsically safety demand. The source will be triggered every few minutes or less, which gives the ability to track seismic velocity changes with high accuracy in time. Quasi-continuous measurement allows to monitor stress field changes, and in consequence, reduce the hazard of rockburst. The WZB type 2 will be compatible with the ARES-5/E seismic system.

Keywords: *seismic source, seismic hazard in mine, rockburst, mining-induced seismic events, seismic mon-itoring system*

Autokompresja jako sposób akumulacji energii odpadowej podczas wynurzania się autonomicznego modułu transportowego wykorzystującego zmianę wyporności

Wiktor FILIPEK[1)], *Krzysztof BRODA*[2)]

[1)] Akademia Gorniczo-Hutnicza w Krakowie, Wydział Inżynierii Lądowej i Gospodarki Zasobami; ORCID: 0000-0001-5472-8214; ResearcherID: W-5254-2018; Scopus: 36185413000; PBN: 5e70922b878c28a047391056

[2)] Akademia Gorniczo-Hutnicza w Krakowie, Wydział Inżynierii Lądowej i Gospodarki Zasobami; ORCID: 0000-0001-8218-9350; ResearcherID: D-2256-2018; Scopus: 55658644400; PBN: 5e70922b878c28a047391048

http://doi.org/10.29227/IM-2024-01-107

Submission date: 20-05-2024 | Review date: 22-06-2024

Abstrakt

Mimo trwającej od kilku lat pandemii Covid-19 nie słabnie zainteresowanie eksploatacją złóż zalegających na dnie mórz i oceanów na dużych głębokościach. Zostało opracowanych wiele nowych koncepcji eksploatacji złóż morskich. Powstało wiele konsorcjów zainteresowanych działalnością górniczą na morzach i oceanach. I chociaż najbardziej zaawansowane przedsięwzięcie Firmy Nautilus-Minerals nie zakończyło się jak dotąd sukcesem ale od strony badawczej i technologicznej poczyniło ogromny krok do przodu. Prawdopodobnie eksploatacja na skalę przemysłową rozpocznie się w najbliższych latach zwłaszcza na wodach EEZ (Exclusiw Economic Zone). W ostatnim czasie władze Wysp Cooka udzieliły trzy licencje na tego typu działalność. Na wodach międzynarodowych musimy niestety jeszcze poczekać na rozwiązania prawne satysfakcjonujące wszystkie zainteresowane strony. Eksploatacja złóż szelfowych prowadzona jest z powodzeniem różnymi metodami w wielu regionach na świecie (Karlic, 1984; Depowski et al., 1998; Abramowski, Kotliński, 2011; Niedoba 2015, SPC 2013; Sharma, 2017) jednak sięgnięcie po złoża masywnych siarczków polimetalicznych czy konkrecji polimetalicznych zalegających na dużych głębokościach stawia przed naukowcami i inżynierami bardzo duże wymagania. Jednym z największych jest opracowanie metody transportu urobku z dna na powierzchnię morza.

Autorzy od kilku lat prowadzą badania teoretyczne i eksperymentalne nowych koncepcji transportu z dna morskiego, wyniki których przedstawili w publikacjach (Filipek, Broda: 2016, 2017, 2018, 2019, Broda, Filipek, Tora 2023).

W trakcie rozważań różnych koncepcji transportu z dna morskiego z wykorzystaniem modułu autonomicznego, zwróciliśmy uwagę na straty energii podczas wymiany medium roboczego między autonomicznym modułem transportowym a otoczeniem (wodą morską). W artykułach (Filipek, Broda 2018, 2019) skupiliśmy się nad pozytywnym aspektem tej wymiany, ale niemniej są to jednak straty energii . W niniejszej publikacji autorzy analizują jaką część tej energii można wykorzystać (w autokompresji) i jaki ma to wpływ na bilans energetyczny modułu transportowego.

Słowa kluczowe: *górnictwo morskie, transport z dużych głębokości, autonomiczny moduł transportowy*

1. Wstęp

Od kilku lat autorzy prowadzą badania związane z transportem urobku z dna morskiego na powierzchnię (Filipek, Broda 2015, 2016, 2017, 2019, 2023, Broda, Filipek, Tora 2023) będącym ciągle największym problemem technicznym w górnictwie morskim (odkrywkowym) a zwłaszcza kiedy transport urobku odbywa się z dużych głębokości. Liczne opracowania dotyczące dotychczas stosowanych rozwiązań opartych o metody: czerpakowo-linową CLB (continuareline bucket), hydrauliczną HP (hydraulic pumping,) air-liftu ALP (air-lift pumping) czy mieszane (Sharma 2017, SPC 2013, The Royal Society 2017) dalekie są od ideału. Ich największą wadą jest duża energochłonność generująca wysokie koszty. Dlatego ciągle prowadzone są badania nad nowymi rozwiązaniami, w których zarówno eksploatacja jak i transport odbywały by się w sposób mało uciążliwy dla środowiska (Jones DO i inni, 2019).

W naszych badaniach naukowych postanowiliśmy spojrzeć na ten problem z perspektywy nowego źródła energii opartego o koncepcję wykorzystania, jako źródła energii do transportu z dna morskiego, procesu przemiany fazowej ciała stałego lub cieczy w stan gazowy lub ciała stałego w ciecz, którą to ideę w formie podsumowania wcześniejszych publikacji autorzy przedstawili w artykule (Broda, Filipek, Tora 2023).

Charakterystyczną własnością odróżniającą tą koncepcję od rozwiązań stosowanych aktualnie jest możliwość wykorzystania (w kolejnym cyklu) części energii, która została wygenerowana lub jest konieczna do zapoczątkowania procesu wynurzania modułu transportowego. W dotychczas stosowanych metodach CLB czy HP, transportu urobku z dna morskiego, całkowita energia, którą musieliśmy użyć jest bezpowrotnie tracona. We wcześniejszych artykułach (Filipek, Broda 2017; Broda, Filipek, Tora 2023) zaproponowaliśmy i omówiliśmy cztery koncepcje wykorzystanie przemiany fazowej do transportu z dna morskiego, które przedstawiono na Rys. 1.

Ciekawym rozwiązaniem wartym wspomnienia jest koncepcja przedstawiona na rys. 1b umożliwiająca odzyskanie nawet do 90% energii. Została ona omówiona w publikacji „The theoretical basis of the concept…" (Filipek, Broda 2017, Broda, Filipek, Tora 2023). Natomiast koncepcje w wersji rys.1c i rys.1d zostały omówiono w kolejnych artykułach (Filipek, Broda 2017, 2018).

W niniejszym artykule koncentrujemy się na nie omawianym do tej pory szczegółowo przypadku rys.1a. W metodzie

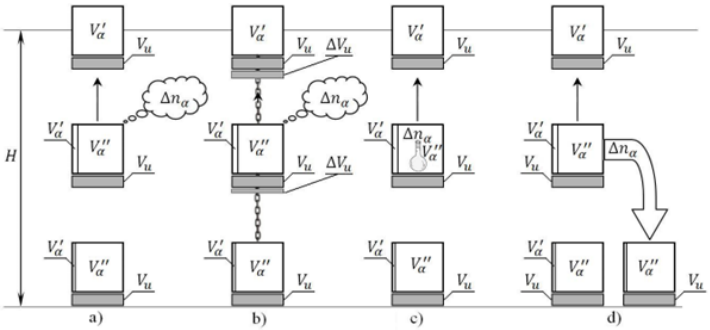

Rys. 1. Ilustracja przedstawiająca cztery koncepcje realizacji wykorzystanie przemiany fazowej z ciała stałego lub cieczy w stan gazowy do transportu urobku z dna morskiego (Broda, Filipek, Tora 2023)

Fig. 1. Illustration showing four concepts for implementing the phase transformation from a solid or liquid to a gaseous state to transport spoil from the seabed (Broda, Filipek, Tora 2023)

tej rozważamy ruch jednego modułu transportowego z danej głębokości na powierzchnię. Na głębokości, z której rozpoczyna się proces wynurzania musimy doprowadzić do sytuacji, w której całkowita gęstość modułu (wraz z transportowanym urobkiem) musi być mniejsza niż gęstość otaczającej go wody. Realizujemy to wykorzystując medium transportowe, którym jest czynnik roboczy – ciecz lub gaz o gęstości mniejszej od wody co automatycznie zainicjuje proces wynurzania. W niniejszej publikacji nie koncentrujemy się na sposobie zainicjowania procesu wynurzania, co omawialiśmy we wcześniejszych artykułach (Filipek, Broda 2016, 2017) przyjmując w naszych rozważaniach, że proces ten (wynurzanie) jest już zainicjowany. Przyjmijmy, że wykorzystanym czynnikiem roboczym jest azot. Jak wiadomo przy tak wysokich ciśnieniach panujących na dnie oceanów w miejscach występowania złóż minerałów interesujących z punktu widzenia gospodarki, gęstość skompresowanego azotu jest znaczna i tak na głębokości 10 km wynosi ok 600 [kg/m^3]. Natomiast na powierzchni (czyli przy ciśnieniu atmosferycznym) wynosi 1.1 [kg/m^3]. Wynika z tego, że przy założeniu stałej objętości zajmowanej przez medium transportowe musimy się pozbyć nadmiaru rozprężającego się azotu, tak aby ciśnienie wewnątrz modułu zrównoważyło się z ciśnieniem otoczenia lub przyjęło wartość bezpieczną dla konstrukcji. Jednak to nie kryteria bezpieczeństwa decydują o konieczności wymiany medium roboczego z otoczeniem, a kryterium fizyczne. Rozważany moduł transportowy po wynurzeniu i rozładowaniu urobku, musi mieć gęstość większą od otaczającej go wody morskiej. We wcześniejszych publikacjach (Filipek, Broda 2017; Broda, Filipek, Tora 2023) przedstawiono kilka sposobów rozwiązania tego problemu. W związku z tym, w niniejszym artykule nie będziemy omawiać tej kwestii. Zaznaczyć jednak należy, że w proponowanych rozwiązaniach konieczne jest wyrównanie ciśnienia wewnątrz modułu z otoczeniem. Realizujemy to jak schematycznie przedstawiono na rys. 1a poprzez upust medium transportowego (w tym przypadku azotu) do otoczenia. Niestety związane jest to z dużą stratą energii.

$$E_{str} = \int_H^0 p(h)V(h)dh \quad (1)$$

Gdzie: E_{str} – całkowita strata energii w rozważanym procesie wynurzania;
p(h) – ciśnienie na danej głębokości;
V(h) – objętość uwolnionego do otoczenia na danej głębokości czynnika roboczego.

Nadmieńmy tu, że swobodne rozprężanie powodujące straty energii, charakteryzujące się zmniejszaniem gęstości modułu, jest cechą pozytywną pozwalającą na zwiększenie masy transportowanego urobku w procesie wynurzania. Natomiast w rozważanej niniejszej publikacji dotyczącej koncepcji rys.1a zajmiemy się próbą wykorzystania tej traconej bezpowrotnie do otoczenia energii i zastanowimy się jaką część tej energii E_{str} jesteśmy w stanie wykorzystać. Przy czym nie zapominając, że cały czas zachodzi swobodna wymiana masy z otoczeniem będąca źródłem energii w procesie autokompresji. Do tego celu wykorzystamy wzmacniacz ciśnienia. Do symulacji zachodzących procesów, z uwagi na to, że przyjętym medium roboczym jest gaz azot, którego gęstość jest ściśle uzależniona od ciśnienia i temperatury (otoczenia), wykorzystamy dane rzeczywiste pobrane ze strony NOAA dla wybranego punktu EX1504L2.

2. Wzmacniacz ciśnienia

Wzmacniacze ciśnienia funkcjonują na rynku od wielu lat pozwalając m.in. na utrzymanie niskiego poziomu ciśnienia w systemach sieci zasilających maszyn, które wymagają wysokiego ciśnienia roboczego. Wzmacniacz ciśnienia posiada trzy przyłącza oznaczone najczęściej jako WE czyli wejście, WY wyjście oraz E odpowietrzanie. Do przyłącza WE podłączamy dostępne źródło sprężonego medium. Na wyjściu WY otrzymujemy wzmocniony sygnał wejściowy (ciśnienie). Natomiast przyłącze E służy do tzw. odpowietrzenia czyli pozbycia się do otoczenia medium nie wykorzystanego w procesie wzmacniania. Zgodnie z przedstawionym schematem wzmacniacza na rys.2 w konstrukcji urządzenia możemy m.in. wyróżnić: komory napędowe A i B, komory sprężania A i B, cztery zawory zwrotne, zawór przełączający oraz regulator ciśnienia. Praca urządzenia odbywa się w dwóch naprzemiennych, powtarzających się cyklach. Sprężone medium poprzez zawór regulacyjny dostarczane jest do komory napędowej A oraz sprężania B poprzez zawory zwrotne, powodując ruch posuwisty tłoczyska. W konsekwencji następuje kompresja medium znajdującego się w komorze sprężania A. Poprzez zawór zwrotny sprężone medium podawane jest na wyjście WY. W tym samym czasie z komory napędowej B poprzez zawór przełączający medium dostarczane jest do zaworu odpowietrzającego E. Po osiągnięciu krańcowego położenia tłoczyska, układ przełącza się w taki sposób, że poszczególne komory pracują w analogiczny jak poprzednio powodując ruch tłoczyska w przeciwna stronę, gdzie komory oznaczone A pełnią funkcję komór B i na odwrót.

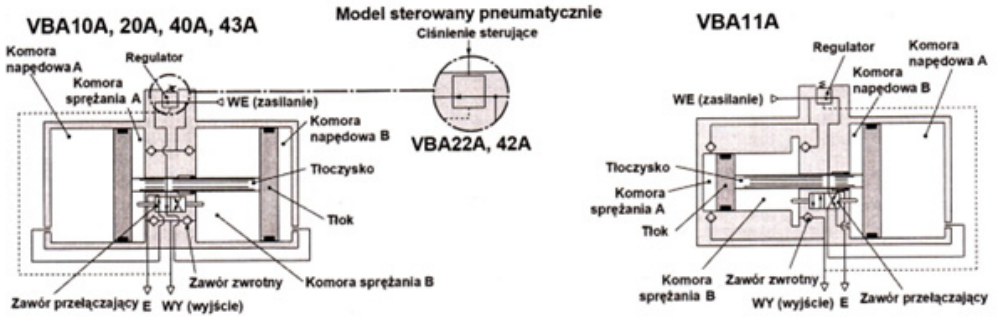

Rys. 2. Schematy przykładowych wzmacniaczy ciśnienia firmy SMC

Fig. 2. Schematics of sample SMC pressure amplifiers (http:\ https://www.smc.eu/pl-pl/products/vba-wzmacniacz-cisnienia~169589~nav)

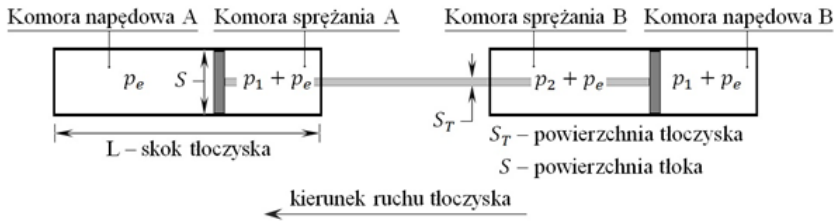

Rys. 3. Schematy pracy wzmacniacza ciśnienia

Fig. 3. Pressure amplifier operation diagrams

Zasada działania wzmacniacza ciśnienia oparta jest o prawo Pascala i jest podobna do zasady działania prasy hydraulicznej (różnica średnicy tłoków przekłada się na różnicę ciśnień). Przykładowe wzmacniacze ciśnienia firmy SMC VBA przedstawia rys.2.

Producent również podaje procedurę doboru modelu wzmacniacza i konfiguracji całego układu sieci zasilającej. W konstrukcji wzmacniaczy ciśnienia należy zwrócić uwagę, że aby zawór przełączający zadziałał, musi tłoczysko wraz z dwoma tłokami posiadać odpowiedni pęd, który kształtowany jest różnicą ciśnień między obszarami ciśnienia wejścia i ciśnienia odpowietrzania. Należy mieć na uwadze, że dodatkowe straty ciśnienia w pracy wzmacniacza (poza zaworem przełączającym); przyłączami (WE, WY, E), oporami ruchu tłoka powoduje praca zaworów zwrotnych. Dla każdego typu wzmacniacza producent podaje charakterystyki tych urządzeń, w szczególności wartości uzyskanego ciśnienia po stronie WY (wzmacnianego) oraz odpowiadający mu wydatek przepływu. Niestety wartości strat producent nie podaje. Z tego też powodu na tym etapie naszych rozważań teoretycznych te straty określimy w sposób pośredni. W tym celu zdefiniujemy współczynnik α (5), którego wartość będzie informowała nas pośrednio o stratach. Straty te związane są ze spadkiem ciśnienia na zaworach zwrotnych i na zaworze przełączającym oraz tarciem elementów mechanicznych. Konstrukcja wzmacniacza ciśnienia kompensuje wymienione straty w bardzo prosty sposób poprzez dobieranie średnicy tłoczyska.

3. Określenie parametrów pracy wzmacniacza ciśnienia pracującego w module transportowym

W celu określenia interesujących nas parametrów, a szczególności ich wpływu na pracę wzmacniacza ciśnienia posłużymy się uproszczonym schematem jego działa przedstawionym na rys. 3. Z uwagi na to, że powyżej zdefiniowaliśmy współczynnik α, którego wartość informowała nas pośrednio o stratach, na schemacie pracy wzmacniacza pominięto zawór regulacyjny, zawory zwrotne, zawór przełączający oraz tarcie elementów mechanicznych. Ponadto z uwagi na fakt, że najistotniejsze jest przedstawienie idei pracy wzmacniacza ciśnienia wybrano jego najprostszą postać składająca się z dwóch identycznych współpracujących ze sobą siłowników o tych samych przekrojach powierzchni tłoka S.

Jak widać na schemacie tłoczyska siłowników o tych samych polach przekroju S_T są ze sobą sztywno połączone stanowiąc tak naprawdę jeden element. Ponieważ tak jak to wcześniej zdefiniowaliśmy, rozważamy dwa takie same siłownik, w związku z tym również skok tłoczyska L jest taki sam dla obu. Przy czym tak zdefiniowany parametr L czyli skok tłoczyska (siłownika pneumatycznego) to odległość pomiędzy końcem tłoczyska w stanie wsuniętym (komora A) i wysuniętym (komora A). Tak przyjęta budowa wewnętrzna wzmacniacza ciśnienia generuje dwa identyczne obszary A i B. Wewnątrz tych obszarów porusza się tłok rozdzielając każdy z nich, na dwa dodatkowe obszary o zmiennej objętości w funkcji ruchu tłoczyska. Komory napędowe A i B są to te obszary, w których zmienność objętości wynika tak naprawdę z ruchu tłoka napędzanego tłoczyskiem. Natomiast komory sprężania A i B są to te obszary, w których zmienność objętości wynika ze zmiany położenia zarówno tłoka jak i poruszającego się w tym obszarze tłoczyska. Przyjmując do rozważań ruch tłoczyska przedstawiony na rys. 3 rozkład sił w siłownikach możemy przedstawić poniższym równaniem:

$$(p_1 + p_e)(S - S_T) - p_e S + (p_1 + p_e)S - (p_2 + p_e)(S - S_T) = 0 \quad (2)$$

Nadmienić trzeba w tym miejscu, że w przypadku ruchu tłoczyska w przeciwną stronę co jest również związane z zamianą wartości w rozważanych obszarach czyli komory oznaczone symbolem A pełnią funkcję komór B i na odwrót, otrzymujemy dokładnie identyczne równanie (2).

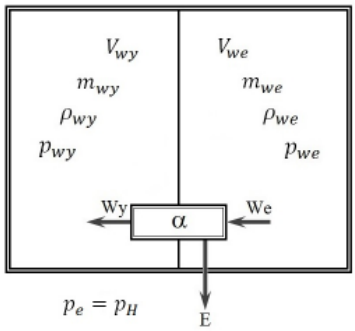

Rys. 4. Schematy modułu transportowego z uwzględnieniem tylko obszaru autokompresji
Fig. 4. Schemes of the transport module taking into account only the autocompression area

Stąd po przekształceniach równania (2) otrzymujemy:

$$p_1(2S - S_T) - p_2(S - S_T) = 0 \tag{3}$$

Czyli

$$p_1(2S - S_T) = p_2(S - S_T) \tag{4}$$

Zdefiniujmy teraz bezwymiarowy współczynnik α, którego wartość zawsze będzie mniejsza od jednego.

$$\alpha = \frac{S - S_T}{S}, \alpha < 1 \tag{5}$$

Po obustronnym podzieleniu równania (4) przez powierzchnię tłoka S i uwzględnieniu współczynnika α mamy

$$p_1(1 + \alpha) = p_2\alpha \tag{6}$$

Z zależności tej (6) możemy wyznaczyć wartość ciśnienia p_2 (7),

$$p_2 = p_1 \frac{1+\alpha}{\alpha} > 2 \tag{7}$$

którego wartość zawsze będzie większa od dwóch.

Możemy również równanie (6) zapisać w innej postaci (8)

$$p_1[(1 - \alpha) + 2\alpha] = p_2\alpha \tag{8}$$

Mnożąc równanie (8) przez powierzchnię tłoka S i uwzględniając chwilowe położenie tłoka (L-x(t)) gdzie x(t) przyjmuje wartości z zakresu od 0 do L otrzymujemy postać (9),

$$p_1 S[(1 - \alpha) + 2\alpha][L - x(t)] = p_2 S\alpha[L - x(t)] \tag{9}$$

która to postać wyraża zasadę zachowania energii ponieważ wymiar jednostki jest [J].

Wróciwszy do równania (8) możemy go przekształcić do postaci (10)

$$2p_1 = p_2 - p_1 \frac{1-\alpha}{\alpha} \tag{10}$$

Uwzględniając ciśnienie p_e czyli otoczenia otrzymujemy następującą postać równania (10)

$$p_{wy} = 2p_{we} = (p_2 + p_e) - p_{str}$$
$$p_{str} = p_{we} \frac{1-\alpha}{\alpha} \tag{11}$$

Analizując równanie (11) widzimy, że aby wzmocnienie wzmacniacza ciśnienia nie było mniejsze niż dwa to suma wszystkich strat ciśnienia nie może być większa od członu p_{str}. Ponadto wyraźnie widać, że przyjęty bezwymiarowy współczynnik α wyrażony zależnością (5) informuje nas w sposób pośredni o stratach w analizowanym urządzeniu. Nadmienić należy również, że w przypadku kiedy p_{wy} osiągnie wartość $2p_{we}$, a nie będzie odbioru medium o ciśnieniu $p_{wy} \leq 2p_{we}$ to układ przestanie pracować osiągając stan równowagi równanie (11).

Należy zwrócić uwagę, że przedstawiony powyżej wywód jest nie do końca precyzyjny i może wprowadzać w błąd. Wiadomo, że wartości ciśnienia w poszczególnych komorach wzmacniacza ciśnienia są ściśle uzależnione od położenia tłoczyska. Natomiast w trakcie wyprowadzenia zależności (11) nic na ten temat nie było mówione. Wyjaśniamy to poniżej. Równanie (2) jest poprawne a więc równanie (11) też. Wspomnieliśmy wcześniej, że równanie (9) tak naprawdę przedstawia zasadę zachowania energii i w rozważanym przypadku spełnia funkcję podobną do równania Bernoulliego (Roberson, Crowe 1995; Roberson, Cassidy, Chaudhry 1995), w którym również występują współczynniki strat tzw. λ – straty liniowe oraz ζ – straty lokalne (Walden, Stasiak 1971). Ponadto równanie Bernoulliego możemy przedstawiać w różnych postaciach, w których poszczególne człony mogą przyjmować jednostki np. wysokości [m], ciśnienia [pa] i dalej będzie ono wyrażało zasadę zachowania energii. Wprowadziwszy współczynnik α możemy zdefiniować straty ciśnienia p_{str} i podobnie jak w równaniu Bernoulliego uwzględnia ono straty na tarcie wewnętrzne oraz straty miejscowe w płynie związane z lepkością i nagłymi zmianami przekrojów itd. Jeżeli ciśnienie w zewnętrznym układzie podłączonym do przyłącza WY jest niższe niż wyznaczone z równania (11) to do momentu kiedy się nie zrównoważą w komorze sprężania następuje spręż do odpowiedniej wartości bez wymiany medium na zewnątrz. Dzieje się to kosztem zmniejszenia objętości komory sprężania B co jest uwarunkowane przesuwaniem się tłoczyska. Tak więc wartość ciśnienia określona równaniem (11) informuje nas o maksymalnej wartości ciśnienia p_{wy} jakie wzmacniacz ciśnienia może wygenerować. Wartość ta jest jednak ściśle związana z osiągnięciem odpowiedniego położenia tłoczyska. Położenie to można wyznaczyć znając wartość p_{wy}. Dla tej wartości należy określić wartość gęstości medium sprężanego i mając tą wartość można wyznaczyć jej objętość, a więc i położenie tłoczyska. Należy jednak zauważyć, że dla gazów zależność gęstości od ciśnienia nie jest liniowa nawet dla

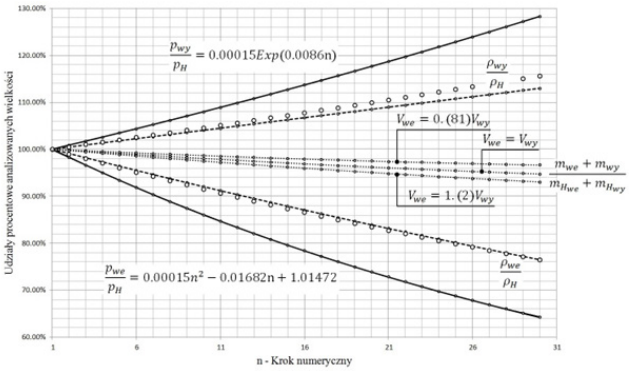

Rys. 4. Schematy modułu transportowego z uwzględnieniem tylko obszaru autokompresji
Fig. 4. Schemes of the transport module taking into account only the autocompression area

przemiany izotermicznej. Dlatego dalsze rozważania należy przeprowadzić dla konkretnego przypadku.

4. Charakterystyka pracy modułu transportowego w procesie wynurzania.

Dla przyjętego punktu odniesienia EX1504L2 maksymalna głębokość na jaką zanurzył się ROV wyniosła 4824.53 [m]. Ciśnienie zarejestrowane na tej głębokości przyjmuje wartość p_H=p_e 492.14 [bar] a temperatura wody morskiej t_e=1.48 [°C]. Gęstość azotu dla przyjętego ciśnienia p_H oraz temperatury t_e wynosi ϱ_H=441.30 [kg/m³] i zakładamy, że jest to wartość, która umożliwia rozpoczęcia procesu transportu urobku przez moduł na powierzchnię. Zmiana wartości gęstości azotu będzie miała oczywiście wpływ na siłę wyporu modułu i tak, gdy wzrośnie rozważany obiekt będzie opadał na dno morskie. Natomiast gdy zmaleje, proces wynurzania modułu transportowego będzie charakteryzował się zwiększeniem jego prędkości poruszania się ku powierzchni. Tak przyjęte parametry odpowiadające za gęstość azotu w module transportowym będą pierwszym poziomem odniesienia (inaczej punktem startowym, punktem bazowym od którego zaczniemy analizę). Schemat modułu przyjętego do analizy przedstawiono na rys.4. Obszar zajęty przez medium czyli w naszym przypadku azot jest podzielone na dwa równe obszary V_{wy} oraz V_{we} a wiec V_{wy}=V_{we}. Na rys.4 umieszczony jest również wzmacniacz ciśnienia, który oznaczony jest współczynnikiem α charakteryzujący starty występujące w nim.

W chwili rozpoczęcia procesu wynurzania ciśnienie w analizowanych obszarach jest równe ciśnieniu zewnętrznemu i wynosi p_{wy}= p_{we}=p_H=p_e Analogicznie jest z wartościami gęstości azotu w rozważanych obszarach ρ_{wy} = ρ_{we} = ρ_H, a co za tym idzie również masy mwy = mwe są sobie równe. W momencie trwania wynurzania parametry fizyczne charakteryzujące pracę modułu transportowego będą ulegały zmianie. Co zostało zilustrowane na rys.5.

Do analizy przedstawionej na rys.5 założono, że wartość bezwymiarowego współczynnika α określającego w sposób pośredni straty wewnętrzne wzmacniacza ciśnienia wynosi 0.95. Na osi argumentów naniesiono kroki, dla których analizowano numerycznie wartości fizyczne obrazujące procesy zachodzące podczas autokompresji modułu transportowego przy wykorzystaniu wzmacniacza ciśnienia zdefiniowanego w rozdziale trzecim. Natomiast oś wartości przedstawia udziały procentowe analizowanych wielkości fizycznych. W miarę postępu procesu wynurzania generuje się różnica miedzy ciśnieniem wewnętrznym w obszarze V_{we} a ciśnieniem otoczenia czyli zewnętrznym. To uruchamia pracę wzmacniacza ciśnienia, który tłoczy medium robocze do obszaru V_{wy} kosztem zasysanego medium z obszaru V_{we}, oczywiście część medium roboczego jest uwalniana do otoczenia za pomocą upustu oznaczonego litera E rys.4. Wzrost masy w obszarze V_{wy} generuje wzrost zarówno ciśnienia p_{wy} (linia ciągła) jak i gęstości ρ_{wy} (linia przerywana). Natomiast w obszarze V_{we} zgodnie z zasadą zachowania masy maleje wartość ciśnienia p_{we} (linia ciągła) jak również gęstości ρ_{we} (linia przerywana). W analizowanym przypadku punktem końca procesu jest osiągnie powierzchni oraz co jest oczywiste ciśnienie otoczenia osiąga wartość ciśnienia atmosferycznego p_{atm} oraz (p_{wy}-p_{atm})=2(p_{atm}-p_{we}) co jest uwarunkowane równaniem (11). Na wykresie rys.5 przedstawiono również liniami kropkowanymi stosunek całkowitej masy czynnika roboczego zawartego wewnątrz moduły transportowego jakim jest w rozważanym przypadku azot w trakcie procesu wynurzania m_{we}+m_{wy} do całkowitej masy w momencie rozpoczęcia wynurzania m_{Hwe} +m_{Hwy}, dla trzech różnych wariantów objętości V_{we} i V_{wy}.

5. Wnioski

W niniejszym artykule skupiliśmy się nad zastosowaniem wzmacniacza ciśnienia do autokompresji. Urządzenie to pracuje autonomiczne jeżeli tylko pojawi się odpowiednia różnica ciśnień między przyłączami WE a tzw. odpowietrzaniem E i nie potrzeba żadnej dodatkowej formy energii do jego zasilania. Dlatego zdaniem autorów jego zastosowanie w transporcie urobku z dna morskiego na powierzchnie otwiera nowe możliwości, które dotychczas wymagały dodatkowego źródła energii. Brak informacji o wewnętrznych stratach ciśnienia analizowanego urządzenia, które jest pomijane przez producentów stwarza problemy natury dokładnego opisu zachodzących procesów w wzmacniaczu ciśnienia. Problem ten rozwiązano definiując bezwymiarowy współczynnik α (5), który w sposób pośredni informuje o stratach wymienionych w niniejszym artykule. Nadmienić w tym miejscu należy również, co w artykule nie zostało poruszane, że za pomocą tego bezwymiarowego współczynnika możemy również modelować wzmocnienie urządzenia (8) co będzie poruszane w kolejnych artykułach. Autorzy zdają sobie sprawę, że zastosowanie wzmacniacza ciśnienia w niestabilnych warunkach pracy wynikających ze zmiany w procesie wynurzania różnicy ciśnień między przyłączami WE a tzw. odpowietrzaniem E, może stworzyć sytuację, że tłoczysko może przyjąć pozycje

(9), która uniemożliwi dalszą pracę wzmacniacza mimo dalszego wzrostu różnicy ciśnienia zasilającego urządzenie. Jest to kolejne zagadnienia do dalszej analizy w kolejnych artykułach. Analiza pracy wzmacniacza wydaje się dość skomplikowana ponieważ równanie wyjściowe (2) zależy od położenia tłoczyska a tak naprawdę od wynikającej z tego położenia gęstości medium w analizowanej objętości, a to generuje wartość ciśnienia. Niestety zależność gęstości od ciśnienia nie jest liniowa. Najkorzystniejsze wydaje się analizowanie pracy wzmacniacza ciśnienia wychodząc z zasady zachowania masy. Przesuwający się tłok przy spełnieniu zasady zachowania masy będzie generował zmianę gęstości, która to wartość będzie odpowiedzialna za wartość ciśnienia, które musi spełniać równanie (2). Tą metodę zastosowano do numerycznej analizy pracy wzmacniacza ciśnienia rys. 5. Dodatkowo w tej analizie musimy uwzględnić wartości V_{wy} i V_{we}, tworzące wspólną przestrzeń fizyczną ze wzmacniaczem ciśnienia, w której zachodzą interesujące nas procesy. Przeanalizowano pracę rozważanego układu dla trzech różnych wartości V_{wy} i V_{we}, co zostało przedstawione na rys. 5 (linia kropkowana). Okazało się że rozkłady zmiany ciśnienia p_{wy}/p_H oraz p_{we}/p_H tak naprawdę pokrywają się dla tych trzech przypadków rys. 5 i maksymalna odchyłka w stosunku do krzywej bazowej $V_{wy}=V_{we}$ (linia ciągła) osiąga maksymalną wartość dla n = 30, czyli osiągnięcia powierzchni, wynosi w obu przypadkach 0.15 [%]. Podobnie jest w przypadku gęstości. Dla $V_{we}=0.(81)$ V_{wy} maksymalna zmiana ρ_{we} wynosi 0.11 [%] a dla ρ_{wy} wynosi 0.07 [%]. Natomiast w przypadku $V_{we}=1.(2)$ V_{wy} maksymalna zmiana ρ_{we} wynosi 0.07 [%] a dla ρ_{wy} wynosi 0.11 [%]. Oczywiście w odniesieniu do krzywej bazowej i dla punktu n = 30. W przypadku upustu masy do otoczenia (krzywe kropkowane) widzimy na rys.5 znaczne odchylenia od krzywej bazowej. W punkcie n = 30 dla $V_{we}=0.(81)V_{wy}$ wynosi -2.01 [%] czyli zmalała wymiana masy z otoczenie a dla $V_{we}=1.(2)$ V_{wy} wynosi 1.84 [%] czyli wzrosła. W przypadku krzywej bazowej maksymalny upust czyli bezpowrotna strata medium do otoczenia wynosi 5.25 [%] w odniesieniu do całkowitej masy medium roboczego w chwili rozpoczęcia wynurzania. Ta niewielka bezpowrotnie tracona (w analizowanym przypadku) masa w medium transportowym przekłada się na znaczny wzrost ciśnienia w obszarze sprężania oraz znaczący spadek ciśnienia w obszarze rozprężania rys.5. Obszar sprężania w naszym rozumieniu związany jest z akumulacją energii. Natomiast obszar rozprężania posiada jeszcze znaczną energię, którą można jeszcze zagospodarować miedzy innymi do zwiększenia sprężu w objętości V_{wy}. W niniejszym artykule nie wyjaśniamy już tej kwestii, z uwagi na fakt, że osiągnięte rezultaty w połączeniu z wcześniejszymi koncepcjami transportu urobku ku powierzchni rys.1 spełniają nasze oczekiwania, pozwalając na ich dalsze rozwinięcie.

Na rys.5 naniesiono również zmianę energii jakie zachodzą w rozważanych obszarach V_{wy} i V_{we} w przypadku $V_{wy}=V\_we$. Przedstawiono je za pomocą kółek. I tak strata energii E_{wy} w stosunku do wartości początkowej w momencie rozpoczęcia procesu wynurzania medium transportowego leży powyżej krzywej obrazującej zmiany gęstości ρ_{wy} (linia przerywana). Natomiast strata energii E_{we} w stosunku do wartości początkowej obrazują punkty, które prawie pokrywają się z krzywą zmiany gęstości ρ_{we} (linia przerywana) rys.5. Całkowita strata energii związana z wymianą masy z otoczeniem w rozważanym przypadku wynosi $E_{str}=3.96$ [%] i jest porównywalna z pozostałymi dwoma analizowanymi wariantami.

Literatura – References

1. Abramowski T, Kotliński R (2011) Współczesne wyzwania eksploatacji oceanicznych kopalin polimetalicznych. Górnictwo i geoinżynieria 35(5):41-61
2. Broda K., Filipek W., Tora B. (2023) Polish Experience in Offshore Mining: The New Concept of Transport Deep-Sea Concretions and Processing; 4GEO, Springer, Springer Nature.
3. Depowski S, Kotliński R, Rühle E, Szamałek K (1998) Surowce mineralne mórz i oceanów, Wydawnictwo Naukowe Scholar, Warszawa
4. Filipek W., Broda K. Theoretical foundation of the implementation of controlled pyrotechnical reactions as an energy source for transportation from the sea bed. Scientific Journals of the Maritime University of Szczecin 48 (120) 2016, pg. 117-124
5. Filipek W., Broda K. Experimental verification of the concept of the use of controlled pyrotechnic reaction as a source of energy as a part of the transport system from the seabed, Scientific Journals of the Maritime University of Szczecin, 49 (121) 2017, 77-83.
6. Filipek W., Broda K. (2017),The Theoretical Basis of the Concept of Using the Controlled Pyrotechnical Reaction Method as an Energy Source in Transportation from the Sea Bed, TransNav the International Journal on Marine Navigation and Safety of Sea Transportation, Vol.11, No. 4, 653-659.
7. Filipek W., Broda K. (2017),Research on the Application of Controlled Pyrotechnic Reaction with the Use of Ammonium Nitrate for Transport from Seabed, TransNav the International Journal on Marine Navigation and Safety of Sea Transportation, Vol.11, No. 4, 647-652.
8. Filipek W., Broda K. (2018) Theoretical research on the gas phase density change in processes occurring during work of the transport module intended for transport from the seabed / W: Proceedings of the international conference on Human safety in work environment : operating machinery and equipment : integrated management systems: quality - environment - safety - technology : October 23–27, 2018, Gdańsk-Nynashamn-Stockholm-Tallinn-Stockholm-Nynashamn-Gdańsk. — Warszawa : STE Group Sp. z o.o., 2018. — (New Trends in Production Engineering ; ISSN 2545-2843 ; vol. 1 iss. 1). — ISBN: 978-83-952420-0-7. — S. 597–604. — Bibliogr. s. 603–604, Abstr.
9. Filipek W., Broda K. (2018) Theoretical research on the stability of the transport module intended for transport from the seabed / W: Proceedings of the international conference on Human safety in work environment : operating machinery and equipment : integrated management systems: quality - environment - safety - technology : October 23–27, 2018, Gdańsk-Nynashamn-Stockholm-Tallinn-Stockholm-Nynashamn-Gdańsk. — Warszawa : STE Group Sp. z o.o., 2018. — (New Trends in Production Engineering ; ISSN 2545-2843 ; vol. 1 iss. 1). — ISBN: 978-83-952420-0-7. — S. 605–612. — Bibliogr. s. 611–612, Abstr.
10. Filipek W., Broda K. (2018) Experimental research on the concept of using an autonomous transport module for transport from the seabed / // W: Proceedings of the international conference on Human safety in work environment : operating machinery and equipment : integrated management systems: quality - environment - safety - technology : October 23–27, 2018, Gdańsk-Nynashamn-Stockholm-Tallinn-Stockholm-Nynashamn-Gdańsk. — Warszawa : STE Group Sp. z o.o., 2018. — (New Trends in Production Engineering ; ISSN 2545-2843 ; vol. 1 iss. 1). — ISBN: 978-83-952420-0-7. — S. 267–275. — Bibliogr. s. 274–275, Abstr.
11. Filipek W., Broda K. (2018) Research on the concept of using calcium carbide as a source of energy for transport from the seabed / W: Proceedings of the international conference on Human safety in work environment : operating machinery and equipment : integrated management systems: quality - environment - safety - technology : October 23–27, 2018, Gdańsk-Nynashamn-Stockholm-Tallinn-Stockholm-Nynashamn-Gdańsk. — Warszawa : STE Group Sp. z o.o., 2018. — (New Trends in Production Engineering ; ISSN 2545-2843 ; vol. 1 iss. 1). — ISBN: 978-83-952420-0-7. — S. 277–284. — Bibliogr. s. 284, Abstr.
12. Filipek W., Broda K. (2019) Theoretical research on mass exchange between an autonomous transport module and the environment in the process of transport from the seabed / W: Advances in marine navigation and safety of sea transportation / eds. Adam Weintrit, Tomasz Neumann. — Boca Raton [etc.] : CRC Press/Balkema : Taylor & Francis Group, cop. 2019. — Publikacja zawiera materiały z: TransNav 2019 : 13th international conference on Marine navigation and safety of sea transportation : 12–14 June 2019, Gdynia, Poland. — ISBN: 978-0-367-35760-3 ; e-ISBN: 978-0-429-34193-9. — S. 143–149. — Bibliogr. s. 148–149, Abstr.. — Abstrakt w: TransNav 2019 : abstracts of papers presented during the 13th international conference on Marine navigation and safety of sea transportation : Gdynia, 12–14 June 2019 / eds. Adam Weintrit, Tomasz Neumann. — [Gdynia : s.n.], [2019]. — S. 71
13. Jones DO, Durden JM, Murphy K, Gjerde K, Gebicka A, Colaço A, Morato T, Cuvelier D, (2019) Existing environmental management approaches relevant to deep-sea mining. Mar Polic 103:172-181
14. Niedoba T (2015) Polymetallic concretions: long-range source of mineral raw materials. Inzynieria Mineralna 1(35):61–74
15. Roberson J.A., Crowe C.T., (1995) Engineering Fluid Mechanics, John Wiley & Sons, Inc.
16. Roberson J.A., Cassidy J.J, Chaudhry M.H., (1995) Hydraulic Engineering John Wiley & Sons, Inc.

17. Sharma R., (2017) Deep-sea mining: resource potential, technical and environmental considerations. Springer International Publishing AG,
18. SPC (2013) Deep sea minerals: sea-floor massive sulphides. A physical, biological, environmental, and technical review. In: Baker E, Beaudoin Y (Eds.), Vol. 1A, Secretariat of the Pacific Community, Sydney
19. The Royal Society (2017) Future ocean resources [https://royalsociety.org/~/media/policy/ projects/future-oceans-resources/future-of-oceans-evidence-pack.pdf]
20. Walden H., Stasiak J., (1971) Mechanika cieczy i gazów w inżynierii sanitarnej. Wydawnictwo Arkady. Warszawa.

Autocompression as a Method of Accumulating Waste Energy during the Emergence of an Autonomous Transport Module using a Change in Buoyancy

Despite the Covid-19 pandemic lasting for few years, the interest in the exploitation of deposits lying at the bottom of seas and oceans at great depths has not been waning. Many new concepts for the exploitation of sea deposits have been developed. Many consortia were established, interested in mining activities in seas and oceans. And although the most advanced venture of Nautilus-Minerals has not been successful so far, it has made a huge leap forward in terms of research and technology. The exploitation on an industrial scale is most likely to start in the coming years, especially in the waters of the EEZ (Exclusive Economic Zone). Recently, for example, the Cook Islands authorities have granted three licenses for this type of activity. In international waters though, we must, unfortunately, still wait for legal solutions satisfying all interested parties. The exploitation of shelf deposits is successfully being carried out with various methods in many regions around the world (Karlic, 1984; Depowski et al., 1998; Abramowski, Kotliński, 2011; Niedoba 2015, SPC 2013; Sharma, 2017); however, reaching for deposits of massive polymetallic sulphides or polymetallic nodules lying at great depths places considerable demands on scientists and engineers. Among the heaviest ones is the development of a method of transporting spoil from the bottom to the sea surface. For several years, the authors have been conducting theoretical and experimental research on new concepts of transport from the seabed, the results of which were presented in numerous publications (Filipek W., Broda K .: 2016, 2017, 2018, 2019, Broda, Filipek, Tora 2023).

While considering various concepts of transport from the seabed using an autonomous module, we paid attention to energy losses during the exchange of the working medium between the autonomous transport module and the surroundings (sea water). In the articles (Filipek W., Broda K. 2018, 2019) we focused on the positive aspect of this exchange, but nevertheless these are energy losses. In this publication, the authors analyze what part of this energy can be used (in autocompression) and what impact it has on the energy balance of the transport module.

Keywords: *marine mining, transport from great depths, autonomous transport module*

Rozkład ciśnienia w ośrodku porowatym podczas zjawiska kolmatacji przebiegającego zgodnie z pierwszą kinetyką bez linearyzacji wyrażenia określającego porowatość rozważanego ośrodka w funkcji położenia i czasu

Wiktor FILIPEK[1)], *Krzysztof BRODA*†[2)]

[1)] Akademia Gorniczo-Hutnicza w Krakowie, Wydział Inżynierii Lądowej i Gospodarki Zasobami; ORCID: 0000-0001-5472-8214; ResearcherID: W-5254-2018; Scopus: 36185413000; PBN: 5e70922b878c28a047391056

[2)] Akademia Gorniczo-Hutnicza w Krakowie, Wydział Inżynierii Lądowej i Gospodarki Zasobami; ORCID: 0000-0001-8218-9350; ResearcherID: D-2256-2018; Scopus: 55658644400; PBN: 5e70922b878c28a047391048

http://doi.org/10.29227/IM-2024-01-108

Submission date: 20-05-2024 | Review date: 28-06-2024

Abstrakt

Zjawisko kolmatacji występuje w przyrodzie wszędzie tam, gdzie dochodzi w ośrodkach porowatych do przepływów cieczy niosących zawieszone cząstki stałe. Nawet „najczystsza" woda dopływająca do studni po pewnym czasie spowoduje jej zakolmatowanie, a tym samym spadek jej wydajności, co jest zjawiskiem negatywnym.

Badania prowadzone w naszym ośrodku od lat 60-tych ubiegłego wieku [1,4-14] doprowadziły do opracowania matematycznego opisu zjawiska kolmatacji [4-8,13,14] oraz przeprowadzenia szeregu eksperymentów ją weryfikujących [9-14]. Uzyskane wyniki wykorzystano również podczas prób uszczelnienia górotworu wokół wyrobiska górniczego [12].

W niniejszym artykule podjęto próbę określenia obszaru K w przypadku przebiegu zjawiska kolmatacji zachodzącego zgodnie z kinetyką pierwszą, oraz podania zależności opisujących rozkład ciśnienia h(x,t) dla przepływu bez kolmatacji i z kolmatacją bez linearyzacji wyrażenia $\varepsilon(x,t)^{-3}$ w otoczeniu ε_o gdzie ε określa porowatość ośrodka w funkcji położenia i czasu.

Określenie obszaru K pozwala nam na jednoznaczne wyprowadzenie dokładnego rozkładu ciśnienia h(x,t) podczas przepływu z kolmatacją przez ośrodek porowaty bez linearyzacji, a następnie porównania rozwiązań układu równań kolmatacji metodą linearyzacji i metodą dokładną przy wykorzystaniu bezwymiarowej postaci funkcji ξ.

W trakcie prowadzenia badań eksperymentalnych próba dopasowania rzeczywistego zjawiska do opracowanego modelu matematycznego obarczona była dużą niepewnością wynikającą prawdopodobnie z zastosowania linearyzacji członu $\varepsilon(x,t)^{-3}$.

W artykule autorzy wyjaśniają co generuje odstępstwo metody przybliżonej od dokładnego rozwiązania oraz zwracają uwagę, że dokładne rozwiązanie bardziej oddaje sens fizyczny matematycznego modelu opisu zjawiska oraz zdefiniowanych współczynników kolmatacji a w szczególności parametru ε_o.

Słowa kluczowe: *filtracja, kolmatacja, przepływ z wymianą masy i pędu, wymiana pędu*

Wstęp

Ze zjawiskiem kolmatacji w przyrodzie mamy do czynienia tam, gdzie występuje przepływ cieczy niosących zawieszone cząstki stałe przez ośrodki porowate. Zjawisko to może mieć znaczenie negatywne, jak w przypadku dopływu wody do studni, powodując zakolmatowanie, a tym samym spadek jej wydajności. Natomiast zależeć nam będzie na jak najintensywniejszym jego przebiegu wszędzie tam gdzie potrzebujemy ograniczyć albo wręcz wyeliminować wodoprzepuszczalność ośrodka porowatego, np. przy uszczelnianiu wałów przeciwpowodziowych, tam czy górotworu przy pracach podziemnych ograniczając dopływ wód do wyrobisk.

Widać więc, że znajomość mechanizmów przebiegu tego zjawiska jak i jego opisu teoretycznego i praktycznego wraz z opracowaniem metod określania parametrów odpowiedzialnych za jego przebieg ma duże znacznie.

Do badań zjawiska kolmatacji [2,3] nasz ośrodek włączył się w latach 60-tych ubiegłego wieku [1,4-14]. Prowadzone w naszym ośrodku badania doprowadziły do powstania teorii kolmatacji [4-8,13,14] oraz przeprowadzenia szeregu eksperymentów ją weryfikujących [9-14]. Zdobyte wówczas doświadczenie wykorzystano również podczas prób uszczelnienia górotworu wokół wyrobiska górniczego [12].

Zjawisko kolmatacji może według teorii kolmatacji przebiegać w różny sposób, opisany trzema kinetykami procesu kolmatacji [5,14]. Niestety w trakcie prowadzenia eksperymentu, czy badań „in situ" bardzo trudno jest określić, według której kinetyki aktualnie przebiega zjawisko kolmatacji. Konieczne więc jest posiadanie metody pozwalającej na określenie w czasie i przestrzeni obszaru K zachodzenia zjawiska dla poszczególnych kinetyk.

W niniejszym artykule autorzy skoncentrowali się na określeniu obszaru K w przypadku zjawiska kolmatacji przebiegającego zgodnie z kinetyką pierwszą, oraz podaniu zależności opisujących rozkład ciśnienia h(x,t) dla przepływu bez kolmatacji i z kolmatacją bez linearyzacji wyrażenia $\varepsilon(x,t)^{-3}$ w otoczeniu ε_o gdzie ε określa porowatość ośrodka w funkcji położenia i czasu.

Rozważania nasze przeprowadzono dla ośrodka jednorodnego charakteryzującego się stałością powierzchni właściwej $\alpha(x) = \alpha$ i stałością współczynnika kolmatacji $\alpha_0(x) = \alpha_0$

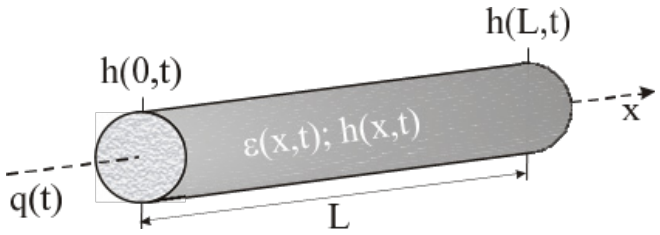

Rys. 4. Schematy modułu transportowego z uwzględnieniem tylko obszaru autokompresji
Fig. 4. Schemes of the transport module taking into account only the autocompression area

$\forall x \in [0, L]$ α(x) = α – powierzchnia właściwa

$\forall x \in [0, L]$ α_o (x) = α_o – współczynnik kolmatacji

Wielkość L opisuje maksymalny liniowy zasięg zjawiska kolmatacji zachodzącego w jednorodnym ośrodku porowatym.

Na Rys.1 przedstawiono taki wyidealizowany ośrodek przyjęty w naszych rozważaniach, gdzie:
q(t) – prędkość filtracji;
ε(x,t) – porowatość ośrodka;
h(x,t) – rozkład ciśnienia;
h(0,t) – ciśnienie na początku rozpatrywanego ośrodka;
h(L,t) – ciśnienie na końcu rozpatrywanego ośrodka;
L – długość ośrodka porowatego.

Według teorii kolmatacji [14] ten przypadek opisany jest układem trzech równań różniczkowych cząstkowych: bilansu transportu (1), kinetyki procesu kolmatacji (2) i ruchu (3)[14].

$$\begin{cases} q(t)\dfrac{\partial N(x,t)}{\partial x} - \dfrac{\partial \varepsilon(x,t)}{\partial t} = 0 \text{ - równanie bilasu transportu} & (1) \\ \dfrac{\partial \varepsilon(x,t)}{\partial t} = -\alpha_o q(t) N(x,t) \text{ - równanie kinetyki procesu} & (2) \\ \dfrac{\partial h(x,t)}{\partial x} = -2a\dfrac{\nu}{g}\dfrac{\alpha^2}{\varepsilon^3(x.t)} q(t) \text{ - równanie ruchu} & (3) \end{cases}$$

gdzie: N(x,t) – koncentracja unoszonych cząstek zawiesiny;
a – współczynnik odstępstwa [7,9];
υ – współczynnik lepkości kinematycznej;
g – przyspieszenie grawitacyjne.

Wyprowadzenie dokładnego rozkładu ciśnienia h(x,t) podczas przepływu z kolmatacją przez ośrodek porowaty – bez linearyzacji

W celu wyznaczenia rozkładu ciśnienia h(x,t), musimy najpierw z równania (1) i (2) wyliczyć funkcję (x,t). W związku z tym przekształćmy równanie kinetyki (2) procesu kolmatacji do poniższej postaci (4) zakładając oczywiście, że $\alpha_o q(t) \neq 0$

$$N(x,t) = -\frac{1}{\alpha_o q(t)}\frac{\partial \varepsilon(x,t)}{\partial t} \quad (4)$$

i wprowadźmy go do równania bilansu transportu (1). Po prostych przekształceniach otrzymamy:

$$\frac{\partial^2 \varepsilon(x,t)}{\partial t \partial x} + \alpha_o \frac{\partial \varepsilon(x,t)}{\partial t} = 0 \quad (5)$$

Powyższe równanie całkujemy względem czasu t otrzymując:

$$\frac{\partial \varepsilon(x,t)}{\partial x} + \alpha_o \varepsilon(x,t) = \phi(x) \quad (6)$$

Nieznaną funkcję φ(x) znajdujemy w oparciu o warunek początkowy (7)

$$\forall x \in [0, L] \quad \varepsilon(x,0) = \varepsilon_o \quad (7)$$

dostając zależność (8)

$$\forall x \in [0, L] \quad \phi(x) = \alpha_o \varepsilon_o, \quad (8)$$

która wstawiona do równania (6) po prostych przekształceniach pozwala zapisać go w poniższej postaci:

$$\forall x \in [0, L]\ \forall t \in R^+ \ \frac{\partial \varepsilon(x,t)}{\partial x} + \alpha_o(\varepsilon(x,t) - \varepsilon_o) = 0 \quad (9)$$

Otrzymane równanie różniczkowe rzędu pierwszego można przedstawić w postaci (10)

$$\frac{d\varepsilon(x,t)}{\varepsilon(x,t) - \varepsilon_o} = -\alpha_o dx \quad (10)$$

lub (11)

$$\varepsilon(x,t) - \varepsilon_o = 0 \quad (11)$$

Rozważmy najpierw zależność (11), z której wynika, że

$$\forall x \in [0, L]\ \forall t \in R^+ \quad \varepsilon(x,t) = \varepsilon_o \quad (12)$$

Natomiast z równania bilansu transportu (1) i warunku $\alpha_o q(t) \neq 0$ otrzymujemy

$$\forall x \in [0, L]\ \forall t \in R^+ \quad \varepsilon(x,t) = \varepsilon_o \Rightarrow N(x,t) = const \quad (13)$$

Ostatecznie uwzględniając równanie kinetyki procesu (2) dochodzimy do spostrzeżenia, że

$$\forall x \in [0, L]\ \forall t \in R^+ \quad \varepsilon(x,t) = \varepsilon_o \Rightarrow N(x,t) = 0. \quad (14)$$

Otrzymana zależności opisuje więc proces przepływu czystej wody przez ośrodek porowaty.

Zajmiemy się teraz członem (10) przy założeniu, że ε(x,t) - $\varepsilon_0 \neq 0$, z którego wynika, że t ≠ 0. Po scałkowaniu równania (10) otrzymujemy zależność (15)

$$ln|\varepsilon(x,t) - \varepsilon_o| = -\alpha_o x + \psi(t), \quad (15)$$

która po prostych przekształceniach i podstawieniu φ(t) = eψ(t) doprowadza do wyniku w postaci równania (16).

$$\varepsilon(x,t) = \varepsilon_o + \phi(t)e^{-\alpha_o x} \tag{16}$$

Musimy teraz określić zależność funkcji φ od czasu - φ(t). Skorzystamy z równania kinetyki procesu (2) i rozwiążemy je dla przypadku, gdy x = 0. Mamy:

$$\frac{\partial\varepsilon(0,t)}{\partial t} = -\alpha_o q(t) N(0,t) \tag{17}$$

Ponieważ do rozważanego obszaru wpływa zawiesina o stałej w czasie koncentracji możemy zapisać warunek brzegowy w postaci:

$$\forall t \in R^+ \quad N(0,t) = n \tag{18}$$

Rozwiązanie ogólne równania (17) z warunkiem brzegowym (18) opisane jest więc poniższą zależnością:

$$\varepsilon(0,t) = -n\alpha_o \int q(t)dt + C \tag{19}$$

Z warunku początkowego (7) wynika, że C = ε_o czyli

$$\varepsilon(0,t) = \varepsilon_o - n\alpha_o \int q(t)dt \tag{20}$$

Stąd po prostych przekształceniach otrzymujemy

$$\phi(t) = -n\alpha_o \int q(t)dt \tag{21}$$

Ostatecznie możemy przedstawić rozwiązanie równania (16) w postaci

$$\begin{gathered}\forall x \in R^+ \ \forall t \in R^+ - \{0\}: \alpha_0 q(t) \neq 0 \\ \varepsilon(x,t) = \varepsilon_o - n\alpha_o e^{-\alpha_o x} \int q(t)dt\end{gathered} \tag{22}$$

przedstawiającej rozkład porowatości ośrodka przy przepływie z kolmatacją, realizowanym przy przyjętych założeniach.

Pozostaje nam teraz tylko sprawa wyjaśnienia, co się dzieje, jeżeli t=0. Jak widać równanie (22) przechodzi w postać (14), co jest przecież oczywiste, bo w chwili zerowej proces kolmatacji spełniający warunek początkowy (7) nie może zachodzić.

Podsumowując teraz nasze dotychczasowe rozważania, poszukiwaną funkcję ε(x,t) ostatecznie możemy przedstawić jak niżej:

$$\forall x \in [0,L] \ \forall t \in R^+: \alpha_o q(t) \neq 0 \quad \varepsilon(x,t) = \begin{cases} \varepsilon_o & \text{– proces bez kolmatacji (23)} \\ \varepsilon_o - n\alpha_o e^{-\alpha_o x} \int q(t)dt & \text{– proces z kolmatacją (24)} \end{cases}$$

Zajmiemy się teraz określeniem obszaru K zachodzenia zjawiska. Z równania (23) wynika, że obszar K dla przepływów bez kolmatacji można przedstawić w postaci

$$\kappa = \{(x,t): x \in [0,L], t \in R^+\}, \tag{25}$$

czyli cały obszar objęty przepływem.

Określenie obszaru K dla przepływu z kolmatacją jest zadaniem skomplikowanym z uwagi na trudność wyznaczenia w sposób bezpośredni czasu zakończenia przebiegu zjawiska. Zatem przyjęliśmy metodę pośrednią. Proces kolmatacji zostanie zakończony jeżeli wszystkie pory ośrodka ulegną wypełnieniu, czyli ε(x,t)=0. W oparciu o to, z równania (24) wynika, że

$$\int_0^{t_{max}} q(t)dt \leq \frac{\varepsilon_o}{n\alpha_o} \tag{26}$$

a w konsekwencji obszar K możemy przedstawić w postaci

$$\kappa = \left\{(x,t): x \in [0,L], t \in [0, t\int_0^{t_{max}} q(t)dt \leq \frac{\varepsilon_o}{n\alpha_o}_{max}\right\} \tag{27}$$

Przejdźmy teraz do wyznaczenia poszukiwanego rozkładu ciśnienia. Wprowadźmy oznaczenie

$$\Omega = 2a\frac{\nu}{g}\alpha^2 \tag{28}$$

i wstawmy je do równania ruchu (3), które w konsekwencji przyjmie postać:

$$\frac{\partial h(x,t)}{\partial x} = -\Omega\frac{q(t)}{\varepsilon^3(x,t)} \tag{29}$$

Scałkujmy go teraz w granicach od x do L.

$$\int_x^L \frac{\partial h(x,t)}{\partial x}dx = -\Omega q(t)\int_x^L \frac{dx}{\varepsilon^3(x,t)} \tag{30}$$

W wyniku całkowania otrzymujemy poniższe równanie określające rozkład ciśnienia w ośrodku porowatym

$$h(x,t) = h(L,t) + \Omega q(t)\int_x^L \frac{dx}{\varepsilon^3(x,t)} \tag{31}$$

Jako pierwszy przypadek rozważymy rozwiązanie powyższego równania dla przepływu bez kolmatacji. Z dotychczasowych naszych rozważań wynika (23), że w takim przypadku ε(x,t) = ε_o, a więc

$$h(x,t) = h(L,t) + \Omega q(t)\frac{1}{\varepsilon_o^3}(L-x) \tag{32}$$

Otrzymana zależność (32) opisująca rozkład ciśnienia przy przepływie bez kolmatacji została zilustrowana graficznie na rys. 2 i jest zgodna z przebiegami obserwowanymi w trakcie eksperymentów.

Drugi przypadek to ten, w którym w trakcie przepływu przez ośrodek porowaty cieczy niosącej zawieszone cząstki stałe dochodzi do ich wymiany z ośrodka ciekłego do stałego – kolmatacji. Prowadzi to w konsekwencji do uzmiennienia rozkładu porowatości co zostało wyrażone zależnością (24).

$$\varepsilon(x,t) = \varepsilon_o - n\alpha_o e^{-\alpha_o x}\int q(t)dt$$

Ponieważ wiadomo [14], że

$$\int q(t)dt = Q(t) \tag{33}$$

to zależność (24) możemy zapisać w postaci (34).

$$\varepsilon(x,t) = \varepsilon_o - n\alpha_o Q(t)e^{-\alpha_o x} \tag{34}$$

Po wstawieniu otrzymanego równania (34) do równania ruchu w postaci (31) otrzymujemy

$$\begin{gathered}h(x,t) = h(L,t) + \Omega q(t)\int_x^t \varepsilon^{-3}(x,t)dx = \\ h(L,t) + \Omega q(t)\int_x^t [\varepsilon_0 - n\alpha_o Q(t)e^{-\alpha_o x}]^{-3}dx\end{gathered} \tag{35}$$

Aby rozwiązać powyższe równanie najpierw obliczmy całkę nieoznaczoną w nim występującą. I tak

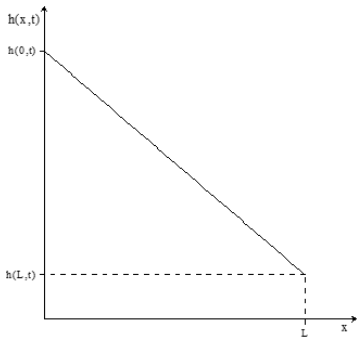

Rys. 2. Rozkład ciśnienia w ośrodku porowatym przy przepływie bez kolamatacji
Fig. 2. Pressure distribution in a porous medium during flow without colmatage

$$\int \varepsilon^{-3}(x,t)dx = \int[\varepsilon_0 - n\alpha_o Q(t)e^{-\alpha_o x}]^{-3}dx = \\ = \frac{1}{2\alpha_o\varepsilon_o^3}\left[2\,ln(\varepsilon_o - n\alpha_o Q(t)e^{-\alpha_o x}) - \varepsilon_o\frac{3\varepsilon_o - 2n\alpha_o Q(t)e^{-\alpha_o x}}{(\varepsilon_o - n\alpha_o Q(t)e^{-\alpha_o x})^2} + 2\alpha_o x + C_1\right] \quad (36)$$

Przechodząc do całki oznaczonej otrzymujemy

$$\int_x^L \varepsilon^{-3}(x,t)dx = \int_x^L[\varepsilon_0 - n\alpha_o Q(t)e^{-\alpha_o x}]^{-3}dx = \\ = \frac{1}{2\alpha_o\varepsilon_o^3}\left\{2\,ln\frac{\varepsilon_o - n\alpha_o Q(t)e^{-\alpha_o L}}{\varepsilon_o - n\alpha_o Q(t)e^{-\alpha_o x}} - \varepsilon_o\left[\frac{3\varepsilon_o - 2n\alpha_o Q(t)e^{-\alpha_o L}}{(\varepsilon_o - n\alpha_o Q(t)e^{-\alpha_o L})^2} - \frac{3\varepsilon_o - 2n\alpha_o Q(t)e^{-\alpha_o x}}{(\varepsilon_o - n\alpha_o Q(t)e^{-\alpha_o x})^2}\right] + 2\alpha_o(L-x)\right\} \quad (37)$$

Wprowadzając nowe oznaczenie

$$\dot{\Omega} = \Omega\frac{1}{2\alpha_o\varepsilon_o^3} = a\frac{\nu}{g}\frac{\alpha^2}{\alpha_o\varepsilon_o^3} \quad (38)$$

możemy podać ostatecznie związek opisujący rozkład ciśnienia h(x,t) dla przepływu z kolmatacją, jak niżej

$$h(x,t) = h(L,t) + \dot{\Omega}q(t)\left\{2\,ln\frac{\varepsilon_o - n\alpha_o Q(t)e^{-\alpha_o L}}{\varepsilon_o - n\alpha_o Q(t)e^{-\alpha_o x}} - \varepsilon_o\left[\frac{3\varepsilon_o - 2n\alpha_o Q(t)e^{-\alpha_o L}}{(\varepsilon_o - n\alpha_o Q(t)e^{-\alpha_o L})^2} - \frac{3\varepsilon_o - 2n\alpha_o Q(t)e^{-\alpha_o x}}{(\varepsilon_o - n\alpha_o Q(t)e^{-\alpha_o x})^2}\right] + 2\alpha_o(L-x)\right\} \quad (39)$$

W tym miejscu warto przypomnieć dotychczasowe przybliżone równanie opisujące rozkład ciśnienia h(x,t) otrzymane przy pomocy linearyzacji wyrażenia $\varepsilon[x,t]^{-3}$ w otoczeniu ε_0 [7,14]. Po drobnych przekształceniach w celu ujednolicenia zapisu, postać tego równania jest następująca

$$h(x,t) \approx h(L,t) + \dot{\Omega}q(t)\left[6Q(t)\frac{n\alpha_o}{\varepsilon_o}(e^{-\alpha_o x} - e^{-\alpha_o L}) + 2\alpha_o(L-x)\right] \quad (40)$$

Z dotychczasowych badań [14] wiadomo, że rozkład ciśnienia przy przepływie z kolmatacją w chwili t = 0 jest taki sam jak dla przepływu bez kolmatacji (32). Czyli jest opisany funkcją liniową o równaniu

$$h(x,t) = h(L,t) + \Omega q(t)\frac{1}{\varepsilon_o^3}(L-x) = h(L,t) + 2\dot{\Omega}q(t)\alpha_o(L-x) \quad (41)$$

Wprowadzając do równania (39) dla t=0 Q(0) = 0 widzimy, że otrzymane rozwiązanie jest analogiczne z równaniem (41), co pokazano poniżej:

$$h(x,t) = h(L.,t) + \dot{\Omega}q(t)\left\{\underbrace{2\,ln\frac{\varepsilon_o - n\alpha_o Q(t)e^{-\alpha_o L}}{\varepsilon_o - n\alpha_o Q(t)e^{-\alpha_o x}}}_{2\,ln\,1=0} - \right. \\ \left. \underbrace{\varepsilon_o\left[\frac{3\varepsilon_o - 2n\alpha_o Q(t)e^{-\alpha_o L}}{(\varepsilon_o - n\alpha_o Q(t)e^{-\alpha_o L})^2} - \frac{3\varepsilon_o - 2n\alpha_o Q(t)e^{-\alpha_o x}}{(\varepsilon_o - n\alpha_o Q(t)e^{-\alpha_o x})^2}\right]}_{\varepsilon_o\left[\frac{3\varepsilon_o}{\varepsilon_o^2} - \frac{3\varepsilon_o}{\varepsilon_o^2}\right] = 0} + 2\alpha_o(L-x)\right\} \quad (42)$$

Na zakończenie tego artykułu chcielibyśmy przedstawić rozkład ciśnienia h(x,t) (39) w funkcji: porowatości ośrodka ε(x,t), rozkładu koncentracji unoszonych N(x,t) oraz wyłapanych P(x,t) cząstek kolmatanta.

Dla rozkładu porowatości opisanego równaniem (24) i z uwzględnieniem równań (33) i (34) rozkład ciśnienia można przedstawić zależnością (43)

$$h(x,t) = h(L,t) + \dot{\Omega}q(t)\left\{2\,ln\frac{\varepsilon(L,t)}{\varepsilon(x,t)} - \varepsilon_o\left[\frac{\varepsilon_o + 2\varepsilon(L,t)}{\varepsilon^2(L,t)} - \frac{\varepsilon_o + 2\varepsilon(x,t)}{\varepsilon^2(x,t)}\right] + 2\alpha_o(L-x)\right\} \quad (43)$$

Z kolei rozkład zatrzymanej masy w ośrodku P(x,t) opisany jest poniższą zależnością [14]:

$$P(x,t) = n\alpha_o Q(t)e^{-\alpha_o x} \quad (44)$$

W konsekwencji więc rozkład ciśnienia h(x,t) możemy przedstawić następująco:

$$h(x,t) = h(L,t) + \dot{\Omega}q(t)\left\{2\,ln\frac{\varepsilon_o - P(L,t)}{\varepsilon_o - P(x,t)} - \varepsilon_o\left[\frac{3\varepsilon_o - 2P(L,t)}{(\varepsilon_o - P(L,t))^2} - \frac{3\varepsilon_o - 2P(x,t)}{(\varepsilon_o - P(x,t))^2}\right] + 2\alpha_o(L-x)\right\} \quad (45)$$

Ponieważ funkcję N(x,t) określającą rozkład koncentracji unoszonych cząstek opisuje zależność (46) [14]

$$N(x,t) = ne^{-\alpha_o x} \quad (46)$$

to rozkład ciśnienia h(x,t) przybierze postać równania (47)

$$h(x,t) = h(L,t) + \dot{\Omega}q(t)\left\{2\,ln\frac{\varepsilon_o - \alpha_o Q(t)N(L,t)}{\varepsilon_o - \alpha_o Q(t)N(x,t)} - \varepsilon_o\left[\frac{3\varepsilon_o - 2\alpha_o Q(t)N(L,t)}{(\varepsilon_o - \alpha_o Q(t)N(L,t))^2} - \frac{3\varepsilon_o - 2\alpha_o Q(t)N(x,t)}{(\varepsilon_o - \alpha_o Q(t)N(x,t))^2}\right] + 2\alpha_o(L-x)\right\} \quad (47)$$

Porównanie rozwiązań układu równań kolmatacji metodą linearyzacji i metodą dokładną

Porównując równania (39) i (40) można zauważyć, że różnią się tylko jednym członem. Jeżeli przedstawimy zależność (40) w formie

$$h(x,t) = h(L,t) + \dot{\Omega}q(t)\cdot A(x,t) \\ A(x,t) = 2ln\frac{\varepsilon_o - n\alpha_o Q(t)e^{-\alpha_o L}}{\varepsilon_o - n\alpha_o Q(t)e^{-\alpha_o x}} - \varepsilon_o\left[\frac{3\varepsilon_o - 2n\alpha_o Q(t)e^{-\alpha_o L}}{(\varepsilon_o - n\alpha_o Q(t)e^{-\alpha_o L})^2} - \frac{3\varepsilon_o - 2n\alpha_o Q(t)e^{-\alpha_o x}}{(\varepsilon_o - n\alpha_o Q(t)e^{-\alpha_o x})^2}\right] + 2\alpha_o(L-x) \quad (48)$$

natomiast równanie (39) w postaci

$$\mathrm{h(x,t)} = \mathrm{h(L,\,t)} + \dot{\Omega}\mathrm{q(t)}\cdot B(x,t) \\ B(x,t) = 6\mathrm{Q(t)}\frac{n\alpha_o}{\varepsilon_o}(e^{-\alpha_o \mathrm{x}} - e^{-\alpha_o \mathrm{L}}) + 2\alpha_o(\mathrm{L-x}) \quad (49)$$

to o odchyłce decyduje wtedy różnica między członami A(x,t) i B(x,t). Najprościej odchyłkę tą możemy zdefiniować w postaci współczynnika ξ(x,t) będącego stosunkiem A(x,t) do B(x,t).

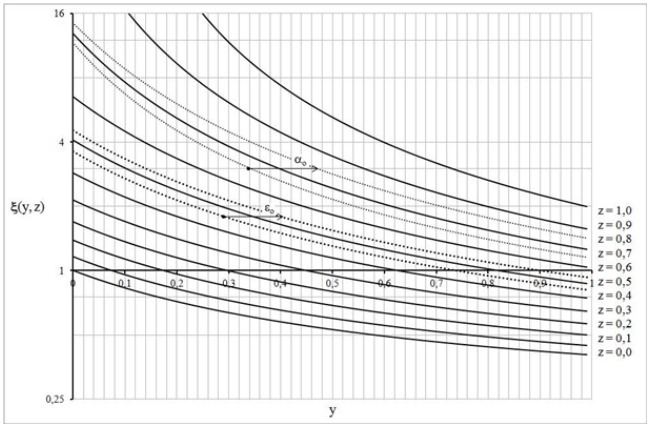

Rys. 3. Graficzna ilustracja zmienności parametru
Fig. 3. Graphical illustration of the variability of the parameter

$$\xi(x,t)=\frac{A(x,t)}{B(x,t)}$$
$$=\frac{2ln\frac{\varepsilon_o-n\alpha_oQ(t)e^{-\alpha_oL}}{\varepsilon_o-n\alpha_oQ(t)e^{-\alpha_ox}}-\varepsilon_o\left[\frac{3\varepsilon_o-2n\alpha_oQ(t)e^{-\alpha_oL}}{(\varepsilon_o-n\alpha_oQ(t)e^{-\alpha_oL})^2}-\frac{3\varepsilon_o-2n\alpha_oQ(t)e^{-\alpha_ox}}{(\varepsilon_o-n\alpha_oQ(t)e^{-\alpha_ox})^2}\right]+2\alpha_o(L-x)}{6\mathrm{Q(t)}\frac{n\alpha_o}{\varepsilon_o}(e^{-\alpha_o\mathrm{x}}-e^{-\alpha_o\mathrm{L}})+2\alpha_o(\mathrm{L}-\mathrm{x})} \quad (50)$$

Z uwagi na nieokreśloność w czasie zakończenia procesu kolmatacji powyższa postać tego równania (50) jest trudna do analizy i sformułowania jakiś ogólnych wniosków. W związku z tym należy je przekształcić do innej postaci, która by odzwierciedlała dowolny fizyczny proces kolmatacji. Wprowadzając bezwymiarową zmienną y

$$\forall x\in[0,L]\ \ y=\frac{x}{L};\ y\in[0,1] \quad (51)$$

Oraz bezwymiarową zmienną z

$$\forall z\in[0,1]\ \ z=\frac{n\alpha_o\mathrm{Q(t)}}{\varepsilon_o} \quad (52)$$

otrzymujemy uniwersalne równanie (53).

$$\xi(y,z)=\frac{2ln\frac{1-ze^{-\alpha_o}}{1-ze^{-\alpha_oy}}-\varepsilon_o\left[\frac{3-2ze^{-\alpha_o}}{(1-ze^{-\alpha_o})^2}-\frac{3-2ze^{-\alpha_oy}}{(1-ze^{-\alpha_oy})^2}\right]+2\alpha_o(1-\mathrm{y})}{6z(e^{-\alpha_oy}-e^{-\alpha_o})+2\alpha_o(1-\mathrm{y})} \quad (53)$$

Ze względu na charakter jednostek wielkości x i L bezwymiarowość współczynnika y jest oczywista. Wątpliwości może wzbudzać bezwymiarowość parametru z, a może powinniśmy zapisać go w postaci funkcji zależnej od czasu z(t). Bezwymiarowość parametru z wynika z warunku (26) określającego czas t zakończenia przebiegu zjawiska kolmatacji i zależności (27) określającej jego obszar. Jeżeli z=0 oznacza to, że proces kolmatacji dopiero rozpoczął się i czas t=0. Natomiast w przypadku gdy z=1 proces kolmatacji zakończył się. Nie posiadamy jednak informacji o czasie jego trwania. Parametr z jest więc bezwymiarowy i informuje nas o stopniu zaawansowaniu procesu bez wnikania w czas jego przebiegu. Tak zdefiniowana funkcja ξ(y,z) (53) daje narzędzie do bezwymiarowego porównania dwóch zależności (39) i (40). Oczywiście w równaniach tych występują parametry takie jak α_o oraz ε_o, ale są to wartości stałe.

Na wykresie rys. 3 przedstawiono liniami ciągłymi zależność bezwymiarowego współczynnika ξ(y,z) od parametru y dla jedenastu wartości z będącymi informacją o stopniu zaawansowania procesu kolmatacji. Tak jak to widać w opisie po prawej stronie wykresu, każda krzywa odpowiada innej wartości z zaczynając od 0 a kończąc na wartości 1, przy przyjętych parametrach α_o oraz ε_o wynoszących odpowiednio 0.5 i 0.7. Ponadto dla z=0,6 co odpowiada stopniu zaawansowania procesu kolmatacji w 60%, naniesiono dwie krzywe oznaczone pogrubionym kropkowaniem w celu zilustrowania, jaki wpływ ma zmiana parametru ε_o na rozkład ξ(y,z). Przyrost wartości został zobrazowany kierunkiem zwrotu strzałki. Krzywe zostały wykreślone dla wartości ε_o=0.4 oraz ε_o=0.6 przy wartości α_o=0.5. Podobnie zilustrowano (krzywe kropkowane) wpływ zmiany parametru α_o dla z=0,8 na rozkład ξ(y,z). Tak jak w poprzednim przypadku, przyrost wartości został zobrazowany kierunkiem zwrotu strzałki. W tym przypadku krzywe zostały wykreślone dla wartości α_o=0.6 oraz α_o=0.8 przy wartości ε_o=0.7.

Oś argumentów y została celowa przesunięta do wartości ξ(y,z)=1. Ta wartość informuje nas, że bez względu na to, którą zależnością będziemy liczyć, (39) czy (40), otrzymamy takie same wartości. Jest to jedyny przypadek, w którym wynik otrzymany metodą przybliżoną pokrywa się z metodą dokładną. Pamiętajmy, że równanie (39) jest równaniem otrzymanym wprost z rozwiązania układu równań (1), (2) i (3), a wersja (40) to tylko forma przybliżona, ale dotychczas była stosowana do analizowania procesu kolmatacji. Stosując zależność przybliżoną (40) dla zakresu ξ(y,z)<1 otrzymane wyniki opisują zawyżony stopień zaawansowania procesu kolmatacji, a współczynnik ξ(y,z) informuje o ile. W przeciwnym przypadku gdy ξ(y,z)>1 otrzymane wyniki opisują zaniżony stopień zaawansowania procesu kolmatacji i w tym przypadku również współczynnik ξ(y,z) informuje nas o ile.

Wnioski:

Przedstawiony tok rozumowania pozwala na dokładniejszy pod względem matematycznym opis przebiegu zjawiska kolmatacji – w oparciu o założenia teorii kolmatacji proponowane przez Profesora Alfreda Trzaskę [14] z uwzględnieniem pierwszej kinetyki procesu kolmatacji. Według dotychczasowej metody, z uwagi na skomplikowaną pod względem matematycznym postać równań różniczkowych opisujących zachodzące zjawisko kolmatacji, przyjmowało się uproszczona postać funkcji $\varepsilon(x,t)^{-3}$ linearyzując tą funkcję w otoczeniu ε_0 [5,14]. Współczesne narzędzia obliczeniowe pozwoliły nam rozwiązać układ równań opisujących pierwszą kinetykę (1),(2),(3) w sposób bezpośredni bez stosowania przybliżeń

w postaci linearyzacji. Potrzeba dokładniejszego rozwiązania wynika z rozbieżności pomiędzy otrzymanymi rozkładami podczas badań laboratoryjnych a przebiegami wynikającymi z symulacji komputerowej opartej o linearyzację członu $\varepsilon(x,t)^{-3}$.

Analizując krzywe na Rys.3 można wysunąć wniosek, że dotychczasowe stosowanie formy przybliżonej opisu procesu kolmatacji obarczone było znaczącym błędem, tym większym im proces zbliżał się do końca. Ponadto formuła ta (40) nie miała mechanizmu, który informował by nas, że proces kolmatacji już zmierza ku końcowi lub się zakończył. Wynika to z faktu, że postać zależności (40) nie uwzględnia warunków (24), (26) przez co funkcja nie zmierza asymptotycznie do określonej wartości. Jest to jedna z przyczyn rozbieżności pomiędzy metodą przybliżoną i dokładną co generuje odchyłkę. Druga przyczyna generowania odchyłki jest związana z tym, że zgodnie z zależnością (49) źle wyznaczona wartość współczynnika B(x,t) ma wpływ na błędną wartość q(t), a to ma wpływ na niewłaściwy rozkład ciśnienia h(x,t). W przypadku przepływu z kolmatacją realizowanego przy stałej różnicy ciśnień, wymuszona różnica ciśnień narzuca jakie wartości może przyjąć iloczyn q(t) B(x,t). Jest to mechanizm samoregulacji procesu i z matematycznego punktu widzenia proces nadal trwa, chociaż fizycznie już się zakończył.

W przypadku funkcji (39) dąży ona do asymptoty zgodnie ze zdefiniowanymi warunkami (24) i (26). Bardzo ważną cechą zależności (39) jest zobrazowanie sensu fizycznego współczynnika kolmatacji $\alpha 0$. Z postaci tej wynika jasno, że może ona przybierać jedynie wartości z przedziału [0,1]. Wartości 0 odpowiada brak wychwytu przepływających cząstek kolmatanta lub przepływ czystej cieczy, a wartości 1 odpowiada sytuacja, w której ośrodek wychwytuje wszystkie przepływające cząstki kolmatanta, czyli wypływa czysta woda, co z fizycznego punktu widzenia jest prawie niemożliwe. Dotychczas stosując metodę przybliżoną przyjmowano ten współczynnik jako parametr empiryczny o wartości umożliwiającej dopasowanie rzeczywistych pomiarów laboratoryjnych do symulacji komputerowej. W ten sposób jego interpretacja fizyczna wzbudzała wiele kontrowersji i była niejasna.

W trakcie prowadzenia badań eksperymentalnych określenie według jakiej kinetyki przebiega proces obarczone jest dużą niepewnością wynikającą prawdopodobnie z zastosowania linearyzacji członu $\varepsilon(x,t)^{-3}$ również w pozostałych kinetykach. Autorzy obecnie pracują nad znalezieniem bezpośredniego rozwiązania również dla kinetyki drugiej i trzeciej.

Literatura – References

1. Broda, K., 2001. Badania eksperymentalne zjawiska kolmatacji jako procesu doprowadzającego do likwidacji wodoprzepuszczalności ośrodków porowatych. Zabezpieczenie i Rewitalizacja podziemnych obiektów zabytkowych – Konferencja Naukowo-techniczna. Kraków-Bochnia 21-22 września 2001, 89-99, ISBN 83-912116-4-9
2. Herzig, J.P.; Leclerc, D.M.; Le Goff, P., 1970. Flow of Suspensions through Porous Media – Application to Deep Filtration. Industrial and Engineering Chemistry, 62,5,8-35
3. Ives, K.J.,1962. Filtration Using Radioactive Algea. Trans. ASCE, 127, part 3, 372-389
4. Litwiniszyn J., 1963. Colmatage Considered as a Certain Stochastic Process. Bull. Acad. Polon. Sci., Ser. Sci. techn., 3
5. Trzaska, A., 1972. New Kinetics Equations of the Colmatage Process and Their Application. Archiwum Górnictwa, 17,4,361-384
6. Trzaska, A., 1983. The Effect of Colmatage on the Porosity of Heterogeneous Porous Media. Archiwum Górnictwa, 28,1,3-11
7. Trzaska, A., 1986. The Distribution of Pressure During the Flow with Colmatage Through Heterogeneous Porous Media. Archiwum Górnictwa, 31,1,175-183
8. Trzaska, A., 1989. On Researches of the Colmatage. Archiwum Górnictwa, 34,3,529 541
9. Trzaska, A., Broda, K., 1991. Comparison of The Actual Course of Colmatage with Its Theoretical Description. Archiwum Górnictwa, 36,4,325-332.
10. Trzaska, A., Broda, K., Filek, K., 1999. Experimental Research of the Influence of the Colmatage Process on Pressure Distribution and Variability of Flow Discharge and Flow with Free Surfaces. Archives of Mining Sciences, 44,4,531 532.
11. Trzaska A., Broda K., 2000. Possibility of Determining Colmatage Parameters and Functions Basing on the Theory of Colmatage and Experiment. Archives of Mining Sciences, 45, 4, 527-542
12. Trzaska, A.; Broda, K.; Rapacz, R., 2001. O możliwości ograniczenia dopływu wód do wyrobisk górniczych. Górnictwo, 25,2,41-48
13. Trzaska A., Broda K., Filipek W., Sobowska K., 2005. The Phenomenon of Colmatage and Its Effect on the Environment. Archives of Mining Sciences, 50, Special Issue, 43-56
14. Trzaska, A; Sobowska, K.; 2007. Kolmatacja przepływy z wymianą masy i zmianą pędu. Uczelniane Wydawnictwa Naukowo-Dydaktyczne AGH, Kraków

Pressure Distribution in a Porous Medium During the Colmatage Phenomenon Accurring According to the First Kinetics without Linearization of the Expression Defining the Porosity of the Considered Medium as a Function of Position and Time

The phenomenon of colmatage occurs in nature wherever there is a flow of fluid carrying suspended solid particles through porous media. Even the "cleanest" water flowing into the well after some period of time will become clogged and therefore its efficiency will decrease, which is a negative phenomenon. Research conducted in our center, since the 1960s [1,4-14], has led to: a theoretical description of the phenomenon of colmatage [4-8,13,14] and a number of experiments verifying it [9-14]. The obtained results were used during tests to seal the rock mass around a mining excavation [12].

This article attempts to determine the area K in the case of the colmatage phenomenon occurring in accordance with the first kinetics, and to identify/formulate relationships describing the pressure distribution h(x,t) for the flow without colmatage and with colmatage without linearization of the expression $\varepsilon(x,t)^{-3}$ in the surroundings ε_o, where ε determines the porosity of the medium as a function of position and time. Determining the area K allows us to clearly derive the exact pressure distribution h(x,t) during flow with colmatage through a porous medium without linearization, and then compare the solutions of the system of colmatage equations using the linearization method and the exact method using the dimensionless form of the ξ function. During the experimental research, the attempt to match the actual phenomenon with the developed mathematical model was burdened with high uncertainty, probably resulting from the use of linearization of the $\varepsilon(x,t)^{-3}$ term. In the article, the authors explain what generates the deviation of the approximate method from the exact solution and point out that the exact solution better reflects the physical meaning of the mathematical model for describing the phenomenon and the defined colmatation coefficients, the parameter ε_o in particular.

Keywords: *filtration, colmatage, flow with mas and momentum exchange*

Importance of Fossil Fuels in Finland's Energy Mix

Tadeusz OLKUSKI[1)], Partrycja ZUBIEŃ[2)]*

[1)] PhD Eng., Associate Professor of AGH University, AGH University of Krakow; ORCID: 0000-0002-6256-9628
[2)] Eng. , President of the „Nova Energia" Student Research Group, AGH University of Krakow; ORCID: 0009-0008-0358-6701
* Corresponding author: olkuski@agh.edu.pl

http://doi.org/10.29227/IM-2024-01-109

Submission date: 09-05-2024 | Review date: 20-06-2024

Abstract

The article presents the energy situation of Finland, with particular emphasis on energy resources. The introduction describes the geographical location of Finland, the population, the political system, and the wealth of Finnish society against the background of the European Union. Attention is paid to relatively low total and per capita carbon dioxide emissions. The energy mix, which is overwhelmingly based on renewable energy sources and nuclear power, especially for electricity generation, is also presented. Despite the fact that Finland has been focusing on increasing the share of renewables in its energy mix for years, as well as developing nuclear power plants, to ensure a continuous supply of energy, it is necessary to import both electricity itself and energy raw materials, with a particular focus on fossil fuels. The main part of the article focuses on presenting the consumption of crude oil, natural gas, and coal in the years 1980–2022. The directions of imports of these energy sources, which have changed after Russia's invasion of Ukraine, are also shown. Ensuring a continuous supply of energy resources from economically and politically stable countries will ensure Finland's energy security and development opportunities in the coming years.

Keywords: *coal, oil, gas, wood, energy resources*

Introduction

Finland is located in the northern part of Europe. It has a population of 5.6 million [18], and its capital and largest city is Helsinki. Finland is a democratic, parliamentary republic. The Finnish Parliament has 200 elected members and exercises legislative power. The prime minister is appointed by the president, who is elected by a direct vote for a term of six years. Energy matters are handled by the Ministry of Economic Affairs and Employment. The ministry's main tasks include developing energy markets and security of supply, promoting renewable energy and energy efficiency, and regulating nuclear power. The ministry is also tasked with implementing emissions trading and coordinating national climate policy preparation and implementation [23]. Finland is one of the richest countries in Europe, with a high quality of life. Finland ranks ninth in the European Union in terms of GDP per capita. This indicator is EUR 39,000 and is well above the EU average (EUR 35,500 thousand). Finland's share in the EU GDP is 1.8% [10]. Finland's energy policy plays a key role in the country's pursuit of sustainable development, economic competitiveness, and minimizing its impact on the environment, with a particular emphasis on carbon neutrality. In 2022, carbon dioxide emissions in Finland amounted to 34.1 million tonnes [1], which is 6.09 tonnes per capita. It is worth mentioning that in 2003 CO2 emissions amounted to 74.9 million tons [1]. Coal-fired power generation is responsible for more than 50% of Finland's emissions, which accounts for less than 5% of total electricity generation [5].

The most important branches of the Finnish economy are the industry, mainly electronics, mechanical, and metal industries, as well as the wood, chemical, and petrochemical industries [27]. The wood industry has been one of the basic industries in this country for years. Forests cover more than 75% of Finland. There are 20.3 million hectares of forest land suitable for timber production and 2.5 million hectares of scrub. According to the Natural Resources Institute Finland, the total annual tree felling in 2023 amounted to about 82 million cubic meters, of which 14% was energy wood, i.e. forest chips for heating and power plants and firewood for single-family houses [21]. The growth of Finnish forests exceeds the annual deforestation, so forest resources are constantly increasing. Therefore, the amount of carbon dioxide sequestered in forests is increasing [15].

Figure 1 shows the location of Finland on the map.

Energy mix

The Finnish energy mix is diverse, however, it is renewable sources together with nuclear energy that are of fundamental importance in this country. Figure 2 shows the percentage share of individual energy sources in 2021 in Finland. It is clear that renewable energy sources account for almost half of the Finnish energy mix. Nuclear power comes second, followed by crude oil, and coal.

Figure 3 shows the percentage share of individual sources in electricity generation in 2021. In this infographic, the most important role is played by renewable raw materials such as biofuels and biomass, mainly forest biomass. Nuclear power comes second, followed by solid fossil fuels, and then natural gas.

Wind energy in the context of renewable energy is one of the fastest growing sectors – the location of the analyzed country offers significant potential in this area. At the end of 2022, 1,393 wind turbines with a total capacity of 5,677 MW were installed. They generated 14.1% of Finland's electricity

Fig. 1. Finland's place on the map of Europe. Source: [3]
Rys. 1. Miejsce Finlandii na mapie Europy. Źródło: [3]

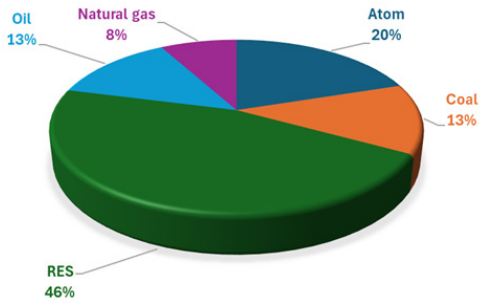

Fig. 2. Finnish energy mix in 2021. Source: own work based on [12]
Rys. 2. Fiński miks energetyczny w 2021 roku. Źródło: praca własna na podstawie [12]

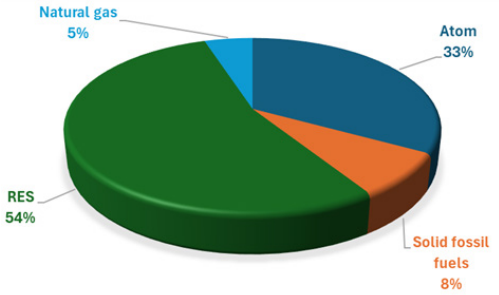

Fig. 3. Finnish electricity mix in 2021. Source: own work based on [12]
Rys. 3. Fiński miks energii elektrycznej w 2021 roku. Źródło: praca własna na podstawie [12]

consumption in 2022. [25]. Hydropower is also crucial to Finland's location due to numerous floods.

Nuclear power also plays a crucial role, accounting for as much as 20% of the country's energy mix in 2021. Currently, there is an increase in interest in this area of energy. This is confirmed by the construction of the first nuclear reactor in Europe in over 15 years in Finland, which began commercial operation in April this year. Moreover, Finland is the first country in the world to conduct activities involving the final disposal of radioactive waste, which is one of the main problems regarding nuclear energy.

Despite Finland's long-standing focus on increasing the share of renewable energy sources in its energy mix, or developing nuclear-based power generation, to ensure continuous energy supplies, it was necessary to import both electricity and energy resources, with particular emphasis on fossil fuels. Figure 4 shows the electricity demand in 2022 by generation source and including imports.

The electricity demand indicated above in 2022 shows that energy imports covered more than 40% of the total demand. In the previous year, i.e. 2021, the total electricity consumption was 1,357 PJ, or as much as 245 GJ/person per year [8].

Energy security

Energy security indicators are very important for a country's energy policy, especially considering the question of energy imports. The analysis of these indicators is accompanied by several benefits. First, it is the ability to assess and manage risks and threats to the energy sector by identifying potential problems – the risk of dependence on energy imports, instability of energy markets, or threats to energy infrastructure. Strategic planning is also an equally important aspect, e.g. in the area of diversification of energy sources, investments related to energy infrastructure, or the issue of energy efficiency itself. All of the above factors strive for the energy security of a given country and the stability of the economy.

Based on publicly available figures, it is possible to present various indicators concerning energy security, depending on the development of the energy sector in a given country.

Considering domestic energy production, energy source, and domestic energy consumption, it is possible to obtain a percentage of the energy independence index, which is a measure of the degree of a country's dependence on energy imports. The higher the value of the energy independence ratio (index), the more self-sufficient the country is in terms of

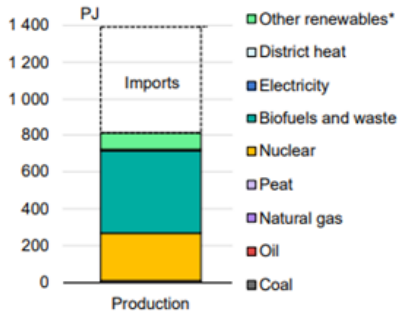

* *Other renewables* include hydro, wind and solar.
Source: IEA (2022).

Fig. 4. Electricity demand in 2022, including generating sources and electricity imports. Source: [11]
Rys. 4. Zapotrzebowanie na energię elektryczną w 2022 roku z uwzględnieniem źródeł wytwórczych oraz importu energii elektrycznej. Źródło: [11]

Fuel	2000	2010	2019	2020
Import Dependency [%]	56.6%	49.1%	42.5%	42.4%
of Solid fossil fuels	97.6%	86.3%	98.9%	92.2%
of Hard Coal	97.7%	85.5%	96.1%	90.0%
of Oil and petroleum products	111.5%	94.2%	98.9%	106.4%
of Crude and NGL	101.5%	101.1%	99.0%	99.7%
of Natural Gas	100.0%	100.0%	100.6%	100.4%

Source: EU energy statistical pocketbook and country datasheets based on Eurostat

Fig. 5. Import dependency ratio for Finland by fuel type in individual years. Source: [12]
Rys. 5. Wskaźnik zależności importowej dla Finlandii z podziałem na rodzaj paliwa w poszczególnych latach. Źródło: [12]

	Gas	Oil	Coal
EU27	44%	26%	54%
FI	67%	84%	55%

Source: Eurostat (nrg_ti_sff, nrg_ti_oil, and nrg_ti_gas)

Fig. 6. Tabular presentation of import dependency ratios on Russian fuels for the European Union and Finland broken down by fuel type. Source: [12]
Rys. 6. Tabelaryczne przedstawienie wskaźników zależności importowej dla Unii Europejskiej oraz Finlandii od rosyjskich paliw z podziałem na typ paliwa. Źródło [12]

energy and less dependent on energy supplies from external sources. In Finland, in 2021, it was 58.5% [6], which means that 58.5% of the country's total energy demand was met by domestic power generation, while the remaining 41.5% had to be imported from other suppliers.

One of the most important energy security indicators, closely related to the energy independence ratio, is the import dependence ratio. Its value is calculated based on data such as import, export, and consumption of the energy source. Figure 5 illustrates in tabular form Finland's import dependencies for individual fuels in the years: 2000, 2010, 2019, and 2020.

In 2020, Finland recorded one of the lowest levels of this indicator among EU countries. This value was 42.4% at that time, which indicates a high level of energy security in the supply of energy resources [2, 12, 26]. Therefore, comparing 2022 with 2000, when this value was at the level of 56.6%, one can notice a significant, positive decrease in this area [12].

An equally important indicator is the one showing the share of renewable energy sources in final energy consumption, which in 2020 for Finland was also one of the highest in the EU and amounted to 27.2% [2]. This figure shows the extent to which Finland is diversifying its energy sources, thus becoming independent of coal or gas supplies from unpredictable countries.

Currently, all of the above indicators have changed positively, unfortunately only as a result of the 2022 Russian invasion of Ukraine. For years, the European Union, including Finland, has underestimated the threats from Russia, even though the security of energy supplies and energy resources is of great importance. Figure 6 shows the import dependency ratios on Russian fuels for the European Union and Finland broken down by fuel type: natural gas, oil, and coal.

Natural gas

Natural gas does not play a significant role in the country's energy policy, as it accounted for only 5% of the primary energy supply in 2021, and in 2022 its share decreased to 3%. Until Russia's invasion of Ukraine, most of the gas was brought in by pipeline from Russia through the Imatra interconnection point. Russia cut off gas supplies in 2022, as state-owned supplier Gasum rejected Gazprom's demand for payment in Russian rubles. However, Finland has not been completely cut off from gas, as the Balticconnector gas pipeline connecting Finland with Estonia was put into operation in 2020 [7]. It allowed gas to be sent from a storage facility in Latvia and from Lithuania from the Klaipeda gas terminal. In 2021, gas imported via the Balticconnector met 23% of the country's needs (Finland 2023) [11]. However, in October 2023, namely on October 8, the gas pipeline was damaged. Initially, the cause of the accident was unknown, but the authorities of Finland, Estonia, and most European Union countries suspected sabotage. As claimed, it could have been an action by Russia against NATO countries [20]. It was later determined that the damage was caused by the Chinese ship Newnew Polar Bear,

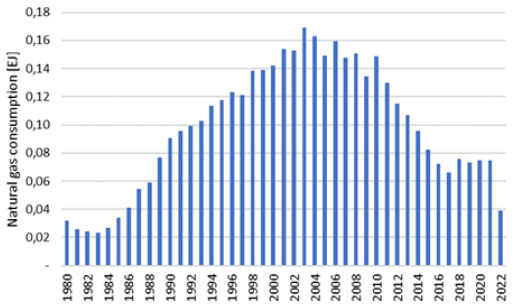

Fig. 7. Natural gas consumption. Source: own work based on [1]
Rys. 7. Zużycie gazu ziemnego. Źródło: praca własne na podstawie [1]

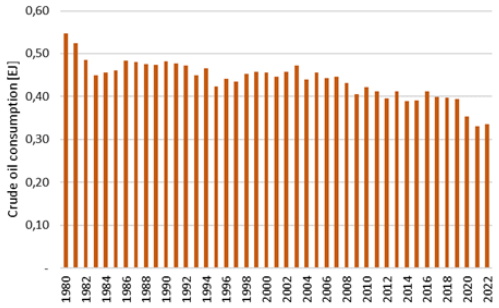

Fig. 8. Crude oil consumption. Source: own work based on [1]
Rys. 8. Zużycie ropy naftowej. Źródło: praca własne na podstawie [1]

flying the flag of Hong Kong, when its anchor hit the gas pipeline. [13, 17]. In April 2024, the repair of the gas pipeline was completed [14, 24]. In addition to the pipeline, three small LNG terminals are also used, and since this year the Floating Storage Regasification Unit has begun operating, allowing for the import of 5 billion m^3 of gas per year. This is a remarkable number for such a sparsely populated country, so there are plans to supply gas to neighboring countries such as Lithuania, Latvia Estonia, and perhaps also Poland [9]. Finland has no problem with access to natural gas.

Fig. 7 shows the consumption of natural gas in the years 1980–2022.

Natural gas consumption has been systematically decreasing for twenty years, so Finland has not and will not have any problem meeting its gas needs in the near future.

Crude oil

Since the end of the 1970s, oil consumption has been steadily decreasing. However, the decline is not as spectacular as in the case of natural gas. Oil is used in transport, and although there are ambitious plans to replace it with biofuels, hydrogen, or to increase the electrification of transport, it is still of great importance to the Finnish economy.

The oil consumption in the years 1980–2022 is presented in Fig. 8.

For many years, Finland imported oil from the Soviet Union and then from Russia. In 2021, imports from Russia accounted for 84% of Finland's oil imports. In 2022, the situation changed dramatically. Imports from Russia amounted to only 17% [19]. Since mid-2022, Finland has completely stopped importing oil from Russia. Currently, crude oil is imported mainly from Norway, but also from the United Kingdom, the United States of America, and Denmark.

Coal

After World War II, coal was one of the primary energy resources not only in Finland but also in other European countries and the United States of America. In the case of Finland, the peak of its consumption fell in 2003. Later, its importance began to decrease, which is related to the energy policy of Finland and the entire European Union.

Figure 9 shows the coal consumption in Finland between 1980 and 2022.

It is clear that the demand for coal is declining, and policies aimed at climate neutrality are further accelerating this process.

Fig. 10 presents a comparison of fossil fuel consumption in Finland in the years 1980–2022. The charts show that the consumption of all fossil fuels is decreasing, but the consumption of natural gas and coal is decreasing the most.

Conclusions

The share of fossil fuels in Finland's energy mix is steadily decreasing. The presented data shows that Finland has not been very severely affected by the lack of energy supplies from Russia. Some of the raw materials have been replaced by supplies from other countries, but in general, Finland has already decided to move away from fossil fuels and replace them with renewables and low-carbon nuclear energy. The consumption of natural gas, oil, and coal is steadily decreasing, which is a result of the government's policy aimed at achieving climate neutrality by 2035. This is more ambitious than the European Union's goal of achieving climate neutrality in 2050 but looking at the direction and pace of change in the country's energy policy, it is quite achievable. Based on the Climate Change Act [22], updated on July 1, 2022, it has become a legal obligation to promote a sustainable economy and protect biodiversi-

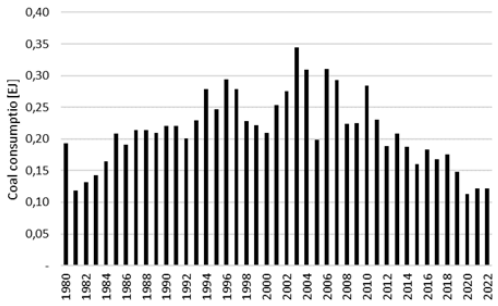

Fig. 9. Coal consumption. Source: own work based on [1]
Rys. 9. Zużycie węgla. Źródło: praca własne na podstawie [1]

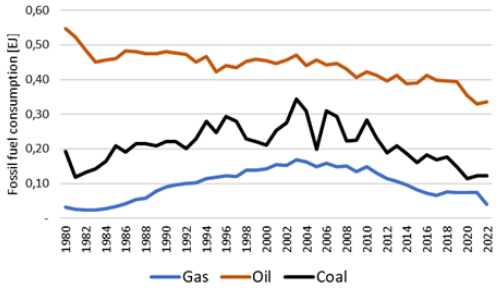

Fig. 10. Comparison of fossil fuel consumption. Source: own work based on [1]
Rys. 10. Porównanie zużycia paliw kopalnych. Źródło: praca własne na podstawie [1]

ty; this can only be achieved by implementing green energy sources that do not negatively impact the environment. This goal was set in the document "Carbon Neutral Finland 2035 - National Climate and Energy Strategy," [4], placing particular emphasis on carbon neutrality, increasing energy efficiency, implementing a national hydrogen strategy, and incorporating new nuclear technologies, with a particular focus on small and modular SMRs (Small Modular Reactors).

Source of financing

The publication of the article was financed by the AGH University of Krakow research subvention no 16.16.210.476.

Literatura – References

1. BP Energy Institute Statistical Review of World Energy 2023
2. BRAUN J., 2023 – Analysis of Poland's Energy Security in Comparison with the Other European Union Countries with the Use of Selected Economic Indicators of Energy Security, OPTIMUM. ECONOMIC STUDIES NR 1 (111) 2023, Maria Curie-Skłodowska University in Lublin
3. Britanica, 2023 – https://www.britannica.com/place/Finland ; accessed on 26.06.2023 r.
4. Carbon neutral Finland 2035 – national climate and energy strategy.
5. Electricitymaps 2023 – https://app.electricitymaps.com/zone/FI - accessed on 26.06.2023
6. Enerdata, 2023 – https://www.enerdata.net/estore/energy-market/finland/ ; accessed on 26.06.2023 r.
7. Energiavirasto 2023 ; https://energiavirasto.fi/maakaasumarkkinat#:~:text=Maakaasua%20on%20saatavilla%20noin%2040%20paikkakunnalla%20Suomessa.%20Suomessa,Suomessa%20tuotettua%20biokaasua%20sy%C3%B6tet%C3%A4%C3%A4n%20maakaasuverkkoon%20verrattain%20v%C3%A4h%C3%A4isi%C3%A4%20m%C3%A4%C3%A4ri%C3%A4.; accessed on: 26.07.2023

8. Energy in Finland 2022, Statistics Finland

9. Euronews 2022 – https://www.euronews.com/2022/12/28/finland-opens-floating-liquified-natural-gas-terminal-to-replace-russian-supply ;accessed on: 5.08.2023

10. European-Union 2024 ; https://european-union.europa.eu/principles-countries-history/eu-countries/finland_pl#:~:text=Trade%20i% 20economy % 20Finland % 20occupies % 20division %C4% 85th % 20location %20w,Finland%20w%20ca%C5% 82co % 20PKB % 20UE % 20wynosi %201% 2C8% 20proc ; accessed on: 24.05.2024

11. Finland 2023 Energy Policy Review, International Energy Agency

12. FINLAND Energy Snapshot, European Comission 2023

13. Ilka-Pohjalainem 2023 – Poliisi selvittää kiinalaisen aluksen liikkeitä Balticconnector-kaasuputken vaurion yhteydessä – merenpohjasta löytyi möykky https://ilkkapohjalainen.fi/ulkomaat/poliisi-selvittaa-kiinalaisen-aluksen-liikkeita-balticconnector-kaasuputken-vaurion-yhteydessa ; accessed on: 24.05.2024

14. Kamiński R., 2024 – Finał prac naprawczych Balticconnector. Operator zapowiada uruchomienie rurociągu https://www.gospodarkamorska.pl/final-prac-naprawczych-balticconnector-operator-zapowiada-uruchomienie-rurociagu-77327 ; acessed on: 24.05.2024

15. Metsateollisuus – https://www.metsateollisuus.fi/uutishuone/metsavarat ; accessed on: 24.05.2024

16. Metsävarat ja metsänomistus – https://forest.fi/fi/artikkeli/tiesitko-taman-euroopan-metsista-metsapinta-ala-puuston-maara-ja-hakkuut-ja-myos-suojeluala-ovat-jatkuvassa-kasvussa/#7680f393 ; accessed on: 24.05.2024

17. POLITICO 2023 – Everything indicates' Chinese ship damaged Baltic pipeline on purpose, Finland says. https://www.politico.eu/article/balticconnector-damage-likely-to-be-intentional-finnish-minister-says-china-estonia/ ; accessed on: 24.05.2024

18. Population, 2023 – https://www.populationof.net/pl/finland/ ; accessed on 30.07.2023

19. Reuters 2023 – https://www.reuters.com/business/energy/finland-replaces-russian-urals-with-oil-norway-uk-us-2023-03-15/; accessed on: 02.08.2023

20. Rzeczpospolita 2023 – https://www.rp.pl/polityka/art39255441-uszkodzenie-gazociagu-balticconnector-sabotaz-na-dnie-baltyku-przeciw-nato ; accessed on: 24.05.2024

21. Suomen metsävarat 2023 – https://mmm.fi/metsat/suomen-metsavarat ; acessed on: 24.05.2024

22. SUOMEN SÄÄDÖSKOKOELMA, 423/2022, Julkaistu Helsingissä 14 päivänä kesäkuuta 2022, The Finnish Climate Act, 14.06.2022

23. Tem.fi ; https://tem.fi/en/energy#:~:text=The%20principal%20tasks%20of%20the%20Ministry%20of%20Economic,energy%20and%20energy%20efficiency%2C%20and%20regulate%20nuclear%20energy ; accessed on 11.08.2023

24. Trusewicz I., 2024 – Balticconnector znów działa. Chińczycy bezkarni. https://energia.rp.pl/gaz/art40118341-balticconnector-znow-dziala-chinczycy-bezkarni ; accessed on: 24.05.2024

25. Tuulivoimayhdistys 2023 – https://tuulivoimayhdistys.fi/en/wind-power-in-finland-2/wind-power-in-finland/about-wind-power-in-finland; accessed on 11.08.2023

26. Visualcapitalist, 2023 – https://www.visualcapitalist.com/visualizing-the-eus-energy-dependency/ ; accessed on26.06.2023 r.

27. Zieliński M., 2019 – Finlandia Informacja o sytuacji gospodarczej i stosunkach gospodarczych z Polską (Finland Information on the economic situation and economic relations with Poland, in Polish). Ministry of Entrepreneurship and Technology

Znaczenie paliw kopalnych w miksie energetycznym Finlandii

W artykule przedstawiono sytuację energetyczną Finlandii szczególny nacisk kładąc na surowce energetyczne. We wstępie opisano położenie geograficzne Finlandii, ludność, system polityczny oraz zamożność społeczeństwa fińskiego na tle Unii Europejskiej. Zwrócono uwagę na stosunkowo niską emisję dwutlenku węgla zarówno ogólną jak i przeliczoną na mieszkańca. Pokazano miks energetyczny, który w zdecydowanej większości bazuje na odnawialnych źródłach energii oraz na energetyce jądrowej, zwłaszcza w zakresie wytwarzania energii elektrycznej. Pomimo tego, że Finlandia od lat koncentruje się na zwiększaniu udziału odnawialnych źródeł energii w swoim miksie energetycznym, a także rozwija elektrownie jądrowe, w celu zapewnienia ciągłych dostaw energii, konieczny jest zarówno import samej energii elektrycznej jak i surowców energetycznych, ze szczególnym uwzględnieniem paliw kopalnych. Właśnie temu zagadnieniu poświęcono dużą część artykułu przedstawiając zużycie ropy naftowej, gazu ziemnego oraz węgla w latach 1980–2022. Pokazano też kierunki importu tych surowców, które uległy zmianie po napaści Rosji na Ukrainę. Zapewnienie ciągłych dostaw surowców energetycznych z państw stabilnych gospodarczo i politycznie zapewni Finlandii bezpieczeństwo energetyczne i możliwość rozwoju w kolejnych latach.

Słowa kluczowe: *węgiel, ropa, gaz, drewno, surowce energetyczne*

Badania zapylenia powietrza w warunkach kopalnianych podczas pracy prototypu kompaktowego suchego odpylacza filtracyjnego

Zbigniew KUCZERA[1)], Rafał ŁUCZAK[5)], Piotr ŻYCZKOWSKI[6)], Zbigniew SZKUDLAREK[2)], Marek KALITA[7)], Piotr KRAWCZYK[3)], Piotr CHONDROKOSTAS[4)]

[1)] AGH Akademia Górniczo-Hutnicza; ORCID: 0000-0001-8130-5102
[2)] Instytut Techniki Górniczej KOMAG ; ORCID: 0000-0001-9066-7543
[3)] Politechnika Warszawska; ORCID: 0000-0001-6270-7544
[4)] 3N Solutions Sp. z o.o.
[5)] AGH Akademia Górniczo-Hutnicza; ORCID: 0000-0001-6897-8679
[6)] AGH Akademia Górniczo-Hutnicza; ORCID: 0000-0003-1573-9943
[7)] Instytut Techniki Górniczej KOMAG; ORCID: 0000-0001-7492-698X

http://doi.org/10.29227/IM-2024-01-110

Submission date: 09-06-2024 | Review date: 01-07-2024

Abstrakt

Artykuł dotyczy zagadnienia zastosowania innowacyjnego rozwiązania służącego do czyszczenia maszyn i urządzeń znajdujących się w wyrobiskach górniczych z zastosowaniem technologii UCT (Underground Cleaning Technology). Podczas czyszczenia podawana jest pod ciśnieniem mieszanina gazów składająca się w głównej mierze z dwutlenku węgla (suchy lód), który sublimując zwiększa efektywność czyszczenia. Podczas prac powstaje zapylenie powietrza wynikające z obecności w wyrobisku nagromadzeń pyłu węglowego i kamiennego oraz z emisji pyłów z procesu czyszczenia. W artykule przedstawiono wyniki pomiarów rozkładu zapylenia na stanowisku pracy oraz w jego otoczeniu. W procesie czyszczenia zastosowano aktywne sposoby redukcji zapylenia powietrza za pomocą suchego odpylacza filtracyjnego. Badaniami objęto również strumień powietrza na wlocie do odpylacza oraz na jego wylocie. Na podstawie wykonanych pomiarów in situ oceniono wpływ metody czyszczenia urządzeń górniczych na stan powietrza w wyrobisku oraz możliwości zastosowania technologii UCT w podziemnych zakładach górniczych.

Słowa kluczowe: *zapylenie powietrza, zwalczanie zapylenia powietrza, suchy odpylacz filtracyjny, frakcja wdychalna, frakcja respirabilna, technologia UCT*

1. Wprowadzenie

W procesie urabiania i transportu węgla oraz skał towarzyszących powstają duże ilości pyłu przemysłowego. Ze względu na miejsce jego powstawania w górnictwie jako profilaktykę zbiorową pracowników wykorzystuje się głównie zraszanie (na organach maszyn urabiających, przesypach, kruszarkach) oraz urządzenia odpylające typu mokrego i suchego współpracujące z systemami wentylacji odrębnej [3, 4, 9]. Zwalczanie zapylenia w kopalniach węgla kamiennego ma na celu ograniczyć [3, 4, 5, 6]:

- powstawanie i osiadania pyłów w strefie niebezpiecznej, ze względu na zagrożenie wybuchem pyłu węglowego,
- negatywne oddziaływanie na zdrowie pracowników spowodowane wdychaniem pyłów przemysłowych zawierających wolną krzemionkę SiO2, która powoduje zwłóknienie tkanki płucnej oraz działa toksycznie również na inne narządy organizmu ludzkiego.

Najprostszą metodą pomiaru stężenia pyłu [mg/m^3] jest oznaczanie wagowe pyłu wdychalnego (frakcja wdychalna) oraz pyłu respirabilnego (frakcja respirabilna) w jednostce objętości powietrza.

W warunkach kopalnianych najczęściej do pomiaru indywidualnej ekspozycji na pył w środowisku pracy pod ziemią używa się pyłomierzy grawimetrycznych CIP 10. Średnie stężenie pyłu przy pomocy CIP 10 oblicza się z zależności zdefiniowanej jako iloraz zmierzonej masy pyłu oraz iloczynu czasu pomiaru i natężenia przepływu powietrza w urządzeniu [9]. Od 21 sierpnia 2018 roku według [11] obowiązujące Najwyższe Dopuszczalne Stężenia (NDS) wynoszą:

- dla pyłów zawierających (wolną) krystaliczną krzemionkę od 2 do 50 mg/m^3 i powyżej 50 mg/m^3: 0,1 mg/m^3;
- dla pyłów węgla (kamienny, brunatny): frakcja wdychalna 10 mg/m^3, frakcja respirabilna 2 mg/m^3.

Według [11] frakcja wdychalna to frakcja aerozolu wnikająca przez nos i usta, która po zdeponowaniu w drogach oddechowych stwarza zagrożenie dla zdrowia, określona zgodnie z normą PN-EN 481. Natomiast frakcja respirabilna to frakcja aerozolu wnikająca do dróg oddechowych, która stwarza zagrożenie dla zdrowia po zdeponowaniu w obszarze wymiany gazowej, określona zgodnie z normą PN-EN 481. W przypadku pyłów węgla obowiązuje jednoczesne oznaczanie stężeń frakcji respirabilnej krzemionki krystalicznej.

2. Sposoby redukcji zapylenia w warunkach kopalnianych

Urządzenia odpylające ze względu na budowę i zasadę działania można podzielić na odpylacze mokre oraz suche. Stanowią one ważny element systemu wentylacyjnego w czasie drążenia wyrobisk, który ma zapewnić bezpieczne warunki

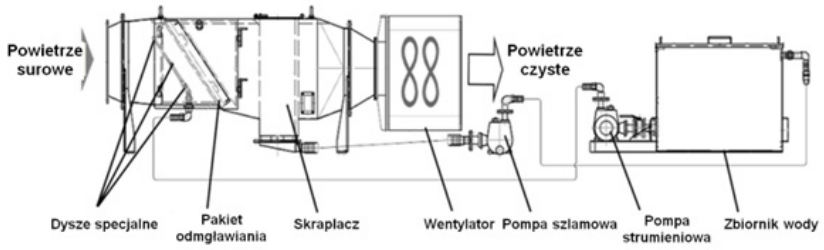

Rys. 1. Budowa i zasada działania odpylacza mokrego HCN firmy CFT [3]
Fig. 1. Construction and principle of operation of the CFT Wet Scrubber - HCN type [3]

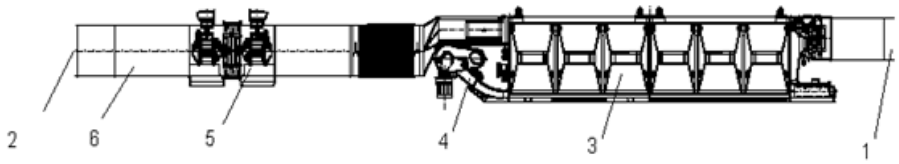

Rys. 2. Budowa suchego odpylacza powietrza typu HBKO 1/500 [3]
Fig. 2. Construction of a dry deduster - HBKO 1/500 type[3]

pracy [5, 6, 8]. Odpylacze mokre działają na zasadzie oczyszczania powietrza zawierającego pył, poprzez przechwycenie cząstek stałych zawieszonych w powietrzu przez kropelki wody, a następnie oddzielenie kropli wody od powietrza. Specjalne dysze generują kurtynę wodną oddziałującą na zasysane zanieczyszczone powietrze. Mieszanina pyłu, wody i powietrza przepływa przez „demister" (odmgławiacz), w którym następuje dalsze ich mieszanie. Skraplacz oddziela szlam i pozostałości wody od powietrza, a oczyszczone powietrze opuszcza system przez wentylator, który wytwarza odpowiednie podciśnienie. Wentylator umieszczony jest w strumieniu powietrza czystego. Oddzielona mieszanina wody i pyłu jest odpompowana do zbiornika w celu sedymentacji. Zbiornik ten może być umieszczony razem z urządzeniem bądź oddzielnie. Oczyszczona po sedymentacji woda ponownie wraca do dysz skraplających przy użyciu pompy strumieniowej [3, 4]. Budowa mokrego odpylacza HCN przedstawiona została na rys. 1 [3].

Redukcja pyłu w powietrzu metodą suchą odbywa się w zakładach górniczych przy pomocy suchych odpylaczy filtracyjnych. Odpylacze suche zatrzymują pył na materiale filtra, a następnie są oczyszczane za pomocą powtarzanego cyklicznie impulsu pneumatycznego, skierowanego w kierunku przeciwnym do zasysanego powietrza [3, 4]. Budowa odpylacza suchego HBKO firmy CFT przedstawia rys. 2.

Odpowiednia numeracja na rysunku 2 oznacza:
1 - wlotowy lutniociąg zasysający powietrze zapylone,
2 - wylot z odpylacza powietrza oczyszczonego,
3 - samonośne elementy filtrujące,
4 - przenośnik zgrzebłowy,
5 - stacja wentylatorów dGAL7-300/300,
6 – tłumik.

Zapylenie powietrza powstaje na każdym etapie eksploatacji górniczej, przygotowania i transportu urobku. Zgodnie z [1, 10] opracowano innowacyjne rozwiązania poprawiające wydajność i bezpieczeństwo pracy maszyn w górnictwie. Określono innowacyjną technologię czyszczenia i konserwacji urządzeń zainstalowanych w strefie zagrożenia wybuchem metanu i/lub pyłu węglowego, w tym w wyrobiskach górniczych – technologia UCT (Underground Cleaning Technology). Technologię UCT opracowała i zaadoptowała do stosowanie w atmosferze kopalnianej firma 3N Solutions. Metoda UCT polega na wykorzystaniu tzw. suchego lodu, to jest dwutlenku węgla w fazie stałej, który kierowany jest na zanieczyszczony element. W wyniku zjawiska sublimacji generowany jest dodatkowy strumień energii pozwalający na oderwanie zanieczyszczeń z czyszczonej powierzchni [1].

UCT umożliwia czyszczenie podzespołów, instalacji, urządzeń zabudowanych w strefach wybuchowym bez konieczności ich wyłączania z eksploatacji i demontażu oraz transportu na powierzchnię lub w strefę niezagrożoną wybuchem. Technologia UCT charakteryzuje się bardzo wysoką skutecznością usuwania zbrudzeń na poziomie 90-95%. Usuwane zanieczyszczenia stanowią zaolejenia, pyły przewodzące i nieprzewodzące, tlenki metali, zanieczyszczenia organiczne, sadze z frontu instalacji, ale również z dalej zdeponowanych podzespołów bez konieczności ich demontażu. Usunięcie szerokiego spektrum zabrudzeń podczas czyszczenia zapobiegnie szybkiemu adsorbowaniu się kolejnych zanieczyszczeń wpływających na obniżenie parametrów pracy i trwałości oraz niezawodności urządzeń. Zalegające i nieusunięte zanieczyszczenia z przestrzeni pracy mogą powodować awarie, które skutkować będą przestojem generującym straty ekonomiczne. Mogą przyczynić się do powstania pożarów oraz powodować szybsze zużywanie się podzespołów, co skutkować będzie koniecznością wyłączenia instalacji lub ich wymiany. Oprócz lepszych parametrów pracy poprawie ulegnie również poziom bezpieczeństwa maszyn oraz osób obsługujących te maszyny. Dokładne usuwanie wszelkich zabrudzeń jest kluczowe dla zachowania prawidłowego i bezpiecznego funkcjonowania urządzeń. Schemat urządzeń układu UCT przedstawiono na rysunku 3.

3. Metodyka badań

Badania kopalniane funkcjonalności użytkowej prototypu suchego odpylacza filtracyjnego (rys. 4) wchodzącego w skład

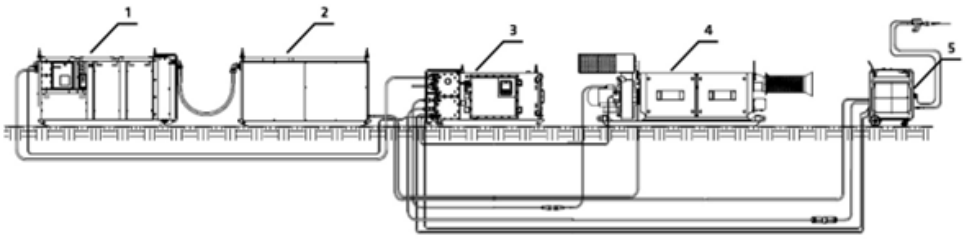

Rys. 3. Schemat układu technologii UCT: 1 – moduł transportowy, 2 – sprężarka, 3 – moduł elektryczny, 4 – odpylacz, 5 – mieszalnik [10]
Fig. 3. UCT technology layout diagram: 1 – transport unit, 2 – compressor, 3 – electrical unit, 4 – deduster, 5 – mixer [10]

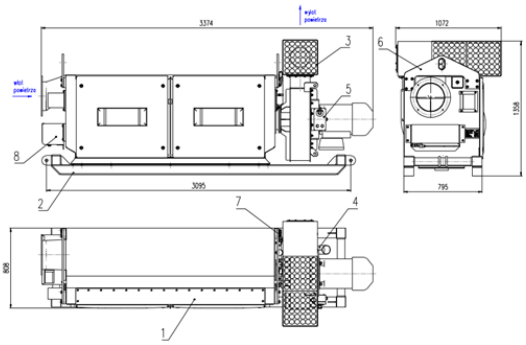

Rys. 4. Budowa prototypowego odpylacza suchego: 1 – zespół oczyszczania powietrza, 2 – zespół odbioru zanieczyszczeń, 3 – dyfuzor, 4 – uchwyt złącza kablowego, 5 – pulpit sterowniczy, 6 – zawiesie, 7 – zespół pneumatyczny, 8 – pneumatyczne sterowanie czyszczeniem [2]
Fig. 4. Construction of a dry deduster prototype: 1 – air purification unit, 2 – pollution collection unit, 3 – diffuser, 4 – cable connector holder, 5 – console, 6 – lifting sling, 7 – pneumatic unit, 8 – pneumatic cleaning control [2]

technologii UCT były przeprowadzone w kopalni węgla kamiennego LW „Bogdanka" S.A. w chodniku taśmowym 2fN w polu Nadrybie. Na rysunku 4 przedstawiono rzut prototypowego odpylacza suchego jako element redukujący zapylenie powietrza w technologii UCT a na rysunku 5 jego widok podczas badań w LW „Bogdanka" S.A.

Badania pilotażowe technologii UCT w atmosferze kolonialnej prowadzono w chodniku taśmowym 2fN, w którym zidentyfikowano następujące zagrożenia naturalne:

- I stopień zagrożenia metanowego,
- pomieszczenie ze stopniem "a" niebezpieczeństwa wybuchu metanu
- klasa B niebezpieczeństwa wybuchu pyłu węglowego,
- zagrożenie wodne I stopień,
- zagrożenie pożarowe IV grupa,
- zagrożenie klimatyczne: niezagrożone/I,
- radiacyjne – niezagrożone,
- wyrzutami gazów i skał – nie występuje,
- tąpaniami – nie występuje.

Chodnik wykonany był w obudowie ŁP o przekroju 16,2 m². Pomiary zapylenia przy pomocy urządzeń CIP 10 dla frakcji wdychalnej i respirabilnej oraz pomiary średniej prędkości powietrza w przekroju wyrobiska zostały przeprowadzone wg. schematu pokazanego na rysunku 6, a stanowisko czyszczenia zostało przestawione na rysunku 7. Na schemacie zaznaczono kolejne punkty pomiarowe: 1 – 1 m od miejsca czyszczenia, 2 – 10 m od miejsca czyszczenia, 3 – przed odpylaczem, 4 – 1 m za odpylaczem, 5 – 1 m od wylotu odpylacza.

Badania miały na celu potwierdzić poprawne działanie prototypu technologii UCT zwłaszcza w kwestii poziomu stężenia pyłu w wyrobisku kopalnianym.

4. Wyniki badań

W wyrobisku górniczym LW Bogdanka - chodnik taśmowy 2fN pomiary zapylenia powietrza wykonywano za pomocą pyłomierzy grawimetrycznych CIP-10. Przed przystąpieniem do badań przeprowadzono szczegółową ocenę stref z wybuchowym pyłem węglowym, w celu wyselekcjonowania stref zabezpieczających, w których badania nie zaburzałyby procesu eksploatacji górniczej i nie wpływałyby na stężenie i rozkład frakcyjny pyłu węglowego oraz intensywność osadzania jego poszczególnych frakcji. Do badań wybrano chodnik taśmowy 2fN zlokalizowany w polu Nadrybie. Zgodnie z Dz.U. 2018 poz. 1286. Rozporządzenie Ministra Rodziny, Pracy i Polityki Społecznej z dnia 12 czerwca 2018 r. w sprawie najwyższych dopuszczalnych stężeń i natężeń czynników szkodliwych dla zdrowia w środowisku pracy [11], pomiarom poddano frakcje wdychalne oraz respirabilne pyłów emitowanych podczas czyszczenia. Pomiary średniego stężenia pyłu frakcji wdychalnej i respirabilnej realizowano metodą grawimetryczną, służącą do oznaczania indywidualnej ekspozycji na pył w środowisku pracy pod ziemią. Średnie stężenie pyłu obliczano z zależności zdefiniowanej jako iloraz zmierzonej masy pyłu oraz iloczynu czasu pomiaru i natężenia przepływu powietrza przez pyłomierz. Pomiarów masy miseczek filtracyjnych przed pomiarami i po, wykonano w laboratorium chemicznym LW „Bogdanka" S.A. Na podstawie zgromadzonych na miseczkach filtracyjnych pyłów, wykonano badania chemiczne stężenia krzemionki krystalicznej frakcji respirabilnej. Wyniki pomiarów laboratoryjnych wyrażono w mg/m³. W sumie podczas prac dołowych z wykorzystaniem prototypu UTC, wykonano 36 serii pomiarowych z wykorzystaniem pyłomierzy CIP-10 (rys. 8).

Rys. 5. Odpylacz suchy podczas badań w LW „Bogdanka”
Fig. 5. Dry deduster during tests at LW "Bogdanka"

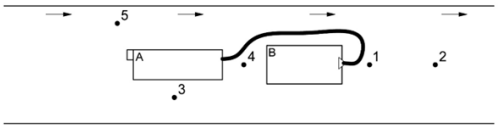

Rys. 6. Schemat pomiarowy badań zapylenia podczas pracy prototypu suchego odpylacza: A – odpylacz, B – stanowisko pracy
Fig. 6. Measurement diagram of air dust tests during operation of the dry deduster prototype: A – deduster, B – workstation

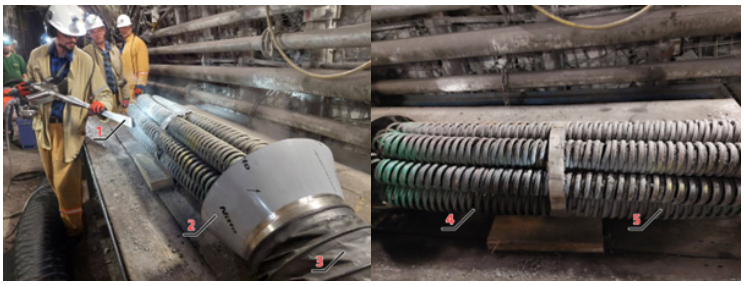

Rys.7. Stanowisko czyszczenia: 1 – dysza, 2 – ssawa, 3 – przewód ssący, 4 – brudna część wymiennika, 5 – czysta część wymiennika
Fig. 7. Cleaning station: 1 – nozzle, 2 – suction nozzle, 3 – suction pipe, 4 – dirty part of the exchanger, 5 – clean part of the exchanger

Badania dotyczyły pomiaru stężenia pyłów frakcji wdychalnej i respirabilnej oraz zawartości krystalicznej krzemionki w pyłach frakcji respirabilnej. W wybranych punktach pomiarowych (rys. 6) zlokalizowane były pyłomierze, które indywidulanie zbierały próbki pyłów frakcji wdychalnej i respirabilnej na wlocie i wylocie z odpylacza oraz w odległości 1 m i 10 m od stanowiska czyszczenia. Na podstawie zebranych prób badawczych (miseczek pomiarowych z materiałem filtracyjnym) przeprowadzono analizę laboratoryjną, na podstawie której określono stężenia zapylenia powietrza w wybranych punktach pomiarowych. Dla uzyskanych wyników określono również maksymalny błąd pomiarowy. Wyniki uzyskanych pomiarów i analiz przedstawiono w tabeli 1 i 2.

Najwyższe stężenia zapylenia powietrza występują w najbliższym otoczeniu miejsca czyszczenia, tj. w odległości 1m od stanowiska operatora oraz w wyrobisku na wylocie z odpylacza. Te dwa punkty pomiarowe zlokalizowane były najbliżej miejsca czyszczenia. Wraz z oddalaniem się od stanowiska operatora stężenia obu badanych frakcji maleją i w odległości 10 metrów stężenie frakcji wdychalnej wynosi tylko 2,1 mg/m^3, a frakcji respirabilnej 1 mg/m^3.

Na rozprzestrzenianie chmury zanieczyszczeń pyłowych duże znaczenie ma prędkość powietrza w wyrobisku kopalnianym. W trakcie procesu czyszczenia mierzono średnią prędkość powietrza w przekroju wyrobiska $v_{śr}$ [m/s] anemometrem skrzydełkowym μAS4 w odległości 1m oraz 10 m przed i za stanowiskiem pracy. W trakcie 24 serii pomiarowych, średnia prędkość powietrza oscylowała w przedziale od 0,66 do 0,72 m/s (tab. 2).

Podsumowując wykonane badania zapylenia, można stwierdzić, że stężenia zanieczyszczeń powietrza nie przekraczają wartości dopuszczalnych określonych w [11]. Stężenie krzemionki krystalicznej również mieści się w przedziale wartości dopuszczalnych (poniżej 0,1 mg/m^3), jednak warto zauważyć, iż w punkcie 1 jak i 4 (według tabeli 1) stężenie to zbliża się do górnej wartości dopuszczalnej, ale jej nie przekracza. Spowodowane to może być emisją wtórną pyłów zalegających na wyposażeniu znajdującym się w wyrobisku oraz ruchem powietrza wywołanym pracą odpylacza i dyszy czyszczącej, a w szczególności nadmuchem strumienia mieszanki czyszczącej przez operatora. W odległości 1m od odpylacza stężenie krystalicznej krzemionki było poniżej progu wykrywalności. Na podstawie wykonanych pomiarów można stwierdzić, iż technologia UCT nie powoduje przekroczeń dopuszczalnych poziomów zapylenia powietrza w wyrobisku górniczym i może być stosowana do wykonywania prac czyszczenia pod ziemią.

Średnie stężenie zapylenia w chodniku taśmowym 2fN wynosiło dla frakcji wdychalnej 288,3 μg/m^3 a respirabilnej 172,6 μg/m^3 (tło zanieczyszczeń). Na stanowisku czyszcze-

Rys. 8. Pyłomierze CIP-10 – chodnik taśmowy 2fN w LW Bogdanka [10]
Fig. 8. CIP-10 dust meters – 2fN belt gallery at LW Bogdanka [10]

Tab. 1. Wyniki pomiarów zapylenia powietrza w chodniku taśmowym 2fN za pomocą pyłomierza CIP-10
Tab. 1. Results of air dust measurements in a 2fN belt gallery using a CIP-10 dust meter

Lp.	Miejsce pobrania próbki	Frakcja wdychalna		Frakcja respirabilna		Stężenie krzemionki krystalicznej - frakcja respirabilna, mg/m^3
		Stężenie, mg/m^3	Błąd pomiaru, mg/m^3	Stężenie, mg/m^3	Błąd pomiaru, mg/m^3	
1	Chodnik taśmowy 2fN - 1m od miejsca czyszczenia	9,40	±1,60	1,95	±1,40	0,089±0,020
2	Chodnik taśmowy 2fN - 10m od miejsca czyszczenia	2,11	±0,66	1,00	±0,66	0,014±0,004
3	Chodnik taśmowy 2fN - przed odpylaczem	5,10	±1,20	1,50	±1,30	0,015±0,004
4	Chodnik taśmowy 2fN - 1m za odpylaczem	7,66	±0,94	1,19	±0,74	0,096±0,032
5	Chodnik taśmowy 2fN - 1m od wylotu odpylacza	3,70	±0,52	1,58	±0,49	Poniżej dolnego zakresu

Rys. 9. Czyszczone urządzenia dołowe
Fig. 9. Cleaned underground equipment

Tab. 2. Wyniki pomiarów średniej prędkości powietrza podczas procesu czyszczenia
Tab. 2. Measurement results of the average air velocity during the cleaning process

Lp.	Proces czyszczenia	Średnia prędkość powietrza w chodniku taśmowym 2fN $v_{śr}$ [m/s]			
		Pomiar 10m przed stanowiskiem czyszczenia	Pomiar 1m przed stanowiskiem czyszczenia	Pomiar 1m za stanowiskiem czyszczenia	Pomiar 10m za stanowiskiem czyszczenia
1.	Czyszczenie silnika kolejki Scharf	0,71	0,68	0,70	0,72
2.	Czyszczenie wyłącznika elektrycznego	0,72	0,69	0,70	0,71
3.	Czyszczenie obudowy lampy elektrycznej	0,69	0,66	0,68	0,70
4.	Czyszczenie podkładek mosiężnych	0,70	0,67	0,69	0,71
5.	Czyszczenie podzespołów hydraulicznych	0,70	0,68	0,69	0,72
6.	Czyszczenie wymiennika chłodnicy powietrza	0,72	0,70	0,70	0,71

nia – stężenie pyłów w powietrzu zasysanym przed odpylacz wynosiło 9400 μg/m³ i dla frakcji respirabilnych 1950 μg/m³, które można uznać jako stężenie na wlocie do odpylacza. Natomiast na wylocie (w strumieniu powietrza oczyszczonego) z odpylacza zarejestrowano wartości odpowiednio 155,7 μg/m³ i 95,8 μg/m³.

Uzyskane wyniki pomiarów potwierdzają wysoką skuteczność odpylania a działanie odpylacza wyraźnie poprawia warunki (obniża stężenie pyłów) w wyrobisku górniczym.

5. Podsumowanie i wnioski

Badania kopalniane efektywności zbierania zabrudzeń oraz efektywności odbierania chmury zabrudzeń przy wykorzystaniu prototypu technologii UCT były przeprowadzone w kopalni węgla kamiennego LW „Bogdanka" S.A. w chodniku taśmowym 2fN w polu Nadrybie. Do badań wytypowano: zespół napędowy (silnik) ciągnika kolejki podwieszanej, wyłącznik elektryczny i jego podzespoły, obudowę lampy, podkładki mosiężne, podzespoły hydrauliki, wymiennik chłodnicy powietrza. Pomiary wykonywane były w różnych odległościach od stanowiska czyszczenia, w celu określenia wpływu technologii UCT na środowisko miejsca pracy oraz jego otoczenie. Z przeprowadzonych badań in situ wynika, że zarówno dla pyłów frakcji wdychalnej jak i respirabilnej nie doszło do przekroczeń średnich wartości zapylenia na stanowisku operatora, jak również w odległości 10 m od miejsca czyszczenia. Zapylenie powietrza na wylocie odpylacza jest bardzo niskie, co poprawia stan powietrza (jego czystość) w wyrobisku. Z tego względu metoda czyszczenia urządzeń dołowych UCT może być stosowana w atmosferze kopalnianej.

Projekt NCBiR POIR.01.01.01-00-0968/20-02: „Opracowanie innowacyjnej technologii czyszczenia urządzeń w warunkach zagrożonych wybuchem metanu i/lub pyłu węglowego w miejscu ich zabudowy z wykorzystaniem dwutlenku węgla w postaci stałej – UCT (Underground Cleaning Technology)".

Literatura – References

1. Dobrzaniecki P., Kaczmarczyk K., Kalita M., Tarkowski A., Nieśpiałowski K., Majewski M., Sinka T., Szkudlarek Z., Janik B.: Technologia czyszczenia elementów maszyn i urządzeń w warunkach górniczych z zastosowaniem suchych gazów. KOMTECH - Innowacyjne Techniki i Technologie w Dobie Zielonej Transformacji, Instytut Techniki Górniczej KOMAG, Gliwice 2021, s. 126-138, DOI:10.32056/KOMAG/KOMTECH2021.13, ISBN 978-83-65593-27-6.
2. Dokumentacja projektowa zespołu odbierającego zabrudzenia IT KOMAG, Gliwice 2022.
3. Kuczera Z.: Metody zwalczania zapylenia w kopalniach podziemnych jako ważny aspekt bezpieczeństwa pracy. W: XXVIII Szkoła Eksploatacji Podziemnej 2019 [Dokument elektroniczny] : Kraków, 25-27.02.2019r.Instytut Gospodarki Surowcami Mineralnymi i Energią Polskiej Akademii Nauk.
4. Kuczera Z., Ptaszyński B.: Zwalczanie zapylenia w górnictwie polskim. Inżynieria Mineralna Z. 2(43) 2019.
5. Kuczera Z., Ptaszyński B.: Ograniczenie zapylenie w przodku drążonego wyrobiska w LW „Bogdanka" S.A. Inżynieria Mineralna Z. 1(41) 2018.
6. Kuczera Z., Ptaszyński B.: Weryfikacja nowego rozwiązania technicznego ograniczającego zapylenie w przodku drążonego wyrobiska w LW „Bogdanka" S.A. Inżynieria Mineralna Z. 1(41) 2018.
7. Materiały udostępnione przez firmę CFT Polska.
8. Prostański D.: Zraszanie powietrzno-wodne jako metoda ograniczenia zagrożenia zapłonem metanu i wybuchem pyłu węglowego oraz redukcji zapylenia powietrza. Instytut Techniki Górniczej KOMAG. 2017.
9. Prostański D, Bałaga M., Kalita M., Siegmund M., Hyła P.: Badanie zapylenia w strefach zabezpieczających. Maszyny Górnicze Z.1, 2016.
10. Raport - Opracowanie innowacyjnej technologii czyszczenia urządzeń w warunkach zagrożonych wybuchem metanu i/lub pyłu węglowego w miejscu ich zabudowy z wykorzystaniem dwutlenku węgla w postaci stałej – UCT (Underground Cleaning Technology). 1/1.1.1/2020 Szybka Ścieżka 1_2020.
11. Rozporządzenie Ministra Rodziny, Pracy i Polityki Społecznej z dnia 12 czerwca 2018 r. w sprawie najwyższych dopuszczalnych stężeń i natężeń czynników szkodliwych dla zdrowia w środowisku pracy. Dz.U. 2018 poz. 1286.

Test of Air Dust in the Mine Conditions during Operation of a Compact Dry Deduster Prototype

In the article the problem of using an innovative solution for cleaning machines and equipment located in mining excavations using Underground Cleaning Technology (UCT) is concerned. During cleaning, an under pressure gas mixture, consisting mainly of carbon dioxide (dry ice), which sublimates and increases the cleaning efficiency, was fed. During the work, air dust from the presence of accumulation of coal and stone dust in the excavation and dust emissions from the cleaning process was created. The results of measurements of dust distribution at the workplace and its surroundings were presented in the article. The active methods to reduce air dust by a dry deduster were used during the cleaning process. The research of the air stream at the inlet and outlet of the deduster was covered. Based on the in situ measurements, the impact of the mining equipment cleaning method on the air condition in the excavation and the possibility of using UCT technology in underground mines was assessed..

Keywords: *air dust, air dust abatement, dry deduster, inhalable fraction, respirable fraction, UCT technology*

Lean Green – Integration of Lean Manufacturing and Sustainable Development in the Light of the Pursuit of Economically and Environmentally Efficient Operations

Konrad PIĘTKA[1)], Paweł BOGACZ[2)]

[1)] M. Sc. Eng.; AGH University of Krakow, Faculty of Civil Engineering and Resource Management, Krakow, Poland; email: pietka@agh.edu.pl; https://orcid.org/0000-0002-2090-3683

[2)] Assoc. Prof., Ph.D., DSc, Eng.; AGH University of Krakow, Faculty of Civil Engineering and Resource Management, Krakow, Poland; email: bogacz@agh.edu.pl; https://orcid.org/0000-0002-0099-6376

http://doi.org/10.29227/IM-2024-01-111

Submission date: 17-06-2024 | Review date: 01-07-2024

Abstract

The concept of Lean Manufacturing is a set of techniques, methods and tools, whose application in manufacturing processes is expected to eliminate wastes and improve their economic efficiency. The challenges of Sustainable Development determine a new approach to conducting manufacturing activities. Issues related to caring for the environment and the social aspects of the business are becoming crucial from the point of view of business stakeholders. The article attempts to juxtapose the classical approach to Lean Manufacturing, presenting its main principles. The authors also highlighted the key legal and formal requirements that determine a different approach to Lean Manufacturing. The main sources of green wastage were then presented and possible ways of correlating the Lean Manufacturing (classical) concept with Lean Manufacturing seen in the light of Sustainability challenges were analysed. This combination was presented as Lean Green, thus indicating the possible relationship between Lean Manufacturing and Sustainability, in its environmental part. Using examples of specific companies, the potential benefits of implementing a Lean Manufacturing concept oriented not only on economic aspects, but above all on environmental benefits, are summarised. A review of the Polish and world literature, an analysis of available sources and the authors' own experience were used.

Keywords: *lean manufacturing, lean green, sustainability, environment, efficiency*

1. Introduction

For years, manufacturing (production) processes have been largely profit-oriented only, doing so by, among other things, minimizing the unit cost of production. The concept of Lean Manufacturing, derived from the Japanese Toyota Production System (TPS), which is one of the strategies for efficient management and organisation of processes, has introduced significant changes in the perception of added value seen from the perspective of the end user, i.e. the customer. In the process of value creation, in addition to profit maximisation, quality embedded in the process, employee involvement in building the organisational culture, elimination of waste and continuous improvement have started to play an important role, with a consequent contribution to the company's flexibility and further improvement of its economic efficiency.

However, in recent times, particular emphasis has been placed on organising manufacturing processes in such a way that their negative impact on environmental, social and employee welfare aspects is also minimized. The measure of the attractiveness of the company, assessed from the point of view of its stakeholders, i.e. end users, suppliers, contractors, etc., it seen through specific actions aimed at carrying out such activities so that they are in line with the idea of Sustainable Development. A strong determinant in the conduct of sustainable activities is the European Union, which, in terms of the European Green Deal strategy and the planned achievement of climate neutrality by 2050, is constructing its legislation since 2019, which in a way, forces operators to focus their attention, mainly on environmental issues. This, in turn, results in the mutual organization of processes in such a way that they are economically optimal, but at the same time environmentally sustainable. Hence, seen over the years, the need to adapt the Lean Manufacturing methodology to these realities is starting to become even greater. An extension of the Lean Manufacturing methodology in this way has become the Lean Green concept, which using lean tools, seeks to develop models for conscious action to improve environmental performance.

This paper, based on the literature review and the authors' own experience, presents the main principles and assumptions of the Lean Green concept. The legal background to the need for integration measures is also outlined. Ways of integrating Lean Manufacturing and sustainable development into the Lean Green concept, for improving both economic and environmental efficiency are analysed and discussed. The environmental benefits of implementing selected Lean Manufacturing tools were also pointed out, indicating in the final conclusions the need to develop the issue in further empirical research.

2. Lean Manufacturing as a Concept Aimed at Improving Economic Efficiency

The concept of Lean Manufacturing was developed and first used by scholars at the Massachussets Institute of Technology. In the mid-1990s, D. Roos, J.P. Womack and D.T. Jones published the book "The Machine That Changed the World" in

Tab. 1. Principles of Lean Manufacturing. Source: own elaboration based on [13]
Tab. 1. Zasady Lean Manufacturing. Źródło: opracowanie własne na podstawie [13]

Criterion of principle	Description
Value	Defining what value is, defined only from the point of view of the end customer. The value should be expressed in terms of a specific product, good or service that will satisfy the customer's needs at a specific price and at a specific time.
Value stream	Identify the value stream. This stream is the set of all activities required to produce a specific product in a process composed of the three most important (in management) tasks, such as: product design, information flow management and physical production execution.
Flow	Creating a flow of value-creating activities - changing the way of thinking.
Pulling	Retrieved from, a 'sucking' system. In such a system, it is the customers who, according to their own needs, "pull" the product from the manufacturers according to their expectations. This avoids a situation in which manufacturers "push", often unwanted, products to customers.
Excellence	The implementation of the preceding actions allows those involved in the process to realise that there is no end to the process of reducing inputs, shortening time, limiting space, reducing costs and eliminating errors has no end, which in the understanding of the concept of Lean Management is at the central point and is referred to, as continuous improvement, from Japanese word "Kaizen".

Tab. 2. Integration of Lean and Green. Source: own elaboration based on [15]
Tab. 2. Integracja Lean oraz Green. Źródło: opracowanie własne na podstawie [15]

Approach	The relationship between Lean and Green	Example
Conflict	The lean approach means less green.	Frequent deliveries increase emissions and emission reduction reduce productivity.
Mild	Lean and Green coexist, but do not complement each other.	The Lean team pursues economic goals, the Green team independently pursues environmental objectives.
Synergistic	Use of tools and techniques lean manafacturing, which aims to eliminate waste in the economically, but inadvertently benefit the environment.	Reducing product waste reduces environmental impact at the same time. Improving economic efficiency in energy consumption translates into environmental benefits.
Symbiotic	Lean and Green are implemented as part of the same strategy as part of a continuous improving of the organisation.	A strategy to reduce environmental losses borne by society during the entire product cycle.

which they compared the parameters of results and expenditures in American, European and Japanese companies. Toyota Motor Production was recognised there as a leader with its Toyota Production System [4]. Many definitions can be found in the literature that attempt to explain the essence of the Lean Manufacturing concept. One of these defines Lean as a method of improving the operation of a company that optimises the creation and flow of value throughout the manufacturing process through the continuous elimination of waste. It aims to build quality into the manufacturing process while embracing the principle of cost reduction [7]. Lean Management is a management methodology, that creates a work culture in an organisation that makes all participants in the organisation interested in continuously reducing costs, increasing quality levels and shortening the delivery cycle. All this is done in order to maximise customer expectations and to adapt seamlessly to the environment [9]. In relation to manufacturing processes, i.e. the company's operational activities, we detail the concept of Lean Manufacturing, which places particular emphasis on the elimination of wastes, as this has a direct impact on an organisation's production efficiency. Sources of wastage are common unproductive losses, such as [6]:

- production of products not ordered by the customer, resulting in increased stocks finished products,
- idle waiting of machines and people for deliveries, that are delayed or for the next steps in the process, which is caused by poor work organisation,
- unnecessary transport of the materials in question between the areas they operate, which refers to unnecessary movement of machinery, as well as the movement of products and raw materials,
- too long to perform certain operations due to poor design of tools and products, rapid wear and tear of equipment, breakdowns, contamination, quality defects,
- excessively high material stocks, which freeze money for the purchase of packaging or raw materials, increase the risk of damage and make it difficult to control the quality control of stored products,
- moving workers around during work to find parts, instructions, tools or aids, refers to poor work organisation and poorly designed workstations,
- deficiencies or errors that need to be corrected or repaired, refers to the cost of scrapping defective products, the disruption of production and the time taken for complaints.

Conducting activities with the use of Lean tools makes it possible to eliminate both the described process "muda", but also overloading or inequalities occurring in processes. The basis for the implementing Lean tools is to rely on the basic principles of Lean Manufacturing, defined by the main criterion that determines each of them. The main principles by criterion of each are shown in table 1.

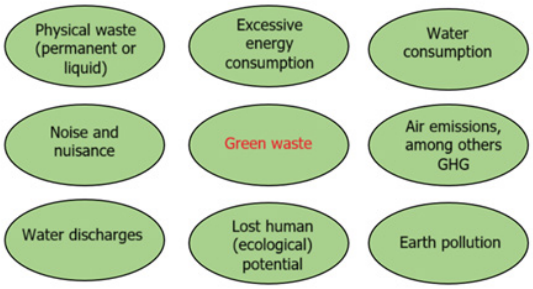

Fig. 1. Sources of green waste. Source: own elaboration based on [15]
Rys. 1. Źródła zielonych marnotrawstw. Źródło: opracowanie własne na podstawie [15]

The key element for implementing Lean Manufacturing in a company is to build awareness and employee culture at all levels of the organisation, so that everyone is involved in the improvement process and is aware of the benefits and tasks resulting from the adopted Lean strategy of efficient operation. Only then can one begin to implement Lean methods and tools, such as 5S, TPM, SMED, Kaizen, visual management, VSM, standardisation work and many others.

3. Sustainable Development and the European Green Deal – a Context for the Conemporary Adaptation of the Lean Manufacturing Methodology

The concept of Sustainable Development is becoming increasingly important for the activities of manufacturing companies operating in European and global value chains. Sustainable development is defined as development, that meets the needs of people today without compromising the ability of future generations to meet their own needs. In order to achieve sustainable development, three key elements need to be coherent: economic growth, social inclusion and environmental protection [20]. In the context of the goals referred to as SDGs (Sustainable Development Goals), included in the "2030 Agenda for Sustainable Development" of the United Nations, it is becoming crucial to work toward responsible production leading to economic growth, while protecting the natural environment and combating climate change. These goals and related targets are global in nature and can be implemented worldwide, taking into account the different conditions of individual countries, their capacities and level of development, and their compatibility with national strategies and priorities [16]. Directive (EU) 2022/2464 of the European Parliament and of the Council of 14 December 2022 amending Regulation (EU) No 537/2014, Directive 2004/109/EC, Directive 2006/43/EC and Directive 2013/34/EU with regard to corporate sustainability reporting, referred to as the Corporate Sustainability Reporting Directive (CSRD). According to it, all large entities and small and medium-sized listed companies will already provide information on: environmental, social and human rights issues and corporate governance in their management report in 2024. This information will be reported according to the common European Sustainability Reporting Standards (the so-called ESRS) [17]. Undoubtedly, individual countries, or communities of countries around the world are pursuing the main objectives, thereby placing a focus on sustainable development. Thus, the European Union is a party to the 2015 Paris Agreement to the United Nations Framework Convention on Climate Change (UNFCC). The Paris Agreement commits to reducing greenhouses gases (GHG) emissions in such a way that the increase in average global temperature compared to pre-industrial levels does not exceed 2°C. In addition, parties are to aim to limit this increase to 1.5°C. According to emission models put forward by the scientific community, including the Intergovernmental Panel on Climate Change (IPCC), this implies a halt to global emissions growth around 2030, followed by a successive reduction so as to reduce global emissions to zero in the second half of the century [19]. Recognised by researchers for years, the need for responsible consumption and production, rising GHG emissions leading to climate change, increasing energy consumption and the finiteness of the earth's resources are among the most serious challenges and dilemmas facing the world. Sustainability, the European Union's existing climate policy and the listed environmental challenges gave rise in December 2019 to the European Green Deal Strategy – a set of initiatives with the overarching goal of achieving climate neutrality by 2050 for all Member States. European Green Deal is also designed to enable a fair energy transition, enable the supply of clean, cheap and secure energy, support among others: the protection of biodiversity, efforts towards a circular economy, promote and support green investments as well as provide their financing.

A tool to support the transition is the EU Taxonomy, which sets out the criteria that an activity must meet to be considered environmentally sustainable (and thus to be able to attract additional funding to carry it out). The EU taxonomy identifies key environmental aspects, referred to as environmental objectives, such as [10]:

- combating and adapting to climate change (reducing CO_2 emissions and improving energy efficiency),
- water management,
- activities for the Circular Economy,
- non-GHG emissions,
- protection of biodiversity.

The EU Taxonomy therefore constitutes a requirement, but also an incentive for economic actors to target their activities to improve environmental performance in terms of the environmental impact of a given activity and thus to obtain 'green fund'.

4. The Concept of Lean Green as a Combination of Lean Manufacturing and Sustainable Development

Lean Green is a manufacturing method that minimizes wastes and maximize environmental protection (first of all minimizing emissions to air, water and soil) through proper process and product design, with sustainability as its main objective [8]. Environmental management tools such as LCA

Tab. 3. The impact of selected Lean Manufacturing tools on environmental added value. Source: own elaboration based on [11] [12]
Tab. 3. Wpływ wybranych narzędzie Lean Manufacturing na środowiskową wartość dodaną. Źródło: opracowanie własne na podstawie [11] [12]

Lean tool	Impact on environmental added value
VSM	Reducing waste, reducing the distance travelled by materials, products, finished goods
5S	Segregation of waste according to label codes, increase in training raising the environmental awareness of employees
TPM	Energy savings, improvement of OEE indicators
SMED	Energy savings resulting from reduced machine changeover time

Tab. 4. Selected environmental benefits and activities in the field of Lean and Green application in the world. Source: own elaboration based on [18] [21]
Tab. 4. Wybrane korzyści środowiskowe oraz działania w kierunku wdrożenia „zielonej i szczupłej" organizacji/produkcji na świecie. Źródło: opracowanie własne na podstawie [18] [21]

Company	Action	Benefit
DuPont	Elimination of landfilling of production waste according to the DMAIC (Lean SixSigma) approach.	The amount of waste landfilled so far has been reduced from 37,000 tonnes to zero. It generated $2.2 million in by-product sales and saved $400,000.
General Electric	Applying the Lean approach to the organization of more than 200 actions searching for opportunities to save energy.	This reduced greenhouse gas emissions by 250,000 tonnes and saved $70 million in energy purchase costs.
3M	Application of Lean, Six Sigma and the 3P (Pollution, Prevention, Pays) pollution prevention program.	Emissions of pollutants into the air were reduced per unit of sale by 61% and the amount of waste generated by 30%, and energy efficiency improved by 27%.
LSI Logic Corporation	Implementation of Lean Green.	By reusing water in the production facility, the manufacturing process need 63 percent less water than it did before.

(Life Cycle Assessment) analysis, the ISO 14001 Environmental Management System, the EMAS Eco-Management and Audit Scheme [1], the ISO 50001 Energy Management System and many others are also tools, that aim to minimize environmental losses. In the Lean Green approach, it is important to also relate it to existing management systems and environmental methods. Lean Green is a specific response to the rising costs of energy procurement, the possible risk of unstable supplies and the accelerating pace of regulatory and/or governmental changes. It is a concept that involves minimization the negative environmental aspects occurring or likely to occur within all types of waste identified in the lean structure of the organisation [5]:

- overproduction, generates more energy consumption than required, related to the infrastructure used to handle redundant products,
- inventory, result in an increase in energy requirements for storage (the need to heat, cool or light warehouses),
- transport requires energy to transport of goods (particularly CO_2 emissions),
- expectation, determines the power consumption during standstill,
- unnecessary movement, increases the need to have space for semi-finished products and work in progress products,
- deficiencies, force additional energy expenditures due to the necessity of corrective actions for production non-conformities (repairs, alterations, reclassification or scrapping),
- errors in the process, result in additional energy use.

Waste resulting from poor environmental performance have been referred to as 'green' wastes. Their main types are shown in figure 1.

The aim of integrating the concept of Lean Manufacturing and sustainable development into the Lean Green approach should be to achieve economic profit and the smallest possible environmental footprint, also referred to as an ecological footprint (minimization the harmful impact of operations on the environment). This combination makes it possible to meet the expectations of sustainable development, but also in the requirements of classically understood economic value. The ways of achieving lean and green maturity when applying the methodologies listed, together with the relationships that may exist between them, are presented in table 2.

The Lean Manufacturing concept is a stimulator for responsible business, so companies applying Lean focus mainly on reducing production time and costs. From the Green point of view, consumer satisfaction is higher the higher the environmental status of a product. By investing in new environmental products, excessive costs are reduced, which are usually incomparable to the benefits that an organisation can gain by implementing green practices [14]. Attempts to date to link and integrate the concepts of Lean Manufacturing and sustainable development in Lean Green involve the definition of so-called environmental added value. It expresses the impact of the use of Lean tools in production processes for selected environmental aspects. In other words, it provides a measure of the environmental benefits of applying the tools of Lean Manufacturing methodology. Table 3. describes how the application of Lean tools can influence the building of environmental added value and thus the environmental management system.

Companies around the world approach the application of Lean Manufacturing tools oriented toward improving environmental performance in different ways. Very often this application is unconscious - oriented towards process optimisation brings economic benefits while having a more or less positive impact on the environment. The environmental benefits could be greater if this started to be done in a systemic and more deliberate way, as shown by the selected examples of Lean and Green application worldwide, summarised in table 4.

Lean Green has applications in various industries. Also in the mining industry its application is possible, but the number of these implementations is so far small and the environmental benefits are seen "incidentally", which requires systematisation and the application of a conscious approach to the development of Lean Green in the mining industry. An example of the implementation of a Lean tool for the mining industry is the introduction of TPM (Total Productive Maintenance) at KGHM Polska Miedź and the consequent elimination of the tube-and-chain conveyor of the crusher dust removal system, thereby achieving zero failure rates and improving energy efficiency by saving 6 kW of energy per shift [22]. Thus, not only an economic benefit but also an environmental benefit (in the spirit of Lean Green) was observed. The mining industry's self-awareness of sustainability is steadily increasing. Not insignificant is also the awareness and expectations of industry stakeholders [23], who determine actions on the part of mining companies towards improving the environmental performance of the processes carried out there.

5. Conclusions

The overriding aim of applying the Lean Manufacturing methodology becomes the pursuit of improving environmental (in addition to economic) efficiency. The analysis of the principles, tools and techniques of Lean Manufacturing juxtaposed with the requirements of sustainable development indicates the need to adapt the methodology and consciously use it to improve the environmental performance of manufacturing processes carried out, as well as a rationale for presenting it as Lean Green. Legal determinants, such as the European Green Deal Strategy and the resulting legal instruments, which place particular emphasis on the prevention of negative climate change, its protection, the creation a circular economy, actions to protect the environment, are a concrete premise for organising manufacturing processes in such a way that they not only bring economic profit, but are continuously improved towards improving environmental efficiency, and thus the impact of these processes on the aforementioned ecological aspects. Of the Lean and Green approaches presented, a symbiotic approach, in which Lean and Green are implemented as part of the same strategy as part of the continuous improvement of the organisation, will yield the best results. The possibilities seen in the literature and previous research to apply selected Lean Manufacturing tools towards building a good environmental impact of manufacturing processes provide excellent material for specific implementations and tests in different industries, as evidenced by examples of Lean and Green implementations applied in companies with different industry specialisations. Increasingly the need to adapt Lean and Green to specific production conditions is becoming apparent, pointing to the need for further empirical research into the adaptability of Lean Manufacturing tools through the lens of environmentally conscious benefits.

Literatura – References

1. Bąk J. (2021), Environmental engineering, Zarządzanie środowiskiem i zarządzenie środowiskowe, Wydawnictwo PK, Kraków, p. 53.
2. Deloitte, Non-financial Reporting 2014, Vol. 6, Pages 348-364, https://www2.deloitte.com/content/dam/Deloitte/lv/Documents/strategy/Nonfinancial_reporting_2015.pdf
3. Corporate Sustainability Reporting Directive European Parliament legislative resolution of 10 November 2022 on the proposal for a directive of the European Parliament and of the Council amending Directive 2013/34/EU, Directive 2004/109/EC, Directive 2006/43/EC and Regulation (EU) No 537/2014 as regards corporate sustainability reporting.
4. Horzela A., Semrau J. (2020) Koncepcja Lean Manufacturing jako narzędzie doskonalenia procesów produkcyjnych 2020 s. 37-49
5. Krzyczkowski M. (2012) Ekologistyka a transport „Logistyka Odzysku" No. 1 (2), p. 14.
6. Liker J.K., Meier D.P. (2011), Droga Toyoty. Fieldbook. Praktyczny przewodnik wdrażania 4P Toyoty, MTBiznes, Warszawa, s.63
7. Lisiński M., Ostrowski B. (2006) Lean management w restrukturyzacji przedsiębiorstwa, Kraków-Kluczbork: Antykwa; Za: J. Czekaj. „Wybrane metody etatyzacji jako instrumenty lean administration". A. Stabryla (red.) (2010) Koncepcja zarządzania współczesnym przedsiębiorstwem. Kraków: Fundacja Uniwersytetu Ekonomicznego w Krakowie.
8. Maruthi, G. D., Rashimi, R. (2015) Green Manufacturing: It's Tools and Techniques that can be implemented in Manufacturing Sectors. Materials Today: Proceedings 2, 3351.
9. Pawłowski, E., Pawłowski, K., & Trzcieliński, S. (2010). Metody i narzędzia Lean Manufacturing, Wydawnictwo Politechniki Poznańskiej, Poznań, s.13.
10. Regulation (EU) 2020/852 of the European Parliament and of the Council of 18 June 2020 on the establishment of a framework to facilitate sustainable investment (hereinafter: "Taxonomy" or "Regulation").
11. Wirkus M., Chmielarz A. (2012) Środowiskowe aspekty wdrażania Lean Manufacturing, w: Materiały konferencyjne: Innowacje w Zarządzaniu i Inżynierii Produkcji, Zakopane, s. 169-176.
12. Wirkus M., Chmielarz A. (2011). Value stream mapping as a tool to improve environmental management system. Inżynieria Produkcji : Innowacje i Technologie przyszłości - Production Engineering ; Innovations and Technologies of the Future, pp. 405-409.
13. Womack P. James, Jones T. Daniel (2012), Lean Thinking. Eliminating waste and creating value, ProdPublishing, Wrocław, ed. 2. pp. 20-40.
14. Wronka A. (2014) Integracja aspektów wyszczuplonego i zielonego zarządzania - Lean Green, Logistyka Odzysku 1/2014(10), Łódź.
15. Zokaei K., Lovins H., Wood A., Hines P. (2013) Creating a Lean and Green Business System. Techniques for Improving Profits and Sustainability, CRC Press Taylor & Francis Group. Boca Raton, London, New York, pp. 46, 56.
16. Dokument elektroniczny: Ministerstwo Rozwoju: Agenda 2030 na rzecz zrównoważonego rozwoju - implementacja w Polsce: https://www.gov.pl/web/rozwoj-technologia/agenda-2030 (access: 20.05.2023).
17. Dyrektywa o sprawozdawczości przedsiębiorstw w zakresie zrównoważonego rozwoju: https://www.gov.pl/web/finanse/dyrektywa-o-sprawozdawczosci-przedsiebiorstw-w-zakresie-zrownowazonego-rozwoju-juz-opublikowana (access: 10.05.2023).
18. Lean Center: https://leancenter.pl/bazawiedzy/lean-green (access: 25.05.2023).
19. Sobolewski M. (2020) Europejski Zielony Ład - w stronę neutralności klimatycznej: http://orka.sejm.gov.pl/WydBAS.nsf/0/5A874F6E5DAB64DCC12585AC002A3997/$file/Infos_275.pdf (access: 10.05.2023).
20. Zrównoważony rozwój i Cele Zrównoważonego Rozwoju: https://www.unic.un.org.pl/strony-2011-2015/zrownowazony-rozwoj-i-celezrownowazonego-rozwoju/2860 (access: 19.05.2023).
21. Gordon J. Pamela (2001) Lean and Green. Profit for your workplace and the environment, Berrett-Koehler Publishers, San Francisco, California, p. XV.
22. Migza M., Bogacz P. (2015) Możliwość wykorzystania narzędzi Lean Management w przedsiębiorstwach sektora górnictwa podziemnego w Polsce, Possibility of using Lean Management tools in underground mining companies in Poland, Przegląd Górniczy, ISSN 0033-216X-2015 t. 71 nr 8, s. 58-61.
23. Bogusz K. (2020) Branża wydobywcza w obliczu wyzwań niesionych przez ideę zrównoważonego rozwoju . Inżynieria Mineralna, 1(1), 131-138. https://doi.org/10.29227/IM-2020-01-21

Lean Green – integracja Lean Manufacturing i zrównoważonego rozwoju w świetle dążenia do prowadzenia działalności efektywnej ekonomicznie i środowiskowo

Koncepcja Lean Manufacturing to zestaw technik, metod i narzędzi, których zastosowanie w procesach produkcyjnych (wytwórczych) ma wyeliminować marnotrawstwo i poprawić efektywność ekonomiczną tychże procesów. Wyzwania zrównoważonego rozwoju determinują nowe podejście do prowadzenia działalności produkcyjnej. Kwestie związane z dbałością o środowisko i społeczne aspekty działalności przedsiębiorstw stają się kluczowe z punktu widzenia interesariuszy biznesowych. W artykule podjęto próbę zestawienia klasycznego pojęcia Lean Manufacturing, prezentując główne zasady i założenia tejże koncepcji. Autorzy zwrócili uwagę na kluczowe wymogi prawne i formalne, które determinują potrzebę odmiennego podejścia do Lean Manufacturing. Przeanalizowano możliwe sposoby korelacji koncepcji Lean Manufacturing (rozumianej klasycznie i zorientowanej na efektywność ekonomiczną) z Lean, widzianym w świetle wyzwań zrównoważonego rozwoju. Połączenie to zostało przedstawione jako Lean Green, wskazując tym samym na możliwy związek między Lean Manufacturing a zrównoważonym rozwojem, w jego części środowiskowej. Zaprezentowano także główne źródła „zielonych marnotrawstw", które można wyeliminować dzięki Lean Green. Na przykładach konkretnych firm zestawiono potencjalne korzyści z wdrożenia koncepcji Lean Manufacturing zorientowanej nie tylko na aspekty ekonomiczne, ale przede wszystkim na korzyści środowiskowe. Wykorzystano przegląd literatury polskiej i światowej, analizę dostępnych źródeł oraz własne doświadczenia autorów.

Słowa kluczowe: *szczupła produkcja, lean green, zrównoważony rozwój, środowisko, efektywność*

Woda jako źródło energii elektrycznej w Polsce

Tadeusz OLKUSKI[1)]*

[1)] dr hab. inż. prof. AGH; AGH Akademia Górniczo-Hutnicza; ORCID: 0000-0001-8081-2348
* Corresponding; olkuski@agh.edu.pl

http://doi.org/10.29227/IM-2024-01-112

Submission date: 21-06-2024 | Review date: 03-07-2024

Abstract

Woda jest niezbędnym składnikiem naszego życia. Odgrywa kluczową rolę we wszystkich procesach biologicznych, procesach przemysłowych, w rolnictwie, transporcie, wytwarzaniu energii elektrycznej i ciepła i w wielu innych dziedzinach życia. Celem artykułu jest pokazanie znaczenia wody w produkcji energii elektrycznej w Polsce. Jak wiemy, energetyka wodna jest jedną z najstarszych form wykorzystywania energii. Już w starożytności wykorzystywana była na przykład do napędu młynów wodnych. W dzisiejszych czasach jej energetyczne wykorzystanie jest zupełnie inne. W Polsce energetyka wodna jest słabo rozwinięta. Moc zainstalowana w elektrowniach wodnych zawodowych wynosi zaledwie 2 292,2 MW, w tym w elektrowniach szczytowo-pompowych 1 792,3. Produkcja energii elektrycznej w elektrowniach wodnych wynosi w Polsce niecałe 2 TWh, co jest wielkością symboliczną, stanowiącą zaledwie 0,6% rocznej produkcji energii elektrycznej w naszym kraju. Polska posiada ponad 700 elektrowni wodnych, ale większość z nich to małe elektrownie wodne nie przekraczające 5 MW mocy. Największymi elektrowniami wodnymi w Polsce są: elektrownia Żarnowiec, elektrownia Porabka-Żar oraz elektrownia Solina wchodząca w skład Zespołu Elektrowni Wodnych Solina – Myczkowce. Wszystkie te elektrownie są elektrowniami szczytowo-pompowymi. Według prognoz światowych pomimo gwałtownego rozwoju fotowoltaiki oraz energetyki wiatrowej energetyka wodna pozostanie do 2030 roku największym na świecie źródłem wytwarzania energii elektrycznej ze źródeł odnawialnych.

Słowa kluczowe: *woda, produkcja energii, elektrownie wodne*

Wprowadzenie

Woda, tak jak i powietrze, jest niezbędnym składnikiem naszego życia. Odgrywa kluczową rolę we wszystkich procesach biologicznych, procesach przemysłowych, w rolnictwie, transporcie, wytwarzaniu energii elektrycznej i ciepła i w wielu innych dziedzinach życia. Jest jedną z najpospolitszych substancji we Wszechświecie. Jest związkiem chemicznym o wzorze H_2O, występującym w warunkach standardowych w stanie ciekłym. W stanie gazowym występuje w postaci pary wodnej, a w stałym stanie skupienia jako lód.

Woda zajmuje ponad 70% powierzchni Ziemi. Zaledwie 2,5% jej zasobów stanowią wody słone, a tylko 0,6% to wody słodkie będące źródłem wody pitnej. Choć wody na Ziemi jest tak dużo to niestety nie we wszystkich regionach jest jej pod dostatkiem. Jak podaje w swoim raporcie „Polska na drodze zrównoważonego rozwoju" Główny Urząd Statystyczny [13] krytyczna jest sytuacja w Afryce Północnej, gdzie roczny pobór wody przekracza ilość odnawialnych zasobów słodkiej wody w tym regionie. Duże jest też prawdopodobieństwo wystąpienia deficytu wody w Azji Środkowej (gdzie pobieranych jest 88% odnawialnych zasobów wód) oraz w Azji Południowej (71%). Niepokojąca staje się również sytuacja w Azji Zachodniej oraz Wschodniej (gdzie relacja ta wynosi odpowiednio 54% i 46%).Jeżeli chodzi o nasz kraj, to pod względem zasobów wody pitnej przypadającej na jednego mieszkańca znajdujemy się na 24 pozycji w Unii Europejskiej wyprzedzając jedynie Czechy, Cypr i Maltę. Najlepsza sytuacja pod tym względem panuje w Chorwacji, Finlandii i Szwecji.

Choć wszystkie zastosowania wody są ważne, to w niniejszym artykule zostanie poruszona kwestia wykorzystywania wody do celów energetycznych.

Woda w procesach wytwarzania energii elektrycznej

Energetyka wodna jest jedną z najstarszych form wykorzystywania energii. Już w starożytności wykorzystywane były młyny wodne, wprawdzie nie do wytwarzania energii elektrycznej, ale do mielenia zboża, w późniejszych czasach również do cięcia i obróbki drewna. Niewątpliwą zaletą wody jest jej niewyczerpalność. Choć w niektórych regionach świata, a ostatnio również w Polsce, wody zaczyna brakować, to jednak jest to odnawialne i niewyczerpywalne źródło energii. Kolejną zaletą energetyki wodnej jest brak emisji gazów cieplarnianych, a także brak wpływu warunków atmosferycznych na jej pracę. Jak podaje IEA (International Energy Agency) energia wodna generuje obecnie więcej energii elektrycznej niż wszystkie inne technologie odnawialne razem wzięte. Pomimo gwałtownego rozwoju fotowoltaiki oraz energetyki wiatrowej energetyka wodna pozostanie do 2030 roku największym na świecie źródłem wytwarzania energii elektrycznej ze źródeł odnawialnych. Po 2030 roku nadal będzie odgrywać kluczową rolę w dekarbonizacji systemu elektroenergetycznego na świecie [8].

W Polsce zagadnienia związane z wykorzystaniem wody reguluje Ustawa Prawo Wodne [19]. Ustawa reguluje gospodarowanie wodami zgodnie z zasadą zrównoważonego rozwoju, w szczególności kształtowanie i ochronę zasobów wodnych, korzystanie z wód oraz zarządzanie zasobami wodnymi. Ustawa reguluje sprawy własności wód oraz gruntów pokrytych wodami, a także zasady gospodarowania tymi składnikami jako mieniem Skarbu Państwa. Przepisy ustawy stosuje się do wód śródlądowych oraz morskich wód wewnętrznych, a także do wód morza terytorialnego w zakresie planowania gospodarowania wodami, ochrony przed zanieczyszczeniem

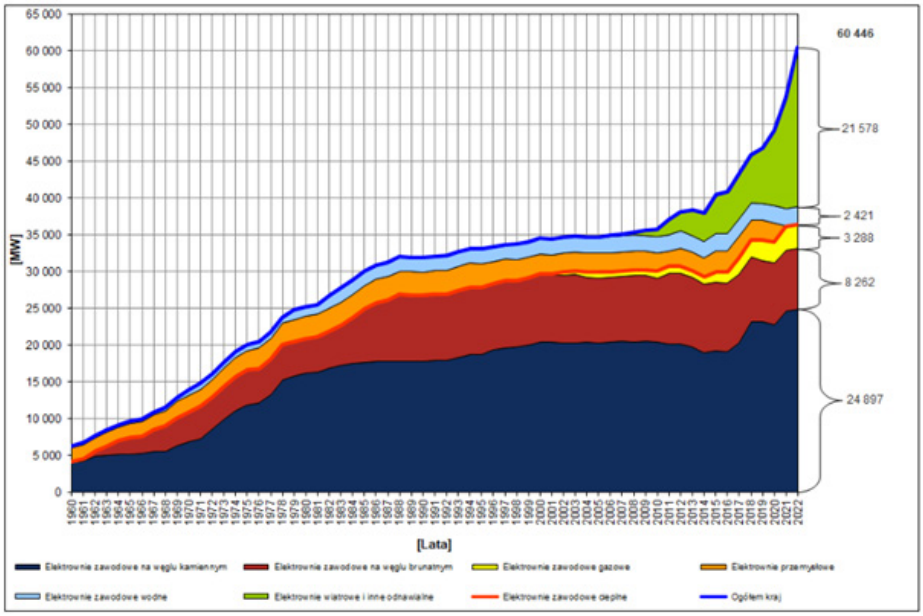

Rys. 1. Moc zainstalowana w Polsce w latach 1960–2022. Źródło: [15]
Fig. 1 Installed power in Poland between 1960–2022 Source: [15].

ze źródeł lądowych oraz ochrony przed powodzią, a w pozostałym zakresie – w przypadkach określonych w ustawie.

Energetyka wodna znalazła również swoje miejsce w ustawie o odnawialnych źródłach energii [18]. W Art. 2 tejże ustawy hydroenergię zdefiniowano jako energię spadku śródlądowych wód powierzchniowych, z wyłączeniem energii uzyskiwanej z pracy pompowej w elektrowniach szczytowo-pompowych lub elektrowniach wodnych z członem pompowym.

Instytucją odpowiedzialną za gospodarowanie wodami w Polsce jest Państwowe Gospodarstwo Wodne Wody Polskie [10]. Do głównych zadań tej instytucji należy:

- Ochrona przed powodzią (zarządzanie ryzykiem powodziowym, tworzenie map zagrożenia powodziowego, planowanie przeciwdziałania skutkom suszy),
- Zarządzanie środowiskiem wodnym (ocena wpływu na możliwość osiągnięcia celów środowiskowych, zarządzanie krajowym planem oczyszczania ścieków, renaturyzacja wód powierzchniowych, wyznaczanie kąpielisk w gminach)
- Zarządzanie korzystaniem z wód (opłaty za usługi wodne, opłaty za zmniejszenie naturalnej retencji terenowej, pozwolenia wodnoprawne i melioracyjne, taryfy wodno-kanalizacyjne).

Energetyka wodna, tak jak i inne formy działalności gospodarczej, posiada nie tylko zalety ale też wady.

Do głównych zalet energetyki wodnej należą:

- Wykorzystywanie odnawialnego źródła energii jakim jest woda,
- Prostota procesu wytwarzania energii elektrycznej,
- Brak emisji gazów cieplarnianych oraz pyłów,
- Długi czas pracy elektrowni wodnych przekraczający niejednokrotnie nawet sto lat,
- Niskie koszty eksploatacji,
- Możliwość szybkiego uruchomienia, gdy zaistnieje taka potrzeba.

Główne wady energetyki wodnej to:

- Ingerencja w środowisko naturalne poprzez wznoszenie konstrukcji spiętrzających wodę,
- Niejednokrotnie konieczność przesiedlania miejscowej ludności,
- Zaburzenia ekosystemów wodnych prowadzące do wyginięcia flory i fauny występującej na obszarach przeznaczonych do zalania,
- Pojawianie się innych gatunków roślin i zwierząt na tych terenach,
- Wzrost występowania pary wodnej w pobliżu zbiornika,
- Wysokie nakłady inwestycyjne,
- Zależność od ilości opadów i poziomu wód,
- Ogromne straty w przypadku uszkodzenia zbiornika.

W Polsce energetyka wodna nie odgrywa znaczącej roli ze względu na brak odpowiednich cieków wodnych. Niemniej jednak 28 lutego 2023 r., Rada Ministrów, przyjęła projekt ustawy o przygotowaniu i realizacji inwestycji w zakresie elektrowni szczytowo-pompowych oraz inwestycji towarzyszących [14], co pozwala mieć nadzieję, że pewne działania w kierunku rozwoju energetyki wodnej zostaną poczynione.

Krajowy System Elektroenergetyczny (KSE)

Moc zainstalowana w Krajowym Systemie Elektroenergetycznym rośnie systematycznie od kilkudziesięciu lat. Na rys. 1 przedstawiono jak wzrastała moc zainstalowana w Polsce w latach 1960–2022.

Od początku lat 60-tych ubiegłego wieku moc zainstalowana w Krajowym Systemie Elektroenergetycznym (KSE) nieustannie wzrasta. Bardzo dynamiczny wzrost występował zwłaszcza w początkowej fazie tego okresu, to znaczy od roku 1960 aż do roku 1989. Przyrost ten wyniósł około 30 GW. Później nastąpiła transformacja polityczna oraz ekonomiczna, co na pewien czas spowolniło zapotrzebowanie na nowe moce wytwórcze w związku z likwidacją wielu zakładów przemy-

Tab. 1. Moc zainstalowana w Polsce na koniec 2022 roku. Źródło: opracowanie własne na podstawie danych [1]
Table 1 Installed capacity in Poland at the end of 2022. Source: own study based on data [1].

Wyszczególnienie	Moc elektryczna zainstalowana [MW]
Elektrownie zawodowe cieplne	
- na węglu kamiennym	21 571,2
- na węglu brunatnym	8 908,4
- na gazie ziemnym	2 464,9
Elektrownie zawodowe wiatrowe	1 871,0
Elektrownie zawodowe wodne	2 292,2
- w tym szczytowo-pompowe	1 792,3
Elektrownie przemysłowe	3 633,5
Niezależne OZE	18 592,8
OGÓŁEM	**60 423,1**

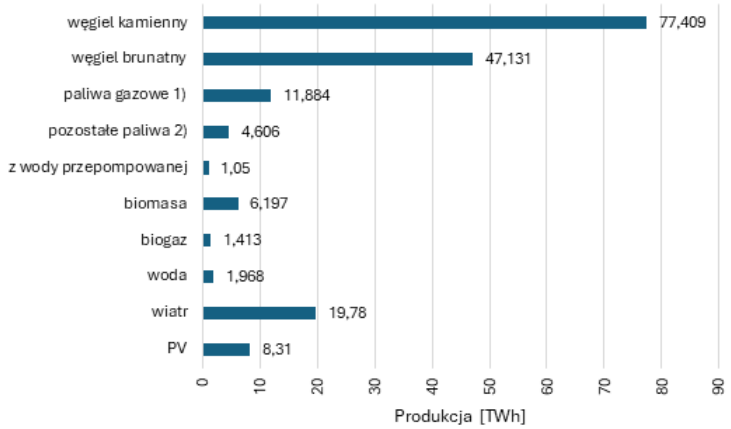

Rys. 2. Produkcja energii elektrycznej w Polsce z podziałem na źródła. Źródło: opracowanie własne na podstawie danych [1]
Fig. 2. Electricity production in Poland by source. Source: own study based on data [1].

słowych w naszym kraju. W 1990 roku pod naciskiem Banku Światowego oraz Międzynarodowego Funduszu Walutowego rozpoczęto restrukturyzację, a de facto likwidację górnictwa węgla kamiennego w Polsce. Wiele zakładów przemysłowych przestało istnieć, więc i zapotrzebowanie na energię elektryczną nie wzrastało. Brakowało też środków finansowych na nowe inwestycje. Wraz z rozwojem gospodarki wolnorynkowej w Polsce zaczęto też oszczędniej gospodarować energią elektryczną, aby nie podrażać kosztów działalności przedsiębiorstw. W pierwszych dziesięcioleciach po II wojnie światowej w systemie dominowały moce na węglu kamiennym i węglu brunatnym. Istniały również elektrownie przemysłowe, które też opalane były głównie węglem. Od 2000 roku zaobserwować można pewną zmianę. Pod wpływem obrońców klimatu zaczęto wdrażać energetykę gazową, która jest mniej inwazyjna dla środowiska naturalnego. Największy przyrost mocy zainstalowanej nastąpił jednak w ostatnich latach. Od roku 2008 gwałtownie zaczęła rozwijać się energetyka bazująca na odnawialnych źródłach energii. Początkowo, do roku 2015, rozwijała się głównie energetyka wiatrowa. Po wprowadzeniu tzw. ustawy odległościowej [20] rozwój energetyki wiatrowej został wstrzymany. Od roku 2017, a zwłaszcza od roku 2019 gwałtownie zaczęła rozwijać się energetyka słoneczna. Dzięki programom pomocowym takim jak Mój Prąd [9], czy też Czyste Powietrze [3] osiągnięto obecnie moc tych instalacji taką jaka zaplanowana została w Polityce energetycznej Polski do 2040 roku [12]. Niestety energetyka wodna pozostaje cały czas na tym samym bardzo niskim poziomie rozwoju, ale wynika to przede wszystkich z warunków naturalnych występujących w Polsce a nie z niechęci decydentów do inwestowania w to źródło energii.

W tabeli 1 przedstawiono moc zainstalowaną w Polsce na koniec 2022 roku.

Największą moc zainstalowaną w Polsce od lat posiadają elektrownie cieplne. Elektrownie na węglu kamiennym posiadają moc 21,6 GW, na węglu brunatnym 8,9 GW, a na gazie ziemnym 2,5 GW. Sytuacja ta powoli się zmienia ze względu na wprowadzanie do systemu odnawialnych źródeł energii, a także, w przypadku węgla brunatnego, zamknięcie w 2018 roku elektrowni Adamów oraz zapowiedzi Zespołu Elektrowni Pątnów-Adamów-Konin (ZE PAK) całkowitego wycofania się z węgla brunatnego do 2030 roku [21].

Wielkość mocy zainstalowanej nie przekłada się bezpośrednio na produkcję energii elektrycznej, gdyż nie wszystkie moce są w równym stopniu wykorzystywane. Na rys. 2 przedstawiono produkcję energii elektrycznej w Polsce w 2022 roku z podziałem na źródła.

Jak widać z rysunku, największa produkcja energii elektrycznej w Polsce w 2020 roku pochodziła z węgla kamiennego i wyniosła 77,4 TWh, następnie z węgla brunatnego 47,1 TWh, a potem z wiatru 19,8 TWh. Mniejsze ilości energii wyprodukowano z paliw gazowych 11,9 TWh oraz z biomasy 6,2 TWh. Produkcja energii elektrycznej w elektrowniach wodnych wyniosła 1,968 TWh, co stanowiło zaledwie 1,1% całkowitej krajowej produkcji prądu. Jeszcze mniej energii elektrycznej wytworzono w elektrowniach szczytowo-pom-

Rys. 3. Elektrownia Żarnowiec. Źródło: [11]
Fig. 3. Żarnowiec power plant. Source: [11]

Rys. 4. Zbiornik górny elektrowni Porąbka-Żar. Źródło: [11]
Fig. 4. Upper reservoir of the Porąbka-Żar power plant. Source: [11]

powych, bo zaledwie 1,05 TWh, co stanowiło 0,6% całkowitej produkcji. Jest to bardzo niewiele chociaż trzeba przyznać, że elektrownie szczytowo-pompowe są bardzo potrzebne w systemie aby zasilić krajowy system elektroenergetyczny (KSE) w godzinach największego zapotrzebowania.

Podział elektrowni wodnych

Elektrownie wodne można klasyfikować ze względu na różne kryteria takie jak topografia terenu czy też różne cechy energetyczne.

Uwzględniając topografię terenu wyróżnia się następujące elektrownie [6]:

- elektrownia zaporowa,
- elektrownia na kanale,
- elektrownia na rurociągu ciśnieniowym,
- elektrownia na kanale i rurociągu,
- elektrownia na sztolni i rurociągu.

Cechy energetyczne brane pod uwagę przy klasyfikacji energetyki wodnej to:

- sposób i stopień wykorzystania energii spływu rocznego,
- zależność mocy i produkcji od warunków wodnych,
- udział produkcji szczytowej, podszczytowej i podstawowej w produkcji rocznej,
- stopień zapewnienia mocy,
- stopień zapewnienia produkcji,
- miejsce pracy na wykresie dobowego obciążenia systemu elektroenergetycznego,
- wpływ pracy elektrowni wodnej na ekonomikę krajowego systemu energetycznego.

Biorąc pod uwagę te kryteria wyróżnia się następujące typy elektrowni wodnych [6]:

- elektrownie przepływowe,
- elektrownie na zbiornikach o dobowej i tygodniowej regulacji,
- elektrownie na zbiornikach wielozadaniowych,
  – wyrównaniu sezonowym i częściowym rocznym,
  – wyrównaniu całkowitym rocznym,
  – wyrównaniu wieloletnim,
- elektrownie w kaskadzie zwartej,
- elektrownie pompowe i elektrownie wodne z pompowaniem.

Największe elektrownie wodne w Polsce

Polska nie posiada zbyt wielu dużych elektrowni wodnych, ale jeśli za kryterium podziału pomiędzy małymi elektrowniami wodnymi a dużymi przyjąć 5 MW, to można wyróżnić dość sporą grupę dużych elektrowni wodnych. W artykule przedstawiono cztery z pięciu elektrowni wodnych, których moc zainstalowana przekracza 100 MW. Wyróżniono cztery, gdyż są to elektrownie szczytowo-pompowe, a piata w kolejności pod względem mocy jest elektrownią przepływową.

Elektrownia Żarnowiec

Największą elektrownią wodną w Polsce jest elektrownia Żarnowiec należąca do Polskiej Grupy Energetycznej S.A.

Rys. 6. Elektrownia wodna Żydowo. Źródło: [4]
Fig. 6. Żydowo hydroelectric power plant. Source: [4]

Rys. 5. Elektrownia wodna Solina. Źródło: [11]
Fig. 5. Solina hydroelectric power plant. Source: [11]

(PGE S.A.) [7]. Elektrownia ta zlokalizowana jest w Czymanowie nad Jeziorem Żarnowieckim w województwie pomorskim na granicy powiatów puckiego i wejherowskiego. Posiada moc zainstalowaną 716 MW (4 turbiny o mocy 179 MW każda). Zbiornikiem dolnym jest Jezioro Żarnowieckie, natomiast zbiornik górny jest całkowicie sztucznym zbiornikiem wybudowanym na płaskim szczycie najwyższego ze znajdujących się w pobliżu jeziora wzgórz morenowych. Pierwsze prace przygotowawcze rozpoczęto w 1972 roku, a uruchomienie elektrowni nastąpiło w 1983 roku [17]. Na rys. 3 przedstawiono widok elektrowni Żarnowiec z lotu ptaka.

Głównymi zaletami tej, ale nie tylko tej elektrowni szczytowo-pompowej, jest łagodzenie krzywej dobowego obciążenia systemu, pokrywanie nagłych ubytków i występujących w systemie przerostów poboru mocy, optymalizowanie pracy krajowego systemu elektroenergetycznego poprzez prowadzenie szybkiej i stałej regulacji dostarczanej do systemu mocy czynnej. Elektrownie szczytowo-pompowe pozwalają na magazynowanie energii elektrycznej w formie energii potencjalnej wody przepompowywanej z dolnego do górnego zbiornika. Odzysk zmagazynowanej energii odbywa się poprzez przepływ wody w odwrotnym kierunku, zasileniu hydrozespołów i oddaniu energii elektrycznej do sieci [15]. Elektrownia ta sterowana jest bezpośrednio przez Krajową Dyspozycję Mocy z Warszawy. Rozruch do pełnej mocy trwa zaledwie 3 minuty.

Elektrownia Porąbka-Żar

Drugą pod względem wielkości mocy zainstalowanej elektrownią wodną w Polsce jest elektrownia szczytowo-pompowa Porąbka-Żar. Elektrownia ta znajduje się w Międzybrodziu Bialskim i posiada moc 500 MW (4 hydrozespoły po 125 MW każdy). Jest to jedyna w Polsce elektrownia podziemna. Budowa elektrowni rozpoczęła się w 1971 roku a jej oddanie do eksploatacji nastąpiło w 1979 roku. Jest to również elektrownia wysokospadowa o spadzie 440 metrów. Umiejscowienie elektrowni wynikało z bardzo korzystnych warunków terenowych, takich jak duży spad przy małej odległości zbiorników od siebie. Na rys. 4 przedstawiono widok zbiornika górnego elektrowni Porąbka-Żar.

Elektrownia składa się z trzech podstawowych części. Jedną z nich jest zbiornik gromadzący wodę mogący pomieścić 2 310 000 m^3 wody. Jest on uszczelniony kilkoma warstwami asfaltu, przełożonych żelbetonem. Drugim elementem elektrowni są dwa szyby wywiercone wewnątrz góry. Mają 4 metry średnicy i są pochylone pod katem 45o względem podłoża. Transportują one wodę do hali elektrowni, oraz gdy jest pompowana do zbiornika górnego. Trzecim elementem są wspomniane wcześniej turbiny. Pełnią one funkcje zarówno turbin jak i pomp. Pompowanie pełnego zbiornika trwa 5 godzin. Następnie woda jest wypuszczana do Zbiornika Międzybrodzkiego [2]. Elektrownia Porąbka-Żar, tak jak i elektrownia Żarnowiec, należą do Polskiej Grupy Energetycznej S.A.

Elektrownia Solina

Trzecią pod względem wielkości elektrownią wodną w Polsce jest elektrownia Solina. Jest to również elektrownia szczytowo-pompowa. Położona jest na rzece San w gminie Solina w województwie podkarpackim. Na rys. 5 przedstawiono widok elektrowni wodnej Solina.

Elektrownia wodna Solina, wchodzi w skład Zespołu Elektrowni Wodnych Solina – Myczkowce, znajduje się na rzece San w miejscowości Solina. Elektrownia Solina jest jedną z największych elektrowni szczytowo-pompowych na dopływie naturalnym zapory betonowej. Moc zainstalowana wynosiła przed modernizacją 136 MW, a po modernizacji wynosi około 200 MW i składa się z 4 hydrozespołów. Budowa zapory w pętli Sanu rozpoczęła się już w 1920 roku lecz z powodu

braku funduszy została przerwana. Po II wojnie światowej powrócono do pomysłu budowy elektrowni wodnej w tym regionie. Najpierw wybudowano zbiornik elektrowni wodnej w Myczkowcach a następnie drugi, dużo większy zbiornik, w Solinie. Elektrownię Myczkowce uruchomiono w 1961 roku, a elektrownię Solina w 1968 roku. W latach 2000–2003 przeprowadzono gruntowną modernizację, co pozwoliło na zwiększenie mocy elektorowi do 200 MW.

Elektrownia Żydowo

Czwartą co do wielkości elektrownią wodną w Polsce jest elektrownia szczytowo-pompowa Żydowo. Znajduje się w miejscowości Żydowo w powiecie koszalińskim i należy do grupy kapitałowej Energa wchodzącej w skład grupy Orlen. Elektrownia wykorzystuje dwa naturalne zbiorniki wodne, jeden – górny, stanowi jezioro Kamienne, a zbiornik dolny jezioro Kwiecko. Obydwa jeziora oddalone są od siebie o około 1,5 kilometra, a różnica poziomów wynosi 80 metrów [4]. Jeziora połączone są trzema stalowymi rurociągami o średnicy pięciu metrów. Budowę elektrowni rozpoczęto w 1964 roku, a zakończono w 1971 roku. Moc zainstalowana tej elektrowni wynosi 167 MW. Na rys. 6 przedstawiono widok elektrowni Żydowo.

Elektrownia ta, podobnie jak 47 innych elektrowni wodnych spośród 727 elektrowni wodnych w Polsce, jest zarządzana przez grupę Energa [5].

Podsumowanie

Największymi elektrowniami wodnymi w Polsce są elektrownie szczytowo-pompowe. Nie są to obiekty zaliczane do odnawialnych źródeł energii, gdyż do pompowania wody do zbiornika górnego wykorzystują energię elektryczną wytwarzaną, w warunkach polskich – głównie z węgla. Łagodzą więc krzywą dobowego obciążenia systemu i pokrywają nagłe ubytki w systemie elektroenergetycznym. Pełnią jednak bardzo ważną rolę magazynów energii i wykorzystywane są w godzinach szczytowego zapotrzebowania na energię elektryczną lub w przypadku awarii innych elektrowni. Pompowanie wody odbywa się w nocy, gdy energia elektryczna jest tańsza i jest jej nadmiar, natomiast wykorzystywana jest głównie w godzinach porannego lub wieczornego szczytu.

Wszystkie cztery elektrownie przedstawione w artykule to elektrownie duże o mocy zainstalowanej przekraczającej 100 MW. Są to największe elektrownie wodne w Polsce o tak dużej mocy. Oprócz wyżej wymienionych jeszcze tylko elektrownia Włocławek ma moc przekraczającą 100 MW, konkretnie 160 MW.

Rozwój energetyki wodnej w Polsce, zwłaszcza tej o dużej mocy, nie ma większych perspektyw głównie z powodu braku odpowiednich cieków wodnych oraz ze względu na ochronę środowiska. Duża energetyka wodna ma bardzo niekorzystny wpływ na środowisko naturalne, więc protesty ekologów są w tym względzie uzasadnione. Należy też brać pod uwagę wysokie koszty budowy tego typu obiektów. Chociaż energetyka wodna w Polsce nie odgrywa znaczącej roli ze względu na brak odpowiednich cieków wodnych to jednak 28 lutego 2023 r., Rada Ministrów, przyjęła projekt ustawy o przygotowaniu i realizacji inwestycji w zakresie elektrowni szczytowo-pompowych oraz inwestycji towarzyszących, co pozwala mieć nadzieję, że pewne działania w kierunku rozwoju energetyki wodnej zostaną poczynione.

Literatura – References

1. ARE 2023 – Statystyka elektroenergetyki Polskiej. Agencja Rynku Energii. Warszawa 2024
2. Budowle https://www.budowle.pl/budowla/elektrownia-porabka-zar dostęp: 07.04.2024
3. Czyste Powietrze https://czystepowietrze.gov.pl/ dostęp: 01.04.2024
4. Energa-wytwarzanie http://www.energa-wytwarzanie.pl/obiekty/lista-obiektow/zydowo%2C51%2Cobiekt.html dostęp: 17.04.2024
5. Energa-wytwarzanie http://www.energa-wytwarzanie.pl/odnawialne-%C5%BAr%C3%B3d%C5%82a-energii/energia-wodna/elektrownie-wodne-duze-segment.html dostęp: 17.04.2024
6. Energia wodna [W:] Podstawy Gospodarki Surowcami Energetycznymi, pod red. E. Mokrzyckiego. Uczelniane Wydawnictwa Naukowo-Dydaktyczne. Kraków 2005
7. GKPGE https://www.gkpge.pl/grupa-pge dostęp: 07.04.2024
8. IEA https://www.iea.org/energy-system/renewables/hydroelectricity dostęp: 27.02.2024
9. Mój Prąd https://mojprad.gov.pl/ dostęp: 01.04.2024
10. Państwowe Gospodarstwo Wodne Wody Polskie https://www.wody.gov.pl/ dostęp: 26.02.2024
11. PGEEO https://pgeeo.pl/nasze-obiekty/elektrownie-wodne/ dostęp: 07.04.2024
12. Polityka energetyczna Polski do 2040 roku (PEP2040) (PEP2040 2021; Ministerstwo Klimatu i Środowiska. Warszawa 2021; Załącznik do uchwały nr 22/2021 Rady Ministrów z dnia 2 lutego 2021 r.
13. Polska na drodze zrównoważonego rozwoju Główny Urząd Statystyczny https://raportsdg.stat.gov.pl/2020/cel6.html dostęp: 20.03.2024
14. Projekt ustawy o przygotowaniu i realizacji inwestycji w zakresie elektrowni szczytowo-pompowych oraz inwestycji towarzyszących (https://www.gov.pl/web/klimat/rzad-przyjal-specustawe-o-elektrowniach-szczytowo-pompowych2 dostęp: 20.05.2024
15. Raport 2022 – Rola elektrowni szczytowo-pompowych w Krajowym Systemie Elektroenergetycznym: uwarunkowania i kierunki rozwoju. Zespół Ekspercki do spraw Budowy Elektrowni Szczytowo-Pompowych. Warszawa 2022
16. Raport PSE 2023
17. Tokarz J., Hryckiewicz L., Elektrownia wodna Żarnowiec – historia i dzień dzisiejszy. Energetyka i Ekologia, sierpień 2003. str. 509-515
18. Ustawa o Odnawialnych Źródłach Energii Dz.U. 2015 poz. 478 Ustawa z dnia 20 lutego 2015 r. o odnawialnych źródłach energii
19. Ustawa Prawo Wodne Dz. U. 2017 poz. 1566, Ustawa z dnia 20 lipca 2017 r.
20. Ustawa z dnia 20 maja 2016 r., poz. 961 o inwestycjach w zakresie elektrowni wiatrowych
21. ZEPAK https://zepak.com.pl/pl/; dostęp: 01.04.2024

Water as a Source of Electricity in Poland

Water is an essential ingredient of our lives as it plays a key role in all biological and industrial processes, agriculture, transport, electricity and heat generation, and other areas of life. The article aims to show the importance of water in electricity production in Poland. As we know, hydropower is one of the oldest forms of energy generation, as it has been used to power watermills from ancient times. Nowadays it is used differently. In Poland, hydropower is underdeveloped. The total installed power in commercial hydropower plants is only 2,292.2 MW, including 1,792.3 in pumped-storage power plants. The production of electricity in hydroelectric power plants in Poland is less than 2 TWh, constituting only 0.6% of the annual electricity production. Poland has over 700 hydroelectric power plants, but most of them are small hydropower plants with less than 5 MW of power. The largest hydroelectric power plants in Poland are Żarnowiec, Porąbka-Żar, and Solina power plants, the latter being a part of the Solina–Myczkowce hydroelectric power plant. All of them are pumped storage power plants. According to global forecasts, despite the rapid growth of photovoltaics and wind power, hydropower will remain the world's largest source of renewable electricity generation until 2030.

Keywords: *water, electricity production, hydropower plants*

Separation of Materials Containing Rare Earth Elements using Screening and Magnetic Separation

Rafał BARON[1)], Paweł FRIEBE[2)], Piotr MATUSIAK[3)], Daniel KOWOL[4)], Tomasz SUPONIK[5)]. Marcin LUTYŃSKI[6)]

[1)] KOMAG Institute of Mining Technology/Division of Preparation Systems, 37 Pszczyńska Street, 44-101 Gliwice, Poland; email: info@komag.eu; ORCID: https://orcid.org/0000-0002-7141-8960
[2)] KOMAG Institute of Mining Technology/Division of Preparation Systems, 37 Pszczyńska Street, 44-101 Gliwice, Poland; email: info@komag.eu; ORCID: 0000-0003-1574-6190
[3)] KOMAG Institute of Mining Technology/Division of Preparation Systems, 37 Pszczyńska Street, 44-101 Gliwice, Poland; email: info@komag.eu; ORCID: 0000-0002-9393-4309
[4)] KOMAG Institute of Mining Technology/Division of Preparation Systems, 37 Pszczyńska Street, 44-101 Gliwice, Poland; email: info@komag.eu; ORCID: 0000-0001-5547-376X
[5)] Silesian University of Technology/Faculty of Mining, Safety Engineering and Industrial Automation, 2 Akademicka Street, 44-100 Gliwice, Poland email: rg@polsl.pl; ORCID: 0000-0002-4251-4275
[6)] Silesian University of Technology/Faculty of Mining, Safety Engineering and Industrial Automation, 2 Akademicka Street, 44-100 Gliwice, Poland email: rg@polsl.pl; ORCID: 0000-0002-0379-3902

http://doi.org/10.29227/IM-2024-01-113

Submission date: 25-06-2024 | Review date: 08-07-2024

Abstract

This article presents research on selected materials with the aim of determining their rare earth element (REE) content and attempting to intensify it. The test material was coal slurry, which is a waste product from the operation of a preparation plant of a closed coal mine. Research on REE concentration intensification tests was carried out using magnetic separation. Laboratory analyses determining the REE content in the samples obtained, were carried out using the inductively coupled plasma ionisation mass spectrometry (ICP-MS) technique. Carrying out this research by the KOMAG Institute of Mining Technology, is a continuation of work related to making mining waste economically useful and determining a new source of REE recovery. Previous research and development work showed REE content (scandium 40.49 ppm) in the coal slurries studied. The result of the work carried out is the determination of the economic utility of REE recovery from the studied waste.

Keywords: *rare earth elements (REE), magnetic separation, coal tailings, coal slurries*

1 Introduction

Rare earth elements, REEs (rare-earth elements), are a group of elements of strategic importance, globally. Their importance is related to the need for their use in modern and advanced technologies. The European Union, including Poland, counts REEs among its 30 economically critical raw materials. According to forecasts, their demand is expected to double by 2060.[1] These elements are widely distributed in nature, but have low concentrations. Deposits that can be economically exploited are few in number and are mainly located in China resulting in the need to import these elements [1,2]. Therefore, many projects are underway to identify new sources of rare earth elements.

In a previous study, REEs with a varying distribution of REEs were shown to contribute to the REE distribution (coal samples, mineral aggregate, energy waste or metallurgical waste). The REE contribution was also shown to vary between the raw sample and the separated grain class in the range 0.045–0 mm [3–9].

This article contains the results of a completed study, extending previous research to determine the REE content of a material sample in specific grain classes. The research included an attempt to increase the concentration of REE content using magnetic separation, which separates material based on differences in magnetic susceptibility.

1.1. Rare earth elements

Rare earth elements, REEs (rare-earth elements), are a group of elements of strategic importance, globally. Their importance is related to the need for their use in modern and advanced technologies. The European Union, including Poland, counts REEs among its 30 economically critical raw materials. According to forecasts, their demand is expected to double by 2060.[1] These elements are widely distributed in nature, but have low concentrations. Deposits that can be economically exploited are few in number and are mainly located in China resulting in the need to import these elements [1,2]. Therefore, many projects are underway to identify new sources of rare earth elements.

In a previous study, REEs with a varying distribution of REEs were shown to contribute to the REE distribution (coal samples, mineral aggregate, energy waste or metallurgical waste). The REE contribution was also shown to vary between the raw sample and the separated grain class in the range 0.045–0 mm [3–9].

This article contains the results of a completed study, extending previous research to determine the REE content of a material sample in specific grain classes. The research included an attempt to increase the concentration of REE content using magnetic separation, which separates material based on differences in magnetic susceptibility.

Fig. 1. Mine heap from which the test sample was taken [own source]
Rys. 1. Hałda odpadów górniczych skąd pochodziły badane próbki

Tab. 1. Overview of the mass distribution of the granulometric classification of coal slurry
Tab. 1. Analiza składu ziarnowego mułów węglowych

No.	Number and identification of the sample	Grain class yield [%]
1.	P8 – Coal slurries >2.0 mm	3.6
2.	P7 – Coal slurries 2.0–1.0 mm	2.1
3.	P6 – Coal slurries 1.0–0.5 mm	11.3
4.	P5 – Coal slurries 0.5–0.25 mm	15.3
5.	P4 – Coal slurries 0.25–0.125 mm	20.5
6.	P3 – Coal slurries 0.125–0.063 mm	13.2
7.	P2 – Coal slurries 0.063–0.045 mm	3.6
8.	P1 – Coal slurries <0.045 mm	30.4
9.	Total	100

Tab. 2. Overview of mass distribution of granulometric classification of basalt aggregate
Tab. 2. Analiza składu ziarnowego kruszywa bazaltowego

No.	Number and Identification of the Sample	Grain Class Yield [%]
1.	P16 – Basalt aggregate >2.0 mm	14.0
2.	P15 – Basalt aggregate 2.0–1.0 mm	2.0
3.	P14 – Basalt aggregate 1.0–0.5 mm	5.8
4.	P13 – Basalt aggregate 0.5–0.25 mm	8.8
5.	P12 – Basalt aggregate 0.25–0.125 mm	12.2
6.	P11 – Basalt aggregate 0.125–0.063 mm	21.1
7.	P10 – Basalt aggregate 0.063–0.045 mm	31.0
8.	P9 – Basalt aggregate <0.045 mm	5.1
9.	Total	100.0

1.2. Magnetic separation

the magnetic separation process is a popular method used in rare earth processing. It is one of the first operations in the processing line (after crushing and grinding) to separate medium and low magnetic susceptibility minerals. (after crushing and grinding) with the aim of separating minerals with medium and low magnetic susceptibility. The product, with a concentrated content of the useful ingredient, is directed to the subsequent processing operations, mainly chemical. The efficiency of the process is highly dependent on:

(1) the strength of the magnetic field,
(2) the degree of loosening of the material layer fed to the separator,
(3) the magnetic susceptibility of the material,
(4) the size of the grains,
(5) the resistance posed by the grains (gravitational and frictional forces) [17,18].

Due to the varying magnetic susceptibilities of grains under the effect of a magnetic field, the material is divided into: paramagnetics, diamagnetics and ferromagnetics. Paramagnetic grains are attracted in the direction of the magnetic field strength, while diamagnetic grains are repelled. Ferromagnetic grains have a higher degree of magnetisation at lower magnetic field strengths, retaining a certain level of magnetism when isolated from the magnetic field.

This type of devices differs in design and in the medium in which the separation takes place (dry and wet separators), but the principle of operation, based on the magnet, is identical. Among others, magnetic wheels, hanging magnets, magnetic rotary drums or flat magnets are used. The principle of operation of dry magnetic separators is based on the use of a rotating drum with magnets. Feed material is transported via a conveyor belt underneath the drum, allowing magnetically susceptible grains to be separated by the magnetic field. The material with higher susceptibility is lifted through the magnetic drum and then placed in a separate hopper. It is possible to adjust the intensity of the magnetic field and thus change the separation limit due to the magnetic susceptibility of the grains [19].

Rare earth elements, with the exception of lanthanum, scandium, ytterbium, lutetium and yttrium, have magnetic susceptibility. REE minerals such as bastnazite, monazite and xenotime have varying magnetic properties, so it is possible to use magnetic separation to intensify the REE contribution [20].

1.3. Research carried out by itg komag related to REE

Due to the lack of REE deposits in Poland and their geopolitical value, it is necessary to identify alternative sources of REE. Work has been carried out at the KOMAG Institute of Mining Technology to determine REE content in the following groups of materials, mainly waste materials from their disposal sites:

(1) hard coals – analyses of type 31 thermal coal showed cerium content of 27.2 ppm (2019) [3],
(2) mining wastes – analyses of wastes constituting coal slurries showed a scandium content of 33.4 ppm (2020) [5],
(3) power plant energy waste – analyses of fly ash and power plant slags showed a cerium content of 34.0 ppm and yttrium content of 29.6 ppm (2019) [6],

Fig. 2. Magnetic separator – vibrating material feeder [own elaboration]
Rys. 2. Separator magnetyczny – podajnik wibracyjny nadawy

Fig. 3. Magnetic separator – reception of diamagnetic material [own elaboration]
Rys. 3. Separator magnetyczny – odbiór produktu magnetycznego

Tab. 3. Overview of outputs of magnetic separation products.
Tab. 3. Analiza wychodów produktów wzbogacania magnertycznego

Lp.	Number and Identification of the Sample	Grain Class Yield [%]
1.	P17 – paramagnetic product with higher susceptibility, coal slurries	0.46
2.	P18 – paramagnetic product with low susceptibility, coal slurries	1.41
3.	Non-magnetic product, coal slurries	98.1
4.	Summary	100
5.	P19 – paramagnetic product with higher susceptibility, basalt aggregate	7.3
6.	P20 – paramagnetic product with low susceptibility, basalt aggregate	12.9
7.	Magnetically not susceptible product, basalt aggregate	79.8
8.	Summary	100

(4) energy waste from landfills – analyses showed a neodymium content of 47.76 ppm (2020) [9],
(5) metallurgical waste – analyses of waste from sludge tanks showed a neodymium content of 17.3 ppm (2022) [21],
(6) mineral raw materials – testing showed a proportion of 45 ppm lanthanum in basalt (151.4 cerium in the finest grain class), 22.0 ppm scandium in halloysite, and 21.8 ppm scandium in sands [4,8],
(7) electronic waste – studies to determine the contribution of REE and attempts to recover elements from hard drives and wind turbine components (unpublished research).

In the present study, analyses were carried out with the application of magnetic separation, where again the REE content of the mining muds and natural aggregate was determined. The study was extended, compared to the previous stages of research, to determine the REE content of individual grain classes (classes differing in grain size).

2. Materials and methods

Material was extracted from the post-mining waste dumps of the DZW (Lower Silesian Coal Basin). The material deposited at the landfill is characterised by a diversified structure due to the method of its disposal and atmospheric influence. The material was collected from three selected locations of the landfill, representing different density structures (Figure 1).

Another test material is natural aggregate, i.e. basalt aggregate. This aggregate comes from the mine, which exploits a basalt deposit located in south-western Poland. This mine produces basalt aggregate in a range of grain sizes. The mine's deposit is excavated using drilling and blasting operations. The plant's technology includes multi-stage grading and crushing. The material used in the research is one of the mine's commercial products and is a 2–0 mm basalt aggregate.

In order to determine the content of rare earth elements in the extracted material, the following laboratory and research methods were used:
(1) granulometric classification and grinding,
(2) magnetic separation,
(3) analysis of REE content by ICP-MS for the obtained products of granulometric classification and magnetic separation.

2.1. Granulometric classification

Based on the results obtained in previous stages [7,9], the REE content was shown to vary according to grain size (grain class). The sieve analysis performed, yielded the following eight grain classes:
(1) >2.0mm.
(2) 2.0–1.0mm.
(3) 1.0–0.5mm.
(4) 0.5–0.25mm.
(5) 0.25–0.125mm.

Tab. 4. Overview of results of REE content in coal slurries, for individual grain classes

Tab. 4. Analiza zawartości REE w klasach ziarnowych, w odpadach węglowych

No.	Number and identification of the sample	Rare earth content [ppm].					
1.	P1 Grain class >2 mm	**Sc**	**Y**	**La**	**Ce**	Pr	Lu
2.		2.35	2.36	2.08	1.86	1.93	2.11
4.		Nd	Sm	Eu	Gd	Tb	**ΣREE**
5.		1.93	1.92	2.44	2.18	1.85	**34.44**
6.		Dy	Ho	Er	Tm	Yb	
7.		2.64	1.86	2.54	1.86	2.53	
8.	P2 Grain class 2–1 mm	Sc	Y	La	Ce	Pr	Lu
9.		2.69	2.72	2.4	2.15	2.22	2.43
10.		Nd	Sm	Eu	Gd	Tb	**ΣREE**
11.		2.22	2.21	2.81	2.52	2.14	**39.67**
12.		Dy	Ho	Er	Tm	Yb	
13.		3.04	2.15	2.92	2.14	2.91	
14.	P3 Grain class 1–0.5 mm	Sc	Y	La	Ce	Pr	Lu
15.		2.11	2.14	1.89	1.69	1.75	1.91
16.		Nd	Sm	Eu	Gd	Tb	**ΣREE**
17.		1.75	1.74	2.21	1.98	1.68	**31.2**
18.		Dy	Ho	Er	Tm	Yb	
19.		2.39	1.69	2.3	1.68	2.29	
20.	P4 Grain class 0.5–0.25 mm	Sc	Y	La	Ce	Pr	Lu
21.		2.68	2.72	2.39	2.14	2.21	2.42
22.		Nd	Sm	Eu	Gd	Tb	**ΣREE**
23.		2.21	2.2	2.8	2.51	2.13	**39.66**
24.		Dy	Ho	Er	Tm	Yb	
25.		3.03	2.28	2.91	2.13	2.9	
26.	P5 Grain class 0.25–0.125 mm	Sc	Y	La	Ce	Pr	Lu
27.		2.84	2.87	2.53	2.26	2.34	2.47
28.		Nd	Sm	Eu	Gd	Tb	**ΣREE**
29.		2.34	2.33	2.96	2.65	2.25	**41.69**
30.		Dy	Ho	Er	Tm	Yb	
31.		3.2	2.26	3.08	2.25	3.06	
32.	P6 Grain class 0.125–0.063 mm	Sc	Y	La	Ce	Pr	Lu
33.		2.44	2.47	2.17	1.94	2.01	2.11
34.		Nd	Sm	Eu	Gd	Tb	**ΣREE**
35.		2.01	2	2.55	2.28	1.93	**35.83**
36.		Dy	Ho	Er	Tm	Yb	
37.		2.75	1.94	2.65	1.94	2.64	
38.	P7 Grain class 0.063–0.045 mm	Sc	Y	La	Ce	Pr	Lu
39.		3.1	3.19	2.6	3	2.2	2.31
40.		Nd	Sm	Eu	Gd	Tb	**ΣREE**
41.		2.53	2.22	2.72	2.54	2.05	**41.27**
42.		Dy	Ho	Er	Tm	Yb	
43.		3.0	2.06	2.86	2.04	2.85	
44.	P8 Grain class <0.045 mm	Sc	Y	La	Ce	Pr	Lu
45.		3.47	4.12	3.04	4.29	2.39	2.38
46.		Nd	Sm	Eu	Gd	Tb	**ΣREE**
47.		3.19	2.45	2.88	2.81	2.13	**46.61**
48.		Dy	Ho	Er	Tm	Yb	
49.		3.12	2.16	3.05	2.11	3.02	

(6) 0.125–0.063mm.
(7) 0.063–0.045mm.
(8) <0.045mm.

The analyses were carried out using a laboratory wet vibrating classifier, in order to correctly separate the fine grains.

The very last material preparation process was to dry the samples in a laboratory dryer to get rid of moisture.

The products were assigned the following designation:

P1. coal slurries in the class >2.0 mm.
P2. coal slurries in the class <2.0–1.0 mm.
P3. coal slurries in the class <1.0–0.5 mm.
P4. coal slurries in the class <0.5–0.25 mm.
P5. coal slurries in the class <0.25–0.125 mm.
P6. coal slurries in class 0.125–0.063 mm.
P7. coal slurries in the class <0.063–0.045 mm.
P8. coal slurries in the class <0.045 mm.
P9. basalt aggregate in class >2.0 mm.
P10. basalt aggregate in class 2.0–1.0 mm.
P11. basalt aggregate in class 1.0–0.5 mm.
P12. basalt aggregate in class 0.5–0.25 mm.
P13. basalt aggregate in class 0.25–0.125 mm.
P14. basalt aggregate in class 0.125–0.063 mm.
P15. basalt aggregate in class 0.063–0.045 mm.
P16. basalt aggregate in class <0.045 mm.

The mass distribution (Tables 1 and 2) of the classification products obtained varied. The finest grains (<0.045mm) presented the highest yield among the analysed grain classes of coal slurry, and in the case of basalt aggregate, the grain 0.063–0.045mm had the highest proportion.

Prior to magnetic separation, the grain class >2mm was crushed in a laboratory grinder, due to the characteristics of the instrument and the testing process.

2. Magnetic separation

Based on information from the literature (magnetic dependencies of individual elements) [20], a magnetic separation test was carried out using a magnetic separator (Fig.2, 3).

Magnetic separation was carried out with the device set at 25V. The selected voltage value determines the magnetic field strength of the device. The value of 25V was chosen based on previous experience.

The separation process consisted of placing 90g (for each material) of raw material in a feeder, which was then transported by conveyor belt. The central separator structure contains a rotary magnet, which causes the separation of grains based on magnetic susceptibility. Three products were thus obtained – with higher, lower and material showing no magnetic susceptibility. The products showing magnetic susceptibility, lifted by the rotary magnet from the conveyor belt, were picked up by suitable slides, while the rest of the material

Tab. 5. Overview of results of REE content in basalt, for individual grain classes

Tab. 5. Analiza zawartości REE w klasach ziarnowych, w bazalcie

No.	Number and identification of the sample	Rare Earth Content [ppm].					
1.	P9 Basalt aggregate >2.0 mm	**Sc**	**Y**	**La**	**Ce**	Pr	Lu
2.		5.83	9.26	30.64	58.3	6.22	0.14
4.		Nd	Sm	Eu	Gd	Tb	**ΣREE**
5.		22.75	4.33	1.47	5.38	0.6	**151.23**
6.		Dy	Ho	Er	Tm	Yb	
7.		3.08	0.54	1.41	0.18	1.1	
8.	P10 Basalt aggregate 2.0–1.0 mm	Sc	Y	La	Ce	Pr	Lu
9.		7.67	10.84	38.08	69.02	7.14	0.17
10.		Nd	Sm	Eu	Gd	Tb	**ΣREE**
11.		26.13	4.99	1.68	6.23	0.69	**179.78**
12.		Dy	Ho	Er	Tm	Yb	
13.		3.5	0.61	1.58	0.21	1.24	
14.	P11 Grain class 1–0.5 mm	Sc	Y	La	Ce	Pr	Lu
15.		8.35	12.47	44.18	81.8	8.92	0.2
16.		Nd	Sm	Eu	Gd	Tb	**ΣREE**
17.		33.2	6.53	2.23	7.84	0.87	**215.25**
18.		Dy	Ho	Er	Tm	Yb	
19.		4.33	0.76	1.91	0.24	1.42	
20.	P12 Basalt aggregate 0.5–0.25 mm	Sc	Y	La	Ce	Pr	Lu
21.		6.08	10.65	41.3	80.82	8.38	0.16
22.		Nd	Sm	Eu	Gd	Tb	**ΣREE**
23.		30.94	5.95	2.03	7.11	0.75	**201.68**
24.		Dy	Ho	Er	Tm	Yb	
25.		3.77	0.66	1.62	0.22	1.24	
26.	P13 Basalt aggregate 0.25–0.125 mm	Sc	Y	La	Ce	Pr	Lu
27.		15.52	18.22	52.37	96.52	10.48	0.26
28.		Nd	Sm	Eu	Gd	Tb	**ΣREE**
29.		38.86	7.66	2.64	9.33	1.06	**264.16**
30.		Dy	Ho	Er	Tm	Yb	
31.		5.46	0.96	2.51	0.32	1.99	
32.	P14 Basalt aggregate 0.125–0.063 mm	Sc	Y	La	Ce	Pr	Lu
33.		17.03	16.42	42.89	80.12	8.67	0.25
34.		Nd	Sm	Eu	Gd	Tb	**ΣREE**
35.		32.46	6.54	2.24	7.97	0.92	**225.14**
36.		Dy	Ho	Er	Tm	Yb	
37.		4.68	0.82	2.12	0.28	1.73	
38.	P15 Basalt aggregate 0.063–0.045 mm	Sc	Y	La	Ce	Pr	Lu
39.		25.2	21.86	52.13	99.32	10.74	0.29
40.		Nd	Sm	Eu	Gd	Tb	**ΣREE**
41.		40.41	8.2	2.78	10.06	1.15	**284.14**
42.		Dy	Ho	Er	Tm	Yb	
43.		5.79	1.04	2.67	0.35	2.15	
44.	P16 Basalt aggregate <0.045 mm	Sc	Y	La	Ce	Pr	Lu
45.		21.85	31.37	82.89	165.06	17.53	0.42
46.		Nd	Sm	Eu	Gd	Tb	**ΣREE**
47.		61.93	12.02	4.08	14.55	1.62	**430.08**
48.		Dy	Ho	Er	Tm	Yb	
49.		8.12	1.45	3.73	0.5	2.96	

Tab. 6. Overview of total rare earth element contents of dry magnetic separation products

Tab. 6. Analiza zawartości REE w produktach wzbogacania magnetycznego

No.	Sample Identification	Raw material	Paramagnetic product with higher susceptibility		Paramagnetic product with lower susceptibility	
		Rare earth content [ppm].	Sample number	Rare earth content [ppm].	Sample Number	Rare Earth Content [ppm].
1.	Coal slurries	263.8	P17	**40.45**	P18	**36.29**
2.	Basalt aggregate	190.0	P19	**26.35**	P20	**212.87**

was removed from the machine using a brush. The resulting product yields are presented in Table 3. The yield of the non-magnetic product was calculated as the difference of 100% and the sum of the yields of the weaker and stronger magnetic products.

The products obtained, were sent to the Laboratory of Materials Engineering and Environment, ITG KOMAG, for determination of rare earth elements. These tests were performed using the ICP-MS method.

3. Materials and methods

Table 4 presents the detailed results of rare earth element content for each analysed grain size class of the coal slurries.

Table 5 presents the detailed results of rare earth element content for each analysed grain size class of the basalt.

Table 6 presents the summarised results of rare earth element content for each analysed magnetic separation product.

4. Discussion

The research found that 16 rare earth elements were included in the samples, with varying proportions of individual elements. To summarise the study of REE content in the individual grain classes of coal slurry, the summed contents of these elements are shown in Figure 4. and are as follows:

P1. (>2 mm)–34.44 ppm.
P2. (2–1 mm)–39.67 ppm.
P3. (1–0.5 mm)–31.2 ppm.
P4. (0.5–0.25 mm)–39.66 ppm.
P5. (0.25–0.125 mm)–41.69 ppm.
P6. (0.125–0.063 mm)–35.83 ppm.
P7. (0.063–0.045 mm)–41.27 ppm.
P8. (<0.045 mm)–46.61 ppm.

Separation of the coal slurries material into grain classes in the magnetic separator did not result in an increase in rare earth element concentrations. The 8 grain classes obtained

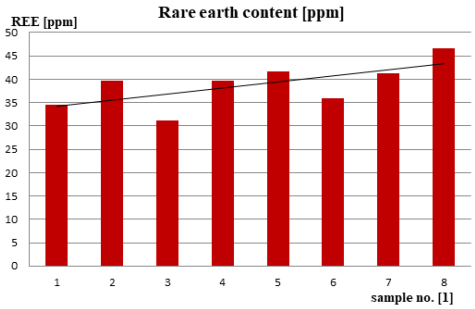

Fig. 4. Graph of REE content in coal slurries
Rys. 4. Zawartość REE w odpadach węglowych

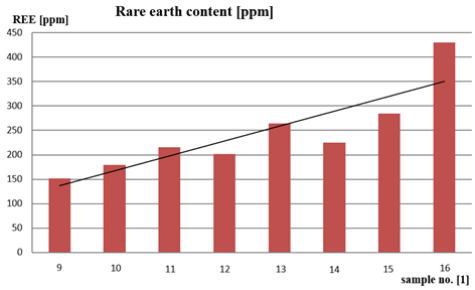

Fig. 5. Graph of REE content in basalt aggregate
Rys. 5. Analiza zawartości REE w próbkach bazaltu

have similar REE contents (average of 40.6 ppm). The highest REE content is represented by the finest grain classes, 0.063–0mm, and the 0.250–0.125mm grain class (above 41 ppm). The contribution of individual elements in the samples, which range from about 1.5 to just over 4 ppm, is negligible.

The total REE contents of the individual grain classes of basalt aggregate are as follows:

P9. (>2 mm)–151.23 ppm.
P10. (2–1 mm)–179.78 ppm.
P11. (1–0.5 mm)–215.25 ppm.
P12. (0.5–0.25 mm)–201.68 ppm.
P13. (0.25–0.125 mm)–264.16 ppm.
P14. (0.125–0.063 mm)–225.14ppm.
P15. (0.063–0.045 mm)–284.14 ppm.
P16. (<0.045 mm) – 430.08 ppm.

Based on the REE content of the different grain classes of basalt aggregate, the graph shown in Figure 5 was made.

The separation of the basalt aggregate into grain classes resulted in an increase in the concentration of rare earth elements in the finest grain classes. An increasing content of rare earth elements in the finest classes was observed. This observation is confirmed by the alignment of the trend line, which clearly increases towards the finest grain classes. The highest total rare earth element content was recorded for grain classes <0.045 mm and was 430.08 ppm. The lowest REE content was recorded for the grain class with the largest grain size and was 151.23 ppm.

Based on the summary of results in Table 6, it can be concluded that the dry magnetic separation had no effect for the coal slurries sample. The results obtained for the REE content are lower than for the raw material. Separation of the basalt aggregate resulted in a higher REE concentration in the less susceptible material to 212.87 ppm compared to the raw material content of 190.0 ppm. The more susceptible product showed a decrease in REE content to 26.35 ppm.

5. Conclusion

In the research carried out in this phase, the work programme consisted of determining new sources of rare earth elements in Poland, using coal slurries and basalt aggregate. The materials were selected and prepared for testing, which was then carried out by determining the proportion of REEs, using the ICP-MS technique.

The tests carried out showed the presence of rare earth elements in the samples analysed. Separation of the raw material into grain classes showed a disproportion of the sought after elements in the different grain classes. The REE content of the finest classes increased relative to the raw sample.

The lack of increase or low increase in rare earth elements in the susceptible products of the magnetic separation process may indicate that the intensity of the applied magnetic field in the equipment used is too low.

At present, the results obtained for the REE content of the samples analysed, do not represent the designated concentration of approximately 1000 ppm [22], which allows an economically viable separation.

The results obtained allow us to conclude that further research is required, by analysing the effect of increasing magnetic field on material separation with the intention of obtaining a product with a higher concentration of rare earth elements. In the further work of ITG KOMAG, related to the search for alternative sources of REE, further research is required using a magnetic separator with a higher field strength. It is also necessary to continue the search for a new group of materials that will contain a higher proportion of REE.

Literatura – References

1. Charalampides G., Vatalis K., Apostoplos B., Ploutarch-Nikolas B. Rare earth elements: Industrial applications and economic dependency of Europe. Procedia Economics and Finance, 2015, Vol. 24, pp.126–135. DOI: https://doi.org/10.1016/s2212-5671(15)00630-9.
2. Balaram V., Rare earth elements: A review of applications, occurrence, exploration, analysis, recycling, and environmental impact. Geoscience Frontiers, 2019, Vol.10, pp.1285–303. DOI: https://doi.org/10.1016/j.gsf.2018.12.005.
3. Baron R. Determination of rare earth elements content in hard coal type 31.1. Management Systems in Production Engineering, 2020, Vol.28, pp. 240–246 DOI: https://doi.org/10.2478/mspe-2020-0034
4. Friebe P., Determining the possibility of using the Polish aggregates for recovery of rare earth elements. Mining Machines, 2021, Vol.3p , pp. 34-43. DOI: 10.32056/KOMAG2021.2.4
5. Baron R., Matusiak P., Kowol D., Talarek M. The Concentration of Rare Earth Elements in the Polish Power Plant Wastes. Arch. Min. Sci, 2022, Vol. 67, pp.25-36. DOI: https://doi.org/10.24425/ams.2022.140700
6. Baron R. Determination of rare earth elements in power plant wastes. Mining Machines, 2020, Vol.4, pp.24-30. DOI: 10.32056/KOMAG2020.4.3
7. Baron R. Określenie koncentracji pierwiastków ziem rzadkich w poszczególnych klasach ziarnowych, dla wybranych materiałów. ITG KOMAG, 2020, (unpublished materials).
8. Friebe P. Tests of neodymium content in selected materials. Mining Machines, 2020, Vol.2, pp.38-47. DOI: 10.32056/KOMAG
9. Baron R. Assessment of rare earth elements content in the material from mine heaps. Mining Machines, 2021 Vol.3, pp.18-27. DOI: 10.32056/KOMAG2021.3.2
10. Mubashir M. Rare Earth Elements- A Review. Journal of Ecology & Natural Resources, 2018, Vol.2, pp.1-6. DOI: https://doi.org/10.23880/jenr-16000128
11. Kanazawa Y., Kamitani M. Rare Earth Minerals and Resources in the World, Journal of Alloys and Compounds, 2006, Vol.408-412, pp.1339-1343. DOI: https://doi.org/10.1016/j.jallcom.2005.04.033
12. Wiejaczka D., Wilczyński W.J. Strategiczne znaczenie metali ziem rzadkich, Przegląd Geopolityczny, 2021, Vol.36, pp.32-53.
13. Polski Instytut Ekonomiczny, Tygodnik Gospodarczy PIE, 2021, Vol.21
14. Kathryn M., Goodenough K.M., Wall F., Merriman D. The Rare Earth Elements: Demand, Global Resources and Challenges for Resourcing Future Generations, Natural Resources Research, 2018, Vol.27, pp.201–216. DOI: 10.1007/s11053-017-9336-5
15. https://www.researchgate.net/publication/349665394_Rare_Earth_Elements, accessed: 27.06.2023
16. https://www.poradnik-inwestora.pl/inwestowanie-metale-ziem-rzadkich/, access 27.06.2023
17. Cieśla A. Dynamiczne działanie pól: elektrycznego i magnetycznego w elektrotechnologiach (na przykładzie separacji). Prace Instytutu Elektrotechniki, 2007, Vol.233, pp.81-93
18. Lewicka E. Innowacyjne technologie produkcji surowców skaleniowych. Górnictwo Odkrywkowe, 2011, Vol.6, pp.115-120
19. Zong Q. Variables and Applications on Dry Magnetic Separator, E3S Web of Conferences 53, 2018. DOI: 10.1051/e3sconf/20185302019.
20. Abaka-Wood G.B., Addai-Mensah J., Skinner W. Review of Flotation and Physical Separation of Rare Earth Element Minerals, 4th UMaT Biennial International Mining and Mineral Conference, 2016, pp. MR55-62.
21. Baron R. Results of pilot research work on the content of rare earth elements in metallurgical wastes from Nowa Huta, Inżynieria Mineralna. 2022, Vol.1, pp.123—127. DOI: 10.29227/IM-2022-01-15
22. Hordyńska M. Popioły elektrowniane w procesach stabilizacji odpadów niebezpiecznych, Doctoral thesis, Wydz. Inżynierii Materiałowej i Metalurgii, Politechnika Śląska, 2003.

Rozdział surowców zawierających pierwiatki ziem rzadkich w procesach przesiewania i separacji magnetycznej

W artykule przedstawiono badania wybranych materiałów mające na celu określenie zawartości pierwiastków ziem rzadkich (REE) oraz próbę ich wzbogacania. Materiałem badawczym była zawiesina węglowa, która jest produktem odpadowym z eksploatacji zakładu przeróbczego zamkniętej kopalni węgla kamiennego. Badania nad testami wzbogacania REE przeprowadzono z wykorzystaniem separacji magnetycznej. Analizy laboratoryjne określające zawartość REE w pobranych próbkach przeprowadzono z wykorzystaniem techniki spektrometrii mas z jonizacją plazmą wzbudzoną indukcyjnie (ICP-MS). Przeprowadzenie tych badań przez Instytut Techniki Górniczej KOMAG jest kontynuacją prac związanych z ekonomiczną przydatnością odpadów górniczych oraz określeniem nowego źródła odzysku REE. Poprzednie prace badawczo-rozwojowe wykazały zawartość REE (skand 40,49 ppm) w badanych zawiesinach węglowych. Wynikiem przeprowadzonych prac jest określenie ekonomicznej użyteczności odzysku REE z badanych odpadów.

Słowa kluczowe: *pierwiastki ziem rzadkich (REE), separacja magnetyczna, odpady węglowe, zawiesiny węglowe*

An Overview of Sustainable Mining Practices for Ecological Rehabilitation of Degraded Lands in the Rovinari Mining Basin (Romania). Case Study: North Pesteana Interior Dump

Izabela-Maria APOSTU[1)], Maria LAZĂR[2)], Florin FAUR[3)], Eugen TRAISTĂ[4)]

[1)] Assist. Prof. Dr. Eng.; University of Petroşani, Faculty of Mining, Department of Environmental Engineering and Geology; email: izabela-apostu@upet.ro, corresponding author; ORCID: https://orcid.org/0000-0002-6456-6148
[2)] Prof. Dr. Eng.; University of Petroşani, Faculty of Mining, Department of Environmental Engineering and Geology; email: marialazar@upet.ro; ORCID: https://orcid.org/0000-0003-2149-6415
[3)] Assoc. Prof. Dr. Eng.; University of Petroşani, Faculty of Mining, Department of Environmental Engineering and Geology; email: florin-faur@upet.ro; ORCID: https://orcid.org/0000-0002-0880-0913
[4)] Assoc. Prof. Dr. Eng.; University of Petroşani, Faculty of Mining, Department of Environmental Engineering and Geology; email: eugen-traista@upet.ro; ORCID: https://orcid.org/0000-0001-6680-5299

http://doi.org/10.29227/IM-2024-01-114

Submission date: 26-07-2023 | Review date: 12-07-2024

Abstract

Open-pit mining, regardless of the nature of deposit and the exploitation type (continuous or discontinuous), produces long-term negative effects on the environment. The immediately visible effects are related to the changes in the morphological configuration and the landscape: the disappearance of the plant cover and topsoil on the entire surface of the mining perimeter, the development of deep open-pits, the appearance of waste dumps, the construction of premises and technological roads, etc. The uncovering of a deposit is carried out by removing the vegetation and excavating the soil, followed by the excavation of the sterile material from the deposit's roof, and is a destructive action with consequences for the local habitat and fauna on long term and sometimes, unfortunately, the effects can be hardly reversible or even irreversible. The environmental component that suffers the most as a result of mining is the soil and with it the entire ecosystem in the area. Soil is a resource that is very difficult to regenerate. Natural soil formation takes a long time, tens and hundreds of years. Therefore, it is important to find and apply solutions to maintain or improve its quality whenever possible or to support the pedogenesis process by applying sustainable practices in order to accelerate it. Some of these practices can be applied even during mining activities. The purpose of this research is to find and recommend the best solutions that can be applied in different stages of the lifecycle of a mine and which, applied together, have a synergistic role and a remarkable effect on the pedogenesis process and on its duration. That is why it is very important to design the mining activity from opening to closing, taking into account the decommissioning of buildings, the rehabilitation and revegetation of degraded lands for the subsequent inclusion in the landscape and the resumption of its functions.

Keywords: *degraded lands, sustainable mining, sustainable practices, anthropogenic soil, pedogenesis, industrial ecology*

1. Introduction

The high level of resource consumption and its continuous growth is amplified by the demographic explosion produced since the middle of the 21st century, registering a tripling of the number of inhabitants of the planet (Wilmoth et al., 2022; Haiwen, 2019). Today, more than 8 billion people live and this number is expected to reach 9 billion by the year 2040. With the demographic explosion and the intensification of industrial processes, the negative impact on the environment has been amplified. As long as only economic development is pursued, without considering the impact on the environment and society, unintended consequences may arise, many of which are irreversible. The intense exploitation of non-renewable resources accentuates the tendency of their exhaustion.

Topsoil (or vegetal soil) is an extremely valuable resource having an essential role in supporting life. The quality and quantity of the soil is affected by human actions carried out day by day, and even more by mining operations.

Instead of natural topsoils, in the mining perimeters and on the related aste dumps, very diverse lithological materials are encountered from a physical, chemical and especially pedological point of view, materials that constitute anthropogenic protosoils. These types of soils lack the essential feature specific to an evolved soil: fertility (Howard, 2017; Zanella et al., 2018; Schaetzl and Anderson, 2005).

Anthropogenic protosoils called anthrisoils are formed on the waste dumps related to the open-pit mining and fall into the class (IX) of undeveloped soils according to (Florea and Munteanu, 2012).

The fact that this resource is difficult to regenerate and that these actions cannot be prevented or removed, requires the finding of appropriate management and exploitation solutions in harmony with the environment. The purpose of the work is to look for sustainable solutions that can be applied from the first stages of the life cycle of a mine and which can ensure the maintenance of soil quality or support the acceleration of the pedogenesis process on waste dumps, but also the quality of the environment in general.

According to the definition of sustainable development, mining activity, which represents the engine of a society's

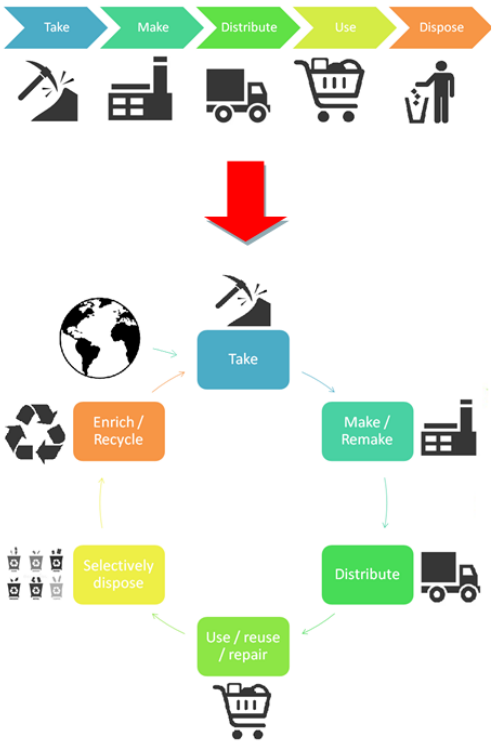

Fig. 1. Linear economy model versus circular economy model
Rys. 1. Model gospodarki liniowej a model gospodarki o obiegu zamkniętym

development, is not a sustainable activity, which is why it is necessary to extrapolate this concept. There is no definition of sustainability that is universally adopted by the mining industry. There are many discussions on this topic, but there are difficulties in applying sustainable development strategies in the mining context, the reasons cited being the multitude of interpretations of this concept of sustainable development.

Applying sustainable practices in the mining industry may sound like an oxymoron. Although the two terms are seemingly incompatible, as long as we do not put an end to the consumption of resources, mining will never end. Sustainable development in the mining sector means that such projects must be financially profitable, technically appropriate, environmentally reasonable and socially responsible (Melan, 2021; Aznar-Sánchez et al., 2019, Hebda 2023). Thus, the best way for the mining industry to coexist with the environment for the purpose of a sustainable development of society from all points of view, is to establish and implement the best sustainable practices applied in conditions of maximum safety and which focus on obtaining favorable results from the point of view of the economy, the environment and the community (Hilson and Murck, 2000; Lazăr, 2010; Miranda et al., 2005; Bastida and Aguado, 2008). At the same time, mining must be in harmony with community expectations, which recognize that the business has a shared responsibility with government and wider society to help facilitate the development of strong and sustainable communities (UNDP, 2018).

The need to redefine the concept of "sustainable development" so as to include the mining industry is even bigger since it is clear to us that ceasing any mining activity is not a feasible choice, given that humanity has and will continue to need mineral raw materials.

Some solutions can be identified by exploring more carefully the concept of industrial ecology, which is relatively recent but still developing. It involves multidisciplinary research combining aspects of engineering, economics, sociology, toxicology, and natural sciences and aims to quantify and document the flow of matter and industrial processes in modern society, focusing on the impact of industrial activities on the environment, taking into account the use and exploitation of natural resources, manufacturing and processing and, crucially, issues involving the storage and/or disposal of waste (Bruel et al., 2018; Cecchin et al., 2020; Walker et el., 2021).

Industrial ecology seeks to understand how industrial activities interact with natural ecosystems. In this context, the idea is promoted that natural systems never leave waste, thus inspiring a sustainable model, where “nothing is lost, nothing is created, everything is transformed” – Antoine Lavoisier.

Industrial ecology looks over the transition from a linear industrial and consumption process (extraction, manufacture, consumption, waste) to a circular one (extraction, manufacture, consumption, recycling or reuse – the concept of circular economy; fig. 1) system in which waste can become resources for new processes, thus minimizing the extraction and consumption of resources. Therefore, the concept of industrial ecology is closely related to that of circular economy (Pont et al., 2019; Sariatli, 2017; Brian, 2004)

Integrating into the process of sustainable industrial development of the main objective of industrial ecology (establishing sustainable practices and responsible methodologies), can lead to an increased level of sustainability of the mining activities.

2. Sustainable solutions and practices in mining industry

For increased efficiency, sustainable practices must be established and applied for each stage of the mining activity. Life cycle analysis identifies those particular aspects that have

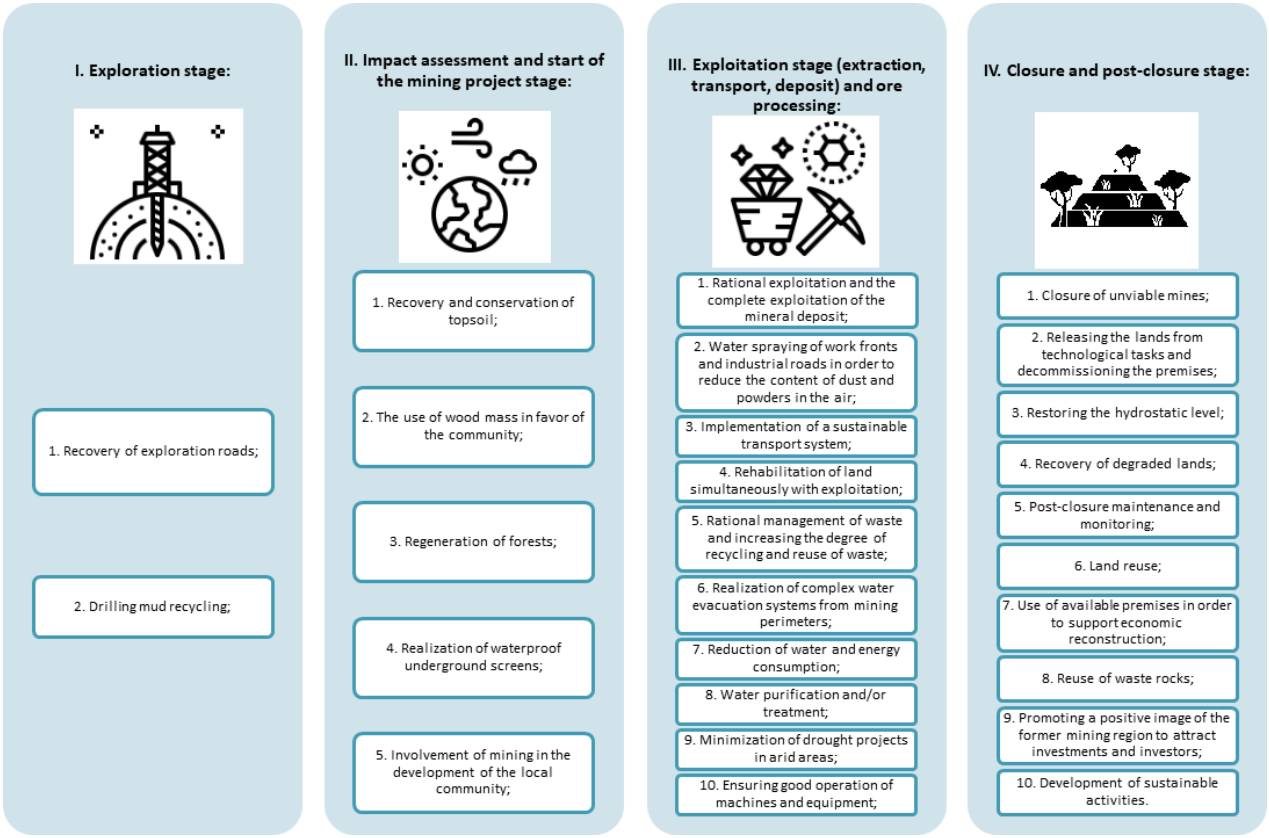

Fig. 2. Sustainable mining practices depending on the main stages of a mining project
Rys. 2. Praktyki zrównoważonego górnictwa w głównych etapach projektu górniczego

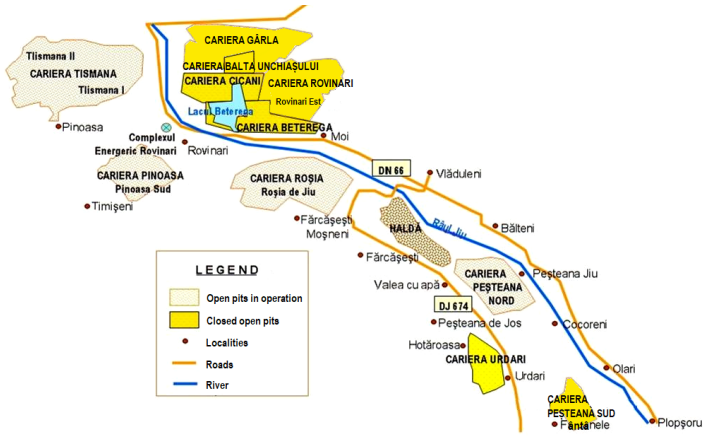

Fig. 3. Rovinari Mining Basin situation plan (***, CEO, 2019–2023)
Rys. 3. Plan sytuacyjny Zagłębia Górniczego Rovinari (***, CEO, 2019–2023

a significant impact on the environment. Thus, the emphasis is placed on the essential aspects involving the reduction of the impact of mining on the environment in the main stages of the life cycle of a mine (Bastida, 2004).

Following the documentation and research carried out (Nyari, 2016; Fodor and Lazăr, 2006; Hilson and Murck, 2000; Lazăr, 2010; Miranda et al., 2005; Bastida and Aguado, 2008; ***, 2006; ***, 2011), several solutions and practices have been identified that can ensure a sustainable development of the mining sector depending to the main stages of a mining project (fig. 2):

In order to intensify the development of mining while improving the ecological, economic, and social sustainability of the mining sector, emphasis must be placed on the application of sustainable practices in all stages of a mining project, from exploration to closure and post-closure, practices that involve reducing the consumption of mineral resources, increasing the degree of resource conservation, recycling and reusing waste and minimizing the impact on the environment.

3. Mining and mining degraded lands in Rovinari Basin - Romania

The Rovinari Mining Basin is located in Gorj county (Romania), in the Rovinari town area. The component mining perimeters (fig. 3) were located on both sides of the Jiu River, in the river meadow area, but also in the hilly areas of the region.

Fig. 1. Linear economy model versus circular economy model

Rys. 1. Model gospodarki liniowej a model gospodarki o obiegu zamkniętym

Mining perimeter	Mining perimeter surface (ha)	Waste dump surface (ha)*
North Pește ana	1176.2	≈ 500
Roșia de Jiu	1738.8	≈ 800
Pinoasa	1581.4	≈ 1000
Tismana I+II	1712.2	≈ 1000
Total	**6208.6**	**≈ 3300**

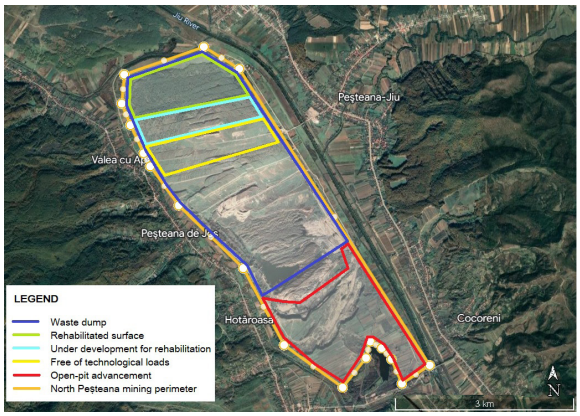

Fig. 4. North Pește ana mining perimeter (***, CEO, 2019–2023)

Rys. 4. Wyrobisko North Pește ana (***, CEO, 2019–2023)

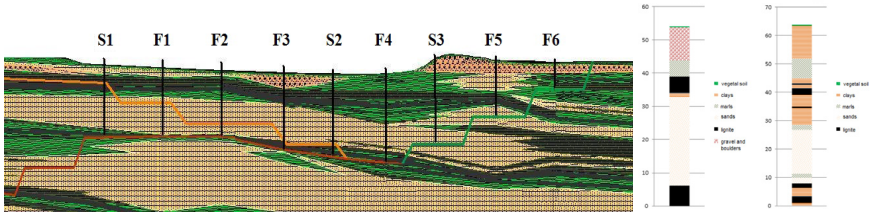

Fig. 5. Location of boreholes and sections and representation of two stratigraphic columns from the Pește ana Nord mining perimeter (Apostu, 2021)

Rys. 5. Lokalizacja otworów i przekrojów oraz przedstawienie dwóch kolumn stratygraficznych z obwodu górniczego Pește ana Nord (Apostu, 2021)

Over time, 12 opne-pits have been put into operation in the Rovinari Mining Basin. Currently, only 5 open-pits are still operational, being united in 4 open-pit mining units (U.M.C.): U.M.C. Tismana (Tismana I + II), U.M.C. Pinoasa, U.M.C. Rosia, and U.M.C. North Pește ana. The other open--pits, Cicani, Balta Unchiașului, Beterega, Urdari, Pește ana Sud, Gârla, and Rovinari Est, ceased their activity as a result of the exhaustion of reserves or the fact that exploitation was no longer technically and economically efficient. Among the closed open-pits, some are used as storage for slag and ash from the Rovinari thermal power plant, others have been returned to the forestry or productive circuit or have reintegrated into the landscape naturally.

Table 1 shows the total surfaces of the active mining perimeters in the Rovinari Mining Basin.

The area of the mining perimeter represents the total area of degraded mining lands (open-pits, dumps, access/technological roads, and other areas occupied by buildings and premises). Of the total area of the 4 active quarry mining units (6208.6 ha), approx. 50% are areas occupied by internal and external waste dumps (***, CEO, 2019–2023).

Considering the size of the Rovinari Mining Basin, but also the lithological constitution of the region, the physical, chemical, and pedological characteristics of the sterile rocks, the mining/dumping methods similar throughout the basin, it was chosen to conduct a case study on the North Pește ana mining perimeter regarding the sustainable practices that can be implemented in order to support and accelerate the pedogenesis process on the waste dumps, considering that the results obtained can be easily extrapolated at least at the level of this basin.

3.1 Case study: North Pește ana mining perimeter

The opening of the North Pește ana open-pit began in 1980s and it is estimated that the exploitation of lignite in this perimeter will cease in 2024 as a result of the exhaustion of the reserve in the license perimeter (***, CEO, 2019–2023; ***, ICSITPML, 2012; ***, ME, 2016).

From an administrative point of view, the perimeter of the North Pește ana open-pit falls within Gorj county, being located within the territory of the Urdari and Bâlteni communes.

From a morphological point of view, the exploitation perimeter of the North Pește ana open-pit is located entirely in the Jiu river meadow area. The minimum altitudes are found in the eastern part of the perimeter, on the old bed of the Jiu river, where the elevation of the land has values between 132 - 136 m. On the western frame, the altitudes have values of 148–150 m. The maximum altitude is 333 m in Bran hill. (Smeu, 2012)

Currently, the excavation activity in the North Pește ana open-pit (fig. 4) is carried out in four excavation steps.

Figure 5 shows the geological profile in longitudinal section of the North Pește ana open-pit and the representative lithology in which sandy, clayey, marly rocks, gravels and boulders predominate, layers between which the exploitable

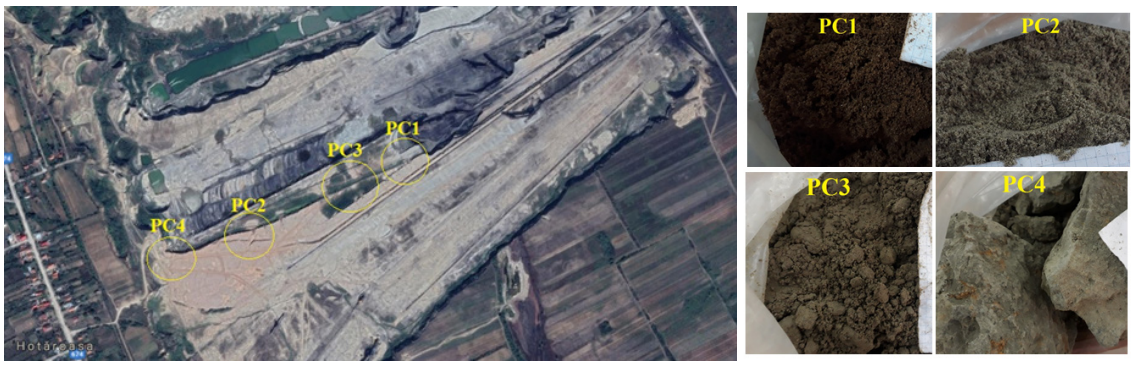

Fig. 6. Sampling points – in-situ slopes
Rys. 6. Punkty poboru próbek – uskoki in-situ

Fig. 7. Sampling points – waste dump
Rys. 7. Punkty poboru próbek – składowisko odpadów

lignite layers are intersposed.

The exploitable layers in the North Peșteana area are layers V–VIII. Excavation is done in parallel blocks, with a width of 40÷45 m. Excavation is carried out with 4 excavators with bucket-wheel excavators. The extracted material is dumped on the front lanes (conveyor belts). Their direction of operation is from west to east, with the distribution equipment located at their end, positioned to discharge either on one of the conveyors in the sterile transport circuits, or on the conveyor in the lignite transport circuit, depending on the excavated rock, respectively sterile or useful.

The sterile rocks from the North Peșteana open-pit are deposited in the internal waste dump with 2 dumping machine. The lignite is stored in the Cocoreni coal deposit located on the right bank of the Jiu River, from where it is delivered to consumers.

3.2 Physical, machanical and podologycal characteristics of sterile rocks

The quality of the topsoil in the mining perimeters is negatively modified by the direct and related activities of lignite exploitation.

In the North Peșteana perimeter, as in the entire basin, the soil is selectively extracted, but it is not enough for revegetation, so it is necessary to analyze the rocks in the intercalations from the point of view of their capacity to represent, under certain conditions, soil substitutes.

To determine the values of the physical characteristics of the rocks from the slopes of the North Peșteana perimeter, 14 samples were taken, 4 samples from the in-situ slopes (PC1 ÷ PC4) and 10 samples from the internal dump (PH1 ÷ PH10) (fig. 6-7; Apostu, 2021).

The physical characteristics of the rocks, resulting from the tests, are shown in table 2 (Apostu, 2021). The rock samples taken were described based on the results as follows: PC1 – Sand (predominantly medium); PC2 – Sand (mainly fine); PC3 – Clayey dusty sand; PC4 – Sandy clay; PH1 – Sandy clay; PH2 – Dusty sand; PH3 – Sand with gravel elements; PH4 – Clay dust; PH5 – Dust; PH6 – Sand (mainly fine) with rare elements of gravel; PH7 – Sand with elements of clay and gravel; PH8 – Sand with elements of clay and gravel; PH9 – Carboniferous rock in dusty clay mass; PH10 – Sand (mainly coarse) with elements of gravel.

According to some research carried out within North Peșteana mining perimeter (Nanu, 2015), the results of the chemical and pedological analyzes carried out on sterile material from the in-situ slopes (P1), the internal dump (P2), and the external dump (P3) show that, according to (Dumitru et al., 2011), they fall into normal load classes (tab. 3) in terms of the content of heavy metals, fluorine, cyanides, phenols, sulfates and hydrocarbons. From a pedological point of view, the waste material is moist to dry (but this characteristic also depends on the weather-climatic conditions), almost totally devoid of humus, generally has a low content in macronutrients (according to DOA, 1997 and Malek et al., 2006 results in a very low N content, low to very low P and moderately to high K) and a moderately acidic pH reaction. The results indicate a reduced cation exchange capacity, the

Tab. 2. Physical characteristics of the waste rocks (Apostu, 2021)

Tab. 2. Charakterystyka fizyczna skały płonnej (Apostu, 2021)

Sample no.	Provenance	Particle size composition, [%]				INDICES OF THE NATURAL STATE												
						Laboratory tests			Calculated				Laboratory tests		Calculated			
		Clay	Dust	Sand	Gravel	Volumetric weight, γ_a [kN/m^3]	Specific weight, γ_s [kN/m^3]	Natural humidity, w [%]	Porozity, n [%]	Pores index, ε	Saturation humidity, w_{sat} [%]	Saturation coefficient, S	Flow limit, W_c [%]	Plastic limit, W_{pl} [%]	Plasticity index, I_p	Consistency index, I_c	Consistency index in saturated state, I_{csat}
PH1	interior dump	24	28	42	6	19.52	26.30	21.68	39.00	0.64	24.33	0.89	36	16.74	19.26	0.74	0.61
PH2		-	38.5	61.5	-	20.56	26.67	23.27	38.38	0.62	23.27	1.00	-	-	-	-	-
PH3		-	-	91	9	20.69	26.67	22.87	37.99	0.61	22.87	1.00	-	-	-	-	-
PH4		20	43	27	10	20.21	26.26	22.47	37.17	0.59	22.47	1.00	37	16.23	20.77	0.70	0.70
PH5		10	55	33.5	1.5	17.77	25.97	20.58	43.24	0.76	29.26	0.89	44	22.73	21.27	1.1	0.67
PH6		-	-	99.5	0.5	15.99	26.64	5.65	43.19	0.76	28.53	0.2	-	-	-	-	-
PH7		-	-	73	27	17.59	26.72	15.19	42.85	0.75	28.07	0.54	-	-	-	-	-
PH8		-	-	78	22	18.82	26.48	18.59	40.07	0.67	25.30	0.73	37.8	22.64	15.16	1.27	0.82
PH9		41	52	7	-	17.40	26.22	27.97	48.14	0.93	35.47	0.79	53.8	24.71	28.09	0.89	0.63
PH10		-	-	89.5	10.5	17.71	26.46	7.24	37.59	0.6	22.68	0.32	-	-	-	-	-
Average		23.75	43.3	60.2	10.8125	18.626	26.439	18.551	40.762	0.693	26.225	0.736	-	-	-	-	-
PC1	intercalations (in-situ slopes)	-	-	100	-	16.10	26.61	7.49	43.71	0.78	29.31	0.255	-	-	-	-	-
PC2		-	-	100	-	15.72	26.64	3.65	43.07	0.76	28.53	0.13	-	-	-	-	-
PC3		7.5	27.5	65	-	19.70	27.11	23.53	41.17	0.7	25.82	0.91	-	-	-	-	-
PC4		33	17	50	-	20.03	26.32	8.44	29.82	0.42	15.96	0.53	47.2	34.95	12.25	3.16	2.55

analyzed samples being prone to acidification (which explains their moderately acidic reaction and low nutrient content).

Tab. 3. Analysis bulletin – sterile material from the North Peșteana perimeter (Nanu, 2015). P1 – in-situ slopes, P2 – interior dump, P3 – external dump

From the process of lignite exploitation through open-pit mining works, there are no emissions of heavy metals that pollute the soil or water (surface or groundwater). The waste resulting from the production process of the lignite extraction units through open-pit mining works – waste dumps – fall into the category of inert-non-hazardous waste deposits. The waste will not undergo any significant disintegration or dissolution or any other significant change that may cause an adverse effect on the environment or harm human health (***, ICSITPML, 2012).

4. Implementation of sustainable practices for ecological rehabilitation of degraded lands on North Peșteana interior dump

4.1 Mining opening stage

In the opening stage of a mining project, numerous changes take place at the level of the local ecosystem, and some of the steps that minimize the impact on the environment and recover a valuable resource are represented by the extraction of topsoil and the regeneration of forests by recovering and planting saplings of trees and shrubs from the lands in the advance areas of the open-pit.

4.1.1 Recovery and conservation of topsoil

Soil management is an important step in the mining activity. Being essential for the development of plants, but difficult to regenerate, it is required to extract it from the lands to be discovered in order to exploit mineral resources, transport and store it in specially spaces, under optimal conditions, or extract it and deposit it immediately on degreaded lands undergoing rehabilitation.

The extraction of topsoil can be done before the discovery of the deposit or simultaneously with the discovery. The most important aspect to check is the thickness of the topsoil layer, according to which the extraction technology is established. Determining the thickness of the topsoil, in order to establish the procedure for removing it, is done manually (pits or trenches). The method of excavating the soil depends on its thickness and is carried out either with bulldozers and scrapers when the soil thickness does not exceed 1 m, or with mechanical shovel excavators or bucket-wheel excavators, when the soil thickness is greater than 1 m. Transport of the topsoil is done by road or rail means or by means of conveyor belts.

Based on the geotechnical boreholes (F1–F6; ***, ICSITPML, 2012) and the sections (S1, S2, S3; Apostu, 2021) drawn in the areas of interest, the stratigraphic columns were made (see fig. 5). The thickness of the topsoil varies between 0.4 and 0.8 m, and the determinations of the physical, chemical and pedological characteristics indicate a good quality and the opportunity to recover the topsoil from on the site studied. Based on this information, it is recommended to take into account the importance of recovering this extremely useful resource by applying the method of extracting the topsoil simultaneously with the discovery with the help of the bulldozer in independent flow (fig. 8).

Tab. 3. Analysis bulletin – sterile material from the North Peşteana perimeter (Nanu, 2015). P1 – in-situ slopes, P2 – interior dump, P3 – external dump

Tab. 3. Wyniki analiz – materiał z North Peşteana (Nanu, 2015)

Chemical analysis							Pedologycal analysis					
Parameter	UM	Limit		Determined value			Parameter	UM	Determined value			Observations
		Alert	Interventio n	P1	P2	P3			P1	P2	P3	
Total cadmium	mg/kg	5	10	0.65	3.0	1.8	pH	unit. pH	5.4	5.6	5.5	moderately acidic
Total lead	mg/kg	250	1000	1.20	3.4	3.2	Combustible parts	%	7.1	7.6	5.6	traces of lignite
Fluorine	mg/kg	500	1000	0	0	0	Moisture	%	35	51	48	wet to dry
Free cyanides	mg/kg	10	20	0	0	0	Humus	%	0	0	2.3	very low to total absence
Phenols	mg/kg	10	40	3	2	0	Bases of exchange	me/ 100 g	2.62	5.85	2.87	reduced
Tone	mg/kg	5000	50000	-	0	-	Exchange cations	me / 100 g	2.15	7.21	3.65	reduced
Polycyclic aromatic hydrocarbons	mg/kg	25	150	2	0	0	Total exchange capacity	me / 100 g	4.77	13.06	6.52	reduced
Petroleum hydrocarbons	mg/kg	1000	2000	75	0	0	assimilable N	%	0.05	0.15	0.10	very low
Copper	mg/kg	250	500	1.10	8.2	6.5	assimilable P	mg %	0.8	1.9	1.2	low to very low
Nickel	mg/kg	200	500	0.35	2.5	2.1	assimilable K	mg %	4.5	6.3	7.2	moderate to high
Zinc	mg/kg	700	1500	8.3	8.6	9.3	-	-	-	-	-	-
Manganese	mg/kg	2000	4000	6.5	10.5	14.6	-	-	-	-	-	-
Chromium	mg/kg	300	600	0.35	1.40	1.35	-	-	-	-	-	-

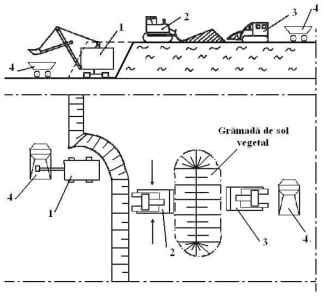

Fig. 8. Extraction of topsoil using the bulldozer in independent flow (Lazăr, 2010): 1 – mechanical shovel excavator; 2 – bulldozer; 3 – bucket loader; 4 – dumping machine

Rys. 8. Zdejmowanie wierzchniej warstwy gleby za pomocą spychacza (Lazăr, 2010)

According to (***, CEO, 2019-2023), as a result of the non-uniformity of the land and the reduced thickness of the topsoil layer, a volume of approximately 500,000 m³ of topsoil was recovered from an area of 137.34 ha.

4.1.1 Regeneration of forests through the recovery of saplings of trees and shrubs

The intensification of the forest regeneration process is possible by starting some projects that involve the afforestation of land areas at least equal to the deforested area for mining. The recovery of saplings of trees and shrubs and their replanting to expand the area of the forest fund by afforestation of lands without forest vegetation, which have no other assigned uses, is a sustainable and cheap solution.

Through forest regeneration activity, the aim is to ensure the integrity and permanence of forests, so as to reduce the current trend of uncontrolled deforestation, depletion of woody mass and/or loss of forests, giving them continuity in terms of production and protection functions.

Such programs existed in the entire Oltenia coal basin (of which Rovinari is also a part). Until 1989s–1990s, the mining operator proceeded to afforest equivalent (even larger) areas, through so-called compensatory afforestation actions, throughout the country (especially in the Moldova area).

4.2 Exploitation stage

4.2.1 Rehabilitation of degraded land simultaneously with the continuation of exploitation

The lignite exploitation activity must ensure the return of the productivity of the affected land as quickly as possible (Ghose, 1989; Ghose, 2005).

The rehabilitation process must start, as far as possible, immediately after the release of the areas of technological burdens, and the opening of the deposit is done progressively, on relatively small areas, enough to ensure the necessary space and allow exploitation to advance to a new front (fig. 9).

In the North Peşteana open-pit, rehabilitation works were carried out on the degraded lands as a result of the construction of the dumps, but in a small percentage. Out of a total area proposed for greening of 637.17 ha (internal dump + external dump), only 90 ha were greened (plantation establishment on the external dump located in the northern part of the perimeter), representing 14.1%. Currently, an area of 65 ha is unde development for rehabilitaion, and another of 73.5 ha is an area free of technological loads, which will also be greened (see fig. 1; ***, CEO, 2019–2023).

The main advantage is that of saving time in favor of the environment, the closure being done immediately after the end of the exploitation of a work front and its release, thus reducing the size of the degreaded land surface, the degree of pollution of environmental factors, and implicitly, the impact on the environment.

Fig. 9. Scheme for the rehabilitation of degraded land simultaneously with the continuation of exploitation (Feng et al., 2019)
Rys. 9. Schemat rekultywacji terenów zdegradowanych przy jednoczesnej kontynuacji eksploatacji (Feng et al., 2019)

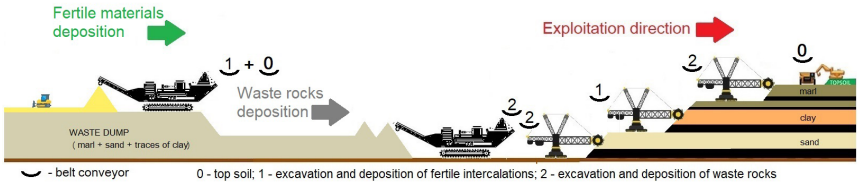

Fig. 10. Scheme of selective exploitation and directed deposition of waste rocks depending to its quality
Rys. 10. Schemat selektywnej eksploatacji i ukierunkowanego składowania skały płonnej w zależności od jej jakości

The rehabilitation of the land also involves leveling, compaction, modeling, revegetation, but also works to restore the hydrostatic level so that the effects of the dewatering are not felt on the reclaimed land surfaces nor in the areas adjacent to the mining perimeter.

4.2.2 Reuse of sterile rocks

In the idea of sustainable development, it is essential to increase the degree of recovery and reuse of waste. Recovery means the extraction of resources from waste that can be reused. Recovery can be done through recycling, reuse, regeneration or any other process of extracting auxiliary raw materials, through which either the material part or the energetic part can be recovered. When it no longer presents any possibility of valorization, it is necessary to dispose of the waste. This process must be done by methods that are not harmful to the environment and do not endanger human health.

4.2.3 Directions for accelerating the restoration of the fertile potential of the lands on the waste dumps

An increasingly studied variant is the use of waste in the pedogenesis process, inert clay and clay-sandy rocks constituting a good base of inorganic matter for the reconstitution of topsoil when it is mixed with biodegradable organic matter and enriched with nutrients necessary for plant growth and life support. Starting from this idea, it is recommended to establish technologies for the selective exploitation of sterile rock layers according to their characteristics, so that the rocks with better physical, chemical and pedological characteristics are deposited at the upper part of the slopes and berms of the final steps of the dump, and those with weaker characteristics are deposited in lower parts.

Analyzing the specialized literature (Scorțariu et al., 2011), it was identified the possibility of combining clays (identified as richer in phosphorus than Romanian soils) with sands, coal dust and coal fragments, all from the same exploitation perimeter, in certain proportions, in order to obtain anthropogenic soils with really good properties.

In Ist and IInd steps of the North Pește̦ana open-pit, clayey and marly rocks predominate, while in IIIrd and IVth steps sandy and clayey rocks predominate.

From a qualitative point of view, coal fragments and coal dust contain free humic acids, which can also be contained in clay rocks, especially in those from the layers immediately adjacent to the lignite layers. In general, clays with a carbon content and implicitly humic acids have a series of valuable properties: the formation of structural soil aggregates, contributing to their loosening which allows its aeration and moistening; hygroscopic retention of water due to humic acids; decomposition of humic substances (Scorțariu et al., 2011).

Depending on the clay particle size, mixtures can be made, or not, including with sandy rocks.

Quantitatively, the clays can be excavated directly from the working slopes and deposited directly on the dumps, areas free of technological load (Scorțariu et al., 2011), leveled and properly compacted, being used as anthropogenic soils on which plant species tolerant to poorer conditions or with minimal nutrient requirements will develop, subsequently enriching the anthropogenic soil with organic material, which will increase its biological diversity. In addition, it is recom-

mended to use compost, manure and organic fertilizers to accelerate the pedogenesis process.

In the North Peșteana open-pit, lignite mining is carried out in continuous flow, using bucket wheel excavators in combination with belt conveyors and dumping machine. The large thickness of the clay layers (generally over 6 m), allows selective exploitation and its direction on lands free of technological loads, leveled and compacted. After depositing the material in deposition cones, it is pushed with the bulldozer and leveled in a layer of 20-30 cm, which is sufficient for the first stage of the pedogenesis process (fig. 10).

Thus, the selective exploitation and directed deposition of the waste rock depending its quality can support the acceleration of the pedogenesis process that begins immediately after the final storage of the waste into the dump, but which naturally requires long periods of time of the order of tens and hundreds of years (Sheoran et. al, 2010).

On anthropogenic soils in the early stages of their formation as fertile soil, in order to support the growth and development of vegetation, it is necessary to apply some amendments (chemical fertilizers, compost, sludge from water treatment plants, manure, wood waste, etc.). Subsequently, the establishment of so-called green cultures is recommended. There are a number of plants recommended as green manures, such as clover, grass, alfalfa, peas, etc. Due to their specificity, these types of crops capture atmospheric nitrogen and retain it in their body, later transferring it, through decomposition, to the soil (Davidescu and Davidescu, 1999). Among their main characteristics are: high installation speed; high degree of germination; fixing nitrogen in the soil (through symbiosis with nitrogen-fixing microorganisms); the production of a plant mass as rich as possible (high productivity); high thread density; low sensitivity; resistance to drought, to low or high temperatures, etc.; increased regeneration capacity after cutting/mowing (case of clover, alfalfa and grass); the vegetation period (of the order of months) that allows the analysis and observations necessary for the proposed research; the sowing and germination period; efficiency on soils poor in organic matter; improving and/or improving the physico-chemical properties of the soil.

5. Final conclusions and recommendations

Lignite represented for a long period of time one of the major sources for the production of energy, so in Romania, as in the whole world, this resource was exploited on a large scale, especially through open mining. The mining of lignite meant and still means the occupation and degradation of large areas of land, which are removed from the natural and/or economic circuit. Closing a quarry involves freeing the working fronts from technological tasks, decommissioning the premises, if they cannot be used for another purpose or if they present insecurity from the point of view of the structure's stability, the rehabilitation of the affected lands, their improvement and revegetation.

In order to facilitate the development and rehabilitation of degraded lands, it is very important that the mining project is planned from the beginning, taking into account the protection of the environment at each stage of its life cycle.

The impact produced by lignite exploitation activities on the soil refers to disturbing the physical-chemical and pedological balance of the geological environment, with significant, unavoidable and irreversible effects, the destruction of the soil on the land surfaces from which it cannot be recovered for various reasons, the degradation of the soils and the decrease of their fertility class on large areas, by changing the initial destination of the agricultural or forestry lands and the organization of exploitation-related activities. This impact can be limited in time and space, but it generates changes and imbalances of all environmental components for a period of several decades, which corresponds to the life cycle of a mining operation (exploration, exploitation, closure and post-closure). What remains behind is a degraded land, morphologically modified, with a lunar aspect and completely devoid of productive function.

The soil is the environmental component that suffers a lot, being affected both qualitatively and quantitatively. Knowing the importance of topsoil as a resource in developing ecosystems and sustaining productivity and life on earth, it is easy to understand why efforts are being made to find solutions for its conservation and correct management or to support the pedogenesis process in the case of lands degraded by various anthropogenic activities.

In order to minimize the impact of mining on the land and, implicitly, on the soil, several solutions and sustainable mining practices were proposed in the paper (considering in particular techniques of selective excavation and directing the sterile material with fertile potential in the upper part of the dumps), which can be applied from the start of the mining works and actual exploitation, practices that support the acceleration of the pedogenesis process and ensure the integration of the degraded land into the landscape and taking over the ecological function it's as early as possible. Due to the similar characteristics of the rocks within the Rovinari mining basin (physical, chemical, pedological characteristics), the research results can be extrapolated, the proposed sustainable practices being valid for the entire basin (with possible adjustments, if necessary) or for other similar mining perimeters.

In the context of sustainable development, the closure of a mining activity does not mean the socio-economic collapse of the affected area, but an opportunity for the development of other businesses. The new activities must have the capacity to ensure: the protection of the environment, the protection of the community and the socio-economic development of the area. Such an activity must fulfill at least two functions: the ecological function and the productive function, aiming to achieve results beyond expectations.

After the recovery of degraded lands, they can be subject to a program to promote the area, depending on the natural, cultural, traditional, touristic objectives that characterize them, so as to attract investors willing to contribute to the socio-economic and ecological reconstruction of the affected localities, in order to develop their own businesses and transform these areas into development poles, by providing jobs that bring benefits to the local communities, taking into account, at the same time, the importance of protecting the environment.

Source of financing: The research on the basis of which this article was written was funded by the University of Petroșani (Romania) through the University Scientific Research Contract no. 4283/31.05.2023.

Literatura – References

1. Apostu, I.M., Geotechnical risks in the conditions of flooding of remaining gaps of lignite open-pits (in Romanian), Universitas PH, Petroșani, 2021.
2. Aznar-Sánchez, J.A., Velasco-Muñoz, J.F., Belmonte-Ureña, L.J., Manzano-Agugliaro, F., Innovation and technology for sustainable mining activity: A worldwide research assessment, Journal of Cleaner Production, 221, pp. 38-54, 2019.
3. Bastida, A. E., Aguado, A. Y., Intensification of mining's contribution to sustainable development in Romania: a legal & political framework (in Romanian), Soros Foundation Romania, Program "Exploitation of Natural Resources - Legal Framework", 2008
4. Bruel, A., Kronenberg, J., Troussier, N., Guillaume, B., Linking Industrial Ecology and Ecological Economics: A Theoretical and Empirical Foundation for the Circular Economy, Journal of Industrial Ecology, 23 (1), pp. 12-21, 2018.
5. Cecchin, A., Salomone, R., Deutz, P., Raggi, A., Cutaia, L., Relating Industrial Symbiosis and Circular Economy to the Sustainable Development Debate. In: Salomone, R., Cecchin, A., Deutz, P., Raggi, A., Cutaia, L. (eds) Industrial Symbiosis for the Circular Economy. Strategies for Sustainability. Springer, Cham, 2020.
6. Davidescu, V., Davidescu, D., Agrichemical Compendium (in Romanian), Romanian Academy Publishing House, Bucharest, Romania, 1999.
7. DOA, Rating for chemical properties of soil in Peninsular Malaysia. Soil Management Division, Department of Agriculture Malaysia, 1997.
8. Dumitru, M., Dumitru S., Tănase, V., Mocanu, V., Manea, A., Vrînceanu, N., Preda, M., Eftene, M., Ciobanu, C., Calciu, I., Rîșnoveanu, I., Soil quality monitoring in Romania (in Romanian), National Research and Development Institute for Pedology, Agrochemistry and Environmental Protection ICPA Bucharest, Sitech PH, Craiova, 2011.
9. Feng, Y., Wang, J., Bai, Z., Reading, L., Effects of surface coal mining and land reclamation on soil properties: A review, Earth-Science Reviews, 191, pp. 12-25, 2019.
10. Florea, N., Munteanu, I., The Romanian Soil Taxonomy System (SRTS) (in Romanian), București, 2012.
11. Fodor, D., Lazăr, M., Occupation and ecological rehabilitation of land in the Oltenia area (in Romanian), Agir Bulletin, 3, 2006.
12. Ghose, M.K., Land reclamation and protection of environment from the effect of coal mining operation, Mine technology, 10(5), pp. 35-39, 1989.
13. Ghose, M.K., Soil conservation for rehabilitation and revegetation of mine-degraded land. TIDEE – TERI Information Digest on Energy and Environment, 4(2), pp. 137-150, 2005.
14. Haiwen, Z., Population growth and industrialization. Published in: Economic Inquiry, 47 (2), pp. 249-265, 2019.
15. Hilson, G., Murck, B., Sustainable development in the mining industry: clarifying the corporate perspective, Resources Policy, 26 (2000), pp. 227-238, Elsevier Science Ltd, 2001.
16. Hebda W., Fossil fuels in the energy transition – the case of Romania, GSM – Mineral Resources Management, Vol. 39 Iss. 4, pp. 85–106, 2023, DOI: 10.24425/gsm.2023.148159
17. Howard, J., Anthropogenic Soils, Progress in Soil Science, 2017.
18. Lazăr, M., Degreaded mining land rehabilitation (in Romanian), Universitas PH, Petroșani, 2010.
19. Malan, S., How to Advance Sustainable Mining, IISD, Earth Neg. Bulletin, 2021.
20. Malek, M.Y., Kamaruzaman, J., Mohd, H.I., Soil Nutrient Varibility Mapping in UiTM Research Station, Arau, Perlis Using Landsat TM and Geostatistical Analysis, Proceedings of the 6th WSEAS International Conference on Remote Sensing, Spain, 2006.
21. Miranda ,M., Chambers, D., Coumans, C., Framework for Responsible Mining: A guide to Evolving Standards, 2005.
22. Nanu, G., Ecological reconstruction of the area related to the Pestana open-pits in the Rovinari mining basin (in Romanian), Doctoral Thesis, University of Petrosani, Petrosani, 2015.
23. 2Nyari, I., Mining of lignite from the Rovinari mining basin in the context of sustainable development (in Romanian), issertation Thesis, University of Petrosani, Petrosani, 2016.
24. Roberts, B.H., The application of industrial ecology principles and planning guidelines for the development of eco-industrial parks: an Australian case study, Journal of Cleaner Production, 12 (8–10), pp. 997-1010, 2004.
25. Sariatli F., "Linear Economy Versus Circular Economy: A Comparative and Analyzer Study for Optimization of Economy for Sustainability" Visegrad Journal on Bioeconomy and Sustainable Development, vol.6, no.1, 2017, pp.31-34.
26. Schaetzl, R. J., Anderson, S., Soils: Genesis and Geomorphology, Cambridge University Press, 2005.

27. Scorțariu, O., Guran, I., Lazăr, M., Obtaining anthropogenic soils from waste rocks for reclamation of damaged land by coal pits from Oltenia, 22nd World Mining Congress&Expo, Istanbul, 2011.

28. Sheoran, V.; Sheoran, A. S.; and Poonia, P., Soil Reclamation of Abandoned Mine Land by Revegetation: A Review, International Journal of Soil, Sediment and Water, 3 (2), Art. 13, 2010. Pont, A., Robles A., Gil, J.A., e-WASTE: Everything an ICT Scientist and Developer Should Know, in IEEE Access, 7, pp. 169614-169635, 2019.

29. Smeu, A. C., Effective solutions for the construction and management of waste dumps from the Rovinari and Motru Mining Basins for recycling in the economic circuit (in Romanian), Doctoral Thesis, University of Petrosani, Petroșani, 2012.

30. United Nations Development Programme (UNDP), Managing mining for sustainable development: A sourcebook, 2018.

31. Walker, A.M., Vermeulen, W.J.V., Simboli, A., Raggi, A., Sustainability assessment in circular inter-firm networks: An integrated framework of industrial ecology and circular supply chain management approaches, Journal of Cleaner Production, 286 (125457), 2021.

32. Wilmoth, J., Menozzi, C., Bassarsky, L., Why population growth matters for sustainable development, United Nations Department of Economic and Social Affairs, Population Division/UNDESA, 2022.

33. Zanella, A., Schad, P., Galbraith, J., Ponge, J.-F. Humusica 2, Article 14: Anthropogenic soils and humus systems, comparing classification systems, Appl. Soil Ecol., 122, pp. 200–203 2018.

34. ***, Case Studies in Sustainable Development in the Coal Industry, Coal Industry Advisory Board, International Energy Agency, 2006. https://www.iea.org/reports/case-studies-in-sustainable-development-in-the-coal-industry

35. ***, Oltenia Energy Complex Documentation (C.E.O.), 2019 - 2023. https://www.gem.wiki/Tismana_1_%26_2_Coal_Mine

36. ***, Ministry of Energy, Lignite Group Report, Lignite - Mining Activity (in Romanian), Mineral Energy Resources Sector, 2016.

37. ***, S.C. - Institute of Scientific Research, Technological Engineering and Design of Lignite Mines - S.A. Craiova (I.C.S.I.T.P.M.L.), Environmental impact study report, continuation of mining works in the license perimeter for U.M.C. Pește ana - North Pește ana open-pit proposed to be located in the extra-urban/intra-urban area of Urdari, Bălteni and Plopșoru communes (in Romanian), Gorj county, symbol 810 - 537, 2012.

38. ***, A guide to leading practice sustainable development in mining, University of New South Wales. Australian Centre for Sustainable Mining Practices. Department of Resources, Energy and Tourism, Canberra, Dept. of Resources, Energy and Tourism, 2011.

Przegląd zrównoważonych praktyk górniczych w zakresie ekologicznej rekultywacji obszarów zdegradowanych terenów górniczych w Zagłębiu Górniczym Rovinari (Rumunia). Studium przypadku: wewnętrzne składowisko w Północnej Pește eanie

Górnictwo odkrywkowe, niezależnie od charakteru złoża i rodzaju eksploatacji (ciągła lub nieciągła), powoduje długotrwałe negatywne skutki dla środowiska. Natychmiast widoczne efekty są związane ze zmianami morfologii i krajobrazu: zanik szaty roślinnej i wierzchniej warstwy gleby na całej powierzchni wyrobiska, rozwój głębokich odkrywek, pojawienie się składowisk odpadów, budowa obiektów, dróg technologicznych itp. Prowadzone jest odsłanianie złoża poprzez usunięcie roślinności i usunięcie gleby, a następnie wydobycie materiału ze stropu złoża, jest to działanie destrukcyjne mające negatywne konsekwencje dla środowiska w tym lokalnych siedlisk fauny. W dłuższej perspektywie, skutki mogą być trudno odwracalne lub nieodwracalne. Elementem środowiska, który ucierpi najbardziej górnictwa jest gleba, a wraz z nią cały ekosystem na tym obszarze. Gleba jest zasobem, który jest bardzo trudny do regeneracji. Naturalne tworzenie się gleby zajmuje dużo czasu, dziesiątki i setki lat. Dlatego ważne jest znalezienie i zastosowanie rozwiązań pozwalających na utrzymanie lub poprawę jego jakości gleby, wspieranie procesu pedogenezy poprzez stosowanie zrównoważonych praktyk. Niektóre z tych praktyk można stosować już podczas działalności wydobywczej. Celem przedstawionych badań jest znalezienie i zarekomendowanie najlepszych rozwiązań możliwych do zastosowania różnych etapach cyklu życia kopalni, które stosowane łącznie pełnią rolę synergistyczną oraz niezwykły wpływ na proces pedogenezy i czas jego trwania. Dlatego bardzo ważne jest zaprojektowanie działalności wydobywczej od otwarcia do zamknięcia, biorąc pod uwagę likwidację budynków, rekultywację i ponowne zazielenienie terenów zdegradowanych.

Słowa kluczowe: *tereny zdegradowane, zrównoważone górnictwo, zrównoważone praktyki, gleba antropogeniczna, pedogeneza, ekologia przemysłowa*

Application of the GNSS Method in the Monitoring of Mine Surface Displacement: A Systemic Review

Hai Van NGUYEN[1)], Khai Cong PHAM[2)], Dung Ba NGUYEN[3)], Long Quoc NGUYEN[2,4)]*

[1)] Faculty of Water Resources Engineering, ThuyLoi University, Vietnam
[2)] Faculty of Geomatics and Land Administration, Hanoi University of Mining and Geology, Vietnam
[3)] Faculty of Surveying, Mapping and Geographic Information, Hanoi University of Natural Resources and Environment, Vietnam
[4)] Innovations for Sustainable and Responsible Mining (ISRM) Research Group, Hanoi University of Mining and Geology, Vietnam
* Corresponding author: haingv@tlu.edu.vn

http://doi.org/10.29227/IM-2024-01-115

Submission date: 26-05-2024 | Review date: 29-06-2024

Abstract

Currently, Global Navigation Satellite System (GNSS) techniques are widely used for monitoring displacement. This study provides an overview of current developments in the application of GNSS technology for determining displacement based on the findings of 52 research publications over the past fifteen years, from 2009 to August 2024. The obtained results indicated that RTK-GNSS and PPP-GNSS are effective methods to monitor deformation, subsidence, and landslides in open-pit, underground, abandoned mines, and waste dumps. Besides, some limitations and benefits of this technology have been mentioned in this paper. Finally, the prospects of developing of GNSS technique combined with AI technology in displacement monitoring of mining areas were also presented. This paper offers a technical reference for expanding the understanding and knowledge of GNSS applications in detecting displacement in mining areas.

Keywords: *displacement, deformation, subsidence, landslide, mine area, GNSS*

1. Introduction

Surface deformations, also known as displacements, are a significant problem in mining due to their negative impact on the environment and construction sites. Since surface displacements are unavoidable, it's critical to keep an eye on the mining regions and their surroundings, which are equally vulnerable to the negative impacts of mining operations [1]. To date, there are many methods to detect deformations in mining areas including leveling, satellite radar interferometry, Global Navigation Satellite System (GNSS), aerial photogrammetry, and airborne LiDAR. Hybrid approaches are also employed, which combine two techniques, such as GNSS and InSAR or GNSS, and leveling, which are complimentary measurements done with a single methodology [1]. The data from conventional measuring methods are discontinuous and only exist in theory at the precise moment of observation, and thus involve a significant field workload. In order to achieve automatic and real-time monitoring, some scientists installed continuously operating GNSS equipment, transmitted the information gathered via a wireless network to a data processing station [2]. According to [3], the GNSS is currently among the most advanced technological tools available. With the emergence of modern satellite positioning systems, GNSS technology such as COMPASS, GPS, GLONASS, GALLIEO has been extensively utilized in spatial information science, military, transportation, and resource exploration [4]. Moreover, integrating InSAR and GNSS data for various applications has been the subject of intriguing papers published by numerous authors such as subsidence analysis [5], landslide back-analysis [6], ground deformation analysis [7], geology [8], etc. Indeed, [9] reviewed on application of GNSS technology for various purposes including atmospheric contribution evaluation and ground deformation identification. [10] provided a summary on the use of the GNSS method in geology and mining on the territory of Bulgaria. [1] conducted an overview of remote sensing and geodetic techniques (including GNSS) for identifying surface displacements induced by mining. Observations made with this technology have some benefits over those obtained with traditional ground approaches because of the high spatial and temporal resolution.

To date, there have been several reviews related to the determination of surface deformation due to mining. [11] provides a comparative discussion of various approaches used to evaluate mining-related subsidence. The obtained results revealed that in the last two decades, the main methods used for the detection and measurement of land subsidence occurrences including GIS and remote sensing, Light Detection and Ranging (LiDAR), and Differential Interferometric Synthetic Aperture Radar (DiNSAR). Similarly, based on a thorough analysis of a significant amount of scientific literature, [1] discussed surface displacement measurement techniques used in underground mining sites in relation to geodetic and remote sensing approaches. While [12] analyzed a large number of published research on mapping and assessing mining-induced subsidence using geographic information systems, [13] presented an overview of techniques for monitor, calculating, and simulating ground subsidence caused by coal mining. Also involved in the review of displacement determination methods, [14] supports the view that an effective and sufficiently precise method for tracking ground displacements brought on by mining-induced earthquakes is InSAR. Besides, from the perspective of subsidence management, recommendations, and methodologies are proposed to enhance the current mine stability evaluation methodologies

[15]. In addition, some reviews of the impact of mining-induced subsidence on the environment are also mentioned. Evaluation of the effects of aquifer system drainage and the spatial extent of ground displacement caused by mining was presented in [16]. In addition, an overview of the relative sea level increase induced by mining-caused displacement in the coastal areas [17]. Thus, although there are many assessments related to aspects of subsidence caused by mining, there is no study that has conducted an analysis of the application of GNSS technology in studying deformation in mining areas. So, in order to fill this gap, this study performs a comprehensive review of the use of the GNSS method in determining surface displacement due to mining. This movement can be horizontal or vertical or landslides in underground, open-pit, closed mines, or waste dump areas.

2. Material and methodology

A systemic review starts with identifying relevant main works and particular concepts, which are then operationalized into search terms and syntax. In this research, they are set up in the following search syntax for this study retrieval: ("Global Navigation Satellite System" OR "GNSS"; AND ("Deformation" OR "Subsidence" OR "Displacement" OR "Landslice"; AND ("Mine" OR "Mining" OR "Open pit mine" OR "Surface mine" OR "Underground mine" OR "Closed mine" OR "Abandoned mine" OR "Waste dump"). This search syntax is used to search systematically in databases of Google Scholar, ScienceDirect, Scopus, and Web of Science. English is the primary language used for searches. A comprehensive collection of scientific literature on many aspects of displacement investigation by GNSS techniques was found out. Book chapters, conference proceedings, and original papers published by international journals following peer review were collected. In January 2024, the data collection was conducted.

The obtained collection, which includes an initial list of 862 contributions, can be regarded as representative of the scholarly literature for the 15-year period 2009–2024 on the use of GNSS technology for displacement detection. The initial conclusion that can be made is that there is a significant amount of literature on the usage of the GNSS method for subsidence analysis, but no study in the world has performed a comprehensive assessment. The abstracts and titles of the research were checked to evaluate whether they agree with the content of this review. Certain study kinds are excluded, including reports and industry trade papers. After a process of screening to remove duplicate entries, documents are sent forward for suitability assessment. Finally, our systematic review of the literature is based on 66 papers in total.

3. Application of GNSS technology in monitoring of mine surface displacement

Mining operations have the potential to deform the surface and harm the ecosystem [18]. Surface deformation from underground mining has a negative impact on locals' quality of life and personal safety. It also creates obstacles to the safe and effective extraction of subsurface resources [19]. According to [20] there are several ways to measure ground deformations, including leveling, laser scanning, synthetic aperture radar, satellite navigation systems, and many more. These days, with the advancement of GNSS technology, mining deformation monitoring technology has become more innovative. The usage of GNSS systems in resource exploration has increased significantly since the emergence of modern satellite positioning systems [21]. Similarly, as the conclusion of the study [22] indicates, at surface lignite mines, several techniques have been developed for detecting ground deformation such as total stations, GNSS, laser scanners, photogrammetry, ground-based radar, drone, etc. For the GNSS approach, they concluded that the precision of this method is adequate for observing ground deformation, even with RTK. Therefore, up to now, many publications have mentioned monitoring surface deformation due to mining using GNSS technology. According to [23], for two decades, the use of global navigation satellite system (GNSS) measurements to monitor deformations induced by underground mining activity has been a global standard. These monitoring techniques combine epoch measurements with one of the following methods: the rapid-static method with double difference (DD) phase observations, the static precise point positioning (PPP) method, the real-time kinematic (RTK) method and PPP, and a postprocessing (P-P) method.

3.1 RTK monitoring technique

3.1.1 Application of GNSS technology in monitoring of deformation in mining areas

As seen in Eq. (1), RTK uses the Double Difference (DD) model to remove the majority of observational errors, leaving just the coordinate and ambiguity parameters to be estimated in a brief baseline [24].

$$\begin{aligned} p_{rb,k}^{ij} &= \rho_{rb}^{ij} + e_{rb,k}^{ij} \\ L_{rb,k}^{ij} &= \rho_{rb}^{ij} + \lambda_k * N_{rb,k}^{ij} + \epsilon_{rb,k}^{ij} \end{aligned} \tag{1}$$

where P and L are the code and phase observations (m), respectively; i and j stand for the non-reference and reference satellites, respectively, and r and b for the rover and reference stations, respectively; N is the integer ambiguity in cycles; ρ is the geometric distance (in meters) between the satellite and the receiver; k is the signal frequency; k is the wavelength of the k-th signal frequency; e and ⎵ are the sum of the measurement error, multipath error, and residual model error for the code and phase observations, respectively [24].

RTK method has been widely utilized in monitoring deformation in mining areas. The GPS RTK method has been applied in subsidence monitoring since the early years of the last decade. In order to meet surface deformation monitoring's precise requirements, [25] proposed a new GPS RTK surveying technique that uses rod measurement. This technique can lessen the influence of multipath error in the U direction, effectively prevent the impacts of vertical deviation and shaking error of the surveying rod, and further increase positioning precision. Similarly, the GPS RTK approach was adopted to enhance the precision and dependability of mine surface subsidence monitoring. Subsequently, the mechanism responsible for the primary systematic mistakes was examined, drawing on several theories and techniques. The accuracy of estimations can be increased by using this method, which can completely remove the inevitable shaking mistake, vertical deflection, and, to some extent, lessen the multipath effect [26].

In this research [20], based on GNSS technology, the findings of two years of ground deformation monitoring in

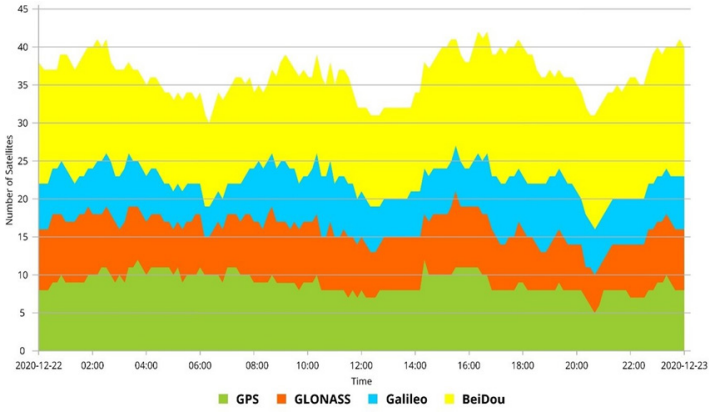

Fig. 1. Number of GNSS satellites visible above the observation location
Rys. 1. Liczba satelitów GNSS widocznych nad miejscem obserwacji

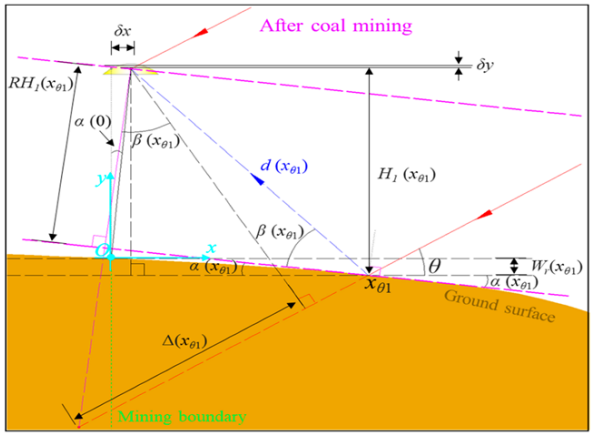

Fig. 2. Reflection model for subsided ground surface caused by underground coal mining [39]
Rys. 2. Model odbicia dla osiadającej powierzchni gruntu spowodowanej podziemną eksploatacją węgla [39]

coal mining regions in Upper Silesia, Poland are presented. Real-time (RT) and near real-time (NRT) GNSS techniques were used to verify the long-term subsidence events, and they were cross-referenced with a daily postprocessing solution. Besides, [27] provided the processing procedure and findings from their analysis of the earth surface displacement data observations during coal mining at the Kostenko mine of the Coal Department of ArcelorMittal Temirtau JSC, Karaganda Coal Basin using the GNSS methods. The obtained results show that the proposed method of observing the displacement of the earth's surface is more economically advantageous and requires significantly less time compared to measurements made using traditional expensive geodetic methods. According to [4], in order to establish real-time and quasi-real-time deformation monitoring methods, the GNSS Continuously Operating Reference Station (CORS) offers services for navigation on the basis of pseudorange measurements and provides carrier phase information. Therefore, in light of mining technology for CORS, They suggested a large-area 3D deformation monitoring system for mining areas. The results showed that the proposed GNSS-RTK can improve the temporal and spatial resolution of the monitoring of mine deformation. In another study, it has proven possible to evaluate displacements both vertically and horizontally with great precision using geodetic networks. The latter is made up of inclinometers and GPS networks to facilitate the detection of horizontal motions, while the former is capable of estimating values of subsidence (e.g., geodetic high-precision leveling systems). This study presented the results and remarks on the usage of a GPS geodetic network for continuous surface deformation monitoring in waste dumps of the Bages region of Catalonia (Spain) [28]. In addition to, utilizing GNSS satellite receivers and robotic total stations to monitor open pit mines is presented in [29]. This study demonstrated the combination of robotic total station equipment and GNSS receivers to provide a completely automated, accurate, efficient, and economical survey monitoring system for large open pit mines. In the study [30], large-scale mobility in the mining area can be detected using continuous-time or GNSS location time series with high sample rates. Therefore, they presented a GPS method for monitoring seismic events and surface displacement that occurs during mining-induced tremors.

Beyond its use for monitoring deformation in surface or underground mines, this technology was applied in closed mines. According to [31], during the time of mine closures, the issue of monitoring surface ground movements in post-mining sites is very crucial. Therefore, the study uses the GNSS to continuously monitor surface movements at the abandoned hard coal mine "Kazimierz-Juliusz" in Poland. Based on the results acquired, it was determined that the best way to meet the needs of ongoing geodetic monitoring in the research region was to conduct GNSS measurements using three navigation systems: GPS, GLONASS, and Galileo. Figure 1 shows the quantity of GNSS satellites that can be seen above the observing site.

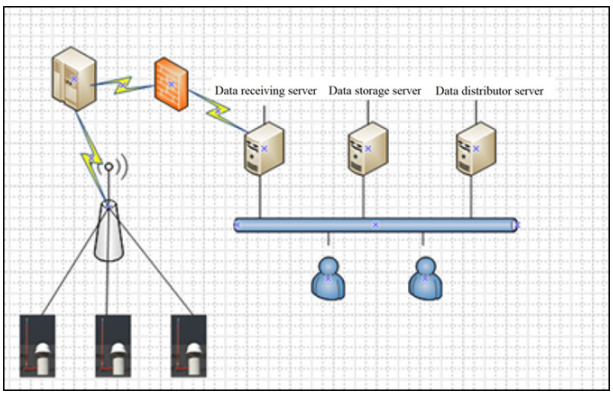

Fig. 3. Schematic diagram of automatic monitoring system [45]
Rys. 3. Schemat ideowy automatycznego systemu monitorowania [45]

In addition to predicting the mining-caused deformation, the GNSS system was also utilized to validate the precision of the displacements determined by InSAR-based methods. According to [32], to fully understand the rule of mining subsidence and to set safe production and construction guidelines for mining areas, it is necessary to measure the surface three-dimensional deformation fields accurately in a mined-out region. Thus, they suggested a better fusion technique to monitor this three-dimensional displacement based on the GNSS and InSAR measurements. This technique can be used to acquire three-dimensional deformation fields, which can then be used as a foundation for safe production in nearby mining sites. In the [33], During the SAR acquisition period, the GPS1 and GPS2 stations were situated in locations that were significantly and insignificantly impacted by underground mining operations, respectively. Similarly, the precision of the DinSAR deformation maps was validated using the GNSS data in [34]. Based on data gathered from the ground network of permanent stations, the GNSS monitoring of ground surface displacements has been carried out. In addition, GNSS data were applied to compare with the results of monitoring ground motion occurrences caused by underground mining operations in Poland based on the interferometric synthetic aperture radar method [35]. The same purpose of assessing accuracy, [36] used the GNSS static monitoring network system situated close to the mining area at the southwest foot of the mountain to determine three-dimensional ground surface displacement data. The findings revealed that there is good agreement between the estimated value identified by InSAR and the displacements measured by GNSS. Another study [37] also used InSAR and GPS measurements to monitor and analyze deformation in the Kunyang phosphate mine fusion. The findings of this study provide a scientific foundation for the management and prevention of landslides, collapses, and other undiscovered geological hazard risks brought on by the mining activities carried out in the Kunyang Phosphorus Mine. Also using this method, [38] introduced an integration process that takes into account the strengths and weaknesses of GNSS and Differential Interferometry SAR (DInSAR) monitoring approaches to monitor deformation in the Upper Silesian coal mining region (southern Poland). Besides, in order to determine the ground surface deformation of underground coal mining, [39] suggested the GNSS approach interferometric reflectometry (GNSS-IR). The GNSS reflection model for the subsided ground surface induced by underground coal mining is illustrated in Figure 2. The results of this study indicate that the navigational GNSS instrument may be considered to be a novel kind of sensor for continuously and economically detecting surface displacement.

Furthermore, the accuracy of the GNSS method is also mentioned in some studies. In the [40], the duration of GPS in ground deformation measurements in mining areas was determined. The results show that a GPS session should last at least twelve hours in order to attain sub-cm precision of height coordinate at a 95% confidence level in a single observation session. Moreover, [41] conducted a study on monitoring local deformation using GNSS in an open pit mine to to solve the issue of how to obtain millimeter accuracy while determining displacements with GPS.

According to [42], high-accuracy geodetic surveys are necessary to determine the deformation indices in areas affected by open pit mines. This allows for the identification of potential dangers. Thus, They discussed the fundamentals of precisely determining three-dimensional displacements using GPS technology. The obtained results indicate that the 3-D coordinates of the observed points can be accurately determined to within 2-3 mm.

3.1.2 Application GNSS technology in monitoring of ground subsidence in mining areas

In addition to determining deformation caused by mining, GNSS methods are also used for monitoring ground subsidence in mining areas. According to [43], in coal-mining regions, the amplitude of ground subsidence can reach up to 10 cm per day and occurs continuously. Thus, timely and accurate monitoring of ground subsidence is essential to ensure the safety of coal-mining regions. This study provides a real-time ground subsidence monitoring system that operates constantly on the Global Navigation Satellite System. Unlike the traditional leveling surveying approach, the suggested method can match the precision requirement of ground subsidence monitoring and offer continuous subsidence information in real-time. In the study [44], to precisely observe large-area mining subsidence, a high-precision GNSS monitoring system was constructed using the neighboring international GNSS service (IGS) stations as reference points. The suggested theory was used to monitor mining subsidence in China's northern Anhui coal mine. The findings revealed that the accuracy

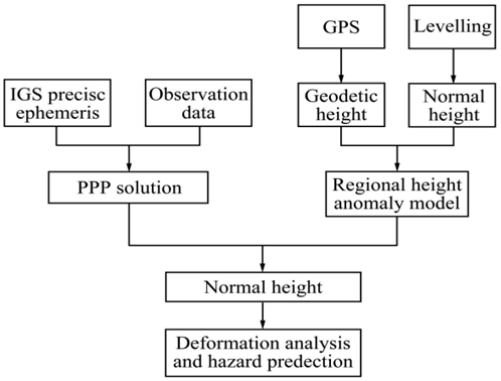

Fig. 4. Vertical subsidence monitoring based on PPP [44]
Rys. 4. Monitorowanie osiadania pionowego w oparciu o PPP [44]

of deformation can reach the millimeter level with four hours of observation. In mining subsidence research, [45] offers a novel technological method for analyzing the law of surface movement. They used time series DInSAR technology in conjunction with a number of GNSS monitoring stations to determine precise, dependable, and fine mining deformation results. Figure 3 shows the automatic monitoring and data distributor system. The findings of the study can offer a solid scientific foundation for computing mining subsidence, evaluating the damage to buildings or structures, evaluating land damage, and supporting environmental control initiatives. To comprehensively evaluate subsidence in mining, [46] presented a weighted total least-squares approach that can be utilized to find the piecewise linear mapping between D-InSAR data and GNSS data. This mapping can be used to improve the findings of traditional D-InSAR monitoring, especially in locations with significant gradient subsidence. In the event of large-gradient subsidence, it is discovered that the improved data is more accurate and dependable than the traditional D-InSAR monitoring data. Additionally, to save expenses and improve security, there is ongoing research into ways to monitor mine subsidence better. As a result, the applicability of numerous novel techniques and equipment is evaluated. UAV, and GNSS are considered a promising method for gathering large amounts of data quickly. Thus, [47] conducted a study to detect mine subsidence using this proposed approach. Overall, the results indicate that UAV photogrammetry and GNSS RTK are both appropriate for monitoring mine subsidence.

3.1.3 Application RTK-GNSS technology in monitoring of landslides in mining areas

[48] described the implementation of a geodetic deformation monitoring method on two significantly damaged and unexplored research locations in India including Bhurkunda coal mines in Jharkhand, and the Sirobagarh landslide in Rudraprayag, Uttarakhand. For the Bhurkunda site (marked by subsidence owing to underground coal mining), A network of 56 GNSS points, densified using Total Station (TS) ground points, was established during three field trips. In order to monitor the recurrent landslides in Sirobagarh caused by the local geology and rainfall, a GNSS network including six control sites was set up over a 500 x 600 m^2 region. According to [49], monitoring landslides caused by waste dumps can be done in a variety of ways these days using GPS, total stations, remote sensing, UAVs, lidar, and other technologies. However, these technologies can only monitor periodically, not continuously in real-time. Therefore, It was decided to use GNSS CORS technology for the design and construction of a real-time waste dump landslide monitoring system. This device gives immediate warning in the event of a landslide and enables continuous real-time monitoring. Additionally, it has the benefit of being inexpensive, adaptable, and simple to install for monitoring stations.

3.2 PPP monitoring technique

According to [24], PPP-GNSS measurement technology is able to make up for RTK's disadvantages in terms of receiver configuration, cost, and range when compared to RTK. Several studies have demonstrated that displacement monitoring can be done using this method. Four continuous operation reference station (CORS) stations in the mining region were used to study the displacement status, and the viability of employing PPP in mining area deformation determination was confirmed in the study [50]. Besides, PPP technology and its application for monitoring mining deformation was presented in [51]. Figure 5 shows the procedure of vertical subsidence determining based on PPP. The obtained results showed that when PPP is employed, multiple quality metrics demonstrate that the precision of deformation monitoring can reach the cm and even mm levels.

In another study [45] found that, by using only one receiver, precise point placement (PPP) eliminates issues brought on by base station limitations when using existing techniques like real-time kinematics. Therefore, they suggested a novel approach to monitor deformation in the mine area through PPP. The results of the monitoring experiment demonstrate that, utilizing this method, the monitoring index of the series under various intervals could be, on average, 1-2 mm, which is significantly better than the original monitoring sequence. As a result, every result demonstrated the method's viability and validity. In the view of [46], the surface of the mining area is prone to disasters including cracking, shifting, and collapse, which can seriously harm the local ecology and human population. Thus, based on the PPP technique, an adaptive filtering algorithm is proposed for deformation monitoring in mining areas. Simultaneously, the actual tests are conducted using the data gathered from the mining engineering practice, and the algorithm's superiority is subsequently confirmed.

With GNSS RTK, landslide deformation in mining area can be precisely observed. But unstable locations can cause reference stations to shift, producing inaccurate data. Thus, [47] suggested a procedure that employs the PPP methodology to identify the reference station's instability and then adjust for the movement of monitoring stations. The results indicated that the suggested method provides reliable and accurate monitoring data, enabling accurate forecasting and early warning systems in the deformation region.

4. Discussion and future perspective

The literature shows that the GNSS technology for monitoring mining-induced subsidence has the advantages of high observing precision, a quick and adaptable network structure and widespread use [48]. Even with their drawbacks, such as inefficiency and a high field workload, they will remain essential for monitoring subsidence in the near future. The experiment results indicate that RTK can be widely employed in small-scale displacement monitoring because it is able to rapidly and precisely acquire positioning information with millimeter-level accuracy. However, it is dependent on a reference station, which is somewhat costly, and is unable to independently establish absolute coordinates [24]. In addition, for monitoring landslides in mining areas, RTK appears to have the fastest reaction time and is typically used to record the abrupt deformation of landslides in real-time. In contrast, because PPP takes a long time to converge and produce high-precision absolute coordinates, it is commonly employed to regularly verify the stability of reference stations [24]. On the other hand, in studying landslides, although PPP can provide absolute coordinates directly without the need for a reference station, its accuracy can only be attained to the centimeter level after tens of minutes, making it suitable for monitoring landslides that vary slowly and occur close to real-time [24].

In addition, previous studies have shown that numerous studies were gathered to confirm the potential application of artificial intelligence (AI) algorithms in the GNSS domain. Deep learning (DL) and machine learning (ML) are the two methods available for achieving intelligence. The two most popular AI methods utilized in the literature to improve GNSS system location accuracy are Support Vector Machine (SVM) and Convolutional Neural Network (CNN) [49]. Although there has not been much research on this application, the deep self-attention neural network approach may be a potent substitute for GNSS coordinate time series prediction, and it will have extensive applications in the domains of early warning for deformation and reference frame maintenance [50]. On the other hand, in the last several years, artificial intelligence (AI) has been used to tackle a number of issues with GNSS, such as accurate location, navigation in challenging environments, and interference cancellation and mitigation [51]. Furthermore, combining machine learning and GNSS technology in determining deformation is not required to 1) preinterpolate GNSS point displacements, and 2) predict GNSS and InSAR point-by-point variance components [52]. With the above analytical advantages, applying AI and GNSS in subsidence monitoring will be effective and highly accurate. However, this proposed method has not been applied in mining areas. Therefore, in the future, scientists need to research to include this method in studies to determine deformation due to mining.

5. Conclusion

This study discusses the utilization of GNSS techniques for monitoring displacement induced by mining based on publications from the last 15 years. The review conducted an analysis 52 papers related to movement monitoring in mining areas by the GNSS method that had been published in scientific journals and M.Sc./Ph.D. theses. The obtained results showed that RTK-GNSS and PPP-GNSS technology can be performed to determine surface deformation, subsidence, landslides in underground, surface, closed mines, and waste dumps. As proven in this paper, although there are some limitations such as inefficiencies and large workloads in the field, GNSS is still necessary to monitor displacement in the near future. In addition, the findings have revealed that RTK in displacement monitoring can quickly obtain monitoring results with millimeter accuracy in stable and reliable reference stations, but its range of services is limited. Moreover, the PPP offers the advantages of not requiring a reference station, cost-effectiveness, and absolute coordinates, which are directly applicable to displacement observing in a vast range, slow-variable, and near real-time, even if it takes tens of minutes to reach steady centimeter-level monitoring precision. On the other hand, the paper also indicated that with many advantages of the combination of GNSS and AI technology, this approach promises to bring many useful applications for monitoring displacement in mine areas.

Conflicts of Interest

The authors declare no conflict of interest.

Literatura – References

1. Owczarz, K. A review of geodetic and remote sensing methods used for detecting surface displacements caused by mining. in IOP Conference Series: Earth and Environmental Science. 2020. IOP Publishing.
2. Lian, X., et al., Determination of the stability of high-steep slopes by global navigation satellite system (GNSS) real-time monitoring in long wall mining. Applied Sciences, 2020. 10(6): p. 1952.
3. Lu, C. The Application of Satellite Navigation System in Deformation Monitoring. in Journal of Physics: Conference Series. 2021. IOP Publishing.
4. Jing-Xiang, G., H.J.P.E. Hong, and P. Science, Advanced GNSS technology of mining deformation monitoring. 2009. 1(1): p. 1081-1088.
5. Heimlich, C., et al., Uplift around the geothermal power plant of Landau (Germany) as observed by InSAR monitoring. 2015. 3: p. 1-12.
6. Bovenga, F., et al., Using C/X-band SAR interferometry and GNSS measurements for the Assisi landslide analysis. 2013. 34(11): p. 4083-4104.
7. Mateus, P., et al., Experimental study on the atmospheric delay based on GPS, SAR interferometry, and numerical weather model data. 2012. 51(1): p. 6-11.
8. ONDREJKA, P., et al., Use of GNSS technology in engineering geology in Slovakia. 2011. 43(2): p. 111-120.
9. Del Soldato, M., et al., Review of works combining GNSS and InSAR in Europe. 2021. 13(9): p. 1684.
10. Kostyanev, S., et al., The use of GNSS technologies for application in mining, geology and geodesy in Bulgaria. 2010. 100: p. 525-534.
11. Behera, A. and K.S. Rawat, A Comprehensive Review on Mining Subsidence and its Geo-environmental Impact. Journal of Mines, Metals & Fuels, 2023. 71(9).
12. Suh, J., An overview of GIS-based assessment and mapping of mining-induced subsidence. Applied Sciences, 2020. 10(21): p. 7845.
13. Cai, Y., et al., A review of monitoring, calculation, and simulation methods for ground subsidence induced by coal mining. International Journal of Coal Science & Technology, 2023. 10(1): p. 32.
14. Hejmanowski, R., et al., An analysis applying InSAR of subsidence caused by nearby mining-induced earthquakes. Geosciences, 2019. 9(12): p. 490.
15. Yu, Y., et al., Subsidence mechanism and stability assessment methods for partial extraction mines for sustainable development of mining cities—A review. Sustainability, 2018. 10(1): p. 113.
16. Guzy, A. and A.A. Malinowska, Assessment of the impact of the spatial extent of land subsidence and aquifer system drainage induced by underground mining. Sustainability, 2020. 12(19): p. 7871.
17. Humphries, L., A review of relative sea level rise caused by mining-induced subsidence in the coastal zone: some implications for increased coastal recession. Climate research, 2001. 18(1-2): p. 147-156.
18. Qingsong, D., et al., Land Use Changes in High Cold-altitude Mining Area Based on Remote Sensing Technology. Environmental Science & Technology (10036504), 2020. 43(12).
19. Liu, P., et al., Impacts of Surface Deformation Induced by Underground Mining of Metal Mines on Above-Ground Structures: A Case Study. Minerals, 2023. 13(12): p. 1510.
20. Tondaś, D., K. Kazmierski, and J. Kapłon, Real-time and near real-time displacement monitoring with GNSS observations in the mining activity areas. IEEE Journal of Selected Topics in Applied Earth Observations and Remote Sensing, 2023.
21. Jing-Xiang, G. and H. Hong, Advanced GNSS technology of mining deformation monitoring. Procedia Earth and Planetary Science, 2009. 1(1): p. 1081-1088.
22. Prokos, A. and C. Roumpos. Ground deformation monitoring techniques at continuous surface lignite mines. in 4th Joint International Symposium on Deformation Monitoring (JISDM). Athens, Greece. 2019.
23. Rodriguez-Lloveras, X., et al., Two decades of GPS/GNSS and DInSAR monitoring of Cardona salt mines (NE of Spain)–natural and mining-induced mechanisms and processes. Proceedings of the International Association of Hydrological Sciences, 2020. 382: p. 167-172.
24. Huang, G., S. Du, and D. Wang, GNSS techniques for real-time monitoring of landslides: A review. Satellite Navigation, 2023. 4(1): p. 5.
25. Liu, C., et al., Mine surface deformation monitoring using modified GPS RTK with surveying rod: Initial results. Survey Review, 2015. 47(341): p. 79-86.

26. GAO, J.-x., et al., A new method for mining deformation monitoring with GPS-RTK. Transactions of Nonferrous Metals Society of China, 2011. 21: p. s659-s664.
27. Issabek, T., V. Dyomin, and D. Ivadilinova, Methods for monitoring the earth surface displacement at points of small geodetic network under the underground method of coal development. Natsional'nyi Hirnychyi Universytet. Naukovyi Visnyk, 2019(2): p. 13-20.
28. Costantino, D. and M.G. Angelini, Geodetic monitoring applied to a mine area. Applied Geomatics, 2011. 3: p. 61-74.
29. Brown, N., S. Kaloustian, and M. Roeckle. Monitoring of open pit mines using combined GNSS satellite receivers and robotic total stations. in Slope Stability 2007: Proceedings of the 2007 International Symposium on Rock Slope Stability in Open Pit Mining and Civil Engineering. 2007. Australian Centre for Geomechanics.
30. Szczerbowski, Z. and J. Jura, Mining induced seismic events and surface deformations monitored by GPS permanent stations. Acta Geodyn. Geomater, 2015. 12(3): p. 179.
31. Sokoła-Szewioła, V. and Z. Siejka, Validation of the accuracy of geodetic automated measurement system based on GNSS platform for continuous monitoring of surface movements in post-mining areas. Reports on Geodesy and Geoinformatics, 2021. 112.
32. Zhou, W., et al., An improved GNSS and InSAR fusion method for monitoring the 3D deformation of a mining area. IEEE Access, 2021. 9: p. 155839-155850.
33. Dai, S., et al., Prediction of Mining-Induced 3-D Deformation by Integrating Single-Orbit SBAS-InSAR, GNSS, and Log-Logistic Model (LL-SIG). IEEE Transactions on Geoscience and Remote Sensing, 2023. 61: p. 1-13.
34. Pawłuszek-Filipiak, K., et al., Assessing the application of GACOS atmospheric correction for DInSAR-based mining deformation monitoring by using Sentinel-1 data in Upper Silesian Coal Basin in Poland. Geodesy and Cartography, 2021. 70(2).
35. Palamà, R., et al., A multi-temporal small baseline interferometry procedure applied to mining-induced deformation monitoring. Remote Sensing, 2022. 14(9): p. 2182.
36. Du, Q., et al., Deformation monitoring in an alpine mining area in the Tianshan Mountains based on SBAS-InSAR technology. Advances in Materials Science and Engineering, 2021. 2021: p. 1-15.
37. Li, Y., et al., Deformation monitoring and analysis of Kunyang phosphate mine fusion with InSAR and GPS measurements. Advances in Space Research, 2022. 69(7): p. 2637-2658.
38. Tondaś, D., et al., Kalman filter-based integration of GNSS and InSAR observations for local nonlinear strong deformations. Journal of Geodesy, 2023. 97(12): p. 109.
39. Bo, H., et al., Estimation of ground subsidence deformation induced by underground coal mining with GNSS-IR. Remote Sensing, 2022. 15(1): p. 96.
40. Wang, G., et al., Mining subsidence prediction parameter inversion by combining GNSS and DInSAR deformation measurements. IEEE Access, 2021. 9: p. 89043-89054.
41. Tiwari, A., et al., Geodetic investigation of landslides and land subsidence: Case study of the Bhurkunda coal mines and the Sirobagarh landslide. Survey review, 2018.
42. Pham, C.K., D.T. Tran, and V.H. Nguyen, GNSS/CORS-Based Technology for Real-Time Monitoring of Landslides on Waste Dump–A Case Study at the Deo Nai South Dump, Vietnam. Inżynieria Mineralna, 2020. 1(2): p. 181-191.
43. Hu, H., et al., Land deformation monitoring in mining area with PPP-AR. 2014. 24(2): p. 207-212.
44. XU, C.-h., et al., Precise point positioning and its application in mining deformation monitoring. 2011. 21: p. s499-s505.
45. Li, R., et al., A New Method for Deformation Monitoring of Structures by Precise Point Positioning. Remote Sensing, 2023. 15(24): p. 5743.
46. Junshan, Y., et al., Adaptive filtering algorithm and its application based on the PPP technique for deformation monitoring in mining area. Bulletin of Surveying and Mapping, (9): p. 129.
47. Wang, D., et al., Stability analysis of reference station and compensation for monitoring stations in GNSS landslide monitoring. Satellite Navigation, 2023. 4(1): p. 29.
48. Lian, X., et al., Residual subsidence time series model in mountain area caused by underground mining based on GNSS online monitoring. International Journal of Coal Science & Technology, 2024. 11(1): p. 27.
49. Jagiwala, D. and S.N. Shah. Possibilities of AI Algorithm Execution in GNSS. in 2022 URSI Regional Conference on Radio Science (USRI-RCRS). 2022. IEEE.
50. Jiang, W., et al., A new deep self-attention neural network for GNSS coordinate time series prediction. GPS Solutions, 2024. 28(1): p. 3.

51. Seyed Mohammad Reza Mosavi and S.B. . Artificial Intelligence Applications in GNSS. The Journal of Global Navigation Satellite Systems, 2020.

52. Ji, P., et al., A new method to obtain 3-D surface deformations from InSAR and GNSS data with genetic algorithm and support vector machine. IEEE Geoscience and Remote Sensing Letters, 2021. 19: p. 1-5.

Zastosowanie metody GNSS w monitorowaniu przemieszczeń powierzchni kopalni: przegląd systemowy

Obecnie do monitorowania przemieszczeń powszechnie stosuje się techniki Globalnego Systemu Nawigacji Satelitarnej (GNSS). Niniejsza praca stanowi przegląd aktualnego rozwoju zastosowań technologii GNSS do wyznaczania przemieszczeń na podstawie wniosków z 50 publikacji naukowych z ostatnich piętnastu lat, od 2009 r. do sierpnia 2024 r. Uzyskane wyniki wskazują, że RTK-GNSS i PPP-GNSS są skuteczne metody monitorowania deformacji, osiadań i osuwisk w kopalniach odkrywkowych, podziemnych, opuszczonych kopalniach i na składowiskach odpadów. Poza tym w artykule wspomniano o pewnych ograniczeniach i zaletach tej technologii. Na koniec przedstawiono także perspektywy rozwoju techniki GNSS w połączeniu z technologią AI w monitorowaniu przemieszczeń obszarów górniczych. W artykule przedstawiono odniesienia techniczne umożliwiające poszerzenie zrozumienia i wiedzy na temat zastosowań GNSS w wykrywaniu przemieszczeń na obszarach górniczych.

Słowa kluczowe: *przemieszczenie, deformacja, osiadanie, osuwisko, teren kopalni, GNSS*

Prediction of Underground Mine's Surface Subsidence using a Recursive Multi-Step Forecasting Model with an Artificial Neural Network

Tam Thanh Thi LE[1)], Trong Gia NGUYEN[1)], Chung Van PHAM[1)], Canh Van LE[1)], Huy Dinh NGUYEN[2)]*

[1)] Faculty of Geomatics and Land Administration, Hanoi University of Mining and Geology, Hanoi, Vietnam; ORCID https://orcid.org/0009-0001-5400-1776
[2)] Faculty of Bridges and Roads, Hanoi University of Civil Engineering, Hanoi, Vietnam; ORCID https://orcid.org/0000-0002-2049-3338
* Corresponding author: phamvanchung@humg.edu.vn

http://doi.org/10.29227/IM-2024-01-116

Submission date: 26-05-2024 | Review date: 30-06-2024

Abstract

The subsidence of the surface due to mining activities is a significant issue in mining areas. Therefore, predicting surface subsidence is a necessary task to ensure safety and production efficiency. This article applied an Artificial Neural Network (ANN) model to predict surface subsidence resulting from underground mining operations in the Mong Dương mine. The ANN model proposed in this research uses a recursive multi-step forecasting model, where the predicted value at the previous step is added to the time series to forecast the next value. The experimental dataset consists of 12 monitoring cycles over 24 months, with a 2-month interval, divided into a training set containing the first 9 measurement cycles and a test set containing the last 3 cycles. First, the K-fold cross-validation method is applied to the training set to determine the best parameters for the model. Then, these parameters are used to predict surface subsidence for the values in the test set. The prediction error depends on the time gap between the last measurement cycle and the forecasting cycle. The relative errors in the tenth cycle for the four points are 0.9%, -1.7%, -1.7%, and 1.4%. These error values increase to 1.4%, -1.8%, -1.8%, and -1.7% in the eleventh cycle and further to 2.0%, -2.2%, -2.2%, and 2.5% in the twelfth cycle. The absolute errors are determined to be small, within the range of 20 mm. These results demonstrate that the proposed method and ANN model are suitable for the time-series monitoring data in mining areas.

Keywords: *surface subsidence, underground mine, artificial neural network, subsidence prediction*

1. Introduction

Vietnam is a country with diverse natural resources, including approximately 70 types of minerals (B. N. Nguyen, Boruff, & Tonts, 2017), among which coal is the primary mineral resource, mostly found in coal mines in Quang Ninh province. Among these, the ratio between underground and surface coal mines is approximately 60% and 40%, respectively, with the total extraction volume expected to increase annually (B.N. Nguyen, Boruff, & Tonts, 2021). Some surface coal mines are planned to be transformed into underground coal mines due to increasing extraction depths, resulting in a rise in the number of underground mines (Q.N. Nguyen, Nguyen, Pham, & Chu, 2021). The contribution of the coal industry in Vietnam is not only economic growth through mineral exports but also energy security through coal-based electricity generation (Dorband, Jakob, & Steckel, 2020).

Despite significant contributions to the economy, mining activities also bring about environmental challenges (Mohsin, Zhu, Naseem, Sarfraz, & Ivascu, 2021), among which land subsidence is a common consequence. Surface subsidence has posed significant risks to infrastructure, the environment, and the safety of workers in mining areas (Marschalko et al., 2012). Although surface subsidence due to mining activities can be measured after the occurrence of subsidence, the effective prediction of mining-induced surface subsidence in the future is also an important task for sustainable mining and resource utilization planning (Ma, Li, & Zhang, 2017). The prediction theories of surface displacement and deformation in mines are divided into three main groups, relying on geometric principles, the continuous mechanical environment, and the random theory. Scientists worldwide have developed many prediction methods based on these theories, which can be grouped into 5 method categories of experimental, intersection surface, influence function, analytical and physical modeling methods (Reddish & Whittaker, 2012).

With the development of computer science, artificial neural networks have been widely applied in various fields, including prediction. Artificial neural networks are capable of connecting and integrating different parameters in identification and forecasting applications. The strength of artificial neural networks is their ability to make good forecasts with complex data. For such data, artificial neural networks provide high generalization in forecasting; moreover, they can also forecast with non-linear variables.

The prediction of displacement resulting from underground mining activities using artificial neural networks has been conducted by many authors, such as the study by Ambrožič và Turk, 2003 to predict surface subsidence due to coal mining at the Velenje mine in Slovenia; Ki-Dong Kim et al, 2009 (Kim, Lee, & Oh, 2009) predicted mining-induced subsidence in the city of Samcheok, South Korea; Saro Lee et al. (2012) (Lee, Park, & Choi, 2012) employed artificial neural networks to forecast subsidence in the Jeong-am mining area, South Korea.

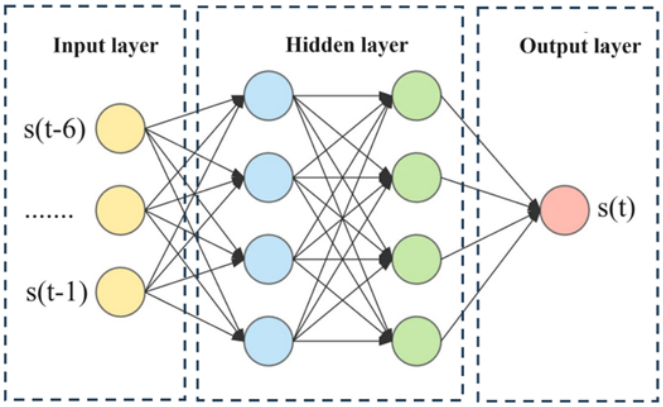

Fig. 1. Structure of an artificial neural network consisting of input layer, hidden layers, and output layer
Rys. 1. Struktura sztucznej sieci neuronowej składającej się z warstwy wejściowej, warstw ukrytych i warstwy wyjściowej

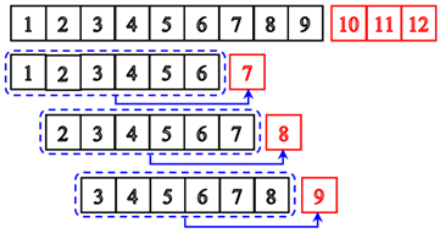

Fig. 2. Recursive multi-step prediction model. Black squares represent the input values of the model and red squares correspond to the output values
Rys. 2. Rekursywny wieloetapowy model predykcji. Czarne kwadraty reprezentują wartości wejściowe modelu, a czerwone kwadraty odpowiadają wartościom wyjściowym

Compared to traditional methods of subsidence prediction relying on a predefined function and its parameters, subsidence prediction using artificial neural networks is a parameter-free method with the ability to forecast for areas with specific geological and topographical characteristics. However, this method requires actual subsidence monitoring data as inputs for network training. This can be much easier to obtain than collecting the necessary influencing factors with high accuracy for the aforementioned traditional methods.

In Vietnam, several prediction studies have been conducted, including constructing forecasting models based on experimental monitoring data (Long et al., 2017; Long, My, & Luyen; L. Q. Nguyen, 2016), and determining parameters of models suitable for specific conditions of each mining area to enhance the accuracy of forecasting results (L. Q. Nguyen, 2016, 2020). Studies on the application of artificial neural networks in surface subsidence prediction in mines have confirmed the superiority of this method over traditional approaches when applied in Vietnam (L. Q. Nguyen, et al., 2023; Q. Nguyen, Nguyen, et al., 2021). Application of artificial neural network using recursive multistep prediction process to predict road subsidence caused by underground mining has been carried out in 2023 (Hung N.V, et al., 2023). A new ANN model with associated "optimal" hyperparameters to predict underground mining-induced land subsidence is proposed (Long Quoc Nguyen, et al., 2023).

In this paper, an artificial neural network (ANN) is applied to predict surface subsidence caused by underground mining in Vietnam. This research contributes methodologically by leveraging advancements in subsidence prediction techniques, thereby supporting sustainable mining operations.

2. Methodology

2.1 Artificial Neural Networks

The artificial neural network (ANN) is one of the artificial intelligence (AI) tools used in surface subsidence prediction due to its ability to learn complex models with a large dataset, thus enabling accurate predictions (Ambrožič & Turk, 2003; Yang & Xia, 2013). ANN models are computational models developed based on the study of the human brain's structure, hence the name ANN (Zou, Han, & So, 2009). They consist of several layers of artificial interconnected neurons, which are divided into input, hidden, and output layers (see Figure 1). The input layer involves input parameters, which are then passed through the hidden layers with computations performed based on weights, resulting in predicted variables estimated in the output layer. The weights are initially assigned random values in the input layer, then propagated through the hidden and output layers. These weights are then recalculated using optimization algorithms such as gradient descent and backpropagation (Amari, 1993). Thus, the ANN model can accurately predict output variables by recalculating weight values.

In an ANN, each layer consists of one or more neurons depending on the specific problem under investigation. In this study, the input layer consists of six neurons corresponding to six previous subsidence measurement cycles from s(t-6) to s(t-1), used to forecast subsidence at time t (denoted as s(t)). The hidden layer(s) comprise one or more layers, each containing a number of hidden nodes. In this research, the optimal number of hidden layers, hidden nodes, and the number of iterations in the backpropagation process are experimentally determined through cross-validation using the k-fold method (Fushiki, 2011).

Tab. 1. Training set consisting of subsidence values for the first nine months (unit: mm)

Tab. 1. Zestaw treningowy składający się z wartości osiadania dla pierwszych dziewięciu miesięcy (jednostka: mm)

Month	Point P1	Point P2	Point P3	Point P4
1	0	0	0	0
2	-22	-25	-24	-15
3	-62	-67	-77	-54
4	-129	-115	-102	-109
5	-198	-192	-183	-165
6	-278	-342	-317	-303
7	-369	-429	-416	-441
8	-452	-558	-547	-569
9	-516	-638	-617	-639

Tab. 2. Comparison between the measured and predicted values at Point P1

Tab. 2. Porównanie zmierzonych i przewidywanych wartości w punkcie P1

Month	Measured (mm)	Predicted (mm)	Abs. Error (mm)	Rel. Error (%)
10	-589	-584	-5	0.9
11	-637	-628	-9	1.4
12	-664	-651	-13	2.0

Tab. 3. Comparison between the measured and predicted values at Point P2

Tab. 3. Porównanie zmierzonych i przewidywanych wartości w punkcie P2

Month	Measured (mm)	Predicted (mm)	Abs. Error (mm)	Rel. Error (%)
10	-725	-737	12	-1.7
11	-761	-775	14	-1.8
12	-797	-815	18	-2.2

Tab. 4. Comparison between the measured and predicted values at Point P3

Tab. 4. Porównanie zmierzonych i przewidywanych wartości w punkcie P3.

Month	Measured (mm)	Predicted (mm)	Abs. Error (mm)	Rel. Error (%)
10	-694	-706	12	-1.7
11	-740	-795	14	-1.8
12	-783	-827	18	-2.2

Tab. 5. Comparison between the measured and predicted values at Point P4

Tab. 5. Porównanie zmierzonych i przewidywanych wartości w punkcie P4

Month	Measured (mm)	Predicted (mm)	Abs. Error (mm)	Rel. Error (%)
10	-711	-701	-10	1.4
11	-762	-775	13	-1.7
12	-814	-834	20	-2.5

2.2 Recursive multi-step forecasting model

A total of 12 subsidence measurements are taken once per month, corresponding to a one-year period. With this number of measurements, we divide the dataset into a training set consisting of the first 9 measurements, and the remaining three measurements are chosen as the test set. To train the model based on the training set, we use the six previous measurements as input and the subsequent measurements as output, as illustrated in Figure 2. This process is called recursive multi-step prediction. Specifically, the first six months are used as input and the seventh month as output. Then, the time series is shifted forward by one step with months two through seven used as input and the eighth month as output. Similarly, month three to month eight are used as input to predict the ninth month. Through this process, the back-propagation algorithm is applied based on the difference between predicted and measured values in months 7, 8, and 9 (see Figure 2). The parameters of the model after the training process are then used to forecast subsidence in months 10, 11, and 12. To do this, values from the fourth to the ninth months are used to predict the subsidence of the tenth month. Then, the predicted value in the tenth month is added to the time series to predict the eleventh month. Finally, a similar process is applied to predict the subsidence of the twelfth month.

2.3 Model Accuracy Evaluation

To evaluate the effectiveness of the surface subsidence prediction using the ANN model, two evaluation metrics are utilized in this study, including absolute (Abs.Err) and relative errors (Rel.Err):

$$Abs.Err_i = \eta_i - \hat{\eta}_i \tag{1}$$

$$Rel.Err_i = \frac{\eta_i - \hat{\eta}_i}{\eta_i} \times 100\%$$

$$r = \frac{\sum_{i=1}^{n}(\eta_i - \overline{\eta_i})\left(\eta_i^p - \overline{\eta_i^p}\right)}{\sqrt{\sum_{i=1}^{n}(\eta_i - \overline{\eta_i})^2 * \sum_{i=1}^{n}\left(\eta_i^p - \overline{\eta_i^p}\right)^2}} \tag{2}$$

(3)

where η_i and η^p are the measured and the predicted values at t_i; $\overline{\eta}$ and $\overline{\eta^p}$ are the corresponding medium values of measured and predicted values, respectively.

3. Results and Discussion

In this study, four Global Navigation Satellite System (GNSS) measurement points in the Mong Duong underground coal mine area were used to test the proposed model. These four points are named P1, P2, P3, and P4, located on the surface within the mining area. As mentioned earlier, each point is measured over 12 measurement cycles at two months apart. The first nine measurement cycles are selected as the training dataset to train the model, and the last three measurement cycles are used as the test dataset for subsidence prediction. The data processing and prediction modules are programmed in Python using the scikit-learn package (Pedregosa et al., 2011). Table 1 shows the subsidence measurements of the four points corresponding to the training dataset of the first nine cycles.

The surface subsidence values for the last three cycles are predicted based on the parameters found from the train-

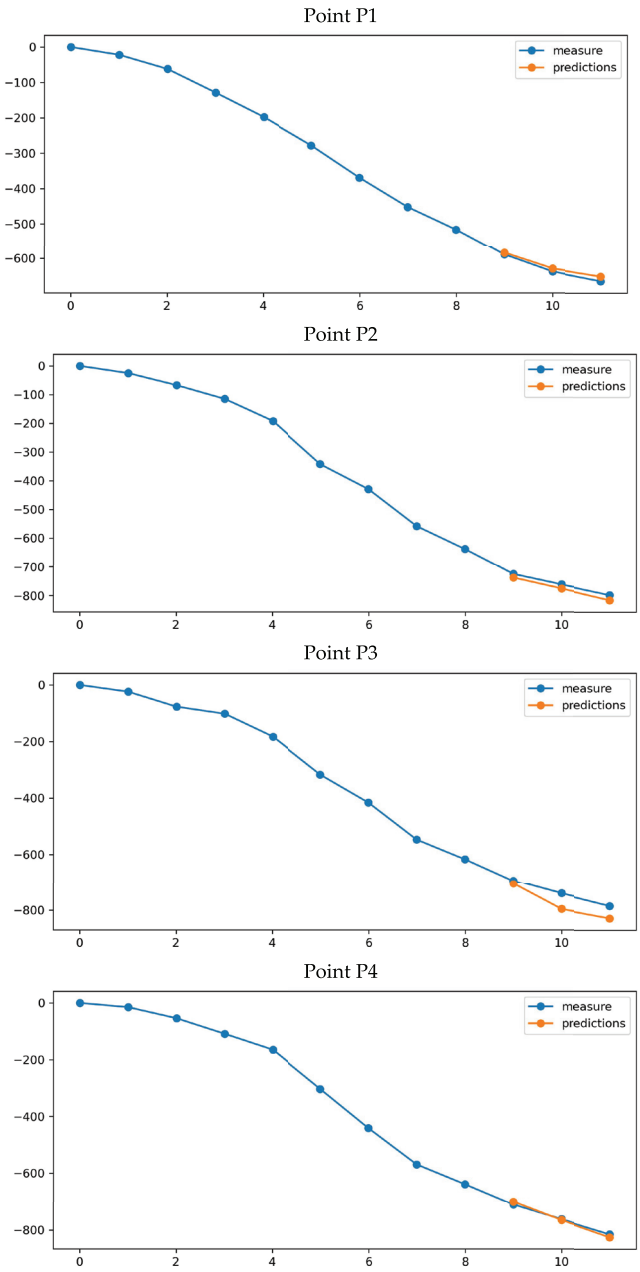

Fig. 3. Comparison between measured subsidence and predicted values
Rys. 3. Porównanie zmierzonego osiadania z wartościami przewidywanymi

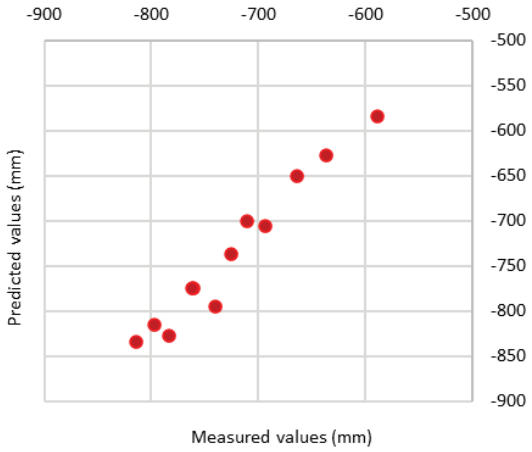

Fig. 4. Correlation between the measured and predicted values of 4 points
Rys. 4. Korelacja między zmierzonymi i przewidywanymi wartościami dla 4 punktów

ing dataset, with the results shown in Table 2 (Point P1), Table 3 (Point P2), Table 4 (Point P3), and Table 5 (Point P4). In these tables, the predicted values are compared with the measured values, from which absolute errors (Abs. errors) are calculated in millimeters 0(mm). Additionally, relative errors (Rel. errors) are computed by dividing the absolute errors by the measured subsidence values, calculated as a percentage (%). The results show a larger discrepancy between the forecasted time and the corresponding time of the last measured value in the training set leading to larger errors. The relative errors in the 10th month for the four experimental points are 0.9%, -1.7%, -1.7%, and 1.4%. These errors increase to 1.4%, -1.8%, -1.8%, and -1.7% in the 11th month, and 2.0%, -2.2%, -2.2%, and 2.5% in the 12th month. The absolute errors are found to be small, within the range of 20 mm. The correlation between the measured and predicted values of 4 points is high with r=0.980. This indicates that the ANN method used in this study can effectively forecast the time series of surface subsidence in mining areas. This is confirmed by the results displayed in Figure 3, where the measured and predicted subsidence values are very close. The correlation coefficients between predicted and measured values for 4 points are plotted in Fig. 4. With high values in the prediction results (r=0.980), it indicates that the predictive model is consistent with the measured data.

4. Conclusion

In this study, we utilized an ANN to forecast surface subsidence caused by underground coal mining at the Mong Duong coal mine, Vietnam. A recursive multi-step prediction process was designed and applied, where the first nine cycles were used as input to train the ANN model. Subsequently, the parameters of the model were used to predict subsidence for the last three cycles.

The parameters of the ANN model, including the number of hidden layers, hidden nodes, and iterations, were determined through the k-fold cross-validation method before being used to identify the model parameters with the training dataset and predict surface subsidence for the test dataset. The proposed ANN model with 'optimized' parameters found in this study has been demonstrated as an effective tool for predicting surface subsidence due to underground mining activities. The absolute errors were determined to be small, within the range of 20 mm. The absolute error depends on the time gap between the forecasted month and the month corresponding to the last measurement in the training dataset. The relative errors in the 10th month were 0.9%, -1.7%, -1.7%, and 1.4%. These errors increased to 1.4%, -1.8%, -1.8%, and -1.7% in the 11th month, and 2.0%, -2.2%, -2.2%, and 2.5% in the 12th month.

Acknowledgment

The authors would like to sincerely thank Hanoi University of Mining and Geology for providing financial support to conduct this study under the project T23-39.

Literatura – References

1. Amari, S. (1993). Backpropagation and stochastic gradient descent method. Neurocomputing, 5(4), 185-196. doi:10.1016/0925-2312(93)90006-O
2. Ambrožič, T., & Turk, G. (2003). Prediction of subsidence due to underground mining by artificial neural networks. Computers & Geosciences, 29(5), 627-637. doi:10.1016/S0098-3004(03)00044-X
3. Dorband, I. I., Jakob, M., & Steckel, J. C. (2020). Unraveling the political economy of coal: Insights from Vietnam. Energy Policy, 147, 111860. doi:10.1016/j.enpol.2020.111860
4. Fushiki, T. (2011). Estimation of prediction error by using K-fold cross-validation. Statistics and Computing, 21(2), 137-146. doi:10.1007/s11222-009-9153-8
5. Kim, K.-D., Lee, S., & Oh, H.-J. (2009). Prediction of ground subsidence in Samcheok City, Korea using artificial neural networks and GIS. Environmental Geology, 61-70.
6. Lee, S., Park, I., & Choi, J.-K. (2012). Spatial Prediction of Ground Subsidence Susceptibility Using an Artificial Neural Network. Environmental Management, 49, 347-358.
7. Long, N. Q., Bui, X.-N., Bui, L. K., Huynh, K. D. V., Van Le, C., Buczek, M., & Nguyen, T. P. (2017). A Computational Tool for Time-Series Prediction of Mining-Induced Subsidence Based on Time-Effect Function and Geodetic Monitoring Data. Paper presented at the International Conference on Geo-Spatial Technologies and Earth Resources.
8. Long, N. Q., My, V. C., & Luyen, B. K. Divergency verification of predicted values and monitored deformation indicators in specific condition of Thong Nhat underground coal mine (Vietnam). Geoinformatica Polonica, 2016(2016)), 15-22.
9. Long Quoc Nguyen, T. T. T. L., Trong Gia Nguyen, Dinh Trong Tran. (2023). Prediction of underground mining-induced subsidence: Artificial neural network based approach. Mining of Mineral Deposits, 17(4).

10. Ma, C., Li, H., & Zhang, P. (2017). Subsidence prediction method of solid backfilling mining with different filling ratios under thick unconsolidated layers. Arabian Journal of Geosciences, 10(23), 511. doi:10.1007/s12517-017-3303-7

11. Marschalko, M., Yilmaz, I., Křístková, V., Fuka, M., Kubečka, K., Bouchal, T., & Bednarik, M. (2012). Optimization of building site category determination in an undermined area prior to and after exhausting coal seams. International Journal of Rock Mechanics and Mining Sciences, 54, 9-18. doi:10.1016/j.ijrmms.2012.05.021

12. Mohsin, M., Zhu, Q., Naseem, S., Sarfraz, M., & Ivascu, L. (2021). Mining Industry Impact on Environmental Sustainability, Economic Growth, Social Interaction, and Public Health: An Application of Semi-Quantitative Mathematical Approach. Processes, 9(6), 972. doi:10.3390/pr9060972

13. Nguyen, B. N., Boruff, B., & Tonts, M. (2017). Mining, development and well-being in Vietnam: A comparative analysis. The extractive industries and society, 4(3), 564-575. doi:10.1016/j.exis.2017.05.009

14. Nguyen, B. N., Boruff, B., & Tonts, M. (2021). Looking through a crystal ball: Understanding the future of Vietnam's minerals and mining industry. The extractive industries and society, 8(3), 100907. doi:10.1016/j.exis.2021.100907

15. NGUYEN, H. V., LE, D. Q., NGUYEN, L. Q., & LIPECKI, T. (2023). Prediction of Road Subsidence Caused by Underground Mining Activities by Artificial Neural Networks. Inżynieria Mineralna, 52(2).

16. Nguyen, L. Q. (2016). Sectional diagram of dynamic subsidence trough at the Mong Duong coal mine: Evaluation and prediction. Journal of Mining and Earth Sciences Vol, 56, 58-66.

17. Nguyen, L. Q. (2020). A novel approach of determining the parameters of Asadi profiling function for predictiong ground subsidence due to inclied coal seam mining at Quang Ninh coal basin.

18. Nguyen, L. Q., Le, T.T.T., Nguyen, T.G., & Tran, D.T. . (2023). Prediction of underground mining-induced subsidence: Artificial neural network based approach. Mining of Mineral Deposits, 4(17), 45-52. doi: https://doi.org/10.33271/mining17.04.045

19. Nguyen, Q., Nguyen, Q., Tran, D., & Bui, X. Prediction of ground subsidence due to underground mining through time using multilayer feed-forward artificial neural networks and back-propagation algorithm–case study at Mong Duong underground coal mine (Vietnam). MINING SCIENCE ANDTECHNOLOGY (Russia), 241.

20. Nguyen, Q. N., Nguyen, V. H., Pham, T. P., & Chu, T. K. L. (2021). Current Status of Coal Mining and Some Highlights in the 2030 Development Plan of Coal Industry in Vietnam. Inżynieria Mineralna. doi:10.29227/IM-2021-02-34

21. Reddish, D. J., & Whittaker, B. N. (2012). Subsidence: occurrence, prediction and control. England: Elsevier.

22. Yang, W., & Xia, X. (2013). Prediction of mining subsidence under thin bedrocks and thick unconsolidated layers based on field measurement and artificial neural networks. Computers & Geosciences, 52, 199-203. doi:10.1016/j.cageo.2012.10.017

23. Zou, J., Han, Y., & So, S.-S. (2009). Overview of Artificial Neural Networks. In D. J. Livingstone (Ed.), Artificial Neural Networks: Methods and Applications (pp. 14-22). Totowa, NJ: Humana Press.

Prognozowanie osiadania powierzchni kopalni podziemnej przy użyciu rekurencyjnego modelu prognozowania wieloetapowego z wykorzystaniem sztucznej sieci neuronowej

Osuwanie się powierzchni z powodu działalności górniczej jest istotnym problemem w obszarach górniczych. Dlatego przewidywanie osiadania powierzchni jest niezbędnym zadaniem, aby zapewnić bezpieczeństwo i efektywność produkcji. W tym artykule zastosowano model sztucznej sieci neuronowej (ANN) do przewidywania osiadania powierzchni wynikającego z podziemnych operacji górniczych w kopalni Mong Dương. Proponowany w tym badaniu model ANN wykorzystuje rekurencyjny model prognozowania wieloetapowego, w którym przewidywana wartość z poprzedniego kroku jest dodawana do szeregu czasowego, aby prognozować następną wartość. Zbiór danych eksperymentalnych składa się z 12 cykli monitorowania w ciągu 24 miesięcy, z dwumiesięcznym odstępem, podzielonych na zestaw treningowy zawierający pierwsze 9 cykli pomiarowych i zestaw testowy zawierający ostatnie 3 cykle. Najpierw metoda walidacji krzyżowej K-fold jest stosowana do zestawu treningowego, aby określić najlepsze parametry dla modelu. Następnie te parametry są używane do przewidywania osiadania powierzchni dla wartości w zestawie testowym. Błąd prognozy zależy od przerwy czasowej między ostatnim cyklem pomiarowym a cyklem prognozowania. Błędy względne w dziesiątym cyklu dla czterech punktów wynoszą 0,9%, -1,7%, -1,7% i 1,4%. Te wartości błędów wzrastają do 1,4%, -1,8%, -1,8% i -1,7% w jedenastym cyklu i dalej do 2,0%, -2,2%, -2,2% i 2,5% w dwunastym cyklu. Błędy bezwzględne są określane jako małe, w zakresie 20 mm. Wyniki te pokazują, że proponowana metoda i model ANN są odpowiednie dla danych monitorowania szeregów czasowych w obszarach górniczych.

Słowa kluczowe: *osiadanie powierzchni, kopalnia podziemna, sztuczna sieć neuronowa, prognozowanie osiadania*